Minimizing Backgrounds for the SuperCDMS SNOLAB Dark-Matter Experiment

— by —

Michael A. Bowles

B.Sc. *Southern Polytechnic State University*, Marietta, GA, 2011
M.Sc. *Syracuse University*, Syracuse, NY, 2013

A dissertation submitted to the Graduate Division
in partial fulfillment of the requirements for the degree of

Doctor of Philosophy in Physics

South Dakota School of Mines and Technology
Rapid City, South Dakota

Date Defended: November 18, 2019

Abstract

Astronomical and cosmological observations indicate that large amounts of some slowly moving, unseen Dark Matter pervades the universe and outweighs normal matter by a factor of five. The Standard Model of Physics has no contender with the properties of this as-yet-undetected particle, so experimentalists build state-of-the-art radiation detectors to attempt to directly measure this Dark Matter. The Super Cryogenic Dark Matter Search (SuperCDMS) at SNOLAB is one such experiment, currently being constructed. This experiment uses ultra-cold, superconducting, high-purity silicon and germanium detectors to measure low-energy nuclear recoils from the elastic scattering of Dark Matter. I contributed to the calibration of the energy scale of low-energy nuclear recoils in CDMS II silicon detectors by computing an improved livetime correction for calibration data to verify the Monte Carlo rate normalization. Results indicate that the phonon collection efficiency of nuclear recoils relative to electron recoils is $95.2^{+0.9}_{-0.7}\%$, and the ionization collection efficiency of low-energy nuclear recoils in silicon is lower than Lindhard prediction, consistent with other recent measurements.

Backgrounds from the progeny decay of the abundant, naturally-occurring radioactive isotope radon-222 obstruct the sensitivity of essentially every dark-matter search. Radon concentrations in the SNOLAB cavern would contribute prohibitively large backgrounds if the volume surrounding the detectors were not purged with a low-flow low-radon gas. By measuring the radon diffusion and emanation, we identified acceptable gasket materials for sealing this radon purge, ensuring that the radon-induced backgrounds will be significantly lower than the other experimental backgrounds. A radon emanation system with a gas handling system and low-background radon detector was commissioned and used to measure the radon emanation of the proposed gaskets. A low-cost apparatus was constructed to measure the radon diffusion of gaskets with a commercial radon detector.

The sensitivity of future generations of dark-matter detectors are expected to be dominated by long-lived low-energy beta- and alpha-emitting radon daughters such as ^{210}Pb on detector surfaces. I describe simulations indicating the detector could also be used to reduce background from material impurities plaguing rare-event searches, the commissioning of a prototype demonstration detector, and a gas handling system necessary to operate the detector. I demonstrated that the gas handling system reduces the otherwise dominant backgrounds by a factor of 62. This detector will therefore be able to detect ^{32}Si and ^{210}Pb 100 times better than currently available screeners.

Acknowledgements

I'd like to thank my advisor, Richard Schnee, for his patience, for letting me learn at my own pace, and especially for providing the financial support to allow me to avoid significant amounts of teaching, to travel to collaboration meetings, conferences, and summer school in Canada! Thanks to Richard, Prisca Cushman, and Juergen Reichenbacher for writing letters of recommendation as I applied to jobs, and thanks to my very patient graduate committee members: Juergen, Frank Strieder, Luke Corwin, and Pat Fleming. Because of your helpful support, I have been more successful than I hoped. Thanks to every encouraging person, too many to name, who took time to thoughtfully discuss physics, constructively criticize my work, and educate me. I would like to especially thank those who helped me get the Nuclear-Recoil Scale paper out: Ray Bunker, Scott Fallows, Dave Moore, Prisca Cushman, Sunil Golwala, Rob Calkins, Alan Robinson, Eric Miller, Paul Brink, Dan Bauer, and the entire SuperCDMS collaboration.

Thanks to everybody–especially Ray, Eric, and Richard–in our group for help with programming, lab work, and the toughest challenge of all: life! I would like to thank my friends for listening to my oft-repeated jokes and unfinished thoughts, and for sharing the joy of laughter and music with me. Finally, I cannot thank my incredible mother and father enough. You taught me about life and the value of grit, you let me play loud and be myself. I dedicate this work to you.

Table of Contents

List of Tables

List of Figures

Chapter 1
Dark Matter

In 1933, F. Zwicky measured the Doppler velocity dispersion of galaxies in the Coma Cluster [3]. He applied the virial theorem to the velocity of orbiting objects to obtain the mass and associated gravitational binding force of the system. Zwicky also measured the light output of the galaxies to estimate the mass of the galaxies and found that the mass from visible matter was not enough to hold the fast-moving galaxies together. He determined that the Coma Cluster contained a large amount of unseen mass he called "dark matter." Prevailing astronomical and cosmological evidence indicates the existence of some as-yet-undetected form of non-luminous matter appearing at galactic and cosmological scales. Many models exists attempting to explain these, and other, observations. A mainstream hypothesis is that this Dark Matter (DM) is composed of one or more elementary particles produced in the early universe [1, 4--8].

The Λ Cold Dark Matter (ΛCDM) model of the universe is a parameterization of the so-called 'Standard Big Bang model of Cosmology' described by 6 parameters [9]. The model attempts to account for features of the observable universe such as the accelerating expansion of the universe (discovered only 20 years ago in 1998), the isotropy (sameness in all directions) and homogeneity (sameness at all locations) of the universe which together are often called the *cosmological principle*. The model also predicts the large-scale structure of the distribution of galaxies at the farthest distances measurable, the abundance of light elements (hydrogen, deuterium, helium, and lithium), and the angular structure of the cosmic microwave background (CMB), the glow left over from the decoupling of photons from matter in the early universe [9, 10]. Finally, gravity, as described by Einstein's general theory of relativity, is assumed to be the main fundamental force relevant to cosmological evolution after the very earliest moments in the universe. This is sensible because the strong and weak forces have very limited range on the order of the size of elementary particles. The electromagnetic force governs intermolecular and chemical interactions and is thus not expected to dominate cosmological evolution.

The cosmological principle implies that the time-dependent expansion of the universe is the same everywhere (*i.e.* homogeneous) and can be quantified by a (unitless) scale factor $a(t)$ which

depends on the distance r between arbitrary fixed points in the universe. The time-dependent scale factor

$$a(t) \equiv \frac{r(t)}{r_0}, \tag{1.0.1}$$

where $r(t)$ is the time-dependent distance between two points (*e.g.* galaxies), the subscript 0 refers to the present, and r_0 is the current distance between the same points. The scale factor is defined such that the present-day scale $a_0 \equiv 1$. This assumption immediately gives rise to Hubble's law since the relative velocity of two objects at any given time

$$v(t) = \frac{\mathrm{d}r}{\mathrm{d}t} = \frac{\mathrm{d}}{\mathrm{d}t}\Big(r_0 a(t)\Big) = r_0 \frac{\mathrm{d}a}{\mathrm{d}t} = \left(\frac{r(t)}{a(t)}\right)\frac{\mathrm{d}a}{\mathrm{d}t}, \tag{1.0.2}$$

will be proportional to their separation

$$v(t) = \mathcal{H}_0 r(t), \tag{1.0.3}$$

where the current value of the Hubble constant $\mathcal{H}_0 \equiv {}^{\mathrm{d}a}/_{\mathrm{d}t} \cdot a^{-1}$[11].

It has been shown that the most general metric describing the four-dimensional manifold of spacetime is given by the Robertson-Walker metric

$$\mathrm{d}s^2 = c^2\,\mathrm{d}t^2 - a(t)^2\left(\frac{\mathrm{d}r^2}{1-kr^2} + r^2\left(\sin^2\theta\,\mathrm{d}\phi^2 + \mathrm{d}\theta^2\right)\right), \tag{1.0.4}$$

where the curvature k is dictated by the geometry of the universe: an open universe has $k = -1$, a flat (closed) universe has $k = 0$ ($k = 1$) [12]. This metric (Eqn. 1.0.4), along with Einstein's field equations, describes the relationship between the matter and the curvature of the universe. To paraphrase John Wheeler: spacetime bends under the influence of matter, which moves under the influence of spacetime. The expansion and evolution of the universe depends primarily on the density of the dominant energy content: radiation, matter, and more recently the dark energy. For an in-depth discussion of the geometry of spacetime see *e.g.* [9, 12] and the references therein.

The Big Bang model of cosmology accounts for the expansion of space which is implied by measurements of the redshift of galaxies, appearing from spectral absorption and emission lines, as well as the apparent time dilation of supernova luminosity light decay [13]. This redshift is an expected result of the Doppler effect in the electromagnetic radiation traveling across vast distances of the ever-expanding universe. This expansion is characterized by a negative pressure of the cosmological constant Λ fighting the gravitational pull between very distant galaxies and galactic clusters. Although there is an incredible discrepancy between the expected vacuum energy density of empty space and the calculated value of Λ as discussed in [14] and references therein, the cosmological constant may be associated with vacuum energy causing weakly-bound galactic clusters, and the universe at large, to expand from one another.

Current models of the universe include another dark component: a gravitationally interacting

particle that does not interact electromagnetically. Dark matter is a hypothetical particle which is hypothesized to account for the gravitational pull observed at galactic scales and up to the largest cosmological scales. The cosmological model postulates that dark matter is 'cold' (*i.e.* slow-moving compared to light, $v \ll c$). Astronomical measurements indicate that dark matter must non-baryonic, because it appears to be collision-less, dissipation-less, and therefore unable to cool by radiating light unlike nuclei. Ordinary matter comprised of atoms and chemical elements makes up only a small portion of the mass-energy density in the universe; the vast majority of matter is invisible.

In this chapter, I describe the evidence and methods used to attempt to detect particle dark matter (**Section 1.1**). I discuss facets of direct-detection experiments and some general properties of dark matter, and the factors that determine an experiment's sensitivity to dark matter (**Section 1.2**). I describe major experimental backgrounds (**Section 1.3**), and focus on dangerous sources of backgrounds (**Section 1.3.1** , **Section 1.3.2**) relevant to the direct-detection experiment SuperCDMS at SNOLAB (**Section 1.4**). Dealing with these dangerous backgrounds is a large focus of this thesis.

1.1 Indirect Evidence For Dark Matter

The evidence for ubiquitous dark matter is abundant, though entirely from astronomical and cosmological measurements. Here, I describe indirect evidence pointing to the existence of dark matter, presumably primordial in nature, existing since the early universe. Galaxy clusters provide strong evidence for the existence of dark matter since their masses can be estimated independently in three ways. The mass can be obtained by comparing the orbital velocity of stars and gas clouds within galaxies to the Keplerian expectation [15], by measuring the energy spectra from X-rays emitted from hot gas in clusters and balancing the gravity and pressure, and finally by measuring the gravitational lensing using static quantities without using dynamical quantities such as velocity [16]. Gravitational lensing, *i.e.* the path-bending of light by large masses, is a natural outcome of general relativity. Light from distant sources, such as galaxies and galaxy clusters, may be redirected by large masses that warp spacetime between an observer and a light source. Calculated values of mass using gravitational lensing may exceed the mass of a galaxy derived from luminosity by a factor of 5 [17].

More evidence for dark matter comes from radiation produced in the early universe. The cosmic microwave background (CMB) is a remnant of the early universe from when the expansion-driven cooling reduced the temperature significantly enough to decouple radiation and matter and allow neutral atoms to form. The CMB is very nearly a perfect blackbody spectrum; the residuals in the temperature anisotropies, about the mean, are $\mathcal{O}$(10's ppm). The angular power spectrum derived from these anisotropies gives rise to peaks and troughs at given angular scales which depend on the matter-energy content of the universe. These peaks are well-predicted by the parameters of the Cosmological model, so high-precision measurements of temperature anisotropies constrain

the components of the model; the power spectrum of the CMB provides exceptionally strong evidence for the existence of particle dark matter that significantly outweighs normal matter in the universe [17, 18].

Historically, evidence for dark matter has come from comparing the motion of visible objects to the predictions of orbital mechanics. Newton's and Kepler's laws of motion, excellently predicts the orbital speed of objects *e.g.* planets in our solar system circling the Sun, as a function of their orbital distance. In this model, orbiting masses moving at speed $v(r)$ accelerating solely due to gravitational forces arising from a total enclosed mass $M_{\rm enc}(r)$ inside the object's orbit at radius r will obey

$$\frac{v^2(r)}{r} = G\frac{M_{\rm enc}(r)}{r^2}. \tag{1.1.1}$$

For a given mass, the speed of an object

$$v(r) = \sqrt{\frac{G\,M_{\rm enc}(r)}{r}} \tag{1.1.2}$$

decreases with the square root of the orbital radius, moving more slowly at larger radii. So measuring the orbital velocities of multiple massive bodies indirectly indicates the enclosed mass profile. The left panel of **Fig. 1.1** shows the orbital speed v of planets in our solar system as a function of their average distance r from NASA data [19]; the Keplerian expectation of speed (Eqn. 1.1.2) from the sun $M_{\rm enc} = 1.989 \times 10^{30}\,$kg shown (dashed) matches the planetary speeds well.

In the right panel of **Fig. 1.1**, galactic rotation curve data (shown dots) from the spiral galaxy NGC 6503 is shown as a function of distance$r$ from the galactic center. The velocity of the matter is much larger than the Keplerian expectation of speed from the mass-derived-from-light [20, 22]. By observing, in the figure, a constant rotation velocity, from an inner radius $r_{\rm i} \approx 4\,$kpc all the way out to the galaxy's edge at $r_{\rm e} \approx 22\,$kpc where the rotational speed of the visible matter

$$v(r_{\rm i} \le r \le r_{\rm e}) = \text{const.} \tag{1.1.3}$$

is independent of radial distance to the galactic center. We infer, from Eqn 1.1.2, that the total enclosed matter content (dark and visible), increases

$$M_{\rm enc}(r_{\rm i} \le r \le r_{\rm e}) \propto r \tag{1.1.4}$$

proportional to the radius, unlike the sum of the disk and gaseous components of NGC 6503. The non-luminous dark matter is assumed to be distributed in a spherically symmetric halo around the 'host' galaxy. The discrepancy between mass-derived-from-gravity and mass-derived-from-light appears in many large systems including individual galaxies, galaxy clusters, even clusters of galaxy clusters, strongly implying that baryonic (visible) matter is separate from the dark (invisible) matter that holds galaxies together. Without a generally large amount of unseen matter spread throughout a galaxy, hydrogen gas at the outer edges of galaxies travel faster than the galactic escape speed

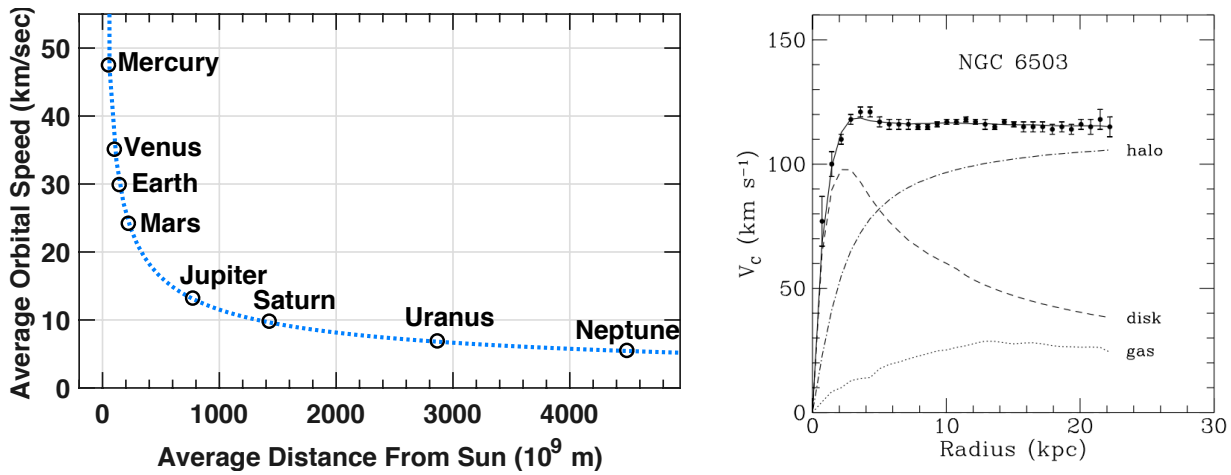

Figure 1.1: Comparison of orbital speeds as a function of distance from the center of bodies in our solar system (left), and the galaxy NGC 6503 (right). **Left:** Average orbital speed v of planets in our solar system versus average distance r from the Sun (○) using data from NASA [19]. The Keplerian expectation $v \propto 1/\sqrt{r}$ (dashed) of planetary orbital speeds using Eq. 1.1.2 assuming the mass of the sun $M_{\text{enc}} = 1.989 \times 10^{30}$ kg, and the gravitational constant $G = 6.674 \times 10^{-11}\,\text{m}^3\,\text{kg}^{-1}\,\text{s}^{-2}$. The Keplerian expectation is essentially perfect for orbiting bodies on stellar distance scales, which implies the matter density at the level of the solar system is dominated by baryonic matter *i.e.* the Sun. **Right:** Rotation curve of the spiral galaxy NGC 6503 (dot) from radio observations of hydrogen gas in the disk from [20]. The expectation from the visible disk material (dashed) and the hydrogen gas (dotted) is not enough to account for the speeds. A dark matter halo (dot dash) encompassing the visible matter (disk and gas) is hypothesized to keep the speed of the gas clouds constant out to the visible galactic edge. Figure from [21].

predicted by Newton's laws using the mass-derived-from light; this material should not be bound to the parent galaxy.

Not all galaxies bear this discrepancy between the observed and expected speed of the visible matter. Recently, evidence of a class of ultra-diffuse, low-mass galaxies, with no appreciable dark matter has been observed [23, 24]. The velocity of the stars in these galaxies appear to be consistent with the Keplerian expectation assuming the enclosed mass is given only by the luminous component. The implications of the evidence are two-fold: since the stars are baryonic, it is inferred that dark matter is apparently not always coupled with normal matter on galactic scales. Also, since gravity appears to be Newtonian at these large scales, modifications of gravity either produce no appreciable changes in the velocity predictions or lead to subtle or outright disagreements with the data. In any event, toppling Einstein's theory of gravity is an undertaking that would require extraordinary evidence since many precision measurements agree with the predictions of this theory: the perihelion advance of Mercury, gravitational red-shift, and also from the gravitational deflection of light-rays by *e.g.* the Sun [25].

More evidence for dark matter comes from Einstein's General Theory of Relativity. Light rays coming from a distant source are predicted to be deflected along the line of sight by intermediate massive objects, *e.g.* a galaxy or a cluster of galaxies. A large concentration of mass may act as a gravitational lens aiming distant light sources at earth along multiple paths. The bending of light is a function of the distance (impact parameter) of the light ray to the intermediate massive object

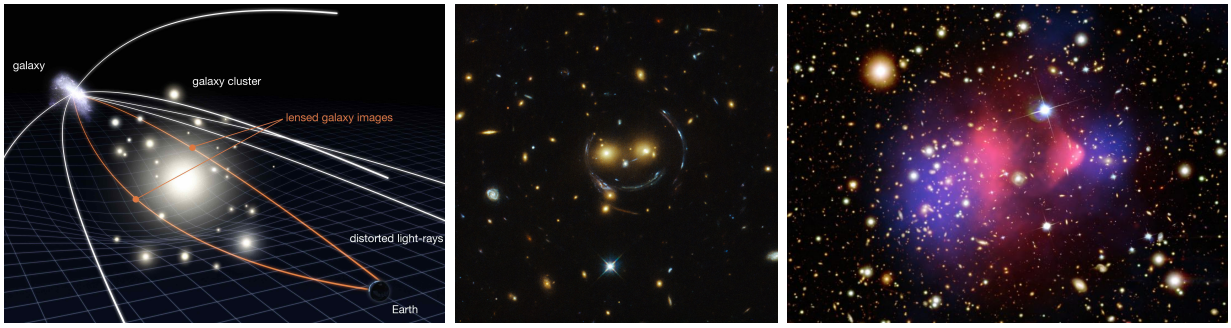

Figure 1.2: Left: Diagram of the gravitational lensing of light by massive, intermediate objects between the background and earth. The mass of intermediate objects may be inferred using the deformed light of the far away light sources. Image adapted from [26]. **Middle:** A famous image of galaxy cluster (SDSS J1038+4849) and gravitational lensing forming an "Einstein ring" that is said to resemble the Cheshire Cat from Alice in Wonderland. This object was observed by Hubble's Wide Field and Planetary Camera 2 (WFPC2) and Wide Field Camera 3 (WFC3) which surveyed strong lensing sources [27]. **Right:** The Bullet Cluster HST observed in Aug. 2004 [16, 29] overlaid with the computed mass distribution from weak gravitational lensing (shown in blue) and X-ray emission from hot gases (shown in pink) from a smaller mass (right) passing through a larger mass (left). The patches of visible, gaseous matter and the invisible mass inferred from lensing appear to have passed through one another, and the normal matter has slowed and deformed into a shockwave from the friction, while the dark matter has passed through apparently without colliding significantly (even with itself).

and the enclosed mass of the object. In the left panel of **Fig. 1.2**, from [26], a few example light rays coming from a distant galaxy are deflected by a large intermediate mass between the source and the earth (orange). Strong lensing occurs when light undergoes significant distortion around an intermediate lens and appears at multiple locations in the sky, whereas weakly lensed light sources do not share this property. In the case of strong gravitational lensing, extra images of *e.g.* a far away galaxy are sometimes stretched in such a way so as to wrap around the intermediate matter forming an "Einstein ring." A strongly lensed galaxy cluster (SDSS J1038+4849) [27] is shown in the middle panel of **Fig. 1.2**. Weak gravitational lensing, also predicted by Einstein's General Theory of Relativity, is not so obvious and may be inferred only by observing small distortions in multiple light sources. By measuring light from many sources with an assumed property, such as circularity, it is possible to use the small, correlated distortions of all the objects in the field of view to deduce the mass of the intermediate lens between the observer and the distant objects. This technique can be used to map unseen matter between distant galaxies and the Earth, see *e.g.* [28] and the references therein.

The right panel of **Fig. 1.2** shows the remnants of a famous galactic cluster collision called the Bullet Cluster, named for the shape of the gas clouds which show a shock wave. The location of gas clouds (shown pink) comes from X-Ray emission measurements, and the location of the inferred dark matter (blue) was calculated by the gravitational lensing deformation of the galaxies seen behind the color patches [16, 29]. The shape of the colorful blobs is a result of the gas clouds passing through one another, deforming the (presumably) initially spheroidal masses, and slowing them significantly during the interaction. The picture shows two types of matter: one visible, gaseous with predictable slowing and shock-wave deformation due to the friction during the collision, and

two collision-less, invisible, undisturbed spherical masses, which have become increasingly separated from one another and the gas clouds. Gravitational lensing calculations imply the total mass of the cluster is much more than that of the luminous, baryonic matter. The gas clouds themselves do not coincide with the (dark) mass that's doing the lensing. This implies that the dark and visible matter are entirely separable components of the massive landscape. Moreover, in a survey of 72 cluster collisions, the computed gravitational centers are well separated from the baryonic, X-ray emitting component [30].

Gravitational forces between galaxies and galaxy clusters provide evidence that baryonic and dark matter may be decoupled; however, the most exceptional evidence for the concordance model of cosmology, and the existence of cold dark matter, comes from measurements (by COBE: the COsmic Background Explorer, WMAP: the Wilkinson Microwave Anisotropy Probe, and Planck) of the Cosmic Microwave Background (CMB) temperature anisotropy [17, 18, 31]. The CMB is microwave radiation from the early universe observed to be essentially uniform in all directions, which was accidentally discovered by astronomers A. A. Penzias and R. W. Wilson in 1964 [32]. The angular variations of the thermal spectrum from the baryon-photon plasma in the early universe carries information about primordial perturbations, and helps to constrain the cosmological parameters describing the contents and age of the universe, and the time of radiation-matter decoupling when the universe became transparent to the CMB. The temperature patterns observed in the CMB were set up by the competition between the inward force of gravity, from both baryonic and dark matter, and an outward photon pressure causing radiation and matter to oscillate in and out of dense regions. Since dark matter is unable to be heated or cool by losing photons it is dissipation-less and is unaffected by the photon pressure. The existence of cold dark matter in the early universe is expected to leave a huge imprint on the CMB since small perturbations in the density of dark matter dominated the gravitational wells which amplify over time, leading normal matter to clump in these overdense regions [9, 33, 34].

According to the ΛCDM model, the early universe was very hot and dense, expanding significantly. The expansion of space stretches the wavelengths of all free-streaming photons like a Universal doppler-effect. This process, called cosmological redshift, reduces the photon frequency ν, lowering their energy $E_\gamma = h\nu$. Up until 380,000 yrs after the big bang, the ambient temperature of the universe was too great for nuclei to form since any nucleus would immediately be photo-disintegrated by photons, and normal matter consisted only of ions with a low number of nucleons, such as doubly ionized helium, and electrons. Photons were frantically scattering off the free electrons and normal matter and radiation were in a state of baryon-photon plasma. At this time, photons were diffusing through the sea of electrons unable to free stream significant distances and the universe was opaque to the CMB [9, 33, 34].

After the expansion-induced cooling of the universe dropped the ambient temperature below

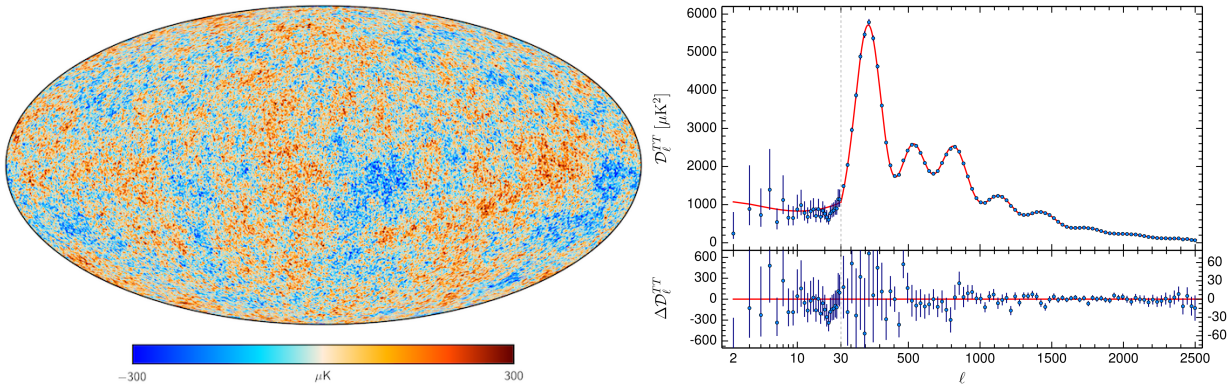

Figure 1.3: Left: Temperature anisotropies across the sky measured by the Planck collaboration where the color scale corresponds to temperature variations $\delta T \in (-300, 300)\,\mu\text{K}$ about the mean temperature $T = 2.725\,\text{K}$. The small hot and cold patches at a given angular separation (ℓ) depend on the curvature of the universe and the density of radiation, and normal and dark matter in the early universe. **Right:** Angular power spectrum (blue dots with 68% C.L. uncertainties) of the cosmic microwave background (CMB) radiation as a function of angular scale ℓ with the best-fit ΛCDM parameter model (red line). The theory corresponds to a spatially flat universe, with $\sim 70\%$ of the energy density in dark energy, 25% of the density in dark matter, and only 5% of the energy from normal matter. The bottom panel shows the residuals of the data and the ΛCDM model fit. Note that for $\ell > 30$ the x-scale is linear and the y-scale of the residuals is a factor of ten smaller, indicated by the right hand y-limits. The prediction agrees very well with the data. Figures from [17].

3,000 K, the average thermal energy of the universe

$$E_{\text{amb}} = k_B\, T = 8.6 \times 10^{-5}\,\text{eV/K} \times 3,000\,\text{K} = 0.25\,\text{eV} \tag{1.1.5}$$

dropped well below the ionization energy of helium $E_{\text{He}} = 26\,\text{eV}$ and hydrogen $E_{\text{H}} = 13.6\,\text{eV}$, so that electrons were, for the first time, captured by protons and helium forming neutral atoms in an event called recombination. As a result, photons in the universe were restricted to interact with electrons at the characteristic energies of the newly formed atoms. At this time, radiation and matter effectively decoupled as photons *everywhere* were scattering off a final electron and the universe then became transparent to the cosmic microwave background radiation. This boundary between the opaque and transparent universe is the surface of last scattering. Photons would now free-stream across the universe, awaiting detection by astronomers and cosmologists. At the time of last scattering, the plasma emitted a thermal distribution of photons, and is observed to be essentially a perfect blackbody spectrum.

Temperature anisotropies in the CMB (shown in left panel of **Fig. 1.3**) are used to put constraints on the energy content of the universe. It's generally possible to predict the patterns in CMB with (and without) dark matter by the strength of peaks in the angular power spectrum of the CMB (shown right panel of **Fig. 1.3**). This angular power spectrum (blue dots) indicates the strength of correlated temperature anisotropies at different angular scales. The amplitude peaks in the CMB in the figure are predicted by the ΛCDM model (shown as a red line). The curvature of the universe, and the density of dark energy, dark matter, baryonic matter, and radiation all significantly impact the amplitude of each peak and their ratios.

These measurements indicate that the universe is mostly ($> 95\%$) dark. At present, the dark sector has a large repulsive component referred to as dark energy, where most of the energy density in the universe is stored. The ΛCDM model parameters measured by the Planck experiment (using CMB data alone) indicate that the dark energy density $\Omega_\Lambda = 0.692 \pm 0.012$ of the total mass-energy density [17]. In the early universe, space was denser so this component was much smaller. There exists evidence for another dark component which interacts gravitationally, which is simply called dark matter (DM). Results from WMAP and Planck are consistent with a spatially flat ($k = 0$) universe that is $t_{\rm univ} = (13.799 \pm 0.038) \times 10^9$ years old [17, 18], with an overall matter density that contributes $(31.5 \pm 1.3)\%$ to the total, with roughly ∼85% of this contained in the cold dark matter. These findings indicate that only 5% of the matter-energy density comes from ordinary matter (*i.e.* protons and neutrons) and dark matter contributes ∼25% of the density, outweighing regular matter by a factor of 5.

After the 13.8 billion year expansion of the universe, the thermal black body spectrum of the CMB has been cosmologically redshifted down by three orders of magnitude to $T_{\rm CMB} = (2.72548 \pm 0.00057)\,{\rm K}$ [35--37]. The cosmic radiation appears to be isotropic to a few parts in 10^5 and very far objects are observed to be isotropic within a few percent. The further away from Earth a telescope measures, the universe appears increasingly homogeneous and less galactic structure is seen, implying that structures observed in the universe today have evolved over time. This high degree of isotropy earlier in the universe is strong evidence for both large-scale isotropy and homogeneity of the observable universe, validating the assumption that the universe is well-modeled by the cosmological principle. The Lambda-CDM model also provides a reasonable account of the light element (*e.g.* hydrogen, deuterium, helium, and lithium) abundance [1, 38]. Since numerous data are so well predicted by this theory that crucially depends on dark matter, scientists conclude that this particle dark matter *may* be detectable.

So what is the dark matter? Theoretical candidates for dark matter are numerous. A few candidates include axions and **A**xion-**L**ike **P**articles (ALPs) [39, 40], **MA**ssively **C**ompact **H**alo **O**bjects (MACHOs) [41] which might consist of brown dwarf stars, large planets, or black holes; primordial black holes [42], gravitinos [43], sterile neutrinos [44], and **W**eakly **I**nteracting **M**assive **P**articles (WIMPs) [6, 45]. For experimentalists, WIMPs are a theoretically-motivated candidate for the particle dark matter that may be detected locally. WIMPs are generally expected to be produced in the early universe. Observations indicate that dark matter does not interact electromagnetically; it therefore is assumed to be electrically neutral. Dark matter has not been produced abundantly by pp collisions at the LHC and apparently bears no strong force interaction and has no color charge. Since all the evidence for particle dark matter relies on its gravitational interaction with visible matter at many distance scales so dark matter is inferred to be massive. Some models assume that these particles will not self-interact significantly and, in this case, the expansion of the universe would reduce the density of these dark particles beyond the point of significant self-annihilation. Unable to pair annihilate, the particles would "freeze out" leaving a relic abundance of

WIMPs [6, 46]. It's usually assumed that a vanishingly small amount of cold dark matter was created after its freeze out in the early universe, so the WIMPs must be long-lived on a cosmological time scale (*e.g.* many billions of years). We expect this relic abundance to be predicted by the ΛCDM model. In order to get the correct relic abundance of dark matter today from thermal production in the early universe, a self-annihilation cross section near the weak force for WIMP masses in the GeV–TeV range is required, see *e.g.* Refs. [8, 33, 47--49] for further discussion. According to the standard model of physics, the only other possible interaction Dark Matter may participate in is the weak nuclear interaction. The term WIMP describes a generic class of particles that are stable, probably heavy, and interact either via the weak force or, more interestingly, through some new force(s) with an interaction cross-section with normal matter that is upper bound by the weak scale. Ultimately, though the effects of dark matter are readily observable, the nature of dark matter is not well-understood. In fact, the dark matter we may eventually detect could exist among an entire dark sector of particles such as dark photons [50], or even be mediated by an undiscovered fundamental force. So we build high-sensitivity experiments to try to directly detect or infer the existence with standard model byproducts of such an elusive particle.

Three complementary methods, shown as arrows in **Fig. 1.4**, are employed by the scientific community to directly measure or indirectly infer the existence of particle dark matter. Dark matter (χ) clumped in astrophysical objects may *self-annihilate* (downwards blue arrow) creating secondary, standard model particles that could indicate the presence of particle dark matter in an indirect experiment. Distinct gamma-ray signatures or neutrinos with very large energies may provide compelling evidence for particle dark matter and so terrestrial experiments like IceCube measure remnants of high-energy neutrinos passing through the Earth [51]. Satellite experiments like PAMELA measure cosmic rays like antiprotons, positrons, and light isotopes and nuclei which may indicate dark matter annihilation in astrophysical sources [52]. However, indirect signals from astrophysical measurements can be ambiguous, potentially explained by phenomena other than self-annihilation of particle dark matter, ultimately limited by our astrophysical ignorance [46].

Dark matter (χ) may also be produced (upwards red arrow) and indirectly detected by *collider experiments* with high-energy standard model particles (SM) and identifying missing transverse momentum from the decay products at the interaction vertex [53]. The goal for *direct-detection* (left black arrow) dark matter experiments is to identify a small energy deposition to a nucleus of the detector's target material (*e.g.* solid-state Ge, Si, NaI, or $CaWO_4$ or liquid Ar or Xe) from a WIMP in our solar neighborhood.

1.2 Direct Dark-Matter Detection

Dark Matter (DM) is a challenging puzzle for the fields of Astrophysics, Cosmology, as well as Nuclear and Particle physics. A simplistic, but reasonable model for DM scattering in normal matter assumes interactions occur only with the nucleus of an atom, because dark matter has

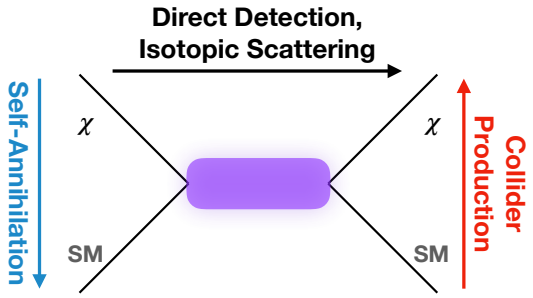

Figure 1.4: Feynman diagram indicating three possible quantum mechanical interactions between Dark Matter (χ) and Standard Model (SM) particles. The arrows indicate the direction of time for each method. Indirect Detection experiments aim to measure standard model particle remnants from Dark Matter *self-annihilating* perhaps at the center of our galaxy or other astrophysical sources. *Direct-detection* experiments use a target material attempting to measure the elastic WIMP-nucleon scattering in a terrestrial target. *Collider experiments* may produce dark matter particles (and other known particles, not pictured) from high-energy SM particles alone; by identifying significant missing transverse momentum, the LHC may find evidence for particle dark matter and discover some production channels from SM particles.

not been found to interact electromagnetically, and therefore won't interact significantly with electrons. The expected recoil energy spectrum for WIMPs is dependent upon the detector, the nature of the nucleon-WIMP interaction *e.g.* spin-dependence, and astrophysical quantities like the dark matter density and velocity distribution in the local stellar neighborhood. Here, I provide a very brief discussion of the factors that determine the sensitivity direct-detection dark matter experiments have to detecting WIMPs. Let's first consider kinematic restrictions on the recoil energies produced by a WIMP in a direct detection experiment. A requirement of the ΛCDM model is that a significant fraction of the dark matter χ needs to be slow-moving (cold) so galaxy formation can occur. With $v_\chi \approx 10^{-3}c$ and since the speed of Earth including its rotation with respect to the Galaxy is also very small $v_{\rm Earth} \lesssim 250\,{\rm km/s}$, the relative speed Δv_χ is still small [54--56]. For an elastic two-body collision, the nuclear recoil energy $E_{\rm R}$ imparted to an atomic nucleus of mass $m_{\rm N}$ by a WIMP of mass m_χ is given by

$$E_{\rm R} = \frac{\mu^2 \Delta v_\chi^2}{m_{\rm N}} \cdot (1 - \cos\theta) \tag{1.2.1}$$

where θ is the center-of-mass scattering angle separating the incoming and outgoing particle momenta, and the reduced mass μ of the DM-nucleus system

$$\mu = \frac{m_\chi m_{\rm N}}{m_\chi + m_{\rm N}}. \tag{1.2.2}$$

There are essentially three cases for a scattering interaction of this nature: the dark matter and target nucleus have roughly equal masses, or either particle outweighs the other considerably. Let's take the best case scenario of a head on collision ($\theta_{\rm CM} = \pi$), so that if the nucleus and DM are of equal mass $m_\chi \approx m_{\rm N}$ (the luckiest case), the reduced mass $\mu = \frac{m_\chi}{2}$ and the recoil energy

$$E_{\rm R} = \frac{m_{\rm N} v_\chi^2}{2}, \tag{1.2.3}$$

because the WIMP transfers all its momentum to the nucleus. If the WIMP greatly outweighs the nucleus, then the reduced mass $\mu = \frac{m_{\rm N}}{1+m_{\rm N}/m_\chi} \approx m_{\rm N}$ and the recoil energy

$$E_{\rm R} = \frac{2 \cdot m_{\rm N}^2 \Delta v_\chi^2}{m_{\rm N}} = 2 \cdot m_{\rm N} \Delta v_\chi^2 \tag{1.2.4}$$

is proportional to the atomic mass, so that targets with a large nucleon number are generally more sensitive–though this is complicated by nuclear physics [56--58]. For a very light WIMP, the reduced mass $\mu \approx m_\chi$ and the recoil energy

$$E_{\rm R} = \frac{2 \cdot m_\chi^2 \Delta v_\chi^2}{m_{\rm N}} \tag{1.2.5}$$

is suppressed by the atomic mass, so light targets (*e.g.* He, Si, F) will bear a larger sensitivity to light WIMPs, whereas high-mass targets (*e.g.* I, Xe) act more like a wall, to which a WIMP can deposit very little energy. Heavy WIMPs produce a target-dependent spectrum essentially independent of their mass. When the (WIMP and target-nucleon) masses are imbalanced, the reduced mass arising from the collision mechanics leaves a lower recoil energy proportional to the smaller of the two masses.

Consideration also needs to be given to the nuclear spin of the target material. For direct detection, there exists a material-dependent complementarity for detectors with different nuclear spins. These couplings are born from the spin dependence, or lack thereof, of the quantum mechanical coupling of dark matter (χ) to standard model (SM) particles. The spin dependence of WIMP-nucleon scattering interactions is treated at length in many Refs. *e.g.* [59] and a generalized effective field theory incorporating the velocity- and spin-dependence in the context of direct detection experiments is described in Refs. [60--64]. For the simplest, spin-independent (*e.g.* scalar) coupling at zero momentum transfer *i.e.* ignoring the nuclear form factor, a coherent interaction with the entire nucleus whose cross-section scales with the square of the target's atomic mass A^2 heavier elements such as iodine ($A_{\rm I} = n + p = 74 + 53 = 128$) or xenon ($A_{\rm Xe} = n + p = 54 + 77 = 131$) are favored. For spin-dependent (*e.g.* axial vector or angular momentum coupled) scattering, odd nuclei targets such as F-19, I-127, Si-29, Ge-73, C-13, and O-17, are favored [65, 66]. The independent single-particle shell model assumes that the total nuclear spin is due to the spin of a single unpaired proton or neutron and is identically zero for even nuclei [4] since the axial couplings of opposite-spin nucleons destructively cancel [66] and interactions occur with only one of the nucleons. The sensitivity of dark matter experiments may be dominated by spin-dependent coupling if the scalar coupling component is significantly suppressed.

Generally, the differential nuclear-recoil rate arising from WIMP interactions

$$\frac{{\rm d}R}{{\rm d}E_{\rm R}} \propto \int_{v \le v_{\rm cutoff}} \frac{{\rm d}v}{v} \mathcal{F}(v) \frac{{\rm d}\sigma}{{\rm d}E_{\rm R}}(v, E_{\rm R}) \tag{1.2.6}$$

where $\mathcal{F}(v)$ is the distribution of WIMP velocities v in the local stellar neighborhood, which is

usually assumed to be an isotropic Maxwell-Boltzmann distribution [56] integrated up the cutoff velocity $v_{\rm cutoff}$, and the differential WIMP-nucleon cross section

$$\frac{\mathrm{d}\sigma}{\mathrm{d}E_{\rm R}}(v, E_{\rm R}) = \frac{\sigma_0}{E_{\rm R}^{\rm max}} F^2(q) \tag{1.2.7}$$

depends on the nuclear form factor $F(q)$, the momentum transfer $q = \sqrt{2\, m_{\rm N}\, E_{\rm R}}$, and the nuclear mass $m_{\rm N}$ of the target [56--58]. The interaction cross section σ is composed of spin-(in)dependent terms $\sigma_{\rm (SI)SD}(q = 0)$ at zero momentum transfer

$$\sigma_{\rm SI}(0)\, F^2_{\rm SI}(E_{\rm R}) + \sigma_{\rm SD}(0)\, F^2_{\rm SD}(E_{\rm R}). \tag{1.2.8}$$

The resulting nuclear-recoil energy distribution is approximately a falling exponential, with no distinguishing features; a detailed description of the mathematics of the expected nuclear-recoil distribution of a direct-detection experiment is given in *e.g.* [56] and a summary is given in *e.g.* [2, 55, 67]. The expected recoil energy of the target nucleus is $\langle E_{\rm R}\rangle \lesssim 100\,\mathrm{keV}$. Very low limits have already been placed on the interaction cross-section of WIMPs of mass $m_\chi \sim (1\text{–}10^3)\,\mathrm{GeV}/c^2$ with normal matter. Due to the recoil energy distribution, the expected scattering rate rises ∼exponentially with lower energy thresholds. Even with state-of-the-art radiation detectors, measuring such low energies is quite a challenge. The WIMP-interaction rate will depend on detection threshold, *i.e.* the energy below which any real event is indistinguishable from noise; the exposure, *i.e.* the detector mass and livetime; the nature of the interaction, *i.e.* detector material and the spin-dependence; and the background rejection and signal-selection efficiencies, which depend significantly on the detector radiopurity and detection technology.

Direct-detection dark matter experiments employ at least three energy channels (shown in **Fig. 1.5**) for identifying the nuclear recoils of a WIMP scatter: light (γ, scintillation), charge (q, *e.g.* e^-h^+-pairs), and vibrations (φ, phonons). The diagram shows the detection channels used by some experiments, along with their target elements. Many direct-detection experiments measure two energy channels simultaneously; this is useful for discriminating against background events occurring in the detection medium. These background events come primarily from electromagnetically interacting particles which generally have different characteristic energy signatures compared to the expected signal for WIMP-nucleon scattering. For example, nuclear recoils are accompanied by very little ionization or scintillation compared to electron recoils of the same recoil energy. As a result, each detector technology has striking advantages and is fundamentally different from the others.

Collecting scintillation produced from an interaction is advantageous because light propagates much more quickly than other quanta. Scintillation signals can be collected in 10's ns, however, only ∼10 γ's per keV deposited are typically released, corresponding to a light production efficiency ∼ 1%, so efficient light collection is very important: LAr and LXe have good scintillation properties [68]. A recoiling nucleus ionizes atoms freeing electrons and a positively charged partner, depending on the media, after a scattering event. An electric field applied across the media drifts these charge carriers

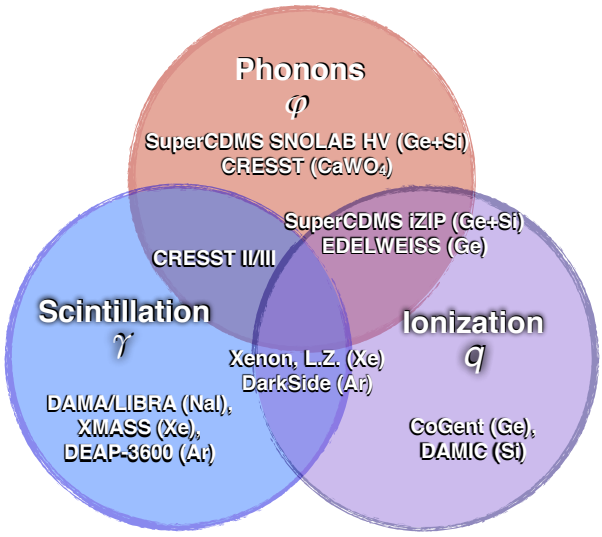

Figure 1.5: Detection channels for directly measuring nuclear recoils produced by WIMP-nucleon scattering. Three energy quanta produced in the WIMP-target media may be detected: phonons (φ, lattice vibrations), ionization (q, charge carriers), and scintillation (γ, photons). Direct detection dark matter experiments (historical and planned) are identified by their detection channel(s) and are shown with the target nuclei.

to sensors. Solid-state detectors measure electron-hole ($e^{-}h^{+}$) pairs, whereas liquid detectors, like LZ [69] and XENON [70], measure electrons, and gaseous detectors, such as DRIFT [71, 72] and NEWS-G [73], can measure ions or electrons. The number of charge carriers per energy is ~ 100 quanta released per keV deposited, corresponding to charge production efficiency$\sim 10\%$, with a marginally improved (statistical) energy resolution over scintillation.

When energy is deposited to a solid-state target, most ($> 90\%$) of the energy is dumped into the system via phonons, *i.e.* quanta of vibrations. Nuclear recoils are characterized by their low charge and light production efficiencies. Using cryogenically-cooled solid-state phonon detectors is a major advantage over the other technologies in that nearly 10,000 phonons per keV of energy deposited may be produced. This has allowed for the development of detectors with robust, low-energy thresholds with exceptional energy resolution such as in SuperCDMS SNOLAB [74]. See Ref. [75] for a description of demonstration detectors fabricated as part of R&D for SuperCDMS SNOLAB which demonstrate sensitivity to single electron hole pairs from the phonons produced by charge carrier motion. Phonons can be divided into two categories: the fast, high-frequency byproducts of initial energy deposition *athermal* phonons, and following a period of equilibration, the slower, low-energy *thermal phonons* [76, 77]. Thermal phonons don't give significant position information about the initial interaction. Detecting athermal phonons may allow three-dimensional reconstruction of particle interactions, but this comes with an added requirement of cooling the target well below LN_2 temperatures (77 K) commonly used for HPGe detectors, and below LHe temperatures (4 K) to *e.g.* ~ 10 milliKelvin [78]. Phonon production and detection is discussed later in the context of SuperCDMS SNOLAB detectors in **Section 1.4** and CDMS II style detectors in **Chapter 2**.

Detectors with super-heated liquid targets with exotic nuclear compositions are used as threshold

detectors. These detectors measure acoustic signals accompanying bubble nucleation from energy deposition to the media from particle interactions [79--82]. The target liquid is held at a pressure below the equilibrium vapor pressure and particles depositing enough energy over a short enough distance will cause the liquid to boil and form a bubble [83, 84]. These detectors may also record visual information to identify multiple nucleation points and veto multiple scatter events uncharacteristic of the very rare WIMP scatter. Some experiments (like bubble chambers) are completely insensitive to electron recoils from gamma and beta radiation since their stopping power in the fluid is too low to cause bubble formation. These detectors have the advantage of not requiring cryogenics or significant photon shielding characteristic of almost all detectors; however, they provide limited event-energy information. The exotic nuclear composition allows the detector to probe spin-dependent interactions. Also, bubble nucleation produces comparatively large dead times, so reducing the rate of background interactions helps maximize the WIMP sensitivity.

Along with the choice of detection technology and target material, there are several other considerations and challenges to commission a direct dark-matter experiment. Understanding the expected signal from WIMPs at the small nuclear-recoil energies $\sim$keV is necessary. The goal for these experiments is to count nuclear recoils from WIMPs within the experimental region of interest (ROI) *e.g.* at an appropriate energy, within the 'fiducial' volume of the detector for which systematic effects are negligible or at least well understood. Background events might end up 'leaking' into the ROI greatly reducing the experiment's sensitivity. The experimental sensitivity to WIMP interactions is dependent on the detector's nuclear recoil response, the target exposure (the product of the detector livetime and mass), the signal acceptance (the fraction of WIMP interactions expected to lie within the experimental ROI), and the background discrimination quality, *i.e.* the rate of background interactions which appear in the signal region.

Because the solar system is traveling through the Milky Way, the nuclear-recoil spectrum from WIMP scattering is expected to vary sinusoidally throughout the year [85]. When the Earth travels parallel to the solar system in June, the rate will be a maximum. The variation throughout the year, until the rate is a minimum in December, is of order 3% [55, 56]. Only experiments with significant sensitivity beyond the current level would be able to detect this annular modulation. For experiments with sensitivity to recoil directionality, the diurnal (*i.e.* daily) modulation of the WIMP-interaction rate due to the Earth's rotation could also provide strong evidence for a WIMP signal [86]. Many radiogenic backgrounds are not expected to temporally vary in this way, though cosmic-ray backgrounds and radon levels–and the associated fast daughter backgrounds–may have a day-night cycle. Regardless, exceptional event discrimination capability and low levels of detector backgrounds are essential for direct-detection dark matter experiments to be maximally sensitive to WIMPs.

WIMPs are expected to interact with an exceptionally low probability, so, even for the largest detectors imaginable, they should only singly scatter. This behavior is similar to that of neutrinos which are also very rarely interacting, but unlike that of muons, photons, or neutrons which can

scatter multiple times throughout a detector. So, detectors which bear even elementary position sensitivity may identify coincident signals in a single detector since a WIMP would never interact twice in a detector. Backgrounds such as these can come from external radiation sources. Typically, a detector is surrounded by some form of shielding and the most basic form of external background prevention is passive shielding to prevent external sources from depositing energy in the detector. Active shields, such as liquid scintillators, measure energy deposition of through-going particles to veto particle interactions which produce coincident signals in the target media from *e.g.* muons, photons, or neutrons.

WIMPs are expected have a uniform interaction likelihood throughout a detector. Since, the penetrative range of radiation exponentially decreases with distance, larger detectors will experience a higher external background near the detector edges, than throughout the bulk. This is advantageous for dense detectors *e.g.* liquid-xenon which are self-shielding against photons. Detectors with position sensitivity generally discriminate against events appearing near detector surfaces or edges where background events are more likely. Fiducialization is performed by reconstructing an event's location within the detection volume and rejecting events where systematic effects are considerable *e.g.* a significantly higher background rate at the detector edges[1], or non-uniformities or time-dependence of the electric field in the target [87].

1.3 Backgrounds for Direct-Detection Dark-Matter Experiments

The active target mass and duration for which particle interactions are recorded play a large role in determining an experiment's WIMP sensitivity. In the best case, the detector sensitivity for an experiment free of backgrounds[2] increases proportionally with the fiducial target mass m and exposure time $t_{\rm exp}$. The goal of an experiment of this nature *i.e.* a rare-event search, is to operate the largest feasible detector for as long as possible free of backgrounds. Very few detectors are free of backgrounds. A detector's WIMP sensitivity is significantly improved by rejecting background interactions. Backgrounds in dark matter detectors are generally classified into two types: nuclear-recoil and electron-recoil backgrounds. Typically background rejection is accomplished on an event-by-event basis from the statistical properties of a large number of signal-like nuclear recoils and background-like electron recoils. Experiments with two detection channels may discriminate against a vast majority of the various backgrounds [88]. A number of rejection techniques exist that are based upon the event's energy, timing or pulse-shape characteristics [89--91], spatial or directional characteristics, and even the temporal variation (in case of a detection). These properties can be used to discriminate between the signal from a WIMP interaction and the detector backgrounds.

In the energy range of interest ($E_{\rm NR} < 10\,{\rm keV}$) for WIMP-induced nuclear recoils, significant

[1] "God made the bulk; surfaces were invented by the devil." -Wolfgang Pauli.

[2] Some novice experimentalists are convinced this isn't possible *in principle*. Consider counting pink elephants in your living room–a well devised experiment *can* be background free.

backgrounds arise from electromagnetic interactions in the detector's target from α's (helium nuclei), β's (electrons), γ's (photons). Photons are problematic for rare-event searches due to their penetrative nature; they may Compton scatter in the target material and produce electron-recoil backgrounds. Generally, the most important primordial (half-lives $t_{1/2} > 10^9$ yrs) elements observed are ^{40}K and members of the ^{238}U and ^{232}Th decay series whose primary photons comprise most of the environmental radiation troublesome for rare-event searches. These elements are generally found in trace amounts in many types of material including rocks and metals comprising the laboratory infrastructure and detector apparatus. Preventing photons from the ambient environment is a concern for almost all dark mater experiments.

The rate of gamma rays incident on the target material may be significantly reduced with passive shielding. High-purity materials with a large number of nucleons such as lead, copper, and cadmium are well-suited for moderating external photon backgrounds. Some materials with a high nucleon number such as gold and platinum are rare and very expensive. Lead is good as a photon shield because it has a low neutron cross section and a low interaction probability with cosmic rays, with little cosmogenic activation. Ancient lead, with a very low Pb-210 activity, is expensive and typically used as an inner gamma shielding, blocking external photons including those from the other, outer shield layers with higher Pb-210 activities. Copper doesn't have as many nucleons as lead, but has only very short-lived radioactive isotopes. Very high-purity copper can be made, and cleaned, in bulk by a variety of methods. Copper electroforming is known to reduce surface contamination and prevent oxide formation [92, 93]. Passive water shields and (active) water cerenkov detectors can also be used as gamma shielding. Detectors with a large enough active volume and position sensitivity may reject photons that multiple scatter, depositing energy in more than one location in the target.

Nuclear-recoil backgrounds can result from neutrons scattering off the target nuclei, and, in future experiments with greater sensitivity, will also arise from coherent neutrino-nucleus scattering, which has recently been measured [94]. Neutrons are uncharged, like WIMPs, and will tend to elastically scatter off nuclei, posing a potentially significant nuclear-recoil background to experiments. Cosmogenic neutrons are produced from spallation reactions of muons on nuclei in the experimental setup or in the surrounding cavern rock. These neutrons can have energies $E_n \gtrsim$ GeV and may be moderated to lower energies by the apparatus surrounding the detector. The resulting neutron energies $E_n \approx$ MeV can produce nuclear-recoil energies $E_{\rm NR} \approx$ keV relevant for dark matter searches. Operating detectors at a deep underground site reduces the flux of high-energy muon-induced neutrons.

Alpha decays can produce radiogenic neutrons from (α, n) reactions in materials with large alpha-capture cross sections. These reactions tend to occur in materials with a low-to-mid-nucleon number, such as those made with hydrocarbons with alpha-emitting radioimpurities *e.g.* teflon and polyethylene. Radiogenic neutrons are also released from spontaneous fission where an atom's nucleus splits into two smaller nuclei and releases neutrons and sometimes photons [95, 96]. Neutrons

tend not to lose any significant fraction of their kinetic energy when scattering off much larger nuclei, which act as a wall to a rubber ball. Materials with an overall low nucleon number are the most efficient neutron moderators. Hydrogen-rich materials such as water, plastics like high- and low-density polyethylene (H/LDPE) can be used to moderate these radiogenic neutrons with $\sim$MeV energies, so that neutron-induced nuclear recoils are below the experimental energy threshold. Polyethylene doped with 5% boron, borated polyethylene (Poly-B) can also be employed [97]. Neutrons from (α, n) reactions and Uranium fission may require some 20 inches of moderator shielding to thermalize the external neutron spectrum to energies below an experiment's detection threshold. Some experiments use active shields such as large water volume with PMT readout [74, 98], doped with gadolinium [99] which moderates neutron flux via neutron capture.

Photons and neutrons are a primary source of electron- and nuclear-recoil backgrounds, respectively, for direct dark-matter detectors. These types of radiation may be moderated by many orders of magnitude with some 10's cm of shielding. Ionizing particles, such as alphas and betas, relevant to backgrounds in dark matter detectors, are shielded by much less material and only pose a problem when the target and near-target materials are contaminated with trace amounts of isotopic impurities.

However, some particle species interact weakly enough with the ordinary matter comprising the target materials of rare-event searches that they cannot be effectively moderated by materials like lead, copper, polyethylene which make up conventional rare-event search shielding. Atmospheric neutrinos–produced by cosmic rays–and solar neutrinos will pass through the Earth. As dark matter experiments employ better detectors, reduce their backgrounds, and reach greater sensitivities, coherent elastic neutrino ν-nucleus scatters (CEνNS) will eventually be detectable [94]. Coherent scattering of solar (atmospheric) neutrinos will ultimately limit the sensitivity of dark matter experiments to low-mass $\lesssim$GeV/c^2 (high-mass $\gtrsim$10 GeV/c^2) WIMPs [94]. The rate of these neutrino interactions will be different for different target materials, the neutrino-floor will eventually limit a detector's dark-matter sensitivity and background estimation and subtraction will need to be performed. The moon may act as a shield to solar neutrinos, so the rate of the backgrounds may have a monthly variation. Measuring the temporal dependence of the resulting low-energy nuclear recoils would be vital to distinguish WIMPs from neutrinos. Future detector generations may eventually require directional sensitivity to distinguish daily, monthly, and annual modulation in signal-like events.

Cosmic rays are high-energy particles, primarily protons, barreling towards the Earth from outer space. High-energy protons scatter in the upper atmosphere and the surface of Earth's crust creating a myriad of particle species in a hadronic cascade that includes neutrons, pions, and kaons. Muonic, electromagnetic, and neutrino components result from these high-energy interactions as well. All particles range out after traveling through Earth's atmosphere and crust except muons and neutrinos. Experiments that are not deep underground see a much larger muon flux [99--101], so rare-event detectors are placed deep underground or inside mountains to use the earth as shielding.

The overburden may vary in composition so it is quoted in meters of water equivalent based on the density of the material (typically rock) above the experiment. For those experiments in mountains such as Gran Sasso (LNGS), shallow-angle muons are less efficiently moderated by the overburden and dominate the flux. While the dominant energy-loss mechanism for muons is ionization, cosmic-ray muons themselves do not typically pose a serious background for dark matter detectors since they may be easily identified by multiple scattering throughout detectors; furthermore, liquid-scintillating active muon-veto shields can be used to veto coincident signals in the target and shielding. Cosmic-ray muons may free high-energy neutrons which need to pass through much more material to thermalize. Muon-induced neutrons produced near dark matter detectors are a source of nuclear-recoil backgrounds.

Along with secondary neutrons, high-energy proton and neutron spallation may produce long-lived radioactive isotopes in detector materials such as germanium [102--104], copper [105, 106], and tungsten [107, 108] which may result in γ-ray emission or tritium production. Tritium (^{3}H) produced in the detector materials before or during fabrication, or even in-situ, will emit low-energy betas during data-taking. Nuclide activation is less problematic when the resulting isotope has a very short half-life of days or weeks. Additionally, cosmic-ray spallation in the upper atmosphere produces many radionuclides such as the beta-decaying ^{14}C and ^{32}Si. Si-32 in the upper atmosphere falls to earth's surface with precipitation and can be found at trace levels in silicates used by the semiconductor industry to fabricate silicon, and these long-lived decays produce electron recoils [109, 110]. Both tritium and Si-32 arise from cosmogenic activation and give rise to low-energy beta-emission throughout the bulk of materials.

Besides external radiation, radionuclide impurities in the detector and near-detector materials also poses a significant source of electron and nuclear-recoil backgrounds. Naturally-occurring neutron-rich isotopes may readily undergo radioactive decay emitting alphas or betas leaving behind a recoil nucleus which may be in an excited eventually giving off photons. These ionizing alpha and beta particles, relevant to backgrounds in dark matter detectors, are effectively shielded by much less material (than photons) and only pose a problem when the target and near-target materials have even trace levels of isotopic impurities. Radioactive elements, *e.g.* inside the bulk of dark matter detectors, are of most serious concern for rare-event searches since shielding may be improved but the detector purity can only be improved by replacing the detectors or radioactive components in the apparatus–which is difficult but not necessarily impossible. The target material of gaseous and liquid detectors may be purified of some radioactive contaminants *e.g.* ^{222}Rn or ^{85}K [98, 111, 112]. Minimizing backgrounds from the radioactivity of detection components and from cosmogenic sources is crucial to improving the WIMP exclusion limits; extensive material screening campaigns are carried out by essentially every rare-event search to obtain the most pure materials and determine sources of radioimpurities that may arise during their fabrication and storage.

Radon-222 poses problematic backgrounds for other rare-event searches such as liquid noble

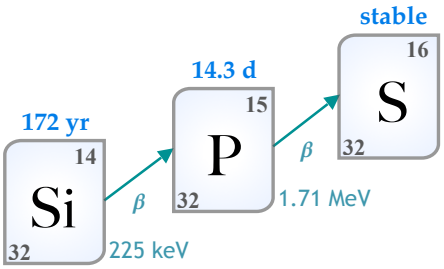

Figure 1.6: Si-32 β decays ($t_{1/2} \approx 172$ yrs, $Q \approx 225$ keV) into P-32 which beta decays ($t_{1/2} = 14.3$ days, $Q = 1.71$ MeV) to the stable ^{32}S.

experiments LZ, PandaX-I, Xenon, DarkSide-50, DEAP, and Si-32 is present in the solid-state silicon CCD-based DAMIC. The next sections describe the nature of these radioactive isotopes and why they are troublesome for these experiments, with particular focus on the experiment I work on: SuperCDMS at SNOLAB. **Chapter 6** describes shortcomings and difficulties measuring radon-222 and its progeny with conventional screening detectors.

1.3.1 Silicon-32

Silicon-based experiments, such as DAMIC [109, 113] and SuperCDMS SNOLAB [74], face a low-energy background from ^{32}Si—a long-lived by-product of cosmic-ray spallation secondaries on argon or chlorine

$$^{40}_{18}\mathrm{Ar} + p \rightarrow {}^{32}_{14}\mathrm{Si} + p + 2\alpha \tag{1.3.1}$$

$$^{37}_{17}\mathrm{Cl} + p \rightarrow {}^{32}_{14}\mathrm{Si} + 2p + \alpha \tag{1.3.2}$$

in the upper atmosphere [114--116]. This isotope may then be transported to the earth by rain and snow [117, 118]. This naturally-occurring radioactive isotope of silicon is expected to be present in sand at low levels, and is problematic for silicon-based detectors since ^{32}Si β-decays to phosphorus and then sulfur [74, 109, 119]. The consecutive beta-decay of ^{32}Si to ^{32}P to ^{32}S

$$^{32}\mathrm{Si} \rightarrow {}^{32}\mathrm{P} + \beta^- + \bar{\nu} \quad (Q = 224.5\,\mathrm{keV}, \quad t_{1/2} \approx 172\,\mathrm{yrs}) \tag{1.3.3}$$

$$^{32}\mathrm{P} \rightarrow {}^{32}\mathrm{S} + \beta^- + \bar{\nu} \quad (Q = 1.709\,\mathrm{MeV}, \quad t_{1/2} = 14.3\,\mathrm{d}). \tag{1.3.4}$$

is depicted in **Fig. 1.6**. Since the ^{32}Si half-life is so long, measuring the level of contamination in silicon substrates may be critical for solid-state detectors such as SuperCDMS and DAMIC. Recently, the direct-detection dark-matter experiment DAMIC reported a measurement on the Si-32 bulk activity

$$A'_{\mathrm{Si}} = (11.5 \pm 2.4)\,\mathrm{events/kg/day} \qquad (95\%\ \mathrm{C.L.}) \tag{1.3.5}$$

of their CCD detectors [110, 120] , corresponding to $\sim 4.3 \times 10^{-20}$ parts ^{32}Si per one part natural ^{28}Si [109]. Because β-decay spectra extend to the lowest energies, ^{32}Si will be produce an unavoidable background in SuperCDMS high-voltage (HV) silicon detectors [74]. If the SuperCDMS SNOLAB

HV detectors are contaminated throughout the bulk of their $m_{\mathrm{Si-HV}} \approx 0.61\,\mathrm{kg}$ at the level DAMIC measured [109], the ^{32}Si-induced β-decay activity

$$\mathcal{R}^{'}_{\mathrm{Si-32}} = A^{'}_{\mathrm{Si}} \times m_{\mathrm{Si-HV}} \approx (7.05 \pm 1.46)\,\mathrm{detector}^{-1}\,\mathrm{day.}^{-1} \tag{1.3.6}$$

across the entire energy region of interest, ignoring the subsequent ^{32}P β-decay. This low level of Si-32 contamination could be the dominant background for the SNOLAB silicon high-voltage detectors [74]; **Section 1.4** discusses this further. The level of Si-32 in Eqn. 1.3.5 is considerably lower than the initially reported [109] activity

$$A^{''}_{\mathrm{Si}} = 80^{+110}_{-65}\ \mathrm{events/kg/day} \qquad (95\%\ \mathrm{C.L.}) \tag{1.3.7}$$

which had a considerably larger uncertainty. If the silicon HV detectors are contaminated throughout their $m_{\mathrm{det}} \approx 0.61\,\mathrm{kg}$ bulk at the level DAMIC measured, the ^{32}Si-induced β-decay activity

$$\mathcal{R}^{''}_{\mathrm{Si}} = A_{\mathrm{Si-32}} \times m_{\mathrm{det}} \approx 49^{+68}_{-40}\,\mathrm{detector}^{-1}\,\mathrm{day.}^{-1} \tag{1.3.8}$$

Dividing the two-sigma results from Eqns. 1.3.7 and 1.3.5, these measurements match at

$$\frac{80 - 11.5}{\sqrt{(65/2)^2 + (2.4/2)^2}} \approx 2.1\sigma. \tag{1.3.9}$$

This doesn't *necessarily* indicate a large variability in the Si-32 contamination of the source. The CCDs used by DAMIC to obtain the above results were fabricated by TOPSiL [121] from silicon of similar characteristics from two different ingots produced in different years, which may explain the difference in ^{32}Si content. The DAMIC CCDs were fabricated from the same type of TOPSiL ingot that was purchased for the SuperCDMS SNOLAB silicon detectors. **Chapter 6** describes an ultra-low-background screener that would be capable of detecting the level of contamination initially reported by DAMIC. The level of Si-32 of these samples will have a large impact on the electron-recoil background rate in SuperCDMS SNOLAB detectors.

1.3.2 Radon Isotopes

Radon is a naturally-occurring, neutron-rich, radioactive noble gas found in trace amounts in the air. Radon has several isotopes originating from the ^{238}U, ^{235}U, and ^{232}Th decay chains. Radon progeny are α-, β-, and γ-emitters [122]. The radon-222 decay chain, shown in **Fig. 1.7** with alpha decay energies and half lives, originates from the primordial isotope ^{238}U and has the longest half-life

$$t_{1/2} = 3.82\,\mathrm{days}. \tag{1.3.10}$$

It is generally the most serious experimental background of all the radon isotopes. Radon's long-lived daughter (Po-210) are accompanied by a potentially low-energy nuclear recoil (Pb-206) that could provide a false positive for a WIMP scatter. Moreover, low-energy electron recoils may be

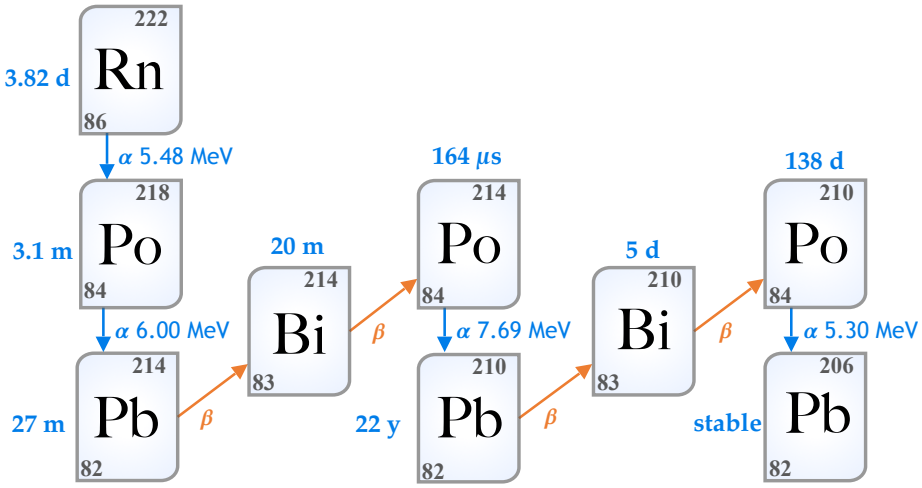

Figure 1.7: Isotopes (abbreviated), with branching fractions >99%, in the ^{222}Rn decay chain shown with proton number Z (lower left), nucleon number $A = N + Z$ (upper right), alpha decay energies E_α (in MeV), and beta decays, with half-lives $t_{1/2}$ from NIST [123]. These are in agreement with NUBASE evaluation of nuclear and decay properties [124]. The so-called fast daughters, on the left, appear before the long-lived daughters, starting with ^{210}Pb, are on the right. Pb-210 has a complicated decay spectrum (shown in **Fig. 1.8**) includes several low-energy β decays, and de-excitation gammas. Figure adapted courtesy of J. A. Street.

mis-reconstructed and appear in the WIMP signal region.

Radon-222 has a propensity to diffuse through materials: it is highly mobile in gases [125], solids such as soils [126, 127], and polymers [128, 129]. Measurements indicate that the ^{222}Rn diffusion coefficient $D_{\text{gas}} \sim 10^{-5}\,\text{m}^2/\text{s}$ in air and noble gases [125]. Radon diffuses significantly in soft materials like polymers and rubbers [127--136]:

$$D_{\text{soft}} \sim \left(10^{-13}\text{–}10^{-9}\right)\ \text{m}^2/\text{sec}. \tag{1.3.11}$$

Metals typically have radon diffusion coefficients

$$D_{\text{metal}} \lesssim (10^{-17}\text{–}10^{-15})\,\text{m}^2/\text{sec} \tag{1.3.12}$$

$\gtrsim 1,000\times$ smaller than plastics [137--139]. Therefore, radon will diffuse from the bulk of non-metals that have trace radium atoms, then emanate into the surrounding atmospheric environment; the radon may subsequently diffuse into other materials.

SuperCDMS SNOLAB will be deployed in an underground mine where the ambient radon concentration $C_{\text{SNO}} \approx 130\,\text{Bq/m}^3$ is large [140]. Lead shielding surrounding the detectors significantly reduces the background from radon daughters. Radon in the cavern must be prevented from mixing with the air within the shielding because high-energy gammas from lead and bismuth decays will singly scatter in the detectors increasing the electron-recoil backgrounds. **Table 1.1** shows the energies and absolute branching fractions for Pb and Bi decays. To keep these decays from dominating the backgrounds in SuperCDMS SNOLAB detectors which cannot employ conventional background discrimination, the lead gamma shielding will be hermetically sealed from the cavern

Table 1.1: High-intensity photons from the nuclear de-excitation of ^{222}Rn daughters from lead and bismuth decays are shown with absolute branching fractions ($\mathcal{F}_B \gtrsim 5\%$) and their approximate energies listed in keV [122, 141].

^{214}Pb $\rightarrow^{214}$Bi		^{214}Bi $\rightarrow^{214}$Po	
Energy (keV)	$\mathcal{F}_B$ (%)	Energy (keV)	$\mathcal{F}_B$ (%)
351.9	37.1	2205.0	4.9
295.1	19.2	1764.5	15.9
241.9	7.5	1238.1	5.9
77.1	11.0	1120.3	15.0
74.8	6.5	609.3	46.1

with a gasket material which must not emanate too much or allow radon to diffuse through it significantly [74]. Radon diffusion measurements of gasket materials for SuperCDMS SNOLAB are discussed in **Chapter 3**. **Chapter 5** describes radon emanation measurements of the same materials, and implications on the expected backgrounds.

Radon daughters (Po, Bi, Pb) are all alpha-, beta-, or gamma-emitting metals [122]. These decays tend to produce positively charged daughters [142--145] that will readily plate-out and stick to surfaces. This is especially true for materials that are low on the triboelectric series which will attract positively charged ions. Teflon is one such material whose fluorine atoms are very electronegative, so must be kept from allowing significant radon daughter accumulation [146, 147]. Radon is troublesome for both rare-event searches and material screening detectors which often have internal backgrounds from radon-222 daughter plate-out [140, 146, 148, 149]. Moreover, these backgrounds may tend to accumulate over time. Surface backgrounds from plate-out are a significant problem for solid-state dark matter experiments like SuperCDMS [59, 88, 140, 150, 151] and liquid noble dark matter experiments like LZ [152] and DarkSide-50 [153, 154]. Solid-state experiments face a similar problem from radon daughters on the surfaces. The beta decays of radon daughters generally produce electron recoils in dark matter detectors. Some radon daughters occur in quick succession and this is helpful for discriminating against some of these backgrounds. There exists a tagging technique of the consecutive ^{214}Bi and ^{214}Po beta decays which occur in about 0.16 millisec, as discussed in *e.g.* Refs. [109, 153, 155--157]. As a result, these decays are not necessarily a significant problem for experiments like LZ. However, the beta-decay of ^{214}Pb to ^{214}Bi poses a problem since the initial ^{214}Pb is not accompanied by another event to help identify it as a background in every case; this 'naked'-beta may be a significant background in LZ [98, 152, 158]. Along with standard Bi-Po analysis [153], DarkSide-50 was able to tag Rn-Po decays in liquid argon [154]. After the ^{214}Po decay, the low-energy beta-emitter Pb-210, whose half life

$$t_{1/2} = 22.3\,\text{yrs}, \tag{1.3.13}$$

will remain on material surfaces for the duration of an experiment. **Fig. 1.8** shows the complicated decay chain of ^{210}Pb, which decays by beta-emission, emits conversion electrons, and gives off 46.5 keV gamma (4%) of the time. Pb-210's daughter ^{210}Bi has a half-life $t_{1/2} = 5$ days, but is not

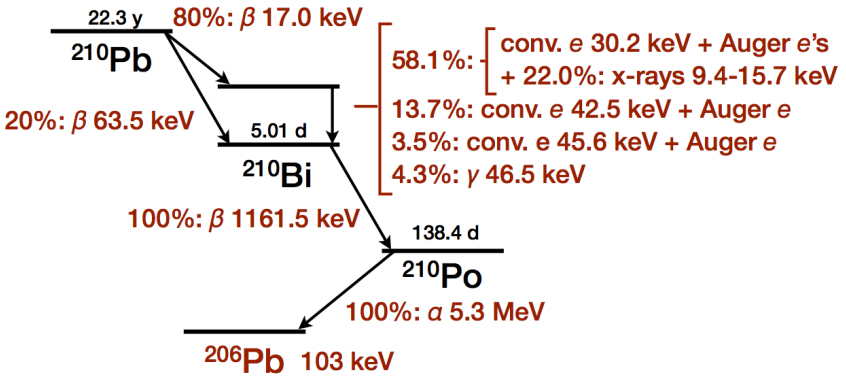

Figure 1.8: Pb-210 decay chain to the stable ^{206}Pb with beta- and alpha-decay Q-values, half-lives $t_{1/2}$, Beta decays of Pb-210 lead to an excited state (46.5 keV) of Bi-210 84% of the time. This energy is released as gammas and conversion electrons. Bi-210 beta decays, some $t_{1/2} = 5$ days later produce Po-210. The 5.3 MeV α decay of Po-210 imparts the stable Pb-206 nucleus $E_{\mathrm{R}} = 103$ keV of kinetic energy. Pb-210 on detector surfaces is problematic for solid-state [88] and liquid noble experiments [152]. Figure from [88].

expected to produce a naked-beta for LZ since no ^{210}Pb will be present in the liquid target [98, 152].

To prevent the myriad of issues from radon contamination, many experiments have devoted significant R&D to measuring the radon emanation of detector components [133, 148, 159--167]. SuperCDMS SNOLAB and LZ are preparing to commission the next-generation of direct-detection dark-matter experiments with the help of our group. By making radon measurements, we have determined the expected background contribution from some components of the apparatus and helped to select materials with as little radon as possible [168]. Directly measuring increasingly low levels (mBq/kg) of Pb-210 contamination is a difficulty that the rare-event search community is working towards very slowly [88, 98, 109]. **Chapter 6** describes an ultra-low-background surface screening detector designed to address issues associated with measurements of low-energy beta decays from *e.g.* Radon-222 progeny and **Chapter 7** describes progress on the commissioning of the corresponding prototype detector at SDSM&T.

After their fabrication, detector materials must be kept sufficiently free of radon daughters before deployment. To this end, detector are often constructed in low-radon environments. Xenon-based experiments [169]: LZ [98, 170, 171], XENON100 [172, 173], XMASS [174], and PANDAX-1 [112], and cryogenic bolometers SuperCDMS [74, 175--178], CUORE [179], Neutrino experiments like Borexino [180--182], SNO+ [183], and Super-K [184, 185], and neutrinoless double-beta decay [186] have performed radon studies attempting to mitigate radon exposure of detector components during construction and/or operation. At SDSM&T, we have a very low radon cleanroom [176, 178, 187], based on a radon mitigation technique developed for Borexino [188]. In this cleanroom, we will be able to commission detectors and avoid radon daughter surface plate-out during fabrication, assembly, and testing. Both SuperCDMS SNOLAB and LZ will utilize radon-mitigation systems to significantly decrease the radon concentrations near the detectors by $\sim 10^3$ during construction [140, 146, 178].

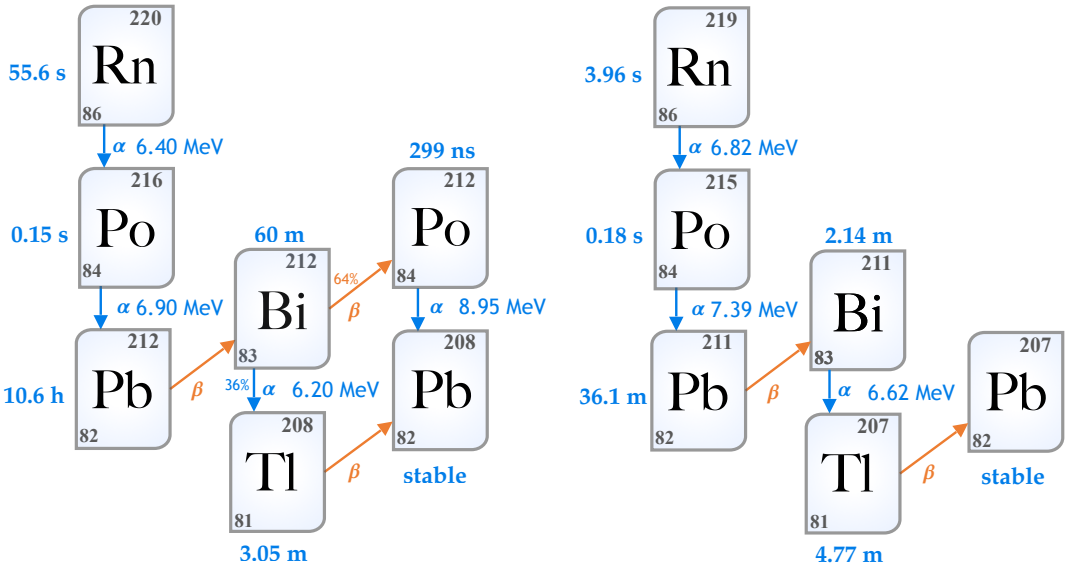

Figure 1.9: Radon-220 and Radon-219 decay chains with half-lives [189], alpha energies, and branching fractions (%). Radon-220 decay chain comes from the Thorium-232 chain and Radon-219 comes from the U-235 chain.

There are at least 3 other, less dangerous radon isotopes besides Rn-222. These short-lived isotopes include ^{219}Rn ($t_{1/2} = 3.96$ sec) and ^{220}Rn ($t_{1/2} = 55.6$ sec), shown in **Fig. 1.9**, come from the primordial ^{232}Th and ^{235}U respectively. ^{218}Rn ($t_{1/2} = 53 \times 10^{-3}$ sec)–not pictured–alpha decays to ^{214}Po feeding the ^{222}Rn chain. The short-lived radon isotopes ^{219}Rn and ^{220}Rn are generally less dangerous than ^{222}Rn because they are so short-lived that they have very little time to diffuse through and emanate from the bulk of materials. In fact, radon-219 progeny decay very quickly to the stable Pb-207 with a total half-life less than 45 minutes. These isotopes may be fed by their long-lived grandparents, and the resulting alpha and beta decays still leave recoiling nuclei which may be wrongly inferred as resulting from WIMP interactions. Though, with back-to-back alpha emission ^{219}Rn at 6.82 MeV ($t_{1/2} = 3.96$ sec) is followed by Po-215 at 7.39 MeV ($t_{1/2} < 2$ millisec), it may be easy to identify the start of this decay chain. For experiments with mobile target nuclei, such as xenon or argon, understanding the radon-daughter mobility in the detection volume can help to veto events that occur at a specific time, energy, and location following the first alpha decay [152, 154]. For solid-state detectors such as SuperCDMS, DAMIC, and CRESST, it may be possible to veto events in a similar time window occurring at a given initial alpha-decay location.

1.4 SuperCDMS SNOLAB

The Super Cryogenic Dark Matter Search (SuperCDMS) experiment is a direct-detection dark-matter search that will use very low background, ultra-cold solid-state detectors to measure the ionization ($e^- h^+$ pairs) and phonons (quanta of lattice vibrations) from WIMP-nucleon scattering.

SuperCDMS at SNOLAB [74, 190] is the latest experimental generation that will use well-

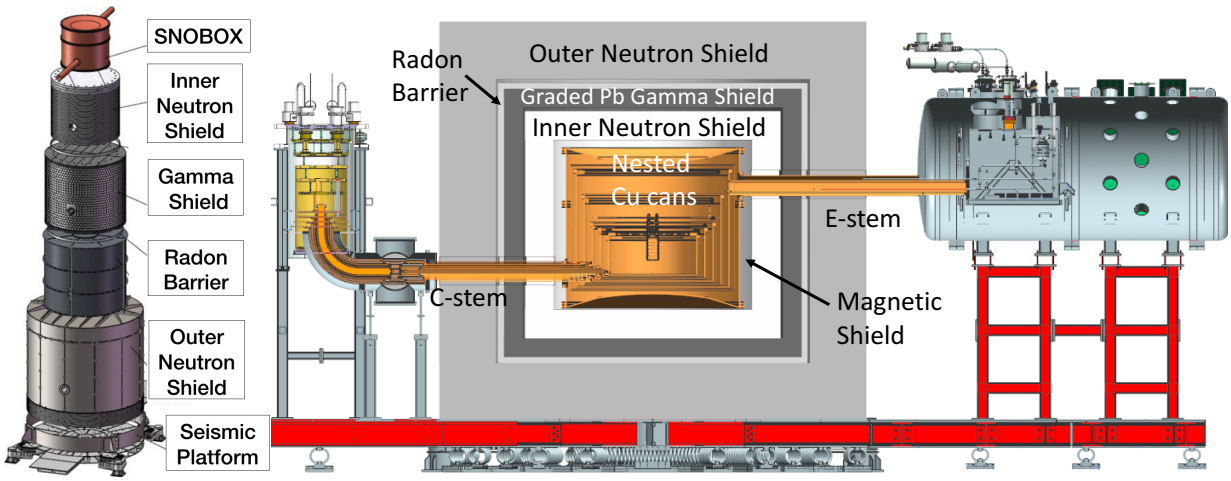

Figure 1.10: Left: Exploded view of shielding layers surrounding the nested copper cans (SNOBOX) housing the detectors. Figure from an unknown SuperCDMS collaborator. **Right:** Cross section of SuperCDMS SNOLAB. The entire apparatus will sit on top of a seismic platform to protect the detectors from seismic events and vibrational noise from the cavern. An outer neutron shield consisting of modular water tanks will moderate neutrons coming from the cavern walls. A graded lead shield, with an inner liner of low-activity ancient lead, will prevent gammas emitted by U/Th/K-bearing rock in the cavern walls from entering the detection volume [106, 192]. An aluminum enclosure (Radon Barrier) surrounding the lead shielding will be purged with low-radon gas to prevent significant radon-induced gamma production within the lead gamma shield. An inner neutron shield made of polyethylene will moderate and absorb radiogenic neutrons from impurities in the outer shielding. The shielding protects the detectors within the nested copper cans from external radiation. A magnetic shield (right) just outside the copper protects the phonon sensors from Earth's magnetic field. A cold finger (C-stem) provides cooling to pass through the shielding to reduce the detector to their critical temperature $T \sim 15\,\mathrm{mK}$, and an electronics feedthrough (E-stem) allows the detector signals to be readout by the data acquisition system. Figure from the SuperCDMS Final Design Report [106].

developed detector technologies to substantially increase the low-mass WIMP sensitivity beyond the previous generations. The apparatus will be deployed in Sudbury, Ontario in the Creighton-Vale mine 2 km underground with a 6010 m.w.e. overburden [191] to reduce the cosmic-ray flux by $\times 1,000$ and the muon-induced neutrons by $\times 250$ [192] compared to the Soudan Mine in Minnesota where earlier CDMS generations were located [89, 193, 194]. The hockey-puck-sized detectors will arranged in towers, housed in six 3/8" thick nested copper cans (SNOBOX) and surrounded by extensive layered shielding (shown as an exploded view in the left panel of **Fig. 1.10**). Groups of high-purity silicon and germanium detectors will be arranged in four vertically stacked towers, cooled with a dilution refrigeration unit to a nominal temperature $T_c \sim 50\,\mathrm{mK}$. The targets are designed to measure the minuscule energy of nuclear recoils from a low-mass WIMP scatter within the crystal substrate with ionization and phonon sensors [74, 78, 195]. A magnetic shield inside all the neutron and gamma shielding ensures the phonon signals remain unperturbed by reducing Earth's magnetic field by $50\times$ [106]. A cross-section of the SuperCDMS SNOLAB apparatus is shown in the right panel of **Fig. 1.10**. The diagram shows the cryostat and detectors surrounded by shielding with electronics (E-stem) and dilution units (C-stem) connections for detector readout and cryogenic cooling power, respectively. The dilution refrigeration (left) passes through all the shield layers to cool the copper cans via the 'C-stem' connection. The cryogenic design of SuperCDMS SNOLAB is described in detail in [196]. The detector signals are fed through the 'E-stem' (right) which passes

through the shield to the DAQ system. The detectors are so sensitive that the apparatus will be placed on top of seismic isolators to reduce environmental microphonic noise (bottom).

The shield design helps to prevent secondary particles produced in the outer shield layers from reaching sequentially deeper layers. Additionally, the design is that the radiopurity of the outer layer materials can be relaxed, but the copper housing the detectors must be of very high radiopurity. The SNOBOX is made of copper cans (6 cm thick in total) that moderate low-energy photons coming from the surrounding lead. This copper slightly reduces the radiopurity requirements on the inner polyethylene layer. Hydrogenous materials generally moderate external neutrons and those produced in the lead shield, and the high-Z lead shields external gammas. An outer neutron shield consists of modular water tanks (60 cm thick) resting on a polyethylene base to reduce the radiogenic cavern neutron flux by $\gtrsim 10^5$ [106] . An aluminum enclosure designed to prevent radon in the cavern environment from mixing with the gas in the graded gamma shielding. Radon present in the lead shielding, emanated from materials within the enclosure, shielding, and from the cavern, will give rise to high-energy photons which pose an otherwise dominant background for the experiment. The ∼9 cm-thick outer lead shield is expected to have a Pb-210 activity < 19 Bq/kg, and the inner lining consists of ∼1 cm-thick ancient lead with a Pb-210 activity < 0.08 Bq/kg [192], designed to reduce the external gamma flux by $\gtrsim 10^6$ [106] to negligible levels below gamma production from the lead itself. A supplementary polyethylene inner neutron shield surrounding the copper cryostat moderates (muon-induced) spallation neutrons and gammas and neutrons from radioimpurities in the lead shield. The shielding is designed to prevent external radiation from reaching the detectors, however, even if they are completely stopped, material impurities in the materials very near and in the detectors is generally expected to be the dominant background. GEANT4 simulations of the energy depositions to the detectors by background sources passing through the SuperCDMS shielding were used to optimize the shield components to meet the background requirements of the experiment.

SuperCDMS has made significant progress, along with the rest of the direct-detection community, increasing the sensitivity to low-energy WIMP interactions. The most significant limitation to WIMP sensitivity generally comes from backgrounds originating from radioimpurities in the apparatus materials. A large focus of my thesis has been on characterizing and using radon detectors (**Chapter 4**) to measure the radon diffusion (**Chapter 3**) and emanation (**Chapter 5**) of materials to reduce these backgrounds as much as possible. I also worked on developing a material screener (**Chapter 6** and **Chapter 7**) that would help identify cleaner materials to significantly reduce the backgrounds from the detection target and surrounding detector components for SuperCDMS and other rare-event searches. This section describes the state-of-the-art detector technology and signal production, the detector design complementarity, the experimental backgrounds, and the projected WIMP sensitivity for SuperCDMS SNOLAB.

1.4.1 Detector Design

The SuperCDMS SNOLAB detectors (shown in **Fig. 1.11**) are cylindrical crystals 33 mm thick, 100 mm in diameter made of high-purity germanium (silicon) of mass 1.39 (0.61) kg operated with two mature and complimentary technology designs. Half of the detectors will be the 'interleaved Z-sensitive Ionization and Phonon mediated' (iZIP) design, operated at a modest bias voltage

$$V_{\mathrm{iZIP}} \sim 4\,\mathrm{V}, \tag{1.4.1}$$

as was the case for SuperCDMS Soudan detectors [76, 197]. These detectors have exceptional nuclear-recoil/electron-recoil event discrimination and event-by-event position reconstruction [198] to fiducialize the active volume of the target–these detectors are expected to run background-free for first 5 years of experimental operation [74]. The other half will be high-voltage (HV) detectors (pictured in **Fig. 1.11**) operated at a much larger voltage bias

$$V_{\mathrm{HV}} \sim 100\,\mathrm{V} \tag{1.4.2}$$

than the iZIP detectors, as was the case for CDMSlite [59, 199, 200]. These HV detectors are operated to achieve exceptional phonon energy resolution and a very low energy threshold [74]. The detector faces (top and bottom) are photolithographically patterned with superconducting sensors determined by the design: the HV detectors will be phonon-only and the iZIP detectors will have grounded phonon sensors interleaved with ionization rails held at potentials $\pm V_{\mathrm{b}}$[3] which measure the image charges on the sensors from the motion of the charge carriers produced by the scattering interaction. The nuclear recoil energy from low-mass WIMPs $m_\chi \approx (1\text{–}10)\,\mathrm{GeV}/c^2$ scattering may be less than the energy threshold for Ge targets, but above the energy threshold for silicon due to its lower atomic mass. Each detector design is optimized for sensitivity to different WIMP-masses: the HV detectors will be more sensitive to WIMPs of mass $m_\chi \lesssim 3\,\mathrm{GeV}/c^2$ owing to their low energy threshold, and the iZIP detectors to WIMPs of mass $m_\chi \gtrsim 3\,\mathrm{GeV}/c^2$.

Interaction sites in the crystals create electron-holes pairs, and create high-frequency (THz) out-of-equilibrium ('athermal') phonons. The initial athermal byproducts, which are characterized by ballistic motion, of the interaction naturally down convert into isotropic thermal phonons (∼μeV) which do not characterize the position of the initial interaction. Traditional calorimeters measure thermal phonons, which are characterized by diffusive motion, and are largely insensitive to the nature of the initial interaction, whereas employing multiple athermal phonon sensors with a fast response time permits us to infer the position and energy of interactions in SuperCDMS detectors. The right panel of **Fig. 1.11** shows the production of high-frequency (Recoil) phonons (φ) both from the WIMP scattering. Charge carriers ($e^- h^+$ pairs) are drifted by the bias voltage V_{b} and measured by ionization sensors (not depicted). The charge-carrier ($e^- h^+$) motion produces a

[3] Where the ± corresponds to the different detector faces–one side has ionization rails at a positive voltage, and rails on the opposite face are at a negative potential.

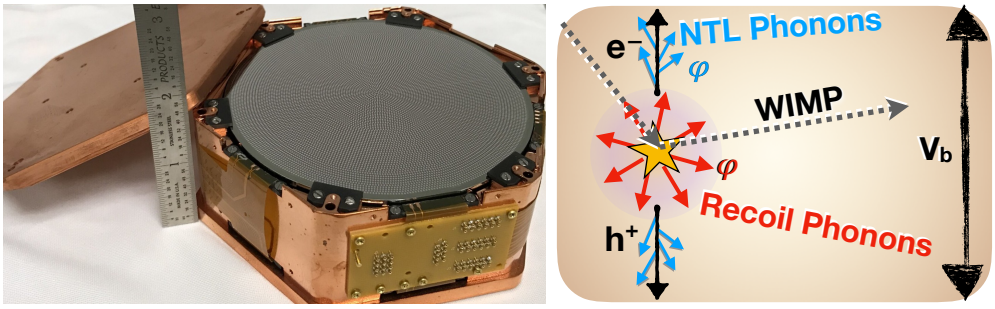

Figure 1.11: Left: SuperCDMS SNOLAB High Voltage detector in copper detector housing. The silicon detectors are $m_{\mathrm{Si}} = 0.61\,\mathrm{kg}$ cylindrical, hockey-puck sized crystals 33 mm thick, 100 mm in diameter with thousands of tiny sensors. Figure by Matt Cherry at UMN. **Right:** Heuristic diagram of phonon production in SuperCDMS style detector. Recoil phonons and electron-hole ($e^- h^+$) pairs are produced at the WIMP scattering site. The detector bias V_{b} does work drifting the charge carriers producing NTL phonons. The number of NTL phonons produced is proportional to the initial number of freed charge carriers, indicated by the ionization energy $E_{\mathrm{Q}} = N_{eh} \cdot \varepsilon_{eh}$ at the interaction site (★). In iZIP detectors, sensors measure the electron-hole pairs and phonons. On the other hand, the HV detectors have such a large bias that the NTL phonons dominate the total phonon signal, so the HV detectors are biased, but are not equipped with ionization sensors. NB: electrons and holes travel in the valleys of the lattice structure, which is not depicted here.

second population of NTL phonons. These phonons propagate through the target crystal until they reach the surface where they are collected by superconducting aluminum collector fins. I will only give a short summary of the signal creation here; an excellent description of TES dynamics and characteristics is given in Refs. [76, 77, 197, 201].

The faces of the crystal are photolithographically patterned with superconducting Transition-Edge Sensors (TESs). As shown in the left panel of **Fig. 1.12**, phonons break Cooper pairs in the Al fins generating quasi-particles which diffuse into and raise the temperature of a tungsten TES on a μsec timescale. In the aluminum, Cooper pairs are only broken by phonons with energy greater than twice the bandgap energy $\gtrsim 340\,\mu\mathrm{eV}$; except for thermal phonons from high-energy events which are directly absorbed by the TES, instead of the aluminum fin, only athermal phonons are detected. The sensor geometry has been designed to maximize the phonon collection [77, 202, 203]. The transition-edge sensors in the SuperCDMS detectors are voltage-biased in their superconducting state to take advantage of Joule heating, where the electrical current produces heat. The crystal is cooled so the TES is held at its critical superconducting-transition temperature where the resistance varies strongly as a function of temperature. This regime is characterized by zero resistance below the superconducting temperature and a narrow transition window to normal, ohmic resistance. Electro-thermal feedback keeps the temperature close the critical temperature T_c as shown in the right panel of **Fig. 1.12**. In the superconducting phase transition (purple), quasi-particle byproducts diffusing from the aluminum deposit energy to the tungsten TES. Then, the TES resistance sharply increases when heated to the normal resistance region (red). For small energy depositions, the resistance increases while the voltage is held constant, so the current and the temperature decrease. Conversely, heat removed from the TES decreases its resistance and the resulting current increase will heat the device back to it's nominal superconducting-transition temperature and resistance; this electro-thermal feedback effect stably biases the TES in its superconducting-transition state.

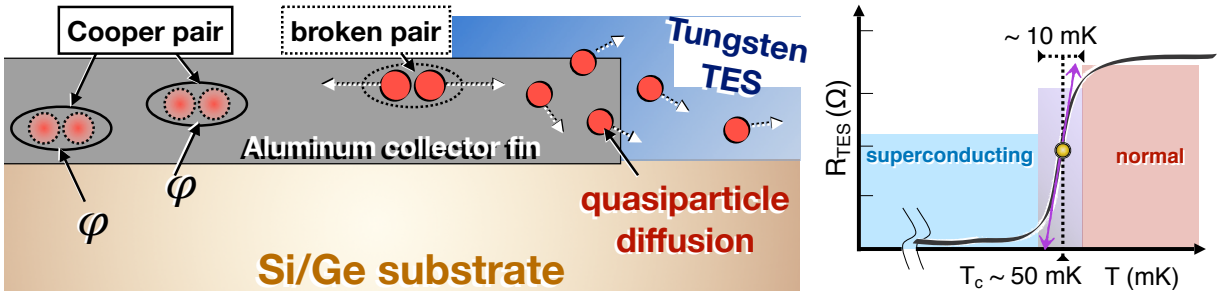

Figure 1.12: Left: Heuristic diagram of Ge/Si detector with superconducting aluminum collector fin and tungsten TES which collect and measure phonons. Athermal phonons (φ) enter the aluminum, break Cooper pairs into quasiparticles which then diffuse to the tungsten TES depositing energy and heating the sensor. **Right:** Resistance versus temperature for the tungsten TES. The TES is voltage biased to keep the resistance near the superconducting phase transition (purple) near the critical temperature $T_c \sim 50\,\mathrm{mK}$. When energy is deposited to the TES, the temperature and resistance rise sharply to the normal resistance region (red) leading to a measurable change in the current passing through the sensor. In turn, the current through the sensor is reduced to keep the voltage constant, and the temperature decreases back to T_c. This occurs more quickly than if the heat were to passively dissipate. If the TES temperature decreases to the superconducting resistance region (blue), the current through the sensor will increase, raising the TES temperature. This returns the sensor to its phase transition at the critical temperature resulting in electrothermal feedback which gives the sensor excellent timing information for the athermal phonons produced by scatters in the substrate.

Electron recoils in Si (Ge) will tend to free one electron-hole ($e^- h^+$) pair per 3.8 (3.0) eV deposited, so the $e^- h^+$ pair creation energy $\varepsilon_{eh} \sim 3.8$ (3.6) eV [204, 205]. Then, the bias voltage applied to the detector causes the electron hole pairs to drift to towards the sensors. These charge carriers accelerate to a terminal drift velocity $v_{eh} \sim 10^6\,\mathrm{cm/sec}$ in $\lesssim 1\,\mathrm{ns}$. As the charge carriers drift, the ionization electrodes sense the image charges, as governed by the Shockley-Ramo theorem [206, 207]. The charge carriers measured by the ionization sensors have an energy

$$E_{\mathrm{Q}} = N_{eh} \cdot \varepsilon_{eh} \tag{1.4.3}$$

where N_{eh} is the number of electron-hole pairs produced and ε_{eh} is the $e^- h^+$ pair creation energy. As the electric field does work $W = e\,V_{\mathrm{b}}$ to drift the charge carriers, a population of cerenkov-like athermal phonons are loosed and sensed in addition to the prompt phonons.

So phonons are produced in (at least) three ways in the detectors. When energy is deposited to the substrate, along with freeing ionization

$$N_{eh} \equiv E_{\mathrm{Q}}/\varepsilon_{eh} \tag{1.4.4}$$

electron-hole ($e^- h^+$) pairs, much of the energy goes into producing *recoil* phonons. Under the influence of the applied electric field, *Neganov-Trofimov-Luke* (NTL) phonons are produced as the charge carriers are drifted toward the detector surface [208--210]. The charges interact with lattice sites as work is being done to move them through the crystal, which releases NTL phonons. The energy of these phonons generated is proportional to the bias voltage V_{b} of the detector, the total

energy of the NTL phonons

$$E_{\mathrm{NTL}} = N_{eh}\, e\, V_{\mathrm{b}} \equiv E_{\mathrm{Q}} \frac{e\, V_{\mathrm{b}}}{\varepsilon_{eh}} \tag{1.4.5}$$

where e is the electron charge. Finally, *recombination* phonons are produced when charge carriers recombine and inject the band gap energy to the lattice. This can occur throughout the crystal at lattice defects, but due to the purity of the crystal, most recombination phonons are produced at the detector surfaces. Since all the energy of the event eventually goes into the phonon system, neglecting energy lost to bulk lattice defects and surface losses, the total phonon energy is

$$E_{\varphi} = E_{\mathrm{R}} + E_{\mathrm{NTL}} = E_{\mathrm{R}} + E_{\mathrm{Q}} \frac{e\, V_{\mathrm{b}}}{\varepsilon_{eh}}. \tag{1.4.6}$$

Electromagnetic backgrounds (γ's, β's, μ's) from external radiation and material contamination tend to interact with electron shells of the targets producing electron-recoil backgrounds. On the other hand, neutrons scatter off nuclei, as is expected for WIMPs, producing nuclear recoils. Particle scattering in the crystal will free charge carriers producing an amount of phonons that is characteristic to the recoil type. The energy in the recoil phonons is proportional to the energy deposited by the scattering particle; a useful form of discrimination lies in the partition between the ionization and athermal phonons produced during the initial energy deposition and the charge carrier drifting. Through a process called quenching, nuclear recoils (between$\sim$ 10–100 keV) are known to produce ionization roughly 4$\times$ less efficiently than electron recoils depositing the same energy, which is discussed in **Chapter 2**. For equal energy deposition nuclear recoils produce fractionally more phonons than electron recoils. The charge production at the scattering site is commonly parametrized with a quantity called the ionization yield

$$\mathcal{Y} \equiv E_{\mathrm{Q}}/E_{\mathrm{R}} \tag{1.4.7}$$

and generally, the fraction of total prompt energy deposited to the ionization, helps to identify the type of recoil. For the (iZIP) detectors which measure the ionization, the ionization yield

$$\mathcal{Y} = N_{eh} \cdot \varepsilon_{eh}/E_{\mathrm{R}}. \tag{1.4.8}$$

The yield for electron recoils in SuperCDMS detectors is assumed to be identically equal to one, since no energy is initially deposited to the phonon system. Combining Eqns. 1.4.8 and 1.4.6, the total phonon energy

$$E_{\varphi} = E_{\mathrm{R}} + E_{\mathrm{Q}} \frac{e\, V_{\mathrm{b}}}{\varepsilon_{eh}} \equiv E_{\mathrm{R}} \left(1 + \mathcal{Y} \frac{e\, V_{\mathrm{b}}}{\varepsilon_{eh}}\right). \tag{1.4.9}$$

By measuring the ionization from the charge carriers, and measuring the total amount of the athermal phonons during a scattering interaction, the recoil energy, type, and interaction position

may be reliably reconstructed. The recoil energy of an event

$$E_{\mathrm{R}} = E_{\varphi} - E_{\mathrm{Q}} \frac{e\, V_{\mathrm{b}}}{\varepsilon_{eh}} \tag{1.4.10}$$

is then estimated by a combination of the phonon and ionization signals by subtracting the NTL energy E_{NTL} from the total phonon energy E_{φ}. The precision of the recoil energy estimate depends on both the phonon energy resolution σ_{φ} and the ionization energy resolution σ_{Q}. The ionization yield

$$\mathcal{Y} = \frac{E_{\mathrm{Q}}}{E_{\mathrm{R}}} = \frac{E_{\mathrm{Q}}}{E_{\varphi} - E_{\mathrm{Q}} \frac{e\, V_{\mathrm{b}}}{\varepsilon_{eh}}} \tag{1.4.11}$$

in SuperCDMS style iZIP detectors. The high-voltage detectors won't have ionization electrodes and since the detectors have a large bias, the phonon signal will be dominated by the NTL phonons. These detectors cannot reliably estimate an event's recoil energy, but the phonon signal will be proportional to the event's ionization.

The drifting electron-hole ($e^{-}h^{+}$) pairs produce NTL phonons before they terminate on the electric-field lines from the bias voltage V_{b}. The left panel of **Fig. 1.13** shows the phonon channel readout configuration for the HV (top) and iZIP (bottom) detectors. The high voltage (iZIP) detectors have two (one) outer channels, 3 (4) middle channels, and a center channel on each face. The middle channels, are rotated by 60 (45) degrees on the opposite faces for increased azimuthal (angular) position reconstruction. The outer channels allow radial position reconstruction to discriminate against side-wall events, which may be dominated by radon exposure and daughter plate-out. The SuperCDMS SNOLAB iZIP detectors will have better position resolution due to the increased number of phonon channels (6) per face over the 4 phonon channels on the SuperCDMS Soudan iZIPs; see *e.g.* [77] for details on optimizing the sensor design. The right panel of **Fig. 1.13** shows the equipotential lines (blue) and electric field lines (red) resulting from the grounded phonon sensors (shown as 0) and interleaved with ionization electrodes at alternating potentials ($\pm V_{\mathrm{b}}$). The sensors are arranged such that charge carriers ($e^{-}h^{+}$) freed near the surface (left star, gray) of the detector will drift to the same side, whereas bulk events (right star, blue) will produce symmetric signals; a similar design is employed by EDELWEISS [211]. The mix of detector types (HV and iZIP) and targets planned for the experiment, as well as flexible detector operation, will allow us to maximize the low-mass WIMP sensitivity with the HV detectors, and characterize the experimental backgrounds with the iZIP detectors. We expect to perform robust background subtraction for the High-Voltage detectors, which lack ER/NR discrimination. To achieve these goals, the detectors will be operated at two bias voltages: $V_{\mathrm{iZIP}} \sim 4\,\mathrm{Volts}$ (iZIP mode), and $V_{\mathrm{HV}} \sim 100\,\mathrm{Volts}$ (High Voltage/CDMSLITE mode). The two detection modes, which I describe here, have complementary strengths which will allow a considerable science reach [75].

The interleaved Z-sensitive Ionization and Phonon mediated (iZIP) detectors will sense the drifted charge carriers with ionization sensors instrumented with charge-integrating amplifiers. The

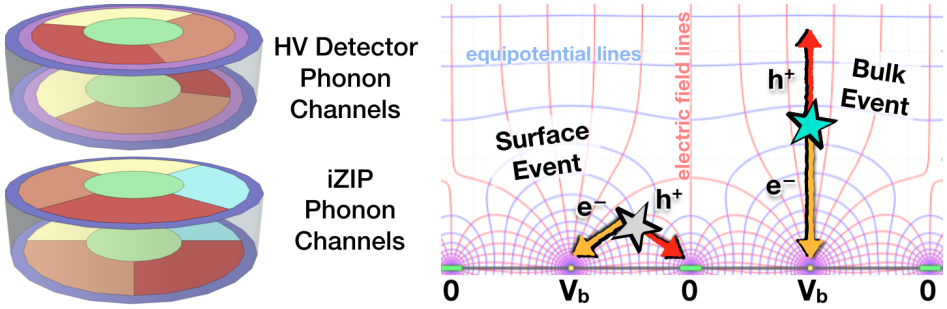

Figure 1.13: Left: Phonon sensor layout for the HV (top) and iZIP (bottom) detectors which are 33 mm thick and 100 mm in diameter. The channels are designed to reconstruct an event's radial, azimuthal, and z-position. On each face, the HV (iZIP) detectors have two (one) outer-ring channels, 3 (4) middle channels, and a center channel. The bottom-face channels of the HV (iZIP) detectors are rotated 60 (45) degrees to provide a finer azimuthal position resolution, compared opposite-side-aligned channels. The outer channel(s) at the detectors' edge allow the radial position to be reconstructed with a high efficiency so that side-wall events can be vetoed; the HV detectors have two outer channels to further improve the radial fiducialization. The sensitivity to the azimuthal position lies in the interleaved geometry of the ionization and phonon sensors. **Right:** For the iZIP detectors, the electric-field lines (red) and equipotential lines (blue) are produced by the grounded phonon sensors (0 V) interleaved with ionization electrodes (yellow dot) at alternating potential ($\pm V_\mathrm{b}$, $\pm V_\mathrm{b}$, ...) of the interleaved ionization electrodes (yellow dot) are shown. The bias V_b of the sensors are positive or negative for a given detector face (top or bottom). An event's position-dependent phonon signal asymmetry allows the detector to be fiducialized along the z-direction to identify and reject surface events occurring far from the bulk of the detector. Surface events (left ★, gray) produce one-sided signals, and bulk events (right ★, blue) produce roughly symmetric signals.

detectors will also measure the athermal phonons produced by the initial recoil and measure the NTL phonons produced by the charge carriers in transit to distinguish the (electron or nuclear) recoil type, and reconstruct the event's energy and position. The iZIP detectors are designed to reconstruct the event position from the ionization signal more than the phonon signal with sensitivity to WIMP masses $m_\chi > 3\,\mathrm{GeV}/c^2$. There are two concentric ionization channels on each face of the iZIP detectors. An advantage of the iZIP detectors is that events in the bulk of the detector material will have nearly symmetric ionization signals on the detector faces, whereas the ionization produced by surface events will be collected by only a single side of the detector. Vetoing these surface events with a charge symmetry requirement will allow us to reject electron recoils from low-energy beta decays and Pb-206 nuclear recoils which both arise from Pb-210 surface contaminants [198].

The phonon energy resolution $\sigma_\varphi \approx 50\,\mathrm{eV}$ is a few times smaller than the ionization resolution $\sigma_\mathrm{Q} \approx 200\,\mathrm{eV}$, so the yield-based discrimination quality is ionization limited. To retain the ionization yield discrimination, the NTL phonon signal must not dominate the prompt phonons produced by the initial recoil. By using the smallest possible voltage bias to ensure the total ionization collection from events in the detector bulk, $V_\mathrm{b} \lesssim 2\,\mathrm{V/cm}$, the recoil energy integrity is minimally reduced by the correlation between the ionization and recoil energy measurements. The ionization signal is used to estimate the NTL phonon contribution

$$E_\mathrm{NTL} \equiv N_{eh}\, e\, V_\mathrm{b} \equiv (E_\mathrm{Q}/\varepsilon_{eh})\, e\, V_\mathrm{b} = \mathcal{Y}\frac{e\,V_\mathrm{b}}{\varepsilon_{eh}} E_\mathrm{R}. \tag{1.4.12}$$

The voltage bias of the iZIPs is such that the energy of the charge carriers

$$e\,V_\mathrm{b} < \varepsilon_{eh} \approx 3\text{–}4\,\mathrm{eV} \tag{1.4.13}$$

is less than the electron-hole pair creation energy. In this case, the NTL phonons do not dominate the total phonon signal. As a result, these detectors have a higher energy threshold $E \approx 1\,\mathrm{keV}$ than the HV design. A strength of the iZIP detector design is that for recoil energies $E_\mathrm{R} > 5\,\mathrm{keV}$, the ionization-yield-based NR/ER discrimination is $\times 10^6$. As a result, the iZIP detectors are expected to be fairly insensitive to variations in detector response and backgrounds. Due to the excellent background discrimination demonstrated in previous detector generations [198], these detectors are expected to operate essentially background-free for the first 5 years of operation [74].

Another set of (high-voltage) detectors will be operated with $\sim 10\times$ larger voltage bias than the iZIPs, to take advantage of the increased NTL phonon production. This will increase the WIMP sensitivity over the iZIP design to WIMP masses $m_\chi < (3\text{–}5)\,\mathrm{GeV}/c^2$. Initial studies of the high-voltage detector performance in CDMSlite-mode are described in Refs. [199, 200, 212]. Unlike the CDMS *low ionization threshold experiment* (CDMSlite) detectors, the SNOLAB HV detectors faces will have a symmetrically applied bias to improve on the one-sided readout of the old detectors, and to improve the uniformity of the electric field. With two-sided readout and field conditions, an event's z-position may be more effectively reconstructed [75, 77, 106]. The phonon sensor geometry of the high-voltage detectors has been optimized exclusively for athermal phonon sensitivity. These detectors lack ionization sensors and are operated closer to the design proposed by Neganov, Trofimov, and Luke [208, 213]. By applying a large voltage bias $V_\mathrm{HV} \sim 100\,\mathrm{V}$, the energy of the charge carrier

$$e\,V_\mathrm{b} \gg \varepsilon_{eh} \tag{1.4.14}$$

greatly outweighs the e^-h^+ pair creation energy. The total phonon energy

$$E_\varphi = E_\mathrm{R} + \frac{E_\mathrm{Q}}{\varepsilon_{eh}} e\,V_\mathrm{b} \approx \frac{E_\mathrm{Q}}{\varepsilon_{eh}} e\,V_\mathrm{b} \tag{1.4.15}$$

is dominated by the NTL contribution. When SuperCDMS detectors are operated in this fashion, the phonon signal provides a very high-resolution measure of the event's ionization. Small-scale detectors have demonstrated phonon energy resolution $\sigma_\mathrm{ph} \sim 14\,\mathrm{eV}$ and phonon threshold efficiency $> 95\%$ with sensitivity to single electronic excitations for one e^-h^+-pair [75]. Nuclear recoils produce less ionization than electron recoils of the same recoil energy, so the phonon energy spectrum for ERs will be stretched to higher energies than NRs of equal energy. Electron-recoil backgrounds are expected to be separable from the low-energy nuclear recoils, which will be aided by characterizing the iZIP detector backgrounds. Even so, the WIMP sensitivity of the HV detectors, unlike the iZIP detectors, are expected to be background-limited [74, 106]. Understanding the SNOLAB detector backgrounds will be critical to obtaining the greatest sensitivity.

1.4.2 Detector Backgrounds

SuperCDMS will be subject to two main categories of background during operation: those appearing in the **bulk** of the detector, and those near the detector **surfaces**. The material radiopurity of the detector substrate is crucially important for SuperCDMS SNOLAB because the dominant background for the HV detectors is expected from the internal contamination of tritium, Si-32, and activated germanium. Cosmic neutron, proton, and muon exposure of the detector before and during operation will produce a population of tritium (^{3}H) from spallation in both germanium and silicon detectors. Tritium is a long-lived ($t_{1/2} = 12.3\,\text{yrs}$) low-energy ($Q \approx 18.6\,\text{keV}$) beta emitter. Due to its low endpoint energy, tritium contamination is difficult to measure, so reducing the potential exposure to cosmic rays is important to prevent this background. The silicon detectors face another background from the production via cosmic-ray spallation of Si-32 in the upper atmosphere [114--116]. . This beta-emitting isotope is long lived ($t_{1/2} \approx 172\,\text{yrs}$), with an endpoint energy $Q \approx 225\,\text{keV}$. The daughter of Si-32, ^{32}P also beta-decays ($Q \approx 1.71\,\text{MeV}$) over a much shorter period ($t_{1/2} \approx 14.3\,\text{days}$). These isotopes are expected to be the dominant source of bulk electron recoils in the silicon HV detectors, so characterizing their rate in the iZIPs will be important for background subtraction efforts [74, 106].

The germanium detectors, when exposed to high-energy cosmic-ray secondaries, will become activated with radioisotopes ^{68}Ge, ^{68}Ga, ^{65}Zn, ^{73}As, ^{57}Co, ^{55}Fe, ^{54}Mn, and ^{49}V. These isotopes decay via K-, L-, or M-shell internal electron conversion with mean lifetimes long enough to provide a background source. These decays are expected to be vetoed with energy cuts around the 24 sharp spectral peaks with very high efficiency due to the detector's exceptional energy resolution.

Some material near the detectors, *e.g.* the copper detector-housing and nickel in the mu-metal shield, may undergo cosmic activation while they are at sea level. Both the detector tower mechanical assembly and the cryostat canisters (SNOBOX) are made of copper whose cosmogenic activation is dominated by $^{57/58/60}$Co. The lead, high-density polyethylene (HDPE), and copper dominate the mass of the construction materials. The lead and HDPE are not expected to pose significant backgrounds and, as a result, do not have the same exposure requirements as the copper and the detectors. The copper and germanium used to build the apparatus are stored underground to reduce the material activation from cosmic-rays.

The contamination of near-detector material such as the detector hardware, cryostat, and shielding, primarily from the ^{238}U and ^{232}Th decay chains, will pose backgrounds. Both of these isotopes may be introduced to materials during manufacturing and have complex decay spectra, whose end-of-chain daughters are already described in **Section 1.3.2**. Both ^{40}K and ^{60}Co are naturally found in the bulk of a wide range of materials, though neither have radioactive daughters. The isotopes will may produce single-scatter electron-recoil backgrounds. Both ICP-MS and HPGe detectors are used by the collaboration to measure the bulk contamination of the apparatus materials.

Radon daughters and dust, bearing U/Th and especially K, in the air will land on material

surfaces. The subsequent radon daughter decay may weakly implant the daughters onto surfaces which do not have a direct line-of-sight to the detectors–radon daughters on line-of-sight surfaces are discussed further below. These surfaces will accumulate the long-lived Pb-210 which has a complex decay spectrum including soft X-rays, alphas, and low-energy betas. The daughter of Pb-210, Bi-210, has a high-energy beta which can produce penetrative Bremmstrahlung X-rays. The daughter of Bi-210, Po-210, will alpha decay which can free neutrons from (α, n) reactions on C-13 present in the hydrocarbons making up the polyethylene shielding. As a result, the exposure of this shielding to the ambient radon concentration $C \approx 130\,\mathrm{Bq/m^3}$ [140] and dust at SNOLAB needs to be restricted.

Gammas and neutrons from radioactive sources in the cavern walls may pass through the shield layers and singly scatter in the detectors producing electron or nuclear recoils. The cavern background is modeled using the gamma spectra from ^{40}K and ^{238}U and ^{232}Th–assuming secular equilibrium– and uniformly in the bulk of the walls and neutrons from ^{238}U spontaneous fission and (α, n) reactions from U- and Th-alphas in the wall. Backgrounds from the gamma sources are expected to be subdominant [74, 106].

Another background comes from radon progeny decays within the lead gamma-shield from radon in the SNOLAB cavern. Due to the penetrative nature of high-energy γ's, the gamma decay of ^{214}Bi/Pb within the lead gamma-shield will produce electron-recoil backgrounds in the bulk of the detectors that would be dominant without mitigation. **Fig. 1.10** shows the lead gamma shielding surrounded by an aluminum enclosure that will be purged with low-radon boil-off nitrogen gas. The radon concentration in the cavern environment $C \approx 130\,\mathrm{Bq/m^3}$ [140] is well above the concentration goal $C_{\mathrm{goal}} = 1\,\mathrm{Bq/m^3}$. This goal for radon in the shielding was determined so that the γ-induced single-scatter electron recoil rate would be less than 2% of the expected total background rate. **Chapter 3** describes radon diffusion measurements of proposed gasket materials sealing the SNOLAB radon-purged lead shielding and **Chapter 5** describes measurements of radon emanation measurements for the same gaskets, the implications on the radon concentration inside the radon purge barrier, and factors leading to the choice of gasket for the radon barrier.

SNOLAB has ~ 6 km.w.e of overburden which reduces the cosmic-ray muon flux by $\times 10^{4\text{–}5}$ [106, 192], secondaries by $\times 10^{4\text{–}5}$ [106, 192], but does not completely mitigate them. Muons may pass through the detector shielding, which does not include an active liquid scintillating muon veto, and directly deposit energy to the detectors causing electron-recoil backgrounds. The lead shield may free high-energy neutrons via spallation, causing nuclear-recoil backgrounds. Most of the cosmic-ray secondaries will produce multiple scatters in the detectors and so are expected to be effectively vetoed. The neutron background contribution to HV detectors from cosmic rays will not be a significant fraction of the total nuclear-recoil background rate [74, 106].

Especially with potential future upgrades, SuperCDMS SNOLAB may be sensitive enough to measure coherent solar neutrino scattering on germanium and silicon nuclei. The ^{8}B decay at the end of solar fusion reaction in the pp-III chain produces a neutrino via ${}^{8}_{5}\mathrm{B} + p \rightarrow {}^{8}_{4}\mathrm{Be} + e^- + \nu_e$.

These ν's may pass through the Earth and coherently scatter causing nuclear-recoil backgrounds; these events will then become a limiting background for the experiment [74]. The background rates in the detectors have been estimated using theoretical values for the neutrino energy spectrum [214] and flux [215], and the coherent neutrino-nucleus scattering cross-section [216]; this background is not expected be significant.

Additional backgrounds are from sources producing events on or even very near the detectors surfaces. These are primarily from detector and copper housing exposure to Rn-222 and subsequent daughter plate-out leading to a host of background types. Sources of radiation that may deposit energy on or near the detector surfaces/faces can be dangerous. Backgrounds of this nature depend on the ^{222}Rn exposure of the detectors, their copper housing, and the readout electronics. This exposure can occur during fabrication, testing, as well as before and during their final deployment. Since radon is so diffusive, and relatively short lived, surfaces not protected from the ambient radon concentration may suffer from radon-daughter plate-out. The subsequent daughter decays may cause the nucleus to become shallowly implanted in the material surface. The decay spectrum of long-lived Pb-210 has two low-energy betas ($Q \approx 17\,\text{keV}$, $Q \approx 64\,\text{keV}$) and a 46 keV gamma. The high energy beta decay ($Q \approx 1.1\,\text{MeV}$) of Bi-120 and the $\sim 5\,\text{MeV}$ alpha emitted by Po-210 are not in danger of being misidentified as a nuclear recoil; however, the accompanying 103 keV full nuclear-recoil energy from Pb-206 may leak into the signal region. Events with coincident energy deposition in adjacent detectors, unlike those aimed into the sidewall or detector housing, will be effectively rejected.

Each background source type described above has been simulated passing through the SuperCDMS shielding geometry using GEANT4. The shielding was generally optimized with some rules of thumb. The irreducible material contamination of the detectors should dominate the single-scatter electron-recoil background rate over the ERs from radon-induced gammas within the shielding. The lead gamma shielding was designed so that the background rate the from ^{40}K, ^{238}U, ^{232}Th will be $< 1\,\text{events}/(\text{kg}\cdot\text{keV}\cdot\text{yr})$ in the Ge HV detectors. The NR rate from fast neutrons emitted from the cavern walls should be less than the expected rate from the unavoidable ^{8}B solar neutrino flux. After determining the optimum shielding geometry from preliminary simulations, the primary background sources above were simulated to obtain the expected event rate [74]. The energy depositions to the simulated detectors from each of the backgrounds above were recorded. Events depositing energy within the HV (iZIP) detector region of interest 3 eV–2 keV (2 keV–50 keV) are tallied, and the resulting energy spectra are scaled to conservative values.

The differential event rate in silicon high-voltage detectors is shown as a function of recoil energy for each of the background sources described above in **Fig. 1.14**. The energy spectra are shown before (left) and after (right) applying event selection criteria cuts. The basic event selection criteria for iZIP detectors include a fiducial-volume definition based on phonon and ionization signals, both radial and z-position. The electron recoil rejection is $\gtrsim 10^6$ for recoil energies $> 2\,\text{keV}$. Given the extensive material selection and assay campaign for the experiment, the electron-recoil background

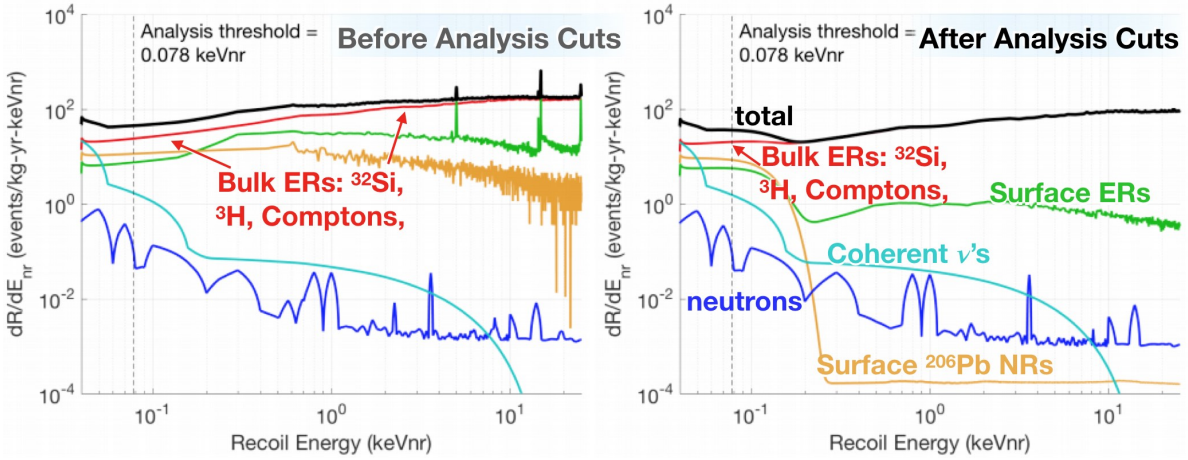

Figure 1.14: Differential background rate in the Silicon HV detectors as a function of recoil energy (converted to nuclear-recoil equivalent $\mathrm{keV_{NR}}$) before (left) and after (right) analysis cuts for the sources described in the text. The analysis threshold $E_{\mathrm{thr}} = 78\,\mathrm{eV_{NR}}$ is shown (vertical dashed). Bulk electron recoils (single-scatter Comptons) from external gammas, and bulk silicon-32 and tritium decays, are the dominant background (red). The other backgrounds are surface electron recoils (green), coherent neutrino scatters (light blue), neutrons (blue), and surface ^{206}Pb nuclear recoils (yellow). Figures adapted from [74].

leakage rate is assumed to be 0 above 2 keV for the entire exposure. Below this energy, the ionization-yield-based discrimination worsens due to the increasing nuclear- and electron-recoil yield-band widths which are expected to overlap significantly below this energy [88, 198]. The energy-dependent event-selection efficiency are applied to the simulated spectra of background events the silicon high voltage detector spectra are shown before (left panel) and after (right panel) cuts in **Fig. 1.14**. The rate of surface Pb-206 (orange) recoils is reduced by $> 10^3$ for recoil energies $E_{\mathrm{R}} > 0.3\,\mathrm{keV}$ after the cuts, due to selection efficiency of surface events. Nuclear-recoil backgrounds from neutrons (dark blue) and neutrinos (cyan) can't be removed by analysis cuts. The leakage rate of surface electron recoils (green) and Pb-206 nuclear recoils (yellow) can be reduced by fiducial volume cuts. The bulk electron-recoil backgrounds from Si-32 and tritium are the dominant background for the silicon HV detectors; these events cannot be removed by analysis cuts–though perhaps with strong a background model may be constructed with iZIP measurements so that we could implement background subtraction for the HV detectors. The nominal background spectrum (black) is used to compute the overall WIMP-nucleon exclusion sensitivity. The background spectra, after applying the event selection criteria, is used to calculate the WIMP-nucleon sensitivity using a large number of simulated set of events determined by the exposure. The expected WIMP spectrum, for a given WIMP mass under the standard halo model [56] and assuming spin-independent WIMP-nucleon interactions applying the event selection efficiency. Initially, SuperCDMS SNOLAB will consist of ten Ge iZIPs, two Si iZIPs, eight Ge HV, and four Si HV detectors. The excluded interaction cross-sections are calculated with the optimum interval method to determine the 90% C.L. upper limits [217, 218] for each detector type using the simulated spectra from pseudoexperiments of their respective backgrounds and the expected WIMP event spectra.

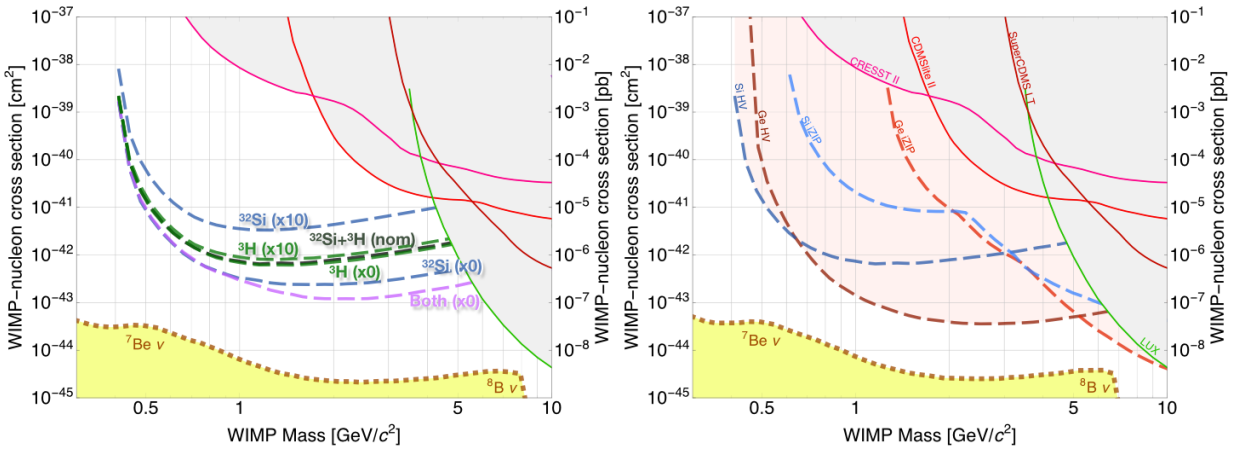

Figure 1.15: Projected WIMP-nucleon sensitivity as a function of WIMP mass for SuperCDMS SNOLAB under standard halo assumptions [56], determined from the optimum interval method [217, 218]. **Left:** with nominal H-3 Si-32 background assumptions (black dashed). Green dashed lines show the effect of varying the H-3 levels from zero (*bottom*) to 3 times (*top*) the nominal exposure with other backgrounds constant. The blue dashed lines correspond to Si-32 levels from to zero (*bottom*) to 20 times (*top*) the nominal bulk activity with nominal H-3 background level. The purple dashed line is the best possible sensitivity corresponding to zero ^{3}H and ^{32}Si contamination; this curve is limited by the irreducible gamma activity from material surrounding the detectors resulting in single-scatter electron recoils. The solid lines, corresponding to published sensitivity limits [199, 200, 219, 220], are labeled in the right image. **Right:** Projected SuperCDMS SNOLAB WIMP-nucleon exclusion sensitivity curves as a function of WIMP mass, assuming nominal backgrounds for the Si (blue) and Ge (red) iZIP and HV detectors. The solid lines are exclusion limits from CRESST-II [219], SuperCDMS [199, 200], and LUX [220]. The dark matter discovery limit which represents the coherent elastic scattering cross-section from ^{8}B solar neutrinos (dotted orange line) from [221]. Figures from [74].

1.4.3 Projected WIMP Sensitivity

The projected WIMP-nucleon sensitivity is shown as a function of WIMP mass in **Fig. 1.15**. The left panel shows the sensitivity of the silicon HV detectors after a two-year exposure with several Si-32 and tritium bulk contamination background level assumptions. The *lowest, pink* curve ('Both') assumes no electron-recoil backgrounds from these sources; in this case, the dominant background is from Compton scatters from external gammas. The nominally assumed bulk rates are shown *middle, black*. The green (blue) dashed lines correspond to H-3 (Si-32) contamination at x0 *bottom* to x3 (x10) *top* the nominal levels. The right panel of **Fig. 1.15** shows the projected sensitivity for all detectors types for a two year exposure, and exclusion curves from earlier CDMSlite measurements [199, 200], CRESST [219], and LUX [220]. The spin-independent WIMP-nucleon cross-section exclusion limit is determined by the optimum interval method based on a single energy interval of the measured spectrum [217, 218]. The kinks in the iZIP detector exclusion curves result from a switch in this optimum energy interval arising from increased backgrounds below 2 keV. No background subtraction is performed with the optimum interval method, so the resulting WIMP sensitivity is conservative. For further discussion on the dependence of the WIMP sensitivity on input parameters such as cosmogenic backgrounds or the ionization yield parametrization, *c.f.* Sec. VII of [74]. The WIMP sensitivity of the Si and Ge high-voltage detectors will be limited by their electron rate backgrounds from bulk silicon and tritium contamination, respectively. The

iZIP detectors will have excellent ionization-based event discrimination, so their WIMP sensitivity is not expected to be limited by the ER background rate; these detectors are expected to run background-free for up to 5 years. However, the HV detectors will not be background-free, though electron/nuclear recoil discrimination may be regained by incorporating charge quantization and iZIP measurements into a background model to subtract from the measured spectrum, to improve the WIMP sensitivity beyond that published in Ref. [74]. With research and development on detectors with lower thresholds–such as those characterized in [75]–and backgrounds, SuperCDMS SNOLAB aims to reach the solar neutrino floor.

1.5 Arrangement of this Thesis

The general focus of this thesis is commissioning and characterizing sensitive detectors to measure very low levels of radon to identify and reduce radon-induced backgrounds for the SuperCDMS SNOLAB Dark Matter experiment. Focus is also given to describing progress made on a prototype screener designed to mitigate surface backgrounds relevant to SuperCDMS SNOLAB and future detector generations. **Chapter 2** discusses the determination of the nuclear recoil scale in CDMS II dark matter detectors as described in the recently published Ref. [2]. I describe the impacts on ionization yield from nuclear recoil energy rescaling, measured with a ^{252}Cf neutron source and compare the results with recent measurements in the literature. **Appendix A** includes tables and plots from the analysis described here not included in the paper [2]. **Chapter 3** describes radon diffusion and measurements of gaskets for the SuperCDMS SNOLAB radon purge barrier. **Chapter 4** describes the ^{222}Rn emanation system at SDSM&T, radon transfer method for placing emanated radon into a detection vessel, the detector backgrounds, transfer and collection efficiency measurements, and improvements and upgrades made to the system, and concludes with a description of the improved gas transfer panel design based on the finding in this chapter. **Chapter 5** describes radon emanation measurements of the same gaskets described in **Chapter 3**, and and includes implications of the gasket materials on the radon concentration and the selected gasket. **Chapter 6** describes an ultra-low-background surface screening time projection chamber: the BetaCage. I describe the superior detector design which makes it a significantly better screener than commercially available systems. I report the main backgrounds and background discrimination techniques, and the detector's sensitivity to alphas and low-energy betas. I describe the characterization of the radon trapping of the gas panel which will reduce the radon-induced backgrounds to sub-dominant levels. I also estimate the detector sensitivity to thin silicon samples bearing surface and bulk Si-32 radioimpurities at the level DAMIC reported. In **Chapter 7**, I discuss a prototype time projection chamber in operation currently undergoing commissioning. I describe the installation of the detector, the data readout, the early calibration data taken, and planned improvements.

Chapter 2

Nuclear-Recoil Energy Rescaling of CDMS II Silicon Detectors

The Cryogenic Dark Matter Search (which includes CDMS and CDMS II) was an early incarnation of SuperCDMS Soudan (decommissioned as of Dec. 2015) and SuperCDMS SNOLAB (under construction as of 2019), designed to measure low-energy nuclear recoils resulting from WIMP scattering in high-purity silicon and germanium semiconductor crystals operated at $\lesssim$50 mK. The detectors used in this CDMS II generation were simpler than the iZIP and HV designs described in **Section 1.4**. In CDMS II, each crystal was instrumented to simultaneously measure the electron-hole pairs (ionization) and athermal phonons created by particle interactions within the crystal [222]. A WIMP, or a neutron, may scatter off a nucleus producing a nuclear recoil (NR), while most other interactions produce an electron recoil (ER). Accurate determination of an event's energy requires a systematic calibration of the recoil energy scale. This energy calibration is generally straightforward for electron recoils due to the availability of a variety of spectral lines from radioactive sources over a wide range of energies. The calibration for nuclear recoils is more difficult. CDMS II used a ^{252}Cf neutron source to perform nuclear-recoil calibrations, and the spectrum of recoil energies in CDMS II detectors resulting from exposure to this source decreases quasi-exponentially with increasing energy and is nearly featureless. For CDMS II detectors, knowledge of the nuclear-recoil energy scale to within $\sim$10% is sufficient to accurately interpret WIMP-search results for WIMP masses greater than a few tens of GeV/c^2, as shown in *e.g.* Sec. 9.2 of Ref. [223]. For lower WIMP masses, however, a more accurate determination of the energy scale is important for a robust comparison of results from different experiments, particularly in light of interpretations of data from several experiments as possible evidence for a low-mass ($\lesssim$10 GeV/c^2) WIMP [224--227].

This chapter describes the determination of the nuclear-recoil energy scale for CDMS II silicon detectors and the implications on the ionization yield produced by nuclear recoils at very low temperature and bias voltage. It draws heavily from (in many cases word-for-word) the previously published work [2], but offers a more detailed description of the analysis and results. A large number

of graduate students, including Scott Fallows [223], Kevin McCarthy [228], Dave Moore [229], and Ray Bunker [67], performed different aspects of the work over a ∼10 year period. Here I describe the CDMS II detectors (**Section 2.1**) and calibrating the ionization and phonon energy scale for electron recoils (**Section 2.2**). **Section 2.3** describes nuclear-recoil calibration data-taking, the data selection cuts, and complications with the data that make the determination of the nuclear-recoil energy scale difficult. *In situ* measurements of elastic neutron scatters in these detectors from a ^{252}Cf source are compared to Monte Carlo simulations of recoiling nuclei in the detectors, which draws on studies by Ray Bunker of the nuclear-recoil spectrum in silicon [2, 67]. **Section 2.4** describes a corrected estimate of the neutron flux incident on each of the detectors which optimizes the agreement between measured and simulated recoil spectra [223]. **Section 2.5** describes the determination of a re-calibrated nuclear-recoil energy scale using spectra from Monte Carlo simulation in the silicon detectors. **Section 2.6** describes the implications on the ionization yield and collection efficiency from applying the improved nuclear-recoil scale to the nuclear-recoil calibration data in CDMS II detectors, as originally described in my CDMS II internal note [230]. **Section 2.6.1** describes my parameterization of a small correction to the mean ionization yield of nuclear recoils due to neutron multiple scattering in the silicon detectors derived by Dave Moore [231]. **Section 2.6.2** describes new ionization yield measurements [232, 233] in silicon and the determination of the average ionization yield in the CDMS II silicon detectors. **Section 2.6.3** describes the ionization collection efficiency of nuclear recoils in silicon and the consistency with recent low-energy ionization yield measurements. **Section 2.7** describes the impact of the improved nuclear-recoil energy scale on the originally published constraints on the WIMP-nucleon spin-independent cross section from the analysis of the final exposure of the silicon detectors [227].

2.1 CDMS II Detectors

The final configuration of CDMS II contained 11 silicon and 19 germanium Z-sensitive Ionization- and Phonon-mediated (ZIP) detectors [194] as shown in (the left panel of) **Fig. 2.1**. Each detector was photolithographically patterned with sensors on both flat faces: two concentric ionization electrodes on one face and four independent phonon sensors on the opposite face (middle panel of **Fig. 2.1**). These were arrayed into five ‘‘towers’’, (right panel of **Fig. 2.1**), each containing six detectors following the designation TxZy where x (1–5) is the tower number and y (1–6) indicates the position within the stack (from top to bottom). We focus here on the silicon detectors used in Ref. [227], which were ∼10 mm thick, 76 mm in diameter, with a mass of ∼106 g each. Of the eleven silicon detectors, two were excluded due to wiring failures leading to incomplete ionization collection, and a third was excluded due to unstable phonon channel response.

The ionization electrodes were biased to 4 V with respect to the phonon electrodes, creating an electric field of 4 V/cm in the bulk of the detector along its z axis [194]. The electrons and holes generated by a particle interaction were separated and drifted across the crystal by the electric field,

Figure 2.1: Left: CDMS II Z-sensitive Ionization- and Phonon-mediated (ZIP) detectors from [234]. **Middle:** Layout of ionization and phonon sensors adapted from [194]. *Top:* Concentric ionization electrodes with a large inner channel $Q_{\rm in}$, and much thinner outer channel $Q_{\rm out}$ which help to fiducialize the bulk of the detector volume where surface backgrounds will not be reconstructed. *Bottom:* Four phonon channels (A, B, C, and D) arranged in quadrants on the ZIP detectors. **Right:** Five detector tower stacks (T1–T5) of six germanium (dark brown) and silicon (light yellow) ZIP detectors adapted from [194]. This analysis includes 8 silicon detectors: `T1Z4`, `T2Z1`, `T2Z2`, `T2Z4`, `T3Z3`, `T4Z1`, `T4Z3`, and `T5Z3`.

generating image currents in the electrodes detected by a JFET-based charge amplifier [235]. By careful neutralization of ionized trapping sites within the crystal with regular exposure to infrared LEDs ("flashing"), the detectors were operated in a metastable state in which trapping of charge carriers in the crystal bulk was low. The ionization collection efficiency for electron recoils was therefore high, despite the relatively modest applied electric field.

In semiconductor devices such as the ZIPs, phonon (φ) energy is generated by three interactions: the initial recoil generates primary phonons, the work done on the charge carriers by the electric field generates Neganov-Trofimov-Luke (or NTL) phonons [208--210], and charge carrier relaxation to the Fermi level at the electrodes generates recombination phonons. When a particle interacts in a ZIP, it deposits a recoil energy $E_{\rm R}$ in the crystal and generates n_Q electron-hole pairs. For electron recoils, this recoil energy $E_{\rm R} = n_Q\epsilon$, where ϵ is the average energy required to create one electron-hole pair.[1] A portion of this energy is stored in the potential energy of the drifting charge carriers and is restored to the phonon system when they relax to the Fermi level at the electrodes, producing recombination phonons.

The work done by the electric field on the n_Q drifting charge pairs results in the Cherenkov-like radiation of an additional population of phonons at near-ballistic energies. These are the so-called NTL phonons which add a contribution

$$E_{\rm NTL} = n_Q(eV_{\rm b}) \tag{2.1.1}$$

to the total phonon signal proportional to the bias voltage $V_{\rm b}$ across the detector. The total phonon energy is therefore $E_\varphi = E_{\rm R} + n_Q(eV_{\rm b})$. It is convenient to express the ionization signal as an

[1] For silicon, $\epsilon = 3.82\,\text{eV}$ above 77 K [236] and is not expected to deviate significantly at lower temperatures.

electron-equivalent energy $E_Q \equiv n_Q \epsilon$ and the total phonon energy as

$$E_\varphi = E_\mathrm{R} + E_Q \frac{eV_\mathrm{b}}{\epsilon} = E_\mathrm{R}\left(1 + y\frac{eV_\mathrm{b}}{\epsilon}\right), \tag{2.1.2}$$

where $y \equiv E_Q/E_\mathrm{R}$ is the ionization yield. With these definitions, an ideal electron recoil has ionization yield $y = 1$. An event's recoil energy is determined by rearranging Eqn. 2.1.2,

$$E_\mathrm{R} = E_\varphi - E_Q(eV_\mathrm{b}/\epsilon), \tag{2.1.3}$$

where E_φ is estimated from the phonon channels and E_Q from the charge channels.

The remainder of the recoil energy is deposited directly into the phonon system as primary phonons. These high-frequency phonons undergo isotopic scattering and cannot travel far from their production sites before down-converting via anharmonic decay [237] into lower-frequency phonons with larger mean free paths, comparable to the thickness of the detector [76]. The lower-frequency ballistic phonons then interact with either the phonon sensors or un-instrumented material at the detector surfaces.

Details of the phonon collection mechanism in SuperCDMS detectors are discussed in Refs. [77, 212, 238]. Past analyses assumed that all three phonon contributions are detected with equal efficiency. This is a plausible assumption because all three mechanisms generally inject energy into the phonon system above the ballistic propagation threshold. All three types down-convert until they become just barely ballistic, so their frequency distributions at the sensors are nearly the same. However, the relative fraction of phonons absorbed by the sensors (compared to other materials) may depend on details of the primary interaction, and even on the relative fractions of primary, NTL, and recombination phonons. Consequently, although the differences are expected to be small, the phonon collection efficiency in CDMS II detectors for nuclear and electron recoils of a given energy need not be identical; this chapter describes measurements of the small difference between these two efficiencies.

2.2 Electron-Recoil Calibration

The response of the ZIP detectors to phonons and ionization from electron recoils is calibrated *in situ* using a gamma-ray source. Event-selection cuts are applied to electron-recoil calibration data to remove events with pathologies, including electronic glitch events, anomalously shaped charge pulses, and periods of high baseline noise. From this sample, only those events occurring within a detector's fiducial volume (or ''bulk'') are selected, thereby avoiding surface events, which can suffer from incomplete ionization collection [239]. We reject events outside the detector's bulk by requiring the signal in the outer ionization electrode be consistent with noise, while the inner ionization signal must exceed a detector- and time-dependent threshold 4.5 standard deviations above the noise mean (as described in Ref. [227]).

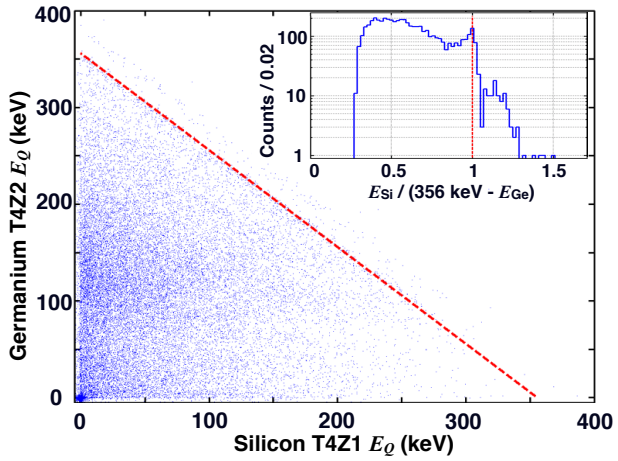

Figure 2.2: Calibration of a silicon detector's ionization energy scale using the ionization collected from ^{133}Ba gamma rays that deposited energy in both the silicon detector (T4Z1) and an adjacent germanium detector (T4Z2). The scatter plot shows the ionization energy E_Q in the neighboring germanium detector as a function of the silicon-detector ionization energy. Events for which the full energy of ^{133}Ba 356 keV gamma rays is deposited in the detector pair follow a diagonal feature (dashed line), enabling calibration of the silicon-detector energy scale and demonstrating linearity of the silicon-detector ionization response up to $E_Q > 350$ keV. **Inset:** Same data histogrammed (with bin width 0.02) to show the ratio of the silicon-detector ionization energy to the expected 356 keV gamma-ray energy less the germanium-detector ionization energy. A peak is clearly visible (dashed line) corresponding to 356 keV gamma rays that are fully contained by the adjacent detector pair.

2.2.1 Ionization Calibration

A ^{133}Ba gamma source with spectral lines at 275, 303, 356, and 384 keV was used to calibrate the ionization energy scale in the detectors. A significant number of these gamma rays are fully contained within a germanium detector, producing clear peaks in histograms of the ionization pulse amplitude [223]. The reconstructed ionization pulse amplitude from the germanium detectors is thus calibrated to an electron-equivalent recoil energy ($\mathrm{keV_{ee}}$) by multiplying by a constant factor chosen such that the observed peaks lie at the appropriate Ba-line energies.

Because of their relatively low stopping power, silicon detectors of this size rarely contain the full energy of the ^{133}Ba gamma rays, so the peaks are not visible. Silicon also has no intrinsic spectral lines at energies below 100 keV. The ionization energy scales in the silicon detectors are therefore calibrated using shared events–a 356 keV ^{133}Ba gamma ray that deposits its energy within adjacent detectors. The ^{133}Ba spectral lines are clearly visible in the sum of ionization energy E_Q in a silicon detector and its germanium neighbor, as shown in **Fig. 2.2**. Ionization energy scales are calibrated first for germanium detectors, and the calibration for silicon detectors is then set so that the shared event lines lie at the appropriate energies. After confirming linearity in the germanium detectors across a wide range of spectral lines, linearity in the silicon detectors is checked implicitly by tracking the total energy of shared 356 keV events as a function of the reconstructed ionization energy in the silicon detector. The position of this peak (shown as a histogram in the inset) varies by less than 5%, demonstrating linearity up to $E_Q \approx 350$ keV.

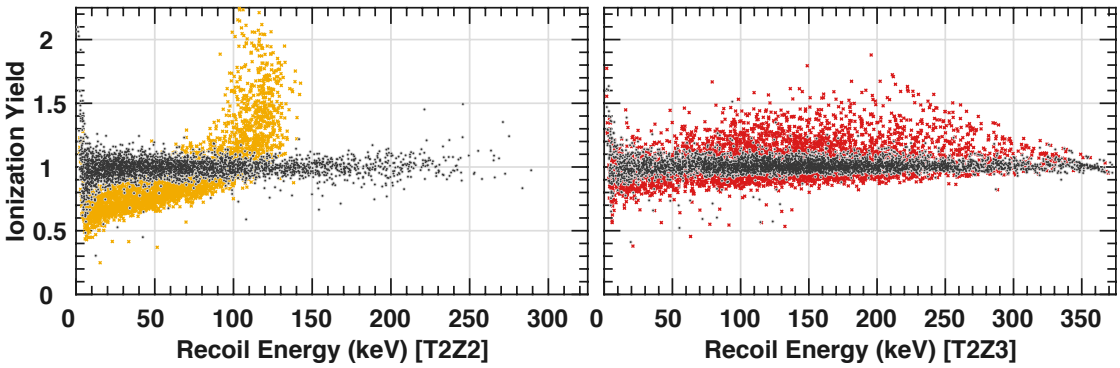

Figure 2.3: Ionization yield versus recoil energy for ^{133}Ba calibration electron recoils in **left:** silicon detector `T2Z2` (**right:** germanium detector `T2Z3`), both prior to applying the position-correction table described in *e.g.* [194, 240] to the phonon signal (light ×) and after (dark •). Electron recoil events are placed to the correct recoil energy and the ionization yield $y \approx 1$ is essentially independent of energy. The resolving power of the ionization yield for electron recoil events in ZIP detectors is improved significantly.

2.2.2 Phonon Calibration

The energy scale for the phonon channels is calibrated using a sample of bulk electron recoils, which should have unity ionization yield; the reconstructed amplitude of the total phonon pulse is scaled so that the inferred recoil energy matches the ionization energy and thus gives $y = 1$ (on average). The measured phonon signals have a significant position dependence that is removed in this process. Based on position-reconstruction parameters derived from the relative amplitudes and timings of the four phonon sensor signals, the broad continuum of ^{133}Ba electron recoils is used to develop an empirical correction table as a function of position, amplitude, and phonon energy [240], as was done for the germanium detectors in Ref. [194]. **Fig. 2.3** shows how application of this position-correction table removes the energy dependence (and improves the resolution) of the ionization yield for electron recoils. The left (right) panel shows the effect on an example silicon (germanium) detector; although the correction (shown as dark points) for the germanium detectors is less significant, the improvement in yield resolution is still clear.

2.3 Nuclear Recoil Calibration Data

Experimental data for this study are drawn from the final runs of these detectors at the Soudan Underground Laboratory, from July 2007 to September 2008, as described in Ref. [227]. Nuclear recoils were provided by a 5 μCu ^{252}Cf neutron source. Neutron capture causes temporary activation of the germanium detectors, so this calibration was performed less frequently than the ^{133}Ba gamma-ray calibration. The period considered here contains six sequences of neutron calibration. During each of these sequences, several data sets were acquired with the source inserted into one of three plastic tubes running along straight paths through the polyethylene and lead shielding to within 10 cm of the copper cryostat cans that housed the detectors, as shown in **Fig. 2.4**. Each tube

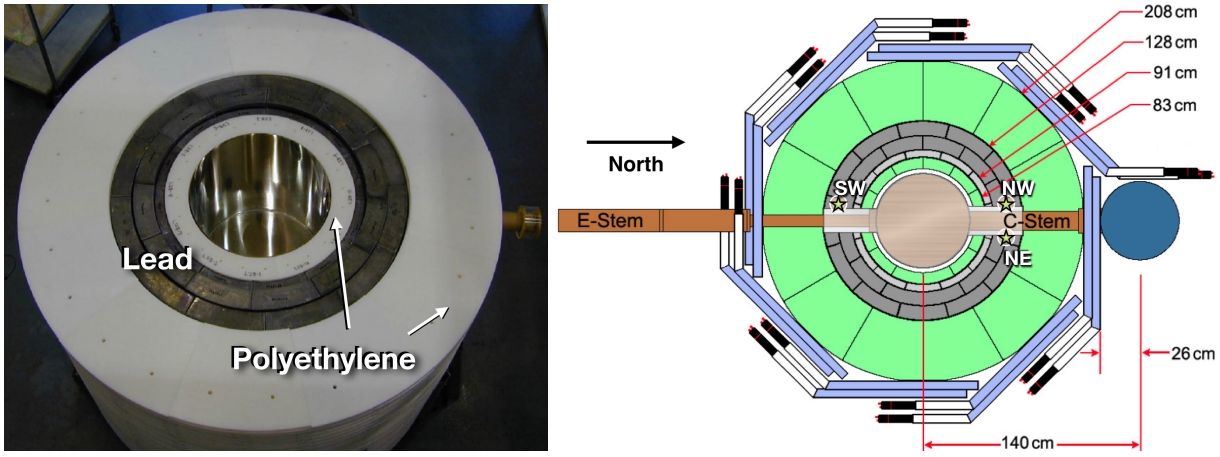

Figure 2.4: Left: CDMS II radiation shielding (photographer unknown). Polyethylene (white) neutron moderator sandwiches the lead gamma shield (dark), surrounding the mu-metal shielding. **Right:** Diagram (top view) of the CDMS II apparatus with calibration source locations (northwest [NW], southwest [SW], and northeast [NE]) indicated by ★. The muon veto panels are shown as the outermost, staggered layers (light blue), surrounding the outer annular layer of polyethylene (green), followed by a layer of low-radioactivity lead bricks (gray), a thin inner layer of ancient lead (light gray), an inner polyethylene shield (green), and finally a mu-metal shield (transparent gray) surrounding the copper cryostats cans (bronze). The mu-metal shield extends into two penetrations that pass through all layers of shielding to enable connections to the electronics readouts ('E-Stem') and the dilution refrigerator ('C-Stem'). CAD drawing adapted courtesy of Susanne Kyre.

was labeled by its nearest inter-cardinal direction: southwest, northwest, or northeast. Because each source position illuminated the detectors with a different relative neutron flux, calibration data were grouped by position and the resulting spectra were normalized separately. Recoil energies for these events were calculated by subtracting the NTL phonon contribution, inferred from the ionization signal, from the total phonon energy. However, unlike the ^{133}Ba data, neutron calibration data have no clear spectral lines. The resulting nuclear-recoil energy scale cannot be directly verified for correctness or linearity.

Instead, a GEANT4 Monte Carlo simulation was performed by Scott Fallows [223] with the goal of finding the linear energy scaling factor $\eta^{\varphi}_{\mathrm{NR}}$–interpreted as the phonon collection efficiency of nuclear recoils relative to that of electron recoils–that minimizes a test statistic comparing the simulated spectra of nuclear recoil energies to the measured spectra. The simulation geometry corresponded to the full experimental apparatus in the five-tower configuration used for CDMS II, including the detectors, support structure, and all shielding. A ^{252}Cf source was simulated separately at the three locations depicted as (★) in the right panel of **Fig. 2.4**. Neutrons from sources at these positions were moderated by part of the inner shielding before reaching the detectors.

A ^{252}Cf input spectrum was used to simulate incident neutron energies, and this spectrum was degraded in energy by propagation through the inner shielding [67]. Features in the input spectrum are washed out to the extent that an independent simulation with a Maxwellian input spectrum produced an identical recoil energy spectrum in the detectors, to within statistical uncertainties. It is therefore inferred that the spectrum of recoil energies for this configuration is largely independent

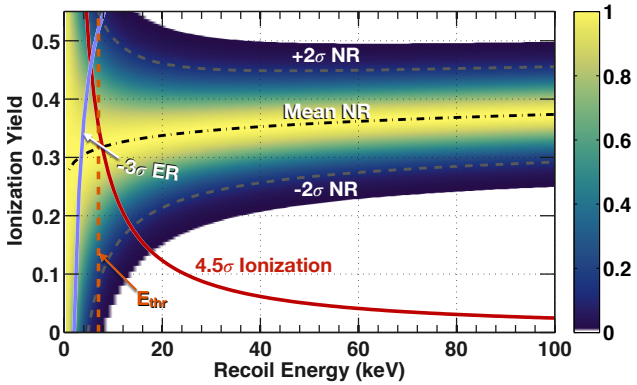

Figure 2.5: Two-dimensional histogram of the probability distribution function of nuclear recoils (NR) for T1Z4. Bins with less than 1% are white. Events selected as WIMPs must lie within the $\pm 2\sigma$ contours (dashed gray) surrounding the nuclear-recoil mean (dot-dash black). Selected events must also lie above the ionization threshold (solid dark red) which was set at 4.5σ above the noise mean, to the right of the analysis threshold (at 7 keV for this run; dashed orange), and below the lower 3σ bound of the electron-recoil (ER) band (solid light purple).

of details of the input neutron energy spectrum and is thus sufficiently accurate. For additional details, see the appendix of the publication [2], which includes work presented in Ray Bunker's PhD thesis [67]. The angular dependence of the differential neutron-scattering cross section for silicon in GEANT4 is known to be incorrect [241], but using the correct dipole anisotropy moment produces an identical nuclear recoil spectrum for neutrons scattering in silicon [242].

These simulated neutron calibration data sets were used to produce the expected energy spectra for nuclear recoil events for each detector and source position. The spectra from measured calibration data were then compared to these expected spectra. In the simulation, an event's recoil energy in each detector was determined by directly summing the energy depositions to recoiling nuclei.

2.3.1 Signal-Selection Cuts and Efficiencies

A sample of good recoil events was selected from the measured calibration data, as described in **Section 2.2**, with the addition of requiring that events fall within $\pm 2\sigma$ of the mean measured nuclear-recoil ionization yield (as shown in **Fig. 2.5**). To correspond to the energy range analyzed in Ref. [227], the reconstructed recoil energy of each event was restricted to lie below 100 keV, to lie above a detector- and run-dependent energy threshold. The analysis energy thresholds ranged from $E_{\mathrm{thr}} = (7\text{–}15)$ keV were determined primarily by the ionization threshold of the detector for the run (also shown in **Fig. 2.5**) [228].

Kevin McCarthy computed the efficiency for the relevant event selection criteria [228]. There are four potentially important energy-dependent efficiencies in this analysis, the forms of which are shown for one detector in **Fig. 2.6**. The first is the efficiency of the hardware phonon trigger which is modeled as an error function, with a width determined by the resolution of the pulse measurement. The second is the efficiency of the ionization-threshold cut, which is the primary determinant of the overall analysis threshold. The cut's main purpose is to remove sidewall surface

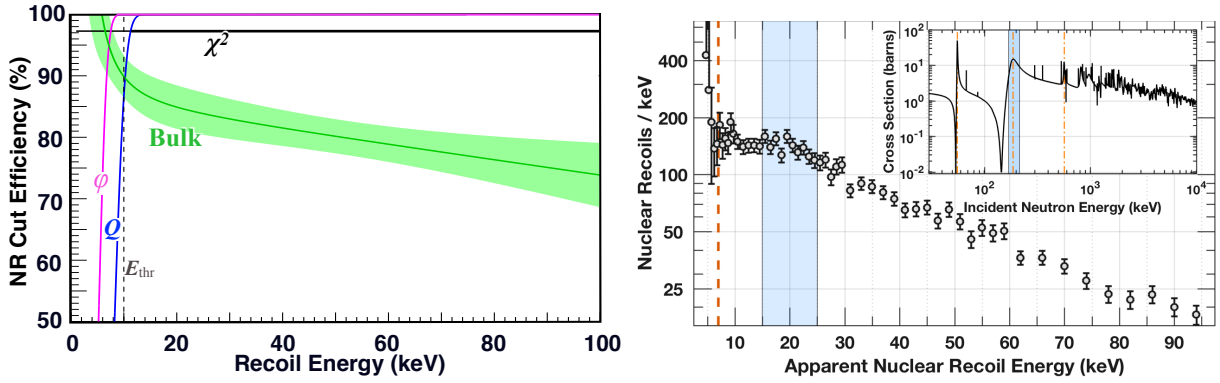

Figure 2.6: Left: Cut efficiencies as a function of recoil energy for T1Z4. The phonon trigger efficiency (φ, magenta) is unity above the run-dependent energy threshold $E_{\rm thr}$ (dashed vertical line at 10 keV). The ionization threshold efficiency (Q, blue) dominates the determination of the analysis threshold. The ionization pulse shape χ^2 efficiency (χ^2, black) has negligible energy dependence. The fiducial-volume cut efficiency (Bulk, green) is shown with shaded 1σ uncertainty band. **Right:** (Log-scale) Efficiency-corrected nuclear-recoil energy spectrum taken during a ^{252}Cf neutron calibration run for detector T2Z1 ($\circ$ with 1σ error bars) as a function of the apparent recoil energy. The detector's analysis energy threshold (vertical dashed line) is 7 keV for this run. The resonance feature (blue fill region) at $E_{\rm R} \approx 20$ keV allows a direct comparison to Monte Carlo spectra. **Inset:** Elastic neutron-^{28}Si scattering cross section as a function of incident neutron energy. The cross section is interpolated from data in the JENDL database [244]. The cross section has three prominent resonances at $E_i \approx 55$, 183, and 550 keV (vertical dashed). The resonance at incident neutron energies $E_i \approx 183$ keV (blue fill region) contributes most significantly to the 20 keV nuclear-recoil energy resonance.

events, which can result in no detected ionization [243]. Its efficiency is calculated analytically for a given recoil energy by finding the integrated fraction of the Gaussian probability distribution (as shown in **Fig. 2.5**) that remains within the bounds of the measured 2σ nuclear-recoil band after removing the portion of the band that falls below the ionization threshold. The efficiency of this cut is estimated in combination with that of the cut requiring events to have ionization yield at least 3σ below the mean of the electron-recoil band. The latter cut ensures that the sample of nuclear recoils is not significantly contaminated by electron recoils.

The remaining efficiencies are those of the χ^2 goodness-of-fit and fiducial-volume cuts. The former rejects poorly shaped ionization pulses and has negligible energy dependence [245], and the latter excludes events occurring in the outer edge of the detector where incomplete ionization collection can cause electron recoils to mimic nuclear recoils [243]. The fiducial-volume cut efficiency is calculated for events in the nuclear-recoil band, including a correction based on an estimate of the number of electron recoils that leak into the nuclear-recoil band [228]. This efficiency has the strongest energy dependence of all the cuts.

After applying these event selection criteria and efficiency corrections, and accounting for the detector masses, the resulting spectra give the raw nuclear recoil rate in counts keV^{-1} kg^{-1} d^{-1}, and as such are directly comparable to the spectra generated by the Monte Carlo simulation. The nuclear-recoil energy spectrum in CDMS II silicon detectors is characterized by a single smooth exponential in the energy range of interest with a prominent feature at $\sim$20 keV caused by a wide nuclear resonance with incident neutrons of $E \approx 183$ keV, as discussed in the appendix of the

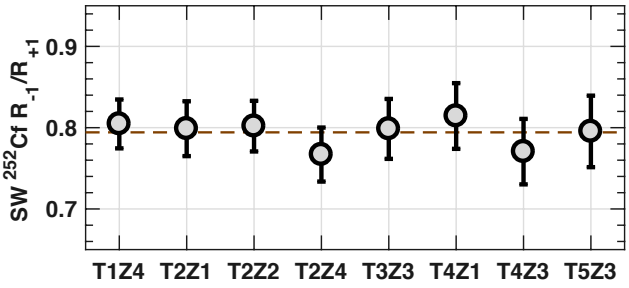

Figure 2.7: Ratio of simulated nuclear recoil rates R_{-1}/R_{+1} for the SW neutron source position with the location of the source varied by ± 1 cm from the nominal source location shown with Poisson uncertainties: $\sigma_{-/+} = \sqrt{\sigma_{+1}^2 + \sigma_{-1}^2}$. The ratio of the detector rates are consistent to within statistical uncertainties, but the overall rate (dashed line) decreases by $\sim 20\%$. Simulations were performed by Scott Fallows [223, 246].

publication [2], and Ray Bunker's PhD thesis [67]. This feature (shown as a blue fill region in the right panel of **Fig. 2.6**) breaks the degeneracy between the Monte Carlo rate normalization and spectral hardness, making it possible to infer the phonon collection efficiency $\eta_{\mathrm{NR}}^{\varphi}$ of nuclear recoils relative to that of electron recoils by comparing measured and simulated spectra without knowing the rate of nuclear recoils.

2.4 Improved Flux-Weighted Livetime for Neutron Calibrations

During the WIMP-search data taking period, the ^{252}Cf neutron source was deployed in one of the three source tubes shown in the right panel of **Fig. 2.4**: southwest (SW), northwest (NW), or northeast (NE), to collect nuclear recoil calibration data. These data are then grouped into series for each of these separate measurements. Sixteen series of neutron data were recorded: 8 series were taken with the source at the SW location, only 2 series were taken from the NW location, and 6 series were taken from the NE. There exists an uncertainty in the placement of the ^{252}Cf source between each calibration, so the overall neutron rate is not used to constrain the energy rescaling factor $\eta_{\mathrm{NR}}^{\varphi}$ because it is not known sufficiently well. As shown in **Fig. 2.7**, variation in source placement of ± 1 cm changes the rate in all detectors by approximately $\pm 10\%$. The placement of the source was done with no way to verify its location with more precision than a centimeter. The resulting spectra cannot be used to scale the Monte Carlo spectra needed to compute the phonon collection efficiency without knowledge of the neutron flux for each detector for each calibration period.

Calibration data (and WIMP search data) are taken in periods of time called 'series' where the nature of the data are intended to be consistent, *e.g.* the neutron calibration data periods do not overlap the low-background periods of WIMP search. There are a few series in the neutron calibration data with very few neutron events. For some series marked as neutron calibration periods, the ^{252}Cf source wasn't placed in the tube, as evidenced by extremely large livetime-to-neutron-count ratio. In particular, the ^{252}Cf calibrations measurements made during Runs 125–128,

from a time between 2007 and 2008, contain three entirely bad series: 171217_1748, 171218_0520, and 180915_1524. Many of the data periods with inconsistent rates were restricted to a subset of the detectors. Because most detectors did not record good nuclear-recoil calibration data throughout the entire exposure, care was taken in forming the overall normalization to account properly for periods of lost live time in the CDMS II detectors.

To account for the series- and detector-dependent neutron exposure, which is not present in the simulated data, I made an estimate of the effective neutron flux for each detector during periods of neutron-calibration data taking using detectors which have reasonable rates. The number of nuclear recoils passing selection criterion cuts, described above in **Section 2.3.1**, with recoil energies $E_{\rm thr} < E_{\rm R} < 100\,{\rm keV}$ was used to improve the estimated livetime for each series. This was done by compensating for lost live time during bad series by weighting the lost live time with the relative neutron rate inferred from periods of good neutron exposure; the efficiency-corrected neutron rate of each detector and the series-total neutron rates were used to identify and correct the detector-dependent neutron rates in 'bad' series using an iterative fitting procedure. A neutron flux-weighted livetime was computed for each detector and used as a stand-in for the livetime of the ^{252}Cf nuclear recoil calibration series.

2.4.1 Initial Estimate of the Series-Total Neutron Rate

Danielle Speller identified the series 171217_1748, 171218_0520, and 180915_1524, as completely bad; these series were removed and no fits, or improved neutron flux estimates were made. After identifying detectors with poor neutron rate measurements in every series, *e.g.* those with exceptionally low rates, or those having large deviations from the mean rates, the rest of the data were used to attempt to estimate the true series-total neutron rate

$$R_{\rm tot}\Big|_{sce.\ pos.} = \sum_{\rm det} R_{\rm det} \tag{2.4.1}$$

for each source position. For a given series, the neutron rate $R_{\rm det}$ in each detector should be some fraction $\mathcal{F}_{\rm det}$ of the total rate measured by all detectors

$$\mathcal{R}_{\rm det} = \mathcal{F}_{\rm det} \times R_{\rm tot} \equiv \mathcal{F}_{\rm det} \times \left(\sum_{\rm det} R_{\rm det} \right) \tag{2.4.2}$$

This is vacuously true when the total rate is zero. When the total rate measured in all detectors is larger in one series than another, for a given neutron source position *e.g.* SW, then each detector may be expected to contribute $\mathcal{F}_{\rm det}$ of the larger total. This linear relationship between the neutron rate in a given detector and the total measured rate allows us to identify poorly operating detectors whose measurements do not coincide with the total. The same relationship should be true when comparing the detector rates to the rates measured in a single detector.

Since (Eqn 2.4.2) holds true, the best-fit fraction of the series-total neutron rate for each detector $\mathcal{F}_{\text{det}} = R_{\text{det}}/R_{\text{tot}}$. The value of this ratio can be computed from a linear fit of the good detector rates, which can be constrained to go through the origin since a total rate of zero means that the detector rates are each identically zero. The best-estimated neutron rate $\mathcal{R}$ for the bad series is obtained by multiplying the linearly-fit coefficient $\mathcal{F}_{\text{det}}$, determined from all neutron-calibration series at a given source position, with the series-total neutron rate

$$\mathcal{R}_{\text{det}} = \mathcal{F}_{\text{det}} \cdot R_{\text{tot}} \tag{2.4.3}$$

for each source location.

After identifying obviously bad neutron-calibration rates, one detector `T5Z3` was selected as good from a by-eye inspection of the neutron rates. Detector `T5Z3` had the fewest bad series (3/16–only the entirely bad series). A linear fit of the neutron rate in each detector to the neutron rate in detector `T5Z3` was performed, and the series-total neutron rates for each calibration period were initially estimated. The true rates in the detectors are proportional to the series-total rate as well as the other detector rates since

$$\mathcal{R}_{\text{tot}} = R_1/\mathcal{F}_1 = R_2/\mathcal{F}_2 = ... \tag{2.4.4}$$

Following the initially computed series-total neutron rate $\mathcal{R}_{\text{tot}}$, an iterative fit procedure was implemented to further improve the estimated series-total neutron rate to compute a neutron flux-weighted livetime, so that Scott could scale the Monte Carlo simulations to account for the loss of exposure.

Each fit iteration assigns the expected fraction $\mathcal{F}_{\text{det}}$ of the (currently best-fit) series-total rate $\mathcal{R}_{\text{tot}}$ to each detector that differs significantly from the expectation. By iteratively fitting the detector rates to the series-total neutron rate $\mathcal{R}_{\text{tot}}$, the best estimate of the total rate was improved. The improved series-total rate $\mathcal{R}_{\text{tot}}$ is determined by summing the observed rates over the good series and the current best-fit detector rates

$$\mathcal{R}_{\text{tot}} = \sum_{\text{good}} R_{\text{det}} + \sum_{\text{bad}} \mathcal{F}_{\text{det}} \cdot \mathcal{R}_{\text{tot}}. \tag{2.4.5}$$

For each iteration, the total rate $\mathcal{R}_{\text{tot}}$ is improved from the improved estimate of the contribution $\mathcal{F}_{\text{det}} \cdot R_{\text{tot}}$. **Fig. 2.8** shows the computed rate for each iteration as the fit quality improves and the total rate converges for each series. The rates in the Northwest source location change by less than $0.05/7.45 \approx 1\%$.

For each iteration, we restrict the candidate series–for which a neutron flux can be calculated–by removing series with neutron rates $R_{\text{det}} < 0.01\,\text{Hz}$ or fewer than 10 neutrons passing the selection cuts. The neutron rates measured by detector `T1Z4` are identically zero for all but the first four series. These are the only series used to determine the contribution to the total rate. After the first iteration, detector-series combinations are replaced if the difference between the observed rates R_{det}

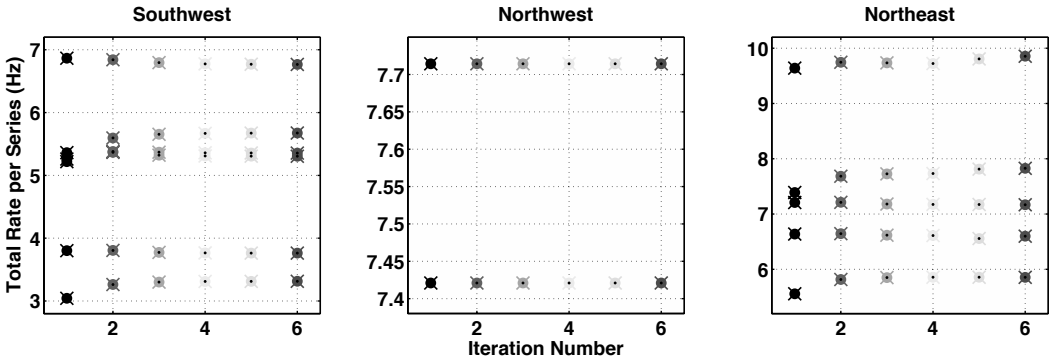

Figure 2.8: Estimated total neutron rate in all detectors for each of the five series for the SW position (*left*), two series for the NW position (*middle*),six series for the NE position (*right*). The series-total neutron rates approach their true value after replacing those data with large residuals (Eqn. 2.4.7). The series-total neutron rate doesn't change significantly for any source position beyond the fourth iteration, and the rates in the Northwest source position change by less than 1%.

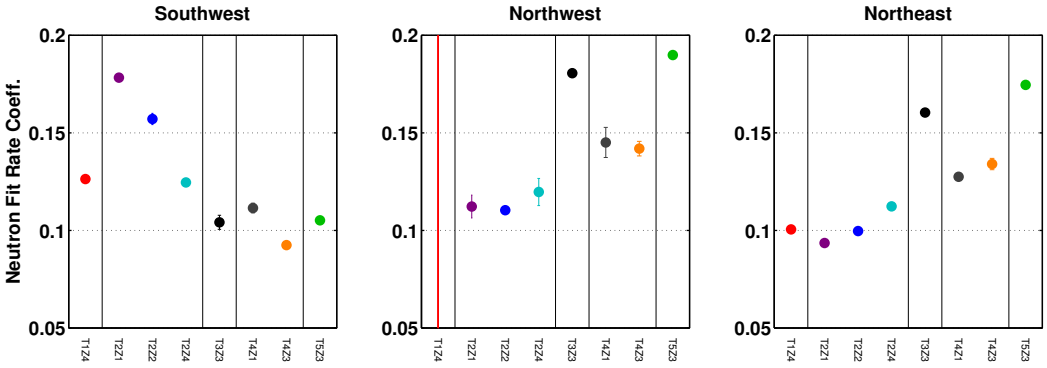

Figure 2.9: Fraction $\mathcal{F}$ of the series-total neutron rate measured by each detector for each neutron source location (panels), after the sixth (final) fit iteration. The vertical black lines separate different towers *e.g.* T1, T2, etc. No suitable neutron data was collected in `T1Z4` for the Northwest position.

and the detector rate $\mathcal{R}_{\rm det}$ expected from the best-fit fraction of the series-total neutron rate,

$$(R_{\rm det} - \mathcal{F}_{\rm det} \cdot \mathcal{R}_{\rm tot}) > \Delta_{\rm thr}. \tag{2.4.6}$$

where the threshold $\Delta_{\rm thr}$ becomes increasingly tight for each iteration

$$\Delta_{\rm thr}({\rm iteration}) = (0.1,\ 0.086,\ 0.073,\ 0.06,\ 0.06)\,{\rm Hz}. \tag{2.4.7}$$

These threshold values $\Delta_{\rm thr}$ chosen are less than $\sim$10% of the rates measured by a given detector. At the final iteration, detectors with neutron rates that differ from the expected values by more than $\Delta_{\mathcal{R}} = 0.06\,{\rm Hz}$ are replaced with the expected fraction of the total (Eqn. 2.4.3). After the bad neutron rates are replaced for each detector, the improved series-total neutron rate is computed.

The best-fit fraction $\mathcal{F}$ of the series-total neutron rate is shown (after the sixth and final iteration) in **Fig. 2.9** for each detector for all ^{252}Cf source positions. The residuals of the detector rates and the best-fit lines versus the series-total neutron rate are shown in **Fig. 2.10** for each calibration location.

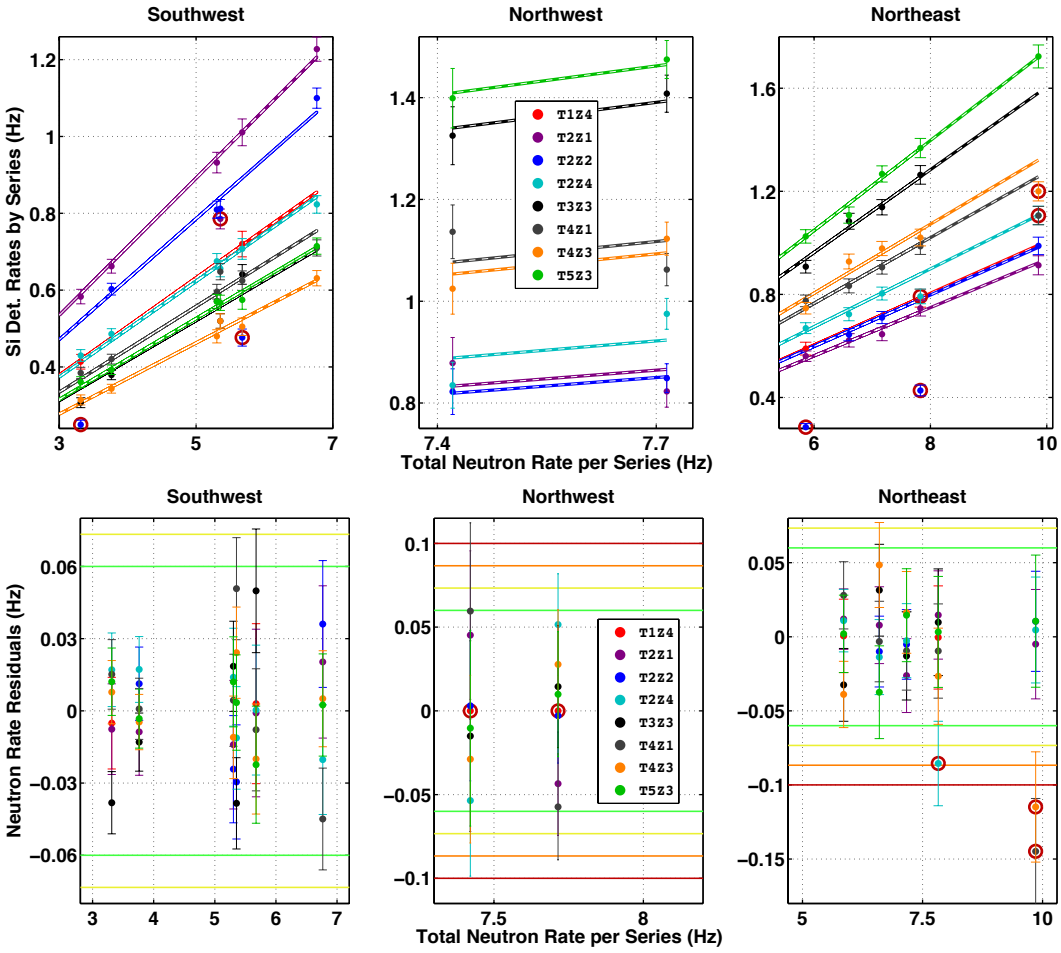

Figure 2.10: Top: Efficiency-corrected neutron rates (dots with 68% C.L. statistical uncertainties) measured in each detector versus the final best estimate of the series-total neutron rate $\mathcal{R}_{\rm tot}$ for each source position. The predicted rate $\mathcal{F}_{\rm det} \times \mathcal{R}_{\rm tot}$ is shown (solid lines) for each detector. Rejected data are circled. In most cases, the fits agree with the accepted individual detector rates within uncertainties. **Bottom:** Residuals of the measured detector rates $R_{\rm det} - \mathcal{F}_{\rm det} \cdot \mathcal{R}_{\rm tot}$ versus the series-total neutron rate $\mathcal{R}_{\rm tot}$. The horizontal lines correspond to the residual threshold (Eqn. 2.4.7) for iterations 2-6; none of these are shown for the SW position. Rejected data are circled. Nearly all of the accepted data agree with the best-fit predicted rate $\mathcal{F}_{\rm det} \times R_{\rm tot}$ within 1.5σ.

The detector rates do not differ significantly from the best-fit expectation (Eqn. 2.4.3). The worst detectors `T1Z4` (shown red) and `T2Z2` (shown blue) have a large fraction of poor data. However, the results are prevented from significantly impacting the final calculation of the flux-weighted livetimes, as described below, because the contribution of the poorly fit data is determined from the reasonable linear fits. The measured data that were rejected and replaced by the predicted rates are circled. The neutron rates in each detector appear to be reasonably well fit to the series-total neutron rate not differing by more than 10%. The top panel shows that the absolute rates $R_{\rm det}$ measured by the detectors varied by as much as a factor of 3, even between good ^{252}Cf calibrations (those for which the detectors were operating properly). However, the relative rates for good calibrations were consistent from series to series as predicted by **Fig. 2.7**.

Table 2.1: Position-total flux-weighted livetimes $\mathcal{L}_{\text{tot}}$ (seconds) for each detector as a function of the source position (Eqn. 2.4.10). **Appendix A** shows the flux weighted livetime for each detector-series combination $\mathcal{L}_{\text{tot}}$ in **Table A.1**.

	T1Z4	T2Z1	T2Z2	T2Z4	T3Z3	T4Z1	T4Z3	T5Z3
SW	1450	6405	7146	9392	7316	9394	9375	9392
NW	X	1780	2167	2167	2167	2167	2166	2167
NE	2069	6695	4881	6584	6409	6409	6385	8061

2.4.2 Determination of the Neutron-Flux-Weighted Livetimes

To appropriately compare the source-position-dependent rates measured by each detector to those predicted by Monte Carlo simulations, the best-fit series-total neutron rates are used to estimate a flux-weighted livetime. In general we expect a flux-weighted exposure quantity (such as the livetime) to scale with the series detector livetime $\mathcal{L}_{\text{det}}$ and scale with the best-fit estimate of the series-total neutron rate, since a larger rate indicates a larger expected exposure. Since some of the detectors have no livetime for a given series, their flux-weighted livetime may not be calculated. Detectors with zero livetime have zero flux-weighted livetime for that series. For each good detector measurement, the flux-weighted livetime assigned to a detector for each series is computed with the best estimate of the improved series-total rate $\mathcal{R}_{\text{tot}}$ from Eqn. 2.4.5

$$\mathcal{L}_{\Phi} = \mathcal{L}_{\text{det}} \times \frac{\mathcal{R}_{\text{tot}}}{\langle R \rangle}, \tag{2.4.8}$$

where the average series-total neutron rate at each position is

$$\langle R \rangle = \frac{1}{N_{\text{det}} \cdot N_{\text{ser}}} \sum_{\text{ser}} \mathcal{R}_{\text{tot}}. \tag{2.4.9}$$

The series-dependent flux-weighted livetimes are shown for each detector and neutron source position in **Appendix A** (**Table A.1**). To apply the computed flux-weighted livetimes to the Monte Carlo spectra for each of the neutron source positions simulated, the flux-weighted livetimes for each source position and detector combination (Eqn. 2.4.8) are summed across all the series

$$\mathcal{L}_{\text{tot}}(\text{det}, \text{sce}) = \sum_{\text{ser}} \mathcal{L}_{\Phi}. \tag{2.4.10}$$

Table 2.1 shows results of the position-total flux-weighted livetimes for the good series measured by each detector. Scott Fallows used my calculated neutron flux-weighted livetimes as a stand-in for the Monte Carlo livetime to improve the correspondence between the measured and simulated nuclear recoil spectra to determine the nuclear recoil energy rescale factor [223].

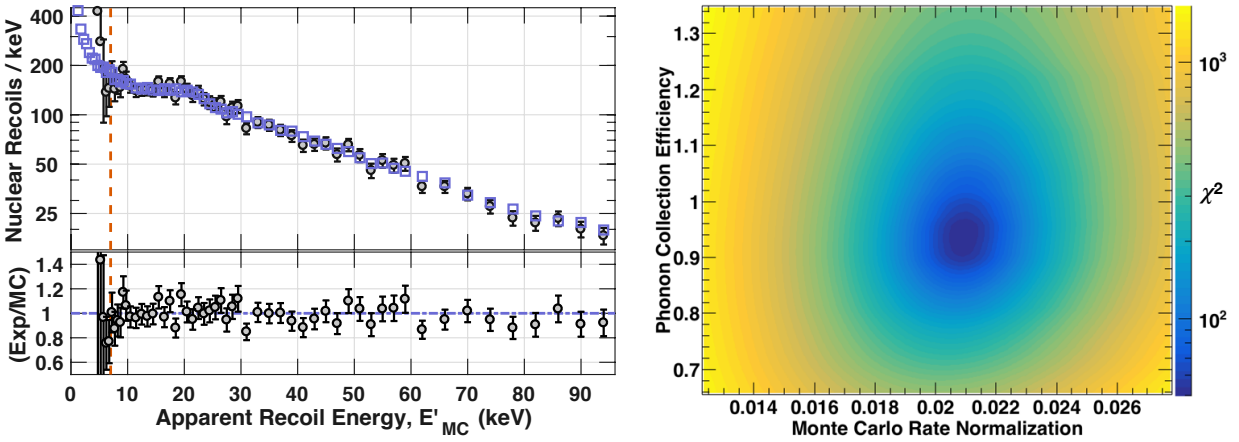

Figure 2.11: Left: *Top:* (Log-scale) Efficiency-corrected nuclear-recoil energy spectrum (same as the right panel of Fig. 2.6) for detector T2Z1 (∘ with 1σ error bars) as a function of the apparent recoil energy (assuming phonon collection efficiency $\eta^{\varphi}_{\mathrm{NR}} = 1$), compared with the corresponding simulated spectrum after application of the overall best-fit energy scale: $E'_{\mathrm{MC}} = 0.95\,E_{\mathrm{MC}}$ (□ with uncertainties smaller than the marker). The detector's analysis energy threshold (vertical dashed line) is 7 keV for this run. *Bottom:* Ratio of the efficiency-corrected nuclear recoil spectrum to the (overall best-fit) rescaled simulated spectrum. **Right:** (Log-scale) Two-dimensional χ^2 contour map from Eqn. 2.5.1 for T2Z1–calculated using simulated and measured data coadded over all source positions–as a function of the phonon collection efficiency $\eta^{\varphi}_{\mathrm{NR}}$ applied to the simulated nuclear recoil energies and the Monte Carlo rate normalization. The simulated nuclear recoil energies are rescaled to $\eta^{\varphi}_{\mathrm{NR}}\,E_{\mathrm{MC}}$.

2.5 Nuclear-Recoil Phonon Collection Efficiency in Silicon Detectors

Scott Fallows performed high-statistics neutron simulations recording neutron-induced nuclear recoils for each of the three neutron source positions passing through the CDMS II shielding geometry [223]. The energy rescaling was determined as a function of detector and source position, by matching the measured nuclear-recoil spectra to the flux-weighted Monte Carlo nuclear recoil spectra. Since the energy rescaling coefficient is determined independent of electron recoils it is interpreted as the phonon collection efficiency $\eta^{\varphi}_{\mathrm{NR}}$ for nuclear recoils (NRs) relative to that of electron recoils (ERs) of the same deposited energy. A test value for this energy rescaling factor $\eta^{\varphi}_{\mathrm{NR}}$ is applied to the recoil energy of each event in the simulated data set prior to binning (as in, *e.g.*, the left panel of Fig. 2.11).

A χ^2 statistic is then constructed from each pair of binned spectra in a way that incorporates the Poisson errors for each energy bin i of both the measured (X) and simulated (μ) rates:

$$\chi^2 = \sum_i \left(\frac{X_i - \mu_i}{\sigma_i} \right)^2, \tag{2.5.1}$$

with $\sigma_i^2 = \sigma_{\mathrm{exp},i}^2 + \sigma_{\mathrm{MC},i}^2$ in terms of the measured ($\sigma_{\mathrm{exp},i}$) and simulated ($\sigma_{\mathrm{MC},i}$) Poisson uncertainties. The energy rescaling is applied to the simulated, rather than the measured, data to avoid problems associated with event energies shifted above or below threshold and to simplify the accounting of

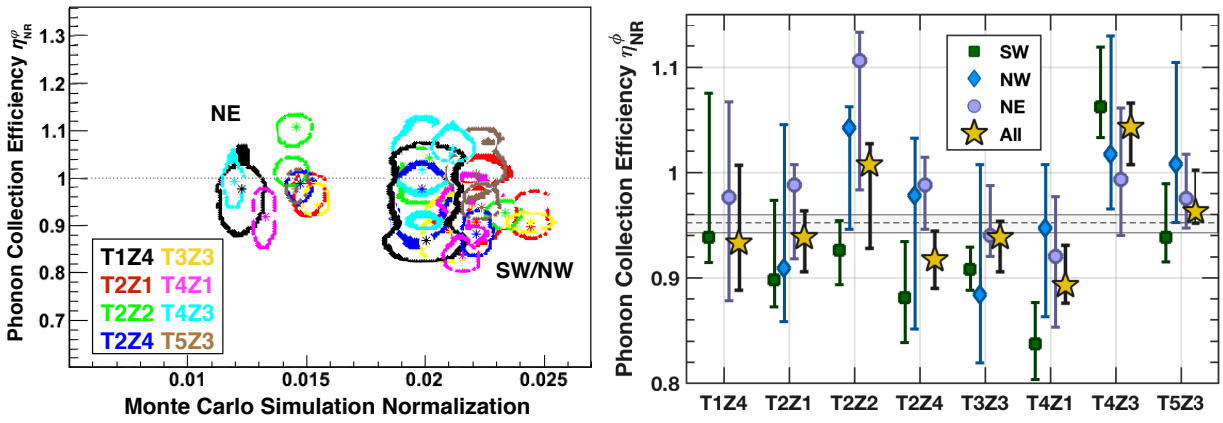

Figure 2.12: Left: (Log-scale) Two-dimensional $\Delta\chi^2 = 4.61$ (90% C.L.) contours for all detectors and source positions as a function of the phonon collection efficiency applied to the Monte Carlo simulated nuclear-recoil energies and the rate normalization of the simulated recoil spectra. The best-fit phonon collection efficiencies are consistent among detectors, and the best-fit Monte Carlo simulated nuclear recoil rate agrees well for the SW and NW positions. The ideal phonon collection efficiency $\eta^{\varphi}_{\rm NR} = 100\%$ is shown (horizontal dotted). Figure adapted from [246]. **Right:** Best-fit phonon collection efficiency for SW (■), NW (♦), NE (●), and coadded (★) ^{252}Cf source positions for each detector with 95% C.L. uncertainties. Most detectors (except for T2Z2 and T4Z3) show an underestimation of nuclear recoil energy. The weighted average over all detectors of the coadded best-fit results (gray fill region) gives $\eta^{\varphi}_{\rm NR} = 95.2^{+0.9}_{-0.7}$ % at 95% C.L. No acceptable NW neutron calibration data sets exist for detector T1Z4.

energy-dependent efficiencies. The rescaled nuclear-recoil energies of the simulated data

$$E'_{\rm MC} = E_{\rm MC}\,\eta^{\varphi}_{\rm NR} \tag{2.5.2}$$

as shown in the left panel of **Fig. 2.11**. For each combination of detector and source position, minimization of this two-dimensional χ^2 was performed by Scott Fallows, scanning over both $\eta^{\varphi}_{\rm NR}$ and the normalization [223]. An overall best-fit $\eta^{\varphi}_{\rm NR}$ for each detector was also determined by performing an additional scan, after coadding data from all three source positions for both the measured and simulated spectra. This overall rescaling $\eta^{\varphi}_{\rm NR}$ is used to scale the apparent nuclear recoil energies by $1/\eta^{\varphi}_{\rm NR}$. **Fig. 2.12** shows the χ^2 statistic as a function of the normalization of the Monte Carlo simulated nuclear-recoil spectrum and phonon collection efficiency $\eta^{\varphi}_{\rm NR}$ for a representative detector.

The final result of the χ^2 minimization is a best-fit phonon collection efficiency $\eta^{\varphi}_{\rm NR}$ for nuclear recoils relative to electron recoils for each detector and source position. As shown in the left panel of **Fig. 2.12**, the best-fit relative Monte Carlo simulated spectrum normalizations from the χ^2 minimization procedure agree at the 90% confidence level for data at the two source positions (SW and NE) with more neutron calibration series, with slightly worse agreement at the third NW position. Moreover, the best-fit energy rescaling factor is independent of the normalization, due to the feature in the spectrum; so the accuracy of the normalization is not important to the results. A weighted average across all silicon detectors, using the best-fit results from the individual-detector fits (coadded over source position), results in an overall phonon collection efficiency for nuclear

Table 2.2: Best-fit phonon collection efficiency $\eta_{\mathrm{NR}}^{\varphi}$ for nuclear recoils relative to electron recoils each detector (95% C.L.), with the minimum χ^2/d.o.f. and p-value. Detectors with higher energy thresholds have fewer energy bins and therefore fewer degrees of freedom.

	T1Z4	T2Z1	T2Z2	T2Z4	T3Z3	T4Z1	T4Z3	T5Z3
$\eta_{\mathrm{NR}}^{\varphi}$ (95% C.L.)	$0.93^{+0.07}_{-0.04}$	$0.94^{+0.03}_{-0.03}$	$1.01^{+0.02}_{-0.08}$	$0.92^{+0.03}_{-0.03}$	$0.94^{+0.02}_{-0.03}$	$0.89^{+0.04}_{-0.02}$	$1.04^{+0.02}_{-0.04}$	$0.96^{+0.04}_{-0.01}$
χ^2/d.o.f.	40.1/42	50.0/48	72.7/48	75.0/48	57.5/48	53.3/42	33.6/37	81.6/48
p-value	.554	.394	.012	.008	.164	.113	.629	.002

recoils

$$\eta_{\mathrm{NR}}^{\varphi} = 95.2^{+0.9}_{-0.7}\% \tag{2.5.3}$$

relative to electron recoils of the same deposited energy. **Table 2.2** lists the best-fit $\eta_{\mathrm{NR}}^{\varphi}$ for each detector (95% C.L.), the best-fit χ^2/d.o.f., and the p-value for each detector. The detectors with the worst fits (lowest p-values) are some of those with the most degrees of freedom (lowest energy thresholds): T2Z2, T2Z4, and T5Z3. Detector T4Z3 has the most significant deviation from the mean efficiency, disagreeing by more than the 95% C.L. mostly due to the best-fit $\eta_{\mathrm{NR}}^{\varphi}$ at the SW position. It is reasonable to assume that the phonon collection efficiency is energy dependent, in which case the recoil spectra would systematically differ from the energy-independent assumption made here. Aside from the small nuclear resonance from incident neutrons of energy $E_{\mathrm{inc}} \approx 180\,\mathrm{keV}$, the measured recoil spectra appear to decrease roughly exponentially across the (10–100) keV region of interest. The discrepancies in the best-fit $\eta_{\mathrm{NR}}^{\varphi}$ between detectors do not appear to be explained by energy dependence in the relative collection efficiency $\eta_{\mathrm{NR}}^{\varphi}$, because the measured and simulated spectral data generally match well both at low energies near the prominent 20 keV feature and at high energies. The residuals are shown for nuclear-recoil energies up to 100 keV in the bottom panel of **Fig. 2.11**.

2.6 Implications on Ionization Yield in Silicon Detectors

The stopping power for charged particles in a target material can be divided into electronic and nuclear components, each with different energy dependence as reported in Ref. [247]. Slow-moving nuclear recoils are not stopped efficiently by electrons and so deposit most of their energy through interactions with the target's nuclei. Because ionization results from electronic excitation, nuclear recoils have a reduced ionization yield y compared to electron recoils of the same energy. The ionization yield of a nuclear recoil varies with the partitioning of energy between electronic and nuclear modes.

The same neutron calibration data discussed in **Section 2.3** were used to infer the ionization yield of nuclear recoils in CDMS II silicon ZIP detectors. The apparent nuclear-recoil energies E'

are rescaled (Eqn. 2.5.2) so that the true nuclear-recoil energy

$$E_{\mathrm{R}}^{\mathrm{true}} = E_{\mathrm{R}}^{'}/\eta_{\mathrm{NR}}^{\varphi}, \tag{2.6.1}$$

and as a result, scaling the apparent ionization yield $y^{'}$ gives the true ionization yield

$$y_{\mathrm{R}}^{\mathrm{true}} = y_{\mathrm{R}}^{'}\,\eta_{\mathrm{NR}}^{\varphi}. \tag{2.6.2}$$

We considered two alternate hypotheses for the nuclear-recoil energy scaling: 1) the nuclear-recoil phonon collection efficiency is consistent across the detectors (as described in the paper [2]), 2) the phonon collection efficiency is detector-dependent, and the best-fit χ^2 is found for each detector separately (given in **Table 2.2**, shown as stars in the right panel of **Fig. 2.12**) .

To determine the impact of the rescaling on the ionization yield tor each detector, the rescaled ionization yield (according to Eqn. 2.6.2) for each nuclear recoil passing quality cuts was binned by rescaled nuclear-recoil energy (Eqn. 2.6.1) from $E_{\mathrm{R}} = (6\text{–}100)\,\mathrm{keV}$ in energy bins of increasing width. The resulting energy-dependent ionization distributions shown (dots with 68% C.L. statistical uncertainties) in **Fig. 2.13** were fit to a 3 parameter gaussian distribution

$$A_y \exp\left(-\frac{1}{4}\left(\frac{y-\mu_y}{\sigma_y}\right)^2\right) \tag{2.6.3}$$

where A_y is the amplitude, μ_y is the mean ionization yield, and σ_y is the standard deviation of the distribution. The fits were performed for each of the 8 silicon detectors for each of the phonon-collection-efficiency hypotheses. The full results of the gaussian fits to the ionization yield (rescaled with the average efficiency $\eta_{\mathrm{NR}}^{\varphi}$) are shown for all detectors (solid lines) grouped by nuclear-recoil energy (panels) in **Fig. 2.13**. The mean ionization yield μ_y is shown (red vertical line), with fill regions indicating the best-fit standard deviation σ_y (wide, light) and the 99.7% C.L. uncertainty δ_μ (dark) on the best-fit mean ionization.

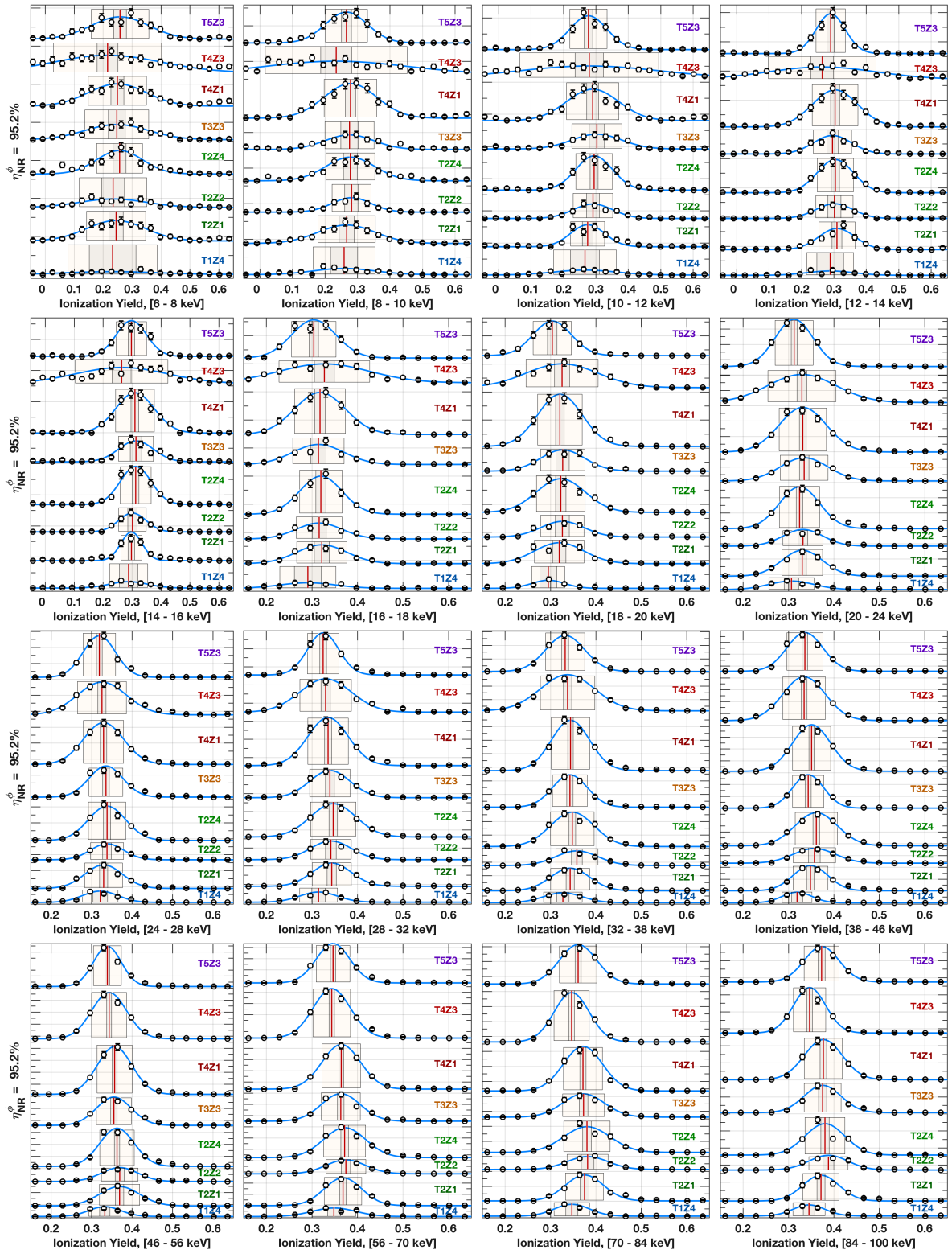

Figure 2.13: Histograms of ionization yield (∘ with 68% C.L. statistical uncertainties) for neutrons in the eight working CDMS II silicon detectors for 16 energy ranges (labeled on the x-axis of each panel) using the average nuclear-recoil energy rescaling $\eta^{\varphi}_{\rm NR}$=0.952. Gaussian fits (solid curves) to the number of events (with a 0.33 yield bin width) with fitted means μ_y are shown (red vertical line), with $3\delta_\mu$ (99.7% C.L.) fit uncertainties on the mean ionization (dark fill), and fitted standard deviation (light fill).

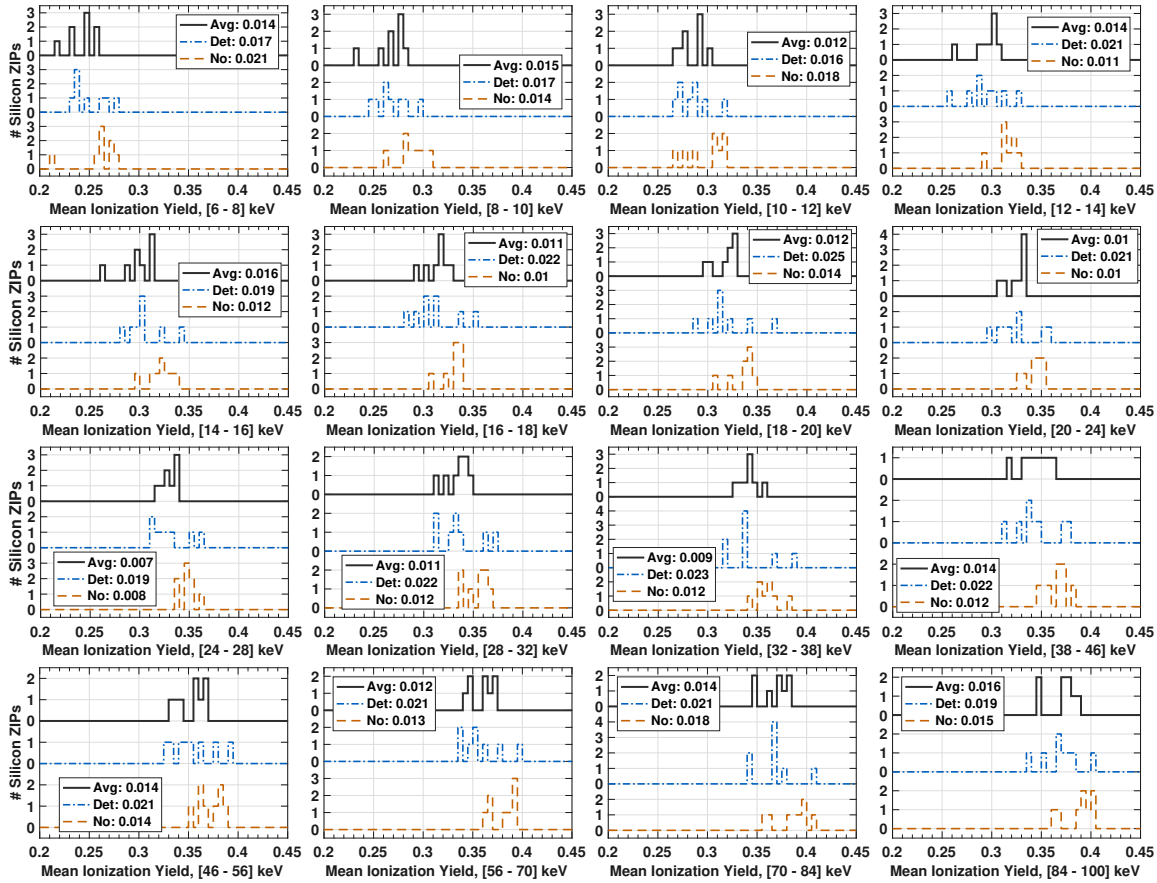

Figure 2.14: Histograms of best-fit ionization yield μ_y for nuclear-recoils in 8 CDMS II silicon detectors for 16 energy ranges (labeled on the x-axis) under three phonon-rescaling hypotheses: 1) $\eta^{\varphi}_{\mathrm{NR}} = 1$ (*bottom curve*: light dashed), 2) detector-dependent $\eta^{\varphi}_{\mathrm{NR}}$ (*middle curve*: dot-dash), and 3) the average $\eta^{\varphi}_{\mathrm{NR}}$=0.952 (*top curve*: dark line), with legend entries indicating the standard deviation $\sigma_Y = {}^1\!/_7 \sum_{\mathrm{det}} (\mu_y(\mathrm{det}) - \langle \mu_y \rangle)^2$ of the distribution of the best-fit ionization yield for all detectors. The standard deviation of the ionization yield distribution is smaller than the other hypotheses for 8 of the 16 energy regions of interest, with 3 of 16 regions having equal or only slightly larger standard deviations.

The results of fits for detector-dependent $\eta^{\varphi}_{\mathrm{NR}}$ are shown in **Fig. A.3** of **Appendix A** and without rescaling in **Fig. A.4**, *i.e.* assuming the phonon collection efficiency for nuclear recoil is the same as for electron recoils of the same deposited energy. Although detector T1Z4 has very few events, the resulting fits are reasonable. Histograms of the best-fit ionization yields μ_y are shown for all detectors (in **Fig. 2.14**) for each rescaling hypothesis (distinguished by the line style) in each nuclear-recoil energy bin (panels). The legend shows the standard deviation of the distribution of best-fit ionization yields for each hypothesis. The standard deviation of best-fit ionization yield among the detectors lower with the average rescaling (Eqn. 2.5.3) than the detector-dependent hypothesis. Even considering small physical differences between the detectors, we expect that using an average scaling over all detectors is more a robust and accurate interpretation of the data, *i.e.*the phonon collection efficiency for nuclear recoils is the same for all detectors. As a result, the average rescaling described in the paper [2] was taken to be the most reasonable; we will not consider the implications of the detector-dependent rescaling hypothesis on the ionization yield of nuclear recoils

in silicon, as described in **Section 2.6.2**.

2.6.1 Neutron Multiple-Scattering Ionization-Yield Correction

The ionization yield of nuclear recoils increases with increasing recoil energy. Hence a multiple-site interaction, for which the ionization is divided among several lower-energy recoils, will produce less ionization (overall) than a single recoil of the same total recoil energy. While WIMPs have a negligible probability of scattering more than once in the apparatus, approximately 30% of neutrons from (2–100) keV scatter off nuclei at multiple locations in a single detector [231]. The resulting inferred ionization yield as a function of recoil energy must be corrected for the small effect of neutron multiple scattering. These multiple-site scatters are not distinguishable from single-site interactions of the same total energy in the CDMS setup. The impact of multiple scattering on ionization yield was determined by Dave Moore [231] using GEANT4 simulations of neutrons passing through the CDMS shielding and detector geometry. For the nuclear recoil calibration data, the fitted means of ionization yield

$$\mathcal{M}_c = \langle y_{\text{sing.}} \rangle / \langle y_{\text{all}} \rangle \tag{2.6.4}$$

are corrected at each energy, which includes a gaussian approximation of the ionization resolution of the silicon ZIP detectors. The left panel shows Dave's original image (Fig. 8 of [231]). The energy-dependent data (I digitally grabbed) is shown in the right panel of **Fig. 2.15** along with the functional form of the correction given in **Table 2.3**. The dashed lines are the parametrized yield corrections in the three energy regions. Since the true ionization yield is larger without the effect

Table 2.3: Results for 3 regimes of polynomial fit (constant, parabola, and line) to the ionization yield corrections calculated by Dave Moore [231]. The multiple scatter correction to the detector-mean ionization $\mathcal{M}_c$ applied to each energy bin is the inverse of the third column.

E_{R} (keV)	Fit Type	Ratio $\langle y_{\text{all}} \rangle / \langle y_{\text{sing.}} \rangle = (\mathcal{M}_c)^{-1}$
0–18	const.	0.9953
18–45	parabola	$2.67 \times 10^{-5} E_{\text{R}}^2 - 2.28 \times 10^{-3} E_{\text{R}} + 1.028$
45–100	linear	$-1.34 \times 10^{-4}\, E_{\text{R}} + 0.985$

of neutron multiple scattering, I scaled the all-detector weighted means determined from Dave's analysis, by the (inverse of the) functional form given in the third column of **Table 2.3**: the ratio of the mean expected ionization yield for single-scatter nuclear recoils to the expected yield from multiple-scatter nuclear recoils at the center of each energy bin (*i.e.* those shown in **Fig. 2.13**). The functional form determined here is chosen for simplicity; the shifts in yield are well-understood and are less than 3% for nuclear-recoil energies $E_{\text{R}} \in$ (10–100) keV. The accuracy of the polynomial(s) describing the average correction therefore has only a small effect on the resultant yield.

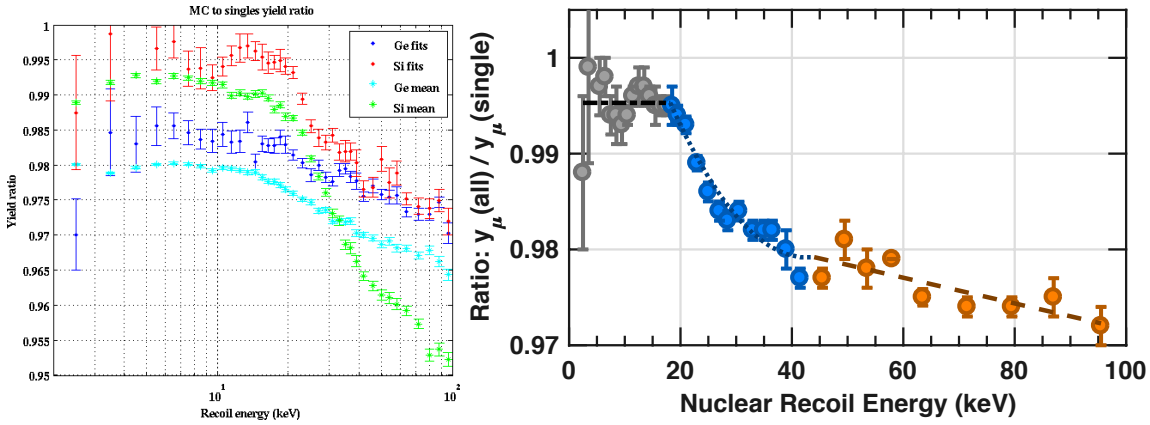

Figure 2.15: Reduction in ionization yield as a function of recoil energy due to Multiple Scatters in CDMS II silicon ZIP detectors. **Left:** Fig. 8 from Dave's analysis [231]: the ratio of ionization yield for single-scatter nuclear recoils to the ionization yield of all nuclear recoils as a function of recoil energy for simulated neutron calibration events. The red (blue) dots are the mean ionization yields for neutron scatters in Ge (Si) from Monte Carlo simulation. The cyan (green) dots are the mean ionization yields for neutron scatters coadded across all Ge (Si) detectors to reduce statistical uncertainties. The neutron multiple scatter ionization yield correction (functional form given in **Table 2.3**) is derived using the coadded silicon data (green points). **Right:** Data for Si nuclear recoils grabbed from the left plot, with polynomial fit results to the coadded silicon simulation results in three energy regimes: a constant derived from the weighted mean of the data for $E_\mathrm{R} \in (0,\, 18)\,\mathrm{keV}$ (dot-dash), a parabola from $E_\mathrm{R} \in (18,\, 45)\,\mathrm{keV}$ (dots), and a (dashed) line from $E_\mathrm{R} \in (45,\, 100)\,\mathrm{keV}$.

2.6.2 Nuclear Recoil Ionization Yield in the Literature

The ionization yield of a nuclear recoil varies with the partitioning of energy between electronic and nuclear modes. The energy dependence of the reduced yield as a function of atomic number Z and atomic mass A was computed by Lindhard in Ref. [247]. The resulting expressions were simplified and reported in Ref. [56]. The expected ionization yield for a nuclear recoil under this Lindhard theory is given by

$$y_L = \frac{k \cdot g(\varepsilon)}{1 + k \cdot g(\varepsilon)}, \tag{2.6.5}$$

where $k = 0.133\, Z^{2/3} A^{-1/2} \approx 0.146$ for silicon, and the transformed energy

$$\varepsilon = 11.5\, E_\mathrm{R}\, Z^{-7/3}, \tag{2.6.6}$$

with the recoil energy E_R given in keV[2]. The function $g(\varepsilon)$ is well-fit by a polynomial in ε with empirically chosen coefficients, described by

$$g(\varepsilon) = 3\,\varepsilon^{0.15} + 0.7\,\varepsilon^{0.6} + \varepsilon. \tag{2.6.7}$$

In silicon, the yield has been measured previously by elastic scattering at 77 K [248--250], 130 K [232], 220 K [233, 251], and 288 K [252], and by utilizing resonances in the scattering cross section to constrain the recoil energy [250]; **Table 2.4** describes the conditions of these yield measurements

[2]NB: The exponent for A in the expression for k in the original Lewin and Smith publication [56] is incorrect.

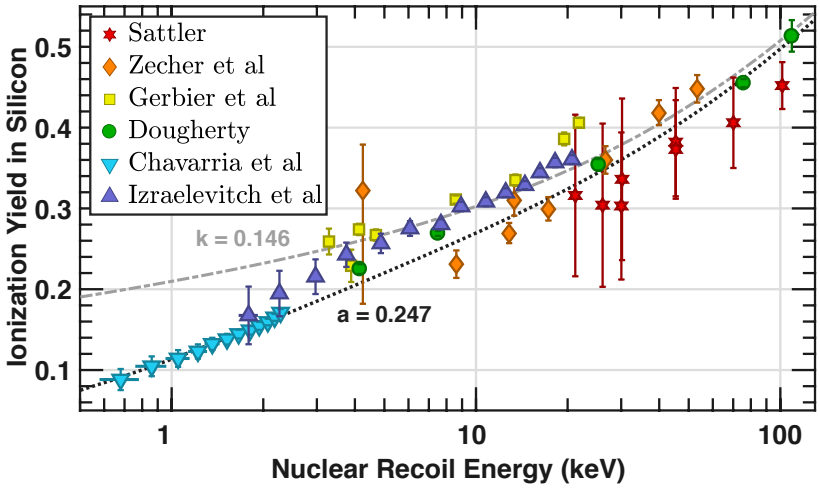

Figure 2.16: Measurements of the ionization yield for nuclear recoils in silicon [232, 233, 248--250, 252]. The light dot-dashed line shows the theoretical prediction y_L for silicon (Eqn. 2.6.5 with $k = 0.146$) from Lindhard [247]. The dark dashed line shows the parameterization y_C (Eqn. 2.6.8 with $a = 0.247$) from Chavarria [253].

Table 2.4: Comparison of nuclear-recoil ionization yield measurements shown in **Fig. 2.16** and **Fig. 2.18**. The detector type, bias, and temperature are included for the references.

Author		Year	Detector Type	(Bias)	Temp. (K)
Agnese	[2]	2018	10 mm silicon	4 V/cm	$\sim 5 \times 10^{-3}$
Gerbier	[249]	1990	3 mm neutron det.	(?)	77
Dougherty	[250]	1991	5 mm neutron det.	1 kV	77
Zecher	[248]	1990	3-mm Si(Li)	(0.24,1, 2) kV/cm	77
Aguirra	[232]	2016	0.5, 0.675 mm CCD	(128 ± 1) V	130
Izraelivitch	[233]	2017	silicon-drift diode	110 V	220
Sattler	[252]	1965	SS lithium drifted	(5–10) kV/cm	288

in silicon. The results of these previous measurements are summarized in **Fig. 2.16**. The light dot-dashed line shows the Lindhard theoretical prediction y_L (Eqn. 2.6.5) for ionization yield in silicon with $k \approx 0.146$ from Ref. [247]. Standard Lindhard theory significantly over-estimates the ionization production for low-energy ($E_{\mathrm{R}} \lesssim 10$ keV) nuclear recoils reported in Refs. [232, 248, 250]. The central values reported in Ref. [252] are also lower than, but not inconsistent with, the Lindhard prediction up to 100 keV, since the data have uncertainties $\sim 25\%$. It is possible that systematic uncertainties in older measurements [248--250] are not accounted for or fully understood. An improved functional form (black dashed) using a parameter $a = 0.247$ [253]

$$y_C = \left(\frac{1}{a\, E_{\mathrm{R}}} + \frac{1}{y_L(E_{\mathrm{R}})} \right)^{-1} \tag{2.6.8}$$

matches the Lindhard expectation y_L for silicon at high energy and fits the data reported in Ref. [232] at low energy. This parameterization was used to report the WIMP-nucleon sensitivity curves in

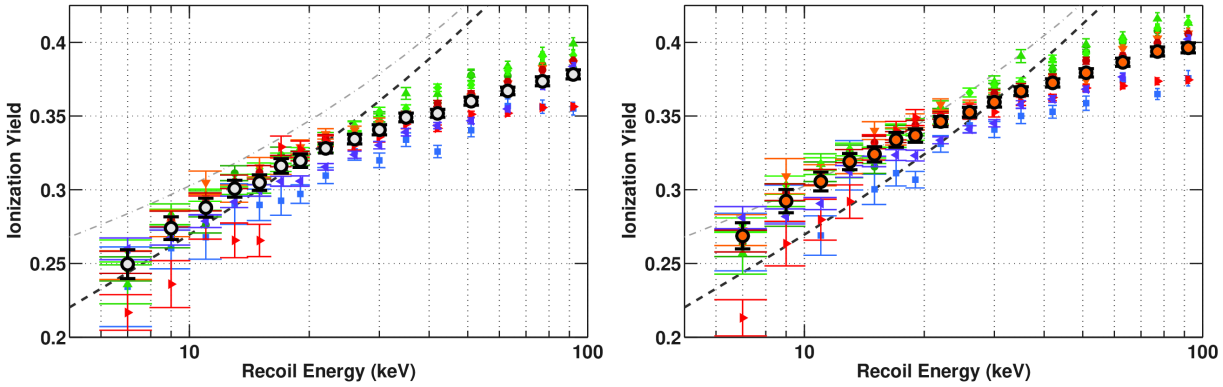

Figure 2.17: Energy-rescaled measurements of the (multiple-scatter corrected) ionization yield *vs.* recoil energy for nuclear recoils in CDMS II silicon detectors with (**left**) and without (**right**) the best-fit average phonon energy rescaling. The error bars indicate the results of the fits to the ionization yield distributions for each detector individually, and weighted means (bold ∘) with 1σ statistical error bars $\sigma_\mu = {}^{\sigma_y}/_{\sqrt{8}}$ given by the standard deviation of the 8 best-fit detector yields (Eqn. 2.6.11) for each energy bin. The light dot-dashed line shows the theoretical prediction y_L for silicon (Eqn. 2.6.5 with $k = 0.146$) from Lindhard [247]. The dark dashed line shows the parameterization y_C (Eqn. 2.6.8 with $a = 0.247$) from Chavarria [253], which fits the existing data reasonably well.

Ref. [232].

The weighted means of best-fit ionization yield μ_y for the eight silicon detectors

$$\Big\langle y(E_{\rm R})\Big\rangle = \mathcal{M}_c(E_{\rm R}) \cdot \left(\sum_{\rm det} \mu_y \times w\right) \times \left(\sum_{\rm det} w\right)^{-1} \tag{2.6.9}$$

where the weights

$$w = \left(\frac{1}{\delta_\mu}\right)^2 \tag{2.6.10}$$

depend on the 68% C.L. uncertainty δ_μ on the best-fit mean ionization yield μ_y for each detector (dark fill regions in **Fig. 2.13**), and include the best-fit phonon energy rescaling ($\eta^{\varphi}_{\rm NR} = 0.952$) and energy-dependent multiple-scattering correction $\mathcal{M}_c$ at the center of the nuclear-recoil energy bin from Eqn. 2.6.4. **Fig. 2.17** shows the ionization yield determined from the Gaussian fits to the nuclear-recoil distribution for each detector (as in **Fig. 2.14** *e.g.*). The uncertainties on the (weighted) means of the ionization yield $\langle y\rangle$, shown in **Fig. 2.17**, are the standard error of the best-fit yields μ_y

$$\sigma_\mu = \frac{\sigma_{\rm y}}{\sqrt{8}} = \frac{1}{\sqrt{8}}\sqrt{\frac{1}{7}\sum_{\rm det}\Big(\langle y\rangle - \mu_y\Big)^2} \tag{2.6.11}$$

where $\sigma_{\rm y}$ is the standard deviation of the best-fit yields, instead of the error on the weighted mean. CDMS II silicon data are consistent with Eqn. 2.6.8 for energies below 20 keV. At high energies, the measured ionization yield is smaller than previous measurements [248, 250, 252], with the size of the discrepancy increasing with energy.

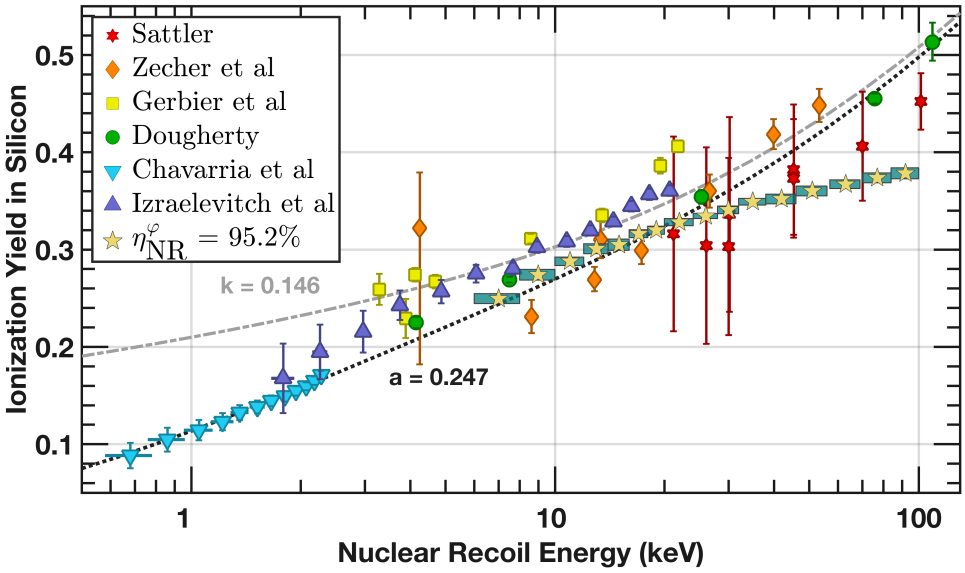

Figure 2.18: Measurements of the ionization yield for nuclear recoils in silicon [232, 233, 248--250, 252]. The light dot-dashed line shows the theoretical prediction y_L for silicon (Eqn. 2.6.5 with $k = 0.146$) from Lindhard [247]. The dark dashed line shows the parameterization y_C (Eqn. 2.6.8 with $a = 0.247$) from Chavarria [253], which fits the existing data reasonably well. Data from this analysis (★) are the weighted means of ionization yield for the eight silicon detectors including phonon energy rescaling ($\eta^{\varphi}_{\mathrm{NR}} = 0.952$) and multiple-scattering corrections, with uncertainty bands representing the standard error of the mean ionization yields (Eqn. 2.6.11) and the nuclear-recoil energy-bin width.

2.6.3 Nuclear Recoil Ionization Collection in CDMS II Silicon Detectors

Comparisons of the CDMS II measurements of the yield to the parametrization that fits the previous measurements shown in **Fig. 2.18** constrain the nuclear-recoil ionization collection efficiency

$$\varepsilon_{\mathrm{coll}} \equiv \frac{\langle y \rangle - y_C}{y_C} \tag{2.6.12}$$

in CDMS II detectors. The nuclear-recoil ionization collection efficiencies for all CDMS II silicon detectors and their weighted mean (Eqn. 2.6.9), with the same fractional uncertainties in **Fig. 2.18**) is shown in **Fig. 2.19**, assuming the same parameterization of ionization yield [253] from **Fig. 2.18**. The figure shows the results of two phonon-collection rescaling hypotheses: best-fit average (*left*) and no rescaling (*right*). The individual detector fits μ_y are inconsistent with one another at the 1σ level. These detector-to-detector variations may correspond to true physical differences between the detectors. The average ionization collection efficiency for nuclear recoils $\varepsilon_{\mathrm{coll}}$ in CDMS II silicon ZIPs is consistent with roughly 100% at nuclear-recoil energies $E_{\mathrm{R}} \lesssim 20\,\mathrm{keV}$. The fit is improved if the ionization-yield parameterization from Eqn. 2.6.8 underestimates the true ionization yield by ∼5% for nuclear recoils $E_{\mathrm{R}} \approx (10\text{–}20)\,\mathrm{keV}$.

There is a reasonable mechanism for producing the ionization collection efficiency observed in CDMS II silicon detectors. The detectors were operated with fields of a few V/cm, much lower than

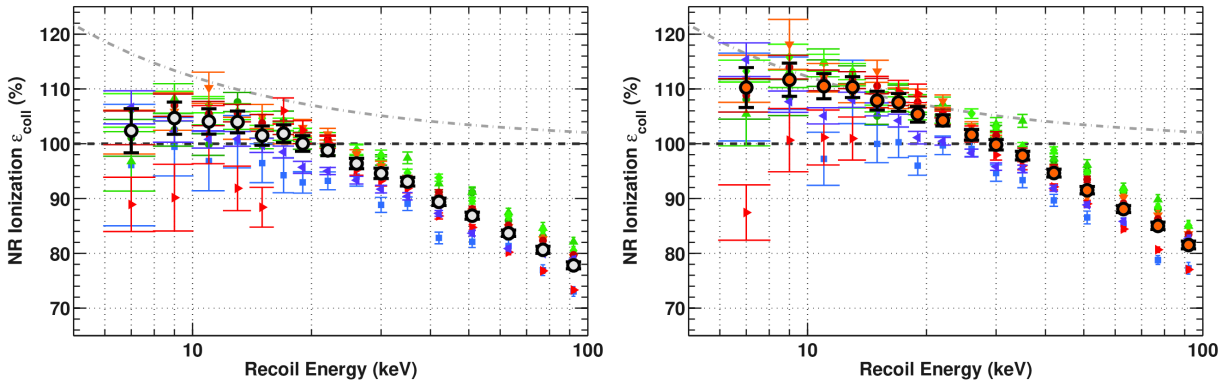

Figure 2.19: Energy-rescaled measurements of the (multiple-scatter corrected) ionization collection efficiency *vs.* recoil energy for nuclear recoils in CDMS II silicon detectors using 2 phonon energy rescaling hypotheses: with the best-fit average (**left**), none (**right**). The error bars indicate the results of the fits to the ionization yield distributions for each detector individually, and weighted means (bold ∘) with 1σ statistical error bars are the standard error of the mean $\sigma_\mu = {}^{\sigma_y}/\sqrt{8}$, where σ_y is the standard deviation of the 8 best-fit detector yields for each energy bin. The ionization collection efficiency assumes the parameterization (dark dashed) for y_C from Ref. [253] in Eqn. 2.6.8. The expected Lindhard ionization from Eqn. 2.6.5 for 100% collection efficiency is shown (light dashed). The yield measurements using the best-fit phonon collection efficiency are consistent with 100% ionization collection efficiency (gray dashed) at energies $E_R \lesssim 20\,\text{keV}$ but gradually decrease with increasing energy to ∼80% at $E_R \approx 100\,\text{keV}$.

those described in Refs. [232, 233, 248--250, 252]. The electric fields reported in Refs. [248, 250, 252] are 60–500× larger than the 4 V/cm electric fields applied to the CDMS II ZIP detectors. Nuclear recoils produce a much denser initial composite of charge pairs than similar-energy electron recoils. It is plausible that the ionization produced by a low-energy nuclear recoil may be fully extracted even at low fields, but the denser ionization produced by higher-energy nuclear recoils cannot be extracted completely at these low fields. The resulting ionization collection efficiency may decrease with increasing energy because the charges are increasingly self-shielded, thus allowing a larger fraction of charge pairs to recombine before they can be drifted across the detector. It is also possible that the lower temperature of the CDMS II detectors relative to those described in Refs. [232, 233, 248--250, 252] (shown in **Table 2.4**) plays a role.

2.7 Implications on WIMP Sensitivity Limits and Conclusions

The revised nuclear-recoil energy scale has a small effect on published CDMS II WIMP sensitivity limits and contours. **Fig. 2.20** shows the shifts in both the spin-independent WIMP-nucleon cross-section exclusion curve and the best-fit WIMP mass region and cross section, both at 90% C.L., from Ref. [227]; the shifts are generally small. For WIMP masses $m_\chi \gtrsim 10\,\text{GeV}/c^2$, the shift is less than 20%, and for WIMP masses $m_\chi \approx 5\,\text{GeV}/c^2$ the upper limit increases by about a factor of two. The best-fit WIMP mass resulting from the revised nuclear-recoil energy scale shifts by <5%.

The measured spectral shape of neutron calibration data in CDMS II silicon detectors provides strong evidence that the phonon collection efficiency η^{φ}_{NR} is almost, but not quite, the same for nuclear

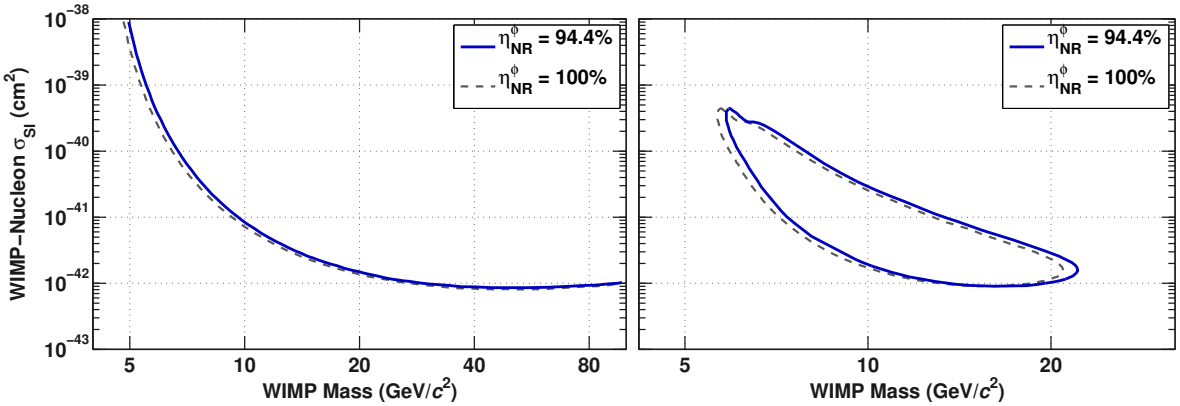

Figure 2.20: (Log-log) 90% C.L. upper limit (**left**) and acceptance contour (**right**) on the spin-independent WIMP-nucleon cross section $\sigma_{\rm SI}$ on silicon, as a function of WIMP mass, as published in [227] (dashed), and using the 1σ lower limit on the best-fit phonon collection efficiency: $\eta^{\varphi}_{\rm NR} = 94.4\%$ (solid). Figure produced from Julien Billiard's work.

recoils as electron recoils. Results are consistent with phonon collection efficiency $\eta^{\varphi}_{\rm NR} = 95^{+0.9}_{-0.7}\%$ for all energies and detectors, with good agreement between measured and simulated spectra down to detector energy thresholds $\sim$10 keV. Any energy dependence in $\eta^{\varphi}_{\rm NR}$ in the 10–100 keV energy range considered here cannot be large. Although similar analysis is possible in germanium, it is prone to systematic uncertainty because the spectrum for this range of nuclear-recoil energies is featureless and decays exponentially. As a result, there is an inherent degeneracy between the neutron rate and the energy scale that is difficult to break in the CDMS setup. Imperfect knowledge of the source strength and position, coupled with inconsistent data quality for the neutron calibrations make a simple comparison of the measured and simulated neutron rates infeasible. The low-energy nuclear resonance in ^{28}Si provides a spectral feature that breaks the degeneracy, making the silicon analysis presented here, and in [2], possible.

The CDMS II silicon ionization measurements described here (and in [2]) support recent findings of Refs. [232, 233] that the Lindhard prediction for nuclear-recoil ionization yield at low energies ($\lesssim$20 keV) is an over-estimate, and that the energy-dependent parameterization of Eqn. 2.6.8 is a more accurate description for nuclear recoils in silicon. The CDMS data suggest that this parameterization may slightly underestimate the true ionization yield of nuclear recoils between (10–20) keV. The inferred reduction in ionization collection efficiency in CDMS II silicon detectors at recoil energies $\gtrsim$20 keV may be due to the field-dependent self-shielding of charge carriers that prevents them from being drifted by the electric field. At higher recoil energies, some ($\lesssim$ 25%) of the ionization produced by the nuclear recoil may recombine. Planned calibration of SuperCDMS SNOLAB [74] silicon detectors will provide improved measurements of the phonon and ionization response, especially at lower energies.

Chapter 3
Radon Diffusion Measurements of SuperCDMS Gaskets

As described in **Section 1.3.2**, the non-chemically interacting nature of radon allows a generally large mobility from the ambient atmosphere to non-metals, and back again, due primarily to its inherent diffusivity. Diffusion is the process resulting from thermally activated random motions that transport matter (*e.g.* nuclei, molecules) from one part of a system to another. Macroscopically, the bulk diffusion of a substance is typified by the motion from areas of high concentration to low concentration, analogous to heat flow. As a result, diffusion is precipitated by a concentration gradient. Microscopically, the motion of each diffusing particle is random and independent of the previous steps as a random walk. So, once the concentration of the diffusant is homogeneous, the concentration is in equilibrium, and molecular diffusion ceases [254, 255]. The subsequent behavior is dominated by self-diffusion, for identical particles, or tracer diffusion, for multi-component systems, where molecular displacement is due to Brownian motion of the particles []. The theory of diffusion in isotropic materials is based on Fourier's work (1822) on heat conduction, which was adopted by Fick (1855). Diffusion (and heat) are underpinned by the hypothesis that the rate of flux ϕ (*i.e.* conduction, transfer) of the diffusing substance along a single dimension x

$$\phi = -D\frac{\partial C}{\partial x} \tag{3.0.1}$$

through a cross section of unit area is proportional to the gradient of the concentration C normal to the cross section. The negative sign arises from the fact that high concentrations diffuse downstreamto regions of space with lower concentrations, as would heat. The diffusion coefficient D is used to quantify the deviation of *e.g.* a population of radon atoms in a material from an initial location.

Diffusion models and measurements (relevant to radon) are discussed at length in many Refs. [125, 127, 254, 255] from as far back as 1915. The time-dependent radon decay concentration $C(x,t) \equiv C$

along a single dimension x in a material with a radon diffusion coefficient D obeys

$$\frac{\partial C}{\partial t} = D\frac{\partial^2 C}{\partial x^2} - \lambda\, C + \lambda\, S, \tag{3.0.2}$$

where S is the radon production density, and $\lambda = 1/\tau = 2.11 \times 10^{-6}$ decays/sec is the radon decay rate related to its lifetime τ. Assuming the radon production density S is zero, inside a semi-infinite material extending from the origin to $\pm\infty$, the steady-state concentration

$$C = \frac{D}{\lambda} \cdot \frac{\partial^2 C}{\partial x^2} \equiv \ell_D^2 \cdot \frac{\partial^2 C}{\partial x^2} \tag{3.0.3}$$

has a solution[1] of the form

$$C(x) = A\, \exp(x/\ell_D) + B\, \exp(-x/\ell_D).$$

For (a semi-infinite) material exposed on one side, the radon concentration will drop off exponentially with a characteristic length scale ℓ_D given by the diffusion length

$$\ell_D = \sqrt{D/\lambda} = \sqrt{D\,\tau}. \tag{3.0.4}$$

Researchers and homeowners use this to qualitatively estimate the effectiveness of *e.g.* a gasket to block radon diffusing from high-activity spaces. The diffusion length of reactive (or decaying) substances is roughly density dependent–varying by *many* orders of magnitude for solids, liquids, and gases. As described in **Section 1.3.2**, radon-222 (and its progeny) cause a variety of backgrounds in dark matter experiments. Radon is highly mobile in room-temperature gases at atmospheric pressure (STP), characterized by a diffusion coefficient of order

$$D_{\text{gas}} \gtrsim 10^{-5}\,\text{m}^2/\text{s} \tag{3.0.5}$$

for air, hydrogen, He, Ne, and Ar, which differ by about a factor of four [125]. Radon is fairly mobile in solids such as soils, in some cases having diffusion coefficients comparable to radon in gases [126, 127, 256--258]. Soft materials, such as plastics and rubbers, have moderate radon diffusion coefficients in the range

$$D_{\text{soft}} \sim \left(10^{-11}\text{–}10^{-6}\right)\ \text{m}^2/\text{s}, \tag{3.0.6}$$

allowing radon to travel a moderate distance

$$\ell_{\text{soft}} = \sqrt{D_{\text{soft}}\,\tau} = \sqrt{10^{-11}\,\text{m}^2/\text{s} \cdot 5.52\,\text{d} \cdot 84,600\,\text{s/d}} = \sqrt{10^{-11}\,\text{m}^2/\text{s} \cdot 4.66 \times 10^5\,\text{s}} = 2.1\,\text{mm}$$

before decaying away [127--136]. Metals and crystals are much more radon-hard [130, 131, 137],

[1] Even time-dependent solutions to the diffusion equation usually include exponential functions–integrated or otherwise.

Table 3.1: Radon diffusion coefficient D and characteristic length scale ℓ_D to an order of magnitude in gases, soils, plastics, and metals at room temperature, with references.

	Gas	**Soils**	**Plastics**	**Metals**
D (m^2/s)	10^{-5}	10^{-8}	10^{-11}	$< 10^{-16}$
ℓ_D	2 m	7 cm	2 mm	<7 μm
Ref.	[125, 257]	[139]	[128, 130--132, 134]	[130, 131, 260]

bearing diffusion coefficients lower than

$$D_{\text{hard}} \lesssim 10^{-16}\,\text{m}^2/\text{s}, \tag{3.0.7}$$

so that radon might diffuse no more than

$$\ell_{\text{hard}} \lesssim \sqrt{D_{\text{hard}}\,\tau} \lesssim \sqrt{10^{-16}\,\text{m}^2/\text{s}\cdot 4.66\times 10^5\,\text{s}} \approx 7\,\mu\text{m}.$$

As a result, low-radon cleanroom environments can be constructed of ∼cm-thick aluminum which will block ambient radon in underground labs from penetrating the walls [175, 178, 179, 259] so radon daughter plate-out can be mitigated [140, 146, 148, 149]. The order of magnitude of these radon diffusion values, including references, are summarized for some materials in **Table 3.1**.

A lead shield, shown in **Fig. 3.1**, surrounding the detection volume (copper SNOBOX) is designed to reduce the external gamma-ray background from the SNOLAB drift by a factor $\times 10^6$ [74]. Without the purged radon barrier, the SuperCDMS SNOLAB high-voltage detector backgrounds, described in **Section 1.4.2**, would be dominated by radon from the cavern environment inside the radon purge barrier surrounding the lead gamma shielding. Prompt decays of ^{214}Po and ^{214}Bi in the ^{222}Rn decay chain include gamma decays at high energies $E_\gamma \approx (0.3\text{–}1.5)$ MeV. Lead-214 produces gammas at $E_\gamma = (352, 295$ and $242)$ keV with appreciable branching fractions $\mathcal{B}_f > 15\%$, and ^{214}Bi beta decays to an excited state of ^{214}Po which emits a photon of energy $E_\gamma = 609$ keV; Table 3 of Ref. [122] shows the decays with branching fractions $\mathcal{B}_f > 1\%$. Without mitigation, the single-scatter bulk electron-recoil rate in the HV detectors would be the dominant background of the experiment. The radon concentration requirement

$$\mathcal{C}_{\text{req}} \leq 1\,\text{Bq/m}^3 \tag{3.0.8}$$

inside the lead shield ensures the rate of prompt ^{214}Po and ^{214}Bi gamma decays in the shielding will contribute $< 2\%$ of the total electron recoil backgrounds [106]. The radon purge design, surrounding the lead shield, from LEMER PAX [261] is shown in the right panel of **Fig. 3.1**. Sources of radon in the lead shielding will contribute to this background rate. The volume $V_S = 5.66\,\text{m}^3$ of air space within the radon purge, surrounding the lead shield, is sealed with a gasket. A purge flow $F_{\text{purge}} \approx (1\text{–}10)$ L/min of liquid nitrogen boil-off with an expected radon concentration $C_{\text{LN}} \lesssim 0.5\,\text{mBq/m}^3$ [165] will flush the gas in the shield and remove radon from the volume. Sources of

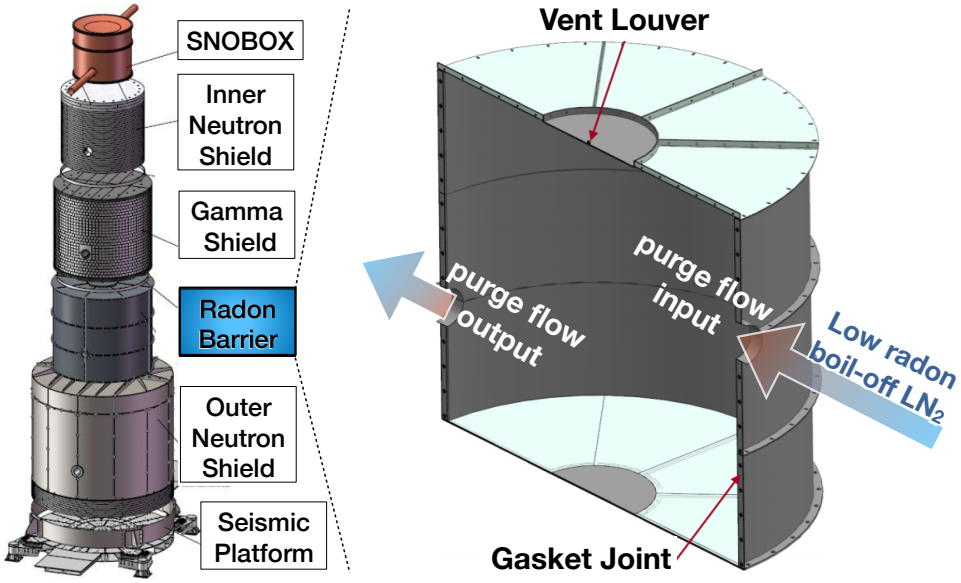

Figure 3.1: Left: Exploded view of shielding layers surrounding the nested copper cans (SNOBOX) housing the detectors. An outer neutron shield consisting of modular water tanks will moderate neutrons coming from the cavern walls. A graded lead shield, with an inner liner of low-activity ancient lead, will prevent gammas emitted by U/Th/K in the cavern walls from entering the detection volume [106, 192]. An aluminum enclosure (Radon Barrier) surrounding the lead shielding will be purged with low-radon gas to prevent significant radon-induced gamma production within the lead gamma shield. An inner neutron shield made of polyethylene will moderate and absorb radiogenic neutrons from impurities in the outer shielding. The entire apparatus will sit on top of a seismic platform to nullify the impact of environmental vibrations in the cavern. **Right:** Cut away of the radon purge lead shield design for SuperCDMS SNOLAB from Lemer pax. A purge flow of boil-off gas from liquid nitrogen (LN_2) will be used to flush radon emanating and diffusing into the lead shield. The vessel will be kept at an overpressure of about 0.42 inches of water, to prevent radon entering through leaky cracks. Cavern radon that diffuses through the gaskets must be reduced as much as possible to prevent significant increase in the backgrounds

radon with an equilibrium strength $\mathcal{S}$ (mBq/sec) will contribute to the radon concentration $\mathcal{C}$ inside the shielding according to

$$\frac{\partial \mathcal{C}}{\partial t} = \frac{F}{V_S} C_{\mathrm{LN}} - \frac{F}{V_S}\mathcal{C} - \lambda \mathcal{C} + \frac{\mathcal{S}}{V_S}. \tag{3.0.9}$$

The steady-state radon concentration as a function of radon sources in the shielding and in the purge flow

$$\mathcal{C} = \left(\frac{F}{V_S} C_{\mathrm{LN}} + \frac{\mathcal{S}}{V_S}\right)\left(\frac{F}{V_S} + \lambda\right)^{-1}. \tag{3.0.10}$$

The radon entering the shielding will come from three sources: radon emanation $\mathcal{S}_{\mathrm{eman}}$ in the purge barrier, and leaks $\mathcal{S}_{\mathrm{leak}}$ and diffusion $\mathcal{S}_{\mathrm{diff}}$ from radon in the cavern environment [140] at a concentration

$$C_{\mathrm{SNO}} \approx 130\,\mathrm{Bq/m^3} \tag{3.0.11}$$

which is much larger than the requirement $\mathcal{C}_{\mathrm{req}}$. Radon leaking into the radon purge barrier will be negligible due to an overpressure (0.42" water) [106]. However, radon that diffused through the

gasket may have a significantly larger radon concentration than the concentration in the purge flow of boil-off liquid nitrogen.

The radon s diffusive flux component $\mathcal{S}_{\text{diff}} = A\phi_D$ (units of mBq/sec) will be proportional to the gasket surface area A, and the radon emanation $\mathcal{S}_{\text{eman}} = \lambda E$ so the equilibrium concentration

$$\mathcal{C} = \left(FC_{\text{LN}} + \lambda E + A\phi_D\right)\left(F + \lambda V_S\right)^{-1}. \tag{3.0.12}$$

This chapter focuses on the impact that radon diffusion has on the steady state concentration $\mathcal{C}$ in the shielding. A general rule of thumb used to block radon diffusion from a high-concentration area is to pick a gasket thickness H at least three times the radon diffusion length of the material [262, 263]. However, a gasket that is only three times thicker than its characteristic diffusion length will reduce the concentration in the secondary volume from the SNOLAB drift to

$$C_{\text{SNOLAB}} \exp(-3) = 130\,\text{Bq/m}^3 \cdot 0.0498 \approx 6.5\,\text{Bq/m}^3 = 6.5 \times \mathcal{C}_{\text{req}}, \tag{3.0.13}$$

is still higher than the requirement. To that end the selected gasket sealing the shield must have a low radon diffusion coefficient. The shielding will be disassembled multiple times. As a result, using a metal gasket with very low radon diffusivity is essentially out of the question, since metal gasket are only expected to function without damage to *e.g.* the knife-edge seal and are not designed for re-use. Since the experiment cannot be built all-at-once, the shielding will be disassembled each time construction resumes. Using a rubbery material is expected to be more cost-effective even in case of full replacement for each assembly. Fortunately, soft materials that are sufficiently thick will significantly reduce the steady-state radon concentration diffusing in from the cavern. The diffusion length of ^{222}Rn in rubbers and plastics [128, 130--132, 134, 262]

$$\ell_{\text{g}} = \sqrt{\frac{D_{\text{g}}}{\lambda_{\text{Rn}}}} \approx \sqrt{\frac{10^{-11}\,\text{m}^2/\text{sec}}{2.1 \times 10^{-6}\,\text{sec}}} \times 1,000\,\text{mm/m} \approx 2.17\,\text{mm} \tag{3.0.14}$$

and in this case the gasket ought to be at least

$$H = 3 \times \ell_{\text{g}} = 3 \times 2.17\,\text{mm} \approx 6.54\,\text{mm}. \tag{3.0.15}$$

In the worst case, a material that's 30× softer will have a radon diffusion length only 5.4× larger, and realistically a $5.4 \times 6.54\,\text{mm} = 3.5\,\text{cm}$ is not explicitly unreasonable. However, we won't need to be quite this strict since the purge flow, will remove some of the radon present in the shield at a low rate. Replacing purge dewars is costly and time consuming due to the dewar refill cost and technician time to move and replace when they run out. As a result, we hope to be able to achieve a sufficiently low radon concentration in the shielding with as little gas as possible. For a modest purge flow $F = 1\,\text{L/min}$, the volume exchange rate

$$\frac{F}{V_S} = \frac{1\,\text{L/min}}{5660\,\text{L}} = 1.76 \times 10^{-4}\,\text{min}^{-1} \approx 0.02\%\ \text{shield–volume exchanges per minute}$$

which corresponds to a replacement time $V_S/F \approx 3.94\,\text{days}$ very close to the radon half-life $t_{1/2} = 3.82\,\text{days}$.

This chapter focuses on constraining the radon diffusion of gaskets materials which will seal the purged radon barrier. The mathematical theory of one-dimensional diffusion is described in **Section 3.1** and **Section 3.2** with the geometric and experimental conditions we used to measure the proposed membranes. I describe aspects of diffusion such as solubility and permeability in **Section 3.2.1**. In **Section 3.2.2**, I derive the theoretically expected radon concentration in an apparatus (described in **Section 3.3**) as used in Ref. [129] report the radon diffusion of thin gaskets and the describe the method to derive the best-fit radon diffusion parameters. **Section 3.3** describes the low-cost experimental apparatus used to measure the radon diffusion, solubility and permeability of three gaskets (**Section 3.4**, **Section 3.5** and **Section 3.6**) proposed for the SuperCDMS SNOLAB radon purge. In **Chapter 5**, radon emanation measurements and radon diffusion measurements described in this chapter are used to estimate the steady-state radon concentration of the SuperCDMS SNOLAB radon purge barrier.

3.1 Radon Diffusion Through a 1D Membrane

Radon diffusion has been mathematically modeled and measured in the literature. Analytic solutions for diffusion of single and multi-dimensional membranes can be derived in some special cases [254, 255, 264], and useful approximations exist in more general cases in materials with *e.g.* complicated geometries or anisotropic diffusion coefficients [254, 255]. Numerical methods have been developed to constrain diffusion and permeability [265, 266]. Experiments to measure radon diffusion have been carried out for decades [125, 126], and rare-event searches have particular interest in the diffusion properties of potential radon barrier materials [128--132, 134, 136, 137].

Understanding the one-dimensional solution to diffusion and decay is useful because the experimental gasket geometry has a high degree of symmetry and the deviation from the one-dimensional diffusion and decay model for the gaskets measured here is dominated by systematic uncertainties in experimental factors *e.g.*humidity due to leaks. By obtaining the general time-dependent solution to radon through a one-dimensional material, the radon flux through the gasket is analytically derived.

For the duration of the experiments described in this chapter, one side of a gasket of length H is held at a constant radon concentration C_H, using the high-activity calibration source described in **Section 4.2.2**. The concentration $C(x,t)$ in the gasket will begin to rise and radon will slowly propagate from the high-radon, or ‘‘hot’’ side at $x = H$ to the low-radon, or ‘‘cold’’ side at $x = 0$. The gasket should have low radon at the start of the experiment with the concentration satisfying the initial condition

$$C \approx 0\,\text{Bq/m}^3, \qquad 0 < x < H \quad t = 0. \tag{3.1.1}$$

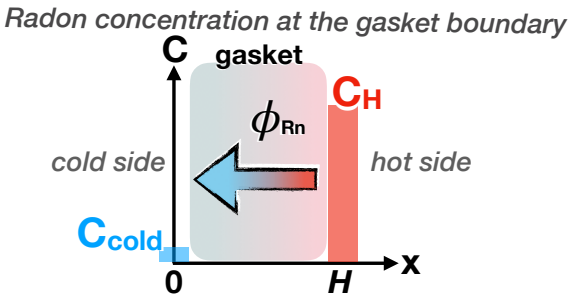

Figure 3.2: Radon boundary conditions for the experiments to determine the diffusion properties of gaskets described in this chapter. The flux boundary of interest is located at $x = 0$, so the radon flux ϕ_{Rn} is leftward moving.

The time-independent boundary conditions for the duration of experiment are given by

$$C(x = 0) = 0\,\mathrm{Bq/m^3}, \qquad t \geq 0 \qquad \text{'cold side'} \tag{3.1.2}$$

$$C(x = H) \equiv C_H = \text{const.}, \qquad t \geq 0 \qquad \text{'hot side'}, \tag{3.1.3}$$

as depicted in **Fig. 3.2**. If the diffusion occurs over a short period of time, as expected for very thin or soft materials, radon decay may be neglected and the solution to the diffusion(-only) equation may be differentiated following Fick's law and multiplying the result by the diffusion coefficient D of the gasket to obtain the radon flux at the cold side

$$\phi_{\mathrm{Rn}}(t) = D\frac{\partial C}{\partial x}\bigg|_{x=0}. \tag{3.1.4}$$

The flux is not assigned a negative sign since the model (specifically the boundary conditions) includes radon diffusing from the right-side at $x = H > 0$, at high concentration, to $x = 0$, at low concentration, traveling along $-\hat{x}$.

I will now describe the general form of the solution to the diffusion-only condition, ignoring the decay of radon during diffusion. It is possible to use the common technique of separation of variables to obtain the linearly dependent solution of the one-dimensional diffusion equation

$$\frac{\partial C}{\partial t} = D\,\frac{\partial^2 C}{\partial x^2}, \tag{3.1.5}$$

where spatial- and temporal-dependence of the concentration C assumes the form

$$C(x, t) = X(x)\cdot T(t), \tag{3.1.6}$$

so that Eqn. 3.1.5 is written with the components as

$$X\frac{\mathrm{d}T}{\mathrm{d}t} = D\,T\frac{\mathrm{d}^2 X}{\mathrm{d}x^2}. \tag{3.1.7}$$

Dividing by the concentration $T(t)\cdot X(x)$, shows clearly that the solutions are independent:

$$\frac{T'}{T} = D\,\frac{X''}{X} = -\kappa^2\,D. \tag{3.1.8}$$

The primes indicate the total derivative (*i.e.* $^{\mathrm{d}}/_{\mathrm{dx}}$, $^{\mathrm{d}}/_{\mathrm{dt}}$) of the function. Then we can separate each of the functions giving equations for space and time

$$T' + \kappa^2 DT(t) = 0 \qquad \text{and} \tag{3.1.9}$$

$$X'' + \kappa^2 X(x) = 0. \tag{3.1.10}$$

The time-dependent solution to Eqn. 3.1.9 can readily be obtained

$$T(t) = \exp(-\kappa^2 D\, t). \tag{3.1.11}$$

Unbounded solutions are of no interest to physical systems, and so we require $\kappa^2 > 0$, ignoring imaginary eigenvalues. This makes intuitive sense because as the diffusing substance spreads, continuity, which is implicitly enforced by Fick's law, requires that the concentration everywhere decreases over time, and so the time-dependent component is expected to be exponential. The spatial equation 3.1.10 is a Sturm-Liouville problem for which the solution is given by

$$X(x) = A\, \cos(\kappa x) + B\, \sin(\kappa x) \tag{3.1.12}$$

and so the general expectation for the radon concentration in the gasket under homogeneous boundary conditions

$$C(x,t) = X(x)T(t) = \Big(A\, \cos(\kappa x) + B\, \sin(\kappa x)\Big) \exp(-\kappa^2 D\, t). \tag{3.1.13}$$

This solution has an oscillating spatial component and a decaying temporal component. Solutions to diffusion (and heat) equations, *i.e.* the values of A and B, under different initial and boundary constraints may be obtained using the method of Laplace transformation and Fourier expansion. The most general solution to the concentration is obtained by summing solutions of the form Eqn. 3.1.14 so that

$$C(x,t) = \sum_{n=1}^{\infty} \Big(A_n\, \cos(\kappa_n x) + B_n\, \sin(\kappa_n x)\Big) \exp(-\kappa_n^2 D\, t). \tag{3.1.14}$$

To determine the time-dependent radon concentration $C(x,t)$ in the gasket that solves Eqn. 3.2.1, we find the concentration $w(x,t)$ that solves the diffusion equation

$$\frac{\partial w}{\partial t} = D\frac{\partial^2 w}{\partial x^2} \tag{3.1.15}$$

without radioactive decay, subject to the initial and boundary conditions in Eqns. 3.1.1, 3.1.2, and 3.1.3. To obtain the solution to the non-homogeneous boundary conditions given in Eqns 3.1.2 and 3.1.3, corresponding to the experimental conditions used to measure the radon diffusion through membranes, we will build the time-dependent solution $w(x,t)$ from a simplified (time-independent)

solution $W(x)$ given by the equilibrium problem wherein

$$D \cdot \frac{\partial^2 W}{\partial x^2} = 0, \tag{3.1.16}$$

subject to $W(x=0) = 0$ and $W(x=H) = C_H$. The concentration $W(x)$ is solved by a line

$$W(x) = a\,x + b \tag{3.1.17}$$

as Fick's law suggests. Then because at $x = 0$, the concentration vanishes $W(0) = 0$, $b = 0$. Then requiring $W(x=H) = C_H$ means that $a \cdot H = C_H$, and the solution to the homogenous problem

$$W(x) = {}^{C_H \cdot x}/_{H}. \tag{3.1.18}$$

Then, we use the homogenous solution $W(x)$ and the time-dependent solution

$$\tilde{v}(x,t) \equiv w(x,t) - W(x), \tag{3.1.19}$$

whose initial condition $\tilde{v}(x, t=0) \neq 0$–unlike that required by the real solution w–we obtain by performing a mathematical trick. With this technique, the non-homogenous boundary conditions inherent to the experiment will be satisfied by the real solution $w(x,t)$ (*i.e.* $w(H,t) = C_H$). Explicitly, this solution

$$\tilde{v}(x,t) = w(x,t) - {}^{C_H \cdot x}/_{H} \tag{3.1.20}$$

will satisfy the (homogenous) boundary conditions

$$\begin{aligned} \tilde{v}(0,t) &= w(0,t) - {}^{C_H}/_{H} \cdot 0 = 0\checkmark \\ \tilde{v}(H,t) &= \underbrace{w(H,t)}_{C_H} - {}^{C_H}/_{H} \cdot H = 0\checkmark \end{aligned}$$

and the initial condition gives rise to a transformed initial $t = 0$ concentration

$$\tilde{v}(x,0) = \cancelto{0}{w(x,0)} - {}^{C_H}/_{H} \cdot x = -{}^{C_H}/_{H} \cdot x. \tag{3.1.21}$$

These equations define the experimental conditions of the transformed solution which, upon subtracting $W(x)$, will give the real solution $w(x,t)$ as a function of time. With this technique, we trade a non-homogeneous boundary condition for a homogenous initial condition. The transformed solution $\tilde{v}$ will solve the diffusion equation

$$\frac{\partial v}{\partial t} = \frac{\partial^2 v}{\partial x^2}, \qquad 0 < x < H, \qquad t > 0 \tag{3.1.22}$$

subject to

$$\tilde{v}(0,t) = 0,\ \tilde{v}(H,t) = 0, \qquad t \geq 0 \tag{3.1.23}$$

$$\tilde{v}(x,0) = -C_H/H \cdot x. \tag{3.1.24}$$

To obtain the solution $\tilde{v}(x,t)$, we use the Fourier method which assumes a series solution of the form

$$\tilde{v}(x,t) = \sum_{n=1}^{\infty} \Big(A_n \cos(\kappa_n x) + B_n \sin(\kappa_n x) \Big) \exp(-\kappa_n^2 D\, t). \tag{3.1.25}$$

The boundary conditions require that the solution vanish at the edges $x = (0, H)$ of the membrane, so the eigenvalues κ_n must take the form

$$\kappa_n = \frac{n\,\pi}{H}, /quad n \in (0,\ 1,\ 2,\ ...). \tag{3.1.26}$$

Since $\cos(n\,\pi)$ is non-zero for integer n, all $A_n = 0$ must identically vanish. Then the solution must take the form

$$\tilde{v}(x,t) = \sum_{n=1}^{\infty} B_n \sin\Big(\frac{n\pi x}{H}\Big) \exp\left(-\Big(\frac{n\,\pi}{H}\Big)^2 D\, t \right). \tag{3.1.27}$$

Now we can use the transformed initial condition (Eqn. 3.1.24)

$$\tilde{v}(x,0) = \sum_{n=1}^{\infty} B_n \sin\Big(\frac{n\pi x}{H}\Big) = -\frac{C_H}{H} \cdot x \tag{3.1.28}$$

to determine the coefficients B_n by integration:

$$B_n = \frac{2}{H} \int_0^H \left(-\frac{C_H}{H} \cdot x \right) \sin\Big(\frac{n\pi x}{H}\Big)\ \mathrm{d}x, \qquad n \in (0, 1, 2, ...). \tag{3.1.29}$$

Note that integration by parts yields

$$\int_0^H x \sin(a\,x)\,\mathrm{d}x = \frac{\sin(a\,x) - a\,x\,\cos(a\,x)}{a^2}.$$

Then, with the appropriate limits and coefficients, the general solution to Eqn. 3.1.29 is

$$B_n = \frac{-2\,C_H}{H^2} \left(\frac{\cancelto{0}{\sin(n\,\pi\,x/H)} - (n\,\pi\,x/H)\cos(n\,\pi\,x/H)}{(n\,\pi/H)^2} \right|_0^H = \frac{2 \cdot C_H}{\pi} \frac{x}{H\,n} \cos\Big(\frac{n\,\pi\,x}{H}\Big) \Big|_0^H.$$

The coefficients B_n can be expressed much more compactly as

$$B_n = \frac{2 \cdot C_H}{\pi} \frac{(-1)^n}{n}, \tag{3.1.30}$$

and $\tilde{v}(x,t)$, the solution to the transformed homogeneous boundary problem, is

$$\tilde{v}(x,t) = \frac{2 \cdot C_H}{\pi} \sum_{n=1}^{\infty} \frac{(-1)^n}{n} \sin\left(\frac{n\pi x}{H}\right) \exp\left(-\left(\frac{n\,\pi}{H}\right)^2 D\,t\right). \tag{3.1.31}$$

To obtain the solution to the non-homogenous boundary problem $w(x,t)$, we substitute this result into Eqn. 3.1.20 ($w(x,t) = \tilde{v}(x,t) + {}^{C_H \cdot x}/_{H}$) so that

$$w(x,t)\frac{C_H \cdot x}{H} + \frac{2 \cdot C_H}{\pi} \sum_{n=1}^{\infty} \frac{(-1)^n}{n} \sin\left(\frac{n\pi x}{H}\right) \exp\left(-\left(\frac{n\,\pi}{H}\right)^2 D\,t\right). \tag{3.1.32}$$

Before deriving the true solution C in the membrane which accounts for radon decay, let us check that this solution solves the conditions. The partial derivative of this equation with respect to time

$$\begin{aligned}\frac{\partial w}{\partial t} &= -\frac{2C_H}{\pi} \sum_{n=1}^{\infty} \frac{(-1)^n}{n} \sin\left(\frac{n\pi x}{H}\right) D \left(\frac{n\pi}{H}\right)^2 \exp\left(-D({}^{n\pi}/_{H})^2 t\right) \\ &= -D\frac{2C_H\pi}{H^2} \sum_{n=1}^{\infty} (-1)^n\, n \times \sin\left(\frac{n\pi x}{H}\right) \exp\left(-D({}^{n\pi}/_{H})^2 t\right).\end{aligned}$$

This is proportional to the second spatial derivative of Eqn. 3.1.32 with respect to space

$$\begin{aligned}\frac{\partial^2 w}{\partial x^2} &= \frac{\partial^2}{\partial x^2}\cancelto{0}{\left(\frac{C_H x}{H}\right)} - \frac{2C_H}{\pi} \sum_{n=1}^{\infty} \frac{(-1)^n}{n} \left(\frac{n\pi}{H}\right)^2 \sin\left(\frac{n\pi x}{H}\right) \exp\left(-D({}^{n\pi}/_{H})^2 t\right) \\ &= -\frac{2C_H\pi}{H^2} \sum_{n=1}^{\infty} (-1)^n\, n \times \sin\left(\frac{n\pi x}{H}\right) \exp\left(-D({}^{n\pi}/_{H})^2 t\right),\end{aligned} \tag{3.1.33}$$

so indeed $\frac{\partial w}{\partial t} = D\frac{\partial^2 w}{\partial x^2}$. It is useful to remind ourselves that the decay-less solution $w(x,t)$ obeys the initial and boundary conditions (Eqns 3.1.1, 3.1.2, and 3.1.3) we impose to determine the gasket's radon diffusion coefficient. Since both x and $\sin(x)$ are odd,

$$w(0,t) = \frac{C_H \cancelto{0}{x}}{H} + \frac{2C_H}{\pi} \sum_{n=1}^{\infty} (-1)^n \cancelto{0}{\sin\left(\frac{n\pi x}{H}\right)} \exp\left(-D({}^{n\pi}/_{H})^2 t\right) = 0. \quad \checkmark$$

The boundary condition at $x = H$ is satisfied since $\sin(n\pi) = 0$ for integer n:

$$w(H,t) = C_H \frac{\cancel{H}^{1}}{\cancel{H}} + \frac{2C_H}{\pi} \sum_{n=1}^{\infty} (-1)^n \cancelto{0}{\sin(n\pi)} \exp\left(-D({}^{n\pi}/_{H})^2 t\right) = C_H. \quad \checkmark$$

3.2 Danckwert's Radon Diffusion Model

An analytic solution for the concentration of reactive and decaying substances wasn't developed until the 1950's when Danckwerts published a solution [264]. For sufficiently radon-hard materials,

a non-zero fraction of the radon entering the gasket will not escape the other side because the mean diffusion time will be comparable to the mean lifetime. The concentration $C(x,t)$ of radon in the (one-dimensional) gasket/membrane obeys

$$\frac{\partial C}{\partial t} = D\frac{\partial^2 C}{\partial x^2} - \lambda C. \tag{3.2.1}$$

The experiment we used to determine the radon diffusion properties of gasket materials is performed by holding a membrane of thickness H at high concentration C_H on one side, and measuring the decay rate of radon from diffusion as a function of time on the other side. The analysis in this section to obtain and verify the concentration closely follows the outline in Crank's text [254]. The correct solution depends on the initial and boundary conditions (Eqns 3.1.2 and 3.1.3) of the experiment and is not obvious. Danckwerts [264] devised a useful integral equation technique to include the effect of reactivity/decay by first solving the decay-less diffusion equation and transforming the result.

Danckwerts showed [264] that the solution $C(x,t)$ to Eqn. 3.2.1, which includes both diffusion and decay, can be derived by applying an integral transformation

$$C(x,t) = w(x,t)\exp(-\lambda t) + \lambda\int_0^t w(x,t)\exp(-\lambda t')\,\mathrm{d}t'. \tag{3.2.2}$$

to the decay-less solution $w(x,t)$. Let us first verify that Eqn. 3.2.2 solves the diffusion equation with decay (Eqn. 3.2.1) by differentiating twice with respect to space and once with time. The time derivative

$$\begin{aligned}\frac{\partial C}{\partial t} &= \frac{\partial}{\partial t}\left(w(x,t)\exp(-\lambda t) + \lambda\int_0^t w(x,t')\exp(-\lambda t')\,\mathrm{d}t'\right)\\ &= \frac{\partial}{\partial t}\left(w(x,t)\exp(-\lambda t)\right) + \lambda\frac{\partial}{\partial t}\left(\int_0^t w(x,t')\exp(-\lambda t')\,\mathrm{d}t'\right).\end{aligned}$$

The derivate of the integral over t' leaves only the upper bound limit of the argument $w(x,t')\exp(-\lambda t')$ at $t'=t$, since the derivative of a constant is zero. The time rate of change of the concentration

$$\frac{\partial C}{\partial t} = \frac{\partial w}{\partial t}\exp(-\lambda t) - \lambda\, w\, \exp(-\lambda t) + \lambda\, w\exp(-\lambda t) = \frac{\partial w}{\partial t}\exp(-\lambda t), \tag{3.2.3}$$

proportional to the original solution. The second spatial derivative of Eqn. 3.2.2

$$\begin{aligned}\frac{\partial^2 C}{\partial x^2} &= \frac{\partial^2}{\partial x^2}\left(w\exp(-\lambda t) + \lambda\int_0^t w\exp(-\lambda t')\,\mathrm{d}t'\right)\\ &= \frac{\partial^2 w}{\partial x^2}\exp(-\lambda t) + \lambda\int_0^t \frac{\partial^2 w}{\partial x^2}\exp(-\lambda t')\,\mathrm{d}t'.\end{aligned} \tag{3.2.4}$$

Since w obeys Eqn. 3.1.15, multiplying Eqn. 3.2.4 by the diffusion coefficient D yields

$$D\frac{\partial^2 C}{\partial x^2} = \frac{\partial w}{\partial t}\exp(-\lambda t) + \lambda\int_0^t \frac{\partial w}{\partial t}\exp(-\lambda t')\,\mathrm{d}t'. \tag{3.2.5}$$

Using the expression for the time derivative obtained in Eqn. 3.2.3 simplifies this result to

$$D\frac{\partial^2 C}{\partial x^2} = \frac{\partial C}{\partial t} + \lambda \int_0^t \frac{\partial C}{\partial t'}\,\mathrm{d}t'. \tag{3.2.6}$$

Since the concentration $C = 0$ everywhere in the gasket at $t = 0$ (Eqn. 3.1.1),

$$D\frac{\partial^2 C}{\partial x^2} = \frac{\partial C}{\partial t} + \lambda\, C + \lambda \cancelto{0}{C(x, t_0)},$$

and Eqn. 3.2.1 is satisfied. Let us now check that this proposed solution solves the experimental boundary conditions that we will impose on the gasket.

$$C(0,t) = \underbrace{w(0,t)}_{0}\exp(-\lambda t) + \lambda \int_0^t \underbrace{w(0,t)}_{0}\exp(-\lambda t')\,\mathrm{d}t' = 0. \quad \checkmark \tag{3.2.7}$$

The concentration at $x = H$

$$\begin{aligned} C(H,t) &= \underbrace{w(H,t)}_{C_H}\exp(-\lambda t) + \lambda \int_0^t \underbrace{w(H,t)}_{C_H}\exp(-\lambda t')\,\mathrm{d}t' \\ &= C_H\left(\exp(-\lambda t) + \lambda \int_0^t \exp(-\lambda t')\,\mathrm{d}t'\right) \\ &= C_H\left(\underbrace{\exp(-\lambda t) - \exp(-\lambda t)}_{0} + \underbrace{\exp(-\lambda 0)}_{1}\right) = C_H, \quad \checkmark \end{aligned}$$

and the initial condition is satisfied trivially since $w(0 < x < H, 0) = 0$. To determine the radon concentration in the gasket, we plug Eqn. 3.1.32 into Danckwert's transformation Eqn. 3.2.2. To compute the solution C, it is convenient to cast $w(x,t)$ in terms of constants

$$a = \frac{C_H x}{H} \qquad b_n = \frac{2C_H}{\pi}\sum_{n=1}^{\infty}(-1)^n \sin\left(\frac{n\pi x}{H}\right), \tag{3.2.8}$$

so that Eqn. 3.1.32 can be expressed

$$w(x,t) \equiv a + \sum_{n=1}^{\infty} b_n \exp\left(-D(n\pi/H)^2 t\right). \tag{3.2.9}$$

Upon suppressing the bounds of the infinite sum, the left-hand term in the transformation

$$\begin{aligned} w(x,t)\exp(-\lambda t) &= \left(a + \sum b_n \exp\left(-D(n\pi/H)^2 t\right)\right)\exp(-\lambda t) \\ &= \left(a\exp(-\lambda t) + \sum b_n \exp\left(-\lambda t - D(n\pi/H)^2 t\right)\right), \end{aligned} \tag{3.2.10}$$

and the right-hand integral term

$$\lambda \int_0^t w(x,t') \exp(-\lambda t')\, \mathrm{d}t' = \lambda \int_0^t \left(a + \sum b_n \exp\left(-D(n\pi/H)^2 t'\right) \right) \exp(-\lambda t')\, \mathrm{d}t'$$
$$= \lambda \int_0^t \left(a \exp(-\lambda t') + \sum b_n \exp\left(-\lambda t' - D\left(n\pi/H\right)^2 t'\right) \right) \mathrm{d}t'. \quad (3.2.11)$$

Defining a factor for the argument of the exponent

$$\beta_n \equiv \lambda + D(n\pi/H)^2, \quad (3.2.12)$$

and distributing the exponential to both a and b_n terms, simplifies Eqn. 3.2.11 to

$$\lambda \int_0^t w(x,t') \exp(-\lambda t')\, \mathrm{d}t' = \lambda \int_0^t \left(a e^{-\lambda t'} + \sum b_n e^{-\beta_n t'}\, \mathrm{d}t' \right)$$
$$= -a\left(e^{-\lambda t} - 1\right) + \lambda \sum b_n \int_0^t e^{-\beta_n t'}\, \mathrm{d}t'$$
$$= a\left(1 - e^{-\lambda t}\right) + \sum b_n \frac{\lambda}{\beta_n}\left(1 - e^{-\beta_n t}\right). \quad (3.2.13)$$

Summing Eqns. 3.2.10 and 3.2.13 as required by Eqn. 3.2.2 yields the concentration

$$C(x,t) = a \exp^{-\lambda t} + \sum b_n e^{-\beta_n t} + a\left(1 - e^{-\lambda t}\right) + \sum b_n \frac{\lambda}{\beta_n}\left(1 - e^{-\beta_n t}\right) \quad (3.2.14)$$
$$= a + \sum b_n e^{-\beta_n t} + \sum b_n \frac{\lambda}{\beta_n}\left(1 - e^{-\beta_n t}\right)$$
$$= a + \sum_{n=1}^{\infty} b_n \left(e^{-\beta_n t} + \frac{\lambda}{\beta_n}\left(1 - e^{-\beta_n t}\right) \right).$$

Then, the general solution to the concentration in the gasket, subject to the conditions in Eqns. 3.1.1, 3.1.2, and 3.1.3, including radon decay, is given by substituting for a and b_n using Eqn. 3.2.8 to get

$$C(x,t) = \frac{C_H x}{H} + \frac{2C_H}{\pi} \sum_{n=1}^{\infty} \frac{(-1)^n}{n} \sin\left(\frac{n\pi x}{H}\right) \times \left(\frac{\lambda}{\beta_n} + \left(1 - \lambda/\beta_n\right) e^{-\beta_n t} \right). \quad (3.2.15)$$

Ref. [129] used this one-dimensional solution to determine the radon diffusion coefficient and solubility of thin samples.

The exact solution everywhere inside the gasket is not needed to find the time-dependent radon concentration on the cold side to where the has radon slowly diffused; however, the time-dependent radon flux $\phi(t)$ supplying the cold-side with radon is needed. The radon flux can be found by applying Fick's law, taking the spatial derivative of the solution at the interface between the gas on the cold-side and the gasket face at $x = 0$ [129, 254, 255, 264]. The time-dependent factors in the

right-hand term can be ignored for now so that

$$\frac{\partial}{\partial x}\left(\frac{2C_H}{\pi}\sum_{n=1}^{\infty}\frac{(-1)^n}{n}\sin\left(\frac{n\pi x}{H}\right)\right)\Bigg|_{x=0} = \frac{2C_H}{\pi}\left(\frac{\pi}{H}\right)\sum_{n=1}^{\infty}\frac{(-1)^n}{n}n\cos\left(\frac{n\pi x}{H}\right)\Bigg|_{x=0}$$
$$= \frac{2C_H}{H}\sum_{n=1}^{\infty}(-1)^n\,.$$

Upon differentiation, the first spatially-dependent term in Eqn. 3.2.15 is a constant, and the time-dependent radon decay flux entering the cold-side per unit area is given by

$$\phi(t) \propto D\frac{\partial C}{\partial x}\Bigg|_{x=0} = C_H\frac{D}{H}\left[1+2\sum_{n=1}^{\infty}(-1)^n\times\left(\frac{\lambda}{\beta_n}+(1-\lambda/\beta_n)\,e^{-\beta_n t}\right)\right]. \tag{3.2.16}$$

This time-dependent flux will determine the radon concentration on the cold-side of the apparatus.

3.2.1 Permeability and Solubility

At the hot-side, the radon concentration in the gas $C = C_H$ is held constant for the duration of the experiment. There exists a material-dependent jump discontinuity at $x = H$, the gas–gasket boundary, quantified by the solubility S of the material (shown graphically in **Fig. 3.3**). The equilibrium radon concentration just inside the material $C(x = H, t \to \infty) = C_g$ is proportional to the hot-side concentration

$$C_g \equiv S\,C_H. \tag{3.2.17}$$

Solubility is related to pore filling on the surface of the material and is sometimes called the coefficient of adsorption [131]. The solubility of the gasket is a function of the gas pressure, temperature, and the presence of other chemicals, especially water. The solubility of radon in solids is known to increase with humidity varying (in nylon foils) by as much as 1,000× at 100% relative humidity [182, 260]. However, measurements at 30% relative humidity indicated no significant

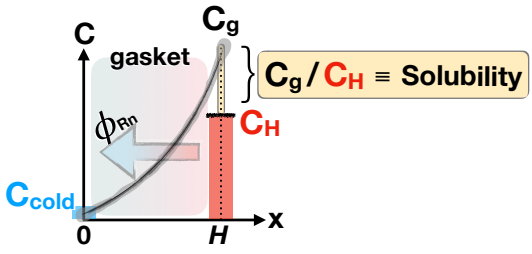

Figure 3.3: Radon solubility S characterizes the jump discontinuity of radon concentration at the boundary between the gasket $C_g = C(x = H)$ and hot-side C_H. The ratio of the equilibrated gasket concentration $C(0 < x < H)$ shown (line) at the surface to the (hot side) radon concentration in the gas is the solubility $S \equiv C_g/C_H$. The discontinuity presumably exists on the cold side as well, however, the model used to derive the cold-side concentration from the boundary flux assumes the concentration is zero. This is the convention taken in Ref. [129].

difference in radon solubility for nylon foils [138]. The cold-side flux of radon sourcing the cold side

$$\phi(t) \equiv SD\frac{\partial C}{\partial x}\bigg|_{x=0} = SC_H\frac{D}{H}\left[1 + 2\sum_{n=1}^{\infty}(-1)^n \times \left(\frac{\lambda}{\beta_n} + (1 - \lambda/\beta_n)\, e^{-\beta_n t}\right)\right]. \tag{3.2.18}$$

This flux is proportional to the gasket's radon solubility and to the membrane's radon diffusion coefficient D; their product is therefore the permeability

$$P = S\,D. \tag{3.2.19}$$

The solubility of radon in solid materials is generally in the range

$$S \sim 1\text{–}20. \tag{3.2.20}$$

Experimentally, we found that large humidities do lead to large radon solubilities so we found it critical to control the experimental conditions during the measurement.

3.2.2 Predicted Cold-Side Radon Concentration

The time-dependent radon concentration $\mathcal{C}$ on the cold side

$$\frac{\partial \mathcal{C}}{\partial t} = \phi(t)\,\frac{A}{V_c} - \lambda\mathcal{C} = \frac{AD}{V_c}\frac{\partial C}{\partial x}\bigg|_{x=0} - \lambda\mathcal{C}, \tag{3.2.21}$$

determined by the flux $\phi(t)$ times the surface area A of the gasket and the cold side volume V_c. In practice, the radon concentration

$$\mathcal{C}(t) = R_{\text{gas}}(t)/V_c \tag{3.2.22}$$

will be measured in a commercial RAD7 alpha counter [267]. The RAD7 infers the radon activity on the cold side by circulating gas decaying at a rate R_{gas} from the cold side of the experimental apparatus into the RAD7 active volume $V_{\text{RAD7}} \approx 800\,\text{cm}^3$ where the alpha decays of ^{218}Po and ^{214}Po are measured. Intuitively, the cold side concentration will increase proportional to the hot-side concentration C_H, solubility S, diffusion D, and inversely proportional to the cold-side volume V_c, and membrane thickness H. A thicker membrane will cause the radon to spend more time in the material. and the decayed radon will never escape the membrane.

The radon decay rate on the cold side, after radon has diffused through the gasket, is given by the solution to Eqn. 3.2.21 which has a general form

$$\frac{\mathrm{d}y}{\mathrm{d}t} + p(t)\,y(t) = \varphi(t). \tag{3.2.23}$$

The solution to Eqn. 3.2.23 can be found using an elementary technique where the left-hand side is forced to take the form of the derivative of a single term. A unique choice of $\mathcal{F}$ transforms

Eqn. 3.2.23 to

$$\frac{\mathrm{d}}{\mathrm{d}t}\Big(\mathcal{F}(t)\,y(t)\Big) = \varphi(t), \tag{3.2.24}$$

so the argument $\mathcal{F}(t)\,y(t)$ is the antiderivative of the original equation $\frac{\mathrm{d}y}{\mathrm{d}t} + p(t)\,y(t)$. Multiplying the Eqn. 3.2.23 by an exponential function (the integrating factor) determined from the product rule so that

$$\frac{\mathrm{d}}{\mathrm{d}t}\Big(\mathcal{F}(t)\,y(t)\Big) = \mathcal{F}\,\frac{\mathrm{d}y}{\mathrm{d}t} + \frac{\mathrm{d}\mathcal{F}}{\mathrm{d}t}\,y(t) \tag{3.2.25}$$

and, by Eqn. 3.2.23, $\frac{\mathcal{F}'}{\mathcal{F}} = p(t)$. By Eqn. 3.2.21, $p(t) = \lambda$, therefore the integrating factor

$$\exp\left(\int \frac{\mathcal{F}'}{\mathcal{F}}\,\mathrm{d}t\right) = \exp\left(\int p(t)\,\mathrm{d}t\right) = \exp\left(\int \lambda\,\mathrm{d}t\right) = \exp\left(\lambda t\right) \tag{3.2.26}$$

and is the multiplicative factor for Eqn. 3.2.23. Then, $\mathcal{F}(t) = e^{\lambda t}$ and

$$e^{\lambda t}\left(\frac{\mathrm{d}y}{\mathrm{d}t} + \lambda\,y(t)\right) = \frac{\mathrm{d}}{\mathrm{d}t}\Big(e^{\lambda t}\,y(t)\Big) = e^{\lambda t}\varphi(t), \tag{3.2.27}$$

so that the solution $y(t)$ to Eqn. 3.2.23 will be determined from

$$\int \frac{\mathrm{d}}{\mathrm{d}t}\Big(e^{\lambda t}\,y(t)\Big)\,\mathrm{d}t = \int e^{\lambda t}\varphi(t)\,\mathrm{d}t. \tag{3.2.28}$$

By the fundamental theorem of calculus, the integral of the total derivative on the left side simplifies to $e^{\lambda t}\,y(t)$. Therefore, dividing by the integrating factor yields the general solution

$$y(t) = e^{-\lambda t}\int e^{\lambda t}\varphi(t)\,\mathrm{d}t. \tag{3.2.29}$$

Applying this technique to Eqn. 3.2.21, using the definition of the flux from Eqn. 3.2.18, the integral

$$\left(C_H\frac{ADS}{H}\right)e^{-\lambda t}\int e^{\lambda t}\left(1 + 2\sum_{n=1}^{\infty}(-1)^n \times \left(\lambda/\beta_n + (1-\lambda/\beta_n)\,e^{-\beta_n t}\right)\right)\,\mathrm{d}t. \tag{3.2.30}$$

The first term in the integral is simply $1/\lambda\exp(\lambda t)$. The summed terms $2\sum_{n=1}^{\infty}(-1)^n$ in the integral become

$$\begin{aligned}
\int e^{\lambda t}\left(\lambda/\beta_n + (1-\lambda/\beta_n)\,e^{-\beta_n t}\right)\,\mathrm{d}t &= \int\left(\lambda/\beta_n e^{\lambda t} + (1-\lambda/\beta_n)\,e^{(\lambda-\beta_n)t}\right)\,\mathrm{d}t \\
&= \frac{e^{\lambda t}}{\beta_n} + \frac{1-\lambda/\beta_n}{\lambda-\beta_n}e^{(\lambda-\beta_n)t} \\
&= \frac{e^{\lambda t}}{\beta_n} - \frac{1-\lambda/\beta_n}{\beta_n(1-\lambda/\beta_n)}e^{(\lambda-\beta_n)t} \\
&= \frac{e^{\lambda t}}{\beta_n}\left(1 - e^{-\beta_n t}\right).
\end{aligned} \tag{3.2.31}$$

By plugging Eqn. 3.2.31 into Eqn 3.2.30, neglecting the multiplicative factor (including the area, hot-side radon concentration, etc), and including a constant of integration r_i

$$R_{\text{gas}}(t) \propto e^{-\lambda t}\left(\frac{1}{\lambda}e^{\lambda t} + 2\sum_{n=1}^{\infty}(-1)^n \times \frac{e^{\lambda t}}{\beta_n}\left(1 - e^{-\beta_n t}\right) + r_i\right) \tag{3.2.32}$$

so the inverse of the integrating factor $\exp(\lambda t)$ is cancelled in each flux term, leaving

$$R_{\text{gas}}(t) \propto \frac{1}{\lambda} + 2\sum_{n=1}^{\infty}(-1)^n \times \frac{1}{\beta_n}\left(1 - e^{-\beta_n t}\right) + r_i\, e^{-\lambda t}. \tag{3.2.33}$$

Including the prefactor $C_H{}^{A\,D\,S}/_{H}$, and dividing out the decay constant λ, the radon decay rate at $t = 0$

$$R_0 \equiv R_{\text{gas}}(t=0) = C_{\text{H}}\frac{ADS}{H\lambda}\left(1 + 2\sum_{n=1}^{\infty}(-1)^n \times {}^{\lambda}\!/_{\beta}\underbrace{\left(1 - \cancel{e^{-\beta 0}}\right)}_{0}\right) - r_i\cancel{e^{-\lambda 0}}^{1}.$$

In the case of a non-zero initial radon activity $R_0 \equiv \mathcal{C}_0\, V$ arising from lab air in the volume V of tubing, RAD7, and cold side at the start of the experiment,

$$R_0 = C_{\text{H}}\frac{ADS}{H\lambda} - r_i \qquad \Leftrightarrow \qquad r_i = \left(R_0 - C_{\text{H}}\frac{ADS}{H\lambda}\right). \tag{3.2.34}$$

Adding the initial concentration $\mathcal{C}_0 = {}^{R_0}\!/_{V}$ from Eqn. 3.2.34 to the time-dependent radon decay rate from Eqn. 3.2.33 divided by the volume yields the radon concentration (decays per unit volume) as a function of time

$$\mathcal{C}(t) = C_{\text{H}}\frac{ADS}{H\lambda V}\left(1 - e^{-\lambda t} + 2\sum_{n=1}^{\infty}(-1)^n \times {}^{\lambda}\!/_{\beta}\left(1 - e^{-\beta t}\right)\right) + \mathcal{C}_0\, e^{-\lambda t}. \tag{3.2.35}$$

The surface area A of the gasket is the length $\mathcal{L}$ times the exposed width w. A gasket of thickness H has a characteristic radon diffusion coefficient

$$\tilde{D} = \lambda H^2.$$

Since $\beta_n \equiv \lambda + D({}^{n\pi}\!/_{H})^2$ (Eqn. 3.2.12),

$$\frac{\lambda}{\beta_n} = \frac{\lambda}{\lambda + D({}^{n\pi}\!/_{H})^2} = \left[1 + D\left(\frac{n^2\pi^2}{\lambda H^2}\right)\right]^{-1} = \left(1 + n^2\pi^2 \cdot {}^{D}\!/_{\tilde{D}}\right)^{-1}.$$

Neglecting the time-dependence of Eqn. 3.2.35, the solubility S and diffusion coefficient D both scale the radon concentration. With this theoretical expression, raising D and lowering S (and vice versa) by a small amount produces a similar goodness-of-fit. As a result, trying to obtain bounds on the diffusion properties of our gaskets is somewhat complicated since the best-fit solubility and diffusion are generally anti-correlated. To avoid this potentially troublesome detail, we substitute

the permeability $P = S\,D$ in the coefficient. The permeability will scale the theoretically expected concentration and the diffusion coefficient D will determine the shape (time-dependence) of the curve. Then, for an experiment where the initial activity $\mathcal{C}_0 = 0\,\mathrm{Bq/m^3}$, the time-dependent radon concentration on the cold side of the gasket (Eqn. 3.2.35)

$$\mathcal{C}(t) = C_{\mathrm{H}}\frac{AP}{H\lambda V}\left(1 - e^{-\lambda t} + 2\sum_{n=1}^{\infty}(-1)^n \times \frac{1}{1 + n^2\pi^2 \cdot D/\tilde{D}}\left(1 - e^{-\beta t}\right)\right). \tag{3.2.36}$$

The steady-state concentration $\mathcal{C}_\infty \equiv \mathcal{C}(t \to \infty)$ for a given gasket geometry (A, H) held on one side at a concentration C_H

$$\mathcal{C}_\infty = C_{\mathrm{H}}\frac{AP}{H\lambda V}\left(1 + 2\sum_{n=1}^{\infty}\frac{(-1)^n}{1 + n^2\pi^2 \cdot D/\tilde{D}}\right). \tag{3.2.37}$$

Chapter 5 will compare the implications (using Eqn. 3.2.37) of the steady state concentration in the large volume of the lead shielding surrounding the SNOLAB detectors. Ultimately, we will use Eqns. 3.2.35 and 3.2.37 to constrain the diffusion coefficient D, solubility S, and permeability

$$P = S \cdot D \tag{3.2.38}$$

of gaskets acquired by SuperCDMS. The diffusion coefficient D and permeability P are determined by minimizing a test statistic

$$\chi^2(D, P) = \sum_t \left(\frac{C_{\mathrm{R7}} - \mathcal{C}}{\delta C_{\mathrm{R7}}}\right)^2, \tag{3.2.39}$$

where the time-dependent concentrations $C_{\mathrm{R7}} \pm \delta C_{\mathrm{R7}}$ are compared to the theoretical expectation $\mathcal{C}(t)$ at a given D and P for the experimental conditions: gasket geometry (A, H) and hot-side concentration C_H. The maximum and minimum values of D and P covered by the $\Delta\chi^2 = 4.61$ bands are the 90% C.L. limits on both parameters [268]; bounds on the solubility are calculated by finding the largest and smallest values of $S \equiv P/D$ along the bounding contours described above.

The diffusion length ℓ is determined by the best-fit D:

$$\ell = \sqrt{\frac{D}{\lambda}}. \tag{3.2.40}$$

The uncertainty σ_ℓ can be determined by propagating the uncertainty on the diffusion σ_D

$$\sigma_\ell = \frac{\partial}{\partial D}\Big(\ell\Big)\sigma_D = \left|\frac{\mathrm{d}}{\mathrm{d}D}\left(\sqrt{\frac{D}{\lambda}}\right)\sigma_D\right| = \frac{1}{\sqrt{\lambda}}\left(\frac{1}{2\sqrt{D}}\right)\sigma_D = \frac{1}{2\,\lambda\,\ell}\sigma_D.$$

The fractional uncertainty

$$\frac{\sigma_\ell}{\ell} = \frac{1}{2\,\lambda\,\ell^2}\sigma_D = \frac{\sigma_D}{2D}. \tag{3.2.41}$$

The time-dependent comparison shown here is the most accurate model of radon diffusion because it includes the effect decay as radon passes through the gasket.

3.3 Experimental Radon Diffusion Apparatus

Using metal plates and a thin gasket (diffusion barrier) through which radon gas will move, we set up an experiment similar to *e.g.* those outlined in Refs.[128, 129, 134, 135] to measure the diffusive flux through a gasket or foil from within a compartment containing high-activity radon gas. The apparatus designed by Eric Miller and Joseph Street is shown in **Fig. 3.4**. The high- and low-activity ('hot' and 'cold') sides are sandwiched between 12"-by-12" aluminum plates a small distance $d_{\text{plates}} \approx 0.5\,\text{cm}$ apart. The cold side of the apparatus is essentially concentric with the hot side separated by a gasket of known thickness H. The high-activity volume is sealed with a thin butyl O-ring or aluminum tape to prevent leaks to the lab. The radon from the hot side diffuses through to the cold side where the gas was continuously circulated with a commercial Durridge RAD7 α counter [267] which measured the radon concentration as a function of time on the cold side. The cold side was also dried with a small desiccant to keep the relative humidity from rising to unacceptable levels due to a leaky RAD7 or poor gas connections.

For most experiments, the cold-side volume is a roughly circular shape concentric with the hot-side volume. The gasket radius $r_{\text{gasket}} \sim 3" \approx 7.6\,\text{cm}$, was kept small so

$$V_{\text{c}} \sim A_{\text{cold}} \times d_{\text{plates}} = \pi\, r_{\text{gasket}}^2 \times d_{\text{app}} \lesssim \pi\,(7.6\,\text{cm})^2 \times 0.5\,\text{cm} \approx 91\,\text{cm}^3,$$

much less than the volume $V_{\text{RAD7}} = 800\,\text{cm}^3$ of the RAD7 alpha detector. The tubing connecting the cold side to the RAD7 consists of no more than $L = 30" \approx 76\,\text{cm}$ of nylon tubing bearing a radius $r = 1/4" \approx 0.64\,\text{cm}$, so the volume of tubing is expected to be much less than the RAD7 inner volume:

$$V_{\text{tube}} = A_{\text{tube}} \times L = \pi\, r^2 \times L \lesssim \pi\,(0.635\,\text{cm})^2 \times 76\,\text{cm} \approx 96.5\,\text{cm}^3 \ll V_{\text{RAD7}}.$$

The total volume of the cold side

$$V_{\text{total}} = V_{\text{c}} + V_{\text{tube}} + V_{\text{RAD7}} \approx (1/8 + 1/8 + 1)\, V_{\text{RAD7}} \approx 1.2\, V_{\text{RAD7}},$$

dominated by the RAD7 internal volume and systematic uncertainties from incorrectly measured tube volume are correspondingly small. A large concentration C_H on the hot-side is determined by the emanation strength of the calibration source discussed in **Section 4.2.2**. A constant flow of nitrogen gas, regulated by an uncalibrated flow meter through the source is expected to a produce an output concentration that is inversely proportional to the through-going flow rate F:

$$C_H = \frac{R_{\text{py}}}{F\tau} = \frac{14.6\,\text{Bq/min}}{F}. \tag{3.3.1}$$

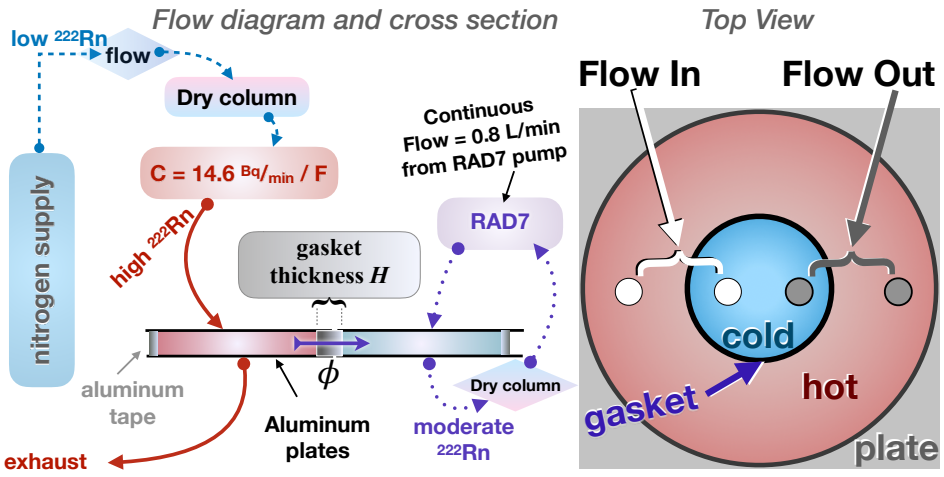

Figure 3.4: Left: Flow path diagram of the experimental apparatus to determine the radon diffusion properties (D, S, P) of proposed gaskets for the radon purge lead shield that will be constructed for SuperCDMS at SNOLAB. A gasket of thickness H separates two volumes sandwiched between two aluminum plates. The boil-off LN_2 gas supply is regulated with a flow meter and fed to a high-activity radon source providing a near-constant output concentration on the 'hot side' (red) where the radon may be measured and exhausted. The radon diffuses through the gasket to the 'cold-side' (blue) of the apparatus where the RAD7 is continuously circulating the diffused radon. A drying desiccant is placed inline to ensure a low relative humidity. **Right:** Top view of the apparatus (gray plate) with flow ports ('in' and 'out') on opposite ends of the hot (red) and cold (blue) sides to encourage thorough gas mixing to achieve a homogenous radon concentration on each side.

Flows of order $F = 2.5\,\mathrm{L/min}$ applied to the calibration source are expected to yield a hot side concentration

$$C_H \approx \frac{14.6\,\mathrm{Bq/min}}{(2.5\times10^{-3})\,\mathrm{m^3/min}} \approx 6,000\,\mathrm{Bq/m^3} \tag{3.3.2}$$

and were changed between experiments, based on the guessed diffusion coefficient, in an attempt to keep the cold-side radon concentration from rising to very high levels. In most experiments, the radon concentration at the output of the hot side was measured by another RAD7. This apparatus was used to constrain the radon diffusion of several gasket materials. Undergraduate Brandon DeVries helped set up the experimental apparatus and monitor the data taking.

3.4 Silicone Diffusion Measurements

A $30\,\mathrm{cm}\times5\,\mathrm{cm}\times5\,\mathrm{mm}$ silicone gasket obtained from Lemer Pax [261] was used to produce a thin gasket sample. The gasket was cut to a total length $\ell = 28\,\mathrm{cm}$, and cut along its $5\,\mathrm{cm}$ side to a thickness $H = 4.5\,\mathrm{mm}$, to avoid long test times. The gasket was placed in a thin configuration with a one-sided surface area

$$A = d_{\mathrm{app}}\,\ell \approx 0.5\,\mathrm{cm}\cdot 28\,\mathrm{cm} = 14\,\mathrm{cm^2}, \tag{3.4.1}$$

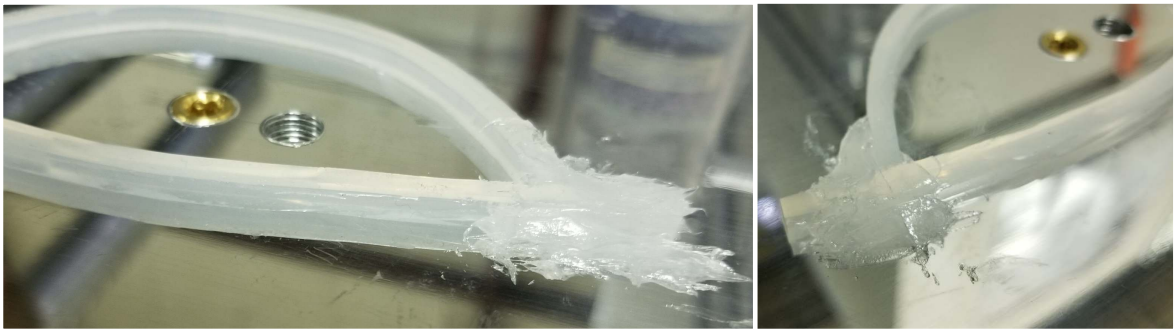

Figure 3.5: Silicone placed in a thin $H = 4.5\,\mathrm{mm}$ almond-shaped geometry to form the cold side. Silicone grease was used to hold the v-shaped edges in place and prevent leaks from the hot side.

forming a 'Vesica Piscis'[2] cold side as shown in **Fig. 3.5**. The diffusion through the silicone gasket was measured three times: only 2 of those were useful for analysis.

3.4.1 First Silicone Measurement

The silicone was initially measured in June 2018 exposed to a radon concentration $C_H = 7.5\mathrm{k}\,\mathrm{Bq/m^3}$. The time-dependent cold-side concentration $\mathcal{C}(t)$ is shown in the left panel of **Fig. 3.6**. The lab air in the cold-side loop has an initial value $\mathcal{C}_0 \approx 40\,\mathrm{Bq/m^3}$. There was no dry stick inline with the cold-side loop, and the relative humidity was $> 10\%$. This measurement constrains the permeability but not the diffusion or solubility. The time-dependent expectation for the radon concentration from Eqn. 3.2.35 is shown (blue line) for the best-fit (D, P) with the 90% C.L. bounds (lines) on the diffusion coefficient. A histogram of the pulls (residuals of the data and the fit divided by the data uncertainties) is shown in the inset. The pulls appear to be gaussian distributed with a mean of zero. The two-dimensional histogram of $\ln(\chi^2)$/number of degrees of freedom, is shown in the right panel of **Fig. 3.6** with the best-fit (D, P) ($\bigstar$) with 90% (99%) C.L. bounds shown as dashed (dotted) bands. The best-fit diffusion coefficient D_I and permeability P_I

$$D_\mathrm{I} = 8.38^{+>10^6}_{-3.99}\,10^{-10}\,\mathrm{m^2/s} \qquad \text{(not well constrained)} \tag{3.4.2}$$

$$P_\mathrm{I} = (8 \pm 1) \times 10^{-10}\,\mathrm{m^2/s} \qquad (90\%\,\mathrm{C.L.}). \tag{3.4.3}$$

While the diffusion is not well constrained by this measurement, the p-value$= 0.0121$, the best-fit diffusion and permeability do indicate a reasonable solubility $S_\mathrm{I} = P_\mathrm{I}/D_\mathrm{I} \approx 1$. If we believe that the permeability is well-measured and that the solubility $S_\mathrm{est} < 10$, then the diffusion coefficient is lower bound

$$P/S_\mathrm{est} = D_\mathrm{est} \gtrsim (8 \pm 1) \times 10^{-11}\,\mathrm{m^2/s}. \tag{3.4.4}$$

The precision of this measurement was presumably limited by the humidity.

[2]The almond shape made from two overlapping circles, like a Venn diagram, comes from the Latin for fish bladder.

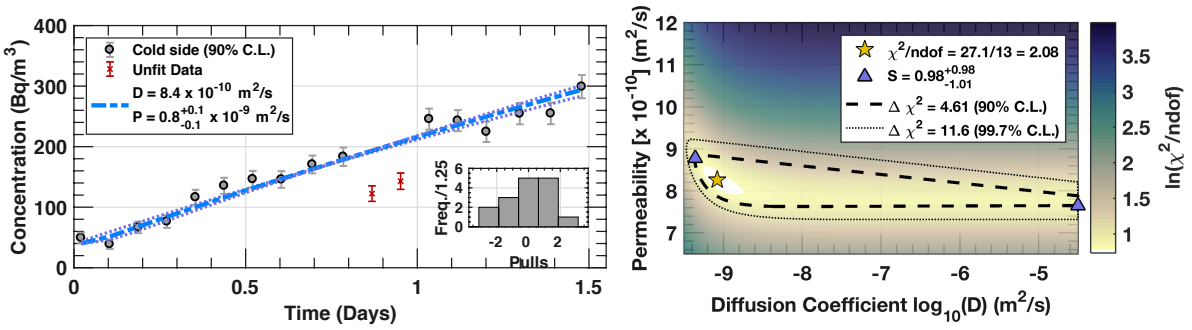

Figure 3.6: Left: Cold-side radon concentration C_{R7} (shown as ◯ with 90 % C.L. statistical uncertainties) versus time from silicone diffusion measurement under the condition of $C_H = 7.5\,\mathrm{kBq/m^3}$ and an initial cold-side concentration $\mathcal{C}_0 \approx 40\,\mathrm{Bq/m^3}$. The theoretical expectation from Eqn. 3.2.35 for the best-fit (D, P) is shown (solid blue line) with 90% C.L. on the diffusion coefficient and permeability (purple dashed). The humidity was high (> 10%) for the first 18 hrs. Some data (shown as red ×) deviate greatly from the prediction and are not included in the fit. **Left Inset:** Histogram of the pulls $P = (C_{\mathrm{R7}} - \mathcal{C}) \cdot \delta_{\mathrm{R7}}^{-1}$ (residuals scaled by the uncertainty). The pulls are roughly gaussian, but their spread is large. **Right:** (Linear versus $\log_{10}$) Colormap of the natural logarithm of the χ^2/number of degrees of freedom, as a function of the diffusion coefficient D and the permeability $P = S\,D$. The $\chi^2/_{\mathrm{ndof}} \approx {}^{27.1}/_{13} = 2.08$. The extent of the dashed (dotted) band corresponds to the 90% C.L.(̃99% C.L.) in each parameter. The permeability is well constrained

3.4.2 Second Silicone Measurement

We repeated the measurement in September 2018 with a dry stick inline with the cold side to prevent significant systematic uncertainties from from humidity dominating the precision of the measurement. A higher hot-side concentration $C_H = 10\,\mathrm{kBq/m^3}$ was used to scale the theoretical curve to a larger concentration. The time-dependent cold-side concentration $\mathcal{C}(t)$, is shown for late times in the left panel of **Fig. 3.7**. The lab air in the cold-side loop has an initial value $\mathcal{C}_0 \approx 0\,\mathrm{Bq/m^3}$. Although the dry stick was included for the second attempt to more strongly constrain the radon diffusion coefficient, this measurement was not ideal. The RAD7 internal pump was not on during the first 3.75 days of measurement, at this time the curve rises well above the lab air concentration $C_{\mathrm{lab}} \approx 100\,\mathrm{Bq/m^3}$. This indicates the measurement did not suffer a large cold-side leak. The cold-side concentration increased to $\mathcal{C} \approx 700\,\mathrm{Bq/m^3}$ about a half a day after we turned on the RAD7 pump. The concentrations measured before the recirculation pump was on are not reliable. Measurements of the radon concentration at late times ($t > 4.4$ days) still constrain the (D, P).

The time-dependent expectation for the radon concentration from Eqn. 3.2.35 is shown (blue line) in the left panel of **Fig. 3.7**. A histogram of the pulls (residuals of the data and the fit divided by the data uncertainties) is shown in the inset. The pulls appear to be gaussian distributed with a mean of zero. The two-dimensional colormap of $\ln(\chi^2)$/number of degrees of freedom is shown in (the right panel of) **Fig. 3.7** with the best-fit (D, P) (★) with 90% (99.57%) C.L. bounds shown as a dashed (dotted) contours. The best-fit diffusion coefficient D_{II} and permeability P_{II}

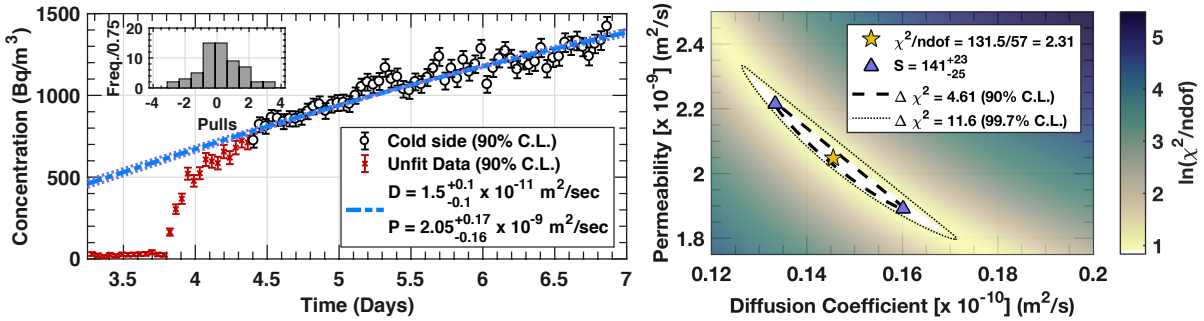

Figure 3.7: Left: Cold-side radon concentration C_{R7} versus time for the second silicone diffusion measurement under the condition of $C_H = 10\,\mathrm{kBq/m^3}$. The cold-side concentrations shown (◯ with 90% C.L. statistical uncertainties) are derived from the weighted means (rebinned 2× into hour-long time bins) of the activities from the RAD7. The RAD7 pump was off for the first 3.75 days during which time the radon concentration from diffusion was not being sampled, those data (shown as red ×) are not included in the fit used to determine the best-fit coefficients for diffusion $D_{\mathrm{II}} = (1.5 \pm 0.1) \times 10^{-11}\,\mathrm{m^2/sec}$, and permeability $P_{\mathrm{II}} = 2.05^{+0.17}_{-0.16} \times 10^{-9}\,\mathrm{m^2/sec}$. The theoretical expectation $\mathcal{C}$ from Eqn. 3.2.35 for the best-fit (D, P) is shown (solid blue line). **Top Left Inset:** Gaussian distributed pulls $(C_{\mathrm{R7}} - \mathcal{C}) \cdot \delta_{\mathrm{R7}}^{-1}$ (residuals scaled by the uncertainty) for fit data per 0.75 for the theoretically expected $(D_{\mathrm{II}}, P_{\mathrm{II}})$. **Right:** Colormap of the natural logarithm of χ^2/number of degrees of freedom, as a function of the diffusion coefficient and permeability. The $\chi^2/\mathrm{ndof} \approx 131/62 = 2.12$ and p-value $< 10^{-4}$. The extent of the dashed (dotted) band corresponds to the 90% C.L. (99.7% C.L.) allowed region in each parameter. Bounds on the best-fit solubility $S \sim 100$ are shown (purple △) at the corresponding (D, P).

$$D_{\mathrm{II}} = 1.45^{+0.15}_{-0.12} \times 10^{-11}\,\mathrm{m^2/s} \qquad (90\%\,\mathrm{C.L.}) \tag{3.4.5}$$

$$P_{\mathrm{II}} = 20.5^{+1.7}_{-1.6} \times 10^{-10}\,\mathrm{m^2sec} \qquad (90\%\,\mathrm{C.L.}) \tag{3.4.6}$$

bear a $\chi^2/\mathrm{ndof} \approx 131/62 = 2.12$ and p-value $< 10^{-4}$ indicate very few random data could give as extreme values on the parameters. The diffusion coefficient is constrained to $\sigma_D/D \sim 0.15/1.5 = 10\%$. The permeability $\sigma_P/P \lesssim 1.7/20.5 = 8\%$ is more well constrained. Since the permeability and diffusion are somewhat anti-correlated, the uncertainties on the solubility are determined from the edges of the 90% C.L. band (dashed line) shown in the right panel of **Fig. 3.7**. Typically the solubility of rubber materials $1 < S_{\mathrm{rubb}} < 20$, so the best-fit solubility

$$S = P_{\mathrm{II}}/D_{\mathrm{II}} \approx 141^{+23}_{-25} \gg S_{\mathrm{rubb}} \tag{3.4.7}$$

appears unreasonably large and bears a $141/25 \approx 5\sigma$ discrepancy with expectation of other soft gasket materials. For the second measurement the diffusion length, determined by the best-fit D known to $\sigma_D/D \approx \pm 10\%$, and so the diffusion length is known to about 5%

$$\ell_S = \sqrt{\frac{D}{\lambda}} = \sqrt{\frac{1.45 \times 10^{-11}\,\mathrm{m^2/s}}{2.11 \times 10^{-6}\,\mathrm{s^{-1}}}}(1 \pm 0.05) \approx (2.6 \pm 0.1)\,\mathrm{mm}. \tag{3.4.8}$$

Measurements of nylon at high relative humidity indicated a large variability on the radon solubility $10^3\times$ [260].

Without the RAD7 pump circulating to dry the cold side air which may include the diffused water vapor from the hot side, the solubility may vary significantly. If this is not the case, either the diffusion coefficient is underestimated, or the permeability is too high, or both. The permeability

from the first and second measurements of this Silicone sample (which are reported at 90% C.L., 1.28σ) are consistent

$$\frac{\mu_2 - \mu_1}{\sigma_T} = \frac{P_{\mathrm{I}} - P_{\mathrm{II}}}{{}^{1}\!/_{1.28}\sqrt{\sigma_{\mathrm{II}}^2 + \sigma_{\mathrm{I}}^2}} = \frac{20.5 - 8.3}{{}^{1}\!/_{1.28}\sqrt{(-1.6)^2 + (1)^2}} = 12.1/1.47 \approx 8, \tag{3.4.9}$$

at 8σ. This indicates poor consistency between the measurements presumably from the experimental conditions. The theoretically expected radon concentrations (shown in **Fig. 3.6** and **Fig. 3.7**) do not deviate significantly from the data. Perhaps the conditions of the first measurement were so poor as to be completely unbelievable or (less likely) the early time measurements of the silicone sample would draw the second measurement into question.

3.5 Zip-A-Way Diffusion Measurements

In an attempt to obtain a cheap solution to the gasket sealing the radon purge barrier. Zip-A-Way [269] is a commercially available caulking substance suggested for use with the radon purge lead shield by Dan Bauer. The gasket was prepared by placing KF flanges in a concentric configuration (as shown in the left panel of **Fig. 3.8**) to achieve a gasket bearing polar symmetry. Zip-A-Way is designed to be used as a beaded caulk in thin strips so the $H = 0.53\,\mathrm{cm}$ thick sample, shown in the right panel of **Fig. 3.8**, took approximately 3 days to dry. Thin beads of this material quickly dry in minutes. Silicone grease was used on the bottom and the ragged edge of the top to prevent leaks and hold the gasket in place. This gasket is much larger (thicker and taller) than the 1/8" bead size recommended by the manufacturer for caulking. The gasket naturally had bubbles which were not feasibly removable from the gasket. The air bubbles within the gasket will allow radon to diffuse to the cold side more quickly, so the diffusion coefficient will be over-estimated by a small amount.

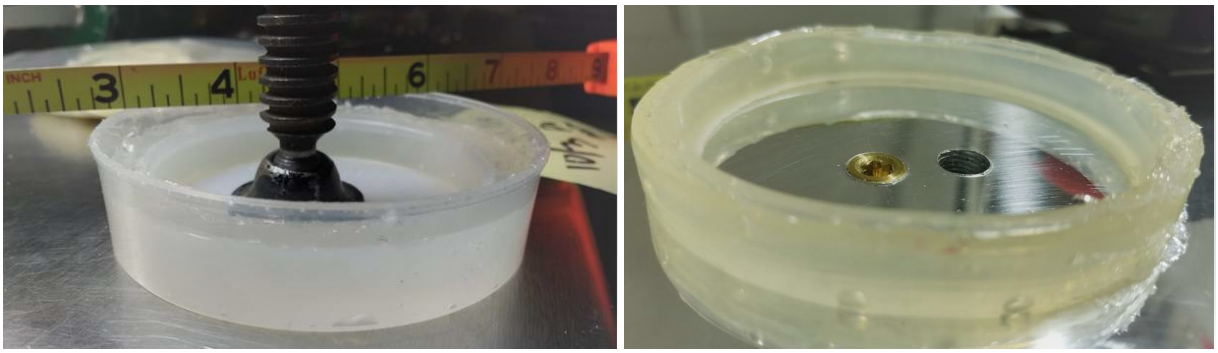

Figure 3.8: Left: Concentric flange caps with Zip-A-Way caulk filled to a height of order $d = 1.25\,\mathrm{cm}$. The inner radius of the sample $r \approx 3.1\,\mathrm{cm}$. After drying for three days, the membrane was removed from the caps and measured for diffusion. **Right:** The membrane was ragged along the top and bottom edges and therefore filled in sparingly with silicone grease to prevent leaks from the high concentration on the hot side. The inner area of the gasket $A \approx 1.25\,\mathrm{cm} \times \pi 3.1\,\mathrm{cm}^2 \approx 35.6\,\mathrm{cm}^2$.

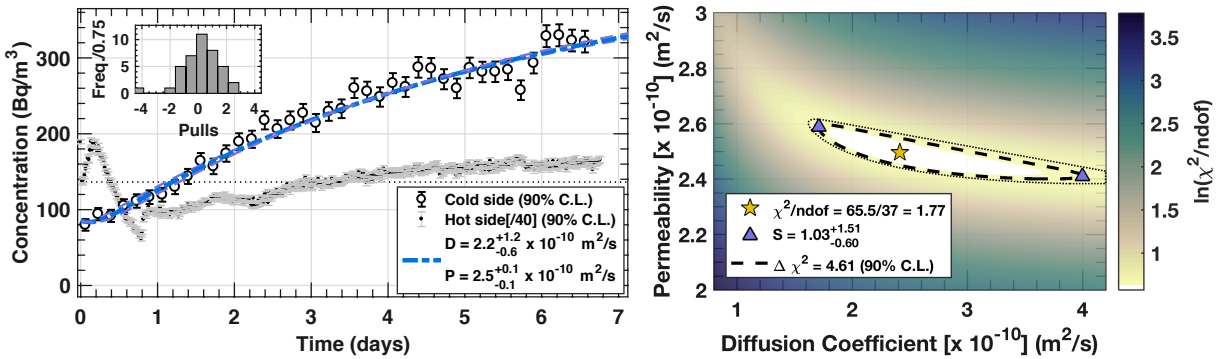

Figure 3.9: Left: Radon concentration versus time from the first Zip-A-Way diffusion measurement. The cold-side concentrations shown (◯ with 90% C.L. statistical uncertainties) are derived from the weighted means (rebinned by ×3) of the activities from the RAD7. The hot-side concentration is shown (small dot) scaled by ×1/40 with 90% C.L. statistical uncertainties. The average hot-side concentration $\langle C_H \rangle = 10\,\mathrm{kBq/m^3}$ is shown (dotted line). The best-fit theoretical expectation from Eqn. 3.2.37 assumes the initial radon concentration $\mathcal{C}_0 = 85\,\mathrm{Bq/m^3}$. **Right:** Two-dimensional histogram of the natural logarithm of the χ^2/number of degrees of freedom, as a function of the diffusion coefficient (D) and permeability P. The best-fit (D, P) is shown (★) at the minimum $\chi^2/\mathrm{ndof} = 60.5/37 \approx 1.64$, with a p-value < 0.0087. The extent of the dashed (dotted) band corresponds to the 90% C.L. (99% C.L.) in each parameter. Bounds on the best-fit solubility $S = 1.13^{+1.61}_{-0.70}$ (90% C.L.) are shown (purple △) at the corresponding (D, P). The permeability is very well constrained with uncertainties of order 4%, whereas the diffusion

3.5.1 First Zip-A-Way Measurement

The time-dependent radon concentration measured by the RAD7 is shown for the first measurement in the left panel of **Fig. 3.9**. The best-fit curve from Eqn. 3.2.35 assumes the initial cold-side radon concentration $\mathcal{C}_0 = 85\,\mathrm{Bq/m^3}$. The best-fit diffusion and permeability

$$D_\mathrm{I} = 2.21^{+0.99}_{-0.55} \times 10^{-10}\,\mathrm{m^2/s} \qquad (90\%\,\mathrm{C.L.}) \tag{3.5.1}$$

$$P_\mathrm{I} = (2.50 \pm 0.08) \times 10^{-10}\,\mathrm{m^2/s} \qquad (90\%\,\mathrm{C.L.}) \tag{3.5.2}$$

are shown with the dashed curves at the 90% C.L. bounds on the parameters. The logarithm of the χ^2/number of degrees of freedom as a function of the permeability and diffusion coefficients is shown as a colormap in the right panel of **Fig. 3.9**. The best-fit $\chi^2/\mathrm{ndof} = {}^{99.0}/_{51} \approx 1.94$, with a p-value $< 10^{-4}$ indicate that the model is imperfect probably based on fluctuations in the hot-side radon concentration. By eye, the prediction of this one-dimensional model appears to be good enough to constrain the radon diffusion of the Zip-A-Way gasket sample. Perhaps simulating the time-dependent hot-side radon concentration would produce even better agreement with the data. This would be computationally very time consuming because each test value χ^2 would be produced from the time-dependent prediction for the pair of (D, P) values shown. We decided that this would not provide an improved understanding of the radon diffusion properties of the Zip-A-Way. The best-fit solubility

$$S = 1.13^{+1.61}_{-0.70} \tag{3.5.3}$$

is shown (purple triangle) at the edges of the dashed curves, and $\mathcal{O}(1)$ is reasonable. The diffusion length is determined by the best-fit D, known to $\sigma_{D_\mathrm{I}}/D_\mathrm{I} \approx 40\%$, and is known to about $\sigma_{\ell_\mathrm{I}}/\ell_\mathrm{I} \sim 20\%$.

$$\ell_\mathrm{I} = \sqrt{\frac{D_\mathrm{I}}{\lambda}} = \sqrt{\frac{2.2 \times 10^{-10}\,\mathrm{m^2/s}}{2.11 \times 10^{-6}\,\mathrm{s^{-1}}}}\,(1^{+0.22}_{-0.12}) = 10.2^{+2.3}_{-1.2}\,\mathrm{mm}. \tag{3.5.4}$$

The ∼40% uncertainty in the radon diffusion coefficient is actually common in the literature for solids. In any event, we made another measure of the Zip-A-Way to measure the variation of the radon diffusion in the gasket.

3.5.2 Second Zip-A-Way Measurement

The Zip-A-Way was measured again with an identical geometry as the first experiment. The time-dependent cold-side concentration $\mathcal{C}(t)$, shown in the left panel of **Fig. 3.10**, had an initial value $\mathcal{C}_0 \approx 20\,\mathrm{Bq/m^3}$. The hot-side concentration is shown (small gray dots) with 90% C.L. statistical uncertainties scaled by $1/40$. The hot-side concentration C_H varied significantly $C_H(t = 0) \approx 7.5\,\mathrm{kBq/m^3}$ to $C_H(t = 10\,\mathrm{days}) \approx 10.5\,\mathrm{kBq/m^3}$ by $\gtrsim 40\%$ during the 10 day measurement. The average $\langle C_H \rangle \approx 4,500\,\mathrm{Bq/m^3}$, used to as the assumed boundary condition for the second measurement, is shown (scaled by $1/40$) as a dotted line.

The fitted data (black dots), corresponding to periods of relatively consistent hot-side radon concentrations C_H from $t_\mathrm{fit} = (1\text{–}7.5)\,\mathrm{days}$, are shown wth the unfit data (red ×) at early and late times. The early times are significantly ($> 3\sigma$) lower than the best-fit theoretical expectation from Eqn. 3.2.37 from the χ^2 minimization. The unfit data at late times also underestimate the radon concentration on the cold side, and may be due to the early hot-side concentration dip at $t \approx 0.8\,\mathrm{days}$ of measurement. Including these data drive the diffusion and permeability to lower values so the reported numbered are conservative.

The best-fit diffusion coefficient and permeability are

$$D_\mathrm{II} = 1.1^{+0.2}_{-0.1} \times 10^{-10}\,\mathrm{m^2/s} \qquad (90\%\,\mathrm{C.L.}) \tag{3.5.5}$$

$$P_\mathrm{II} = (1.27 \pm 0.04) \times 10^{-10}\,\mathrm{m^2/s} \qquad (90\%\,\mathrm{C.L.}) \tag{3.5.6}$$

bear a $\chi^2/\mathrm{ndof} = 61.5/57 = 1.08$. The best-fit solubility $S_\mathrm{II} = P/D \approx 1.27/1.1 \approx 1.18$. Since the permeability and diffusion are anti-correlated, the uncertainties on the solubility are determined from the edges of the 95% C.L. band shown in the right panel of **Fig. 3.10**. The diffusion length is determined by the best-fit D, and (half of) the fractional uncertainty ($\sigma_D/D \approx^{+17\%}_{-12\%}$)

$$\ell_\mathrm{II} = \sqrt{\frac{D}{\lambda}} = \sqrt{\frac{1.1 \times 10^{-10}\,\mathrm{m^2/s}}{2.11 \times 10^{-6}\,\mathrm{s^{-1}}}}(1^{+8.7\%}_{-6.1\%}) \approx (7.2 \pm 0.6)\,\mathrm{mm}. \tag{3.5.7}$$

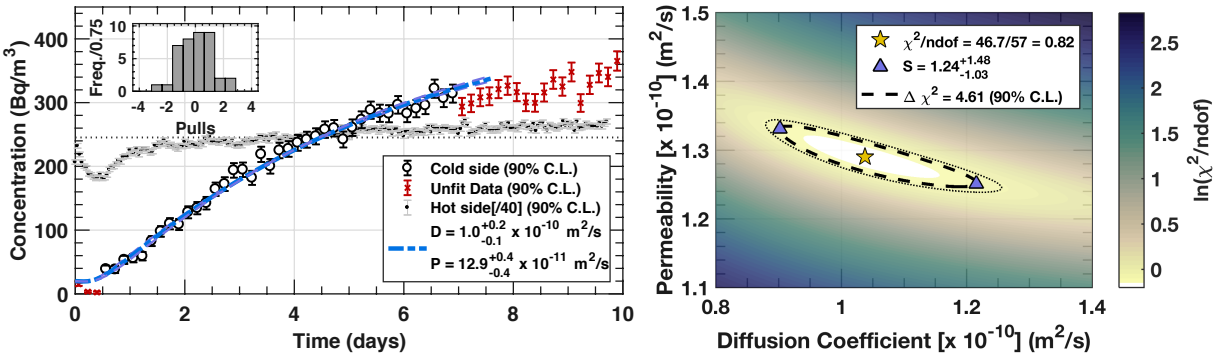

Figure 3.10: Left: Radon concentration versus time for the second Zip-A-Way diffusion measurement. The cold-side concentrations $C_{\rm R7}$ (◯) are derived from the weighted means (rebin=×3) of the activities from the RAD7 shown with 90%C.L. statistical uncertainties. Some data (red ×) were not used in the fit since they generally bring down the expected values and produce wider best-fit (D, P). The hot-side concentrations $C_H(t)$ during the measurement are shown (scaled by $\times 1/40$, with 90%C.L. statistical uncertainties) as light dots, and the dotted line represents the assumed C_H used for the theoretical expectation in Eqn. 3.2.35 to produce the best-fit (D, P). The best-fit expectation from Eqn. 3.2.35 assumes the initial radon concentration $\mathcal{C}_0 = 20\,\mathrm{Bq/m^3}$. **Right:** Two-dimensional histogram of the natural logarithm of the χ^2/number of degrees of freedom, as a function of the diffusion coefficient $\log_{10}(D)$ and permeability $\log_{10}(P)$. The best-fit (D, P) is shown (★) at the minimum $\chi^2/\mathrm{ndof} = 61.5.0/57 \approx 1.08$, with a p-value $< 10^{-4}$. The extent of the black (purple) band corresponds to the 90%C.L. (99%C.L.) in each parameter. The permeability is very well constrained with uncertainties of order 3%. The diffusion coefficient has uncertainties at the 20% level.

3.6 EPDM Diffusion Constraints

A 30 cm sample with a 15 mm-5 mm cross-section of self-adhering ethylene propylene diene terpolyme, which is also known as EPDM, was sent to SDSM&T from Lemer Pax [261]. The 5 mm tall EPDM sample was cut into a strip of thickness $H_{\rm EPDM} = 2.7\,\mathrm{mm}$ to avoid complications testing the original 15 mm thickness and to avoid very long test times. The left panel of **Fig. 3.11** shows the thin strip of self-adhering EPDM placed in a circular geometry on the bottom metal plate. The time-dependent radon concentration for the EPDM test is shown in the middle panel of **Fig. 3.11**. There was not enough data taken to place satisfactory constraints on the diffusion coefficient D. The right panel of **Fig. 3.11** shows the χ^2 versus permeability under several assumption of diffusion coefficient: $D = (10^{-10}, 10^{-9}, 10^{-8})\,\mathrm{m^2/s}$. The best-fit permeability for each of these cases are within

$$\frac{\delta P}{P} \lesssim {}^{0.06}/_{5.7} \approx 1.0\% \tag{3.6.1}$$

of each other. Each of these diffusion coefficients produce almost identical expected concentrations $\mathcal{C}(t)$ for this short experiment. It is reasonable to assume the diffusion coefficient $D \approx 10^{-10}\,\mathrm{m^2/s}$ and the permeability

$$P = (5.78 \pm 0.06) \times 10^{-9}\,\mathrm{m^2/s} \qquad (68\%\ \mathrm{C.L.}) \tag{3.6.2}$$

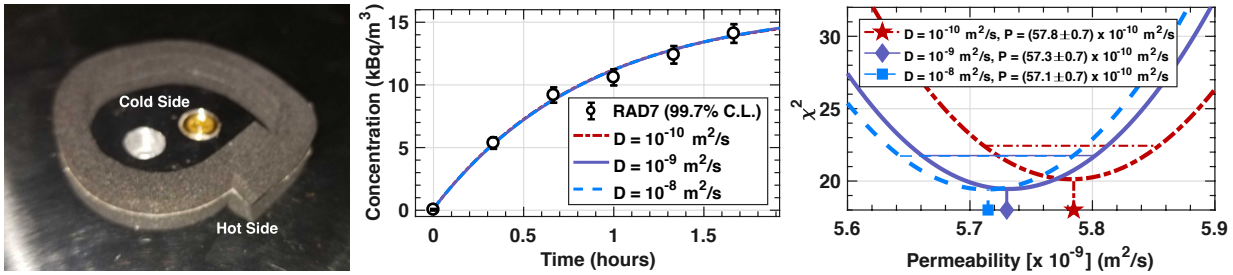

Figure 3.11: Left: Circular experimental configuration of $H_{\text{EPDM}} = 2.7\,\text{mm}$ EPDM on the aluminum apparatus. **Middle:** Radon concentration versus time from the first EPDM diffusion measurement. The cold-side concentrations are shown (◯) with 99.7% C.L. statistical uncertainties from 15 minute time bins. The best-fit theoretical expectation from Eqn. 3.2.37, bears an initial radon concentration $\mathcal{C}_0 = 0\,\text{Bq/m}^3$ and is shown for three diffusion coefficients $D = (10^{-8}, 10^{-9}, 10^{-10})\,\text{m}^2/\text{s}$ (overlapping) along with the best-fit permeability coefficients $P_{\text{EPDM}} \approx 5.7 \times 10^{-8}$. For diffusion coefficients this large, the expected concentration changes only by a small amount. **Right:** χ^2 versus permeability P for the three diffusion coefficients $D = (10^{-10}, 10^{-9}, 10^{-8})\,\text{m}^2/\text{s}$ hypotheses with similar goodness of fit χ^2/number degrees of freedom $\leq 20/4 = 5$ with a p-value $= .000499$. near permeabilities $P = 5.7$–$5.8 \times 10^{-9})\,\text{m}^2/\text{s}$. The uncertainties $\sigma_P = ^{+0.07}_{-0.07} \times 10^{-10})\,\text{m}^2/\text{s}$ are the same for all the diffusion hypotheses.

and the solubility cannot be reasonably constrained either, however, assuming $D > 10^{-10}\,\text{m}^2/\text{s}$ the solubility

$$S = \frac{P}{D} \lesssim \frac{5.8 \times 10^{-9}\,\text{m}^2\text{s}}{10^{-10}\,\text{m}^2/\text{s}} \lesssim 60. \tag{3.6.3}$$

In total, 5 more attempts were made to measure the radon diffusion of the EPDM sample in both circular and rectangular geometries, all of these suffered from leaks, *i.e.*the cold-side concentration equilibrated over a period of 10 minutes, much slower than the 120 minute period shown in **Fig. 3.11**. We attempted to block the cracks between the sample geometries using silicone grease and more EPDM at the gasket edges with no success.

3.7 Conclusions

The results from the chapter will be used to determine the gasket we select to seal the SuperCDMS SNOLAB radon purge barrier, which will also be informed by radon emanation measurements (**Chapter 5**) of the same gaskets. Measuring the radon diffusion properties of materials is difficult since the relative humidity in the environment can change the permeability. Researchers have used several formalisms to constrain the diffusion of gases through membranes [265], [134, 136], [132],[130], [260], [262], [263]. In the literature, constraints on the radon diffusion coefficient for thin membranes vary significantly from $\sigma_D \sim$ (5–50)% [129, 134, 135, 262, 265] or are sometimes not reported at all [128, 131]. While the constraints on the silicone and EPDM samples are not impressive, we will find that this has no bearing on the expected radon reduction in the radon purge barrier.

Chapter 4
Radon-222 Emanation at SDSM&T

As described in **Section 1.3.2**, radon-222 is problematic for many-rare event searches, as a result of its diffusive nature and complex decay chain, shown in the left panel of **Fig. 4.1**. The α decay of trace ^{226}Ra ($t_{1/2} \approx 1,600$ years) supplies materials with ^{222}Rn on very long time scales. Assuming that no radon is in a vessel at the time a material is sealed, the radon decay rate will grow in with a mean lifetime $\tau = 5.52$ day [122, 270] according to

$$R(t) = R_{\text{eqbm}}\left(1 - \exp\left(\tfrac{-t}{5.52\,\text{d}}\right)\right). \tag{4.0.1}$$

The right panel of **Fig. 4.1** shows some example times and the grow-in fraction of the equilibrium decay level for a sealed radon source. The radon decay rate is 95% of the maximum rate after only 16.6 days.

The Radon Emanation System (R.E.S.) at SDSM&T, shown in **Fig. 4.2**, is used to measure the ^{222}Rn emanation rate of potential detector and infrastructure materials for both the SuperCDMS and LZ dark matter experiments. The Radon Emanation System has two vacuum vessels–one 13 L and one 300 L where large samples emanate radon. We use a custom-made gas-handling system with electropolished stainless steel tubing to direct radon from the emanation chamber to a small detection vessel. The vacuum chambers are housed in an acrylic clean tent with a small ante-room for putting on a cleanroom gown, and a High Efficiency Particulate Air (HEPA) filter to remove U/Th-laden dust [271]. We let a sample outgas and emanate ^{222}Rn in one of these electropolished stainless-steel, vacuum-tight vessels for a couple of weeks. The emanation chambers are equipped with pressure gauges, inlet and outlet valves connecting to the gas panel, and KF-25 flange connections for an auxiliary vacuum pump. The pressure gauges allow us to identify leaks and significant outgassing. The auxiliary pump is used to purge ambient gas from leaked-in lab air and outgassed contaminants before emanation. The time planned to allow a material to emanate radon depends on the expected level of contamination and the amount of outgassing. Larger radon contamination in a sample allows shorter emanation times, whereas the outgassing of molecules, such as water and hydrocarbons, tends to shorten the total available emanation time since transfers

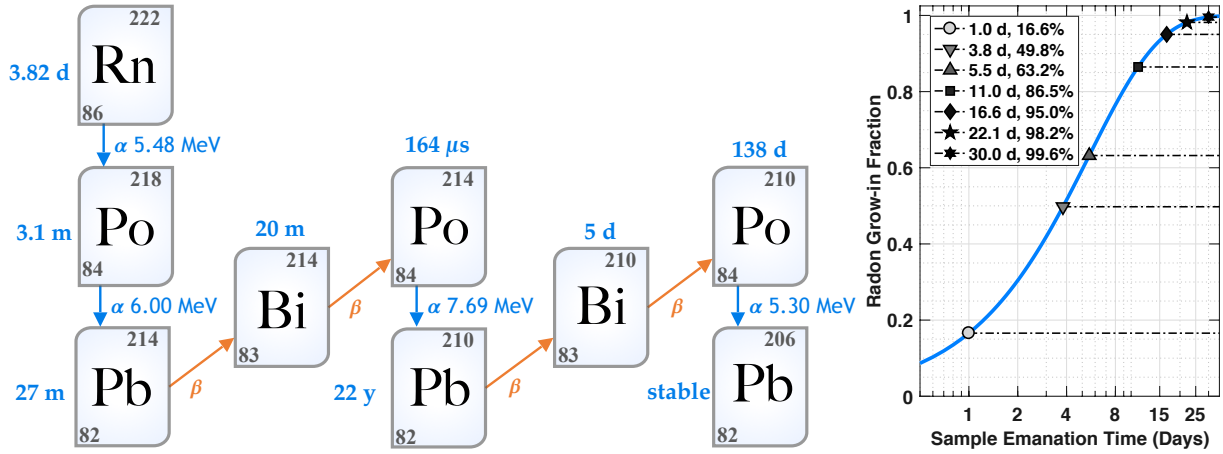

Figure 4.1: Left: Isotopes (abbreviated), with branching fractions >99%, in the ^{222}Rn decay chain shown with proton number Z (lower left), nucleon number $A = N + Z$ (upper right), half-lives $t_{1/2}$, alpha decay energies E_α (in MeV), and beta decays according to NIST [123] and the International Conference on Nuclear Data for Science and Technology [122]. Fast daughters are on the left; long-lived daughters, starting with ^{210}Pb, are on the right. Pb-210 has a complicated decay spectrum including low-energy β decays. Figure adapted courtesy of J. A. Street. **Right:** Radon grow-in fraction (solid blue) of the equilibrium radon decay $R(t)/R_{\mathrm{eqbm}}$ rate as a function of time, according to Eqn. 4.0.1, assuming the rate of ^{226}Ra decays ($t_{1/2} = 1,600\,\mathrm{yr}$) in a material is constant. Emanation fractions are shown for a few times in the legend indicating *e.g.* that the radon decay rate is 86% of the maximum rate after only 11 days. As a result, we typically would not choose to emanate a sample for much longer than 2 weeks.

with fewer outgassed molecules are much less likely to fail.

The gas panel piping is made with electropolished stainless steel (SS) to significantly reduce radon emanation [137, 272--275] and outgassing [276, 277]. **Fig. 4.3** shows the gas panel schematic designed by R. W. Schnee, R. Bunker and sent to Swagelok [278] for fabrication. The gas panel is equipped with a carbon trap and two brass wool traps. The panel has a carrier-gas input that feeds to the carbon trap, which was characterized, by me, and installed after the initial installation of the R.E.S. at SDSM&T. This trap is cryogenically cooled with dry ice (solid CO_2), which sublimates near 196 K = −77°C in a bath of isopropyl alcohol (IPA). At this temperature, the trap effectively scrubs the carrier gas of radon contaminants from the LN_2 dewar by physical adsorption to the carbon surface for up to 2 days. The trap output can be fed to either of two emanation chambers housing either a material for assay or a gaseous calibration source. The chambers both feed to 2 sequential brass wool traps, the first with a large volume (615 cm^3) and the second with a small volume (46.6 cm^3), each equipped with a pressure gauge and a reusable relief valve (instead of one-shot rupture disks) to prevent accidentally overpressuring the gas panel and making a bomb.

Low-radon boil-off gas from a liquid nitrogen (LN_2) dewar is used as a carrier gas to transfer the radon from the emanation vessel to the large brass wool trap cooled to LN_2 temperature (77 K). For the samples emanated in the large (small) chamber, the radon adsorbs to the metal surface of the trap for a period of 5 (0.5) hrs while the nitrogen gas flows to the vacuum pump. After this, the sample is sealed, the trap is heated, and the sample is transferred to another, already cooled secondary (small) brass wool trap over a period of (20–30) mins. This process of adsorption,

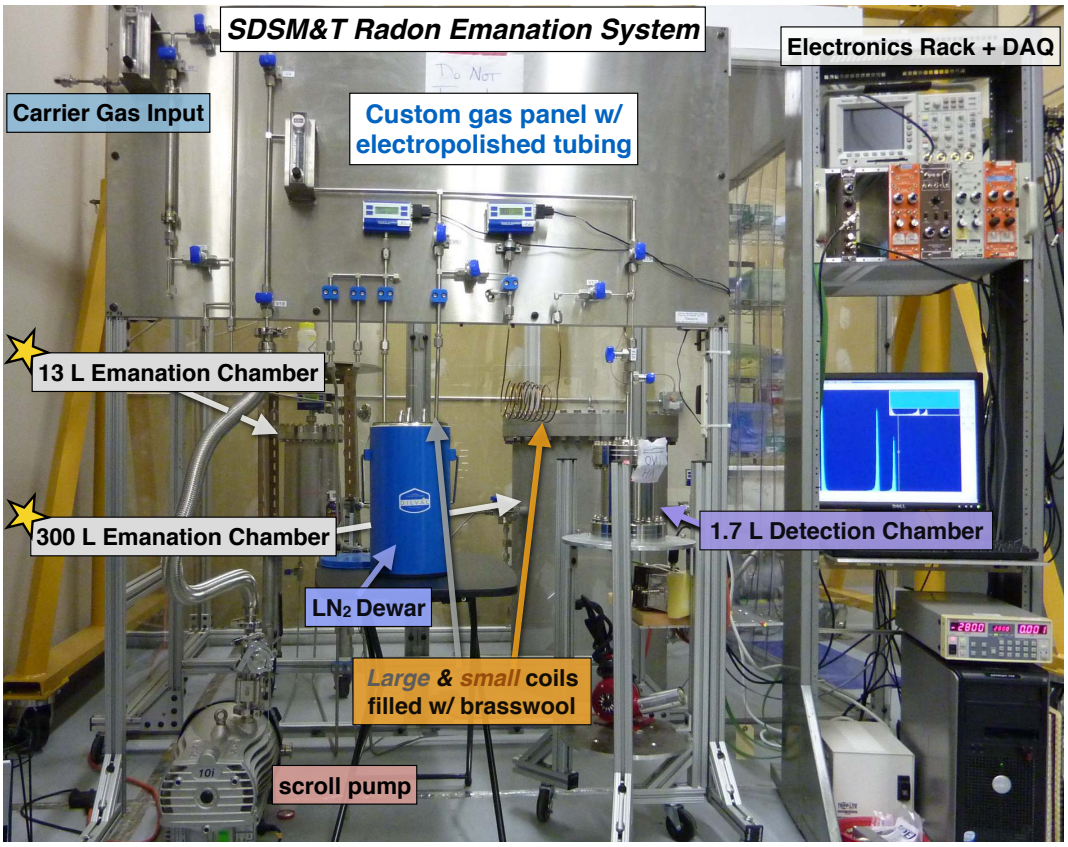

Figure 4.2: SDSM&T radon emanation system gas panel (foreground), electronics rack and DAQ (right), and low-dust cleanroom tent (background). R.E.S. gas panel is outfitted with connections to 13 L and 300 L emanation chambers (★) located in the acrylic clean tent outfitted with a HEPA filter to prevent dust accumulation in the vessels during sample transfers. Boil-off gas from a LN_2 dewar (not shown) is used to transfer radon from the chambers to cryogenic brass wool traps (orange box). When submerged in LN_2, the large (left) and small (right) coiled brass wool traps adsorb the radon sample to their surfaces. Following the concentration of sample radon in the small trap, we finally transfer the radon to the 1.7 L detection chamber. Inside the volume, a silicon pin-diode detector held at high negative voltage collects the positively charged fast daughters of Rn-222: Po-218 and Po-214 (^{21x}Po ions). A filter box circuit (under the detection vessel) sends signals from the detector to an amplifier in the electronics rack and data acquisition (DAQ) system. The amplified signal is output to a multi-channel analyzer (MCA), and histograms of the pulse height spectra produced by the alpha decay of ^{21x}Po ions (bright blue peaks on DAQ screen) are periodically saved on a computer. The spectra are analyzed offline and compared with backgrounds spectra taken before and after the sample's radon assay for $^{218/214}$Po as shown on the screen of the computer. Figure adapted courtesy of R. Bunker.

desorption, and re-adsorption to the brass wool surfaces effectively concentrates the radon by a factor of $\times$6,500 (280) for the large (small) emanation chamber. Following this concentration of radon onto metal traps, we heat the sample so that it can be displaced into the detection chamber, which has been evacuated to low pressure ($P < 5$ Torr). After heating the small trap, we place the rest of the gas panel at a high pressure $P \approx 1,000$ Torr; with this fresh nitrogen, we flow 100 Torr of boil-off gas through the trap to carry the sample radon into the detection vessel.

The detection chamber is a 1.7 L electropolished stainless-steel vacuum vessel with a silicon pin diode α detector. Once inside, radon will decay to produce (mostly) positively charged ^{218}Po ions which recoil and are slowed by the carrier gas. After thermalizing, the ions diffuse in the presence

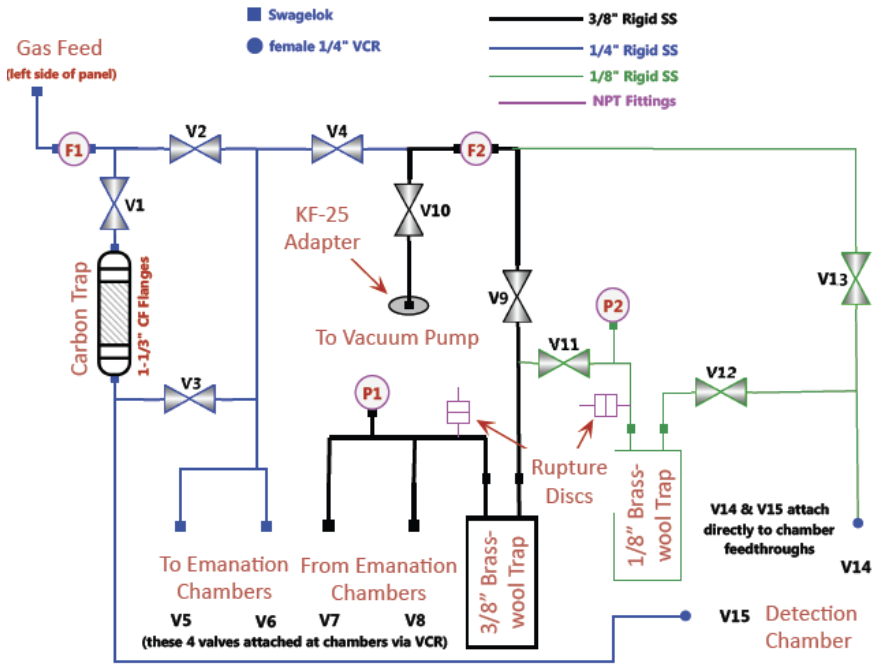

Figure 4.3: SDSM&T R.E.S. gas-handling piping and instrumentation diagram (P&ID) sent to Swagelok. The gas panel is used to transfer radon from the emanation vessels to a small detection chamber. The gas panel has a carbon trap at the input of the panel. The output of the trap connects (V3,V4,V10) to the vacuum pump for trap regeneration (described in **Section 4.6.5**), and (V3,V5/V6) to the small or large emanation vessel. The input gas flows through the chamber, back to the panel (via V7/V8) fed to a 3/8" brass wool trap equipped with a pressure gauge (P1). The trap connects (via V9, V10) to the scroll pump or (via V11) to a second 1/8" brass wool trap which is also equipped with a pressure gauge (P2). The small trap connects to the scroll pump (V12,V13,V10) and the detection chamber (V12,V14). The flow meter (F2) is used to monitor the output flow during radon concentration to both brass wool traps. Figure courtesy of R. Bunker.

of a large electric field and are collected to the surface of a silicon pin diode detector held at an electric potential offset of -2 kV. Po-218 daughters not collected may be collected later as ^{214}Pb, ^{214}Bi, or ^{214}Po. Over a period of days, $\sim$ 6 MeV α decays from the short-lived ^{218}Po and ^{214}Po directed into the detector, shown in the left panel of **Fig. 4.1**, generate small voltage signals that are fed to shaping and amplification electronics. A custom filter box biases the detector, holds the detector at -2 kV, and sends the signal to a preamp. The signal is then sent to a shaping amplifier, and subsequently a multi-channel analyzer (MCA) emulator. Pulse-height spectra from the α energy deposition of fast radon daughters are analyzed offline to infer the strength of the radon emanated from the sample.

In this chapter, I describe the components the Radon Emanation System (R.E.S.) at SDSM&T such as the emanation chambers, custom gas-handling system, data acquisition system (DAQ), and their purpose. In the following sections (**Section 4.1**—**Section 4.3**), I describe radon emanation mechanisms, sample preparation and procedures (**Section 4.1.1**), leaks, outgassing, and their prevention (**Section 4.1.2**). I give a brief overview of radon adsorption and elution at cryogenic temperatures (**Section 4.2.1**), describe the calibration source preparation, the determination of

the radon transfer efficiency (**Section 4.2.2**), and the development and validation of an improved radon transfer method (**Section 4.2.5**). I then describe the radon detection vessel, hardware, and electronics (**Section 4.3.1**), radon daughter collection and detection efficiencies (**Section 4.3.2**), and hardware improvements that greatly improved the sensitivity of the detector (**Section 4.3.3**). I then discuss the detector backgrounds (**Section 4.4**), and simulations and measurements I performed to mitigate the most serious backgrounds from radon back-diffusion in the detection vessel (**Section 4.5**) and radon from the LN_2 carrier-gas dewars (**Section 4.6**).

4.1 Sample and Vessel Preparation

The radon emanation system is designed to measure very low levels of radon. For the rare-event search community, radiopure materials of interest have U/Th decay concentrations [133, 139, 161, 162, 279--282]

$$\tilde{R} \approx (10\text{–}10^5)\ \mu\text{Bq/kg}. \tag{4.1.1}$$

Measuring such low levels of radon is complicated by many factors. Plastics and soft materials may have density $\rho \sim 500\,\text{kg/m}^3$corresponding to a radon emanation density (*i.e.* radon production per unit volume)

$$C_{\text{mat}} = \tilde{R}\,\rho \sim 10^5\,\mu\text{Bq/kg} \times 500\,\text{kg/m}^3 \approx 50\,\text{Bq/m}^3.$$

which is lower than the SDSM&T lab air radon concentration $C_{\text{air}} \sim 100\,\text{Bq/m}^3$. The equivalent lab-air volume (nominal radon content) carrying a radon decay rate similar to the level expected to emanate from a sample $R = 10\,\text{mBq}$ is only

$$V_{\text{eq}} = R/C_{\text{air}} = \tfrac{10\,\text{mBq}}{100\,\text{Bq/m}^3} = 0.1 \times 10^{-3}\,\text{m}^3 = 0.1\,\text{L},$$

which poses a problem for measuring small amounts of radon. Radon is generally non-interacting and therefore can diffuse into and through materials. Samples of interest meant for radon emanation assay must spend time in lab air before they are put into an emanation chamber. During this time, ambient radon diffuses into the material, increasing the radon concentration above the natural production from radium decays. As described in **Section 3.2.1**, materials are characterized by their radon permeability

$$P = S\,D. \tag{4.1.2}$$

The solubility of radon in materials is typically greater than 1 [130], so radon tends to get sucked in by materials intended for assay leading to a greater radon concentration than the ambient exposure conditions, which is already larger than the bulk radium decay concentration! So, unfortunately, materials of interest act like radon sponges, requiring us to take great care both when preparing

samples and when analyzing data.

During the emanation period, before the transfer, radon from the lab will diffuse back out of the material, contaminating the emanation chamber with radon not originating from radium decays in the bulk of the material itself, but from its recent radon exposure history. In order to minimize this effect, we perform repeated pressurization and evacuation of the vessels (aka 'fill and flush'). After each evacuation, the gas is replaced with high-pressure LN_2 boil-off. Flushing the emanation chambers removes lab-air radon, back-diffused radon, and outgassed molecules. Flushing the panel and the detection chamber before transfers helps to avoid cross-contamination between samples and calibration measurements. Between every assay, the background rate of the detector is measured by filling it directly with LN_2 boil-off.

Diffusion is a thermally activated process leading to the random motion of particles in materials. At room temperatures, non-metal materials allow radon to travel significantly before decaying [127, 129, 258], so some radon produced in the bulk of these materials will escape, leading to the so-called diffusion emanation of radon. Radon diffusion is the dominant mechanism for contributing to the radon emanation of soft plastics and rubbers where thorough surface preparation can be employed.

Radon contamination from material surfaces can also contribute to rare-event search backgrounds, from *e.g.* material manufacturing or processing. Radium on or just barely below material surfaces will give rise to radon. The nuclear recoil energy $E_{\mathrm{NR}} = 86.3\,\mathrm{keV}$ (103 keV) imparted to a ^{222}Rn (^{220}Rn) atom by the α decay of radium may free the radon from material surfaces [133, 148, 170]. For dense materials (*i.e.* metals), recoil emanation is the dominant radon release mechanism since radon has a range of about 150 Angstroms in stainless steel [282, 283] and won't originate from the bulk.

Radon atoms produced by the decay of ^{226}Ra recoil with 86.3 keV of kinetic energy and can travel 5 meters in 100 mTorr of nitrogen gas, or 500 μm in 100 Torr of nitrogen [170, 283]. If the vessel pressure housing the sample is too low, the radon atoms ejected from the surface by radium decay may fail be slowed insufficiently for traversing the emanation vessel causing the atoms to become embedded in the chamber walls, where they will stay. It is important therefore to measure this radon emanation. To reduce the inefficiency associated with radon embeddings so that the recoil and diffusion emanation mechanisms can be identified, the radon-emanation vessel pressure must be tuned based on the expected range of the nuclear recoil of radon atoms. Since radon diffusion through metals is negligible, measuring the recoil emanation, *i.e.* radon arising from surface contaminants, cannot be done at very low pressure. Emanation from the nuclear recoil of radium decay cannot be reliably measured below (1-10) Torr due to the 8 cm diameter of the small emanation chamber, depending on the sample geometry with the chamber. To measure the surface radon content (via recoil emanation) the vessel pressure is set to

$$P_{\mathrm{recoil}} \approx 100\,\mathrm{Torr}.$$

Below this pressure, there is expected to be a significant loss of radon atoms which will tend to

stick to the walls. It is possible to isolate the diffusion emanation component, neglecting surface contamination by emanating the sample below this pressure. To effectively sample only the diffusion emanation component due to bulk radon production, the vessel pressure is set to

$$P_{\text{diffusion}} = (20-30)\,\text{mTorr}.$$

This low pressure also makes measuring the outgassing of molecules easy with rate-of-rise tests (described in **Section 4.1.2**).

Samples are typically emanated and transferred at least twice. The first emanation typically has a portion of out-gassed radon arising from the material's exposure to the lab air. Typically, radon emanation is performed at a moderate vessel pressure $P \approx 100\,\text{Torr}$ which allows us to measure the combined recoil and diffusion emanation and obtain the largest possible signal. A second emanation can be done at low pressure to sample the diffusion emanation alone. Due to the tight schedule of material screening, and the fact that many emanated samples had low radon, low pressure (diffusion-only) emanations were not usually carried out.

4.1.1 Sample Placement and Cleanliness Protocols

Dust usually contains significant amounts of primordial U/Th/K. Radon atoms produced by the decay of U/Th are likely to escape the dust molecule and be transferred to the detection vessel along with the radon emanated from the material itself. To prevent this likely background source, the emanation chambers are housed in a low-dust, acrylic cleanroom with a High-Efficiency Particulate Air (HEPA) filter. The HEPA filter does not remove the chemically inert radon from air, but it removes particulates that may contain U/Th contaminants, and it reduces radon progeny in the air. In order to reduce dust on the samples under assay, we prepare samples by wetting 'lint-free' wipes with isopropyl alcohol (IPA) and wiping away the surface dust before placing the samples inside one of the vessels, such as the small emanation chamber, shown in **Fig. 4.4**. In the past, we used KIMTECH brand KIMWIPES [284]. These have a higher particle shedding than Berkshire brand [285] low-lint wipes, which we now use to clean the surfaces of samples and vacuum vessels.

When placing a sample in the small chamber, we start by disconnecting the KF-25 flange on top of the vessel and unfastening the 24 bolts without yet removing the lid. To view dust accumulation with a UV light during the vessel cleaning and sample placement, a nylon black-out cloth is moved over the chamber. We then remove the chamber lid, placing it right-side up on top of the large chamber with lint-free wipes to keep dust from settling on the inner lid. Beyond using IPA-wetted wipes to clean sample surfaces, we also remove dust from the inner vessel surface using nylon brushes and a UV light (under a black-out cloth) to illuminate dust dirt and dust (which fluoresces under UV) inside the S.E.C., as shown in **Fig. 4.4**. Nylon brushes help to remove lint introduced by the wipes, though some dust remains attached to the inner vessel surface as shown in the right panel of **Fig. 4.4**. We avoid vigorously moving when under the cloth with the chamber.

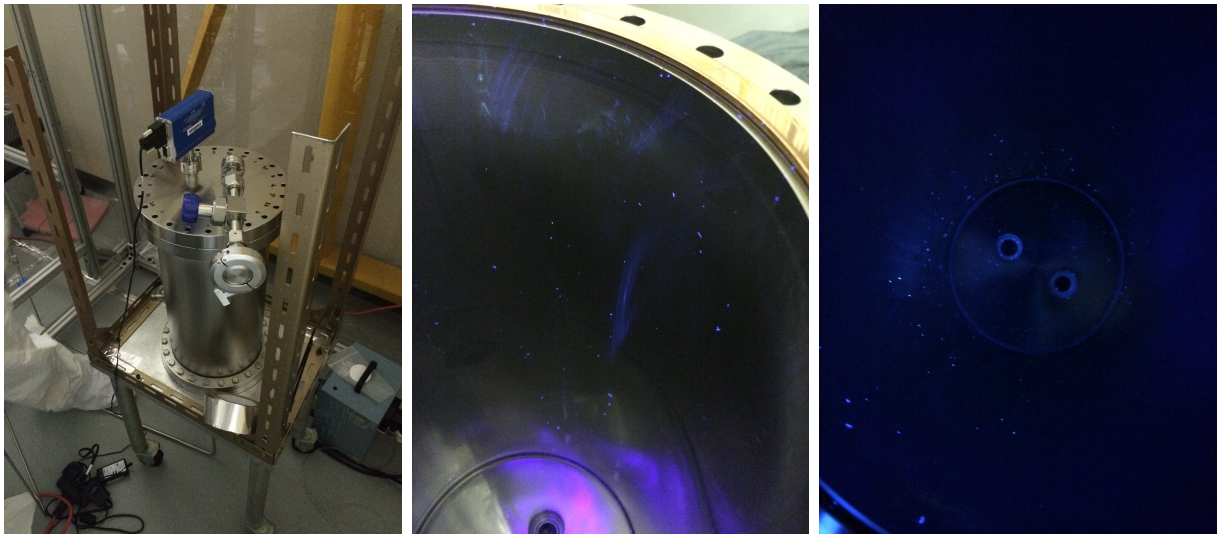

Figure 4.4: Left: Small emanation chamber, with bolts removed, in the HEPA-filtered cleanroom tent. **Middle:** Inside of emanation chamber, without the black-out cloth, shown with UV light illuminating dust, dirt, and lint inside the S.E.C.. **Right:** S.E.C. after cleaning the surface with IPA, using lint-free wipes, and finally applying nylon brushes from bottom to top. Some dust remains in the chamber even with vigorous wiping and scrubbing.

The temperature inside the cloth is increased due to the UV lamp, and the smell of IPA is quite strong; small breathing breaks are useful to avoid getting light-headed during long cleaning periods. Lint-free wipes are used to clean the inner surface of the chamber where dust has been identified and nylon brushes may be used to remove lint introduced by the wipes. After the vessel is clean, we slowly debag the sample under the cloth and place it in the chamber. Then we remove the cloth, replace the vessel lid, and optionally the copper gasket as well.

4.1.2 Outgassing and Leaks

Similar to radon emanation from materials, outgassing is the release of gas atoms or molecules [276, 277, 286] (such as water or hydrocarbons) which includes desorption, leaks of molecules from thin cracks, gaseous release from slow chemical reactions such as oxidation, phase transitions such as sublimation (solid to gas) and evaporation (liquid to gas). Boiling is not considered outgassing because it is the liquid to vapor phase transition, which can occur before evaporation. Outgassing by desorption is the release of gas that has accumulated on materials during atmospheric exposure. A sample that outgasses in the sealed vessel raises the pressure in a vessel. These molecules leaving material surfaces will prevent a system from reaching a minimum vacuum predicted by the vessel volume and vacuum pumping speed. In a real vacuum system, the time-dependent desorption rate Q_d leads to a pressure rise that is described, to first order, by a power law

$$Q_d(t) \propto t^{-\alpha} \tag{4.1.3}$$

and may exhibit a slower outgassing after long times, requiring a secondary Q_d curve to match with experimental data [287]. For plastics and rubbers, the coefficient $\alpha \sim 2$–4 which indicates a distribution of binding energies between the outgassed byproducts and the material surface [277]. As a result, the pressure contribution from these materials starts at $\gtrsim 25\times$ larger than at late times. A single fingerprint exposed to vacuum may have a gas load $\sim 10^{-5}\,\mathrm{Torr\,L/s}$ [276]. To prevent outgassing due to oils on our skin, nitrile or latex gloves are imperative for sample placement in the emanation chambers.

Materials having a high capacity to soak in atmospheric contaminants, characterized by their permeability $P = SD$–the product of solubility S and diffusion coefficient D–will outgas, resulting in a rising pressure of the vessel in which they are sealed. Carbon dioxide and other gases may adsorb to or penetrate the surface of plastics and rubbers which have radon diffusion coefficients $D_{\mathrm{soft}} \sim (10^{-12}$–$10^{-6})\,\mathrm{m^2/s}$ [129--131, 134, 135]. The dominant source of outgassing for such materials is from the material itself! Soft materials can outgas in a sealed vessel for ∼weeks. Samples, such as metals, with small diffusion coefficients of order $D \lesssim 10^{-12}\,\mathrm{m^2/s}$ will outgas only for a short period, because water moisture and gases won't penetrate the surface significantly before being sealed in an emanation chamber. In the small emanation chamber, outgassing may initially produce pressure changes (10–100) mTorr/min. and eventually asymptote. Outgassing can also be detected in the ($\times$20 larger) large emanation chamber, but the impact on the rate of rise for the same sample is only $^{13}/_{300} \approx 4\%$ that of the small chamber for the same initial pressure.

Outgassing poses three problems for radon emanation measurements. The first is the potential for mistaking the resulting rate of rise at early times as arising from a poor vacuum seal. The second is the presence of *e.g.* water molecules which may condense on the surface of the small cryogenic trap during radon transfer. If enough condensation occurs, the flow of the carrier gas may cease entirely preventing the complete transfer of radon. Preventative measures must be taken to avoid these blockages for large amounts of plastic and rubber components. As described in **Section 4.3.2**, the third comes from transferring these molecular contents to the detection vessel. These electronegative molecules can neutralize the positively charged fast radon daughters and prevent them from being collected, reducing the detector's radon sensitivity [144].

Some material preparations are known to reduce outgassing significantly [276, 288, 289]. Degreasing, polishing, exposure to UV light, and bake-out (a process of heating components), can be employed to reduce outgassing. Samples can be cleaned by applying *e.g.* alcohol or other chemicals to remove surface impurities not intrinsic to the component. Shining UV light in photon-stimulated desorption can increase pump-down speed of vacuum systems by desorbing monolayers of water [290]. Bake-out is typically performed in an oven and can help to speed up the outgassing of soft materials such as polyethylene, polyurethane, and PTFE [286--288]. and can reduce the average outgassing of harder materials such as aluminum, copper, titanium, and stainless steel by orders of magnitude [287, 289]. After the material has returned to room temperature, the outgassing is reduced. For vacuum vessels, pump-down speed generally improves and the minimum pressure of

the vacuum vessel may be lowered significantly. In the lab at SDSM&T, we use a silicone heating tape that has a maximum temperature 300°F, to speed up the outgassing process. We wrap a vacuum vessel in the tape and use a scroll pump to remove outgassed molecules shortly after they leave the material surface. By flushing the emanation chamber and restarting the emanation, we can mitigate the impact of outgassing of materials intended for assay.

Leaks are troublesome for samples emanating little radon. Samples are typically emanated in the chambers well below atmospheric pressure. Given radon's nefarious, diffusive nature, the vessels hermetically sealing the emanated radon until transfer time need to be really leak tight. We can determine the worst-case impact of a leak by assuming no radon decays occur after they enter a chamber of volume V_{cham}, or alternatively, that the leak occurs over a much shorter timescale than the mean lifetime of radon. In this case, the rate of radon decays ΔR added to a chamber by a leak leads to a pressure increase ΔP_{cham} in the chamber that is proportional to the concentration of radon C_{lab} in the lab. The upper bound on the added radon decay rate

$$\Delta R = V_{\text{cham}} \times C_{\text{lab}} \times (\Delta P_{\text{cham}}/P_{\text{lab}}). \tag{4.1.4}$$

The radon detector has a an approximate background and minimum detectable activity $\sim 0.2\,\text{mBq}$. For a maximum acceptable radon level $R_{\text{max}} = 0.2\,\text{mBq}$ added to the 300 L vessel, given a lab-air radon concentration $C_{\text{lab}} = 100\,\text{Bq/m}^3$ and pressure $P_{\text{lab}} = 680\,\text{Torr}$, the maximum allowable pressure change due to a leak is found by solving Eqn. 4.1.4 for the added pressure:

$$\Delta P_{\text{cham}} = \frac{R_{\text{max}}}{V_{\text{cham}}} \cdot \frac{P_{\text{lab}}}{C_{\text{lab}}} = \frac{0.2\,\text{mBq}}{0.3\,\text{m}^3} \cdot \frac{680\,\text{Torr}}{100\,\text{Bq/m}^3} \lesssim 5.0\,\text{mTorr}. \tag{4.1.5}$$

This calculation conservatively overestimates the radon transferred to the detection vessel by assuming that no lab-air radon decays during the emanation or transfer. The added radon decay rate is shown (in **Fig. 4.5**) as a function of vessel pressure change, due to leaks in vessels of three volumes: (13, 30, and 300) L. During emanation, the small (large) chamber should leak no more than 105 (5.0) mTorr of lab air to prevent radon in the lab contributing to the decay rate of the sample radon. Leak rates as low as $Q_{\text{VCR}} \approx (10^{-12}\text{–}10^{-10})\,\text{Torr L/sec}$ are achievable with Vacuum Coupling Radiation (VCR) gaskets [291]. These gaskets are used exclusively in all 3 of the SWAGELOK gas panels at SDSM&T, save for a single carrier-gas input. The over-pressure provided by the low-radon dewar guarantees no radon will leak in from the lab environment at the panel input. Leaks can be hard to identify especially in a 300 L volume since, by the ideal gas law $P \propto {}^{NT}/_{V}$, the change in pressure will be proportional to the atoms N added divided by the vessel volume. A leak rate high as the worst VCR connection $Q_{\text{VCR}} = 10^{-10}\,\text{Torr L/sec}$ guarantees that for a $t_{\text{eman}} = 15\,\text{day}$ emanation in the enormous 300 L emanation chamber, only

$$\begin{aligned} \Delta(PV) &= Q \times t_{\text{eman}} \\ &= 10^{-10}\,{}^{\text{Torr L}}/_{\text{sec}} \times 15\,\text{days} \times \left(84.6 \times 10^3\,{}^{\text{sec}}/_{\text{day}}\right) \\ &\approx 0.13 \times 10^{-3}\,\text{Torr L} \end{aligned} \tag{4.1.6}$$

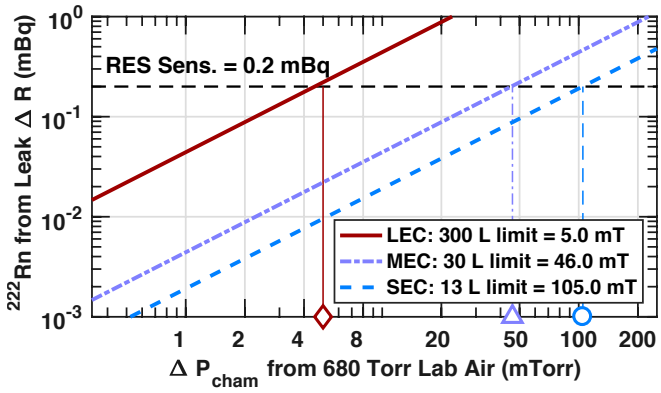

Figure 4.5: ^{222}Rn decay rate ΔR added to 13 L small emanation chamber (SEC, blue dash), hypothetical 30 L medium emanation chamber (MEC, purple dot-dash), and 300 L large emanation chamber (LEC, red solid) as a function of the change in pressure ΔP due to leaked-in lab air. The curves, from Eqn. 4.1.4, assume the lab is at $P_{\text{lab}} = 680$ Torr, and carries a radon concentration $C_{\text{lab}} = 100\,\text{Bq/m}^3$. The 0.2 mBq sensitivity of the R.E.S. shown (horizontal dashed) is a useful comparative upper limit for the pressure increase allowed by a given chamber. This calculation conservatively assumes that radon added to the chamber from leaks does not decay between the time the radon enters the vessel to the time of assay.

of lab air will enter the vessel. Since the decay activity of the lab air $\tilde{C} \approx 0.1^{\text{Bq}}/_{\text{L}\,680\,\text{Torr}}$, the radon added to the vessel

$$\begin{aligned} \Delta R_{\text{leak}} &= \Delta(PV) \times \tilde{C} \\ &= 0.13 \times 10^{-3}\,\text{Torr L} \times 0.1^{\text{Bq}}/_{\text{L}\,680\,\text{Torr}} \\ &\approx 0.02\,\mu\text{Bq} \ll 10^{-3}\,R_{\text{max}} \end{aligned} \tag{4.1.7}$$

and the purity of the emanated radon will remain unspoiled by the lab's high-activity radon.

To prevent leaks during sample replacement, we use a torque wrench to re-seal the lid of the emanation and detection chambers using a non-sequential star pattern as shown in **Fig. 4.6**. The left panel shows a 24-bolt star pattern example from [292], and the right panel shows the 20-bolt star pattern written with sharpie on the bottom flange of the detection chamber. The patterns are created by forming a cross with the first four bolts: bolt '2' is placed across from '1', and bolts '3' and '4' are opposite each other forming a cross with the first two bolts. The pattern may be inexact, not exactly as described in **Fig. 4.6**, as long as the angular separation between subsequent bolts is large enough to distribute the pressure evenly across the flange. The star pattern and torque wrench are used to set an even pressure for bolts on opposite sides of the lid. The detection chamber uses the same bolt sizes as the small emanation chamber and therefore is sealed with the same torque. The detection chamber flanges have 18 bolts and the small (large) emanation chambers has 24- (48-)bolt vacuum flanges. To re-seal the small (large) emanation chamber lid, we use a torque wrench set to no more than

$$\tau_{\text{nom}} \leq 142\,\text{in lbs}\ (40\,\text{ft lbs}) \tag{4.1.8}$$

to guarantee a sufficient chamber-lid pressure. When resealing the chamber, we initially set a snug

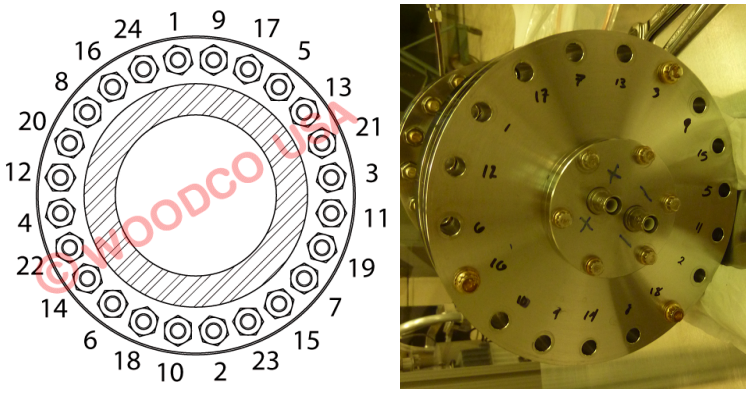

Figure 4.6: **Left:** 24-bolt star-pattern tightening sequence from [292]. **Right:** Sequence used on the 20-bolt HV feedthrough flange of the radon detection vessel.

tension in the bolts by hand. Ref. [292] suggests using an incremental increase in the applied torque taking 4 star-pattern passes at 25, 50, 75, and 100% of the nominal torque, followed by another pass at the maximum torque. Sometimes, a final pass might help spot bolts with a low pressure. Big leaks $\gtrsim$1 Torr/day might warrant replacing the copper gasket seal. Most torque loss is expected to occur within the first day, so tightening the bolts a day after sealing might be useful [292], especially if a new copper gasket has been used.

We measure the leak rate of each vacuum vessel using a multi-purpose Pfeiffer helium leak checker [293]. We seal and evacuate the vessel with a roughing pump before connecting the leak checker. After connecting the leak checker, the vessel pressure is measured and we spray lab-grade helium gas[1] in a small area near potential leak sites. The leak checker pumps the gas in the vessel and a leak rate is inferred from helium measurements. The worst VCR connection may produce a leak rate $Q_{\text{leak}} \leq 9 \times 10^{-9}\,\frac{\text{Torr}\cdot\text{L}}{\text{sec}}$ and, for 15 day leak (Eqn. 4.1.7), lead to an additional $\Delta R_{\text{leak}} \leq 1.8\,\mu\text{Bq}$ of radon in the chamber, which is acceptable for the emanation and detection chambers. In practice, if the vessel in question can't reach $\mathcal{O}$(mTorr), we can replace the copper gasket; this is somewhat tough to accomplish on the large emanation chamber, due to the small diameter of the gasket. It is much easier to replace when the vessel flange is upside-down on the floor.

The small (large) emanation chamber can be pumped to $\sim$ 4.0 (6.5) mTorr with no sample. Outgassing samples may prevent the vessel pressure from reaching 20 mTorr even under constant evacuation with a scroll pump. A rate-of-rise test may be performed by pumping the chamber to its lowest achievable pressure and sealing the chamber. During the resulting pressure rise, we note the vessel pressure over time, frequently recording the pressure at early times to measure the asymptotically decreasing pressure rate-of-rise. When the vessel has been evacuated to its minimum

[1]NB: Some samples, such as photomultiplier tubes, may be damaged if they are exposed to helium, so using the leak checker is not an option.

pressure, leaks from the lab will produce a pressure change

$$\frac{\mathrm{d}P}{\mathrm{d}t} \approx \text{constant} \tag{4.1.9}$$

that remains constant in time. Before beginning the sample emanation, it must be confirmed that the chamber is below the acceptable leak rate for the chamber (using Eqn. 4.1.4 or **Fig. 4.5**). Otherwise the lab air leaking in to the chamber will contaminate the sample measurement; it may be difficult to determine with a residual gas analyzer (RGA) whether the pressure increase is due to outgassing of the sample or from a leak.

The desorption rate of outgassing samples will eventually reach an equilibrium wherein the vessel pressure no longer rises appreciably. If the pressure increases at a decreasing rate and begins to asymptote, then the increase in pressure was dominated at early times by outgassing and may be dominated at late times by a leak. If the pressure continues to increase indefinitely, then a linear rate-of-rise indicates a leak in the chamber which may require bolt-tightening or gasket replacement. If it is not possible to use a helium leak checker, a residual gas analyzer may help ensure that the pressure rise is due to soft sample outgassing, in which case, it may be helpful to evacuate the emanation vessel for hours–days before beginning the sample emanation. Once a vessel is determined to be leak free, and the sample no longer outgasses significantly, an emanation can begin. In case there's a leak we can't address, the radon emanation is performed with the vessel pressure well above atmospheric pressure $P_{\text{eman}} \approx 1,000\,\text{Torr}$ so outward leaks prevent lab air from entering the vessel. There is an efficiency loss associated with this emanation method due to the radon leaking out of the vessel. The radon loss may be assumed to be proportional to the pressure loss from leaks. A conservative upper bound on this loss of emanated radon can be estimated by assuming the leak brings the vessel from 1,000 Torr to atmospheric pressure

$$\epsilon_{\text{over-pressure}} = \frac{680\,\text{Torr}}{1000\,\text{Torr}} \approx 70\%. \tag{4.1.10}$$

This is an overestimate since not all the emanated radon will be in the vessel at the time it is sealed. In practice, we usually don't have leaks large enough to warrant over-pressured emanation.

4.2 Radon Transfer

After the radon emanation period has completed, the radon is transferred to the detection chamber with the gas panel (shown in **Fig. 4.3**). The emanation vessels house potentially large amounts of material and the detection volume is considerably smaller. As a result, the sample must be concentrated as much as possible during radon transfer. To achieve this, we trap the sample using cryogenically cooled materials on which radon will stick. We use radon from a high-activity source to measure the effectiveness of the transfers. This section describes the physics of radon adsorption, and passage through an adsorbing bed (**Section 4.2.1**). I also describe the preparation

of our gaseous calibration-source (**Section 4.2.2**), a simplified determination (**Section 4.2.3**) and measurement of the radon transfer efficiency (**Section 4.2.2**, **Section 4.2.4**), and the procedures to ensure a $\sim 95\%$ radon transfer efficiency to our 1.7 L detection vessel (**Section 4.2.5**).

4.2.1 Radon Adsorption at Cryogenic Temperatures

Radon is an inert, noble gas having essentially no chemical interactions, so the only relevant interactions for radon adsorption are physical in nature. In order to capture radon that has been successfully removed from the emanation chamber, we take advantage of low-temperature physical interactions radon has with some solids. I forgo the discussion of strictly chemical phenomena, relying on as little chemistry as possible since...

> "The literature pertaining to the sorption of gases by solids is now so vast that it is impossible for any, except those who are specialists in the experimental technique, rightly to appraise the work, which has been done, or to understand the main theoretical problems which require elucidation."
>
> –J. E. Lennard-Jones, 1932 [294]

Molecules interact with material surfaces–in this case an 'adsorbent' or 'substrate'–with forces from either the physical *Van der Waals* interaction or from the 'chemical' hybridization of electron orbitals with the atomic substrate. Van der Waals interactions arise from correlated polarization fluctuations of nearby particles. Physical adsorption or 'physi-sorption' comes from the characteristically weak *Van der Waals* forces (of order 10–100 meV) between atoms, and does not arise from chemical electronic bonds at much greater energies than (1–10) eV. Chemical adsorption involves a significant perturbation of the molecular electronic structure. The physical adsorption from a gas to an adsorbent *e.g.* the column of trapping material that we call 'a trap', occurs when molecular forces between the absorbent and gas ions overcome the inter-molecular attractive forces of the gas itself. Ions with low kinetic energy may be temporarily attached to the surface of certain materials. Gas phase molecules may form multilayers during physical adsorption.

Gaseous Elution Across an Absorbent In order to transfer and concentrate radon from our (large) emanation vessels to our (small) detection chamber, we flow nitrogen through the vessel and capture the radon onto cold brass wool traps. Radon atoms will move across the brass wool (the adsorbent) surface repeatedly adsorbing and de-sorbing as the carrier gas brings more of the sample radon into the trap. Radon will preferentially adsorb to the surface of certain materials, such as carbon or metals, compared to other gases *e.g.* helium, nitrogen, and neon. As the carrier gas passes along the bed of adsorbent, the competing adsorption and desorption result in radon moving orders of magnitude more slowly than the carrier gas [112, 174, 188, 295--298]. The average total time a carrier spends to pass an adsorbing material is called the *elution* or *breakthrough* time $t_{\text{B.T.}}$ and is proportional to the dynamic adsorption coefficient k_a, which characterizes the

temperature-dependent stickiness between the adsorbent and carrier. The breakthrough time for radon traveling through an ideal trap at temperature T (K) is given by

$$t_{\text{B.T.}} = \frac{k_a(T)\, m}{F}, \tag{4.2.1}$$

which depends on the coefficient k_a (units of inverse density: $\text{m}^3\,\text{kg}^{-1}$), the trap mass m (kg), and the flow rate F (STP $\text{m}^3\,\text{s}^{-1}$). The dynamic adsorption coefficient k_a obeys a temperature-dependent Arrhenius relation

$$k_a \propto \exp(^{-E_a}/_{k_b T}) \tag{4.2.2}$$

depending on the activation energy E_a, similar to diffusion, and increases substantially at low temperatures [112, 169, 174, 188, 295, 297]. The dynamic adsorption coefficient also depends on the surface area per mass S ($\text{m}^2\,\text{g}^{-1}$) of the adsorbent [142, 188, 295]. Radon adsorption onto activated charcoal has been studied in *e.g.* Refs. [142, 171, 185, 188, 295, 296, 299, 300] and the coefficient k_a has been determined experimentally to be

$$k_a(T) = (0.0070\, S - 3.51) \exp\left(\frac{\mathcal{H}_a}{R}\left(\frac{1}{T} - \frac{1}{273}\right)\right), \tag{4.2.3}$$

where the heat of adsorption $\mathcal{H}_a$ is material dependent, and the gas constant $R = 8.31\,\text{J}\,\text{mol}^{-1}\,\text{K}^{-1}$. Note that, as mentioned in Hallin's note [142], this formula is different from that given in the original Strong and Levins paper [295], incorporating a sensible sign change in the exponential, since hotter temperatures lead to less effective radon adsorption and therefore quicker radon breakthrough. The equation also bears a normalization factor in the denominator. These changes bring the formula into agreement with figure 5 in the original paper [295]. The original paper gives an adsorption heat

$$\mathcal{H}_a \approx 29 \times 10^3\,\text{J/mol} \tag{4.2.4}$$

for carbon [142, 188, 295], and I use this value throughout this thesis. The surface area per mass of carbon $S \approx (800\text{–}1500)\,\text{m}^2/\text{gram}$ [295, 296, 301, 302]. Radon adsorption onto carbon has been studied in an attempt to prevent radon from nearing rare-event search detectors since radon's complicated decay scheme with alphas, high-energy betas, and penetrating gammas poses significant backgrounds for many experiments. Radon removal from xenon has been studied in *e.g.* Ref. [296], for XMASS [174], for PandaX-1 [112], and radon in nitrogen for SuperCDMS SNOLAB in *e.g.* [178], and CUORE [179], as well as others like Borexino [182], and SNO+ [183].

Metal and Carbon Traps For the radon emanation system, radon is initially trapped and sealed in a small volume. The sample is then heated and transferred again to another, smaller trap, and following a secondary heating is then placed in the small detection vessel. Because the diffusion coefficient of materials is temperature dependent [130, 133, 170, 277, 303--305], the adsorbents may release internal radon when reheated. Metals are useful as a trap material because they have

much lower radon diffusion coefficients than other materials, so radon is significantly less likely to emanate from or diffuse into (and subsequently back out of) the metal. Metals such as copper can have a high enough dynamic heat of adsorption–of the order of carbon [306]–to be useful for capturing radon, especially at cryogenic temperatures. Metals may also be low enough in bulk uranium so that, coupled with their generally low diffusion coefficient, their radon emanation will be very low! With some surface preparation, metal traps are good for capturing the sample radon and not releasing extra radon, even if heated above room temperature for secondary transfer to the detection volume. Carbons, on the other hand, have a larger diffusion coefficient than metals so diffusion emanation may be higher for the same level of radium contamination per volume. At an increased cost, carbon can be prepared to have a very high surface-area-to-mass ratio; carbon can also be prepared at high isotopic purity bearing very-low levels of radon emanation [171].

The gas panel at SDSM&T used for radon transfers is outfitted with two brass wool traps cooled by liquid nitrogen to 77 K. Each trap captures and concentrates the sample radon in a small volume before transfer to the detection chamber for assay. Radon emanating from the inner surfaces of LN_2 dewars may contaminate sample transfers, by passing through the emanation chamber and getting trapped along with the sample in the brass wool traps. We overcome this by passing the carrier gas through another cryogenic trap at the panel input to scrub the gas before it reaches the emanation vessel. We use a carbon trap submerged in a 10 L Nalgene dewar filled with isopropyl alcohol (IPA), cooled with solid CO_2 which sublimates (phase transformation from solid to gas) very near the IPA freezing temperature at $196\,\mathrm{K} \approx -77^{\circ}\mathrm{C}$. Radon in the carrier gas is prevented from ever reaching the emanation vessel, brass wool traps, and the detector. Characterization of the carbon sample at the input of the gas panel that prevents radon from LN_2 dewars dominating the sample radon is described in **Section 4.6**.

4.2.2 Determining the Radon Transfer Efficiency

To determine the transfer efficiency $\varepsilon_{\mathrm{tr}}$, *i.e.* the fraction of radon transferred from the emanation vessel via the traps to the detection chamber, we use a commercially available Pylon brand radon source (RN-1025) [307] to prepare a known quantity of ^{222}Rn. Radon samples prepared for the transfer efficiency measurements described here were specifically prepared to provide a substantially higher event rate $S \gtrsim 0.1$ events/peak/second than the detector background $B \lesssim 2$ events/peak/day in the $^{218/4}$Po energy region of interest. Since the detector backgrounds are low, the total measured rate S will depend on the rate of signal events R and background rate B such that

$$S_{\mathrm{tot}} = R + B = R\,(1 + {}^{B}/_{R}) \approx R,$$

because the detector backgrounds $B \ll R$ are much lower than the prepared calibration rate. The Pylon source is a $V = 0.106\,\mathrm{L}$ vessel with ^{226}Ra salt that decays producing gaseous ^{222}Rn that diffuses from the substrate. The vessel has flow-through input/output gas ports useful for continuous

Table 4.1: Radon emanation efficiency $\varepsilon_{\text{eman}} = R/R_{\text{eqbm}}$ as a function of time. After a 3.82 day sample emanation, the radon decay rate in the gas is half the equilibrium bulk emanation. The grow-in is linear for early times with $^{\text{d}\varepsilon_{\text{eman}}}/_{\text{d}t} \approx t/\tau$.

time (days)	4/24	0.50	1.00	3.82	5.52	11.0	16.6	22.0	30.0
R/R_{eqbm} (%)	2.97	8.66	16.6	50.0	63.2	86.5	95.0	98.1	99.6

or short-term use. The radon from the source has an equilibrium decay rate

$$R_{\text{py}} = 117.479\,\text{kBq}\,(1 \pm 0.04) \tag{4.2.5}$$

with a fractional decay-rate uncertainty $^{\delta R}/_{R} = 4\%$ specified by the manufacturer. To prepare the source, N_2 gas is used to purge the built-up radon. Ref. [308] suggests flowing 10 or more vessel volumes V_{py} of carrier gas

$$V_{\text{purge}} \geq 10\,V_{\text{py}} = 10 \times 0.106\,\text{L} \approx 1.1\,\text{L} \tag{4.2.6}$$

through the vessel to ensure basically none of the old radon will be in the volume for the planned calibration. Historically, a purge of the source was typically performed for an excessively long time $t_{\text{purge}} \gtrsim 20\,\text{min}$ at $F = 10\,\text{L/min}$ for a gas purge volume

$$V_{\text{purge}} = F \cdot\, t_{\text{purge}} \approx 20\,\text{min} \times 10\,\text{L/min} \approx 2,000\,V_{\text{py}}. \tag{4.2.7}$$

We can relax this requirement with a purge flow of 5 lpm, flowing for $t_{\text{purge}} = 1\,\text{min}$, still achieving $5\,\text{L}/0.106\,\text{L} \gtrsim$ 45 volume exchanges. Following this very modest flow-through time, the Pylon is effectively purged of the built-up radon. As described below, the source can be sealed for a time to build-up a huge radon decay rate, or it can be used continuously with a through-going gas source so that the output activity will depend on the flow rate.

For single-use build-up, the Pylon can be sealed for a time t_{build} during which the radon emanates into the small Pylon vessel volume, before subsequent transfer to a vessel all at once. The radon decay rate in the vessel is found with the emanation grow-in Eqn. 4.0.1 using the equilibrium production rate from Eqn. 4.2.5. **Table 4.1** shows a few values of the emanated fraction of the equilibrium decay rate, allowing a quick estimate of the calibration source strength. For example, according to Eqn. 4.0.1 and **Table 4.1**, the rate of radon decays in the gas is 98.1% the equilibrium decay rate after 22 days of emanation.

In practice, boil-off from a liquid nitrogen dewar is fed to the vessel to purge the radon. The source is then sealed and allowed to build up for $t_{\text{build}} \approx$ (2–4) hours. The output of the Pylon is then connected to the gas panel to transfer to one of the emanation vessels. The Pylon is transferred to the emanation chamber over a very short time $t_{\text{tr}} \lesssim 2.5\,\text{min}$. The fraction of the total preparation time spent transferring the calibration source to the vessel $t_{\text{tr}}/t_{\text{build}} \lesssim 2.5\,\text{min}/120\,\text{min} \approx 2.1\%$ of the build-up period.

The radon from the source may also be accurately calculated when it is flushed continuously. If the source is being flushed with external gas, then the steady-state radon decay rate provided at the output of the Pylon vessel is found by taking the time derivative of the grow-in fraction from Eqn. 4.0.1 evaluated at $t = 0$,

$$\left.\frac{\mathrm{d}R}{\mathrm{d}t}\right|_{t=0} = \frac{R_{\mathrm{py}}}{\tau} = \frac{117.479\,\mathrm{kBq}}{5.52\,\mathrm{day}} = 21.3\frac{\mathrm{kBq}}{\mathrm{day}} \times \frac{1\,\mathrm{day}}{1,440\,\mathrm{min}} = 14.6\,\mathrm{Bq/min}. \tag{4.2.8}$$

This linear equation is also fairly accurate for short, single-use cases where the grow-in period is much less than the half-life of radon. The linear prediction of the total radon decay rate from Eqn. 4.2.8 for a very long 4 hr calibration build-up is $R_{\mathrm{lin}} = 14.6\,\mathrm{Bq/min} \cdot 4 \cdot 60\,\mathrm{min} \approx 3.50\,\mathrm{kBq}$. The grow-in prediction from Eqn 4.0.1 gives an accumulated radon decay rate

$$R(4\,\mathrm{hr}) = 117.479\,\mathrm{Bq}\Big(1 - \exp(^{-4}/_{24\cdot 5.52})\Big) \approx 3.49\,\mathrm{kBq} \tag{4.2.9}$$

deviating only 1.5% from the true value.

The expected radon concentration at the output of the Pylon source is an example of a general problem we will encounter in several forms: radon concentration in a vessel with radon sources and sinks. Low-radon nitrogen flowing at F into the Pylon has a characteristic volume-replacement time $t_{\mathrm{rep}} = (F/V)^{-1}$, which is the duration to flow a full vessel volume V of carrier gas through the source. While gas flows out (at the input flow rate) the steady-state radon concentration C in the vessel is determined

$$\frac{\partial C}{\partial t} = \frac{F C_{\mathrm{LN_2}}}{V} + \frac{R_{\mathrm{py}}}{\tau\, V} - \frac{FC}{V} - \frac{C}{\tau}. \tag{4.2.10}$$

where $C_{\mathrm{LN_2}}$ is the input-gas radon concentration. We can simplify Eqn. 4.2.10 by considering a few factors. The radon concentration of the nitrogen (at $C_{\mathrm{LN_2}} \lesssim 1\,\mathrm{mBq/m^3}$) is many orders of magnitude lower than the Pylon $C \sim 10\,\mathrm{kBq/m^3}$, and so the first term can safely be ignored. For usable flow rates, the volume replacement time is much smaller than the mean lifetime of radon $\tau = 5.52\,\mathrm{days}$. In this case, very few radon decays occur after emanating from the source, so we can also ignore the radon decay term. The steady-state output concentration of this source, at moderate flow-replacement, is found by setting Eqn. 4.2.10 to zero so that

$$\frac{F\,C}{V} = \frac{R_{\mathrm{py}}}{\tau\, V}, \qquad \text{for} \qquad t_{\mathrm{rep}} = {}^{V}/_{F} \ll \tau. \tag{4.2.11}$$

Thus, the concentration is inversely proportional to the flow rate

$$C_{\mathrm{py}} = \frac{R_{\mathrm{py}}}{F\tau} \tag{4.2.12}$$

and independent of the vessel volume. This intuitively makes sense, if we assume complete mixing of the gas inside the vessel volume only volumetric flow rate has an impact on the activity at the output. Preferential flow paths inside a volume (*e.g.* due to input and output ports very near to each other) may prevent near-ideal gaseous mixing from occurring. Eqn. 4.2.12 is useful for

describing the expected equilibrium concentration from radon breakthrough in carbon samples as described in **Section 4.6**.

Calibration Sample Reduction and Decay Historically, radon is transferred (over a short time $t_{\text{tr}} = 2.5\,\text{mins}$) to either emanation chamber after a 2 hr build-up period $t_{\text{build}} = 2 + 2.5/60\,\text{hr} \approx 2.042\,\text{hr}$ so that the radon in the chamber, including the source's systematic uncertainty, is given by

$$\begin{aligned} R_0 &= R_{\text{py}} \times \left(1 - \exp(^{-2.04\,\text{hr}}/_{24\cdot 5.52\,\text{hr}})\right) \\ &\approx (117.5 \pm 4.7)\,\text{kBq} \times 1.52\% \\ &\approx (1,800 \pm 70)\,\text{Bq}. \end{aligned} \tag{4.2.13}$$

A decay rate this large is unnecessary for calibrating a detector sensitive to decay rates as low as 1 mBq. As described in **Section 4.5**, radon will diffuse into the few non-metal components in the vessel, similar to lab-air diffusing into samples before an emanation. So following a high-rate calibration, radon will back-diffuse out of the epoxy and teflon; this produces an irreducible detector background for $\mathcal{O}(\text{days})$. As a result, we avoid placing high decay-rate calibration samples in the detector. To avoid a large uncertainty in the overall decay rate due to a potentially short source preparation time, the transfer time is done over a small fraction of the build-up time, so that the uncertainty in the transfer time is much less than the Pylon source uncertainty

$$\delta t_{\text{tr}}/t_{\text{build}} < {}^1/_{10} \cdot \delta R_{\text{py}}/R_{\text{py}} = 0.4\%.$$

The radon activity in a vessel (*e.g.* gas panel, detection chamber, or emanation chamber) is reduced by introducing a new supply of low-radon gas that mixes with the high-radon sample. Following this pressure increase, radon is removed by partially evacuating the vessel. Then, assuming the radon is well-mixed, the fraction of atoms removed during the vessel evacuation is expected to be proportional to the fraction of the pressure removed. The reduction η_{red} of radon decays in the vessel, after n_{flush} pressure swings, from P_i down to P_f is given by the successive ratio for each swing

$$\eta_{\text{red}} = \prod^{n_{\text{flush}}} P_f/P_i. \tag{4.2.14}$$

Performing a pressure swing takes a considerable amount of time for the large emanation chamber due to its volume. To accurately estimate the radon intended for transfer, one should account for the decay of radon in the vessel during the pressure-reduction phase. For a three-hour reduction, the radon content will have naturally decayed to $\exp(^{-3}/_{24\cdot 5.52}) \approx 97.8\%$ of the initial value. The total source reduction from the pressure reduction from Eqn. 4.2.14 and radioactive decay

$$\eta_{\text{total}} = \eta_{\text{red}} \exp(-t_{\text{red}}/\tau). \tag{4.2.15}$$

with a systematic uncertainty

$$\frac{\sigma_\eta}{\eta_{\text{total}}} = \sqrt{\left(\frac{\sigma_{\text{red}}}{\eta_{\text{red}}}\right)^2 + \left(\frac{\sigma_t}{\tau}\right)^2} \approx \sqrt{\left(\sum_{P_i \neq P_f} \left(\frac{\sigma_P}{P}\right)^2\right) + \left(\frac{1\,\text{hr}}{5.52 \times 24\,\text{hr}}\right)^2} \tag{4.2.16}$$

where the accuracy[2] of the pressure gauges $\sigma_P/P \lesssim 5\%$ is summed over for every unique pressure measurement made during the reduction of the sample concentration. The calibration source decay rate, just before a transfer begins, is then computed from Eqn. 4.0.1 using the grow-in t_{build} and transfer time t_{tr}. The systematic uncertainty associated with a $t_{\text{tr}} = 2.5\,\text{min}$ transfer, following a $t_{\text{build}} = 2\,\text{hr}$ build-up period

$$\frac{\sigma_t}{t_{\text{build}}} \lesssim \frac{2.5}{2 \times 3600} \approx 0.035\% \tag{4.2.17}$$

is much smaller than the 4% systematic uncertainty on the calibration source. In this case, using two consecutive $\times 100$ pressure reductions from *e.g.* (700–7) Torr over a $t_{\text{red}} = 40\,\text{min}$ period will leave

$$\eta_{\text{red}} = (7/700)^2 = 10^{-4}$$

of the sample, and radon decays leave $\exp(-40/1440 \cdot 5.52) = 99.4\%$ of the sample, so the radon in the vessel ready for transfer

$$\begin{aligned} R_{\text{trans}} &= R_0\,\eta_{\text{red}}\,\exp(-t_{\text{red}}/\tau) \\ &= (1,800 \pm 70)\,\text{Bq} \times 10^{-4} \times 99.4\% \\ &= (178.8 \pm 7.1)\,\text{mBq}. \end{aligned} \tag{4.2.18}$$

During radon transfer, carrier gas flows into the emanation chamber, knocking the sample radon into the evacuation flow path where it is captured by cryogenically cooled brass wool traps as described in **Section 4.2.1** above.

Measuring the Radon Transfer Efficiency The transfer efficiency ε_{tr} of placing the radon in the detection chamber via the brass wool trap is determined by calculating and comparing the expected radon prepared in the transfer vessel to the measured decay rate following a transfer. Radon transfers were originally performed with the emanation chamber held at a single, low pressure $P_{\text{tr}} = 200\,\text{Torr}$, with a constant carrier-gas flow rate $F_{\text{tr}} \sim 10\,\text{L/min}$. Measurements of transfers performed by Megan Stark and Ray Bunker with a constant vessel pressure and analyzed by Megan indicate (in **Fig. 4.7**) that the average transfer efficiency varied significantly:

$$\varepsilon_{\text{tr}} \approx (50 \pm 20)\%. \tag{4.2.19}$$

[2]The pressure gauges are not calibrated; their digital display shows 4 digits of precision.

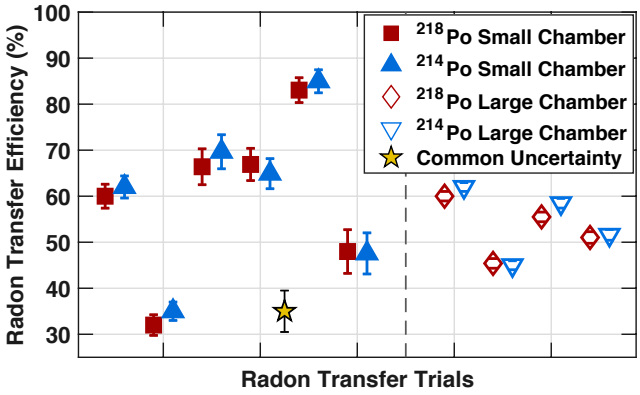

Figure 4.7: Radon transfer efficiency for ^{218}Po (□) and ^{214}Po (△) isotopes for 6 radon transfer trials from the small (solid) and 4 from the large (empty) emanation chambers shown with poisson uncertainties (errorbars). M. Stark and R. Bunker performed the transfers and analyzed the data. The common systematic uncertainty $\sim 4.1\%$ (shown as ★) is dominated by the 4% statistical uncertainty of the Pylon source, and includes a 1% upper limit on the uncertainty in the initial transfer (> 99 %) of radon to the chambers. The average radon transfer efficiency for constant vessel pressure varies significantly, and is typically no more than 70%.

Even with hours long flow-through periods, the average (constant-pressure) radon transfer efficiency is an unacceptably low 65%. The gas replacement of the vessels is a non-trivial function of position that assumedly depends on the carrier-gas flow path. Our small emanation chamber has input and output flow ports on the bottom vacuum flange very near to each other (< 3" apart). Our large emanation chamber, by nature, houses as much material as possible so a sample's geometry may partially block the flow path of some radon gas in the vessel, potentially leading to worse transfer efficiencies.

Our group had plans to test a method of radon transfer where the emanation chamber pressure would vary. This idea is based on taking advantage of the ideal gas law. The mean free path λ is the average distance traveled by a particle between collisions. For a gas at a given temperature T and pressure P

$$\lambda(P,T) = \frac{k_B T}{\sqrt{2} P \sigma_{\text{coll}}}, \tag{4.2.20}$$

where the collision cross-section $\sigma_{\text{coll}} = \pi d_{\text{m}}^2$ depends on the molecular diameter d_{m} [277, 309]. For a gas of a given temperature, $\lambda \cdot P =$ constant, so as the ambient pressure decreases in a vessel, gas atoms travel farther before a collision, which can be used to increase the radon transfer efficiency by reducing the vessel pressure. Radon has diameter $d_{\text{Rn}} \approx 450 \times 10^{-12}\,\text{m}$ [310], so that at room temperature a purely radon gas at $P = 200\,\text{Torr} = 200 \times 133.3\,\text{N/m}^2$ will have a mean free path

$$\begin{aligned} \lambda_{\text{Rn}} &= \frac{1.38 \times 10^{-23}\,\text{J/K} \cdot 293\,\text{K}}{\sqrt{2}\pi\, 450^2 \times 10^{-24}\,\text{m}^2 \cdot 2.66 \times 10^{-4}\,\text{J/m}^3} \\ &= \frac{4.04 \times 10^{-21}\,\text{J}}{5.73 \times 10^{-15}\,\text{J/m}} \approx 674\,\text{nm}. \end{aligned}$$

This is an underestimate since the collision diameter of radon significantly exceeds that of nitrogen

and the velocity distribution will be higher for trace radon diffusing in nitrogen. Even for pure nitrogen which has a diameter $d_{\mathrm{N}} = 310 \times 10^{-12}\,\mathrm{m}$, some 68% of the diameter of radon and with 47% the cross-sectional area of radon, the mean free path is doubled for the same ambient temperature. Although the pressure decrease from *e.g.* (200–50) Torr won't allow radon to travel the distance of the emanation vessel (diameter near 20–60 cm) the gas will diffuse $\sim 4\times$ faster. Then by the ideal gas law

$$P\,V = n\,RT \tag{4.2.21}$$

we expect that reducing the initial emanation vessel pressure P_i during a radon transfer, where the temperature T and volume V don't change,

$$P_f = 1/4 \cdot P_i \tag{4.2.22}$$

by a factor of 4, would leave the same fraction of the radon atoms $f_{\mathrm{left}} = n_f/n_i = 1/4$ in the vessel, and the radon removal (*i.e.* transfer) efficiency would be

$$f_{\mathrm{transfer}} \equiv 1 - f_{\mathrm{left}} = 1 - {}^{n_f}/_{n_i} = 1 - 1/4 = 3/4. \tag{4.2.23}$$

Eric Miller devised a test to measure the radon transfer efficiency while varying a transfer vessel pressure, in an attempt improve on the constant-pressure efficiency $\varepsilon_{\mathrm{tr}} \sim 50\%$. The test uses the same sample of radon for multiple assay periods: the sample radon is transferred back and forth between the brass wool traps and detector several times in a row. This sample radon is first transferred to the detection chamber and measured. Following this first assay, the radon in the detection chamber was transferred back to the brass wool traps with a backwards-flow technique. Prior to re-placing the sample in the detection chamber, while the sample is sealed in the trap, the detection chamber previously full of high-activity calibration radon was repeatedly evacuated (*i.e.* filled and flushed) leaving only 10 ppb of the un-transferred radon remaining in the detection vessel. This is expected to leave a negligible cross-transfer radon concentration. The process is repeated to obtain a measure of the variation since the constant-pressure transfer efficiencies vary by $\sim 40\%$. Two set of tests will be performed: one with transfer vessels held at a constant pressure, and one with varying pressure. The radon is put in the small chamber, then moved to the traps, and first assayed in the detection chamber. Then radon is transferred backwards, and then re-transferred for subsequent assay.

While in the detection chamber, radon initially decaying at a rate $\tilde{R}_0$ in a sealed vessel t days ago will give rise to a time-dependent decay rate

$$\tilde{R}(t) = \tilde{R}_0 \cdot \exp(-t/5.52\,\mathrm{d}). \tag{4.2.24}$$

The measured radon decay rate $R(t)$ will be a function of the polonium ion collection ϵ_C and

detection $\epsilon_{\mathcal{D}}$ efficiencies[3]:

$$R(t) = \epsilon_{\mathcal{C}}\,\epsilon_{\mathcal{D}}\,\tilde{R}(t). \tag{4.2.25}$$

To infer the real radon decay rate from a single measurement, these efficiencies, and their associated systematic uncertainties, must be well-known. The radon transfer efficiency $\varepsilon_{\mathrm{tr}}$ between two consecutive assays I and II

$$\varepsilon_{\mathrm{tr}} \equiv \frac{\tilde{R}_{\mathrm{II}}(t=0)}{\tilde{R}_{\mathrm{I}}(t=0)} \tag{4.2.26}$$

the ratio of real (initial) decay rates before $\tilde{R}_{\mathrm{I}}$ and after $\tilde{R}_{\mathrm{II}}$ the transfer. Since the efficiencies are common to both measurements, the radon transfer efficiency is

$$\frac{\tilde{R}_{\mathrm{II}}}{\tilde{R}_{\mathrm{I}}} = \frac{\epsilon_{\mathcal{C}}\epsilon_{\mathcal{D}}\,R_{\mathrm{II}}}{\epsilon_{\mathcal{C}}\epsilon_{\mathcal{D}}\,R_{\mathrm{I}}} = \frac{R_{\mathrm{II}}(t=0)}{R_{\mathrm{I}}(t=0)} \tag{4.2.27}$$

independent of the detection and collection efficiencies, and is simply the ratio of the measured rates! In other words, the efficiencies and the corresponding systematic uncertainties will also cancel which allows us to put tighter bounds on the transfer efficiencies than a single measurement alone. Moreover, the accuracy for any decay rate measurement for a single transfer is limited by the 4% systematic uncertainty in the expected decay rate of the high-activity radon source. By repeatedly transferring the sample several times in a row, we obtain a measure of the transfer efficiency which is independent of the above mentioned sources of systematic uncertainty. So these tests allow a much more precise determination, and comparison, for both of the radon transfer methods.

4.2.3 Decay-Corrected Radon Determination

Ideal sample transfers, from *e.g.* the detection vessel, to the transfer trap, and back to the detection vessel, performed at arbitrary times will result in measured rates that appear continuous from before to after the transfer, decaying with the radon mean lifetime. The determination of the initial decay rate may be simplified by multiplying the measured rates by

$$f_{\mathrm{c}}(t) = \exp\left({}^{t}\!/_{5.52\,\mathrm{d}}\right), \tag{4.2.28}$$

to account for the radioactive decay occurring since the initial transfer at $t = 0$. Neglecting the naturally occurring statistical fluctuations, the corrected decay rate at each time t, following the initial transfer ending at $t_0 = 0$, is time-independent, indicating the initial decay rate R_0 in the detector

$$R_{\mathrm{c}}(t) \equiv R(t) \cdot f_{\mathrm{c}}(t) = R_0 \cdot \exp\left({}^{-t}\!/_{5.52\,\mathrm{d}}\right) \cdot \exp\left({}^{t}\!/_{5.52\,\mathrm{d}}\right) = R_0. \tag{4.2.29}$$

[3]The collection and detection efficiencies are discussed further in **Section 4.3.2**.

Radon undergoing transfer at an arbitrary time will have a corrected rate that appears constant with time, albeit with increasing fractional uncertainties as the rates become less statistically significant. Computing the average of the corrected rates R_c

$$\langle R_{\mathrm{c}}(t)\rangle \equiv \langle R \cdot f_{\mathrm{c}}\rangle = R_0 \tag{4.2.30}$$

will further improve the determination of the initial decay rate for a given transfer. In fact, plotting both the measured rates $R(t)$ and the decay-corrected rates R_{c} for each transfer test allows an easy by-eye determination of the initial decay rate (R_{I} for the first transfer, and R_{II} for the second transfer) and taking the ratio of these constants will give the radon transfer efficiency

$$\varepsilon_{\mathrm{tr}} = \frac{\langle R_{\mathrm{II}} \cdot f_{\mathrm{c}}\rangle}{\langle R_{\mathrm{I}} \cdot f_{\mathrm{c}}\rangle}. \tag{4.2.31}$$

The measured decay rate R and its associated statistical uncertainty σ_R, in a given time bin Δt are given by

$$R \pm \sigma_R \equiv \frac{N}{\Delta t} \pm \frac{\sqrt{N}}{\Delta t}, \tag{4.2.32}$$

determined by the number N of events measured in that time bin. The decay-correction f_{c} (Eqn. 4.2.28) is applied to the rate

$$R_{\mathrm{c}}(t) = (R \pm \sigma_R)\, f_{\mathrm{c}} \equiv \left(\frac{N}{\Delta t} \pm \frac{\sqrt{N}}{\Delta t}\right) \cdot \exp\left(\frac{t}{5.52\,\mathrm{d}}\right). \tag{4.2.33}$$

The weighted mean of the decay-corrected rates

$$\Big\langle R_{\mathrm{c}}(t)\Big\rangle = \frac{\sum R_{\mathrm{c}}(t) \cdot w(t)}{\sum w(t)} \tag{4.2.34}$$

is more robust than the nominal arithmetic average, and is computed by summing over all measurement times for the given transfer, where the weights

$$w(t) \equiv \left(\frac{1}{\sigma_{R_{\mathrm{c}}}}\right)^2 = \left(\frac{1}{\sigma_R\, f_{\mathrm{c}}}\right)^2 = \left(\frac{\Delta t}{\sqrt{N}}\right)^2 \cdot \exp\left(-\frac{t}{5.52\,\mathrm{d}}\right)^2.$$

The uncertainty on the decay-corrected weighted mean

$$\sigma_{\langle R_{\mathrm{c}}\rangle} \equiv \left(\sqrt{\sum w(t)}\right)^{-1}, \tag{4.2.35}$$

so that the best estimate of the initial decay rate

$$R_0 = \langle R_{\mathrm{c}}\rangle \pm \sigma_{\langle R_{\mathrm{c}}\rangle}. \tag{4.2.36}$$

The transfer efficiency

$$\varepsilon_{\text{tr}} \pm \sigma_{\varepsilon} = \frac{\langle R_{\text{II}} \cdot f_{\text{c}} \rangle}{\langle R_{\text{I}} \cdot f_{\text{c}} \rangle} \pm \sqrt{\left(\frac{\sigma_{\langle R^{\text{I}} \cdot f \rangle}}{\langle R^{\text{I}} \cdot f \rangle} \right)^2 + \left(\frac{\sigma_{\langle R^{\text{II}} \cdot f \rangle}}{\langle R^{\text{II}} \cdot f \rangle} \right)^2}, \tag{4.2.37}$$

depending on the quadrature sum of the fractional errors of the decay-corrected weighted means. By taking the ratio of consecutive measurements, we avoid the systematical uncertainties from the calibration source, and those from the detection and collection efficiencies. Correcting for the decay of radon simplifies the determination of the initial decay rate, and using the weighted mean improves the accuracy further. So by measuring the sample multiple times, and a little mathematical work we simplify the analysis significantly.

4.2.4 Constant-Pressure Transfer Efficiency

Transfers were performed with the vessels held at a constant pressure to get a measure of the average transfer efficiency without using pressure swings. A simplified diagram of the transfer paths between the chambers and traps, with the nitrogen supply, valve (×), and scroll pumps providing the flow direction is shown in **Fig. 4.8**. The tests use a forward flow configuration to move the sample from the emanation chamber to the traps and then the detection chamber. A radon sample was prepared with the Pylon source over a $t_{\text{build}} \approx 2.16\,\text{hr}$ period, and placed in the small emanation chamber, by flowing nitrogen through the source vessel for two minutes to raise the small chamber pressure by some 500 Torr with an expected efficiency $\varepsilon_{\text{SEC}} \approx 100\%$. The expected sample rate rate

$$R_{\text{samp}} = R_{\text{py}}\ \varepsilon_{\text{build}} = 117.479 \times 10^3\,\text{Bq}\ \left(1 - \exp(-2.16\,\text{hr}/24{\cdot}5.52\,\text{hr})\right) \approx 1847\,\text{Bq}.$$

After a $t_{\text{wait}} = 4.1\,\text{day}$ decay period, the sample was decreased by reducing the pressure from $P_i = 597\,\text{Torr}$ to $P_f = 3.87\,\text{Torr}$, so the initial radon expected for the first constant-pressure transfer

$$\begin{aligned} R_0 &= R_{\text{samp}}\ \eta_{\text{decay}}(t_{\text{wait}})\ \eta_{\text{red}} \\ &= 1847\,\text{Bq}\exp(-4.1\,\text{day}/5.52\,\text{day}) \times 3.87/597 \\ &\approx 5.802\,(1 \pm 0.04)\,\text{Bq} \approx 20.8\text{k}\,\text{decays/hr}. \end{aligned}$$

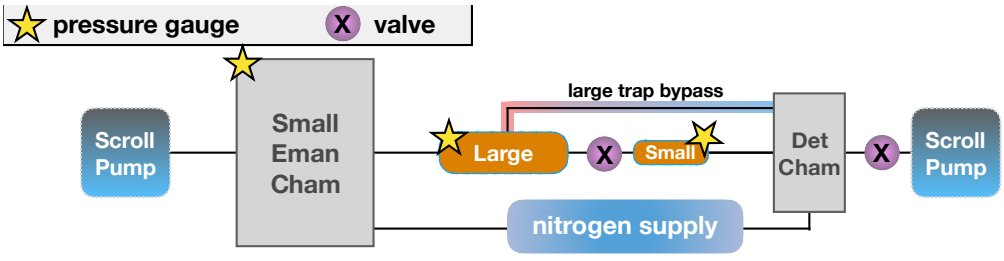

Figure 4.8: Simplified gas panel connections between the chambers and traps, showing the valves (purple ×) and pressure gauges (★).

These tests infer the radon decay rate using the ^{218}Po decays. The total ^{218}Po detection (and collection) efficiency $\varepsilon_{\mathrm{Po}} = \epsilon_{\mathcal{C}}\,\epsilon_{\mathcal{D}} \approx (18.8 \pm 0.7)\%$ which reduces the expected signal to

$$R_{\mathrm{exp}} = \varepsilon_{\mathrm{Po}} R_0 \approx 0.18 \times 20.8\mathrm{k\,cts/hr} \approx 3,740\,\mathrm{counts/hr}. \tag{4.2.38}$$

The sample was transferred to the large trap using a constant vessel pressure $P_{\mathrm{tr}} \approx 100\,\mathrm{Torr}$, to the small trap performed (as typical) at constant pressure, and finally to the detection chamber. The decay-corrected ^{218}Po alpha-decay rate from the first transfer

$$R^{\mathrm{I}}(t=0) = \left\langle R^{\mathrm{I}} f_{\mathrm{c}}(t) \right\rangle \approx 2.5\,\mathrm{k\,cts/hr}, \tag{4.2.39}$$

indicating a much lower initial sample decay rate than the expected decay rate R_{exp} of the Pylon sample. The first transfer efficiency bears the systematic uncertainty of the calibration source $\delta R_{\mathrm{py}} = 4\%$ so that

$$\varepsilon^{\mathrm{I}}_{\mathrm{tr}}|_{P=\mathrm{const.}} \equiv \frac{\left\langle R^{\mathrm{I}} f \right\rangle}{R_{\mathrm{exp}} \pm \delta R_{\mathrm{py}}} \approx (65 \pm 4)\%,$$

similar to the efficiency measured by Ray Bunker and Megan Stark in our early transfers (see **Fig. 4.7**). After the first assay, the backwards-flow method was used to transfer the sample via the large trap bypass (highlighted in red/blue in **Fig. 4.8**) directly to the large trap, using the scroll pump to evacuate the small chamber and pull the sample from the detection chamber to the large trap.

During the backwards flow, the transfer pressure of the detection chamber and the large trap was $P_{\mathrm{tr}} \approx 80\,\mathrm{Torr}$ and the S.E.C. was at lower pressure $P_{\mathrm{S.E.C.}} \approx 7\,\mathrm{Torr}$. Following the initial sample capture, the trap was heated, and the detection chamber and small trap were evacuated to $P_{\mathrm{det}} = 950\,\mathrm{mTorr}$. The sample was placed back in the detection chamber by over-pressuring the small emanation chamber and waiting for the pressure as read by the small trap to reach $P_{\mathrm{det/sm}} \approx 117\,\mathrm{Torr}$. This is similar to the method used for transfers from the small trap to the detection chamber wherein the gas panel is brought to very high pressures while the small trap and detection chamber at $P_{\mathrm{det/sm}} < 1\,\mathrm{Torr}$ and high pressure gas forces the sample from the small trap into the detection vessel. This process was repeated 2 more times to achieve three separate measures of the constant-pressure transfer efficiency.

The time-dependent pulse-height spectra for each of the four steady-pressure transfers is shown in the left panel of **Fig. 4.9** with the ^{218}Po region of interest highlighted ($\circ$), and vertical dashed lines indicating the transfers separating each assay. The right panel shows the measured ^{218}Po rates $R(t)$ (Eqn. 4.2.25) and the decay-corrected rates $R(t)\,f_{\mathrm{c}}$ (Eqn. 4.2.29). It is easy (by-eye) to determine a correct assessment of the decay rate, for each transfer with the decay-corrected rates. The measured rates and ($\varepsilon \lesssim 40\%$) transfer efficiencies of repeated constant-pressure transfers are summarized in **Table 4.2**. The calculated efficiencies of the transfers performed at constant pressure are typically $\sim 50\%$,

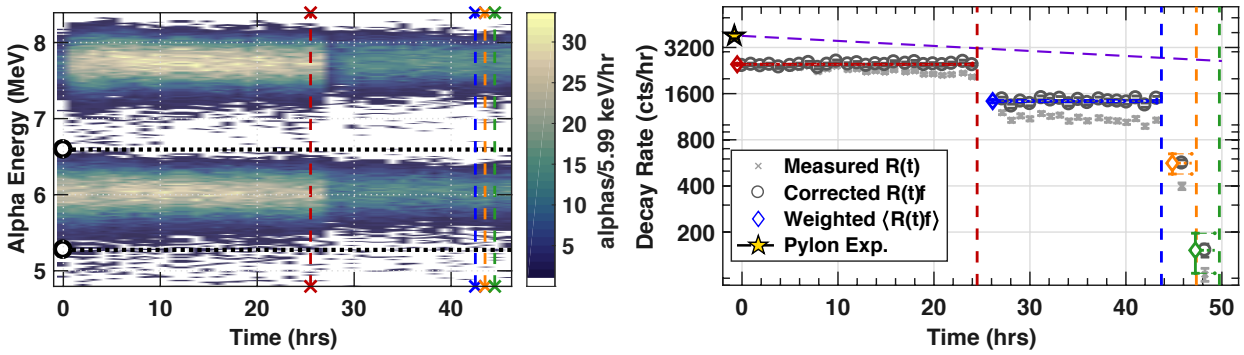

Figure 4.9: Left: Two-dimensional histogram of polonium alpha decays as a function of time due to $\sim 6\,\mathrm{Bq}$ sample of ^{222}Rn gas with the ^{218}Po region of interest shown ($\circ$ with horizontal dashed). Most empty bins are white: the $\sim$ hour-long time gaps are depicted but the surface plot is interpolated and thus the count rate appears non-zero. **Right:** (Semi-logarithmic) ^{218}Po rate as a function of time and expected rate ($R_{\mathrm{py}}(t=0), \bigstar$) with $\pm 4\%$ rate uncertainty and predicted time-dependent decay rate (purple dashed). Measured ^{218}Po rates are shown (light $\times$) with 68% C.L. statistical uncertainties. Decay-corrected rates are shown (dark $\circ$) with decay-corrected uncertainties. Weighted means for the decay-corrected rates are shown ($\Diamond$) with 95% C.L. weighted uncertainties (light dashed). Transfers shown in red, blue, orange vertical dashed lines and the Transfer times are shown as red, blue, orange, and green vertical dashed lines.

Table 4.2: ^{218}Po decay-corrected weighted means, and Pylon expectation, with constant-pressure transfer efficiencies and naive transfer efficiency uncertainties computed as the quadrature sum of the fractional uncertainties of the decay-corrected weighted means. The decrease in efficiency may be due to increased wait time, during the each subsequent transfer during the last step when the sample expands from the trap to the detection chamber.

		(cts/hr)			
Pylon	--	3810	(95% C.L.)		
		$\langle R \cdot f_{\mathrm{c}} \rangle$	$\sigma_{\langle Rf \rangle} / \langle R \cdot f_{\mathrm{c}} \rangle$ (%)	ε (%)	$\sigma_\varepsilon / \varepsilon$ (%)
I	$\varepsilon_{\mathrm{lg}}\varepsilon_{\mathrm{sm}}$	2490	0.4	65.3	--
II	$\varepsilon_{\mathrm{lg}}\varepsilon_{\mathrm{sm}}$	1430	0.7	57.5	4.6
III	$\varepsilon_{\mathrm{lg}}$	563	5.0	39.4	2.3
IV	$\varepsilon_{\mathrm{lg}}$	153	9.7	27.0	5.1

4.2.5 Variable-Pressure Transfer Efficiency

The variable pressure transfer was performed by postdoc Eric Miller and lab technician John Harrison. Following a purge of the Pylon vessel, there was a $t_{\mathrm{grow-in}} = 4.1\,\mathrm{hr}$ grow-in period with an expected sample decay rate

$$R_{\mathrm{samp}} = R_{\mathrm{py}}\ \varepsilon_{\mathrm{grow-in}} = 117.479 \times 10^3\,\mathrm{Bq}\ \left(1 - \exp(^{-4.1\,\mathrm{hr}}/_{24.5.52\,\mathrm{hr}})\right) \approx 3,580\,\mathrm{Bq}.$$

Following this a wait time $t_w \approx 17.8\,\mathrm{hr}$, expected to leave 87% of the originally placed sample in the chamber. Near the end of this wait period, the sample was reduced by evacuating and refilling ($\times 3$ flush and fill) leaving only

$$\eta_{\mathrm{red}} \quad = \quad \prod_{j=1}^{N_{\mathrm{red}}} \left(P_f/P_i\right)_j = \frac{49.5}{527} \times \frac{57.6}{523} \times \frac{49.4}{515} \approx 0.978\%. \tag{4.2.40}$$

The ^{222}Rn decay rate from the calibration source sample available to transfer from the S.E.C. following the decay and reduction is expected to be

$$\begin{aligned} R_0 &= R_{\text{samp}}\ \eta_{\text{decay}}(t_{\text{wait}})\ \eta_{\text{red}} \\ &= 3,580\text{Bq} \times 0.978\% \times 87\% \approx 3.06\,(1 \pm 0.04)\,\text{Bq} \approx 11\text{k}\,\text{decays/hr}. \end{aligned}$$

The total ^{218}Po detection (and collection) efficiency $\varepsilon_{\text{Po}} = \epsilon_{\mathcal{C}}\,\epsilon_{\mathcal{D}} \approx 0.18$ reduces the expected decay rate to

$$R_{\text{exp}} = \varepsilon_{\text{Po}} R_0 \approx 0.18 \times 11\text{k}\,\text{cts/hr} \approx 1,980\,\alpha' s\,\text{detected/hr}.$$

The sample transfer from the small emanation chamber to the large trap was performed by reducing the pressure $P_i = 80\,\text{Torr}$ to less to than $P_f = 10\,\text{Torr}$, $N_{\text{sw}} = 5\,\text{times}$, so the naively expected transfer efficiency as given by Eqn. 4.2.50 is

$$\varepsilon_{\text{tr}} \approx 1 - (P_f/P_i)^{N_{\text{sw}}} = 1 - (1/8)^5 \approx 1 - 3 \times 10^{-5} \approx 100\%. \tag{4.2.41}$$

Following the transfer to the large trap via the bypass, the large trap was evacuated with the sample to a low pressure $P = 2.14\,\text{Torr}$ and then transferred to the small trap as usual with a $\approx 20\,\text{minute}$ flow at $100\,\text{Torr}$. The sample was finally transferred to the detection vessel by bringing the small trap and detection chamber to low pressure $\mathcal{O}(1\,\text{Torr})$, over-pressuring the gas panel $\mathcal{O}(1{,}000\,\text{Torr})$, and opening the flow path from the gas panel across the small trap to the detection chamber. The weighted mean of the ^{218}Po decay-corrected rate

$$R^{\text{I}}(t=0) = \left\langle R^{\text{I}} \times f_{\text{c}} \right\rangle \approx 2.028 \pm 0.045\text{k}\,\text{cts/hr} \approx 1.028 \times R_{\text{exp}} \tag{4.2.42}$$

from the first transfer, lasting only a single hour is some 2.8% higher(!) than the decay rate of the initial Pylon sample R_{exp}, within the 4% systematic uncertainty of the calibration source. Since the transfer efficiency, and any other efficiency for that matter, can not exceed 100%, we can use the manufacturer's 4% fractional uncertainty to calculate the 95% C.L. (2σ) upper limit on the initial Pylon decay rate

$$R_{95\%} = (1 + 2\sigma)\,R_{\text{exp}} = (1 + 2{\cdot}4\%) \times 3.06\,\text{Bq} = 3.30\,\text{Bq}. \tag{4.2.43}$$

The corresponding 95% C.L. lower limit on the (forward flow) large and small trap transfer efficiency using swung pressures is

$$\varepsilon_{\text{tr}} \equiv \left(\varepsilon_{\text{sm}}\varepsilon_{\text{lg}}\right)_{\text{forw}} \equiv \frac{\left\langle R^{\text{I}} f \right\rangle}{R_{95\%}} \approx \frac{3.15}{3.30} \approx 97\% \tag{4.2.44}$$

very nearly ideal. The sample was then transferred via the bypass, using a backwards flow, to the large trap with swung pressures. The transfer pressure of the detection chamber and the large trap was $P_{\text{tr}} \approx 80\,\text{Torr}$ while the S.E.C. was being evacuated to low pressure $P_{\text{S.E.C.}} \sim 10\,\text{Torr}$. The trap was then heated and the detection chamber and small trap were evacuated to $P_{\text{det}} \approx 1\,\text{Torr}$.

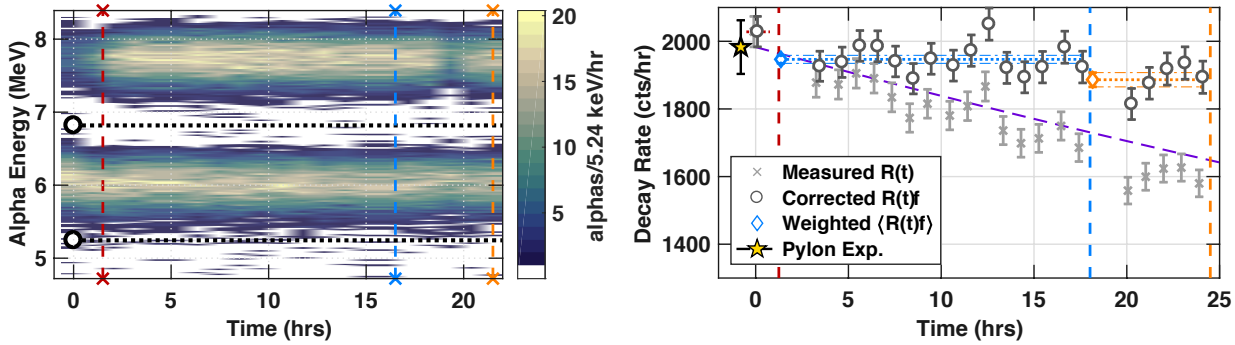

Figure 4.10: Left: Two-dimensional histogram of polonium alpha decays as a function of time from $\sim 3\,\mathrm{Bq}$ of $^{222}\mathrm{Rn}$ with the $^{218}\mathrm{Po}$ region of interest shown ($\circ$ with horizontal dashed). Most empty bins are white: the $\sim$ hour-long time gaps are depicted but the surface plot is interpolated and thus the count rate appears non-zero. **Right:** $^{218}\mathrm{Po}$ rate as a function of time and expected rate ($R_{\mathrm{py}}(t=0), \bigstar$) with $\pm 4\%$ rate uncertainty and predicted time-dependent decay rate (purple dashed). Measured rates are shown (light $\times$) with 68% C.L. statistical uncertainties. Decay-corrected rates are shown (dark $\circ$) with decay-corrected uncertainties and weighted means for the decay-corrected rates are shown ($\Diamond$) with 95% C.L. weighted uncertainties (light dashed). Transfer times are shown as red, blue, and orange vertical dashed lines.

The sample was placed back in the detection chamber by over-pressuring the panel again to get a measure of

$$\left(\varepsilon_{\mathrm{lg}}\right)_{\mathrm{back}}\left(\varepsilon_{\mathrm{sm}}\varepsilon_{\mathrm{lg}}\right)_{\mathrm{forw}}. \tag{4.2.45}$$

The mean decay-corrected $^{218}\mathrm{Po}$ rate for this second transfer was

$$\left\langle R^{\mathrm{II}}\right\rangle \approx 1,950\mathrm{cts/hr}. \tag{4.2.46}$$

The final test was performed by transferring the sample via the bypass to the large trap, and included reducing the pressure from $P_i = 40\,\mathrm{Torr}$ to less than $P_f = 10\,\mathrm{Torr}$, $N_{\mathrm{sw}} = 5\,\mathrm{times}$, for a naive efficiency $\varepsilon_{\mathrm{tr}} = 1 - (1/4)^5 \gtrsim 99.9\%$. Then by bringing the large brass-wool trap and detection chamber to very low pressure $\mathcal{O}(1\,\mathrm{Torr})$, The sample was then transferred from the large trap back through the bypass straight to the detection chamber to measure

$$\left(\varepsilon_{\mathrm{lg}}\right)_{\mathrm{back}}\left(\varepsilon_{\mathrm{lg}}\right)_{\mathrm{forw}}. \tag{4.2.47}$$

by flowing nitrogen until the large trap was 150 Torr and then sealing the detection chamber at 111 Torr. The final mean decay-corrected $^{218}\mathrm{Po}$ rate for this second transfer was

$$\left\langle R^{\mathrm{III}}\right\rangle \approx 1,870\,\mathrm{cts/hr}. \tag{4.2.48}$$

very near to the expected sample decay rate. The results of these transfer efficiency measurements are shown in **Fig. 4.10**. The left panel shows the pulse-height spectra for the three transfers as a function of time, and the $^{218}\mathrm{Po}$ regions of interest. The right panel shows the measured, decay-corrected, and weighted means of the $^{218}\mathrm{Po}$ α decays as a function of time.

The uncertainties on the weighted means are $\times 1.2$–2 smaller than the statistical uncertainties

alone. These are combined to compute the naive transfer efficiency uncertainties $\delta\varepsilon$ for each transfer. **Table 4.3** shows the calculated ^{218}Po rates, transfer efficiencies, and naive uncertainties with transfers performed (by E. Miller and J. Harrison) with swung vessel pressure. These data show that the sample transfer procedures using swung pressures

$$\varepsilon_{\text{tr}} \approx 95\%. \tag{4.2.49}$$

The constant-pressure transfer efficiency appears to be >3 more efficient than that of the variable-pressure method. These tests also served to determine that, coupled with swinging pressures, transferring the sample from the large brass wool trap directly to the detection chamber doesn't significantly lower the radon transfer efficiency. Therefore, the small trap, which concentrates the sample by $\eta_{\text{conc}} = {}^{615\,\text{cm}^2}/_{46\,\text{cm}^2} \approx 13.4$, isn't necessary to achieve $\varepsilon_{\text{tr}} \gtrsim 95\%$.

Table 4.3: ^{218}Po decay-corrected weighted means, and Pylon expectation, with variable-pressure transfer efficiencies and transfer efficiency uncertainties computed as the quadrature sum of the fractional uncertainties of the decay-corrected weighted means. Transfers performed by E. Miller and J. Harrison.

Run	Path	$\langle R \cdot f \rangle$ (cts/hr)	$\sigma_{\langle R \rangle}$ (%)	ε (%)	$\sigma_\varepsilon/\varepsilon$ (%)
Pylon	--	<2140 (95% C.L.)			
382	$\varepsilon_{\text{lg}}\varepsilon_{\text{sm}}$	2028	2.2	>94.7	4.6
383	$\varepsilon_{\text{lg}}\varepsilon_{\text{sm}}$	1946	0.6	96.0	2.3
384	ε_{lg}	1886	1.1	96.9	1.3

Pressure Swings During Radon Transfer to Large Trap In order to achieve a higher transfer efficiency to the large trap, we intermittently discontinue the input flow to the emanation vessel during a transfer and allow the emanation vessel to pump down to a much lower pressure. By restricting the flow temporarily, the pressure inside the small (large) emanation chamber decreases by a factor of $P_i/P_f \approx 4$, from 160–40 Torr (200–50 Torr), as depicted in **Fig. 4.11**. The resulting pressure decrease removes radon along with the gas in the vessel, and also serves to increase the diffusion of radon atoms still in the vessel during the pump down. As the vessel pressure goes down, the radon far from the flow ports is likely to diffuse closer to the flow path and be transferred to the brass wool traps. Once the vessel is at low pressure, the input gas flow is resumed allowing the vessel pressure to rise back up to 160 (200) Torr. We then repeat this process 2 more times. The ideal gas law implies that (with an unchanging vessel volume and temperature) the number of atoms present in the chamber is directly proportional to the pressure. So, assuming the radon equilibrates sufficiently during these N_{sw} pressure swings, the transfer efficiency

$$\begin{aligned} \epsilon_{\text{naive}} \equiv 1 - f_{\text{left}} &= 1 - (P_f/P_i)^{N_{\text{sw}}} \\ &= 1 - ({}^1\!/_4)^3 = (100 - 1.56)\% \approx 98.5\%, \end{aligned} \tag{4.2.50}$$

leaving a mere $f_{\text{left}} = 1.56\%$ of the emanated radon in the vessel–slightly higher than the measured transfer efficiencies in **Table 4.3** and **Fig. 4.10**. Using four of these quarter-pressure swings provides

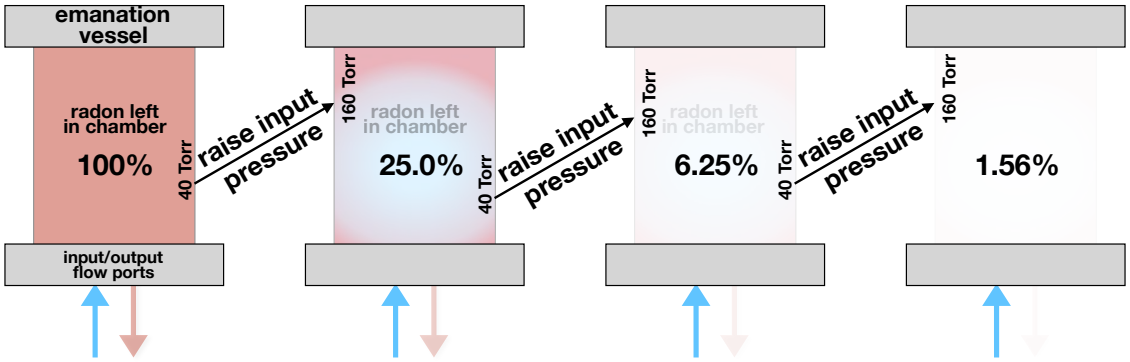

Figure 4.11: Pressure swings showing radon-222 (red patches) in a closed vessel after the vessel is evacuated to 1/4 its initial pressure P_i removing 75% of the radon. The input (blue, up) and output (red, down) flow ports are spaced close together so that presumably, radon inside the vessel farther from the ports is less likely to be transferred. So to avoid this problem, we restrict flow during a transfer at the chamber input and let the pressure in the vessel decrease by $\times 4$, and then reintroduce flow on the input port thereby bringing the pressure of the emanation vessel back to $\sim$160 Torr. The ^{222}Rn is homogenized before the reintroduction of pressure to the chamber. Each pressure swing allows $\gtrsim 75\%$ of the radon to be removed from the vessel where it will adsorb to the 77 K large (615 cm^3) brass wool trap.

a consistently higher transfer efficiency to the large brass wool trap than performing the radon transfer at constant vessel pressure. The small emanation chamber takes $t_{\text{tr}} \lesssim 1$ hr to perform 4 pressure swings, however, the large emanation chamber takes $t_{\text{tr}} \sim 5$ hrs.

Using the principle of cryogenic radon adsorption and employing pressure swings, we can reliably transfer $\gtrsim 95\%$ of radon from both large (300 L) and small (13 L) emanation vessels to cryogenic brass-wool traps. Following the radon capture onto the LN_2-cooled (77 K) large brasswool trap, the emanation vessel is left to pump down to $P_{\text{eman}} = \mathcal{O}(10\,\text{Torr})$ and the first trap $\mathcal{O}(P_{\text{I}}) = 5$ Torr where the radon is sealed and heated for transfer to the second brasswool trap. The second trap is cooled and evacuated to a pressure $P_{\text{II}} < 1/2\,\text{Torr} < P_{\text{I}}$ to initially encourage flow from the large to the small trap once flow begins. The radon in the first trap is flowed at $F \sim 5$ L/min to the secondary trap at moderate pressure $P_{\text{II}} \approx 100$ Torr. This low pressure is used to avoid condensing the nitrogen carrier onto to 77 K brasswool traps. The large trap has a volume $V_{\text{lg. trap}} = 615\,\text{cm}^3$, and so the number of large trap volumes passed during the large-small trap transfer corrected for the reduced pressure is

$$F \cdot t_{\text{purge}} \times \left(\frac{P}{P_{\text{atm}}}\right) \approx 5\,\text{L/min} \cdot 20\,\text{min} \times \underbrace{\left(\frac{100}{760}\right)}_{0.13} = 13.1\,\text{L} \approx 21\,V_{\text{lg. trap}}$$

enough to ensure all the radon gets captured on the small (46.6 cm^3) brass wool trap. Given the number of volume exchanges, the expected transfer efficiency from the large trap to the small trap

$$\epsilon_{\text{lg}} > 99\%. \tag{4.2.51}$$

is very nearly ideal.

Following the 20 min transfer from the large trap, the small trap is evacuated to a pressure $P_{\text{sm.}} \lesssim$

0.5 Torr in preparation of the final transfer of the sample radon to the detector volume. We transfer the sample to the detection chamber, along with 100 Torr of low radon-activity LN_2 boil-off, which has a negligible radon decay rate [165, 182]

$$R_{\text{gas}} = C_{\text{gas}} \cdot V_{\text{cham}} \times \left(\frac{P}{P_{\text{atm}}} \right) \approx 500 \ \mu\text{Bq/m}^3 \cdot 1.7 \text{ L} \times 0.13 = 0.11 \ \mu\text{Bq},$$

$\times 2,000$ below the sensitivity of the detector, of order $\sim$0.2 mBq. We don't use the carbon trap when transferring the warmed radon gas in the small trap to the detection chamber because this radon is negligible, at the detection chamber pressure. After over-pressuring the gas panel to 1,000 Torr, we open the valves across the low-pressure small trap and to the gas input of the detection chamber. This procedure helps to ensure that very little back-flow of sample radon occurs. The volume of the small trap and pressure gauge, and the piping connected to the detection chamber

$$(V_{\text{sm}} + V_{\text{gauge}}) + V_{\text{pipe}} \approx (46.6 + 1.9)\,\text{cm}^3 = 48.5\,\text{cm}^3, \tag{4.2.52}$$

some 28.5 times smaller than the $V_{\text{cham}} \approx 1.7$ L detection vessel. If the radon equilibrates and is evenly spread throughout the trap, piping, pressure gauge and vessel volume we expect

$$\epsilon_{\text{sm}} = \frac{V_{\text{cham}}}{V_{\text{cham}} + V_{\text{sm}} + V_{\text{gauge}} + V_{\text{pipe}}} = \frac{1.7}{1.7 + 0.0485} \approx 97.2\% \tag{4.2.53}$$

of the sample radon to remain in the chamber. In practice, using the across-trap pressure gradient from the over-pressured gas panel (and low pressure detection chamber) ensures the radon will be transferred very quickly to the detection chamber. Eqn. 4.2.53 is a fairly pessimistic lower limit to the expected small-trap-to-detection chamber transfer efficiency. The product of the naive transfer efficiency expected from the pressure swings (Eqn. 4.2.50), the large-trap transfer efficiency (Eqn. 4.2.51), and the small-trap transfer efficiency

$$\epsilon_{\text{naive}} \times \epsilon_{\text{lg}} \times \epsilon_{\text{sm}} = 98.5\% \times 99\% \times 97.2\% = 94.8\% \tag{4.2.54}$$

is consistent with the measured transfer efficiencies $\varepsilon_{\text{tr}} \approx 95\%$ (**Section 4.2.5**, **Table 4.3**) we demonstrated with the improved pressure swing method.

4.3 Detecting Radon Daughters

After radon is placed in the detection vessel along with 100 Torr of LN_2 boil-off, radon will radioactively decay producing positively charged polonium ions which can be electrostatically collected and identified based on their subsequent α decay energies. Understanding the collection of the polonium ions and their detection efficiency, as well as the detector backgrounds, is critical to make a radon measurement.

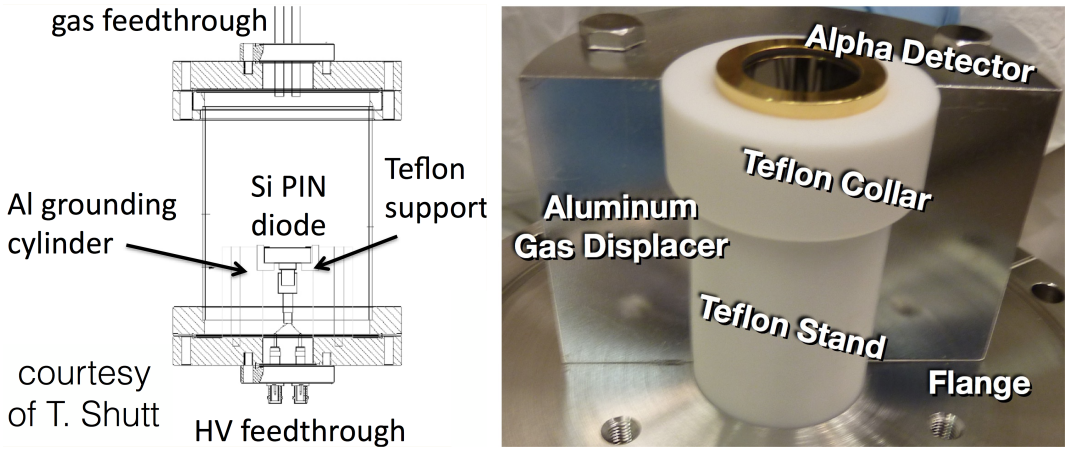

Figure 4.12: Left: Cross section of the radon detection vessel shown with gas feedthrough (top), HV feedthrough (bottom), aluminum gas displacers ('grounding cylinder') shaped like half moons, silicon pin diode detector, and teflon support. Schematic provided by Tom Shutt. **Right:** Inside of the radon detection vessel with HV feedthrough flange disconnected from the chamber body, one aluminum gas displacer attached to the flange, silicon detector sitting in the teflon collar on top of a 3.5" teflon stand. This teflon prevents arcing from the signal lines to the grounded aluminum gas displacers, as described in **Section 4.3.3**.

4.3.1 Radon Detection Vessel and Electronics

A custom-made 1.7 L detection vessel, cross-section shown left in **Fig. 4.12**, was manufactured by Kurt J. Lesker based on a design from collaborators at Case Western Reserve University [311] based on SuperK and Borexino radon counters [144, 180]. Electropolishing metal components reduces radon emanation [137, 272--275] and outgassing [276, 277] and thus the detection vessel is made of electropolished stainless steel to reduce U/Th emanation. Inside the detection vessel is a commercially available ORTEC 300-AS [312] silicon pin diode detector shown in the right panel of **Fig. 4.12**. The detector sits on top of a (white) cylinder teflon collar. The figure shows one electropolished aluminum gas-displacer stand attached to the high-voltage feedthrough flange. This HV feedthrough provides the voltage from the filter box, to set the bias voltage to operate the diode; it also places the detector at $\mathcal{O}$(kV) potential offset needed to collect the positively charged polonium ions. The teflon collar sits on a 3" tall teflon stand and centers the detector in the vessel fitting snugly in the aluminum gas displacers. Electrical insulation from the teflon protects the diode from arcing to the grounded aluminum gas displacers. As described in **Section 4.3.3**, Torr seal epoxy prevents arcing from the small feedthrough electrodes to the grounded feedthrough itself, and a 0.5-cm-thick, hollow teflon cylinder insulates the high voltage signal wires from the aluminum stands and chamber.

We use an analog BERTAN 380N high voltage supply, shown in the left panel of **Fig. 4.13**, to apply $\mathcal{O}$(kV) negative electric potential offset to the detector. The circuit diagram for the filter box-detector-preamp circuit is shown in the right panel of **Fig. 4.13**. The filter box (labeled 'bias box') has carefully chosen resistors and capacitors which form a voltage divider ($R1$, $R2$, $R3$) that sets the detector (labeled C_d) to a moderate 50 V bias. The filter box also serves to set the detector

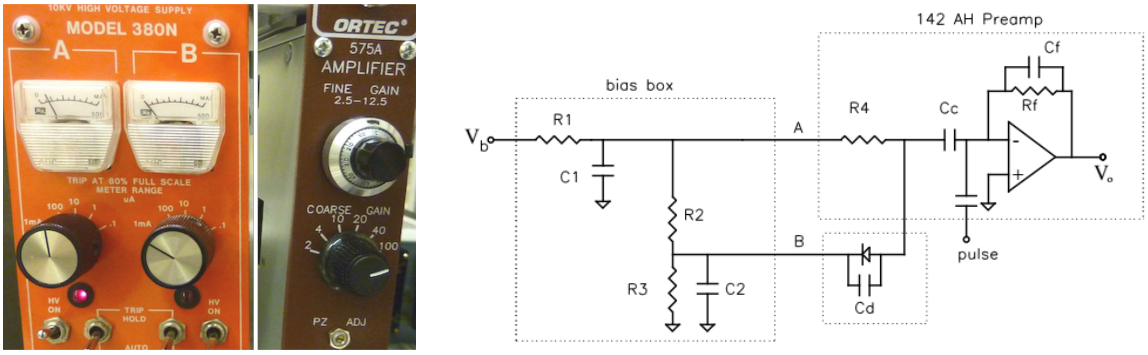

Figure 4.13: Left: Analog BERTAN 380N high voltage supply and ORTEC 575A amplifier. **Right:** Circuit diagram of filter box ('bias box'), ORTEC 300-AS silicon pin diode alpha detector, and ORTEC preamplifier (142 AH Preamp). The voltage divider allows the $C_d = 300\,\text{nFarad}$ detector to be placed at -2 kV relative to the vessel, while the bias across the diode is set to 50 V. The preamplifier is very sensitive to microphonic vibrations and is therefore placed on a cushy foam pad, directly underneath the detection chamber. Output of the preamp ('pulse') is sent to the ORTEC amp and subsequently to the MCA emulator where pulse height spectra are readout and intermittently saved.

at (negative) high voltage offset by

$$V_{\text{offset}} = -2\,\text{kV} \equiv I \times (R_1 + R_2 + R_3) \tag{4.3.1}$$

from the grounded vacuum feedthrough, aluminum stands, and chamber walls to electrostatically collect charged radon daughters. The resistors are chosen so that the voltage across the detector

$$V_{\text{bias}} \equiv V_a - V_b = 50\,\text{V}. \tag{4.3.2}$$

Using Ohm's law and a little algebra yields

$$\begin{aligned} V_{\text{bias}} &= (V_{\text{offset}} - I\,R_1) - (V_{\text{offset}} - I\,R_1 - I\,R_2) \\ &= V_{\text{offset}} \left(\frac{R_2}{R_1 + R_2 + R_3} \right). \end{aligned} \tag{4.3.3}$$

The values of the resistors are determined by requiring a sufficiently low current $I \lesssim 5\,\mu\text{A}$ so that

$$R_1 + R_2 + R_3 \gtrsim \frac{V_{\text{offset}}}{I} \approx \frac{2\,\text{kV}}{5\mu\text{A}} = 500\,\text{G}\Omega. \tag{4.3.4}$$

The values of the capacitors C_1 and C_2 need to be chosen so the pulses are not filtered to prevent significant reverse-biasing of the detector as the voltage decreases to $V_{\text{offset}} = 0\text{V}$. Undergraduates Woodlin Smith and Brandon DeVries used a Simulation Program with Integrated Circuit Emphasis (SPICE) program [313] to determine the order of the second capacitor $C_2 \sim 1\,\text{nF}$ to prevent the diode from being destroyed[4].

The output of the detector is sent along custom-made 6" SHV cables (which add minimum impedance to the detection circuit) to the filter box connecting to an ORTEC 142B preamplifier [314, 315] which smooths the incoming charge traces. An ORTEC 575A amplifier [316, 317] applies

[4]The internal notes were not posted to the group wiki page.

×10 gain factor to the analog pulses from the preamp so the pulse height can be determined by an ORTEC multi-channel analyzer (MCA) emulator running MAESTRO software Version 6.08 [318, 319]. Pulse height spectra are saved automatically at regular intervals (typically 1 hr time bins) with a computer for offline analysis.

4.3.2 Radon Daughter Collection and Detection

The radioactive decay of radon produces a $\mathcal{O}(5\,\mathrm{MeV})$ alpha particle leaving behind a recoiling polonium nucleus. Radioactive decay satisfies both conservation of momentum and energy. For simplicity let us assume that the radon atoms in the vessel are at thermal energies near $1\,\mathrm{eV} \ll \mathcal{O}(5\,\mathrm{MeV})$ α decay energies so the initial momentum of the radon atom is 0 before decay, and so the momenta of the alpha and polonium cancel:

$$m_\alpha \cdot \vec{v}_\alpha = -m_{\mathrm{Po}} \cdot \vec{v}_{\mathrm{Po}}. \tag{4.3.5}$$

The alpha and daughter move in opposite directions, with the ion traveling at $v_{\mathrm{Po}} = {}^{m_\alpha}\!/_{m_{\mathrm{Po}}} \cdot v_\alpha$, and the alpha moving at $v_\alpha = {}^{m_{\mathrm{Po}}}\!/_{m_\alpha} \cdot v_{\mathrm{Po}}$. The rest mass of radon $m_{\mathrm{Rn}} = 222.018\,\mathrm{amu}$ [320], the alpha $m_\alpha = 4.003\,\mathrm{amu}$ [321], and the polonium ion $m_{\mathrm{Po}} = 218.009\,\mathrm{amu}$ [322]. Given that $1\,\mathrm{amu}\,c^2 = 931.49\,\mathrm{MeV}$, the combined rest energy of the decay progeny Po and the alpha

$$(m_{\mathrm{Po}} + m_\alpha)\,c^2 = (218.009 + 4.003)\,\mathrm{amu}\,c^2 = 222.012\,\mathrm{amu}\,c^2. \tag{4.3.6}$$

The difference between the rest energy and that of the radon atom is the kinetic energy shared by the daughters:

$$\Delta_{\mathrm{decay}} = (222.018 - 222.012)\,\mathrm{amu}\,c^2 = 0.006\,\mathrm{amu} \times 931.49\mathrm{MeV/amu} = 5.58\,\mathrm{MeV}.$$

The total energy given to the polonium and alpha can be derived from the excess decay energy and the energy of the alpha itself $E_\alpha = 6.0\,\mathrm{MeV}$. However, a simpler comparison can be made by considering the fraction of total kinetic energy imparted to the polonium

$$\begin{aligned} \frac{E_{\mathrm{Po}}}{E_{\mathrm{Po}} + E_\alpha} &= \frac{E_{\mathrm{Po}}}{E_{\mathrm{Po}} + {}^1\!/_2\, m_\alpha \left({}^{m_{\mathrm{Po}}}\!/_{m_\alpha} \cdot v_{\mathrm{Po}}\right)^2} \\ &= \frac{E_{\mathrm{Po}}}{E_{\mathrm{Po}} + E_{\mathrm{Po}} \cdot {}^{m_{\mathrm{Po}}}\!/_{m_\alpha}} = \frac{1}{1 + {}^{m_{\mathrm{Po}}}\!/_{m_\alpha}} \\ &= \frac{1}{1 + {}^{218.009}\!/_{4.003}} = {}^1\!/_{55.46} = 1.80\%. \end{aligned} \tag{4.3.7}$$

The kinetic energy of a singly-charged polonium ion $E_{^{218}\mathrm{Po}} = 1.8\% \times 6.0\,\mathrm{MeV} \approx 108\,\mathrm{keV}$, much greater than the potential energy from the electric 2 kV potential. The calculation can be carried out for radium decays, using the radium decay energy $E_{\mathrm{Ra}} = 4.87\,\mathrm{MeV}$, so that the nuclear recoil

energy of a radon atom

$$E_{\mathrm{Rn}} = E_{\mathrm{Ra}} \frac{1}{1 + {}^{222}/_{4}} = 0.0177 \times 4.87\,\mathrm{MeV} = 86.1\,\mathrm{keV}. \tag{4.3.8}$$

The relativistic expression for kinetic energy is

$$T = (\gamma - 1) m_{\mathrm{rest}} c^2, \qquad \text{where} \qquad \gamma^2 = \frac{1}{1 - \beta^2} \tag{4.3.9}$$

where the Lorentz factor γ depends on the velocity fraction of light speed $\beta = {}^{v}/_{c}$. Then,

$$T = (\gamma - 1) m_{\mathrm{rest}}\, c^2 = (\gamma - 1) 218\,\mathrm{amu} \times 931 \frac{\mathrm{MeV}}{\mathrm{amu}\, c^2} c^2 \approx (\gamma - 1)\, 203\,\mathrm{GeV}. \tag{4.3.10}$$

Then polonium atom is given only 100 keV, so the Lorentz factor γ is exceedingly small:

$$\gamma - 1 = \frac{100\,\mathrm{keV}}{203\,\mathrm{GeV}} \approx 0.5 \cdot 10^{-6}, \tag{4.3.11}$$

and the Newtonian expression for kinetic energy is accurate to better than 0.1%. Since the nuclear recoil imparts non-relativistic speed to the polonium atom, it is traveling at

$$v_{\mathrm{Po}} = \sqrt{\frac{2 \cdot E_{\mathrm{NR}}}{m}} \approx \sqrt{\frac{2 \cdot 100\,\mathrm{keV}}{203\,\mathrm{GeV}/c^2}} \approx \sqrt{10^{-6}\, c^2} = 10^{-3} c. \tag{4.3.12}$$

After the radon atoms have been transferred to the detection vessel, the radon alpha decay in the nitrogen carrier gas produces the short lived ($t_{1/2} \approx 3\,\mathrm{min}$) polonium-218. As described in **??**, the recoil distance of heavy atoms depends on the ambient gas pressure, and at very low detection chamber pressures $\mathcal{O}$(mTorr), radon decays imbue Po-218 ions so much energy that they cannot thermalize in the gas. The recoiling atoms will typically travel from across the entire $\sim 15\,\mathrm{cm}$ distance of the vessel becoming embedded in the chamber walls, never to be detected. To overcome the inefficiency associated from losing these embedded radon atoms, the detection vessel pressure $P_{\mathrm{det}} = 100\,\mathrm{Torr}$. At this pressure, collisions with gas molecules in the detection chamber slow the Po-21x ions after the initial $\sim 100\,\mathrm{keV}$ kick from the α decay [170, 283].

The ^{218}Po positively charged ~88% of the time [143, 144, 323, 324]. Charged polonium production and neutralization in noble gases has been measured [143, 144, 325, 326], and simulated for xenon experiments [297, 327, 328], and discussed in *e.g.* [142, 329]. Positively charged ions in the chamber are attracted to the detector surface held at a potential

$$V_{\mathrm{offset}} = -2\,\mathrm{kV} \tag{4.3.13}$$

with respect to the grounded detection vessel. Besides the small cut separating the half-moon shaped gas displacement stands, the detection chamber is cylindrically symmetric. The collection efficiency of polonium ions generally increases as the inactive gas fraction goes down. An improved vessel design would have an electric field geometry with a magnitude large enough to ensure all

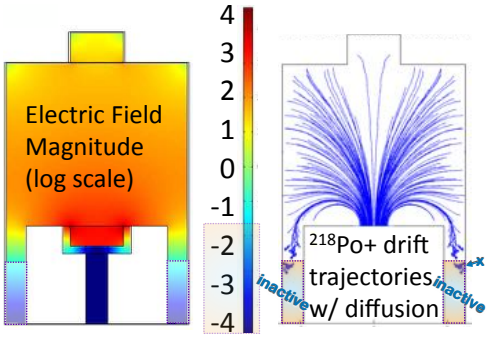

Figure 4.14: Cross-section of the radon emanation system detection chamber depicting the results of a COMSOL simulation performed by D. Seymour [327, 328]. Figure adapted from [327]. **Left:** Colormap of the (logarithmic) magnitude of the electric field inside the detection vessel with the detector held at -1 kV and the walls and detector stand grounded. **Right:** ^{218}Po ion trajectories (blue lines) through low pressure gas under the influence an electric field, including ion diffusion. The lowest set of blue dots (labelled 'inactive' ×) indicate that the polonium ions this far from the detector experience such a low electric field that they diffuse until they radioactively decay.

decays occur long after the ions are collected. In practice, gas displacers that span the diameter of the vessel itself would help achieve that goal. Regions in the detection chamber *e.g.* below the horizontal plane of the upward facing aluminum gas displacers and very near the corners have very-low electric fields; the charged ions in these places are not effectively attracted to the detector. Low-energy ^{218}Po ions thermalize and diffuse until they decay or stick to a surface. **Fig. 4.14** shows a cross-section of the detection chamber with the results of a COMSOL [330] multi-physics simulation [327, 328]; the left panel shows a two-dimensional colormap of the logarithm of the magnitude of the electric field in the detection chamber. Even in the upper corners of the chamber, the field strength is approximately 3–4 orders of magnitude smaller than the strength near the detector. As the polonium ions move under the influence of the electric field, they also diffuse in the low pressure gas, as shown in the right panel of **Fig. 4.14**; the diffusion of polonium ions under the influence of kV potentials at low nitrogen pressure is described in Refs. [297, 328].

By preparing and transferring a known quantity of radon (as described in **Section 4.2.2**) from the large and small emanation chambers with the help of R. Bunker, M. Stark calculated the ^{21x}Po collection efficiency $\epsilon_{\mathcal{C}}$ for electric potential offsets in the range $V_{\text{offset}} = (0\text{–}3)\,\text{kV}$ and pressures $P = 10\text{–}760\,\text{Torr}$. The left panel of **Fig. 4.15** shows that the collection efficiency of polonium ions

$$\epsilon_{\mathcal{C}} \approx 50\% \tag{4.3.14}$$

for this detection vessel and does not appear to change significantly near the nominal offset $V_{\text{offset}} = -2\,\text{kV}$ and chamber pressure $P = 100\,\text{Torr}$. Therefore the R.E.S. detector is expected to produce consistent results with inconsistent detection conditions. Along with ^{218}Po, the positively charged ^{214}Po ions can also be collected. Measurements longer than several hours typically indicate that alpha rates measured $R_{214} > R_{218}$. This small discrepancy in the rates depends on the amount of electronegative content of the outgassed molecules (*e.g.* water vapor, carbon dioxide, or hydrocarbons) which neutralize the ^{21x}Po in the gas sample before they can be electrostatically collected [142--145].

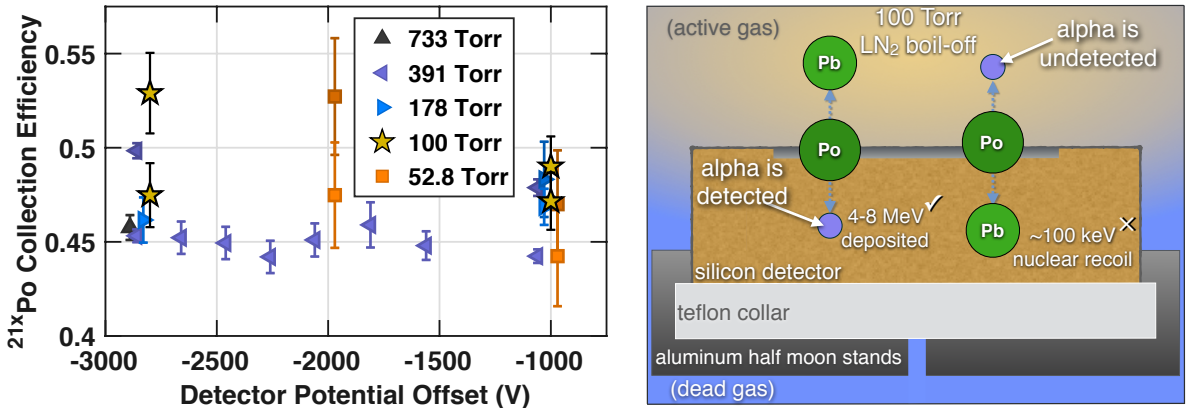

Figure 4.15: Left: ^{218}Po (^{214}Po) ion collection efficiency with statistical uncertainties shown light (dark) as a function of voltage offset of the detector and detection chamber pressure–symbols indicate pressure range from $P_{\text{cham}} = (11\text{–}730)$ Torr. Megan Stark and Ray Bunker carried out the measurement, data collection, and analysis. The collection efficiency $\epsilon_{\mathcal{C}} \approx 50\%$ does not vary strongly with the vessel pressure or the detector voltage near the nominal operating pressure (★). **Right:** Cross section of silicon PIN diode detector (yellow), placed inside a teflon collar (white) separating the detector at HV from the grounded aluminum gas displacer (dark). (In)active gas regions in (blue) yellow consist of $P_{\text{cham}} \approx 100$ Torr of boil-off gas from a LN_2 dewar. This gas sufficiently slows $E_{\text{NR}} \sim 100$ keV recoiling polonium ions from radioactive decays. Electrostatic collection of positively charged polonium ions (dark green) diffusing in the gas is then possible. Following ion collection, the geometric efficiency for detecting ($E = 4\text{–}8$ MeV) α's (purple) from subsequent radioactive decay $\epsilon_{\mathcal{D}} \approx 50\%$. If the lead atom (light green) is aimed into the detector, the $\mathcal{O}(100\,\text{keV})$ nuclear recoil energy won't be identified as an alpha decay.

This is not expected to be an issue in our detector since we use very pure LN_2 boil-off and the trace water content condenses on the surface of the 77 K brass wool traps during the transfer.

Once the polonium ions are collected on surface of the pin diode,approximately 50% of α decays are directed into the detector and are subsequently counted, as shown schematically in the right panel of **Fig. 4.15**. The (geometric) detection efficiency for each of the fast alpha-emitting daughters (Po-218 and Po-214) is very close to

$$\epsilon_{\mathcal{D}} \approx 50\%. \tag{4.3.15}$$

These (well-aimed) alpha decays produce voltage proportional to the energy deposited in the detector. The small current travels through the filter box, to a preamp, shaping amplifier, and finally to a multi-channel analyzer (MCA) where the pulse height spectra can be histogrammed as a function of time. Events with characteristic polonium α decay energies E_α =6.0 MeV for Po-218, and 7.8 MeV for Po-214 (shown in **Fig. 4.1**), indicate the presence of ^{222}Rn

4.3.3 Improving the Detection Sensitivity

In an effort to improve the sensitivity limit of the radon detector, we made hardware upgrades and developed software and procedural improvements. The section describes physics and measurements related to electronics improvements to reduce detector noise and arcing.

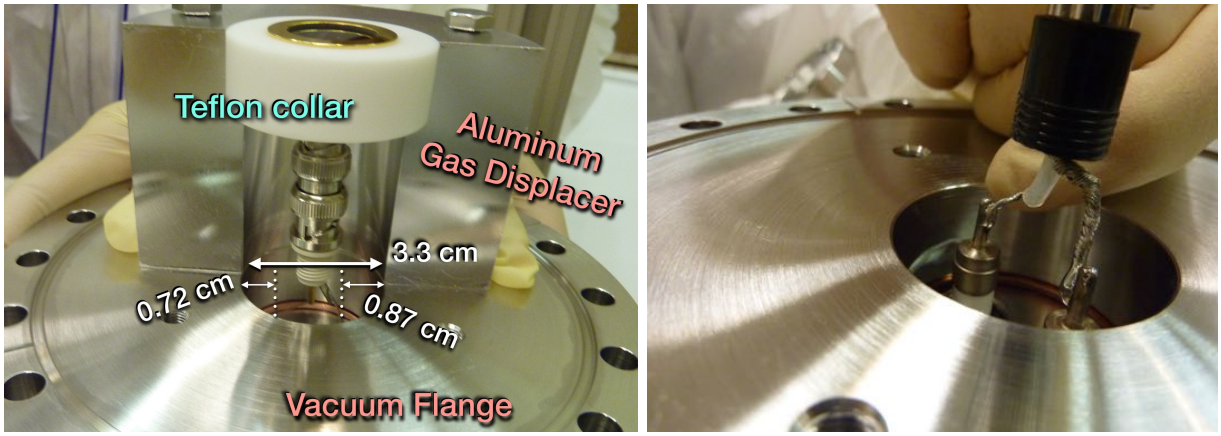

Figure 4.16: High-voltage signal feedthrough flange and inner-detection volume assembly. **Left:** Silicon pin-diode α detector inside teflon collar, with the signal feedthrough flange (hidden) bolted to the vacuum flange, surrounded by one (of the two) half-moon-shaped aluminum gas-displacement stands. The dimensions within the vessel separating the grounded components from the high voltage feedthrough electrodes are of order 1 cm. **Right:** Close-up on the signal feedthrough and vacuum flange, with no detector attached. The distance between the high-voltage electrode and the displacer stand is about a finger's width.

Preventing High-Voltage Breakdown

The aluminum gas displacer surrounding the detector increases the detector's $^{218/4}$Po ion collection efficiency by eliminating inactive ('dead') locations in the vessel. The inner detection vessel dimensions are shown in the left panel of **Fig. 4.16** with a few approximate dimensions from the displacer size. The early feedthrough assembly is shown in the right panel where two high-voltage signal wires are held at 1,950 V and 2,000 V, to bias the detector at 50 V.

Gas discharge occurs when electrical current flows between electrodes at a significant voltage difference. When subjected to very large electric fields, electrons in matter are separated from their ions and *e.g.* gases become conductive, and electrical breakdown can occur. Ionization by collision, photo-ionization–ion formation from the interaction of a photon with an atom or a molecule–and so-called secondary ionization processes all contribute to the flow of current between electrodes in matter [331, 332]. Intuitively, the phenomenon of breakdown can be understood by first considering a neutral gas within a large electric field. The density of ambient gas atoms, and therefore electrons, at low pressures eventually fails to contribute any electrons to the current breakdown, whereas at very high pressures, atoms prevent the flow of current between electrodes at large potential differences [331--335]. F. Paschen published a paper in 1889, describing the results of studies on the breakdown voltage of parallel plates in a gas as a function of pressure and gap distance. The electrical breakdown of gases is described by a non-linear relationship between the product of pressure and gap length $P{\cdot}\ell$ and the voltage applied V [333] with a large effect at moderate values of $P{\cdot}\ell$ where there are enough electrons to form a current between electrodes at low voltage separation, and the gas density is low enough to allow current to flow.

The Townsend mechanism of avalanching is a model of the exponential current growth at

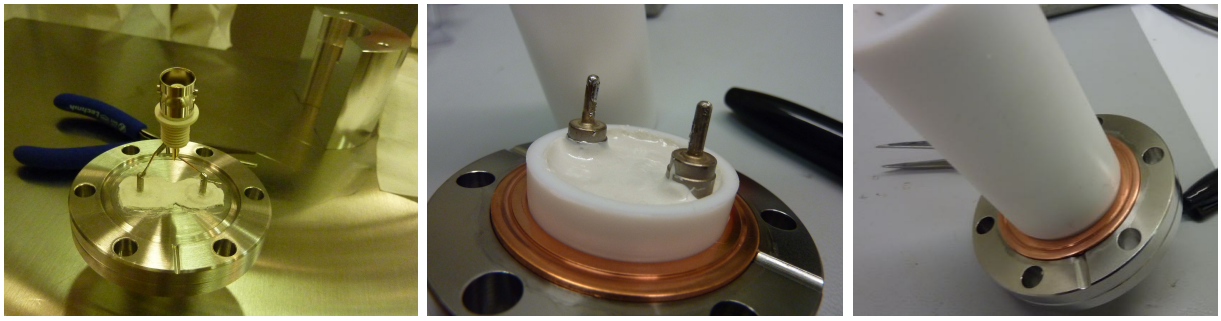

Figure 4.17: Left: First attempted configuration of epoxy potting for the high-voltage feedthrough. This configuration failed to provide sufficient insulation between the high voltage of the electrodes coming from the signal feedthrough. **Middle:** Second configuration of epoxy potting formed by mixing two-part epoxy paste and evacuating the paste during the curing process. This configuration reduced the arcing somewhat at pressures above 1 Torr. **Right:** Tubular teflon stand, lathed to fit snugly inside the copper gasket of the high-voltage feedthrough and aluminum gas displacers. This teflon, along with the second configuration of epoxy significantly reduced arcing at pressures $P \approx 2$–25 Torr from the 2 kV signal wires to the grounded half-moon stands and feedthrough.

pressures corresponding to $P{\cdot}\ell$ values of 1000 Torr cm and below [331, 332, 334, 336]. Under the theory given by F. Paschen in *e.g.* Refs. [332--334], the breakdown voltage in gases as a function of pressure P and electrode gap length ℓ is given by

$$V_{\text{breakdown}}(P\ell) = \frac{B \cdot P\ell}{C + \ln(P\ell)} \qquad \text{where} \qquad C = \ln\left(\frac{A}{\ln(1+\gamma^{-1})}\right). \tag{4.3.16}$$

For air, the empirically determined constants are approximately

$$A = 15\,\text{cm}^{-1}\,\text{Torr}^{-1}, \quad B = 365\,\text{V}\,\text{cm}^{-1}\,\text{Torr}^{-1}, \quad \text{and} \quad \gamma \approx 0.01, \tag{4.3.17}$$

so that $C \approx 1.18$ [337, 338]. Townsend's secondary ionization coefficient γ is the number of secondary electrons produced per incident particle (such as a photon, ion, etc.) and is of order 10^{-3}–10^{-2} for nitrogen and even lower for electronegative gases such as oxygen and CO_2 [331]. The Townsend coefficient is generally poorly known [334]. There is a 'non-Paschen' region at $P{\cdot}\,\ell$ above the theoretically proposed maximum, characterized by a lower breakdown voltage and a large standard deviation between measurements [339].

Borexino's work on a high-voltage alpha counter [144] showed reduced a ^{21x}Po ion collection efficiency at voltages below 3 kV. As a result, the intended R.E.S. alpha detection vessel was planned to be operated with the detector held at a voltage offset $V_{\text{offset}} = 4$ kV, at a pressure $P \approx (1$–$10)$ Torr. Early alpha spectroscopy measurements taken at electric potentials $\mathcal{O}(3\,\text{kV})$ showed indications of arcing to the high voltage feedthrough lines coming from the signal feedthrough flange, to the half-moon shaped aluminum gas displacers within the detection chamber. The geometry, including estimates of length within the vessel are shown in the left panel of **Fig. 4.16** which shows that the likely gap lengths ℓ are close to 1.0 cm. To quantify the improvement of the breakdown voltage for each attempted fix, I compared the breakdown Paschen theory for a gap length chosen by the dimensions inside the chamber.

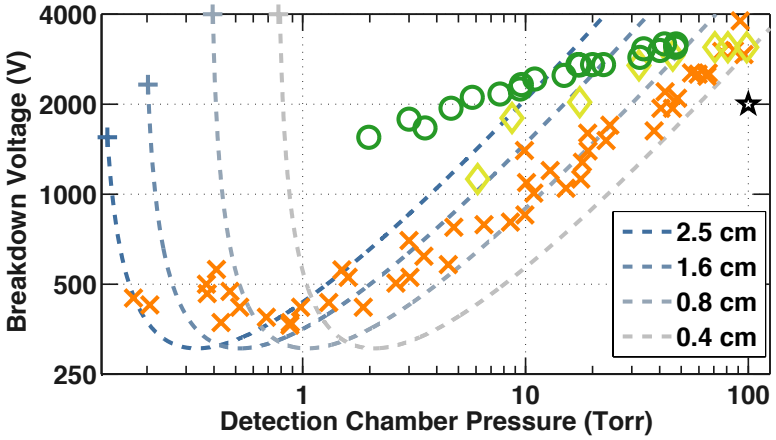

Figure 4.18: Measurements of breakdown voltage as a function of detection chamber pressure P for several insulation configurations. The theoretical expectations (Eqn. 4.3.16) are shown (dashed) for likely arcing gap lengths in air ($0.4 < \ell_{\text{air}}/\text{cm} < 2.5$). Data taken with the lathed teflon stand and collar are shown in two configurations. The teflon and first epoxied feedthrough (yellow ◊), and with kapton (orange ×) both fail to provide sufficient insulation between the aluminum gas-displacers and the signal electrodes. Data taken with the teflon stand and the second epoxied feedthrough are shown (green ○) to be sufficiently insulating down to pressures $P \approx 2\,\text{Torr}$. The nominal chamber pressure $P = 100\,\text{Torr}$ and detector voltage offset $V = 2\,\text{kV}$ are shown (★).

I used the HV supply to bias the feedthrough flange and detector, and to infer arcing of the different insulating configurations by a flickering current. The operating current of the detector is nominally 3 μA, so the HV supply current was limited to 10 μA, three times the nominal, to prevent potentially damaging the diode. I monitored the voltage on the BERTAN high voltage supply, noting the voltage when a trip occurred. Initially, I attempted to reduce arcing in the detection chamber with electrically-insulating Kapton tape in the vessel. Kapton is a registered trademark of the DuPont corporation. Kapton is a so-called polyimide foil, with a high dielectric constant $\mathcal{O}(30\,\text{kV/cm})$ [340] and is commonly used in particle physics experiments and industry to provide very good electric insulation. Even so, Kapton tape (some 5-50 mil thick) wrapped around the signal electrodes in varied geometries did not provide enough insulation (shown as × in **Fig. 4.18**) to prevent arcing at the relevant voltages.

Epoxy is often used as an insulator for high voltage applications to stop electrical breakdown that could occur inside the detection chamber. We applied a two-part epoxy to the feedthrough flange to prevent the electrodes from arcing to the surface of the feedthrough. We first potted the high-voltage feedthrough with a small amount of epoxy, shown in the left panel of **Fig. 4.17**; this failed to alter the arcing behavior. Following the first attempt to stop the arcing in the detection vessel, we applied epoxy to another flange. The second attempt to cure the epoxy was done with considerably more epoxy. During the potting of the second feedthrough flange, we mixed the paste, which hardens quickly, to decrease the potential instances of bubbles. This epoxy improved the arcing as shown (◊) in **Fig. 4.18**.

The dielectric constant of PTFE (teflon is manufactured by DuPont) is measured to prevent arcing for electric fields <11.8 kV/mm [341]. Ray Bunker and I lathed a cylindrical teflon sample

into a tall hollow cylinder of thickness $H \gtrsim 0.4\,\text{cm}$, shown in the right panel of **Fig. 4.17**. The outer diameter was chosen to sit inside the aluminum gas displacement stands, and shield the bare signal cables (a mere 50 V apart) from the 2,000 V potential difference to the grounded displacement stands. The teflon cylinder is placed on the feedthrough flange, inside the copper gasket, sitting under the teflon collar upon which the detector rests. Measurements of arcing in the detection chamber with the second epoxy configuration and the teflon (shown as ∘ in **Fig. 4.18**) indicate the insulation at pressures $P > 4\,\text{Torr}$ is sufficient for the potential offsets $V_{\text{offset}} \lesssim 2,000\,\text{V}$.

Fig. 4.18 shows the results of many (P, V) measurements I took using kapton tape, two potted-feedthrough configurations, and teflon. The predicted breakdown voltages from Paschen's model (from Eqn. 4.3.16) are shown for gaps of length $\ell = (0.4\text{–}2.5)\,\text{cm}$; theory curves are undefined below pressures $P \approx (0.1\text{–}1.0)\,\text{Torr}$, shown (+). Breakdown measurements taken in all the configurations, at chamber pressures $P < 100\,\text{Torr}$, are consistent with gap lengths $\ell \sim 1\,\text{cm}$ arcing inside the detector volume geometry (dashed curves in **Fig. 4.17**). We were not able to use Kapton to effectively prevent arcing in the detection volume. However, by applying epoxy and a custom-made teflon stand and collar, we are able to prevent arcing in the chamber for pressures 10× lower than we ultimately chose to use.

Reducing Spectrum Noise with a Common Ground

Early measurements of LN_2 boil-off and lab air indicated the presence of noise events extending to the energies corresponding to the polonium alpha decay regions of interest. **Fig. 4.19** shows the pulse height spectra (gray histogram in the top right panel) for a 0.87 day lab-air measurement containing a large number of events near the $^{218/4}$Po alpha decays between 6–8 MeV increasing exponentially with decreasing energy. The spectrum shown has alphas from ^{214}Po decays ($E_\alpha = 7.69\,\text{MeV}$) around channel 1,000 with a channel-to-energy conversion factor roughly 8 keV/channel. These noise events even extend up to the maximum channel ($\sim 2,000$) of the multi-channel analyzer with ×2 the energy of ^{214}Po. As a result, the detector's sensitivity to very-low levels of radon was greatly reduced. Suspecting ground loops in the system, Ray Bunker and I added grounding lines connecting the isolation transformer (white box), to the high-voltage supply, preamplifier, amplifier, and filter box, shown in left panel of **Fig. 4.19**. This technique reduced the steady ∼33 mV peak-to-peak noise to $\leq 5\,\text{meV}$, reducing the noise events in the ^{21x}Po α decay R.O.I. by ∼×50.

4.4 Detector Backgrounds

Now that we have demonstrated radon may be transferred and measured successfully in the detection volume, it is useful to describe the detector backgrounds. Preventing dust contamination in the emanation chambers and on the sample has already been discussed in **Section 4.1.1**. The impacts of emanation chamber leaks and the outgassing of lab-air radon diffused from samples after

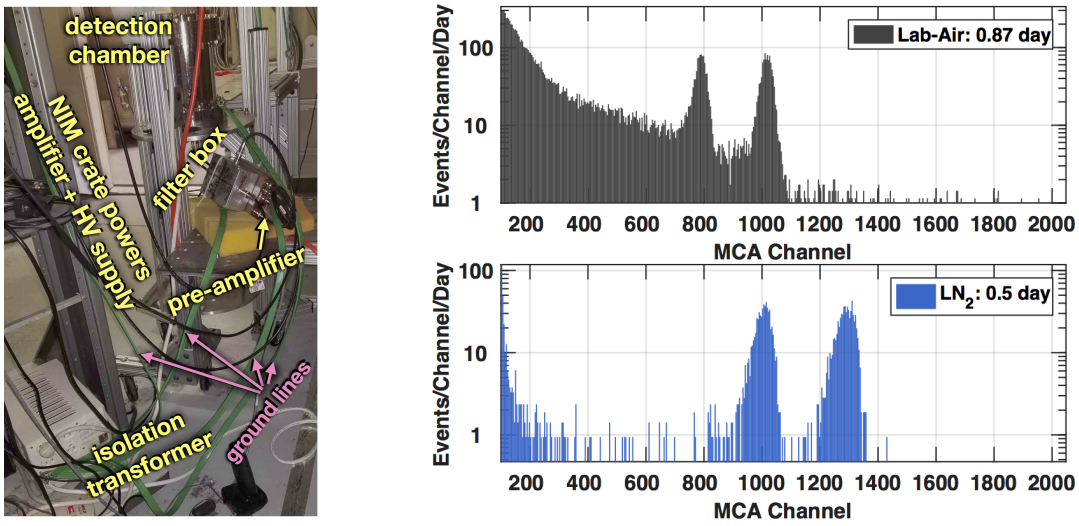

Figure 4.19: Left: Back of the Radon Emanation System DAQ and electronics rack, with grounding cables (green) connecting all the detector components to a common grounded isolation transformer to avoid ground loops. The components having a common ground are the detection chamber, filter box, preamplifier, and the NIM crate powering the amplifier and high-voltage supply. In the Syracuse lab, we used the copper wall pipes, while at SDSM&T we use an isolation box plugged into a clean power supply in the Foundation lab. **Right:** (Log-scale) Pulse height spectra taken before (top/gray) and after (bottom/blue) adding grounding lines and isolation transformer to the detection circuitry. *Top:* Histogram of lab-air taken in the Syracuse sub-basement for 0.87 days. The peak at channel 800 (1,000) from ^{218}Po (^{214}Po) has a large number of background events extending up to twice the energy of ^{214}Po α decays: $2 \times E_\alpha \approx 15$ MeV. *Bottom:* Histogram of lab-air taken in the Syracuse sub-basement for 0.5 days after installing common grounding lines attached to the preamp, amplifier, and NIM crate powering the HV supply.

being sealed in the chamber has been discussed in **Section 4.1.2**. Radon is also expected to emanate from the inner surfaces of the emanation chambers, gas-handling system piping, the components of the detection chamber, as well as the boil-off gas dewars used for radon transfers. Emanation from the chamber, piping, and panels contribute to the radon-blank (*i.e.* empty chamber) transfers. This section gives an overview of the background sources internal to the detection vessel **Section 4.4.1** and the radon-blank rate **Section 4.4.2**–both of which are generally much smaller than the other sources of radon. This will lead to a discussion of mitigating the largest background sources: radon diffusing into components inside the detection vessel and back-diffusing during subsequent assays (discussed in **Section 4.5**), and radon emanating from the walls of a LN_2 dewar during transfer (discussed in **Section 4.6**).

4.4.1 Radon Internal to the Detection Chamber

Between every sample assay, calibration transfer, and sample-free ('radon-blank') chamber measurement we fill and flush the detection vessel and gas panel with low-radon nitrogen, to significantly reduce sample cross-contamination. Subsequently, with no sample radon, we measure the internal detector backgrounds and monitor the intermittent noise of the detector. The vessel components naturally have some very-low level of radium contamination that will lead to some non-zero radon background. Most of the components in the detection vessel such as the vessel walls,

the gas and signal feedthroughs, and the gas displacers are electropolished metals. Due to their very low diffusion coefficient, only the recoil emanation from radium on the surface of these metal components contribute to the radon backgrounds. The only non-metal components are the teflon collar and stand, and the Torr seal epoxy; as described in **Section 4.3.3**, these non-conducting materials with a high dielectric constant are necessary to prevent arcing from the high-voltage signal electrodes to the grounded gas displacers. The radon diffusion coefficient of the teflon collar and stand are $\gtrsim$1,000$\times$ larger than the metal components, and are therefore expected to be the worst contributor to the overall internal background rate even if the bulk radium impurities and inner surface area are each $\times$10 larger for the metal than the teflon. Measurements with only the LN_2 boil-off over the course of years indicate an internal chamber background in the (6–8) MeV energy region of interest for $^{218/4}$Po alpha-decay peaks

$$B_{\text{int}} \lesssim 2\,\text{events/peak/day}. \tag{4.4.1}$$

Naively, we expect this rate from the vessel components to grow in with the mean lifetime of radon τ as $B_{\text{int}}(t) = B_{\text{eqbm}}\left(1 - e^{-t/\tau}\right)$, due to the emanation of components. However, these backgrounds appear to be fairly constant with no measured/significant time dependence. The teflon components and epoxy appear to produce low radon emanation, and internal radon sources seem to quite low. All other sources of detector background will not grow-in with time and so the rate of events in the region of interest for the Po-21x is modeled by

$$R_{\text{tot}} \equiv S(t) + B_{\text{int}} = S_0 \exp(-t/\tau) + B_{\text{int}}, \tag{4.4.2}$$

where S_0 is the strength of the radon source intended for assay and B_{int} is the rate of non-signal events in the Po-21x region of interest determined for each assay by measuring pre- and post-assay background runs.

Muons from cosmic rays deposit energy that depends on the kinetic energy and angle of passage through the detector. No studies have been performed that definitively identify the cosmic-ray muon flux, as a result the average level of backgrounds seen (Eqn. 4.4.1) must encompass the coincidence of the muon rate with the $^{218/4}$Po region of interest. No further studies of cosmic rays are planned.

Another internal source of radon background arises due to the back-diffusion of radon from components originating from a previous measurement. The radon calibration source employed by our group, when concentrated into the 1.7 L detection volume, produces quite a large activity:

$$C_{\text{sce}} \sim {}^{10\,\text{Bq}}/_{1.7\,\text{L}} \approx 6,000\,\text{Bq/m}^3. \tag{4.4.3}$$

The metal components in the detection volume will not allow radon to diffuse into their surfaces and therefore pose no risk of back-diffusion. Some fraction of radon from these large concentrations are likely to diffuse into the softer components within the detection vessel–this is discussed further in **Section 4.5**.

4.4.2 Radon-Blank Transfer Backgrounds

Sources of backgrounds other than the detector's internal radon are associated with radon-blank transfers *i.e.* radon from emanation and leaks that enters the vessel simultaneously with the sample. Once inside the detector these backgrounds will decay with the half life of radon and cannot be discriminated from the emanated sample. Mitigating these backgrounds is critical to reach the best sensitivity of the detector.

A radon-blank transfer includes radon emanating from the chamber walls over the days–weeks-long emanation. The emanation vessel is emptied and cleaned in preparation for a radon-blank emanation, transfer, and assay. A radon-blank emanation won't be subject to material outgassing, and the emanation chambers are initially pumped down to $P \approx 10\,\text{mTorr}$ to identify and mitigate leaks. Subsequently, the chamber pressure is brought to $P \approx 100\,\text{Torr}$ to include the recoil emanation of radon due to the surface radium contamination of the vessel walls. The inner surfaces of the small and large emanation chambers are electropolished, like the detection chamber and gas displacers, with an expected surface emanation density $\mathcal{R} \sim 1\,\mu\text{Bq/m}^2$ [137]. Radon emanated from the inner surfaces of the large emanation chamber, with a height $H = 1\,\text{m}$, and circumference $C = 1.93\,\text{m}$ is expected to have negligible contribution compared to the internal detector backgrounds:

$$R_{\text{surf.}} = A \times \mathcal{R} = \left(\frac{(1.93\,\text{m})^2}{2\,\pi} + (1.93\,\text{m})\,1\,\text{m} \right) \times \frac{\mu\text{Bq}}{\text{m}^2} \approx 2.52\,\mu\text{Bq}.$$

Radon present in the gas panel before the sample transfer will have no impact on the backgrounds due to the repeated evacuation of the gas handling system and detection chamber. However, radon emanating from the piping of the gas panel as well as lab air leaking into the piping will contribute to the blank rate of radon. Since the inner surfaces of the gas panel piping, which consist of no more than $\ell \lesssim 25\,\text{m}$ of piping with an average diameter $d \lesssim 1\,\text{cm}$, the total radon emanated from during a 12 hr transfer time is negligible

$$\begin{aligned} R_{\text{panel}} &= \ell(\pi\,d) \times \mathcal{R} \cdot \left(1 - \exp(-0.5/5.52)\right) \\ &\lesssim 25\,\text{m} \times (1\,\text{cm}\,\pi)^{\mu\text{Bq}/\text{m}^2} \cdot 0.08 \approx 9\,\mu\text{Bq}. \end{aligned}$$

Leaks in the piping are also expected to be negligible since the leak rate of the VCR connections in the gas panel $Q_{\text{VCR}} \lesssim 10^{-11}\,\text{Torr L/sec}$ will only impact the radon-blank transfer backgrounds during the time of transfer. For a $\Delta t = 8\,\text{hour}$ transfer, the amount of leaking lab air

$$Q_{\text{VCR}}\,\Delta t \lesssim 10^{-11}\,\text{Torr L/sec} \times\ (3600\,\text{sec/hr} \times 8\,\text{hr}) \approx 3 \times 10^{-7}\,\text{Torr L}$$

Assuming the radon activity in the lab $C = 0.1\,\text{Bq/L}$, the number of radon atoms ρ_{Rn} introduced at $P_{\text{atm}} \approx 680\,\text{Torr}$

$$\rho_{\text{Rn}} = \tau \cdot \frac{C}{P_{\text{atm}}} \approx \left(5.52 \times 84.6 \times 10^3\,\text{sec}\right) \cdot \frac{0.1\,^{\text{atoms}}/_{\text{sec L}}}{680\,\text{Torr}} \approx 70\,^{\text{atoms}}/_{\text{Torr L}}.$$

If all the radon that leaks into the piping during a transfer is captured and placed in the detection chamber, leaks occurring during the 8 hr transfer would yield only

$$Q_{\mathrm{VCR}}\Delta t \times \rho_{\mathrm{Rn}} \approx 3\times10^{-7}\,\mathrm{Torr\,L}\times 70\,{}^{\mathrm{atoms}}/_{\mathrm{Torr\,L}} \approx 20\times10^{-6}\,\mathrm{atoms\ per\ transfer.}$$

Early measurements indicated radon-blank rates of order

$$B_{\mathrm{blank}} \lesssim 0.4\,\mathrm{mBq} \tag{4.4.4}$$

which were dominated by the radon in the boil-off carrier gas. Commercial LN_2 dewars are known to contain trace amounts of U/Th in the walls of the vessel and therefore will emanate radon. Large chamber transfers can take up to $\Delta t_{\mathrm{trans}} \approx 8$ hours, and are performed at an average flow $F \approx 10$ standard liters per minute, with the vessel varying at low pressures $P = (50\text{–}200)$ Torr. The activity of radon in the carrier gas (boil-off LN_2) with a concentration $C_{\mathrm{LN_2}} \approx 0.5\ {}^{\mathrm{mBq}}/_{\mathrm{m}^3}$ [165]

$$\begin{aligned} R_{\mathrm{LN_2}} = C_{\mathrm{LN_2}}V &= C_{\mathrm{LN_2}}\,F\,\Delta t_{\mathrm{trans}}\,({}^{P}/_{P_{\mathrm{atm}}}) \\ &= 0.5\ {}^{\mathrm{mBq}}/_{\mathrm{m}^3}\cdot 0.010\ {}^{\mathrm{m}^3}/_{\mathrm{min}}\cdot 480\ \mathrm{min}\cdot \cancel{({}^{100}/_{680})}\,0.147 \\ &\approx 0.35\ \mathrm{mBq}. \end{aligned}$$

This radon will be captured by the brass wool traps, along with sample, producing a background of radon contaminating the sample proportional to the transfer-time. It is critical to remove this background, which would lessen the detector sensitivity from the nominal $\mathcal{O}(0.2\,\mathrm{mBq})$.

Section 4.6 describes radon adsorption measurements of a carbon trap used to remove the radon. By scrubbing the minuscule radon in the carrier gas with a cryogenically-cooled carbon trap at the gas panel input, we can ensure no extra radon is introduced to the detection chamber along with the sample. Due to minimum cosmic ray interactions, and low internal and radon-blank backgrounds, subsequent measurements of the radon-blank rate were consistent with the detector backgrounds

$$B_{\mathrm{blank}} + B_{\mathrm{int}} \lesssim 2\,\mathrm{events/peak/day}.$$

4.5 Radon Back-Diffusion in the Detection Chamber

With minimum cosmic-ray interactions, and low internal and radon-blank backgrounds, we discovered an unexpected radon source internal to the detection vessel during a low-background measurement. Following a high-radon, calibration transfer, we measured count rates of the short-lived ${}^{218/4}$Po, well above the internal backgrounds ~ 2 cts/peak/day for a 10 day period. The LN_2 sample is expected to produce a very-low activity $C_{\mathrm{LN}}\,V_{\mathrm{cham}} \times {}^{P'}/_{P_{\mathrm{atm}}} \lesssim 0.13\,\mu\mathrm{Bq}$. Therefore, the $\mathcal{O}(100\,\mathrm{cts/peak/day})$ rate of ${}^{218/4}$Po α decays shown in **Fig. 4.20** in the 100 Torr of LN_2 boil-off following the transfer and measurement of a whopping 100 Bq of calibration radon was unexpected.

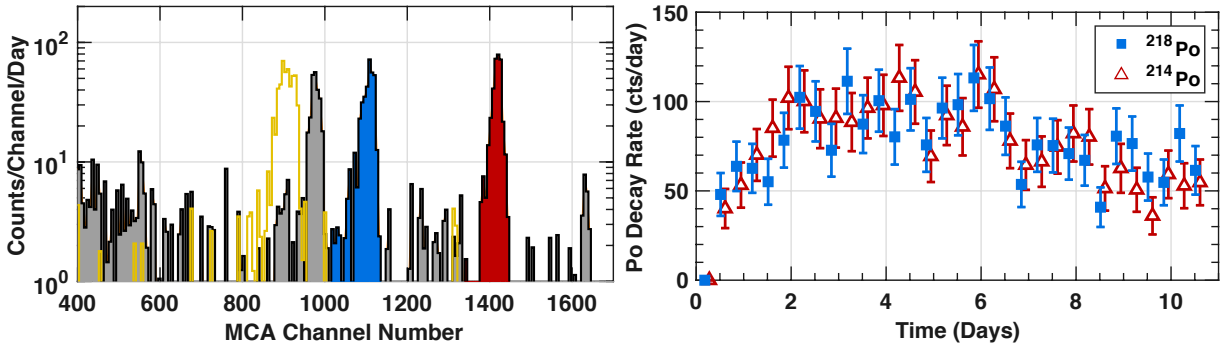

Figure 4.20: $^{218/4}$Po measured decay rates during a LN_2 boil-off background run following a 100 Bq exposure to radon for hours. **Left:** Cumulative pulse height spectra (gray fill) with $^{218(4)}$Po region of interest shown in blue (red) with a background run (yellow line) shown for comparison. Though the gain is different in the background run, the measured ^{210}Po rate (peak near channel 900) is comparable, as expected given its long grow-in time following the 22 yr half-life of ^{210}Pb. The rate of events above the ^{210}Po peak is much smaller than the previous LN_2 assay, indicating a big leak or a radon source. **Right:** Time-dependent ^{21x}Po decay rates. Measuring 100 cts/peak/day during a background run was a huge shock to us.

This prompted us to investigate sources of radon both inside and outside of the detection vessel.

Every radon measurement begins only after purging the gas panel and detection chamber by evacuating the pressure to 10 Torr and reintroducing 1,000 Torr of nitrogen (*i.e.* filling and flushing) four times so the reduction (from Eqn 4.2.14)

$$\eta_{\text{red}} \approx (10/1000)^4 = 10^{-8}, \tag{4.5.1}$$

leaving an expected 1 µBq of radon–only a minuscule 10 ppb of the $\mathcal{O}(100\,\text{Bq})$ in the detector. A leak could provide this amount of radon to the detection volume, but the time dependence of the radon decay is inconsistent with the expected linear increase due to a leak from lab air. Including the detection $\epsilon_{\mathcal{D}} \sim 50\%$ and collection $\epsilon_{\mathcal{C}} \sim 50\%$ efficiencies indicates a true decay rate

$$R_{\text{max}} = \epsilon_{\mathcal{C}}\epsilon_{\mathcal{D}} \times 100\,\text{cts/day} \approx 400\,\text{decays/day}. \tag{4.5.2}$$

The pressure change ΔP_{cham} (Eqn. 4.1.5) needed in the $V_{\text{cham}} = 1.7\,\text{L}$ detection vessel to provide 400 decays/day given $C_{\text{lab}} \approx 100\,\text{Bq/m}^3$ at a pressure $P_{\text{lab}} = 680\,\text{Torr}$

$$\begin{aligned}\Delta P_{\text{cham}} &= \frac{R_{\text{max}}}{V_{\text{cham}}} \cdot \frac{P_{\text{lab}}}{C_{\text{lab}}} = \frac{400\,\text{decays/day}}{0.0017\,\text{m}^3} \cdot \frac{680\,\text{Torr}}{100\,\text{Bq/m}^3} \\ &\approx \frac{0.0058\,\text{Bq}}{0.17\,\text{Bq}} \cdot 680\,\text{Torr} \approx \frac{3.12}{0.17}\,\text{Torr} \approx 18\,\text{Torr}\end{aligned}$$

which is not too large to be unreasonable, given the small volume of the chamber–it is conceivable that during early runs, when the pressure of the detection chamber was read by the small-trap gauge, no one noticed a small pressure rise from 100 Torr to 118 Torr. We certainly would have noticed a pressure change this large in later measurements. Also, given the huge pressure difference between the lab and the vessel, leaks introducing radon would continue to rise linearly until the

pressures equilibrated. Instead, the decay rates increased for only a two day period, hovered near 100 cts/day for about 4 days, and subsequently decreased over a 10 day period. Moreover, the detection chamber configuration (*i.e.* the panel connections, vessel bolts, and detector) wasn't changed before or after the calibration transfer of Pylon, and radon due to this leak rate would be the same order of magnitude for other LN_2 measurements, which was not observed. Although the polonium decay rates shown in **Fig. 4.20** do not obey the expected time-dependence of radioactive decay for a freshly sealed source, presumably, the radon source was inside the detection chamber.

Since the rate was much higher than other background measured at other times, the only plausible cause for this is the sequestration and delayed release of radon in the vessel components from the previous high-rate calibration measurement.

In order to understand the decay rates shown in **Fig. 4.20**, predict the general behavior of diffusing radon, and prevent significant contamination of future assays, I describe the steady-state solution to the one-dimensional radon decay and diffusion equation and perform simulations of radon diffusing into and, more importantly, back out of a moderately radon-hard material representing the teflon stand. The stand itself has polar symmetry, so the one-dimensional diffusion and decay simulations are expected to be representative of the radon behavior in the teflon. I describe how to calculate the back-diffused flux of radon following vessel evacuations, and present simulated results. I also compare the simulation results of materials with several diffusion coefficients, near the expected level of HDPE $D \sim 10^{-11}\,\mathrm{m}^2/\mathrm{sec}$, to the measured $^{218/4}$Po α decay rates in the background run following the high-activity calibration transfer. I then give a generalized (non-analytic) form for back-diffusing radon from a single, high-activity exposure of the teflon in the detection chamber, useful for determining how long the back-diffusion induced by the calibration run will take to fall below the level of the detector backgrounds.

4.5.1 Steady-State Radon Diffusion and Decay

The time-dependent ^{222}Rn concentration $C(x,t) \equiv C$ describing diffusion, decay, and production within a one-dimensional material, with a radon diffusion coefficient D spanning x obeys

$$\frac{\partial C}{\partial t} = D\frac{\partial^2 C}{\partial x^2} - \lambda_{\mathrm{Rn}} C + \rho, \tag{4.5.3}$$

where the radon production ρ spanning the material is uniform, radon decays reduce the concentration everywhere proportional to the decay constant $\lambda_{\mathrm{Rn}} = 2.1 \times 10^{-6}/\mathrm{sec}$, and the diffusion coefficient for materials of interest–typically 'poly' plastics such as high- and low-density polyethylene (HDPE/LDPE) and rubbers such as silicone–are in the range $D \sim (10^{-12}\text{–}10^{-9})\,\mathrm{m}^2/\mathrm{sec}$, *c.f.* [134]. Obtaining the analytic solution to the steady-state concentration is useful to understand the diffusion of radon into 'soft' materials, since for a given depth the time to equilibrate will be different.

Sourceless Steady-State Solution I start by solving the 'source-less' equation which neglects radon production in the teflon, so that $\rho = 0$. The concentration $C(x,t)$ inside a material with low radon production and emanation is found by solving

$$\frac{\partial C}{\partial t} = D\frac{\partial^2 C}{\partial x^2} - \lambda C. \tag{4.5.4}$$

The general steady-state solution C to Eqn. 4.5.4 is given by the sum of exponentials:

$$D\frac{\partial^2 C}{\partial x^2} = \lambda C \quad \rightarrow \quad C(x) = c_1\,\exp(x/\ell) + c_2\,\exp(-x/\ell),$$

where the characteristic distance scale is the radon diffusion length $\ell = \sqrt{D/\lambda}$. It is convenient to check the analytic solution when it is cast

$$C(x) \;=\; \kappa\Big(a\exp(x/\ell) + b\exp(-x/\ell)\Big). \tag{4.5.5}$$

Now let us assume that at the boundaries $x = 0$ and $x = d$, the material is held at constant concentration $C_0 \equiv C(x=0)$ and $C_d \equiv C(x=d)$. The coefficients a and b of the exponential terms and the normalization constant κ satisfy

$$\begin{aligned} a &= C_d - C_0\exp(-d/\ell) \\ b &= C_0\exp(d/\ell) - C_d \\ \kappa &= 0.5\,\mathrm{csch}(d/\ell). \end{aligned} \tag{4.5.6}$$

The hyperbolic trigonometric function is given (for $x \neq 0$) by

$$\mathrm{csch}(x) \equiv 1/\sinh(x) = 2\,\Big(\exp(x) - \exp(-x)\Big)^{-1}, \quad \text{where} \quad \sinh(0) = 0. \tag{4.5.7}$$

The coefficients from Eqn. 4.5.6 can easily be shown to solve the source-less diffusion and decay Eqn. 4.5.5 by evaluating the steady-state boundary conditions $C(x = 0, d)$. Since $\exp(0) = 1$,

$$\begin{aligned} C(x=0) &= \kappa\Big(a + b\Big) \\ &= 0.5\,\mathrm{csch}(d/\ell)\Big(C_d - C_0\exp(-d/\ell) + C_0\exp(d/\ell) - C_d\Big) \\ &= \frac{1}{2\sinh(d/\ell)}\,C_0\,\Big(\underbrace{\exp(d/\ell) - \exp(-d/\ell)}_{2\cdot\sinh(d/\ell)}\Big) = C_0 \quad \checkmark \end{aligned} \tag{4.5.8}$$

and so the $x = 0$ boundary is appropriately solved. Evaluating the concentration at the other boundary $C(x = d)$ with the above coefficients from Eqn. 4.5.6 gives

$$\begin{aligned} C(x=d) &= \kappa\Big(a\exp(d/\ell) + b\exp(-d/\ell)\Big) \\ &= \kappa\Big(\big(C_d - C_0\exp(-d/\ell)\big)\exp(d/\ell) + \big(C_0\exp(d/\ell) - C_d\big)\exp(-d/\ell)\Big). \end{aligned} \tag{4.5.9}$$

This long expression can be simplified by noting that the C_0's are left with no prefactors and

$$\begin{aligned} C_d &= \kappa\Big(C_d \exp(d/\ell) \cancel{- C_0 + C_0}^{\,0} - C_d \exp(-d/\ell)\Big) \\ &= \frac{1}{2\sinh(d/\ell)}\, C_d \Big(\underbrace{\exp(d/\ell) - \exp(-d/\ell)}_{2\cdot\sinh(d/\ell)}\Big) = C_d \quad \checkmark \end{aligned}$$

so the secondary boundary condition is also found to match with the coefficients given in Eqn. 4.5.6. The coefficients (Eqn. 4.5.6) are implicitly defined as functions of the diffusion coefficient. The steady-state solution including a constant source ρ of radon production is easily shown to be the sourceless solution Eqn 4.5.5 minus an offset

$$C_{\text{sce}} = C(x) + \rho/\lambda. \tag{4.5.10}$$

The second spatial derivative (diffusion term) leaves no remaining source-dependent term. Then transforming the decay term

$$-\lambda C_{\text{sce}} = -\lambda\Big(C(x) + \rho/\lambda\Big) = -\lambda C(x) - \rho \tag{4.5.11}$$

exactly cancels the constant offset introduced. The teflon in the detection vessel has an essentially negligible radon emanation so the radon production ρ can safely be ignored for the purposes of understanding the radon backgrounds measured in this assay, and, more generally to avoid radon resulting from high-exposure periods. Unfortunately, no analytic solution exists for the amount of radon that enters and escapes (via back-diffusion) from a *single* side of a material of a given thickness and permeability, for a given exposure concentration and duration. It is useful to simulate the concentration of radon in a material of a given thickness and hold the boundary concentration at a constant strength for a given exposure. This will be the first step to gain understanding of the radon diffusion into and out of the teflon for the somewhat complicated exposure period before the high-radon background measurement 'Run 128' that motivated this work studying back-diffusing radon.

4.5.2 Single-Exposure Radon Diffusion Simulation

Obtaining the analytic solution to the steady-state concentration is useful to understand the time scale of radon diffusion into 'soft' materials from very-high external sources. Here, I simulate the diffusion of radon into teflon using a constant, high-activity boundary concentration to understand the time dependence of diffusion for a single exposure. The largest portion of exposed teflon is a cylinder–lathed by me with R. Bunker's help (as described in **Section 4.3.3**) to a thickness $d_{\text{tef}} \approx 4\,\text{mm}$. The outer lateral surface area of the teflon is calculated from the height $H_{\text{cyl}} = 6.60\,\text{cm}$ and the outer radius $R_{\text{out}} = 1.90\,\text{cm}$:

$$A_{\text{tef}} = \pi \cdot R_{\text{out}} \times H_{\text{cyl}} = \pi \cdot 1.9 \times 6.6\,\text{cm}^2 \approx 39\,\text{cm}^2. \tag{4.5.12}$$

Using MATLAB's `pdede`, I numerically solved the one-dimensional, time-dependent source-less, diffusion and decay Eqn. 4.5.4 for the ^{222}Rn concentration $C(x,t)$ on a $d_{\text{tef}} = 4\,\text{mm}$-long line representing teflon in the detection chamber with $D = 10^{-12}\,\text{m}^2/\text{s}$ with a diffusion length

$$\ell = \sqrt{D/\lambda} = \sqrt{10^{-12}\,\text{m}^2/\text{s} \cdot 4.66 \times 10^5\,\text{s}} \approx 0.69\,\text{mm}.$$

The radon concentration inside the teflon determined by the solver already includes the effect of radioactive decay, and it ignores the production of radon by radium decays, which is sensible given the generally low background levels in the detector. The simulation was updated at 10 minute intervals where the ^{222}Rn decay probability for such a short time $\lambda\Delta t \approx 2.1 \times 10^{-6}/\text{sec} \cdot 600\ \text{sec} \approx 1.26 \times 10^{-3}$. The simulation is one-dimensional, so to bring the concentration to sensible units, the area A_{tef} will scale the radon flux diffusing into and out of the material.

The total radon activity at a time t inside the 4-mm-deep teflon is calculated by integrating the concentration at every point in the teflon

$$R_{\text{tef}}(t) = \int_{\text{all}} C(x',t)\,\text{d}V' \equiv A_{\text{tef}} \int_0^{d_{\text{tef}}} C(x',t)\,\text{d}x'. \tag{4.5.13}$$

which is equivalent, in this case, to multiplying the integrated concentration by the area. Following an exposure lasting $t = t_{\text{exp}}$, Eqn. 4.5.13 can be used to compute the number of radon atoms $N_{\text{Rn}} = \tau \times R_{\text{tef}}(t_{\text{exp}})$ accumulated in the teflon. The MATLAB simulation can not be run with boundary values or initial concentration conditions set too low. The teflon in the detection chamber emanates very little radon, so the initial radon-decay concentration within the teflon (not including the boundaries) at $t_0 = 0\,\text{days}$ was set to

$$C_{\text{teflon}}(t_0) = C\Big(x = (0, 0.4)\,\text{cm}, t = 0\Big) = 0.1\,\text{Bq/m}^3. \tag{4.5.14}$$

The high-activity radon concentration at the teflon-gas interface (defined at the origin $x = 0$)

$$C_{\text{gas}}(t_0) = C\Big(x = 0\,\text{cm}, t = (0, t_{\text{exp}})\Big) = 100\,\text{Bq}/1.7\,\text{L} = 58\,\text{kBq/m}^3 \tag{4.5.15}$$

to mimic the exposure of the teflon before the background run with back-diffused radon. The opposite ($x = 0$) boundary is set to

$$C_{\text{inner}}(t_0) = C\Big(x = 0.4\,\text{cm}, t = (0, t_{\text{exp}})\Big) = 0.1\,\text{Bq/m}^3. \tag{4.5.16}$$

The boundary conditions (Eqns. 4.5.14, 4.5.15) are held constant for the entire duration of exposure. The concentration $C(x, t_{\text{exp}})$ inside the teflon resulting from exposures lasting

$$t_{\text{exp}} = 0.5, 1.5, 3.8, 5.5, 40\,\text{days} \tag{4.5.17}$$

are shown in **Fig. 4.21**. The diffusion length $\ell \approx 700\,\mu\text{m}$ of radon in the teflon is shown as vertical line. For a half day exposure, less than 10% of the radon has diffused beyond the diffusion length.

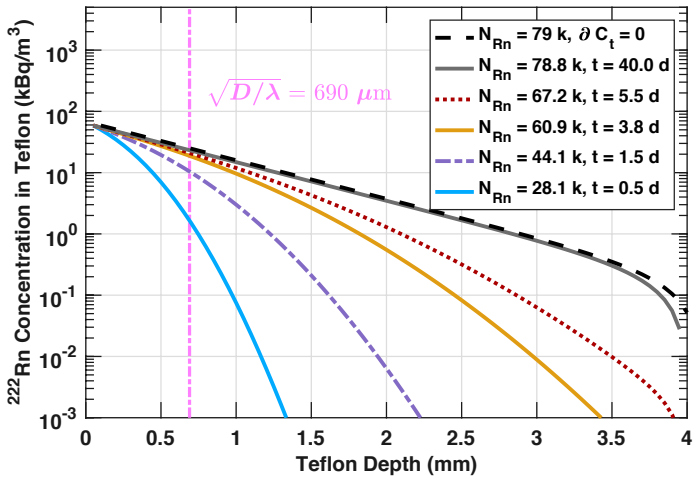

Figure 4.21: Simulated ^{222}Rn concentration as a function of distance from the teflon–gas interface ($x = 0$ mm) at the ends of 5 exposure times: $t_{\rm exp} = 0.5$, 1.5, 3.8, 5.5, and 40 days (colors) compared with the steady-state solution (dashed black). The boundary concentration $C_{\rm gas} = R_{\rm gas}/V_{\rm det} = 100\,{\rm Bq}/1.7\,{\rm L} \approx 58\,{\rm kBq/m^3}$ during exposure. The number of radon atoms diffused into the 4 mm thick teflon at the end of exposure $N_{\rm Rn} = \tau \times R_{\rm tef}(t_{\rm exp})$ from Eqn. 4.5.13, is shown in the legend. The diffusion length of teflon $\sqrt{D/\lambda} = 690\,\mu$m is shown (vertical line). The number of atoms $N_{\rm Rn}$ in the teflon after 40 days of exposure is 99.7% of the steady state solution (dashed black $\partial C_t = 0$) from Eqns. 4.5.5, 4.5.6.

Teflon exposed for 40 days has 99.7% of the radon content of the steady-state solution with the same boundary conditions.

The initial high-radon concentration is some 10^6 times larger than the low activity LN_2 boil-off used for background runs during which period radon in the teflon will make its way out of the teflon and back into the gas. In order to understand the time-dependence of back-diffusing radon, these results are used as the initial condition for the evacuated, low-concentration period where back-diffusion will occur.

4.5.3 Back-Diffusion Radon Simulation

Following an accumulation of radon in the teflon, the chamber is evacuated repeatedly to prepare for the next assay. I simulated this by setting the boundary condition at the teflon-gas interface $C_{\rm gas} = 0.1\,{\rm Bq/m^3}$. The repeated evacuation will remove all the radon in the gas, but radon may still diffuse back out of the teflon into the gas. The total radon in the vessel, following an evacuation, will be given by the sum of radon in the gas and teflon components. By suppressing the integration limits in Eqn. 4.5.13 the total decay rate is

$$R_{\rm tot}(t) = R_{\rm gas} + R_{\rm tef} = R_{\rm gas}(t) + \lambda A_{\rm tef} \int C(x',t)\,{\rm d}x'. \tag{4.5.18}$$

After an exposure lasting $t_{\rm exp}$, the evacuation of radon from the vessel leaves the initial amount of radon $R_0 \equiv R_{\rm tef}(t_{\rm exp})$ in the vessel which is determined by the radon in the teflon at that time. This distribution $C(x, t_{\rm exp})$ will be the initial condition in the teflon for the upcoming back-diffusing time. We also know that the total radon in the gas and teflon will decay with the lifetime of radon,

so at a time after the flush $t = t_{\text{exp}}$, the radon obeys

$$R_{\text{tot}}(t) \equiv R_{\text{tef}}(t_{\text{exp}}) \exp(-t/\tau) = \lambda A_{\text{tef}} \exp(-t/\tau) \int C(x', t)\, \mathrm{d}x'. \tag{4.5.19}$$

The simulation doesn't track the rate of radon decays in the gas from the teflon back-diffusion, so that is calculated manually. It can be calculated using Eqns. 4.5.18 (4.5.13) and 4.5.19:

$$R_{\text{gas}}(t) = R_{\text{tot}}(t) - R_{\text{tef}}(t) = \lambda A_{\text{tef}} \Big(\exp(-t/\tau) \int C(x', t_{\text{exp}})\, \mathrm{d}x' - \int C(x', t)\, \mathrm{d}x' \Big). \tag{4.5.20}$$

Fick's law [342] determines the radon flux ϕ_{esc} (the transfer rate of radon atoms per unit area) at a boundary. The radon flux entering the gas from the teflon boundary is proportional to the slope of the concentration at the boundary at a given time [254, 255, 264]

$$\phi_{\text{esc}}(t) = -D \frac{\partial C(x,t)}{\partial x}\bigg|_{x = 0\,\text{cm}} \tag{4.5.21}$$

since the radon leaving the teflon is exactly what has entered the gas. The negative sign is necessary since the radon flux travels from high concentration to low concentration analogous to heat flow. The flux contributes to the total decay rate in the gas which can be obtained by solving

$$\frac{\partial R_{\text{gas}}}{\partial t} = \phi_{\text{esc}}(t) \times A_{\text{tef}} - \lambda R_{\text{gas}}. \tag{4.5.22}$$

However, using Eqn. 4.5.20 is easier in practice. Right after a flush is performed, the slope of the concentration (and therefore the back-diffused flux) is a maximum, and so radon pours out of the teflon over a period of days. The total amount radon in the teflon, determined by Eqn. 4.5.13, decreases as radon back-diffuses into the gas. These equations determine the amount of radon back-diffusion to expect from the teflon sample during the complete evacuation of a vessel following a high exposure period as performed after every calibration.

To understand the impact of back diffusion on a background run I simulated a $t = 1\,\text{day}$ exposure to $C = 58\,\text{kBq/m}^3$ and imitated a primary evacuation by setting the boundary concentration for the rest of the simulation to $C_{\text{gas}} = 0.1\,\text{Bq/m}^3$. A subsequent, secondary flush at a later time t'_{fl} was performed by subtracting the total back-diffused radon R_{gas} (scaling the flux by the area to obtain a decay rate) from the total R_{tot} at that time

$$R_{\text{evac}}(t = t'_{\text{fl}}) = R_{\text{tot}}(t = t'_{\text{fl}}) - R_{\text{gas}}(t = t'_{\text{fl}}). \tag{4.5.23}$$

Fig. 4.22 shows 3 curve types representing the total radon decay rate (dashed blue-ish), radon in a teflon sample (dashed gray), the back-diffused radon, from Eqns. 4.5.23 and 4.5.20 (solid red–yellow curves). Following the exposure ($t < 0$) and the primary evacuation ($t = 0$) on the graph, 5 secondary flushes were simulated at times $t_{\text{fl}} = 1, 2, 4, 12, 24$, and 48 hrs removing $R_{\text{evac}}(t_{\text{fl}})$. In practice, we already know to evacuate the detection vessel (and gas panel) prior to an assay. The separation of the radon decay rate in the gas for each secondary flush, makes it clear that late-time

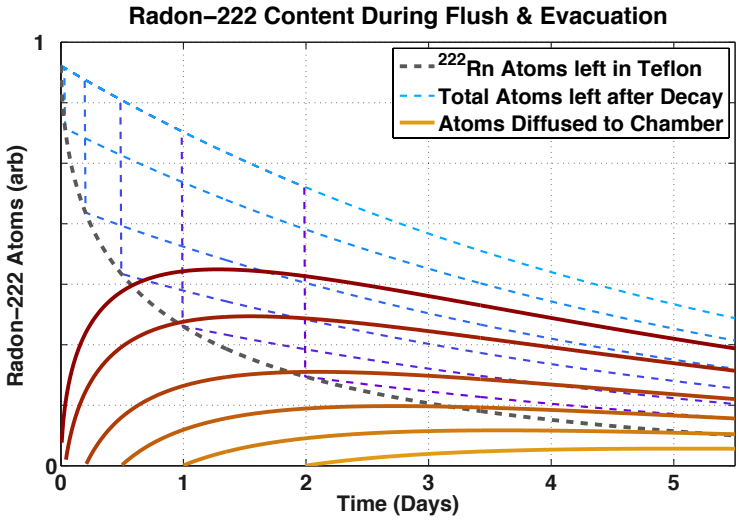

Figure 4.22: Time dependence of the number of radon atoms N_{Rn} in teflon (gray dashed), gas (red–yellow solid, 'diffused to chamber'), and their sum (blue–purple dashed). All radon initially starts in the teflon and back-diffuses into the gas following an evacuation at $t = 0$, and the total number of atoms falls exponentially. The curve colors represent solutions given a secondary flush at 5 times $t_{\mathrm{fl}} = 1, 2, 4, 12, 24, 48$ hrs, following a high exposure. The radon that back-diffuses before the second flush time is removed, and only the radon left in the teflon after a given flush is available to back-diffuse into the chamber. The vertical (blue–purple) dashed lines joining the total number of atoms to the total number in the teflon represent the amount of radon removed $R_{\mathrm{evac}}(t_{\mathrm{fl}})$ from the vessel by a flush from Eqn. 4.5.23.

flushes are more crucial to preserving low back-diffused radon rates in the detection vessel.

Comparing Run 128 with Simulation The teflon had an extended calibration-exposure period before the Run 128 background measurement including 5 hours at high exposure $C_1 = 12.6\,\mathrm{kBq/m^3}$, 3.8 days at medium exposure $C_2 = 1.499\,\mathrm{kBq/m3}$, and 2.06 days of exposure to $\mathrm{LN_2}$ gas $C \approx 1\,\mathrm{mBq/m^3}$. I ran three simulations, each with a different diffusion coefficient

$$D_{\mathrm{tef}} = (5, 10, 30) \times 10^{-12}\,\mathrm{m^2/sec}, \tag{4.5.24}$$

near that of high-density polyethylene (HPDE) [133]. The left panel of **Fig. 4.23** shows the predicted number of radon atoms diffused into the teflon as a function of time, during the high-activity calibration period, which lasted 2 weeks, before the Run 128 background measurement. The right panel shows the measured ^{21x}Po decay rates in the detection vessel compared to the decay rates predicted by Eqn. 4.5.20, using three diffusion coefficients D_{tef} (Eqn. 4.5.24). The predictions agree the measured rates within an order of magnitude. The results are potentially more convincing given that the solubility of teflon was assumed to be 1 (correct to with an order of magnitude) and could account for the discrepancy if *e.g.*the diffusion parameters of teflon $D = 5 \times 10^{-12}\,\mathrm{m/s^2}$ and $S \approx 2$. Regardless of the exact parameter values, these results indicate that back-diffused radon from high-activity exposures will swamp assays of low-radon samples.

The time-dependent behavior of diffusion into the teflon is crucial for short periods of high

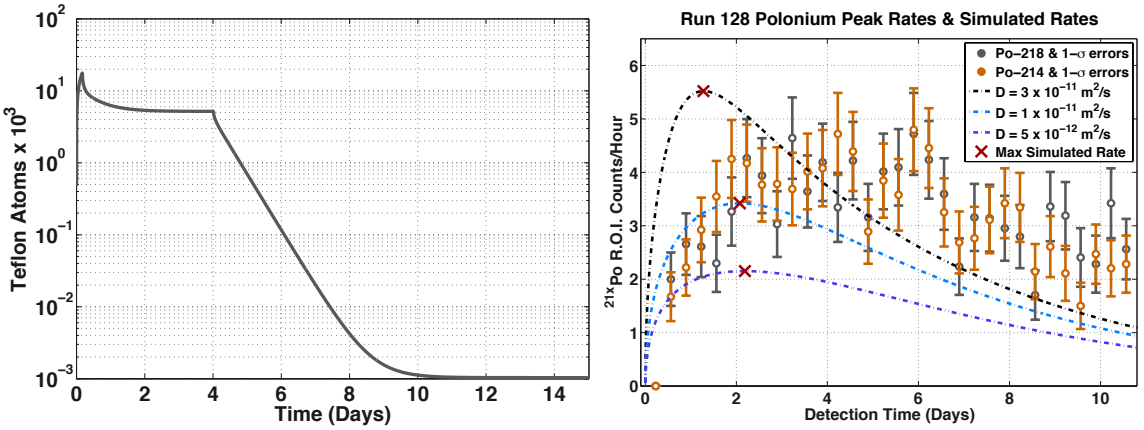

Figure 4.23: Left: Simulated radon content in teflon with a diffusion coefficient $D = 10^{-12}\,\mathrm{m}^2/\mathrm{s}$, as a function of time during the high-exposure calibration period of the Run 127 calibration run. The rate increase rapidly in the first few hours. Then, following the decrease of the boundary radon in the gas, radon in the teflon approaches a temporary equilibrium, until $t = 4\,\mathrm{days}$ where the boundary is lowered again, and the radon approaches zero. **Right:** $^{218/4}$Po alpha decay rate with 68% C.L. poisson errors as a function of time for post-calibration radon assay. Curves indicate simulation results of radon back-diffused from the teflon arising from the calibration exposure. The radon diffusion coefficients chosen are 5, 10, and 30× HPDE $D_{\mathrm{sim}} \approx 10^{-12}\,\mathrm{m}^2/\mathrm{sec}$ (purple, blue, black dashed lines). For modest, hours-long exposures of order 10 Bq, radon will back-diffuse from the teflon and will dominate low-radon assays for up to a week. .

exposure. It is useful to generalize these results for a less complicated (single) radon exposure similar to that used when determining the transfer or collection efficiency *c.f.* **Section 4.2**, and **Section 4.3.2**. To recap the steps: we a transfer high-activity source for calibration, or sometimes an unexpectedly high sample during an assay, which is then measured for a period of hours or days. During this time, some radon in the gas diffuses into the small teflon. The detection volume is flushed with repeated evacuation leaving ∼(10 ppb) of the sample in the vessel following the measurement. To compare the expected back-diffusion, I simulated the same 4 mm deep teflon, with a diffusion coefficient $D = 10^{-12}\,\mathrm{m}^2/\mathrm{s}$ to compare the back-diffusion of radon, including the effect of decaying boundary conditions of the gas, as would be expected for a real measurement, for 5 exposure times. Afterward, the concentrations at the teflon boundaries C_{far} and C_{gas} are set to $C_{\mathrm{evac}} = 0.1\,\mathrm{Bq}/\mathrm{m}^3$, to simulate the effect of radon being flushed from the detection vessel; this is done in practice with 4 fill-and-flush evacuations as described in **Section 4.2**. The time-dependent boundary conditions of the teflon (as shown in the left panel of **Fig. 4.24**) are updated in 10 minute time intervals for the 5 high-radon exposure periods $t_{\mathrm{exp}} = 1$, 4, 24, 72, and 120 hours. The initial gas concentration for each exposure period was set to $C_{\mathrm{gas}}(t = 0) = 1\,\mathrm{Bq}/1.7\,\mathrm{L} = 588\,\mathrm{Bq}/\mathrm{m}^3$. Following this, the gas concentration is reset to a very low concentration for 16 days, to simulate flushing the detection chamber. During this time, the sequestered radon will back-diffuse. The boundary conditions are

$$C_{\mathrm{gas}}(t) = \begin{cases} C_{\mathrm{exp}} = \frac{1\,\mathrm{Bq}}{1.7\,\mathrm{L}} \times \exp(-\lambda_{\mathrm{Rn}} t) & \text{if } t < t_{\mathrm{exp}} \\ C_{\mathrm{flush}} = 10^{-3}\ \mathrm{Bq}/\mathrm{m}^3 & \text{if } t > t_{\mathrm{exp}}. \end{cases} \tag{4.5.25}$$

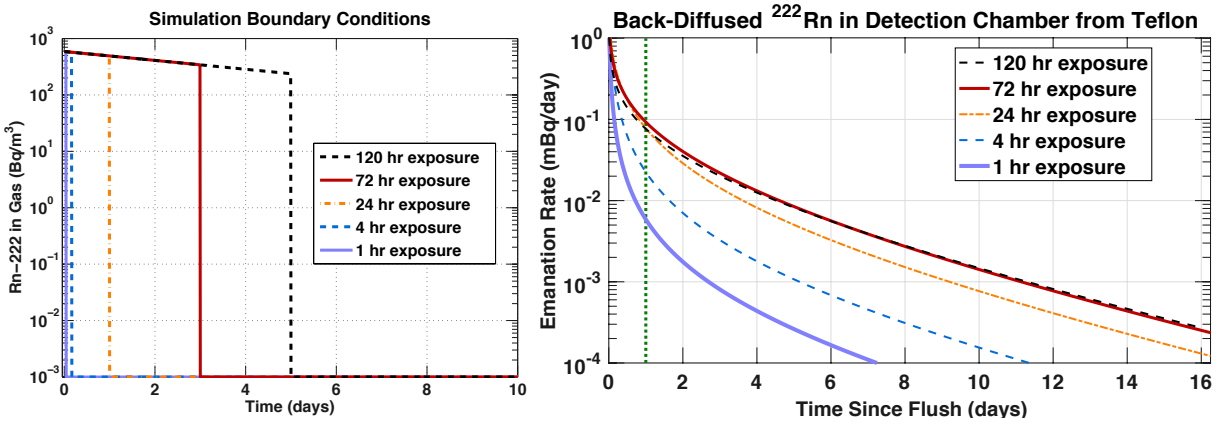

Figure 4.24: Left: Simulated teflon boundary ^{222}Rn concentration in the gas versus time for 5 exposure periods. **Right:** Simulated ^{222}Rn emanation rate due to back-diffusion from the teflon as a function of time calculated using Eqn. 4.5.21. Note the 120 hr exposure back-diffusion is lower than the 72 hr exposure. This trend is expected since the exposure time is a significant fraction of the 5.52 day radon mean lifetime. The radon that would back-diffuse has entered the teflon, and decayed to ^{218}Po while diffusing inside, never to escape. The total amount of radon in the vessel at the time of evacuation for a very long exposure is a smaller fraction due to decay.

4.5.4 Conclusions

The right panel of **Fig. 4.24** shows the expected radon decay rate in the detection chamber for 5 different exposure periods resulting from radon that has diffused into and, days later, back out of the teflon. Simulations indicate that we need to wait about 7 days for the back-diffusion of ^{222}Rn into the active detection volume to be reduced by $\lesssim 10^{3-4}$ of the original exposure. To account for the back-diffusion of radon from the teflon following the high-exposure period, first pick the approximate exposure time. Calibration assays to calculate transfer or collection efficiencies may range from 4 hrs to several days. Scale the y-axis values in the figure, which corresponds to $R = 1$ Bq to the expected exposure (*e.g.* for a 55 mBq sample, typical of a very-hot sample, multiply the y-axis values by 0.055). This calculation neglects the $\varepsilon_{\text{tr}} \approx 95\%$ and the detection and collection efficiencies; similar to the analysis in **Section 4.2.3**, scale the measured rates during exposure to obtain the expected contribution to the next assay. For a 1 hr exposure, the back-diffusion rate is $\times 100$ lower after a day. The R.E.S. is sensitive enough to detect better than 0.5 mBq in a few days. Then a 1 hour exposure of 50 mBq would allow for a background run potentially the very next day. By understanding the effects of radon back diffusion internal to the detection chamber, we can plan the calibration source strength with more consideration by balancing the expected statistical uncertainty with the wait-time predicted by my simulations.

4.6 Radon-Blank Backgrounds from Gas Dewars

Commercial LN_2 dewars are known to contain trace amounts of U/Th in the walls of the vessel. Since the inner surface area of the dewar wall above the liquid-gas interface increases

with nitrogen use, the radon concentration in the gas will increase. The R.E.S. at SDSM&T is outfitted with a very large 300 L vacuum vessel where hundreds of samples emanate radon. Large chamber transfers–described in significant detail in **Section 4.2.2**–can take up to 8 hours. Such transfers are performed at an average flow $F \approx 10$ standard liters per minute, with the vessel varying at low pressures $P = (50\text{–}200)$ Torr. The boil-off LN_2 carrier gas with a concentration $C_{LN_2} \approx 0.5\ {}^{mBq}/_{m^3}$ [165] is expected to have a radon decay rate

$$\begin{aligned} R_{LN_2} = C_{LN_2} V &= C_{LN_2}\, F\, \Delta t_{trans}\, ({}^{P}/_{P_{atm}}) \\ &= 0.5\ {}^{mBq}/_{m^3} \cdot 0.010\ {}^{m^3}/_{min} \cdot 480\ min \cdot \cancel{(100/680)} \to 0.147 \\ &\approx 0.35\ mBq. \end{aligned} \tag{4.6.1}$$

This radon will be captured by the brass wool traps, along with radon from the sample, producing a background of radon contaminating the sample is proportional to the transfer-time. It is critical to remove this background, which would lessen the detector sensitivity from the nominal $\mathcal{O}(0.2\,mBq)$. We do so by passing the nitrogen carrier gas through a cryogenically cooled carbon trap. The focus of this section is measurements made by me (with some previous work by R. Bunker and M. Stark) to characterize the temperature-dependent radon trapping of the carbon trap. **Section 4.6.1** describes a mathematical model for the elution (or breakthrough) of radon undergoing continuous adsorption and desorption. I describe radon breakthrough measurements at 3 temperatures taken with a trap housing a 28.5 gram sample of synthetic carbon. Room-temperature measurements were made by Megan Stark and Ray Bunker (**Section 4.6.2**), and radon breakthrough measurements with a thermal bath of ice water $T = 273\,K$ (**Section 4.6.3**), and solid CO_2 $T = 196\,K$ (**Section 4.6.4**) along with determination of the breakthrough time of the trap are presented here. I also compare the data to theoretical expectations to verify the radon adsorption in the trap will be sufficient for long radon transfers. Results of a long breakthrough test and subsequent regenerative flow using the full sample of carbon are also presented (**Section 4.6.5**).

4.6.1 Chromatographic Plate Model of Radon Elution

A common framework for describing radon breakthrough (passage/elution) is the chromatographic plate model [188, 295]. Under this model, a gas such as radon passes a column of length L divided equally into n theoretical stages (or plates). The stages in the column are each $H_{stage} = L/n$ tall, within which the gaseous and adsorbed phases are assumed to be completely equilibrated. Following Chapter 4 of A. Pocar's thesis [188], the rate of radon decays at a given (theoretical) stage of the trap can be modeled under the assumption that the radon source input to the column is a constant input (*i.e.* step function, 'Heaviside' distribution). For these measurements of breakthrough time, the input concentration of the carbon trap is constant provided by the high-activity Pylon brand [307] radon source with a constant flow rate, until radon breakthrough occurs.

Following Pocar, the time-dependent radon concentration $y_j(t)$ at each j^{th} stage in the trap, can

be modeled using a dimensionless time parameter $\xi = t/t_{\text{B.T.}}$ describing the number of characteristic breakthrough times $t_{\text{B.T.}}$ at a time t. The expected activity for each stage ($0 < j \leq n$) is composed of two general terms and is described by

$$y_j(t) = A_0 \left(1 - \exp(-n\xi) \sum_{k=1}^{j} \frac{(n\xi)^{j-k}}{(j-k)!}\right) + \sum_{k=1}^{j} y_k(0) \frac{(n\xi)^{j-k}}{(j-k)!}, \tag{4.6.2}$$

owing to the input concentration source of strength A_0, and the initial radon concentration $y_j(t=0)$ at each j^{th} stage in the trap. Given the high activity of the input source, and that the breakthrough measurement begins after an initial purge of nitrogen gas as described in **Section 4.2.2**, it is reasonable to assume the initial activity at each stage is zero, since $y_j(t=0) \ll 1{,}000\,\text{Bq/m}^3$ the nominal equilibrium concentration.

To measure the breakthrough time of a step input we compare the output concentration of the carbon trap measured by the RAD7 and fit the activity in the n^{th} (final) theoretical stage to a functional form

$$y_n(A_0, \xi) = A_0 \left(1 - e^{-n\xi} \sum_{k=1}^{n} \frac{(n\xi)^{n-k}}{(n-k)!}\right) + \cancel{\text{I.C.}}^{\,0},$$

where we ignore the initial concentrations I.C. so

$$y_n(A_0, \xi) = A_0 \left(1 - e^{-n\xi} \left[\frac{(n\xi)^{n-1}}{(n-1)!} + ... + \frac{(n\xi)^2}{2!} + n\xi + 1\right]\right). \tag{4.6.3}$$

As described in **Section 4.2.2**, the high-activity radon source used in these tests produces $R_{\text{py}} = 14.6\,\text{Bq/min}$ when using a continuous flow-through source of carrier gas. The concentration at the output of the source, flowing into the trap input, for a relevant flow rate $F \approx 10\,\text{L/min}$ is expected to be

$$C_{\text{input}} = \frac{R_{\text{py}}}{F\tau} = \frac{14.6\,\text{Bq/min}}{10\,\text{L/min}} \approx 1460\,\text{Bq/m}^3, \tag{4.6.4}$$

equal to the equilibrium concentration A_0. The best-fit elution parameters A_0, $t_{\text{B.T.}}$, and n are determined using Eqn. 4.6.3; however, it is convenient to recast Eqn. 4.6.3 in terms of the breakthrough volume $V_{\text{B.T.}} \equiv F \times t_{\text{B.T.}}$ for runs where radon breakthrough has occurred. The dimensionless time ξ is then a function of flow F and breakthrough volume $V_{\text{B.T.}}$ as

$$\xi = {}^{t}\!/_{t_{\text{B.T.}}} = {}^{t\,F}\!/_{V_{\text{B.T.}}}. \tag{4.6.5}$$

The output concentration y of the n^{th} stage as a function of time

$$y_n(F, V_{\text{B.T.}}) = \frac{R_{\text{py}}}{F\tau} \left(1 - \exp\left(-n{\cdot}t\ ({}^{F}\!/_{V_{\text{B.T.}}})\right) \sum_{k=1}^{n} \frac{\left(n{\cdot}t\ ({}^{F}\!/_{V_{\text{B.T.}}})\right)^{n-k}}{(n-k)!}\right). \tag{4.6.6}$$

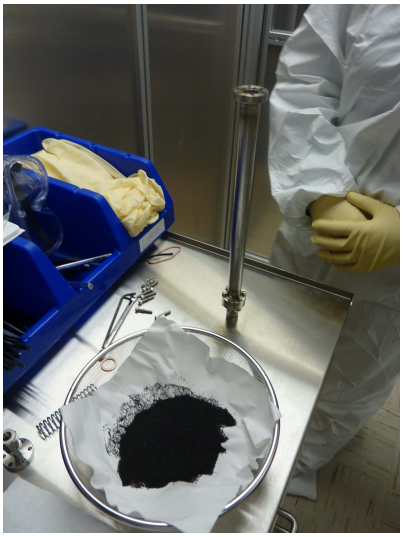

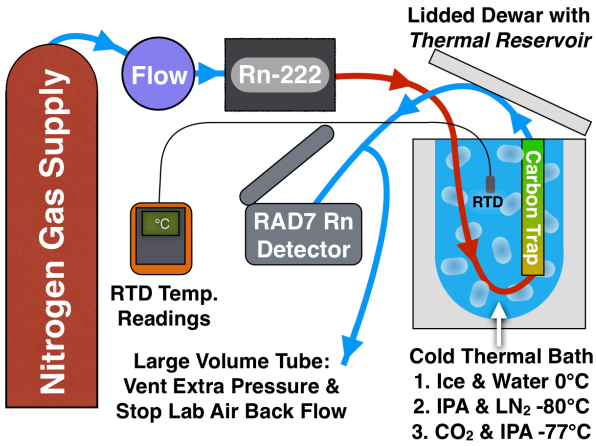

Figure 4.25: Left: Preparation of carbon sample for placement in a stainless-steel tube in the Syracuse low-radon cleanroom. Picture courtesy of R. Bunker. **Right:** Experimental set-up used to measure the carbon trap breakthrough time submerged in cold baths. Nitrogen gas flows continuously through a high-activity ^{222}Rn source producing a high concentration $C_{\text{input}} \approx 1,000\,\text{Bq/m}^3$ well above the lab air concentration $\sim 100\,\text{Bq/m}^3$. For the room temperature tests, performed by Megan and Ray, the trap was not placed in a temperature bath. For the cold tests, which I performed, the dewar was filled with ice water ($T = 273\,\text{K}$), or isopropyl alcohol (IPA) cooled to its freezing temperature ($T = 196\,\text{K}$) with either sparing LN_2 or solid CO_2 (dry ice). Dry ice sublimates 3°K below the IPA freezing temperature. The thermal bath temperature was monitored with a resistive temperature device (RTD) in the liquid. The trap output was connected to a RAD7, sampling the concentration continuously at $F_{\text{R7}} = 0.8\,\text{L/min}$, and to a long tube to prevent over pressure in the RAD7. The radon activity at the trap's output was measured in 10 minute intervals until the output concentration equilibrated to a high concentration A_0 after radon breakthrough.

It is worth noting that for very long breakthrough times approaching the 3.82 day half-life of radon, the concentration strength $^{R_{\text{Py}}}/_{F\tau}$ will be reduced by the decay of radon, by the factor $\eta = \exp(^{-t_{\text{B.T.}}}/_{5.52\,\text{d}})$.

4.6.2 Previously Measured Radon Breakthrough (293 K)

Megan Stark and Ray Bunker tested a 28.5 gram sample of etched SARATECH synthetic carbon expected to have low radon activity because a separate batch was measured in Ref. to be $\lesssim$ 2 mBq/kg [171]. At this level the sample would emanate less than $28.5\,\text{gm} \times 0.0017\,\text{mBq/gm} \approx 50\,\mu\text{Bq}$. The carbon was placed inside a stainless steel tube (the 'trap'), shown in the left panel of **Fig. 4.25**, and tested for radon breakthrough at room temperature. They used flow rates $F \approx 0.05,\ 0.25,\ 1,$ and 10 L/min through the high-radon source, directed through the carbon trap at room temperature and into a RAD7 electrostatic commercial radon detector [267, 343] measuring output concentrations as a function of time.

The radon breakthrough times measured at room temperature vary significantly for low flows $F \leq 0.94\,\text{L/min}$. In some case, the two day tests had no radon breakthrough. The continuous pumping speed of the RAD7 is merely $F_{\text{R7}} = 0.8\,\text{L/min}$. It is conceivable that with the impedance of the high-

activity source and trap, the transport of radon through the apparatus at flows $F \leq 0.94\,\mathrm{L/min} \approx F_{\mathrm{R7}}$ may be dominated by diffusion. The radon breakthrough times measured at room temperature with a flow $F \sim 9.4\,\mathrm{L/min}$ vary significantly from $t_{\mathrm{B.T.}} \sim 10\,\mathrm{min}$ to $t_{\mathrm{B.T.}} \sim 40\,\mathrm{min}$. Breakthrough times larger than 10 min, for such a small sample of carbon, are not convincing. Flow through the packed carbon geometry may be significantly reduced, preventing an a precise measurement to within an order of magnitude. For tests at flows $F > 0.94\,\mathrm{L/min}$ (larger than the RAD7 pumping speed), the breakthrough volumes measured are of order

$$V_{293\,\mathrm{K}} = F \times t_{\mathrm{B.T.}} \sim 10\,\mathrm{L/min} \times 10\,\mathrm{min} \approx 100\,\mathrm{L},$$

consistent with the expectation (from Eqn. 4.6.21) of carbon's surface area per mass $S \sim 1,300\,\mathrm{m^2/gram}$ [171, 188], and a dynamic heat of adsorption $\mathcal{H}_a \approx 29 \times 10^3\,\mathrm{J/mol}$. A breakthrough volume $V_{293\,\mathrm{K}} = 100\,\mathrm{L}$ is insufficient for radon-assay transfers, which may require $\Delta t_{\mathrm{trans}} = 8\,\mathrm{hrs}$

$$V_{\mathrm{tr}} = F_{\mathrm{tr}} \times \Delta t_{\mathrm{trans}} \gtrsim 10\,\mathrm{L/min} \times 480\,\mathrm{min} = 4.8\,\mathrm{m^3} \approx 50\,V_{293\,\mathrm{K}}. \tag{4.6.7}$$

As a result, we needed to take advantage of the exponential increase of the radon adsorption onto carbon and resultant breakthrough volume of carrier gas at cold temperatures.

Preparing the Source and the Cold Bath Apparatus I constructed an apparatus to measure the breakthrough time of radon at cold temperatures; a simple diagram is shown in the right panel of **Fig. 4.25**. I used a nitrogen dewar and a flow meter nominally set to $F_{\mathrm{nom}} = 9.4\,\mathrm{L/min}$ passing through the high-activity radon source. The source was fed to a carbon trap in a small dewar where ice water and cryogenics (CO_2 and LN_2) could be used to cool the trap. A RAD7 pumping continuously sampled the output of the trap at

$$F_{\mathrm{R7}} = 800\,\mathrm{mL/min} \ll F_{\mathrm{nom}} \approx 9.5\,\mathrm{L/min}.$$

The RAD7 measures the ^{222}Rn concentration via the short-lived ^{218}Po α decay in 10 minute intervals for $\sim 1.5\,\mathrm{hrs}$. A soft plastic tube, more than 20 ft long, was connected in parallel to the RAD7 at the trap output to avoid damaging the RAD7 with the $\mathcal{O}(10\,\mathrm{L/min})$ flow rate. The tube also prevents lab air back-diffusing into the input of the alpha counter.

For cold tests, the trap was submerged and cooled in two thermal baths with ice water $T_{\mathrm{ice}} = 0°\,\mathrm{C}$ and $T_{\mathrm{IPA}} = -77°\,\mathrm{C}$ near the freezing temperature of 'high-grade' isopropyl alcohol (IPA) obtained by the chemical storeroom on SDSM&T campus. I used solid blocks of CO_2 to cool the trap, pouring sparing amounts of LN_2 to keep the thermal bath cold, after the bath reached T_{IPA}. I used a resistive temperature device (RTD) in the liquid to monitor and adjust any increase to the trap temperature. The RTD was calibrated in ice water and carries a negligible uncertainty $\delta_{\mathrm{syst.}} \approx \pm 0.05\,°\mathrm{C}$. While monitoring the RTD, I added coolant (LN_2, CO_2, or ice) as necessary to keep a consistent bath temperature.

Before I could measure the radon adsorption of the same 28.5 gram sample of synthetic charcoal in the trap, I had to regenerate the trap and purge the radon source. I first measured concentration at the output of trap, at room temperature, to verify the concentration at the trap output

$$C_n \lesssim 50\,\mathrm{Bq/m^3} \ll 1,000\,\mathrm{Bq/m^3} \approx A_0$$

was much less than the nominal equilibrium concentration. Since the calibration radon is at such high levels, small deviations in this initial output will have little impact on the output concentration and the final result is impacted negilibly.

Following the trap regeneration, I purged the radon source by flowing nitrogen gas at $F_{\mathrm{purge}} \gtrsim 10\,\mathrm{L/min}$ for $t_{\mathrm{purge}} \gtrsim 20\,\mathrm{minutes}$, which gives an expected number of volume exchanges

$$N_{\mathrm{vol.\ exch.}} = \frac{V_{\mathrm{flow}}}{V_{\mathrm{py}}} \gtrsim \frac{20\,\mathrm{min}\cdot\ 10\,\mathrm{L/min}}{0.106\,\mathrm{L}} \approx 1,900 \tag{4.6.8}$$

removing all previously built-up radon. Once a steady trap temperature was achieved, I could begin measuring the radon concentration by ceasing the Pylon purge flow and connecting the radon source output to the carbon trap. For each breakthrough test, the radon concentration at the output of the carbon trap was measured until either breakthrough occurred, or the experiment failed in some way such as using all the gas in a dewar and losing flow, nylon tubing breaking at very low temperatures, or heating overnight resulting in inconsistent trap temperatures and pre-mature radon breakthrough.

4.6.3 Radon Breakthrough in Ice-Water (273 K)

For a successful breakthrough measurement, I determined the best-fit parameters from Eqn. 4.6.6, by picking the minimum χ^2

$$\chi^2(n, V_{\mathrm{B.T.}}, F) = \sum_t \left(\frac{C_n - y_n(V_{\mathrm{B.T.}}, F)}{\sigma_C} \right)^2, \tag{4.6.9}$$

where $y_n(V_{\mathrm{B.T.}}, F)$ is the theoretical expectation determined from Eqn. 4.6.6, the time-dependent measured concentrations $C(t) = C_n \pm \sigma_C$ are summed over all measurement times t. This process of determining the best-ft model parameters is described in chapter 14 of *Numerical Recipes* [268], and chapter 3 of Knoll's *Radiation Detection and Measurement* [207]. The best-fit parameters $(n, V_{\mathrm{B.T.}}, F)$ minimize the χ^2 and produce the best theoretical expectation of the concentration as a function of time under the chromatographic plate model. Large χ^2 values indicate a poor fit of the proposed theory $y_n(V_{\mathrm{B.T.}}, F)$ to the measured time-dependent data $C(t) = C_n \pm \sigma_n$. For infinitely many measurements, the χ^2 approaches the number of degrees of freedom ν of the fit if the model is correct. The number of degrees of freedom

$$\nu_{\mathrm{single}} = N_{\mathrm{data}} - m_{\mathrm{single}} - 1 = N_{\mathrm{data}} - 4$$

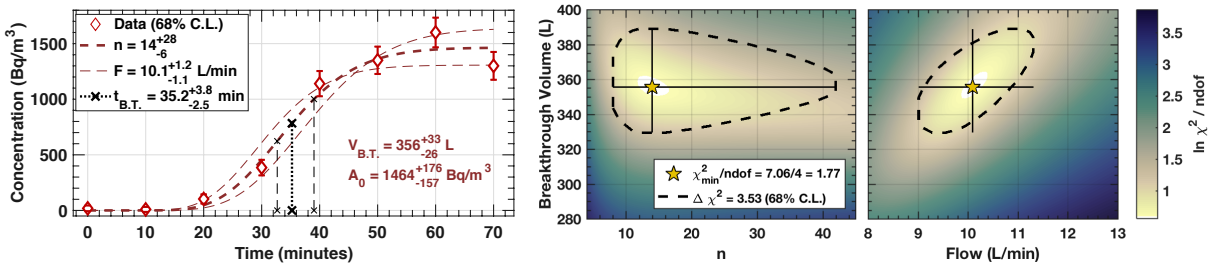

Figure 4.26: Left: Radon concentration ($\Diamond$ with 1σ statistical uncertainties) as a function of time for the Oct. 3 measurement at the output of a 28.5 gram carbon trap at $T = 0\,^{\circ}\mathrm{C}$ at a nominal flow $F_{\mathrm{nom}} = 9.4\,\mathrm{L/min}$. The best-fit radon concentration (dashed) from Eqn. 4.6.6 is shown with $\pm 1\sigma$ flow uncertainty. The best-fit parameters are $n = 14^{+28}_{-6}$, $V_{\mathrm{B.T.}} = 356^{+33}_{-26}\,\mathrm{L}$, and $F = 10.1^{+1.2}_{-1.1}\,\mathrm{L/min}$. The derived breakthrough time $t_{\mathrm{B.T.}} = 35.2^{+3.7}_{-2.5}\,\mathrm{min}$ (shown as $\times$). The best-fit equilibrium concentration $A_0 = 1460^{+180}_{-160}\,\mathrm{Bq/m^3}$. The goodness of fit $\chi^2_{\mathrm{min}}/\mathrm{ndof} = 7.06/4 \approx 1.77$ with a p-value $= 0.13$. **Right:** Two-dimensional colormaps of the χ^2 for the model parameters $V_{\mathrm{B.T.}}$, stages n (*left*), and $V_{\mathrm{B.T.}}$ and flow rate F (*right*), at the best $n = 14$ with best-fit parameters ($\bigstar$) shown with errorbars indicating 68% C.L. derived from $\Delta\chi^2 = 1$.

depends on the number of data points N_{data} and the number of fit parameters $m_{\mathrm{single}} = 3$ (n, V, F) for a single measurement. The appropriate confidence limits to the best-fit parameters are found by varying a single parameter $x \in (F, V, n)$ (about the best-fit triplet) until the χ^2 deviates by a given amount. The value of χ^2 at a test value x' gives rise to a difference

$$\Delta\chi^2(x') \equiv \chi^2(x') - \chi^2(x_{\mathrm{best}}) = \chi^2(x') - \chi^2_{\mathrm{min}}. \tag{4.6.10}$$

For a two-parameter model, when $\Delta\chi^2 = 2.30$ (4.61), the maximum and minimum parameters give the 68.3% (90%) confidence intervals. A table in Chapter 15 (p. 697) of Numerical Recipes [268] gives a list of $\Delta\chi^2$ and the corresponding significance for a given number of fit parameters.

First Breakthrough Measurement

The first ice water test on October 3, 2015 was performed for 70 minutes while the flow meter was set to $F_{\mathrm{nom}} = 9.4\,\mathrm{L/min}$. I noted the temperature, using an RTD in the bath, every 3–5 minutes. I stirred the bath frequently and the temperature didn't deviate significantly during the test. The results of the first test at ice-water temperatures are shown in **Fig. 4.26**. The left panel shows the radon concentration C_n as a function of time at the output of the carbon trap with the best-fit curve from Eqn. 4.6.6. The best-fit breakthrough volume

$$V_{\mathrm{B.T.}} = 357^{+33}_{-29}\,\mathrm{L} \qquad (68\%\,\mathrm{C.L.}), \tag{4.6.11}$$

and the flow $F = (10.2 \pm 1.2)\,\mathrm{L/min}$. The number of best-fit stages for the carbon trap $n = 14^{+28}_{-6}$ with a wide range of theoretical stages giving an acceptably similar goodness of fit to the data. The 68% uncertainties on the model parameters are derived from the maximum and minimum parameters enclosed by the $\Delta\chi^2 = 3.53$ contours shown in the right panel of **Fig. 4.26** and the

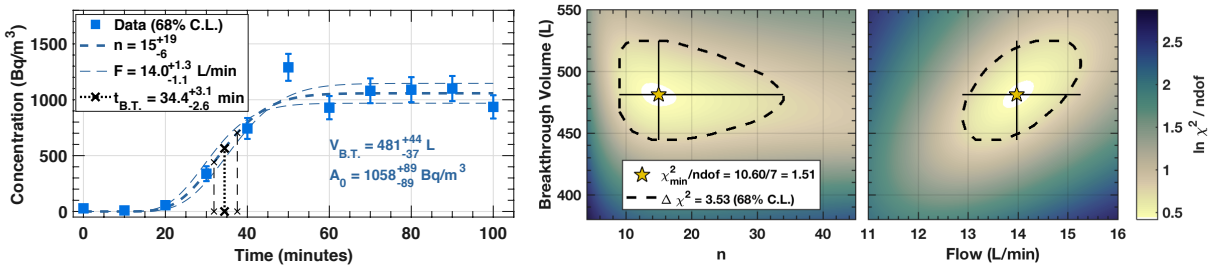

Figure 4.27: Left: Radon concentration (□ with 1σ statistical uncertainties) as a function of time for the second measurement on Oct. 14 at the output of a 28.5 gram carbon trap at $T = 0\,^{\circ}\mathrm{C}$. The best-fit concentration from Eqn. 4.6.6 (dashed) is shown with $\pm 1\sigma$ flow uncertainty. The best-fit parameters are $n = 15^{+19}_{-6}$, $V_{\mathrm{B.T.}} = 481^{+44}_{-37}\,\mathrm{L}$, and $F = 14.0^{+1.3}_{-1.0}\,\mathrm{L/min}$, and the derived breakthrough time $t_{\mathrm{B.T.}} = 34.4^{+3.1}_{-2.6}\,\mathrm{min}$ (shown as ×), and derived equilibrium concentration $A_0 = (1060 \pm 90)\,\mathrm{Bq/m^3}$. The goodness of fit $\chi^2/\mathrm{ndof} = 10.6/7 \approx 1.51$ with a p-value = 0.16. **Right:** Colormap of $\ln(\chi^2/\mathrm{ndof})$ as a function of $V_{\mathrm{B.T.}}$ and n (*left*), and $V_{\mathrm{B.T.}}$ and F (*right*) with best-fit parameters (★) shown with errorbars indicating 68% C.L. derived from $\Delta\chi^2 = 3.53$. The χ^2 vs. n has been interpolated and (at 68% C.L.) the best-fit number of stages $n_{\mathrm{II}} = 15^{+19}_{-6}$.

best-fit breakthrough time

$$t^{\mathrm{I}}_{\mathrm{B.T.}}(273\ \mathrm{K}) = 35.2^{+3.9}_{-2.6}\,\mathrm{min} \qquad (68\%\,\mathrm{C.L.}).$$

The uncalibrated flow meter was set to $F = 9.4\,\mathrm{L/min}$ and was assumed to have a 10% uncertainty, and the fit results indicate a fractional uncertainty $^{\delta F}/_{F} = 1.2/10.2 \approx 11.9\%$, with the best-fit flow deviating from the nominal flow $F_{\mathrm{nom}} = 9.4\,\mathrm{L/min}$ by only 7.5%. The best-fit flow F indicates the expected equilibrium concentration for the measurement

$$A_0 = \frac{R_{\mathrm{py}}}{F\,\tau} = \frac{14.6\,\mathrm{Bq/min}}{10.2^{+1.1}_{-1.1}\,\mathrm{L/min}} \approx 1456^{+179}_{-144}\,\mathrm{Bq/m^3} \qquad (68\%\,\mathrm{C.L.}). \tag{4.6.12}$$

The goodness of fit $\chi^2_{\mathrm{min}}/\mathrm{ndof} = 7.07/4 \approx 1.77$ (calculated from Eqns. 4.6.9 and 4.6.10) with a p-value = 0.13. See Refs. [268, 344] for more detail on statistical inference with the χ^2 and p-value.

Second Breakthrough Measurement

Measuring the trap a second time was prudent to determine if the number of stages or the breakthrough volume would vary significantly, since they are expected to be fixed properties of the carbon trap geometry. Therefore, the radon breakthrough was measured again at 273 K in an ice-water bath on October 14, 2015 for 100 minutes while the flow meter was again set to $F_{\mathrm{nom}} = 9.4\,\mathrm{L/min}$. The temperatures were consistent throughout data taking. The results of the second ice-water test are shown in **Fig. 4.27**. The left panel shows the radon concentration at the output of the carbon trap with the best-fit curve indicating the best number of theoretical stages $n = 15$ is consistent with the first measurement, as expected. The right panels show the χ^2 near the best-fit $V_{\mathrm{B.T.}}$ versus (left) n and (right) F. The best-fit breakthrough volume

$$V^{\mathrm{II}}_{\mathrm{B.T.}}(273\ \mathrm{K}) = 481^{+44}_{-37}\,\mathrm{L} \qquad (68\%\,\mathrm{C.L.}). \tag{4.6.13}$$

is considerably larger than the first breakthrough measurement. Using the lower bound uncertainty on the larger measurement, and the upper bound uncertainty on the smaller measurement indicates the second breakthrough volume is consistent at the 2.5σ level with the first measurement

$$\frac{\mu_2 - \mu_1}{\sqrt{\sigma_2^2 + \sigma_1^2}} = \frac{481 - 357}{\sqrt{(-37)^2 + 33^2}} \approx 2.5. \tag{4.6.14}$$

The apparent flow $F_{\mathrm{II}} = (13.9^{+1.3}_{-1.0})\,\mathrm{L/min}$ is 47% larger than the nominal flow and inconsistent with the first measurement. The fractional uncertainties on this second measurement are larger on the breakthrough volume ($\pm 4.2\%$ vs ± 2.8) and smaller on flow ($\pm 3.9\%$ vs ± 3.5) with comparable uncertainties on the number of theoretical stages $n_{\mathrm{I}} = 14^{+48\%}_{-24\%}$ vs $n^{\mathrm{II}} = 15^{+44\%}_{-28\%}$. The second breakthrough time

$$t^{\mathrm{II}}_{\mathrm{B.T.}}(273\ \mathrm{K}) = \frac{V^{\mathrm{II}}_{\mathrm{B.T.}}}{F^{\mathrm{II}}} = 34.5^{+3.2}_{-2.7}\,\mathrm{min} \qquad (68\%\,\mathrm{C.L.}),$$

is consistent at 1σ with the first measurement. The goodness of fit $\chi^2_{\mathrm{min}}/\mathrm{ndof} = 10.67/7 \approx 1.52$ and p-value $= 0.16$ indicates the chosen parameters of the theory match the data reasonably well. The breakthrough times measured above are consistent at the 1σ level. The flow meter was not calibrated for these measurements, so a difference $\sim 20\%$ is not unreasonable; however, the 36% higher computed flow rate seems suspiciously large and potentially indicates that the flow rates may vary significantly during the tests, or that there may be some unknown source of systematic uncertainty. For a single trap under the same flow rate, the number of theoretical stages n, and the breakthrough volume $V_{\mathrm{B.T.}}$ really ought to be the same. So given that the computed flows differ by 40%, one might naively expect the apparent flows and breakthrough times to differ, with a consistent number of stages, which are consistent to much less than 68% C.L., and breakthrough volume, which has not been observed.

Combined Ice-Water Breakthrough Results

I performed a global fit to the datasets for a range of stages n and volumes $V_{\mathrm{B.T.}}$, allowing the best-fit (apparent) flow for each experiment ($F_{\mathrm{glob-I}}$, and $F_{\mathrm{glob-II}}$) to be independent in an attempt to improve the fit results. The globally-best-fit trap parameters (n_{st}, $V_{\mathrm{B.T.}}$) were selected from the minimum total goodness-of-fit parameter

$$\chi^2{}_{\mathrm{glob}}(n, V_{\mathrm{B.T.}}) = \chi^2_{\mathrm{I}} + \chi^2_{\mathrm{II}} = \chi^2(n, V_{\mathrm{B.T.}}, F_{\mathrm{glob-I}}) + \chi^2(n, V_{\mathrm{B.T.}}, F_{\mathrm{glob-II}}) \tag{4.6.15}$$

with unconstrained flows. The nominal flows for each experiment need not be related or constrained, though the single-data fits indicate they are near 10–14 L/min. The results of the global fit are shown in **Fig. 4.28**. The best-fit global breakthrough volume

$$V^{\mathrm{glob}}_{\mathrm{B.T.}}(273\ \mathrm{K}) = 425^{+13}_{-8}\,\mathrm{L}, \tag{4.6.16}$$

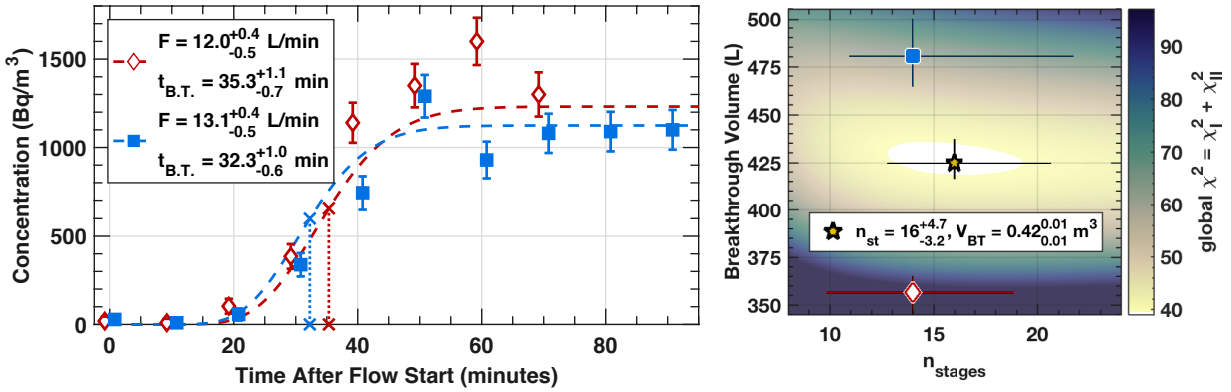

Figure 4.28: Left: Radon concentration (1σ statistical uncertainties) as a function of time for both measurements of a 28.5 gram carbon trap at $T = 0\,^{\circ}\mathrm{C}$. The best-fit concentration from Eqn. 4.6.6 with global best-fit trap parameters $n_{\mathrm{st}} = 16$, $V_{\mathrm{B.T.}} = (420 \pm 10)\,\mathrm{L}$, and the (independent) best-fit flow for each experiment $F_{\mathrm{glob-I}} = 12.0^{+0.4}_{-0.5}\,\mathrm{L/min}$ and $F_{\mathrm{glob-II}} = 13.1^{+0.4}_{-0.5}\,\mathrm{L/min}$ are shown (dashed). The goodness of fit $\chi^2/\mathrm{ndof} = 38.9/14 \approx 2.78$ and the $p-$value $= 0.38 \times 10^{-3}$, indicate a poor fit. **Right:** Two-dimensional colormap of χ^2 near the best-fit parameters $V_{\mathrm{B.T.}}$ versus n_{st} for the best-fit flows $F_{\mathrm{I/II}}$ with best-fit global trap parameters (★) shown with errorbars indicating 68% C.L. derived from one-dimensional $\Delta\chi^2 = 1$ with fit results from the single breakthrough measurements (Eqns. 4.6.11 ◊, and 4.6.13 □). The number of stages is consistent at better than 1σ between all fits. The breakthrough volumes are consistent at about 3σ.

inconsistent at the 3σ level with both measurements $V^{\mathrm{I/II}}_{\mathrm{B.T.}}(273\ \mathrm{K})$. The best-fit flows for each of the (combined) measurements $F_{\mathrm{glob-I}} = 12.0^{+0.4}_{-0.5}\,\mathrm{L/min}$ are inconsistent with F_{I} at about 3σ, and $F_{\mathrm{glob-II}} = 13.1^{+0.4}_{-0.5}\,\mathrm{L/min}$ is consistent with F_{II} at about 2σ. The derived equilibrium concentrations $A_{\mathrm{I}} = 1233^{+31}_{-43}\,\mathrm{Bq/m^3}$, $A_{\mathrm{II}} = 1125^{+31}_{-43}\,\mathrm{Bq/m^3}$ are brought closer to agreement with each other, and consistent with their respective initial measurements at 3σ. However, by eye, the time-dependent concentrations for each measurement do not appear to equilibrate to the same value. Perhaps this is incorrect, and they do have a close equilibrium concentration and the confusion between the datasets arises due to the measured value at 60 minutes which appear to diverge in opposite directions for each measurement, which would bifurcate the apparent best-fit flows which are nominally equal. The flows were set with a passive flow meter, as opposed to a mass flow controller. It is reasonable to assume the flows for each measurement differ by 20%. The flows are also expected to fluctuate, perhaps in a diverging manner. Combining the data doesn't improve the fit results with a somewhat higher

$$\chi^2_{\mathrm{min}}/\mathrm{ndof} = \frac{\chi^2_{\mathrm{I}} + \chi^2_{\mathrm{II}}}{n_{\mathrm{I}} + n_{\mathrm{II}} - n_{\mathrm{parm}} - 1} = \frac{19.7 + 19.1}{8 + 11 - 5} = \frac{38.9}{14} \approx 2.78 \tag{4.6.17}$$

for the global fit. The $p-$value $= 0.367{\times}10^{-3}$ is significantly lower than the single data fits. Altering the fit constraints to require only the number of stages to be shared would not change the fit results drastically from the single fits, since the number of stages in the global and single fits are consistent. In this case, the breakthrough volumes would diverge significantly, as observed for the single fits. However, the global-fit $n^{\mathrm{glob}} = 16^{+4.7}_{-3.2} = 16^{+29\%}_{-20\%}$, has a smaller fractional uncertainty than the ${}^{\delta n}/_{n} \approx^{+45\%}_{-25\%}$ for the single fits.

The best-fit breakthrough times $t_{\text{B.T.}} \approx 35\,\text{min}$, which dictates the time-dependent shape of the theoretical curves, and the number of stages $n \approx 15$ are consistent for separate breakthrough measurements. We expect the breakthrough volume and the theoretical number of stages each to be the same for a given trap [188]. The tests were performed with the same nominal flow, so the breakthrough volume should be the same and the breakthrough time $t = V/F$ should differ by the ratio of the flows. To understand the discrepant best-fit flows and volumes, it is useful consider the systematic effect of two cases of leaks in the experimental apparatus: before and after the high-activity calibration source.

A gas leak occurring before the radon source will push radon through the source more slowly than the nominal flow. This will lead to a lower flow than indicated by the flow meter at the input of the calibration source and a higher equilibrium concentration, and a larger breakthrough time. However, a gas leak after the source will carry away the high-activity radon $\mathcal{A}(t)$ from the source, leading to a potentially lower measured radon output activity. If the pressure at the location of the leak is not much higher than the ambient lab air pressure, then lab air may enter the apparatus at the leak location and be carried to the RAD7 which will measure an artificially low concentration that will be a mix of the lab air

$$A_{\text{measured}} = \mathcal{A}(t) \times (1 - f_{\text{leak}}) + A_{\text{lab}} \times f_{\text{leak}} = \mathcal{A}(t) - \big(\mathcal{A}(t) - A_{\text{lab}}\big) f_{\text{leak}}, \tag{4.6.18}$$

where the fraction of gas measured by the RAD7 A_{measured} is composed of the fraction f_{leak} of leaked-in lab air at a concentration A_{lab} and $(1 - f_{\text{leak}})$ of the activity $\mathcal{A}(t)$ from the source output. A leak of this nature will give rise to slightly larger concentrations at early times–which ought to start at at an activity $A_0 \approx 0\,\text{Bq/m}^3$, and slightly lower concentrations than the nominal equilibrium at late times.

If a leak was present in the system, it is reasonable to assume that the second measurement with a computed average flow $\sim 40\%$ larger than the nominal flow, and an equilibrium concentration $\sim 40\%$ lower than the first measurement, suffered from a leak carrying the high-activity gas away before it could be sampled by the RAD7. Assuming the lab air concentration $A_{\text{lab}} \approx 50\,\text{Bq/m}^3$, and the input equilibrium concentration $\mathcal{A}_0 = 1,400\,\text{Bq/m}^3$ (before the leak, indicated by the first measurement whose breakthrough time is consistent), using the best-fit equilibrium activity $A_{\text{measured}} = 1,000\,\text{Bq/m}^3$, results in the leak fraction

$$f_{\text{leak}} = \frac{\mathcal{A}_0 - A_{\text{measured}}}{\mathcal{A}_0 - A_{\text{lab}}} = \frac{(1,400 - 1,000)\,\text{Bq/m}^3}{(1,400 - 50)\,\text{Bq/m}^3} = \frac{400}{1350} \approx 28\%. \tag{4.6.19}$$

This hypothesis may explain why the number of stages and breakthrough times are consistent between measurements sharing the same nominal flow. In any event, measuring the adsorption and breakthrough at colder temperatures is useful since radon transfers take about an hour (5 hours) for the small (large) emanation chamber.

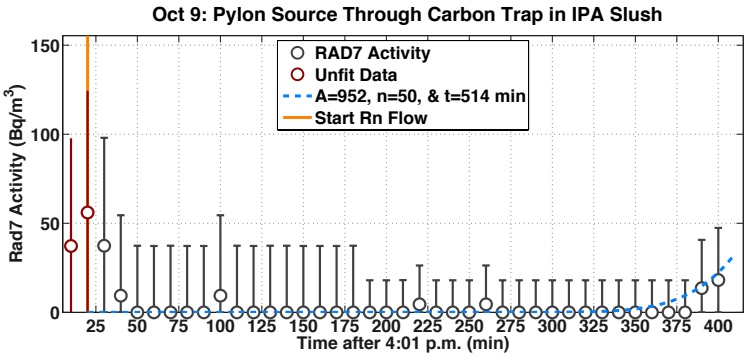

Figure 4.29: Radon concentration with statistical uncertainties (68% C.L.) as a function of time at the carbon trap output at IPA freezing temperature $T \approx -80 \pm 10\,^{\circ}\mathrm{C}$ with colder temperatures due to the occasional LN_2 cooling. Although this test ended early due to overnight heating, a conservative lower limit, based on the measurement duration and nominal flow, can be placed on the breakthrough volume $V_{\mathrm{B.T.}} \lesssim 10\,\mathrm{L/min} \times 396\,\mathrm{min} \approx 4\,\mathrm{m}^3$.

4.6.4 Lower Limits on Radon Breakthrough in Dry Ice (196 K)

After the ice water measurements we decided to use dry ice (sold CO_2) and isopropyl alcohol (IPA) bath to cool the trap below 200 K. For the IPA slush bath (196 K), I prepared the trap for use with a 10 L nalgene dewar filled with IPA by one of two methods. For one preparation, I poured LN_2 until an IPA ice crust formed and used a non-metallic stirrer to break the ice and mix the slush until an IPA ice ball formed. For another test, I used solid dry ice pellets and blocks. I monitored the temperature of the bath intermittently while adding LN_2 or CO_2 about once an hour to re-cool the slush to keep the temperature deviation of the thermal bath $\delta T_{\mathrm{bath}} \lesssim 5\,^{\circ}\mathrm{C}$ per hour. I built a custom-fitted two-piece foam dewar cover to lessen environmental heating of the trap during data taking. This inspired an elegant solution to help keep the carbon trap and liquid nitrogen traps on the R.E.S. gas panel cold in-situ. We use a two-piece foam cover to fit easily around the carbon trap. Even with this extra dewar insulation, due to the small amount of dry ice I purchased, hourly cooling was still necessary and heating in the middle of the night occurred for two of the CO_2 measurements. The other two measurements failed due to loss of nitrogen dewar pressure and shattered hard nylon tubing. No dry-ice test ran for longer than 6,6 hours.

An example measurement including 6 hrs of data with no breakthrough is shown in **Fig. 4.29**. Without the equilibrium concentration after radon breakthrough, there is no way to estimate the flow F from the output concentration $C \propto F^{-1}$. Without significant time series data taken of the concentration rising during elution, the number of theoretical stages may not be well bound. However, it is possible to estimate conservative lower limits on the breakthrough time $t_{\mathrm{B.T.}} = {}^{V_{\mathrm{B.T.}}}/_{F}$ of the trap at 196 K from the duration of the test. The longest test ran for $t_{196\,\mathrm{K}} \approx 400$ minutes $= 6.6$ hrs. Since the breakthrough volume of carrier gas passed through the trap depends on the flow which is unknown, we need to estimate the average flow during the measurement. The best-fit flows $F_{273\,\mathrm{K}} \approx (10\text{–}14)\,\mathrm{L/min} = (12 \pm 2)\,\mathrm{L/min}$ computed from the ice-water tests can help give a lower bound on the radon breakthrough volume of gas for 28.5 grams of carbon. Using uncertainties

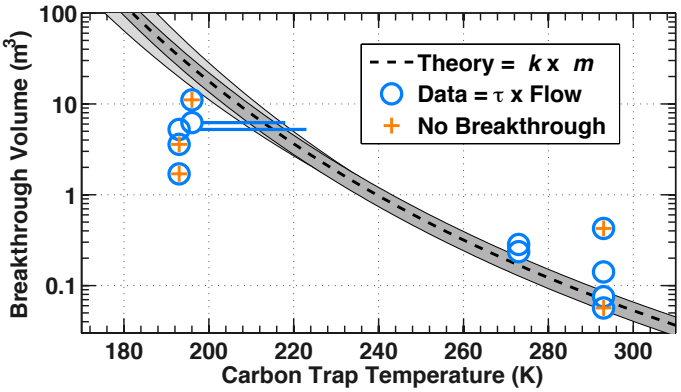

Figure 4.30: Radon breakthrough volume measurements (◯) taken with a 28.5 gm carbon trap as a function of temperature. The theoretical expectations [188] shown (dashed line) include a $\delta k_a = 15\%$ uncertainty (light gray fill region) and $\delta \mathcal{H}_a = 10\%$ uncertainty (dark gray fill region). The uncertainty in the breakthrough volume for the ice water measurements $\mathcal{O}(3\%)$ are smaller than the markers. Lower-limits on the breakthrough volume $V_{\text{low}} = F\, t_{\text{meas}}$ for dry ice tests with no breakthrough are shown (+) with the measurement time using a conservative flow $F = 10\,\text{L/min}$. Dry-ice measurements shown with horizontal errorbars indicate the minimum and maximum temperatures (> 99%C.L.) for tests where overnight heating occurred. The breakthrough volume of the trap at room temperature are unconvincing, and are > 5× too small for the transfers planned R.E.S.transfers. The cold tests confirm the expectation from Eqn. 4.6.21.

on the expected flow for the ice water test, which were carried out at the same nominal flow as the dry ice experiments, and a $m = 28.5\,\text{gram}$ carbon trap, gives an expected breakthrough volume

$$V_{\text{B.T.}}\big|_{196\,\text{K}} \gtrsim F \times t_{196\,\text{K}} \approx (12 \pm 2)\,\text{L/min} \times 400\,\text{min} \approx 4.8\,(1 \pm 0.17)\,\text{m}^3. \tag{4.6.20}$$

This volume provides the amount of LN_2 carrier gas needed to perform an 8 hour radon transfer with the large emanation chamber at a flow 10 L/min.

The breakthrough volume measurements at room temperature, ice water, and dry ice temperatures are summarized in **Fig. 4.30**. The theoretical curve $V_{\text{thy}} = k_a(T) \cdot m$ uses an assumed value for the adsorption coefficient, as given in **Section 4.2.1** by

$$k_a(T) = (0.0070\,S - 3.51)\exp\Big(\tfrac{\mathcal{H}_a}{R}(1/T - 1/273)\Big), \tag{4.6.21}$$

with the heat of adsorption $\mathcal{H}_a \approx 29 \times 10^3\,\text{J/mol}$, and the assumed surface area per mass $S = 1342\,\text{m}^2/\text{gram}$ for the $m = 28.5\,\text{gram}$ carbon sample.

4.6.5 In-Situ Radon Breakthrough Evaluation (196 K)

Following the ice water and CO_2 tests described in **Section 4.6.3** and **Section 4.6.4**, Rashyll Leonard and Eric Miller installed a 70 gram carbon trap on the R.E.S. gas panel, as shown in **Fig. 4.31**. The left panel shows the initial sketch inside the dewar; the right (middle) panel shows the trap following installation with(out) the dewar. The carbon trap is designed to be deployed in a dewar filled with isopropyl alcohol (IPA) and solid dry ice sublimating at $T_{CO_2} \approx -80\,°\text{C}$ just below

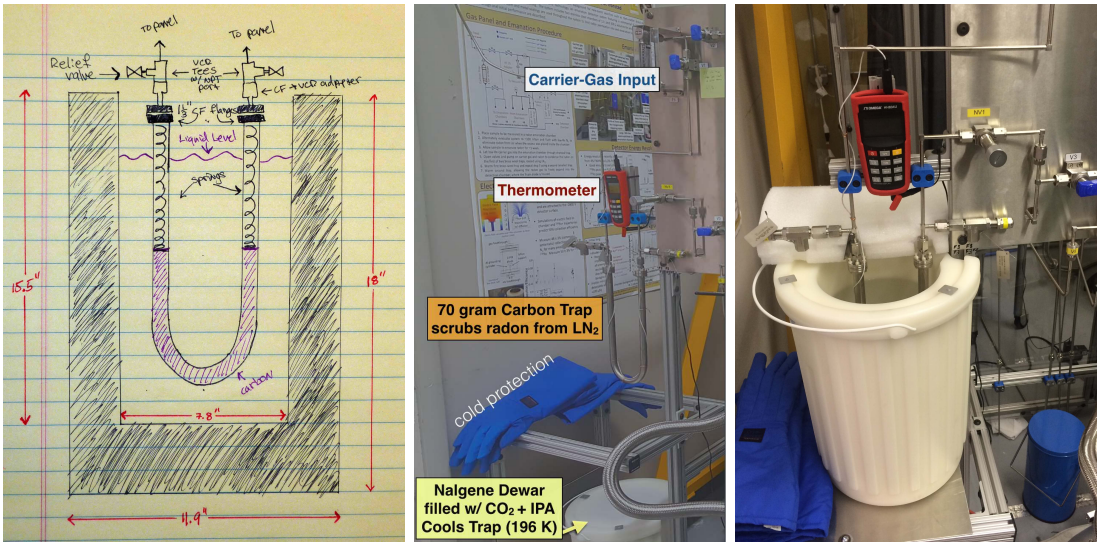

Figure 4.31: Left: Dimensioned sketch (by R. Leonard) of the carbon (purple) trap inside the Nalgene dewar (shaded black). **Middle:** Thermometer wrapping around the 3/4" metal trap ensures that we can monitor the IPA bath temperature with the RTD and add CO_2 as necessary. **Right:** Carbon trap at the panel input placed inside a Nalgene dewar. We place CO_2 (196 K) in an IPA bath and use foam covers, inspired by my initial breakthrough tests of the 28.5 gram carbon sample, to insulate the cold IPA. Figures courtesy of R. Leonard.

the IPA freezing temperature $T_{\text{IPA}} \approx -77\,^{\circ}\text{C}$ with a two-piece foam cover that fits snugly inside the dewar lip. The tests described in **Section 4.6.3** showed that the 28.5 gram carbon trap at T_{IPA} provides sufficient radon adsorption for a radon transfer at a flow rate $F_{\text{tr}} = 10\,\text{L/min}$ lasting

$$t_{\text{B.T.}}(196\,\text{K}) = \frac{V_{\text{B.T.}}}{F_{\text{tr}}} = \frac{5\,\text{m}^3}{10\,\text{L/min}} \approx 8.3\,\text{hrs}. \tag{4.6.22}$$

Rashyll Leonard and I used solid CO_2 to cool the newly installed carbon trap to 196 K in preparation of an in-situ breakthrough measurement of the carbon trap. We used a flow meter to set the flow through the high-activity Pylon source to $F_{\text{nom}} = 20\,\text{L/min}$. The output of the carbon trap was evacuated by the scroll pump. We measured the radon concentration at the output of the trap with a RAD7 pumping continuously, sampling gas from the scroll pump. The breakthrough test continued with no increase in radon activity at the trap output for 2.7 days, before we stopped the test for the weekend. This dry ice test did not heat significantly overnight due to the mass of dry ice used. This test may have used in excess of 25 lbs of dry ice over the two day period, compared to the 5–10 lbs used in the 28.5 gram configuration. For this test, it is possible only to estimate a lower limit on the breakthrough volume of carrier gas

$$V_{\text{B.T.}} = F \cdot t_{\text{B.T.}} > F_{\text{nom}} \cdot t_{\text{meas}},$$

based on the measurement time $t_{\text{meas}} = 2.7\,\text{days}$ and the nominal flow rate $F_{\text{nom}} = 20\,\text{L/min}$. This corresponds a breakthrough volume

$$V_{\text{B.T.}} \geq (2.7\,\text{days} \cdot 1440\,\text{min/day})\,20\,\text{L/min} \times 1\,\text{m}^3/1000\,\text{L} \approx 75\,\text{m}^3 \tag{4.6.23}$$

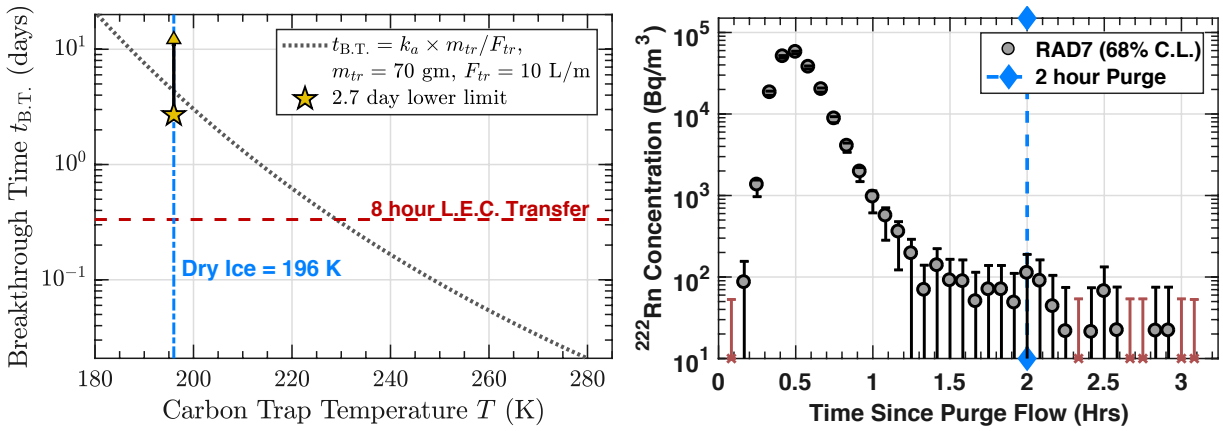

Figure 4.32: Left: Radon breakthrough time versus trap temperature for the 70 gram carbon trap. The theoretical expectation for the breakthrough time (from Eqn. 4.6.21) assumes a conservatively high transfer flow $F_{\rm tr} = 10\,{\rm L/min}$, resulting in a shorter period before breakthrough. The 2.7 day lower limit on breakthrough time $t_{\rm B.T.}$ (★) is shown at the carbon trap temperature $T_{\rm CO_2} = 196\,{\rm K}$ (blue dot dash). A long $t = 8\,{\rm hr}$ large emanation chamber transfer is shown (dashed red) for reference; the trap is expected to provide radon-free LN_2 boil-off for up to 5 days. **Right:** Radon concentration measured by the RAD7 (○) versus time while purging the R.E.S. carbon trap. Intervals with no counts are shown (red ×'s). The radon concentration appears to decrease by 3 orders of magnitude in the hour-long period from about (0.5–1.5) hrs. Before a radon transfer begins, the carbon trap is regenerated by purging for two hours (blue ◊) with the dewar and scroll pump.

which is sufficiently large compared to the gas volume needed for a radon transfer through the 300 L large emanation chamber. Radon transfers from the large chamber typically take 6 hours, with an output flow in the range $F = 1$–$10\,{\rm L/min}$. The flow rate for transfer $F_{\rm tr} \approx 10\,{\rm L/min}$, so a radon transfer could take

$$t_{\rm max} = {}^{F_{\rm nom}}\!/_{F_{\rm tr}} \times t_{\rm meas} \approx {}^{20}\!/_{10} \times 2.7\,{\rm d} \approx 5.5\,{\rm days}$$

before radon emanating from within the dewar would pass completely through the trap and pose a background to the radon assay. The lower-limit on breakthrough time we demonstrated is compared to the theoretical expectation for the $m = 70\,{\rm gm}$ trap, and a flow $F_{\rm tr} = 10\,{\rm L/min}$ in the left panel of **Fig. 4.32**.

Radon from the (low-activity) carbon sample will diffuse and emanate from the surface of carbon during the time preceding a transfer when it is not in use. Because the emanation rate is expected to be low radon trapped from the previous transfer poses a larger contaminant threat. To avoid capturing this contaminant in the brass wool traps along with the radon transferred from the emanation chamber, we need to remove the radon in the trap before cooling the trap with dry ice and starting the transfer. Rashyll and I measured the regeneration of the carbon trap following the 2.7 day breakthrough test to understand how long this pre-transfer purge should take. The trap was warmed to near room temperature and we flowed LN_2 boil-off through the trap evacuating the adsorbed (and emanated) radon with a scroll pump. The pump output was fed to a RAD7 measuring the concentration in 5 minute intervals for ≈ 3 hours with the dewar regulator set to $P = 0\,{\rm psig}$ applied at the trap input (corresponding to about $P_{\rm atm} = 680\,{\rm Torr}$ atmospheric pressure

in SD) and $P_{\text{out}} \approx 50\,\text{Torr}$ at the trap output.

The radon activity during this regenerative purging of the carbon trap is shown the right panel of **Fig. 4.32**. The radon concentration increases substantially as the trapped radon is released, followed by a significant decrease in output concentration over an hour and a half period. Most of the captured radon makes its way to the output after 60 min of flow. An order-of-magnitude estimate on the activity released during a true regeneration may be made by considering the radon from the LN_2 dewar with an activity $C_{\text{LN}} \leq 1\,\text{mBq/m}^3$ [165] trapped during a $t_{\text{trans}} = 8\,\text{hr}$ transfer, performed with a transfer flow $F \approx 10\,\text{L/min}$, and a trap pressure $P_{\text{trap}} \approx 50\,\text{Torr}$. The rate of radon decays in the carrier gas is expected to be no more than

$$\begin{aligned} R_{\text{trapped}} \leq C_{\text{LN}} V_{\text{trans}} &= C_{\text{LN}_2}\, F\, t_{\text{trans}}\, (P_{\text{trap}}/P_{\text{atm}}) \\ &= 1\,\text{mBq/m}^3 \cdot 0.010\ \text{m}^3/\text{min} \cdot 480\ \text{min} \cdot \cancel{(50/680)} \to 7.35\% \\ &\approx 0.35\ \text{mBq}. \end{aligned} \tag{4.6.24}$$

To obtain a worst case, we may neglect the radon decay during the first 8 hr transfer which leaves

$$\exp(-8/24/5.52) \approx 95\% \tag{4.6.25}$$

of the contaminant. The decay of this sample occurring over the 4 day period between the transfers, while the sample is emanated, leaves $\eta_{\text{decay}} = \exp(-4/5.52) \approx 48\%$ of the trapped radon. Assuming the radon trapped by the carbon R_{trapped} before the purge shares the same time-dependent regenerative reduction, as shown in the right panel of **Fig. 4.32**, the radon removed before the first hour would be well above 95% of the radon purged before the first 2 hrs of the regenerative flow. In this case, an hour of flow might reduce the trapped radon R_{trapped} by some $\eta_{\text{regen}} = 0.05$ of the originally captured 0.35 mBq so the unremoved radon from the previous transfer

$$R_{\text{unremoved}} = \eta_{\text{decay}} \eta_{\text{regen}} R_{\text{trapped}} = 0.48 \times 0.05 \times 0.35\,\text{mBq} \approx 8.5\,\mu\text{Bq}, \tag{4.6.26}$$

well below the 0.2 mBq detector sensitivity. We purge the carbon trap at room temperature because desorption is more effective at higher temperatures. By flowing boil-off N_2 through the trap to the auxiliary vacuum pump for

$$t_{\text{regen}} = 2\,\text{hours}, \tag{4.6.27}$$

we remove the previously trapped radon which desorbed from the surface of the carbon. After a two-hour regenerative purge, a radon transfer can begin.

4.7 Conclusions

I have helped commission the R.E.S. at SDSM&T by installing a potted HV feedthrough and teflon stand and collar to prevent arcing in the detection chamber. Installing an isolation transformer and grounding lines to the electronic components and detection vessel, the noise environment is reduced significantly so that we can perform low-background radon assays. We measured the radon transfer efficiency of two methods, free of systematic uncertainties. Varying the pressure of the 300 L emanation vessel by a factor of four, three times, yields a radon transfer efficiency $\gtrsim 95\%$. I helped reduce the two dominant detector backgrounds: from radon in the carrier gas and from back-diffused radon in the detection chamber. By measuring the temperature-dependent radon adsorption onto the carbon sample, radon transfers may be performed from our 300 L vessel for 16 hours before radon from the dewar will contribute to the detector backgrounds. By simulating and measuring radon back-diffusion in the teflon collar, we know the minimum wait time before a low-background assay can be performed.

Chapter 5
Radon Emanation Measurements of SuperCDMS Gaskets

Radon (specifically ^{222}Rn) has become an increasingly relevant background to rare-event searches. Radon emanation measurements are critical to obtain greater experimental sensitivities [159--162, 280, 282, 345] by helping these experiments reduce detector backgrounds, and SuperCDMS SNOLAB is no exception. Prompt decays of ^{214}Po and ^{214}Bi in the ^{222}Rn decay chain produce gammas at high energies $E_\gamma \approx (300\text{–}1.5)\,\mathrm{MeV}$. During operation, radon inside the lead gamma shielding will decay and eventually produce high-energy photons that will produce single-scatter electron-recoil backgrounds in the detectors. A lead shield, shown in **Fig. 3.1**, surrounding the detection volume (copper SNOBOX) is designed to reduce the external gamma-ray background from the SNOLAB drift by a factor $\times 10^6$ [74]. Though the iZIP detectors will have essentially perfect rejection based on the ionization yield, the High Voltage detectors, described in **Section 1.4.2**, may have no such discrimination capability and will be dominated by such events. By surrounding the shielding with a hermetically sealed radon purge barrier, using low-radon purge gas, the radon concentration will be reduced significantly. The radon purge design, surrounding the lead shield, from Lemer pax [261] is shown in the right panel of **Fig. 3.1**. The radon concentration requirement

$$\mathcal{C}_{\mathrm{req}} \leq 1\,\mathrm{Bq/m^3} \tag{5.0.1}$$

inside the lead shield ensures the rate of prompt ^{214}Po and ^{214}Bi gamma decays in the shielding will contribute $< 2\%$ of the total electron-recoil backgrounds [106]. A purge flow $F_{\mathrm{purge}} \approx (1\text{–}10)\,\mathrm{L/min}$ of liquid nitrogen boil-off with an expected a radon concentration $C_{\mathrm{LN}} \lesssim 0.5\,\mathrm{mBq/m^3}$ [165] will flush the gas in the shield and remove radon from the volume. The outer volume of air space surrounding the lead gamma shield $V_S = 5.66\,\mathrm{m^3}$ is sealed with a gasket from the ambient cavern, with a radon concentration $C_{\mathrm{SNO}} \approx 130\,\mathrm{Bq/m^3}$ [140]. To be most effective, the gasket material sealing the inner volume shield should neither produce radon nor allow radon to diffuse from the cavern environment. The proposed gaskets have already measured for radon diffusion (**Chapter 3**).

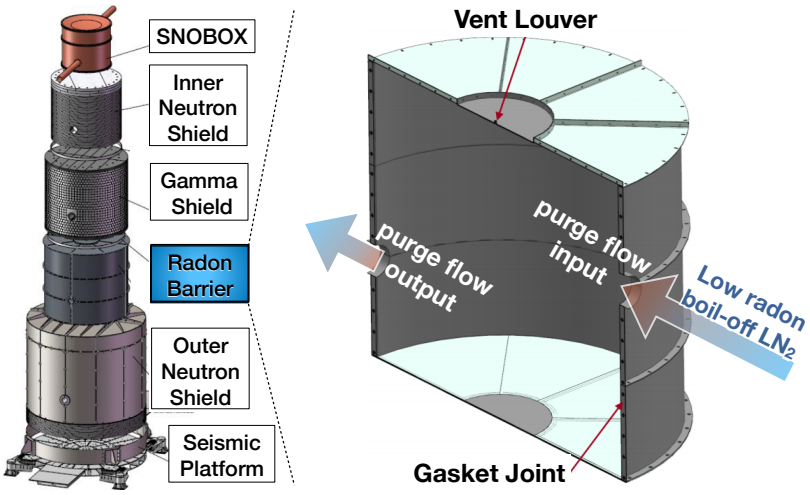

Figure 5.1: Left: Exploded view of shielding layers surrounding the nested copper cans (SNOBOX) housing the detectors. A graded lead shield, with an inner liner of low-activity ancient lead, will prevent gammas emitted by U/Th/K-bearing rock in the cavern walls from entering the detection volume [106, 192]. An aluminum enclosure (Radon Barrier) surrounding the lead shielding will be purged with low-radon gas to prevent significant radon-induced gamma production within the lead gamma shield. **Right:** Cut away of the radon purge lead shield design for SuperCDMS SNOLAB from LEMER PAX. The radon concentration requirement $\mathcal{C}_{\rm req} \leq 1\,{\rm Bq/m^3}$ for the experiment will keep the single-scatter electron-recoil backgrounds from prompt gamma decays to $< 2\%$ the overall experimental background requirement. A modest purge flow $F \sim {\rm L/min}$ of boil-off gas from a liquid nitrogen (LN_2) dewar will flush radon emanating inside the enclosure. The vessel will be kept at an overpressure of about 0.42 inches of water, to prevent radon entering through leaky cracks. Radon emanation from the gasket may significantly increase the backgrounds, therefore gaskets sealing the purge barrier along a $L_{\rm gasket} = 53\,{\rm m}$ total joint length need to be moderately radiopure.

Radon emanation of the gasket will also contribute to the steady-state radon concentration in the enclosure. The radon concentration $\mathcal{C}$ inside the shielding will depend on the flow rate F, the radon sources $\mathcal{S}$, and the radon concentration $C_{\rm LN}$ in the LN_2 boil-off purge flow:

$$\frac{\partial \mathcal{C}}{\partial t} = \frac{F}{V_S} C_{\rm LN} - \frac{F}{V_S}\mathcal{C} - \lambda \mathcal{C} + \frac{\mathcal{S}}{V_S}. \tag{5.0.2}$$

The steady-state radon concentration in the shielding

$$\mathcal{C} = \left(\frac{F}{V_S} C_{\rm LN} + \frac{\mathcal{S}}{V_S}\right)\left(\frac{F}{V_S} + \lambda\right)^{-1}. \tag{5.0.3}$$

Here, the radon sources $\mathcal{S}$ consist of the emanation λE (units of mBq/sec) and diffusion $A\phi_D$ (units of mBq/sec) from the high-radon cavern environment that will be proportional to the gasket surface area A. The steady-state radon concentration

$$\mathcal{C} = \left(F C_{\rm LN} + \lambda E + A\phi_D\right)\left(F + \lambda V_S\right)^{-1}. \tag{5.0.4}$$

This concentration will approach the purge gas concentration $C_{\rm LN}$ for high enough flows. Replacing purge dewars is costly and time consuming due to the dewar refill cost and technician time to move and replace when they run out. Conservatively, underground work takes 2–3× longer than above ground work. As a result, we hope to be able to achieve a sufficiently low radon concentration in the

shielding with as little carrier gas, time, and work as possible. For a modest purge flow $F = 1\,\mathrm{L/min}$, the volume exchange rate

$$\frac{F}{V_S} = \frac{1\,\mathrm{L/min}}{5660\,\mathrm{L}} = 1.76 \times 10^{-4}\,\mathrm{min}^{-1} \lesssim 0.02\%\ \text{shield–volume exchanges per minute,}$$

corresponding to a replacement time $V_S/F \approx 3.94\,\mathrm{days}$, very close to the $t_{1/2} = 3.82\,\mathrm{day}$ half-life of radon. In the following paragraphs, I will assume that radon emanation is the only source $\mathcal{S} \equiv \lambda E$ in the enclosure. To achieve a concentration $\mathcal{C}_{\mathrm{req}}$, the strength of radon sources inside the shielding must not exceed

$$\lambda\, E < \mathcal{C}_{\mathrm{req}}\,(F + \lambda V_S) - F \cdot C_{\mathrm{LN}}. \tag{5.0.5}$$

We can safely ignore C_{LN} which is much smaller ($\times 2000$) than the radon requirement $\mathcal{C}_{\mathrm{req}} = 1\,\mathrm{Bq/m^3}$, so at the nominal purge flow $F = 1\,\mathrm{L/min}$, the equilibrium radon emanation of the gasket could contribute no more than

$$\begin{aligned} E \lesssim \mathcal{C}_{\mathrm{req}}\,(F/\lambda + V_S) &\approx 1\,{}^{\mathrm{Bq}}/_{\mathrm{m}^3} \left(\frac{10^{-3}\,\mathrm{m^3/min}}{1.27 \times 10^{-4}/\mathrm{min}} + 5.66\,\mathrm{m^3} \right) \\ &\approx (7.87 + 5.66)\ \mathrm{Bq} = 13.53\,\mathrm{Bq}. \end{aligned} \tag{5.0.6}$$

The total length L of the gasket material to be deployed in the joints of the cylindrically symmetric radon purge barrier of diameter $D = 3.278\,\mathrm{m}$ and height $H = 2.966\,\mathrm{m}$ will be

$$L = 4H + 4\pi D = 4\,(2.966\,\mathrm{m} + 3.278\pi\,\mathrm{m}) = 53.0\,\mathrm{m} \tag{5.0.7}$$

as a result of the 4 seams around the circumference and 4 seams separated by 90° running vertically along the enclosure. If the radon source is due to gasket emanation alone (Eqn. 5.0.6), and conservatively assuming that all of this radon goes into the enclosure, the emanation per unit length

$$\tilde{E} \leq 13.5\,\mathrm{Bq}/53\,\mathrm{m} \approx 255\,\mathrm{mBq/m}. \tag{5.0.8}$$

A gasket of density $\rho = 500\,\mathrm{kg/m^3}$, and (rectangular) cross sectional area $A = (5 \times 15)\,\mathrm{mm^2}$, with a mass per unit length $\tilde{M} \equiv \rho \times A = 500\,\mathrm{kg/m^3} \times (75 \times 10^{-6})\,\mathrm{m^2} = 0.0375\,\mathrm{kg/m}$ sealing the radon purge barrier will produce a radon emanation density per unit mass

$$\tilde{A} = \frac{\tilde{E}}{\tilde{M}} \approx 255\,\mathrm{mBq/m} \times 26.6\,\mathrm{m/kg} = 6.8\,\mathrm{Bq/kg}.$$

Although this is not a tough requirement to meet, the gasket emanation will not be the only source of radon in the shielding. Dust on the lead bricks and the inner neutron shield surfaces, and radon in the cavern diffusing through the gasket will all contribute to the steady-state concentration $\mathcal{C}$ in the lead-gamma shielding enclosure. The surface of the lead bricks and neutron shielding will be cleaned, though presumably the radon emanation from these surfaces will be non-zero. If the radon emanation of the gasket contributes only 10% of the total radon source, conservatively allowing the

dust and diffusion to produce 90% of the requirement, the emanation per length should not exceed

$$\tilde{E} \lesssim 10\% \, \mathcal{S} = 1.3 \, \mathrm{Bq}/53 \, \mathrm{m} \approx 25 \, \mathrm{mBq/m}, \tag{5.0.9}$$

for a flow $F = 1 \, \mathrm{L/min}$, or about $\tilde{E} \approx 10 \, \mathrm{mBq/m}$ at zero flow.

This chapter describes the mathematical model used (**Section 5.1**) to analyze the radon assay data taken (**Section 5.2**) with the R.E.S. system I helped to commission as described in **Chapter 4**. I describe the radon emanation (per unit length) of gaskets: EPDM (**Section 5.2.1**), Zip-A-Way (**Section 5.2.3**), and Silicone (**Section 5.2.4**) whose radon diffusion, solubility, and permeability were measured in **Chapter 3**. Finally, this chapter combines the results from the radon diffusion and emanation measurements to describe implications on the radon purge barrier surrounding the lead shielding (**Section 5.3**).

5.1 Inferring the Radon Emanation of Samples

Counting experiments such as dark matter experiments are inherently poisson distributed observations as discussed in chapter 7 of *Numerical Recipes* [268], appendix B of Knoll's *Radiation Detection and Measurement* [207], and many others. The Poisson distribution is a discrete, one-parameter distribution that describes the probability of an integer number n of events happening in a given time interval t (or space) if the events occur independently of one another at a constant rate μ/t. The Poisson probability P of detecting n events in a given time interval from a phenomena which produces an average number of events μ

$$P(\mu, n) = \frac{\mu^n \cdot \exp(-\mu)}{n!}. \tag{5.1.1}$$

From repeated measurements, we expect that during a assay of the detector backgrounds, the rate of ^{21x}Po events is roughly constant. As described in the previous chapter (**Section 4.4**), the radon emanation system detector background rate is quite low:

$$B_{\mathrm{bkgds}} \lesssim 2 \, \mathrm{cts/peak/day}. \tag{5.1.2}$$

A common framework to determine the number of events expected in a given counting experiment is the maximum likelihood method. In plain words, the likelihood is the probability of observing the given data (*e.g.* a number of events). If we make k (time-dependent) observations of a number events

$$\mathbf{N} \equiv n(t_i) = n_i = (n_1, n_2, n_3, ..., n_k) \tag{5.1.3}$$

which are drawn from an underlying Poisson distribution with an expected number of events μ at each time t_i, the likelihood of observing this data is the product of probabilities (Eqn. 5.1.1)

$$\mathcal{L}(\mu;\mathbf{N}) = \prod_{i=1}^{k} P(\mu,\mathbf{N}) = \prod_{i=1}^{k} \frac{\mu^{n_i}\cdot\,\exp(-\mu)}{n_i!} = \exp(-k\,\mu)\prod_{i=1}^{k}\frac{\mu^{n_i}}{n_i!} \tag{5.1.4}$$

To estimate the value of μ, we determine the value of μ that maximizes the likelihood. Alternatively, we can compute the minimum of the negative log-likelihood (as a function of the parameter μ) of observing the data

$$\mathbf{L}(\mu;\mathbf{N}) = -\ln\big(\mathcal{L}(\mu;\mathbf{N})\big). \tag{5.1.5}$$

For the case outlined above, k time-dependent observations of, *e.g.* background, events obtained from a distribution of constant rate of events, the negative loglikelihood

$$\mathbf{L}(\mu;\mathbf{N}) = -\ln\left(\exp(-k\,\mu)\prod_{i=1}^{k}\frac{\mu^{n_i}}{n_i!}\right) = k\mu - \ln\left(\prod_{i=1}^{k}\frac{\mu^{n_i}}{n_i!}\right) \tag{5.1.6}$$

simplifies the function whose extremum we need to compute significantly since the logs of a product is the sum of the logs:

$$\mathbf{L}(\mu;\mathbf{N}) = k\mu - \sum_{i=1}^{k}\ln\left(\frac{\mu^{n_i}}{n_i!}\right) = k\mu - \sum_{i=1}^{k} n(t_i)\ln\mu + \underbrace{\sum_{i=1}^{k} n(t_i)!}_{\partial/\partial\,\mu\to 0} \tag{5.1.7}$$

It is an easy exercise to find the maximum of a one-parameter function: take the derivative of Eqn 5.1.7 with the respect to the parameter μ and find the value where the derivative is zero, and confirm the concavity of the function. Since we take a derivative w.r.t. μ, the maximum likelihood value of μ will be independent of the final term with factorials, so it is ignored. The derivative of the negative log-likelihood

$$\frac{\partial\mathbf{L}(\mu;\mathbf{N})}{\partial\mu} = k + \sum_{i=1}^{k}\frac{n(t_i)}{\mu} \tag{5.1.8}$$

is then set to zero. Under this framework, the best-estimate of the parameter μ for Poisson-distributed data

$$\mu = \frac{1}{k}\sum_{i=1}^{k} n(t_i) = \frac{1}{k}\times(n_1 + n_2 + \,...\, + n_k) \tag{5.1.9}$$

is the mean of the measurements of events $n(t_i)$, as one might naively expect.

We typically use a log-likelihood approach using background (*i.e.* radon-blank) measurements before and after the assay to determine the strength of the radon emanation. During the course of a sample assay, radon introduced to the detector, initially decaying at $R(t=0)\equiv R_0$, will decay a

rate

$$R(t) = R_0 \exp(-\lambda\, t). \tag{5.1.10}$$

The total number of events measured in a given time is expected to have a constant component from the detector backgrounds, and an exponentially decaying component from the sample of interest decaying. In this case, not only are the data time-dependent (Eqn. 5.1.3), but the underlying distribution (μ in Eqn. 5.1.1) is drawn from the time-dependent poisson distribution

$$\mu \to \mu(t) \equiv \mu_{\mathcal{S}} \exp(-\lambda\, t) + \mu_{\mathcal{B}} \tag{5.1.11}$$

the constant backgrounds $\mu_{\mathcal{B}}$, and the exponential decay with another parameter $\mu_{\mathcal{S}}$ describing the initial number of atoms expected to decay in the first time t_1 in the detection vessel following the radon transfer.

The radon detection vessel internal backgrounds are modeled as a constant $\mu_{\mathcal{B}}$, and the radon introduced to the detector will decay with $\tau = 5.52\,\text{days}$. The event rate R_{tot} in the region of interest for the Po-21x decays in the detector are both modeled

$$R_{\text{tot}}(\mu_{\mathcal{S}}, \mu_{\mathcal{B}}) \equiv \mu_{\mathcal{S}} \exp(-\lambda t) + \mu_{\mathcal{B}} \tag{5.1.12}$$

where $\mu_{\mathcal{S}}$ is the strength of the radon source intended for assay and $\mu_{\mathcal{B}}$ is the rate of non-signal events in the Po-21x region of interest determined for each assay by measuring pre- and post-assay background runs.

Transfers of radon, performed as described in **Section 4.2.5**, were used to determine the total efficiency ε_{T} for collecting and detecting Po-218 $\varepsilon_{\text{T}}^{218} \approx 0.18$, and the total efficiency for collecting and detecting Po-214 $\varepsilon_{\text{T}}^{214} \approx 0.23$. The emanation grow-in period $1 - \exp(-t_{\text{eman}}/\tau)$ is also applied to the measured ^{21x}Po decay rates. The pre- and post-assay runs, consisting of the time-dependent $\mathbf{N}_{\mathcal{B}}$ events in each polonium peak, are used to estimate the level of detector backgrounds. Therefore, the log of the total likelihood

$$\mathbf{L}(\mu_{\mathcal{S}}, \mu_{\mathcal{B}}; \mathbf{N}_{\mathcal{S}}, \mathbf{N}_{\mathcal{B}}) \;=\; \sum^{k_{\mathcal{B}}} f_{\mathcal{B}}(\mu_{\mathcal{B}}; \mathbf{N}_{\mathcal{B}}) + \sum^{k_{\mathcal{S}}} f_{\mathcal{S}}(\mu_{\mathcal{S}}, \mu_{\mathcal{B}}; \mathbf{N}_{\mathcal{S}}) \tag{5.1.13}$$

depends on the sample decay model (Eqn. 5.1.12) given the time-dependent efficiency-corrected events $\mathbf{N}_{\mathcal{S}}(t_k)$ measured in each polonium peak during the assay

$$f_{\mathcal{S}}(\mu_{\mathcal{S}}, \mu_{\mathcal{B}}; \mathbf{N}_{\mathcal{S}}) = R_{\text{tot}}(\mu_{\mathcal{S}}, \mu_{\mathcal{B}}) - \mathbf{N}_{\mathcal{S}} \ln\left(R_{\text{tot}}\right) \tag{5.1.14}$$

the test value of the source strength $\mu_{\mathcal{S}}$, and the test value of the internal detector backgrounds $\mu_{\mathcal{B}}$. The likelihood of obtaining the background model B, given the number $\mathbf{N}_{\mathcal{B}}(t)$ of background events measured

$$f_{\mathcal{B}}(\mu_{\mathcal{B}}; \mathbf{N}_{\mathcal{B}}) = \mu_{\mathcal{B}} - \mathbf{N}_{\mathcal{B}} \ln\left(\mu_{\mathcal{B}}\right) \tag{5.1.15}$$

looks the same as the sample decay model $R_{\rm tot}(\mu_{\mathcal{S}}, \overset{0}{\mu}_{\mathcal{B}})$ with a source of zero strength.

By applying the detection efficiency to each polonium peak, the time-series alpha-decay rate is used to define the negative log-likelihood $\mathcal{L}$ as a function of radon decay rate and constant backgrounds. We then evaluate the negative log-likelihood (NLL) $\mathbf{L}$ on a grid of signal $\mu_{\mathcal{S}}$ and background $\mu_{\mathcal{B}}$ rates. The confidence limits for the strength sample and background are constructed from the two-dimensional negative log-likelihood distribution. The 68 (95, 99.7)% C.L. bounds are set by finding the minimum negative log-likelihood $\mathbf{L}_{\rm min}$ in the two-dimensional parameter space of the sample decay rate $\mu_{\mathcal{S}}$ and average background $\mu_{\mathcal{B}}$ and finding the largest and smallest value of each for which the difference

$$\Delta\,\mathbf{L}(\mu_{\mathcal{S}}, \mu_{\mathcal{B}}) = \mathbf{L} - \mathbf{L}_{\rm min} = 1.15\ (3.09,\ 5.9). \tag{5.1.16}$$

Table 5.1 shows the negative log-likelihood $\Delta\,\mathbf{L}$, for a few levels of confidence and the significance σ for a model with 2 free parameters [1]. We use negative log-likelihood formalism to place bounds on

Table 5.1: The negative log-likelihood $\Delta\,\mathbf{L}$ for common levels of confidence and the significance σ for a model with 2 parameters [1].

$\Delta\,\mathcal{L}$	C.L. %	σ
1.15	68.27%	1
3.09	95.45%	2
5.9	99.73%	3

the sample radon emanation.

5.2 Measuring SuperCDMS Gasket Radon Emanation

We have emanated, transferred, and analyzed samples to understand the impact of radon emanation on the steady-state radon concentration in the SuperCDMS SNOLAB radon purge barrier. This section describes the proposed gasket samples, radon emanation conditions, and analysis results obtained using the R.E.S. gas-handling system and low-background α detector described in **Chapter 4**. Selecting a gasket of sufficiently low radon emanation and diffusion will prevent the radon-induced detector backgrounds.

5.2.1 EPDM Sample I

A $L = 63\,$cm sample of self-adhering ethylene propylene diene terpolyme (EPDM) cellular foam gasket with a 15 mm-by-5 mm cross-section, shown in the left panel of **Fig. 5.2**, was sent to SDSM&T from Lemer Pax [261]. For the $t_{\rm eman} = 9\,$day radon emanation, the emanation efficiency $\epsilon_{\rm eman} = 1 - \exp(-9/5.52) \approx 80.4\%$. The emanation in the 13 L emanation chamber

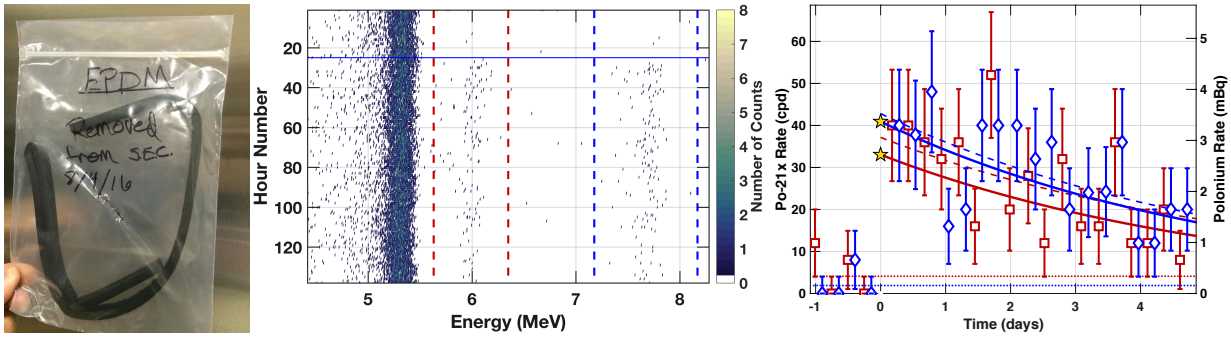

Figure 5.2: Left: A $L = 63\,\text{cm}$ sample sample of EPDM from Lemer Pax [261]. **Middle:** Pulse height spectra (colormap) as a function of time for the EPDM assay. The ^{21x}Po α decay regions of interest shown (vertical dashed) are conservatively wide. The t_{bgd} $\sim$1 day pre-assay background run and the $t_{\text{asy}} \sim 4\,\text{day}$ sample assay separated by a horizontal line. The background rate in each polonium peak is approximately 2 counts per day, well below the ~ 40 counts per day detected! **Right:** Efficiency-corrected $^{218/(214)}$Po rates are shown $\square$ ($\diamond$) in 6 hr time bins with statistical uncertainties (68% C.L.) separated (vertical lines) from the efficiency-uncorrected pre-assay background run. The best-fit value $R_{\text{fit}} = (2.9 \pm 0.6)\,\text{mBq}$ determined from the negative log-likelihood method for both polonium peaks.

was carried out in June, 2016 at a pressure $P_{\text{eman}} \approx 100\,\text{Torr}$ to measure the recoil and diffusion emanation. The time-dependent pulse height spectra are shown, in the middle panel of **Fig. 5.2**, for the t_{bgd} $\sim$1 day pre-assay background run and the t_{asy} $\sim$4 day sample assay separated by a horizontal line. The ^{21x}Po regions of interest are shown as vertical lines near $E_{218} = 6.0\,\text{MeV}$, and $E_{214} = 7.9\,\text{MeV}$.

Fig. 5.2 shows the pulse height spectra (middle panel) and efficiency-corrected ^{21x}Po α decay rates $R_\varepsilon \pm \sigma_{R_\varepsilon}$ (right panel) in each $\Delta t = 6\,\text{hr}$ time bin. The best fit ^{218}Po decay rate $R_{218} = 2.7^{+0.5}_{-0.6}\,\text{mBq}$ (68% C.L.) and the ^{214}Po decay rate $R_{214} = (3.1 \pm 0.5)\,\text{mBq}$ (68% C.L.) and the best-fit radon emanation

$$R_{\text{fit}} = 2.9^{+0.5}_{-0.6}\,\text{mBq} \qquad (95\%\,\text{C.L.}), \tag{5.2.1}$$

determined from the combined negative log-likelihood, corresponds to a radon emanation per unit length

$$\tilde{E} = \frac{R_{\text{fit}}}{L} \approx \frac{(2.9 \pm 0.6)\,\text{mBq}}{63\,\text{cm}} = (4.6 \pm 0.9)\,\text{mBq/m}. \qquad (95\%\,\text{C.L.}) \tag{5.2.2}$$

This EPDM gasket has an equilibrium well below the 10 mBq/m benchmark, and when deployed as a $L_{\text{gasket}} = 53.0\,\text{m}$ gasket, would emanate

$$E_{\text{tot}} = \tilde{E} \cdot L_{\text{gasket}} \lesssim 5.5\,\text{mBq/m} \cdot 53\,\text{m} \approx 300\,\text{mBq} \qquad (95\%\,\text{C.L.}) \tag{5.2.3}$$

in the $V_S = 5.66\,\text{m}^3$ volume of SuperCDMS SNOLAB radon purge barrier. Then, for the zero-flow steady-state radon concentration

$$\mathcal{C} \lesssim E_{\text{tot}}/V_S = 300\,\text{mBq}/5.66\,\text{m}^3 \approx 53\,\text{mBq/m}^3 \tag{5.2.4}$$

is approximately 19× below the requirement $\mathcal{C}_{\text{req}} \leq 1\,\text{Bq/m}^3$! This EPDM sample is an excellent candidate to seal lead-gamma shielding since it is self-adhering and thus easy to apply and remove, which will be necessary during construction

5.2.2 EPDM Sample II

A second $L = (38 \pm 3)$ inch sample of EPDM with a 5 mm-8 mm cross section, shown in **Fig. 5.3**, was sent to SDSM&T from Lemer Pax. This sample was spongy and stretchy so there are somewhat large uncertainties on the sample length; as we'll see, this has little bearing on selecting a gasket of sufficiently low radon emanation per length. The gasket was cut into two halves and the strip was removed to expose the adhesive side on the bottom of each sample half. These separate halves were then adhered to one another, and a zip tie was used to keep the sample halves secure during the week-long radon emanation periods as shown in the left panel of **Fig. 5.3**. The sample was measured for radon emanation twice to ensure the outgassing of radon from the lab air, as described in **Section 4.1.2**, did not contribute to the radon sample.

This second EPDM sample was emanated for a $t_{\text{eman}} \approx 7\,\text{day}$ period, and transferred for a $t_{\text{asy}} \approx 1\,\text{day}$ assay since the statistical uncertainties $\sigma_{\text{stat}} \lesssim 5\%$ smaller than the systematic expected from the radon detection, collection, and transfer efficiencies. **Fig. 5.4** shows the (efficiency-corrected) time-dependent ^{21x}Po decay rates $R_\varepsilon \pm \sigma_{R_\varepsilon}$ with pre- and post-assay background runs. For the period of data directly after the first radon assay, the detector backgrounds were significantly larger than usual as a result of the radon back-diffusing from the teflon in the detection vessel. The best-fit radon emanation

$$E_{\text{II}} = 55.2^{+2.8}_{-2.7}\,\text{mBq} \tag{5.2.5}$$

was determined from the sum of the (^{21x}Po) negative log-likelihoods shown in the right panel

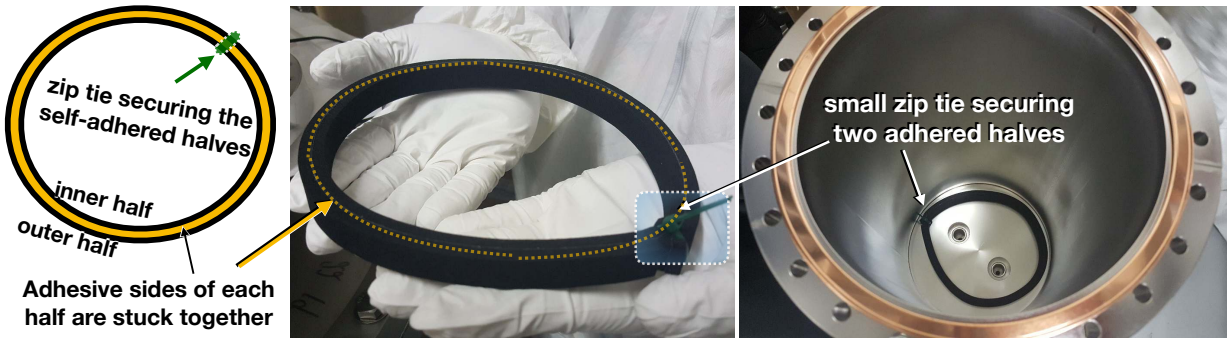

Figure 5.3: Left: Diagram of the EPDM sample halves (black) adhered to one another and secured with a zip tie. **Middle:** A $L = (38 \pm 3)$ inch sample of EPDM from Lemer Pax [261]. After cutting the sample in half, the adhesive side of the gasket sample were connected, arranged into a circle and cinched with a zip tie. **Right:** EPDM sample in the small emanation chamber.

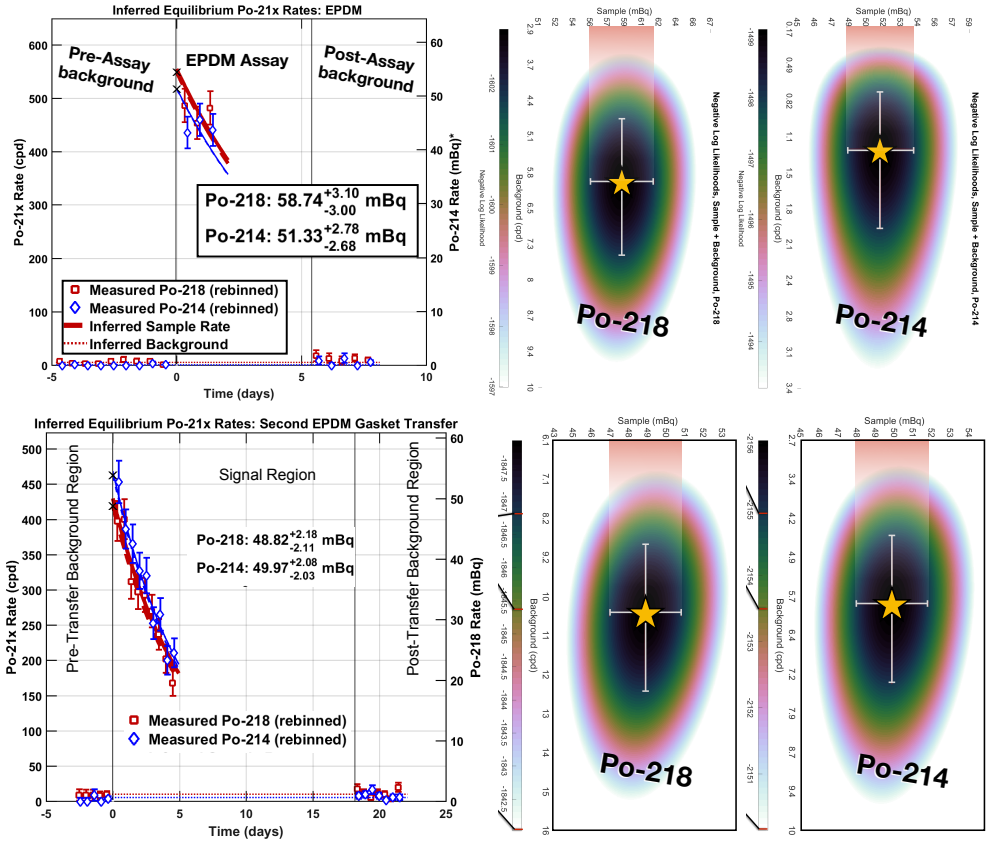

Figure 5.4: Top Left: Efficiency-corrected ^{21x}Po α decay rates $R_\varepsilon \pm \sigma_{R_\varepsilon}$ shown with statistical uncertainties (68% C.L.) in 12 hr time bins. **Right:** Negative log-likelihood distribution as a function of the sample emanation and the detector background for both ^{21x}Po peaks shown with best-fit value (★) $R \approx 55$ mBq with errorbars determined from the $\Delta\mathcal{L} = 1.15$ indicating 68% C.L. bounds on the sample and background. The combined best-fit ^{222}Rn emanation rate $R_{\text{rn}} = 55.2^{+2.8}_{-2.7}$ mBq (68% C.L.) . The radon emanation per unit length $\tilde{E} \lesssim (55 \pm 3)\,^{\text{mBq}}/_{\text{m}}$ at 95% C.L. **Bottom Left:** Efficiency-corrected ^{21x}Po α decay rate shown with statistical uncertainties (68% C.L.) in 12 hr bins. **Right:** Negative log-likelihood distribution as a function of the sample emanation and the detector background for both ^{21x}Po peaks shown with best-fit value (★) $R \approx 50$ mBq with errorbars (68% C.L. bounds) determined from the $\Delta\mathcal{L} = 1.15$. The combined best-fit ^{222}Rn emanation rate $E_{\text{II}} = (50 \pm 2)$ mBq (68% C.L.).

of **Fig. 5.4**. The radon emanation per unit length

$$\tilde{E}_{\text{II}} = E_{\text{II}}/L \approx \frac{55.2^{+2.81}_{-2.71}\,\text{mBq}}{(97 \pm 8)\,\text{cm}} \approx (52 \pm 5)\,\text{mBq/m}, \tag{5.2.6}$$

is 10× larger than that of the previously measured EPDM sample which emanated $\tilde{E} \lesssim 5.5$ mBq/m.

The second EPDM sample was emanated again for a period $t_{\text{eman}} \approx 8$ days. During this period, radon in the detection vessel from the first assay diffused out of the teflon and the radon was not transferred until the backgrounds in the detector returned to $B \sim 2$ cts/peak/day. The bottom left panel of **Fig. 5.4** shows the time-dependent ^{21x}Po decay rates with pre- and post-assay background runs in 12 hr time bins. The second emanation period has a slightly lower inferred equilibrium

^{222}Rn emanation than the first emanation period. The best-fit radon emanation shown (★)

$$E_{\mathrm{II}} = (50 \pm 2)\,\mathrm{mBq}, \tag{5.2.7}$$

determined from the negative log-likelihood distribution from the ^{214}Po measurement shown in the right panel of **Fig. 5.4**. The Po-218 peak overlapped with the α decays from long-lived Po-210 on the detector surface and so only decays from the Po-214 were used to constrain the radon emanation. The α decay rates measured during the second assay were lower than the first period. We infer that this was due to in part to radon outgassing during the first emanation sample from the initial room-air exposure during sample placement. This first measurement provides a reasonable conservative upper limit. The best-fit limits on the second emanation are consistent with the first emanation

$$\frac{55.2 - 50}{\sqrt{(2.7^2 + 2^2)}} \approx 1.5\sigma. \tag{5.2.8}$$

The discrepancy can be reasonably explained from radon back-diffusing (or outgassing) from the bulk of the material arising from the initial exposure to high concentration in the laboratory. The first emanation period was $t_{\mathrm{eman}} \approx 7\,\mathrm{days}$, during which period lab-air radon would outgas at a decreasing rate (Eqn. 4.1.3) proportional to $1/t^{2-4}$ [277]. In the worst case, the amount radon of outgassed $\mathcal{O}$ during a given emanation will be

$$\mathcal{O} \lesssim \int_{t_0}^{t_f} 1/t^2 \; \mathrm{d}t = \left(\frac{1}{t_0} - \frac{1}{t_f}\right). \tag{5.2.9}$$

Though this integral diverges for arbitrarily small t_0, we can assume an initial outgassing time $t_0 \sim 1\,\mathrm{hour}$ after sealing. During this time the vacuum vessel was purged of high-radon lab air with liquid nitrogen boil-off before the emanation period began. Then, assuming $t_0 \approx 0.05\,\mathrm{days}$, the magnitude of the integral (neglecting radon decay, and ignoring units in the interest of comparison) indicates that the outgassed radon $\mathcal{O}_{\mathrm{I}} \sim 1/0.05 - 1/7 \sim 10$. The second emanation period $t_{\mathrm{eman}} \approx 8\,\mathrm{days}$ took place immediately following the first emanation, so the integral for the second emanation $\mathcal{O}_{\mathrm{II}} \sim 1/7 - 1/15 \sim 0.1$ is $100\times$ smaller than that of the first emanation period. The radon emanation per unit length computed from the second transfer

$$\tilde{E}_{\mathrm{II}} = E_{\mathrm{II}}/L \approx \frac{(50 \pm 2)\,\mathrm{mBq}}{(97 \pm 8)\,\mathrm{cm}} \approx (52 \pm 5)\,\mathrm{mBq/m}. \tag{5.2.10}$$

We see that EPDM gaskets may vary in their radon emanation depending on the production batch. Working with the vendor, Lemer Pax, will be possible to select gaskets with lower radon emanation. These gaskets are self-adhering and therefore very easy to use!

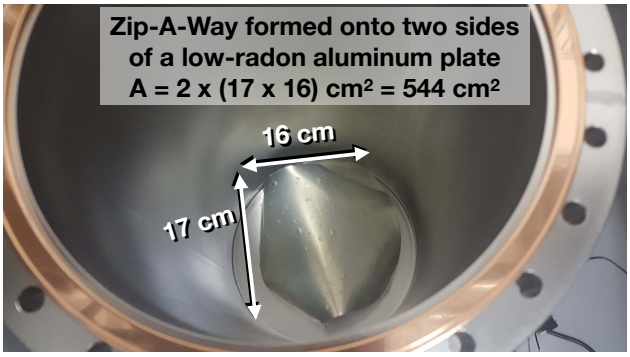

Figure 5.5: Zip-A-Way formed onto low-radon aluminum plate. The total material surface exposed is $A_Z = 2 \times (17 \cdot 16)\,\mathrm{cm}^2 = 544\,\mathrm{cm}^2$.

5.2.3 Zip-A-Way

Zip-A-Way [269] is a commercially available removable weather stripping manufactured by Red Devil. This caulking substance was suggested for use as a gasket to seal the SuperCDMS radon barrier by Dan Bauer. This material is designed to be applied as a beaded caulk in thin strips. We purchased several bottles for the radon diffusion (**Section 3.5**) and emanation measurements described here. The sample was prepared for radon emanation by emptying one full 300 mL bottle onto two sides of an aluminum foil of area $A_{\mathrm{foil}} = (17 \cdot 16)\,\mathrm{cm}^2 = 272\,\mathrm{cm}^2$ as shown in **Fig. 5.5**. The radon emanation $R_{\mathrm{foil}} \lesssim 70\,\mu\mathrm{Bq}$ of the foil previously measured was determined to be at approximately the same level as the detector backgrounds $B \approx 2\,\mathrm{cts/peak/day}$. This plate will contribute somewhat less radon than this because the radon will have to diffuse through the Zip-A-Way.

The time-dependent ^{21x}Po rates for three Zip-A-Way assays are shown in **Fig. 5.6** with the best-fit ^{214}Po decay rate $R_{214} \approx 0.00^{+0.22}_{-0.00}\,\mathrm{mBq}$ (68% C.L.) determined by Eqn. 5.1.12 consistent with zero for all three measurements. During the emanation assays, the Po-218 and Po-210 peak overlap significantly enough that the radon emanation was determined using only the Po-214 α peak. The combined ^{214}Po negative log-likelihood results for all three assays: $R_{\mathrm{I}} = 0.00^{+0.21}_{-0.00}\,\mathrm{mBq}$ (68% C.L.), $R_{\mathrm{II}} = 0.00^{+0.10}_{-0.00}\,\mathrm{mBq}$ (68% C.L.), and $R_{\mathrm{III}} = 0.10^{+0.22}_{-0.10}\,\mathrm{mBq}$ (68% C.L.) were consistent with zero radon emanation! The best-fit combined results indicate the radon emanation

$$R_{\mathrm{Z}} = 0.0^{+0.9}_{-0.0}\,\mathrm{mBq} \qquad (68\%\,\mathrm{C.L.}) \tag{5.2.11}$$

so that the $A_Z = 544\,\mathrm{cm}^2$ sample has an upper bound best-fit

$$\tilde{E}_{\mathrm{Z}} = \frac{R_{\mathrm{Z}}}{A_{\mathrm{Z}}} < \frac{180\,\mu\mathrm{Bq}}{544\,\mathrm{cm}^2} = 3.3\,\mathrm{mBq/m}^2 \qquad (\mathrm{at}\ 95\%\,\mathrm{C.L.}) \tag{5.2.12}$$

^{222}Rn emanation per unit area. This is not as low as the aluminum plate which bears an expected

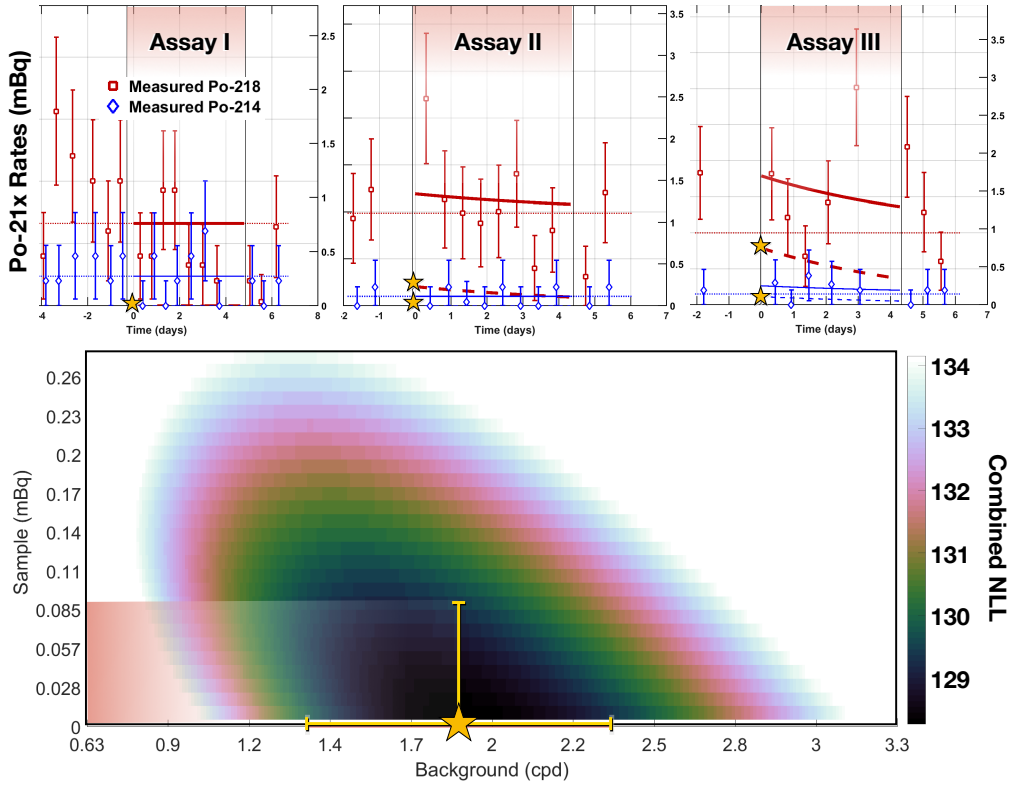

Figure 5.6: Top: Efficiency-corrected $^{218/(214)}$Po rates are shown □ (◇) in 6 hr time bins with statistical uncertainties (68% C.L.) separated (vertical lines) from the efficiency-uncorrected pre-assay background run, for 3 emanation periods (panels). The best-fit background rates are shown (dotted lines), with the total polonium rates (solid), and best-fit polonium decay rates (★). **Bottom:** Combined negative log-likelihood distribution as a function of the sample emanation and the detector background. The combined best-fit ^{222}Rn emanation rate $E_Z = 0.00^{+0.09}_{-0.00}$ mBq (68% C.L.) consistent with zero shown (★) determined from the $\Delta\mathcal{L} = 1.15$.

radon emission

$$\tilde{E}_{\mathrm{Al}} = E_{\mathrm{Al}}/A \lesssim \frac{70\,\mu\mathrm{Bq}}{544\,\mathrm{cm}^2} \approx 1.2\,\mathrm{mBq/m^2} \qquad (\text{at } 95\%\,\text{C.L.}) \tag{5.2.13}$$

considerably higher than *e.g.* electropolished stainless steel $\tilde{E}_{\mathrm{SS}} \approx 1\,\mu\mathrm{Bq/m^2}$ [137]. To apply these results to the case of Zip-A-Way used as thin gasket sealing the SuperCDMS radon purge barrier, we might assume a gasket would be $H = 1$-cm wide. Then we can convert the computed radon emanation per unit area to emanation per unit length under the assumed 1 cm thickness. The surface area measured then corresponds to a gasket of length

$$L_{\mathrm{gasket}}\,A_Z/H = 544\,\mathrm{cm}^2/1\,\mathrm{cm} = 5.44\,\mathrm{m}. \tag{5.2.14}$$

In this case, the material would bear a radon emanation per unit length

$$\frac{R_Z}{L_{\mathrm{gasket}}} < \frac{180\mu\,\mathrm{Bq}}{5.44\,\mathrm{m}} = 0.033\,\mathrm{mBq/m} \qquad (\text{at } 95\%\,\text{C.L.}). \tag{5.2.15}$$

This is also well below the requirement for the SuperCDMS SNOLAB radon purge barrier. In thin

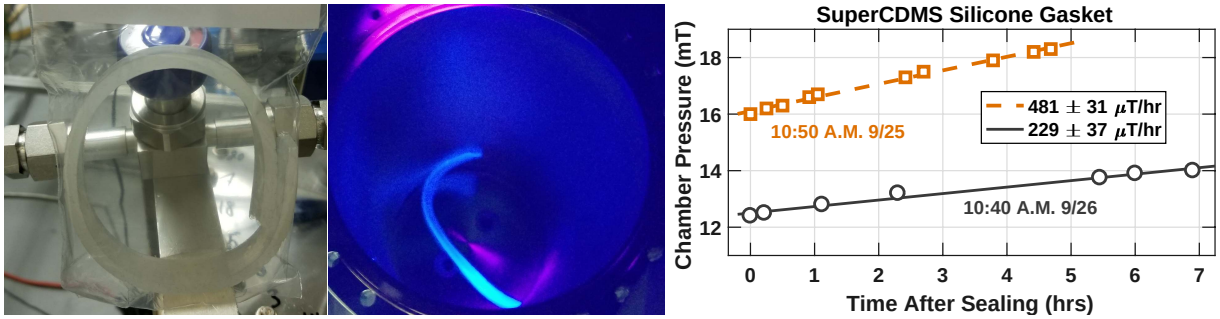

Figure 5.7: Left: Silicone sample bagged, in the small emanation chamber, and illuminated by a UV light. **Right:** Silicone gasket Pressure rate-of-rise in the small vacuum chamber as a function of time before (light □, dashed) and after (dark ○, solid) the application of 300°F silicone heating tape for a bakeout period of 2.5 hours. During the backout period, the vacuum vessel was evacuated with a scroll pump and the outgassing was reduced by a factor of two from ∼ 0.48 mTorr/hr to ∼ 0.23 mTorr/hr.

beads, this caulk does dry very fast–we believe this substance would be great to patch leaks, though given its liquid form, would be hard to apply as a gasket alone.

5.2.4 Silicone

We received a $L = 30$-cm-long sample of Silicone rubber with a cross sectional area: 15 mm by 5 mm $= 0.75\,\mathrm{cm}^2$ from Lemer Pax [261] shown in the left panel of **Fig. 5.7**. We cleaned the surface of the rubber with isopropyl alcohol and sealed the sample in the S.E.C. evacuating the vessel to a pressure $P = 16$ mTorr to measure outgassing. The right panel of **Fig. 5.7** shows a fairly linear vessel pressure rate-of-rise from 16 mTorr to 18 mTorr over a 5 hour period at an average pressure rise 481 μTorr/hr. We concluded this was due to outgassing and applied a heating strap to the small chamber for a short time, to speed up the outgassing. The strap reached $T = 300$°F during which period we continuously evacuated the vessel for t_{evac} ∼2.5 hours. After this, we measured the pressure rate of rise from a lower initial pressure, indicating the accelerated outgassing was successful. The small emanation chamber was evacuated to $P = 12$ mTorr to measure the pressure rate-of-rise, over a 7 hour period, which had fallen by a factor of two to 230 μTorr/hr. We then emanated the silicone sample at $P_{\mathrm{ema}} \approx 100$ Torr. We emanated the sample consecutively for two emanation periods $t_{\mathrm{eman}} = 8\,(14)$ days with an emanation grow-in efficiency $\epsilon_{\mathrm{eman}} = 76.5\%\,(92.1\%)$.

Fig. 5.8 shows the time-dependent Po-21x event rates (shown in 12 hour periods) for the first (left panel) and second (right panel) emanation assays with the surrounding background runs. The best-fit decay rates in the Polonium 21x regions of interest ^{218}Po: $R_{218} = 0.16^{+0.31}_{-0.16}$ mBq (68% C.L.), and ^{214}Po: $R_{214} = 0.03^{+0.20}_{-0.03}$ mBq (68% C.L.) are consistent with zero. The best-fit background-corrected Polonium 21x decay rates $R_{218} = 0.06^{+0.21}_{-0.06}$ mBq (68% C.L.), and $R_{214} = 0.00^{+0.08}_{-0.00}$ mBq (68% C.L.) are consistent with zero at 1σ. The ^{218}Po peaks overlapped with the lower energy ^{210}Po α peak and therefore the best-fit radon emanation

$$E = 0^{+86}_{-0}\,\mu\mathrm{Bq} \qquad (95\%\ \mathrm{C.L.}), \tag{5.2.16}$$

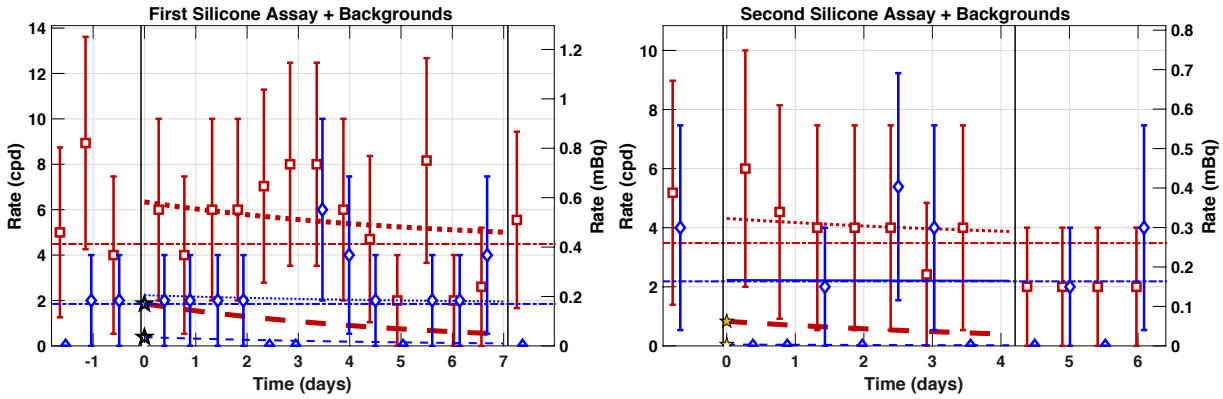

Figure 5.8: Efficiency-corrected $^{218/(214)}$Po rates during 2 assay periods are shown □ (◇) separated (vertical lines) from the efficiency-uncorrected pre- and post-assay background runs. The decay rates are shown in 12 hr bins with statistical uncertainties (68% C.L.). The best-fit ^{222}Rn emanation $R = 0.00^{+0.08}_{-0.00}$ mBq for the sample determined from the combined negative log-likelihood of the time-dependent ^{214}Po rates for both the assays, and the surrounding background measurements.

consistent with zero is determined from the negative log-likelihood from the efficiency-corrected ^{214}Po rates, during the assay periods, and the corresponding background runs. The 30-cm sample of silicone is measured to have a radon emanation per unit length

$$\tilde{E} \equiv E/L \lesssim 0.86\,\text{mBq}/0.30\,\text{m} = 2.9\,\text{mBq/m} \qquad (95\%\ \text{C.L.}). \tag{5.2.17}$$

This is about 50× better than the assay results of the second EPDM sample from Lemer Pax. This Silicone sample is very-low radon, however, it is less suited for use as a gasket for the SuperCDMS radon purge barrier since it is not self-adhesive, and would presumably sustain damages from the repeated application and removal during the detector commissioning.

5.3 Impacts of ^{222}Rn Emanation and Diffusion for SuperCDMS Shielding

Table 5.2 reports the radon emanation results of the proposed gaskets for the SuperCDMS radon purge barrier. The resulting emanation per length can be used to compute the level of radon added to the shielding from the gasket emanation. The Silicone and Zip-A-Way gaskets were consistent with zero radon emanation, but neither are suited to be deployed as a the sole gasket sealing the radon purge barrier. A gasket of length L_g with ^{222}Rn emanation per unit length $\tilde{E}$ will contribute as much as $E = \tilde{E} \times L_\text{g}$ to an enclosed volume. **Fig. 5.9** shows the steady-state radon concentration

$$\mathcal{C} \;= \left(FC_\text{LN} + \lambda\tilde{E} \times L_\text{g}\right)(F + \lambda V_S)^{-1}\,. \tag{5.3.1}$$

in the $V_S = 5.66\,\text{m}^3$ radon purge barrier as a function flow F for a $L_\text{gasket} = 53\,\text{m}$ gasket for each of the emanated samples, using the 95% C.L. upper limits for the emanation per length, and the

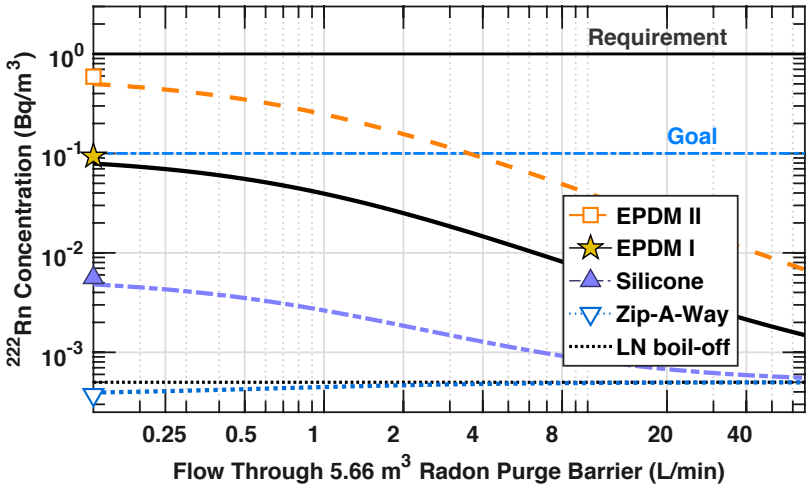

Figure 5.9: Radon concentration in the 5.66 m^3 radon purge barrier surrounding the lead-gamma shielding as a function of flow rate F resulting from radon emanation of gasket (symbols) materials, including a conservative value for contribution $C_{\rm LN} = 0.5\,{\rm mBq/m^3}$ from the liquid nitrogen boil-off purge gas (dotted). The radon concentration requirement $\mathcal{C}_{\rm req} = 1\,{\rm Bq/m^3}$ (horizontal solid) and goal $\mathcal{C}_{\rm goal} \equiv 0.1\,\mathcal{C}_{\rm req}$ (horizontal dashed) are shown. The zero-flow equilibrium concentration is shown (symbols indicated in the legend) on the y-axis for each of the gaskets measured. The radon emanation per length used here to determine the steady-state concentration corresponds to the 95% C.L. upper limit (2σ) for each gasket. Combined emanation results from both silicone and Zip-A-Way shown (triangles) are consistent with zero radon emanation. The planned gasket (★, EPDM I) beats the radon concentration goal even at zero flow.

radon concentration the purge gas $C_{\rm LN} = 0.5\,{\rm Bq/m^3}$ is conservatively chosen.

The impact of diffusion can be found from the steady-state Danckwert's model of radon diffusion under simple assumptions. Using the Danckwert's formulation (Eqn 3.2.37) for the equilibrium 'cold-side' concentration, under steady one-sided (hot-side) exposure, the steady-state concentration $\mathcal{C}_\infty \equiv \mathcal{C}(t \to \infty)$ for a given gasket geometry (A, H) held on one side at a concentration C_H will be given by

$$\mathcal{C}_\infty = C_{\rm H}\frac{A\cdot DS}{H\lambda V_S}\underbrace{\left(1+2\sum_{n=1}^{\infty}\frac{(-1)^n}{1+n^2\pi^2\cdot D/\tilde{D}}\right)}_{\text{of order 1}} \sim C_{\rm H}\frac{L\,w\cdot P}{H\lambda V_S}, \tag{5.3.2}$$

Table 5.2: Summary of radon emanation measurements for gaskets with 68% C.L. either determined from a negative log-likelihood analysis incorporating backgrounds, or by fitting to a conservative background free model with 95% C.L. uncertainties. The sample length is used to report the ^{222}Rn emanation per unit length. The silicone and Zip-A-Way samples were consistent with zero and are upper limits (95% C.L.).

Material	L (cm)	E (mBq)	E/L (mBq/m)	notes
EPDM I	64	(3.9 ± 1)	(6.2 ± 1.6)	
EPDM II	(97 ± 8)	(50 ± 4)	(52 ± 5)	
Silicone	30 cm	$0.00^{+0.08}_{-0.00}$	<2.9	
Zip-A-Way	5.4 m	$0.00^{+0.09}_{-0.00}$	<0.033	1 cm equiv

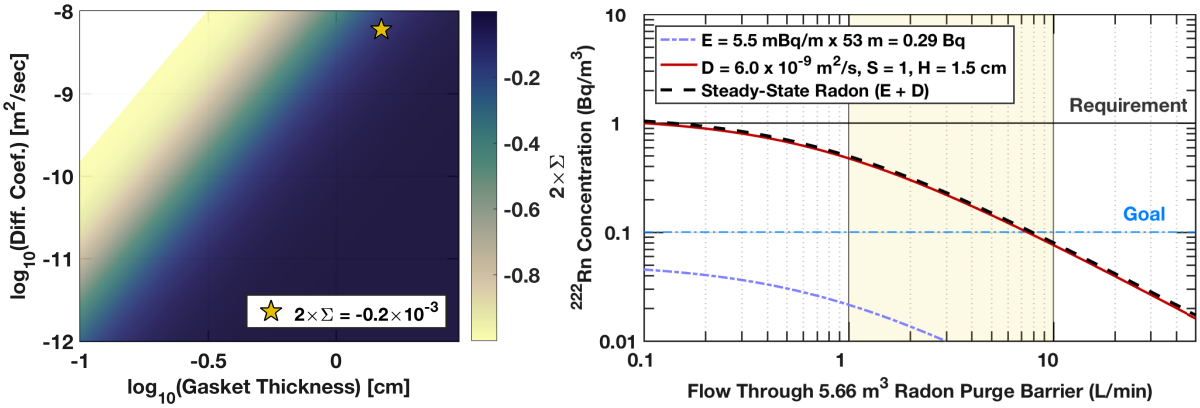

Figure 5.10: Left: (Colormap) Deviation of the summed terms in Eqn. 5.3.2 from 1 as a function of the $\log_{10}$ of the diffusion coefficient D and the $\log_{10}$ gasket thickness H. For the planned 1.5-cm-thick EPDM gasket, shown (★) with a conservative diffusion coefficient $D = 6.0 \times 10^{-6}\,\mathrm{m}^2/\mathrm{s}$, the deviation from one is less than 1 part in one thousand. **Right:** Steady-state radon concentration (dashed) in the $5.66\,\mathrm{m}^3$ radon purge barrier versus flow rate F resulting from radon emanation (dot-dash) and diffusion (solid) of the planned 15 mm-thick EPDM gasket. The radon concentration requirement $\mathcal{C}_{\mathrm{req}} = 1\,\mathrm{Bq/m}^3$ (horizontal solid) and goal $\mathcal{C}_{\mathrm{goal}} \equiv 0.1\,\mathcal{C}_{\mathrm{req}}$ (horizontal dashed) are shown. Reasonable flow rates $F = (1\text{–}10)\,\mathrm{L/min}$ are indicated by the light fill region. The diffusion dominates the expected radon in the radon purge barrier. For a purge flow $F = 1\,\mathrm{L/min}$, the steady-state radon concentration $\mathcal{C} \approx 0.5\,\mathrm{Bq/m}^3$ is half the SNOLAB requirement, and at a flow a $F \approx 8\,\mathrm{L/min}$, the radon concentration in the purge barrier $\mathcal{C} \approx 0.1\,\mathrm{Bq/m}^3$ meets the goal!

given that the exposed surface area A of the gasket is the length $L = 53\,\mathrm{m}$ times the exposed width $w \lesssim 1\,\mathrm{cm}$, where the characteristic radon diffusion coefficient $\tilde{D} = \lambda H^2$. As shown in the left panel of **Fig. 5.10**, twice the value of summed terms in Eqn. 5.3.2 exceed 1, by less than 1 part in a thousand for a 15 mm gasket with a diffusion coefficient $D = 6 \times 10^{-9}\,\mathrm{m}^2/\mathrm{s}$ For the case of the SNOLAB cavern, we assume a 'hot-side' concentration $C_H \approx 130\,\mathrm{Bq/m}^3$. Then, a gasket of radon permeability $P = 6 \times 10^{-9}\,\mathrm{m}^2/\mathrm{sec}$, with a thickness $H = 1.5\,\mathrm{cm}$ and an exposed width $w = 0.5\,\mathrm{cm}$ gives a (zero-flow) equilibrium concentration

$$\begin{aligned} \mathcal{C} \sim C_{\mathrm{H}} \frac{L\,w P}{H \lambda V_S} &= 130\,\mathrm{Bq/m}^3 \frac{53\,\mathrm{m} \cdot 0.5\,\mathrm{cm} \cdot (6 \times 10^{-9}\,\mathrm{m}^2/\mathrm{sec})}{1.5\,\mathrm{cm} \cdot (2.11 \times 10^{-6}/\mathrm{sec}) \times 5.66\,\mathrm{m}^3} \\ &\approx 1.2\,\mathrm{Bq/m}^3 \end{aligned} \tag{5.3.3}$$

about the level of the radon concentration requirement $\mathcal{C}_{\mathrm{req}} \leq 1\,\mathrm{Bq/m}^3$! The right panel of **Fig. 5.10** shows the steady-state radon concentration

$$\mathcal{C} = \left(\lambda \times V_S(\mathcal{E} + \mathcal{D}) + C_{\mathrm{LN}} V_S\right) (F + \lambda V_S)^{-1} \tag{5.3.4}$$

in the radon purge barrier versus flow F where the source of radon emanation $\mathcal{E}$ is much less than the radon diffusing $\mathcal{D}$, through a 15 mm gasket with a diffusion coefficient $D = 6.0 \times 10^{-6}\,\mathrm{m}^2/\mathrm{s}$, from the $130\,\mathrm{Bq/m}^3$ SNOLAB cavern. The radon concentration requirement $\mathcal{C}_{\mathrm{req}} = 1\,\mathrm{Bq/m}^3$ ensures that the contribution of radon-induced electron recoils are less than 1% the rate of backgrounds from ^{32}Si and ^{3}H in the high voltage detectors.

During construction and commissioning, the SuperCDMS shielding will be opened and closed multiple times. The planned gasket will need to be easy to work with: application ought to be quick with little thought required, and removal should be easy as well. Both Silicone and Zip-A-Way have better diffusion properties than the EPDM gasket, but the Silicone lacks adhesive and the Zip-A-Way is designed for use as in thin beads. We plan to use a self-adhering $H = 1.5\,\text{cm}$-thick EPDM gasket to seal the radon purge barrier, and the Zip-A-Way caulking substance is planned for use to patch leaks. These gaskets are both low cost and easy to use. For the gaskets measured in this thesis, radon diffusion from the cavern environment will dominate the concentration within the enclosure surrounding the lead shielding. Since diffusion is expected to dominate, the Zip-A-Way can also be used to improve the radon-reduction of EPDM gasket by lining the inside and/or outside of the adhesive gasket. This will help to ensure that human error will not play a role in the mitigation (or lack thereof) of the steady-state ^{222}Rn concentration in the radon purge barrier!

Chapter 6

The BetaCage: Low-Background Surface Screening TPC

Sensitive assay of low-energy beta- and alpha-emitting radio-impurities, *e.g.* ^{210}Pb, ^{32}Si, and ^{3}H, especially of material surfaces is necessary to meet the background goals of direct-detection dark-matter experiments to push to greater sensitivities [141]. Very few detectors are expected to be background-free, so the radio-purity of materials in an experimental apparatus hugely impact the detector's expected sensitivity. Uranium and thorium decay to radon and eventually lead, are present in dust. As described in **Section 1.3.2**, ambient radon, present in the air at concentrations $C_{\mathrm{Rn}} \sim 100\,\mathrm{Bq/m^3}$, is problematic for such experiments for many reasons. Due to its long half-life and chemically inert nature, radon readily diffuses through non-metals. Radon has many daughters which produce de-excitation gammas, high- and low-energy beta's, and alphas. Materials exposed to airborne radiation sources like radon may be subject to charged radon daughter plate-out during fabrication and installation. Detector surfaces and experimental support structures are of primary concern in this case since these long-lived contaminants can cause a variety of backgrounds. Nonpenetrating radiation from ^{210}Pb on material surfaces is a dominant background for many dark matter detectors. By limiting radon exposure during periods of construction and storage, and employing surface cleaning techniques, these surface radiation backgrounds can be significantly reduced. However, material screening and selection efforts have become a very large focus of dark matter experiments to minimize the detector backgrounds and increase the WIMP sensitivity as much as possible.

Pb-206 nuclear recoils on detector surfaces present from pre-deployment radon exposure were the dominant background for the *SuperCDMS Soudan* experiment [59, 88, 150, 151]. Measurements of gasket materials described in **Chapter 3** and **Chapter 5** of this thesis allow us to conclude that the radon present in the lead gamma shielding will be mitigated so as to contribute less than 2% of the bulk electron recoils backgrounds for the SuperCDMS SNOLAB silicon high-voltage detector backgrounds. Therefore, the backgrounds are expected to be dominated by electron recoils from the

low-energy beta-emitters Si-32 and Tritium [74]. Tritium decays are expected to be the dominant background for the germanium HV detectors above recoil energies $E_{\mathrm{R}} \approx 0.2\,\mathrm{keV}$ as well [74]. Material screening for both thee low-energy beta-emitters may become a primary concern for future detectors. For the high voltage detectors, radon daughter plate-out on detector surfaces before deployment provides the secondary (dominant) backgrounds in the low-energy regime where dark matter will produce the largest signal. The decays from long-lived daughters, like ^{210}Pb, produce both electron recoils and low-energy $E_{\mathrm{R}} < 103\,\mathrm{keV}$ ^{206}Pb nuclear recoils [74]. CRESST II was also subject to ^{206}Pb nuclear recoil backgrounds on the surface of their detectors [346], developing surface-alpha rejection techniques [347] and improved detectors to overcome these events [348] The silicon-based direct-detection dark matter experiment DAMIC will also suffer non-negligible backgrounds from Si-32 low-energy beta decays [109, 110, 120]. These events will limit the experiment's sensitivity, so measuring trace Si-32 contamination will be increasingly relevant for future silicon-based detectors. The liquid-noble dark matter experiments such as LZ [98], XENON1T [349, 350], DarkSide [351], and DEAP [352] will also suffer from radon-induced surface-alpha emission backgrounds leading to (α, n)-reactions on the PTFE and surface recoils which may be reconstructed as a signal event. Many screening devices exist which help identify low levels of radioactive contaminants, however they are generally insufficient to meet the stringent radiopurities requirements for experiments like SuperCDMS.

Intrinsic or High-purity Germanium (HPGe) detectors are an industry standard for screening the bulk gamma emission of small to medium-sized samples to determine isotopic content of *e.g.* U/Th/K/Cs. These detectors are operated at LN_2 temperature (77 K) and measure ionization produced from photons depositing some or all of their energy in the detectors. They are known for their $\mathcal{O}$(keV) energy resolution [353] and good intrinsic backgrounds due to exceptional isotopic purity during detector fabrication. They typically have an energy threshold around tens of keV, but some detectors manufactured by ORTEC [98, 354] boast an energy threshold as low as 3 keV. The energy thresholds are limited because a vacuum window separates the detector and the samples, and they suffer from inactive layers where low-energy electrons will be stopped when they enter the active detection region. For these reasons, high-purity germanium detectors are insufficient for screening very-low-energy electrons without accompanying high-energy ($> 100\,\mathrm{keV}$) gamma-ray emission. Even special-purpose detectors with very thin dead layers *e.g.*, Si(Li), B-implanted HPGe, or silicon surface-barrier detectors, are inadequate as there remains a vacuum window that may stop or scatter some particles, introducing backscattering effects which will distort low-energy emission spectra. HPGe detectors are naturally somewhat ineffectual at identifying trace Pb-210 from it 46.5 keV gamma-emission which has a minuscule 4% branching fraction. Detection volumes are usually somewhat limited so measuring a lot of material may not be possible. Moreover, due to the amount of trace radioactivity, assays take a long time to obtain statistically significant results with low uncertainties.

Mass spectrometry is an analytical technique that ionizes chemical species by breaking molecules

up into ions, which are then accelerated and selected by their mass-to-charge ratio using electric and magnetic fields. These detectors are useful for long-lived isotopes where an HPGe detector may require impractical assay times. The ion detector consists of a series of dynodes which release an electron when first struck by the sifted ion, and then by amplifying the current up to measurable levels with subsequent dynodes which cause larger electron avalanches [355]. Mass spectroscopy is sensitive enough only for some beta-emitting isotopes without an incredibly low ppt sensitivity, and is destructive, requiring significant sample processing that may introduce new contaminants. This process may also obscure the relation between the intrinsic contamination level and the measured signal. The raw material cost required to produce processable samples for each material is typically quite high [356]. Sample analysis is quite fast (of order hours) to obtain sensitivity at the ppb or even ppt levels [357] but the amount of mass processed is small $\sim 10's$ grams. SuperCDMS collaborates with chemists operating an inductively-coupled plasma mass spectrometer (ICP-MS) at PNNL who have measured uranium and thorium contamination at the ppb level [358]. It would be difficult to achieve a substantially better sensitivity which is limited by the amount of raw material processed per sample, which is not expected to increase significantly.

Counting the alpha emission of materials is useful since many low-backgrounds experiments face U/Th contamination with numerous alpha emitting daughters and may be made of materials which can undergo (α, n) reactions, due to their high neutron-interaction cross section such as $\alpha + {}^{19}_{9}\mathrm{F} \rightarrow {}^{22}_{11}\mathrm{Na} + n$. XIA [359--362] has designed a gaseous, windowless, ultra-low background alpha counter for screening thin samples $< 5\,\mathrm{cm}$. Alpha particles emitted from the surface of the material will deposit energy in the argon creating an ionization track which is drifted by a large potential to produce two pulses from concentric anode plates: one inner signal plates and an outer (veto) guard channel. Pulse-shape discrimination is employed to identify alphas from the samples. The detector discriminates signal events against backgrounds from the expected rise-time from the drift time of the electrons from an alpha track extending from the sample where it originated. Signal events have a rise time equal to the drift time of the detector. Signal alphas produce far larger signals in the central anode than the veto channel, unlike alphas from the walls of the detector itself which produce comparable signals in the inner and outer channels. Alphas from the anodes will have much smaller pulse heights dictated by the much smaller rise time, since the alpha track won't drift across the total height of the detector. The background rejection ratio is claimed to be 50,000:1 [363]. The device has an appreciably large $0.18\,\mathrm{cm}^2$ counting area and has demonstrated backgrounds $<2\,\alpha\text{'s}\,\mathrm{khr}^{-1}\,\mathrm{cm}^{-2}$ [361]. Background leakage rates from misidentified pulses with a clear dependence on the detector overburden suggests these backgrounds originate from cosmogenic sources [362, 363]. Underground deployment is expected to reduce the source of these events and potentially improve the associated systematics. The XIA is background-limited and isn't sensitive enough to meet all of SuperCDMS's radio-purity validation assay requirements for this reason, as well as geometric limitations on samples.

Similar to the Universities of Alabama and Maryland, we operate a radon emanation system at

SDSM&T (described in **Chapter 4**) consisting of large volume (13 L and 300 L) vacuum chambers for samples which may not bear an agreeable (*i.e.* very thin) geometry for use with the XIA. In this system, radon emanates from within the material bulk over a period of weeks, and the sample radon is transferred to a small detection volume using low-radon carrier gas pushed through cryogenic traps. Therein, the sample adsorbs to the cold metal traps and is concentrated to a very small volume for transfer to a small detector. In the detection volume, positively charged Po ions resulting from the alpha decay of radon are collected on the surface of a pin-diode detector and the characteristic energies of the alpha emitting Po-218 and Po-214 are used to infer the radon emanation of the sample. We achieve a generally signal-limited sensitivity of about $\mathcal{O}(0.2\,\mathrm{mBq})$ and have successfully estimated the radon emanation rate of many components for both LZ and SuperCDMS.

Other screening methods such as neutron activation and liquid scintillation are also employed to measure the intrinsic radio purity for rare-event searches. Neutron Activation Analysis (NAA) is an irradiative process where a sample is exposed to a large neutron flux which activates nuclei in the sample. The sample is then assayed for γ-emission to determine the isotopic composition of the material. NAA relies on elements which may decay with half lives of many years and is suitable for measuring K, Th, and U. It may take up to eight weeks from the beginning of sample preparation until the final data analysis may be completed, though early results may be available after 2-3 weeks. It is suitable for some non-metallic materials such as teflon, boasting beyond ppt sensitivity [357]. Neutron activation, like gamma ray detection, may allow for the measurement of many isotopes at the same time. Neutron activation is ineffective on *e.g.* Cu and Pb–which are used is significant quantities as gamma-shielding for rare-event searches. Ge as the target material for low-temperature bolometers. A serious drawback to NAA is that the irradiated sample will remain radioactive for years after the isotopic analysis. In this case, verifying a batch of materials from a vendor and using a non-irradiated sample from the same batch would be necessary. Another potential drawback is requirement of a neutron source in a safe irradiation facility which makes the technique somewhat more expensive than passive assay techniques like alpha counting and use of HPGe detectors.

Liquid scintillation counters work by mixing sample material, typically alpha- and low-energy beta-emitters, in luminescing liquids *e.g.* Zinc sulfide. Liquid scintillation cocktails absorb the decay products (α, β) emitted by radioisotopes in the sample and release the energy as light. The radioactive energy is (mostly) absorbed, and re-emitted and absorbed) by the solvent molecules. The energy will then reach the scintillators (fluors and phosphors) which get excited and undergo subsequent decay to the characteristic ground state of the scintillator. The photon emission results in light signals detectable by photomultiplier tubes (PMTs) placed near the liquid scintillators. To be an efficient LSC, the solvent (comprises $> 60\%$ of the solution) should collect as much energy from the initial decay as possible and release the energy to the scintillator, and not through some other mechanism. The efficiency loss due to the absorption of primary α- or β-energy or of the secondary photons by the solvent is called quenching. The solvent should not significantly quench

Table 6.1: List of long-lived beta-emitting or electron-capture isotopes that are not detectable by gamma screening or by mass spectroscopy (MS) less sensitive than 1 ppt, indicating effective screening method by emission of their beta electrons or alphas ('β/α'), only by their beta emission or by MS with sensitivity between 1 ppb and 1 ppt ('β/MS$^{\text{ppt}}$'), or by their betas only. Table reproduced from [365].

Method	Long-Lived Beta-Emitting or Electron-Capture Isotopes
β/α	^{210}Pb ^{208}Po ^{209}Po ^{228}Ra ^{227}Ac ^{252}Es
β/MS$^{\text{ppt}}$	^{10}Be ^{36}Cl ^{79}Se ^{97}Tc ^{107}Pd ^{135}Cs ^{137}La ^{154}Eu ^{209}Po
β only	^{3}H ^{14}C ^{32}Si ^{63}Ni ^{90}Sr ^{106}Ru ^{113m}Cd ^{147}Pm ^{151}Sm ^{171}Tm ^{194}Os ^{204}Tl

(self adsorb) the resultant scintillation from the flour/phosphor. The counting efficiencies, under ideal conditions, range from about 30% for tritium (H-3), a low-energy beta emitter with $Q \approx 18$ keV, to nearly 100% for phosphorus-32, a high-energy beta emitter, $Q \approx 1.7$ MeV. Commercial liquid scintillators are background-limited at ∼1 count/minute from cosmic rays, environmental radiation, and from the gamma shielding [364].

Generally, HPGe γ-ray assays, ICP-MS, and neutron activation analysis cannot be easily implemented to detect ^{210}Pb or its daughters at the mBq/kg level [98]. Commercial detectors are either too insensitive to low-energy betas (HPGe), assay such little material (HPGe and ICP-MS), suffer unrejectable backgrounds (alpha counters and LSC), or take too long to process sample (HPGe, NAA). **Table 6.1** shows long-lived beta-emitting or electron-capture isotopes that are not detectable by gamma screening or by mass spectroscopy (MS) less sensitive than 1 part per trillion (ppt). An ideal detector would place the sample directly in the detection medium (*e.g.* a gas) both to produce the largest detectable signal possible and to help eliminate backscattering and dead layer effects present in HPGe detectors. A detector with a large active area, a very small amount material surface area in the fiducial volume, and with very few internal backgrounds will be limited by the amount of signal events/contamination present in the sample. A detector with excellent position sensitivity will be able to further reduce the rate of backgrounds both internal and external to the detector. With enough shielding, the external backgrounds may be reduced below the level of radioactivity from the shielding itself. A detector with essentially zero external backgrounds may have improved sensitivity by employing detector materials and shielding of the highest radiopurity. Amplifying the detectable quanta, *e.g.* by operating the detector as a proportional counter, will also improve the signal-to-noise ratio and thus the detector sensitivity. These principles were used to design an ultra-low-background time projection chamber under development at SDSM&T: the BetaCage, which is the focus of this chapter. Given the limitations of current material screening technologies described above, my advisor, and some of his colleagues now on SuperCDMS, LZ, and other dark matter detectors, worked on developing a better detector. At SDSM&T, we are commissioning a small-scale prototype detector called the ProtoCage (which is discussed in **Chapter 7**) and a corresponding gas panel to reduce the most significant backgrounds, described in this chapter. This device will be much more sensitive to such surface and bulk radioactive sources from long-lived U-238 daughters, like ^{210}Pb, as well as Si-32 and H-3 that limit the current WIMP sensitivity and

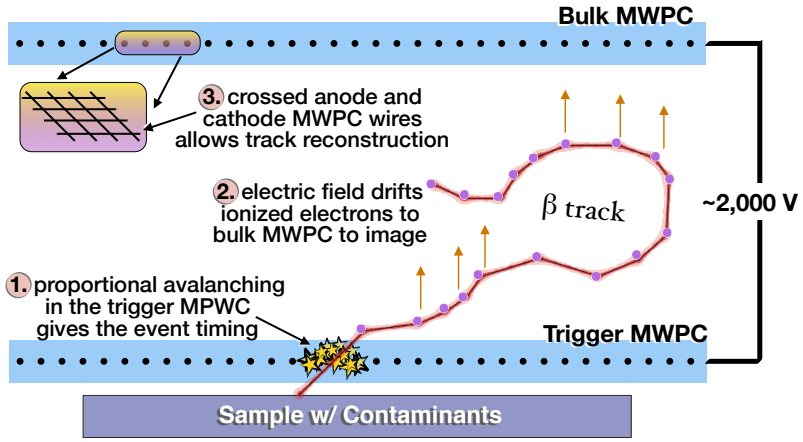

Figure 6.1: An ionization track produced by a βranging out in the fill gas of the BetaCage. **1.** A sample near the bottom MWPC provides timing information so the vertical (z) extent of the track ('β track') may be reconstructed. The ionization track is amplified (★) by operating the MWPCs as proportional counters where avalanching will ionize $\gtrsim 10^4\times$ electrons initially freed in the fill gas. **2.** An electric field from the ∼2 kV MWPC voltage separation drifts the ionized electrons towards an upper imaging MWPC. **3.** Track reconstruction is performed via the crossed anode/cathode grid configuration.

will continue to plague future generations of direct-detection dark-matter detectors.

In this chapter, I describe an ideal detector the *BetaCage*–a screener being developed at SDSM&T–which does not bear the flaws of the detectors described above. I discuss the principles of the detector design, signal creation and collection (**Section 6.1**) and the detector backgrounds and expected α- and low-energy β-sensitivity (**Section 6.2**). I describe a radon breakthrough measurement made with the gas handling system which ensure the dominant backgrounds will be reduced by $\gtrsim 50\times$ (**Section 6.3**). **Section 6.4** describes calculations and GEANT4 Monte Carlo simulations to determine the BetaCage's sensitivity to ^{32}Si β-decays throughout the bulk and on the surface of thin silicon samples, employing the same technique DAMIC used to measure the Si-32 in their thin detectors. In **Chapter 7**, I describe the ongoing development and commissioning of a small-scale prototype surface-alpha screening detector at SDSM&T which is expected to be signal-limited.

6.1 BetaCage Detector Design

The BetaCage [366--370] is a proposed ultra-low-background time projection chamber (TPC) designed to screen α's and low-energy β's emitted from surfaces (and in some cases the bulk) of materials with trace radio-impurities. The BetaCage will use three multi-wire proportional chambers (MWPC), operated as a time projection chamber (TPC), strategically surrounding a sample intended for assay. Multi-Wire Proportional Chambers have thin wires in a liquid or gas at such potentials that attract and detect the motion of electrons and ions. A simplified cross-sectional mock-up of the detection design is shown in **Fig. 6.1**. To identify byproducts (ionization) of the

surface contaminants (*e.g.* Pb-210), we measure the energy of tracks produced by alphas and low-energy betas from the sample. **1.** A *trigger* MPWC placed very near (∼1 cm) to the sample surface measures a small portion (∼1 keV) of the ionization deposited to the gas by an α or β originating from the sample. Each MWPC consists of 3 wire-planes containing two cathode planes sandwiching a central, crossed anode plane. The cathode and anode sense wires in will be separated by a voltage

$$V_{\mathrm{MWPC}} \sim 2,000\,\mathrm{Volts}$$

to provide proportional amplification of the ionization produced near the MWPCs. This MWPC directly above the sample will provide a reliable trigger start-time for particles coming from sample surfaces. **2.** The ionization track forms as the particle ranges out in the drift region of the fill gas, and is carried upwards by a homogeneous electric field

$$E_{\mathrm{drift}} \sim 50\,\mathrm{V/cm}.$$

The ionization produced in the drift region is imaged by a secondary *bulk* MWPC

$$z_{\mathrm{drift}} = 40\,\mathrm{cm}$$

above the trigger MWPC. The vertical extent of the drift region is chosen to range-out α's and low-energy β's emitted from the sample in neon gas. Neon has a large enough stopping power to contain the full spectrum of electrons from likely low-energy beta-emitters such as ^{14}C ($Q \approx 156.5\,\mathrm{keV}$, $t_{1/2} = 5,734\,\mathrm{yrs}$),^{32}Si ($Q \approx 225\,\mathrm{keV}$, $t_{1/2} = 172\,\mathrm{yrs}$), ^{210}Pb ($Q \approx 65\,\mathrm{keV}$ and $Q \approx 18\,\mathrm{keV}$, $t_{1/2} = 22.3\,\mathrm{yrs}$), and ^{3}H ($Q \approx 18.6\,\mathrm{keV}$, $t_{1/2} = 12.3\,\mathrm{yrs}$) in a 30-cm-high drift region. **3.** The anode and cathode grids in the MWPCs have a wire spacing (pitch) and inter-grid spacing $s = 0.2\,\mathrm{inches}$ ($\approx 5\,\mathrm{mm}$) which will provide xy-position information about the track of ionization in the drift region. The time profile of charge collection in the bulk MWPC will allow us to determine the spatial profile of the ionization track, in the z-direction, while the trigger MWPC provides a start time to establish the absolute z-location of the entire track. The detector will accommodate large-area samples to the maximize sensitivity to trace contaminants from sample up to area

$$A = (78 \times 58)\ \mathrm{cm}^2 \approx 0.45\ \mathrm{m}^2 \tag{6.1.1}$$

spanning the length and width of the open MWPCs. The third *veto* MWPC will help to identify through-going particles, though we expect that this MPWC is not a necessity. The design of BetaCage relies on track reconstruction to efficiently identify and discriminate against ionization tracks not originating from the sample [275, 365, 371].

The BetaCage will be deployed about an hour north of SDSM&T at the Sanford Underground Research Facility (SURF), in Lead, South Dakota. This laboratory is deep underground at the 4850 level of the Black Hills State University Underground Campus (BHUC). The significant ∼4,300 m.w.e. overburden will reduce the incident cosmic-ray flux by $\gtrsim 10^6\times$ that at the surface [98,

372--374]. In addition to using Earth's crust to mitigate these minimum interacting particles, low-background assay devices such as the BetaCage basically always require shielding to protect against the ambient photon flux coming from U/Th/K present in the rocks and dust in the lab environment. The gamma shielding for the BetaCage will consist of $\sim 20\,\mathrm{cm}$ of lead, with a small amount of ancient lead inside the outer layers of less radiopure lead, along with a 1 cm low-oxygen copper liner–oxygen-free electronic (OFE) or oxygen-free high thermal conductivity (OFHC). These high-Z materials are expected to prevent all external γ's from entering the acrylic gas vessel inside the shield [371]. Within the lead and copper gamma shielding is an acrylic gas containment vessel that also provides gamma moderation, especially for gammas produced on the inner surface of the lead shielding.

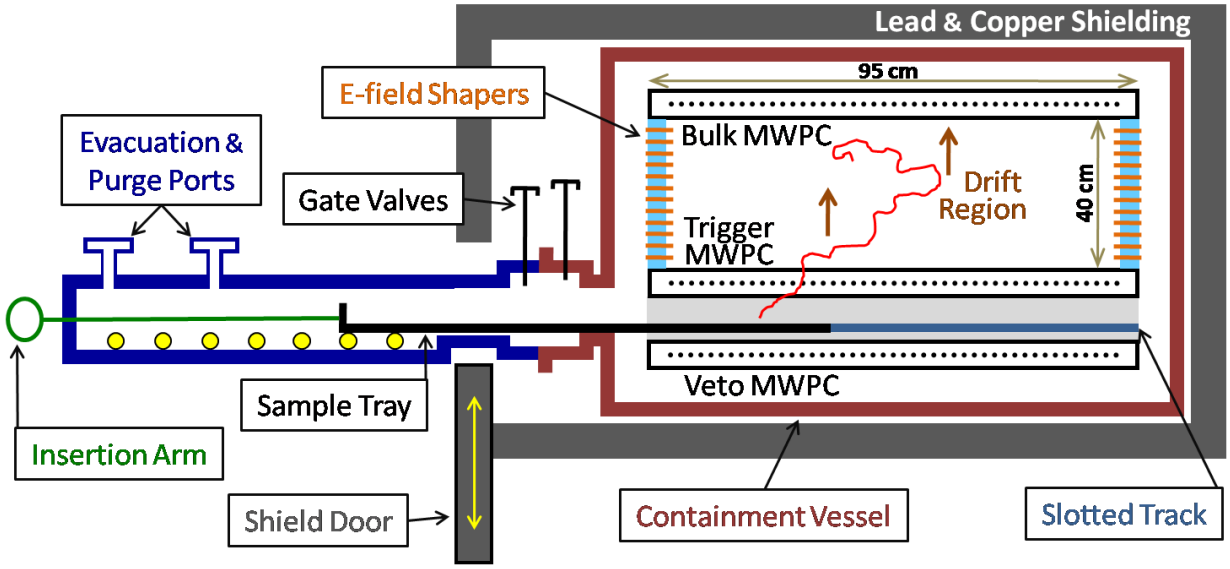

Figure 6.2: Side view of the BetaCage with an example event (red line) with the drift-field direction shown (arrows) pointing to the imaging 'bulk' MWPC. The shielding (gray) will consist of 10-cm-thick lead outside and 5-cm-low-activity lead and a 1-cm-thick low-oxygen copper liner to shield external gamma radiation. The shield surrounds an acrylic gas-containment vessel (dark red) which, along with the copper liner, moderates gammas from the surface of the lead shielding. Inside the gas vessel are (from top to bottom) the Bulk, Trigger, and Veto MWPCs (horizontal dotted), separated by electric-field shapers (blue/orange), which keep the electric field homogeneous in the 40-cm-tall drift region between the trigger and bulk MWPCs. With a simple field geometry reconstruct ionizing particle tracks in the gas is essentially trivial. Directly under the trigger MWPC is the sample tray area which is fed via a load-lock mechanism to keep contaminants from entering the detection volume with every sample change. Figure courtesy of R. Bunker.

Fig. 6.2 shows a cross section of the detector with lead and copper gamma-shielding surrounding the gas containment vessel where the three MWPCs (Bulk, Trigger, and Veto) form a time projection chamber. Ionization tracks produced in the drift region will be reconstructed to veto background events to achieve an unprecedented sensitivity to surface contaminants. The BetaCage will be constructed from materials of high radio-purity to reduce the internal backgrounds as low as possible [375]. We will construct the BetaCage at SDSM&T where we have a radon-mitigated low-dust cleanroom where the radon concentration C $<1\,\mathrm{Bq/m^3}$ which will reduce radon

daughter accumulation on the wires [146, 175--178, 187]. **Section 6.2** describes the impact of these backgrounds in more detail.

Noble gases such as Ar, Ne, and Xe (but not Rn!) are popular for ionization detectors. Gases containing few trace α-, β-, and γ-decaying isotopes are more suited to low-background measurements. Argon is also a suitable fill gas for the TPC design that is cheaper than and twice the density of neon. Unfortunately, the naturally-occurring beta-emitting isotope ^{39}Ar ($Q \approx 565\,\mathrm{keV}$, $t_{1/2} = 169\,\mathrm{yrs}$) would not be purified from the argon fill gas after purchase. The gas is supplied to the inner volume of the acrylic via the purge port, and an evacuation port will allow us to flush the volume of gas following periods of installation, calibration, and troubleshooting. A sample placement tray between the veto and trigger MWPCs with gate valves and a load-lock mechanism will allow the reuse of the fill gas. The fill gas may be continuously, or periodically, scrubbed of the most dangerous background radon, discussed in **Section 6.2.3** and **Section 6.3**, with a gas handling system described therein.

A large electric field between the anode and cathode sense wires of each MWPC will cause a proportional avalanching to amplify the number of electron-ion pairs freed by the ionizing particle. Proportional avalanching or gas amplification, occurs very close to the anode sense wires since the magnitude of an electric field

$$\left|\vec{E}\right| \propto \frac{1}{\left|\vec{r}_{\mathrm{wire}} - \vec{r}_{\beta}\right|} \tag{6.1.2}$$

with a cylindrical symmetry increases dramatically as the electron approaches the wire *i.e.* $\left|\vec{r}_{\mathrm{wire}} - \vec{r}_{\beta}\right| \to 0$. When the electric field experienced by an electron is large enough, So electrons in the gas are drifted in a homogenous electric field until they approach the anode wires. When the local electric field is large enough, electrons will no longer drift at at constant speed but will accelerate sufficiently so as to ionize secondary electrons. These electrons, produced in the vicinity of the large electric field, will then accelerate and ionize another generation of electrons [207, 376, 377]. **Fig. 6.3** shows a diagram of the first two generations of secondary electrons after an initial ionizing electron bumps into an atom producing an electron-ion pair, accelerated in opposite directions along the direction of the local electric field. The MWPCs of the BetaCage will be held at an anode-cathode potential difference $V_{\mathrm{MWPC}} \approx 2,000\,\mathrm{V}$, in the so-called proportional regime as discussed in Refs. [207, 376, 377]. The electron-ion pairs separate, drift in opposite directions, and induce a large signal on the wires, that is then shaped by an amplifier and may be digitized for offline analysis and track reconstruction. Proportional avalanching of the primary ionization will provide gain $G \sim 10^4$ sufficient to overcome electronics noise [240, 375].

A complicating factor for gas detectors of this nature is that at high electric-field strength, electrons from the inner shells of atoms in the fill gas become excited rather than being completely ionized. Following this initial excitation, a (visible or UV) photon may be emitted during the

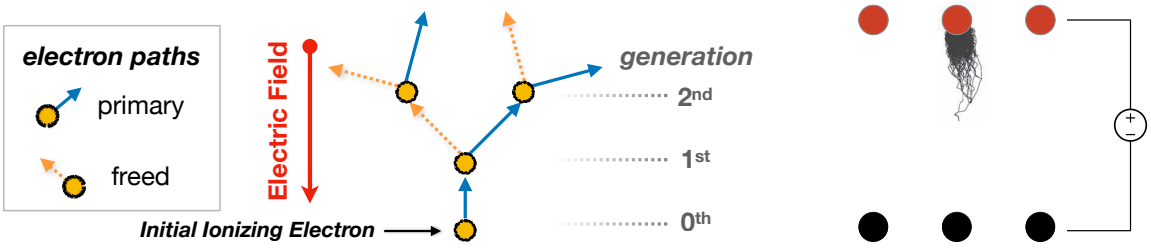

Figure 6.3: Townsend avalanching of electrons (○) under the influence of an electric field. **Left:** Diagram of avalanching with initial ionizing electron with 2 doubling generations. The electron starts at the bottom, accelerating upwards freeing a secondary electron, and both of the electrons free secondary electrons, until the electrons reach the sense wire. **Right:** Garfield simulation of an electron avalanche formation (ion trajectories not shown) in an MWPC plane, very near to an electrode. Image modified from [378].

de-excitation. This photon will have a long mean free path and may start another avalanche not local to the initial ionization leading to a non-linear relation on the energy deposited by the initial ionizing particle, and the detected pulse. If these photons are not quenched, the signal measured by the wire detector will no be longer proportional to the signal complicating the spectroscopic process. By using another 'quench' gas, typically of an organic vapor or a halogen gas *e.g.* CO_2 (carbon dioxide) or CH_4 (methane) [376, 377], which absorbs these photons. This quench gas preferentially absorbs photons without becoming ionized. This mechanism helps to keep the ionization collected by the sense wires proportional to the ionization produced by particles coming from the sample.

MWPCs are position-sensitive by nature because differences in the pulse shape arising from distance-dependent impedance of the signal arriving in the amplifier [240]. MWPCs typically have crossed anode and cathode grids so that localized ionization can be used to determine the trajectory of a charged particle passing through the detection medium (fill gas). As described in Refs. [376, 377], a set of one-dimensional wire detectors, with a pitch s has an ideal 'sub-pixel' position resolution

$$\Delta x_{\text{res}} = \frac{s}{\sqrt{12}} \approx 28\%\, s \tag{6.1.3}$$

some three times smaller than the actual wire spacing. The wire planes of the BetaCage will have a pitch

$$s_{\text{MWPC}} = 5.08\,\text{mm}, \tag{6.1.4}$$

we conservatively expect one-dimensional $\Delta x_{\text{res}} \approx 1\,\text{cm}$ position resolution in both wire plane directions. This will help us tag spatially-correlated α's or β's emitted from isotopes with multiple decay progeny. The bread and butter of the device will be measuring the complicated low-energy decay spectrum of ^{210}Pb. The sensitivity of the BetaCage to ^{210}Pb will be enhanced by the high-energy ^{210}Bi β-decay which occurs $t_{1/2} \approx 5\,\text{days}$ after the Pb-210 decay. By establishing a measure of the sample's surface-event multiplicity, the sensitivity to very low levels of α- and β-emitters will be improved beyond those described in Boqian's PhD thesis [371]. The dark matter experiment DAMIC used this technique to measure both Si-32 and Pb-210 contamination in the bulk of their

silicon CCD detector. In **Section 6.4.5**, I describe simulations of consecutive beta-emission from ^{32}Si/^{32}P which I use to determine the BetaCage's sensitivity to trace Si-32 contamination within and on the surface of thin samples. This technique will also be applicable to the sequential beta decays of ^{210}Pb/^{210}Bi.

6.2 BetaCage Background Rejection and Expected Sensitivity

The BetaCage is designed to be an incredibly sensitive alpha and low-energy beta surface screening detector to identify radioisotopes not suited for gamma-ray or mass spectroscopy. The strength of the BetaCage as a surface-assay device lies in the fiducialization from the ionization track reconstruction. In general, charged particles (α's and low-energy β's) coming from the surface of the sample will pass through the wires of trigger MWPC, and range out in the fill gas between the trigger and bulk MPWCs (*i.e.* the drift region). As result, the device will not record data unless the trigger grid registers a pulse. Events originating the drift region (below the bulk MWPC)–by volume the largest active region of the detector–not extending as down to the trigger MWPC are naturally vetoed. Tracks of ionization extending to the outer-(x, y) edge (about 1–2 cm) of the device will be vetoed. External particles entering the top of the device are expected to deposit energy to the bulk MWPC. The most signal-like of such events will produce temporally-coincident signals in the trigger and bulk MWPC and stop on the sample itself. Events depositing energy to the bulk MWPC will thus be vetoed. The BetaCage detector design minimizes internal backgrounds due to the TPC materials and provides excellent rejection of unavoidable backgrounds. The left panel of **Fig. 6.4** shows several example tracks in the BetaCage and the corresponding rejection techniques for background events labeled (A)–(E). The signal-selection criteria for the BetaCage can be summarized in the following energy deposition E_{dep} requirements: events selected as signal-like will be

1. **Triggered**: $E_{\text{dep}} > 1\,\text{keV}$ in the trigger MWPC
2. **Contained**: $E_{\text{dep}} > 5\,\text{keV}$ in the drift gas and $E_{\text{dep}} < 1\,\text{keV}$ in the bulk MWPC
3. **Not vetoed**: $E_{\text{dep}} < 1\,\text{keV}$ in the outer veto region (outer 1-2 cm in any MWPC)
4. **Bragg-like**: Energy deposition $\mathrm{d}E/\mathrm{d}x$ will increase further from the sample as the particle ranges out

Events from the sample should have enough energy deposition ($E_{\text{dep}} > 1\,\text{keV}$) to trigger the detector–**A** fails this criteria. Essentially all external particles, and those from the TPC components themselves are expected to be vetoed by their timing and energy deposition. Signal-like events should deposit little energy ($E_{\text{dep}} < 1\,\text{keV}$) to the outer edge of the detector region–events such as **B** and **C** fail these criteria. Signal-like events will be required to deposit sufficient energy ($E_{\text{dep}} > 5\,\text{keV}$) in the drift region with an ionization track whose lowest extent is consistent with the drift time corresponding to the drift length *i.e.* the distance trigger MPWC to the bulk MWPC–events like **D** fail this requirement. Events originating above the trigger MWPC, aimed towards the sample

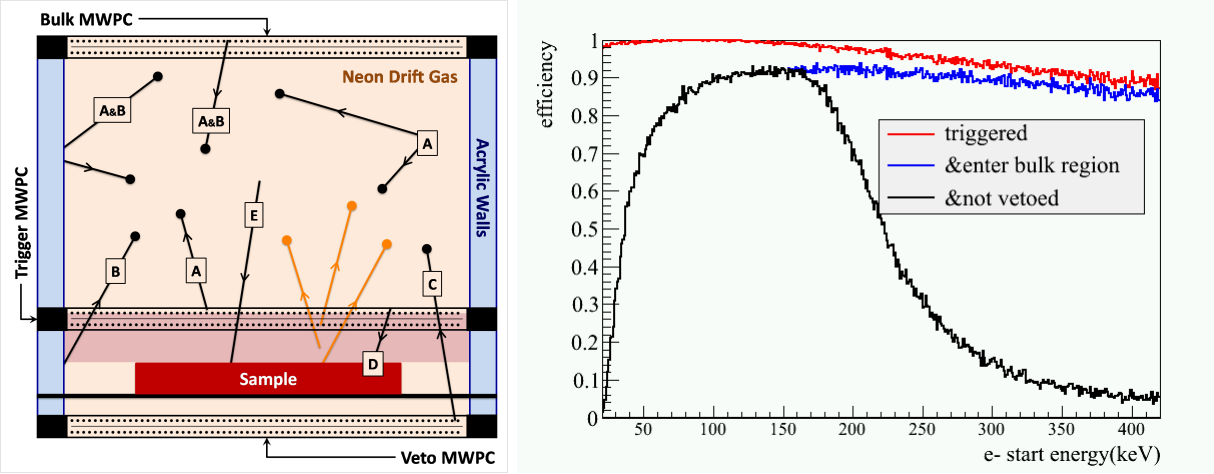

Figure 6.4: Left: Examples of background tracks we can reject (dark lines) due to their energy deposition profiles: **(A)** insufficient energy in the trigger MWPC, **(B)** lack of containment in the fiducial drift region, **(C)** too much energy in the veto MWPC, **(D)** insufficient energy in the bulk MWPC, or **(E)** uniform or 'backwards' $\mathrm{d}E/\mathrm{d}x$. Background discrimination is less effective (light lines) for betas or alphas emitted from the drift gas and cathode wires directly above the sample, or from the surface of the sample itself, following Rn-daughter implantation or Compton scattering. Events from the trigger grid, aimed upwards are expected to produce signals which do not appear (by timing) come from the sample surface. Figure courtesy of R. Bunker. **Right:** Signal selection efficiency versus initial kinetic energy for electrons emitted from a thin region 0.4 cm below the trigger grid. The curves show the effect of successive application of energy deposition cuts: $E_{\mathrm{dep}} > 1\,\mathrm{keV}$ in the trigger grid ('triggered', red), $E_{\mathrm{dep}} > 5\,\mathrm{keV}$ in the bulk gas between the trigger and bulk MWPCs ('enter bulk', blue), and $E_{\mathrm{dep}} < 1\,\mathrm{keV}$ in the outer veto region of the MPWCs and $E_{\mathrm{dep}} < 1\,\mathrm{keV}$ in the bulk MWPC ('not vetoed', black). Figure from [371].

will likely have energy deposition profiles inconsistent with the expected Bragg-peak–events such as **E** will fail this criteria. The signal-selection efficiency was determined by Boqian [371] and is shown in the right panel of **Fig. 6.4**. By simulating electrons from 0.4 cm under the trigger grid, and applying the criteria described above, the efficiency $\epsilon \approx 90\%$ for measuring electron with initial energies $E = (50\text{–}150)\,\mathrm{keV}$. The efficiency drops off at higher energies since electrons travelling through the drift region will curve enough to deposit $> 1\,\mathrm{keV}$ to the outer edge of the detector and be vetoed.

6.2.1 Detector Backgrounds

Similar to dark matter detectors, photons are problematic for the BetaCage because they may Compton scatter in the sample of interest freeing electrons that mimic signal events coming from the sample surface. Shielding made from materials with a large number of protons (high-Z) such as copper, cadmium, and lead are quite effective at stopping the ambient gamma-ray flux [379]. The BetaCage detector is designed to completely prevent external photons from entering the fiducial volume of the detector. As described in Boqian's thesis, more than 99.99% of external photons will be blocked by the lead shielding [371]. These materials themselves may contain U/Th/K throughout their bulk and may especially have U/Th daughters on their surfaces, especially the long-lived ^{210}Pb, from exposure to radon during fabrication or storage. Only *ancient* lead, which is

particularly expensive, is free from the beta-emitting ^{210}Pb and ^{210}Bi. The BetaCage shielding will be thick enough that the rate of ambient gammas reaching the fiducial volume of the detector will be negligible compared to gammas emitted from surface of the lead shield itself! This is advantageous to the design since using cleaner lead will reduce the rate of these surface-events further and may be done anytime funding is available. These lead-surface gammas will be significantly moderated by the 1 cm low-oxygen copper shielding and the acrylic gas containment vessel which prevents the unsafe fill gas from mixing with the lab.

The fill gas has such little mass that Compton scatters from gammas in the fiducial volume of the detector will be a negligible small source of signal-like events. Using argon gas will contribute ^{39}Ar beta decays throughout the fill gas. Neon has no naturally-occurring beta-emitting isotopes but is more expensive than argon since it is at a lower concentration in the atmosphere. Unfortunately, neon is less well studied than argon-based gases [376] which are the basis of many high-energy particle physics experiments [380] and direct-detection dark matter detectors [351, 352]. So as with the shielding, by using more expensive materials, beta-backgrounds from the gas may be reduced significantly. The quench gas methane (CH_4) may give rise to small amounts of low-energy β's from tritium (^{3}H, $Q = 18.6\,\text{keV}$) and ^{14}C ($Q \sim 156\,\text{keV}$). A large fraction of β's decaying in the detector's drift region between the trigger and bulk MWPCs aimed at the sample will be identified, and vetoed, by their head-tail energy deposition. The tritium contribution will depend on the cosmogenic activation of the gas. The radioactive isotope C-14 exists naturally at

$$^{14}\text{C}/^{12}\text{C} \lesssim 10^{-10} \tag{6.2.1}$$

of the ^{12}C abundance, and may be as low as $\sim 10^{-16}$ [381, 382]. The carbon will contribute only $\sim$8% of the mass of the quench gas and so the rate of these backgrounds will be negligible.

The BetaCage operates with a minimum surface area of material in the fiducial trigger volume of the detector which can be a source of backgrounds. The only truly dangerous events come from the anode wires of the trigger grid (orange lines in **Fig. 6.4**) because the sense wires are the only non-gaseous material in the fiducial volume of the detector. The total surface area of the wires (given the 0.2 inch wire pitch) in the trigger MWPC

$$A_{\text{MWPC}} \;=\; n_{\text{cath}} \times A_{\text{cath}} + n_{\text{an}} \times A_{\text{an}} = n_{\text{cath}} \times C_{\text{cath}} \ell_{\text{cath}} + n_{\text{an}} \times C_{\text{an}} \ell_{\text{an}} \tag{6.2.2}$$

given two cathode planes with $n_{\text{cath}} = 153$ wires of length $\ell_{\text{cath}} = 78\,\text{cm}$ wires of radius $r_{\text{cath}} = 12.5\,\mu\text{m}$, and a single anode plane with $n_{\text{an}} = 114$ wires of length $\ell_{\text{an}} = 58\,\text{cm}$ wires of radius $r_{\text{an}} = 62.5\,\mu\text{m}$ is

$$\begin{aligned} A_{\text{MWPC}} &= 2 \cdot 153 \times (2\pi r_{\text{cath}} \ell_{\text{cath}}) + 114 \times (2\pi r_{\text{an}} \ell_{\text{an}}) \\ &= 306\,(2\pi\, 0.36\,\text{cm}^2) + 114\,(2\pi\, 0.097\,\text{cm}^2) \\ &= 767\,\text{cm}^2 \approx 17\%\, A_{\text{B.C.}} \end{aligned} \tag{6.2.3}$$

17% of the 0.45 m^2 sample surface area. Radon daughters (^{214}Pb, ^{214}Bi, ^{210}Pb, and ^{210}Bi) may deposit energy in the sample region, trigger grid, and drift regions and become misidentified as a sample-surface event. To reduce the pre-fabricated radon daughter concentration on these surfaces [274], the wires used to string the MWPCs will be electropolished as described in [275]. During construction, the MWPCs will be strung in the low-radon cleanroom at SDSM&T which is described in *e.g.* [177, 178, 187]. This reduced-radon, low-dust environment is expected to reduce radon daughter plate-out by orders of magnitude [146] with a demonstrated radon concentration $C < 67\,\mathrm{mBq/m^3}$ (90% C.L.) consistent with zero [178]. Even with initially clean wires, radon daughters (^{214}Pb, ^{214}Bi) may lead to non-negligible backgrounds during operation. This is because the radon decay products are mostly positively charged [143, 144, 323, 324] and will likely plate-out onto the most negative surface [279, 383] either the anode wires of the trigger MWPC, or surface of the sample. Though, no radon daughter after ^{214}Po is expected to freely decay in gas [384], the long-lived ^{210}Pb will accumulate on the wire surfaces and lead to alpha- and beta-emission from ^{210}Po and ^{210}Bi which will lead to backgrounds for beta-screening [371, 385]. Events from the wires are expected to be less serious due to the timing profile of the event, but ^{222}Rn daughters plated-out onto sample will be indistinguishable from sample-surface events. So, ultimately ^{222}Rn in the fill gas is the expected to cause the most serious backgrounds.

6.2.2 Surface-Alpha Sensitivity

For α screening, the TPC design will allow us to achieve excellent background event rejection. The BetaCage will be very effective as an alpha screener because α's deposit energy in short, dense, straight, high-energy tracks dissimilar to other types of background. Alphas deposit energy with a corresponding a Bragg peak that leads to more energy deposition at the end of the track. As a result, alphas emitted from the sample are expected to be reconstructed with essentially 100% efficiency. Gamma rays from natural radioactivity are not energetic enough $E_\gamma \lesssim 3\,\mathrm{MeV}$ to be mistaken for $E_\alpha \sim 6\,\mathrm{MeV}$ alphas from the sample surface. Similarly, betas from radioimpurities in the TPC materials or fill gas won't deposit enough energy to be misidentified as an alpha. The XIA UltraLo-1800 argon gas chamber is a very sensitive commercially available alpha-screening detector discussed in the beginning of **Chapter 6** which has demonstrated a sensitivity to surface-alpha emission as low as $20\,\mathrm{m^{-2}\,day^{-1}}$ [359]. There is a systematic uncertainty associated with detector background subtraction due to the ambiguous pulse-shape of cosmic muon backgrounds [362, 363]. The ionization produced by muons depositing their energy in the drift region will be linear and very weakly ionizing. In the BetaCage, minimum ionizing muons are expected to be vetoed with 100% efficiency because they will typically produce a coincident signal in both the bulk and trigger MWPC. This is because more than 99% of minimum ionizing muons will deposit more than 0.8 keV, well above the expected electronics noise, within the first 2 mm of gas, and the other 1% of these muons will deposit energy far enough away (vertically) from the trigger grid that they could not be mistaken for a surface alpha, which at most will travel 10 cm, depositing many 10's of keV per

mm [386].

It is conceivable that $\mathrm{d}E/\mathrm{d}x$ rejection will be possible and the energy near the sample will be up to $\times 4$ more than that collected near the trigger grid and head-tail rejection may be performed to discriminate against events not emitted form the sample surface. Alphas whose tracks originate outside of the fiducial volume will be vetoed easily. The only potentially impacting backgrounds for surface-alpha screening come from alpha decays from the radon decay chain very near to the sample and on the wires. The gas volume between trigger grid and sample is a very small $\sim 1\,\mathrm{cm}$ region so this is only expected to be a problem in case of poor energy resolution, in which case, a $5.48\,\mathrm{MeV}$ $^{222}\mathrm{Rn}$ alpha may be misidentified as a $5.3\,\mathrm{MeV}$ $^{210}\mathrm{Po}$ alpha. Alphas on the anode wires of the trigger grid that are aimed up will have the wrong energy deposition profile. For these events, too little ionization will be deposited below the trigger region, producing a timing profile after the initial pulse is recorded that is inconsistent with those originating on the sample surface. Alphas from the wires that are aimed down will end on the sample and produce an energy deposition profile that does not agree with the expected Bragg-peak *i.e.* much less energy will deposited in the drift region than from a surface alpha that will range out well above the trigger grid. These will also be rejected by their timing profile since $\sim$5 MeV surface α's will have a $\sim 9\,\mathrm{cm}$ track length in a neon-based fill gas.

The most significant α screening background is expected to come from radon daughter plate-out onto the sample itself. The rate of these backgrounds will depend on the radon reduction of the purifying gas handling system, described in **Section 6.3**. We expect to veto these events by their timing, lack of energy deposition to the bulk gas region, and energy deposition profile. We expect an alpha background $B_\alpha \lesssim 100\times$ lower than the XIA due to the reliable track reconstruction and background rejection. Ultimately, we expect to be able to run the TPC free of α-backgrounds, with rare backgrounds from radon daughter plate-out onto the sample during assay. The surface-alpha emission sensitivity of the BetaCage

$$\lesssim 0.1\ \mathrm{alpha's\,m^{-2}\,day^{-1}} \tag{6.2.4}$$

is expected to be signal-limited owing to the fiducialization from ionization track reconstruction.

6.2.3 Low-Energy Beta Sensitivity

The potential power of the detector as a low-energy beta screener is a large motivation for its development. The signal-selection efficiency and backgrounds for low-energy beta-screening were studied in the PhD thesis of Boqian Wang [371] and are summarized here. Minimum ionizing muons will pose no background because fewer than 1% of muons will deposit $E_{\mathrm{dep}} \lesssim 0.8\,\mathrm{keV}$ in the bulk MWPC. In the worst case, their straight ionization deposits will lead to secondary electrons from the muon's lightly ionized path. The lead shielding is expected block all external gammas from reaching the inner detection volume. Past efforts [387, 388] and simulations [379] indicate

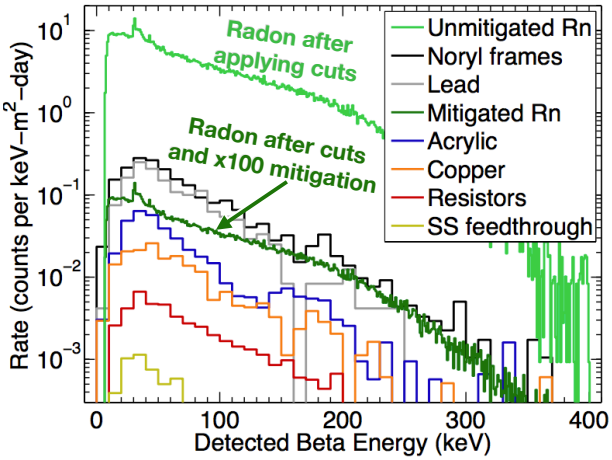

Figure 6.5: Results of Boqian Wang's simulations of backgrounds sources as a function of energy deposited to the fill gas from [371, 385]. The lead-surface gamma backgrounds (top, gray) dominate over the internal U/Th backgrounds from the TPC components which are shown separated by source (wide binned histograms) from top to bottom: lead shielding surface, noryl MWPC frames, acrylic containment vessel, copper liner, field-shaping resistors, and stainless steel feedthroughs. Backgrounds from radon (narrow binned histograms) are shown (light green) after applying the data-selection cuts which reduce the event rate 10× and even at this level, the radon-induced events will dominate all other backgrounds. By employing a radon-mitigation system (the focus of **Section 6.3**) that can reduce the radon levels by 100× (dark green), these radon-induced backgrounds will sub-dominant to the lead-surface gammas and the internal U/Th backgrounds from the TPC components.

that the 15-cm-thick lead shield will reduce the backgrounds from cavern photons below that from the inner, clean lead. Boqian simulated photons from the U/Th decay chains coming from the bulk of the TPC materials scaled to upper limits or measurements of material-contamination levels from [389--391]. The rate of backgrounds expected for each component after applying the signal-selection criteria, described in **Section 6.2**, to simulated events coming from the internal components from the BetaCage is shown (wide binned histograms) in **Fig. 6.5**. His simulations show that photons from the surface of the inner lead shielding (gray curve) will dominate those from the apparatus itself [371]. The calculations made by Boqian [371, 385] assume that the radon decay rate

$$R_{\mathrm{Rn}} = 1,300\,{}^{222}\mathrm{Rn}\,\mathrm{decays/day} \tag{6.2.5}$$

present in the the detector (not shown) is supported by the emanation of the TPC components or from the fill gas. These radon decays will lead some signal-like to beta's originating on the trigger grid wires and in the drift region gas from ^{214}Pb, ^{214}Bi, ^{210}Pb, and ^{210}Bi. This is conservative since the planned materials have already been assayed [385, 386]. Applying data-selection cuts to simulated events reduces the rate of β backgrounds by 10× as shown (thin-binned histogram, top light-green curve) in **Fig. 6.5** [371, 385]. Radon-induced backgrounds are expected to be dominant by a significant amount. To improve the outlook of the detector, w23se will employ a radon mitigating gas handling system, described in **Section 6.3**, outfitted with a carbon sample, like that described in **Section 4.2.1** and **Section 4.6**, that will capture radon in the cryogenically-cooled

gas. We expect an overall equilibrium decay rate $R_{\mathrm{Rn}} \lesssim 1,000\,^{222}\mathrm{Rn}$ decays per day from radon emanation that, with careful material selection, may be reduced further [370, 371]. The goal for the BetaCage is to obtain materials $\lesssim 10\,^{222}\mathrm{Rn}$ atom decays per day come from radon emanation, so that about 1 radon atom decays per day in the BetaCage some $\sim 10^3\times$ smaller than assumed. With a radon mitigating gas handling system reducing the rate of decays by $100\times$ to $13\,^{222}\mathrm{Rn}$ atom decays per day (as shown in the plot) the backgrounds are expected

$$\mathcal{R}_{\mathrm{B.C.}} = 3\times10^{-5}\,\mathrm{keV}^{-1}\,\mathrm{cm}^{-2}\,\mathrm{day}^{-1} \tag{6.2.6}$$

across the energy region of interest. Then, with a sample $A_{\mathrm{samp}} = 0.45\,\mathrm{m}^2$ filling the active area, and a low-energy region of interest spanning $E_{\mathrm{ROI}} = 200\,\mathrm{keV}$, the background event rate will be

$$\begin{aligned} R_{\mathrm{B.C.}} &= \mathcal{R}_{\mathrm{B.C.}} \cdot E_{\mathrm{ROI}} \cdot A_{\mathrm{samp}} \\ &= (3\times10^{-5})\,\mathrm{keV}^{-1}\,\mathrm{cm}^{-2}\,\mathrm{day}^{-1} \cdot 200\ \mathrm{keV} \cdot 0.45\,\mathrm{m}^2 \\ &= 60\,\mathrm{events}\,\mathrm{m}^{-2}\,\mathrm{day}^{-1} \cdot 0.45\,\mathrm{m}^2 \\ &\approx 27\ \mathrm{events/day} \lesssim 1.13\ \mathrm{events/hr}. \end{aligned} \tag{6.2.7}$$

a modest $\sim 1.1\,\mathrm{events/hour}$. The discovery significance of a counting experiment quantifies the ability to distinguish signal events of interest, above the detector backgrounds. The discovery significance σ_{disc} from a counting experiment such as the BetaCage measuring a sample of area A_{samp} for a time t_{asy}

$$\sigma_{\mathrm{disc}} \equiv \frac{S}{\sqrt{B}} = \frac{\mathcal{S}A_{\mathrm{samp}} \cdot t_{\mathrm{asy}}}{\sqrt{\mathcal{B}A_{\mathrm{samp}} \cdot t_{\mathrm{asy}}}} \tag{6.2.8}$$

where the total number of signal events S from a rate density $\mathcal{S}$ (events per unit area per time), above a given number of background events B with a rate density $\mathcal{B}$. With such incredibly low backgrounds, a three sigma discovery (Eqn. 6.2.8) could be placed on a sample emitting

$$3\sqrt{\frac{\mathcal{B}}{t_{\mathrm{asy}} \cdot A_{\mathrm{samp}}}} = 3\sqrt{\frac{60\,\mathrm{events}\,\mathrm{m}^{-2}\,\mathrm{day}^{-1}}{7\,\mathrm{days} \cdot 0.45\,\mathrm{m}^2}} \approx 24\,\beta' s\,\mathrm{m}^{-2}\,\mathrm{day}^{-1} \tag{6.2.9}$$

from a $0.45\,\mathrm{m}^2$ sample spanning the entire active area, in only 2 days. The BetaCage will be sensitive enough that a 3 sigma discovery significance can be made on a sample emitting

$$3\sqrt{\frac{27\,\mathrm{events}\,\mathrm{day}^{-1}}{14\,\mathrm{days}}} \approx 4\,\beta' s\,\mathrm{day}^{-1} \tag{6.2.10}$$

$4\,\beta$'s per day, in only 14 days. In **Section 6.4**, I will use Eqn. 6.2.8 to estimate the signal discovery potential for electrons resulting from surface and bulk $^{32}\mathrm{Si}$ contamination of thin samples, by using spatially correlated β's. Employing background subtraction will further strengthen the surface

screener to sensitivity to emission rates as low as

$$0.1\,\beta' s\,\mathrm{m}^{-2}\,\mathrm{day}^{-1}. \tag{6.2.11}$$

This sensitivity is orders of magnitude better than existing screening technologies. In particular, measuring ^{210}Pb contamination on material surfaces will be much easier with the BetaCage, since HPGe detectors infer ^{210}Pb levels from the 46.5 keV gamma line, which only has a 4.25% branching fraction–as opposed to the entire $Q \approx 64\,\mathrm{keV}$ beta-emission spectra. Also, HPGe detectors have *significantly* higher backgrounds and a much lower solid angle for signal detection. Directly measuring the low-energy beta spectra from Pb contamination will allow $\gtrsim 100\times$ greater sensitivity!

6.3 Radon Mitigation in the BetaCage

We expect radon-daughters to be the dominant background for low-energy beta screening with the BetaCage. In principle, the emanation can be beaten down by material selection and our goal will be to reduce the radon emanation to 10 ^{222}Rn decays per day, so the background level (after applying cuts) will be only be one radon decay per day, $\sim 20\times$ below the lead-surface gammas and U/Th backgrounds. If we can do this, then sensitivity of the BetaCage will be limited by the level of radon present in the neon- or argon-based fill gas. As described in **Section 4.6**, radon will emanate from the walls of the fill gas dewar [392]. The BetaCage will be housed in a volume

$$V_{\mathrm{BetaCage}} \lesssim 1\,\mathrm{m} \times 1\,\mathrm{m} \times 0.6\,\mathrm{m} = 0.6\,\mathrm{m}^3, \tag{6.3.1}$$

large enough to accommodate the acrylic field cage and the high voltage wiring soldered to the G10 boards lining the MWPCs. The BetaCage can be operated with neon or argon gases. I could not find a reference with a measurement of the radon concentration in neon gas. Since argon is planned for the prototype, I will briefly describe that here. The radon concentration in commercial argon gas

$$C_{\mathrm{Ar}} = (0.01\text{–}10)\,\mathrm{mBq/m}^3 \tag{6.3.2}$$

has been found to vary by a factor of a thousand [392], with a maximal contribution

$$\begin{aligned} R_{\mathrm{Ar}} &\leq C_{\mathrm{max}} \cdot V_{\mathrm{vessel}} = 10\,\mathrm{mBq/m}^3 \cdot 0.6\,\mathrm{m}^3 = 6\,\mathrm{mBq} \\ &= 21.6\,\mathrm{decays/hr} \approx 520\,\mathrm{decays/day} \end{aligned} \tag{6.3.3}$$

well above those from the internal components and lead-surface gammas. After applying event-selection cuts, only $\approx$10% of the decays will result in backgrounds, still $\sim 50\times$ the background goal. At the time of the fill, the true radon decay rate will be lower because they will occur outside the sensitive detection volume. This background may be avoided by waiting until the decays are

significantly lower than that of emanation ($\sim 10^3$/decays/day) Under the most favorable condition

$$R_{\mathrm{Ar}} = 0.01\,\mathrm{mBq/m^3} \cdot 0.6\,\mathrm{m^3} = 6\,\mu\mathrm{Bq}, \tag{6.3.4}$$

or 0.52 decays/day before analysis cuts, which will contribute about 5% of the radon decay goal after cuts. Since these backgrounds are not in our control, and may be $\gtrsim 50\times$ larger than the other backgrounds, a radon mitigating gas handling system will be employed. A gas handling system at SDSM&T (left panel of **Fig. 6.6**) is equipped with a cryogenic trap for capturing radon, so that we need not rely on a consistently pure supply of gas. To ensure these radon-induced backgrounds can be made sub-dominant, This section is focused on describing the impact of a measurement I made of radon-reduction of the gas handling system.

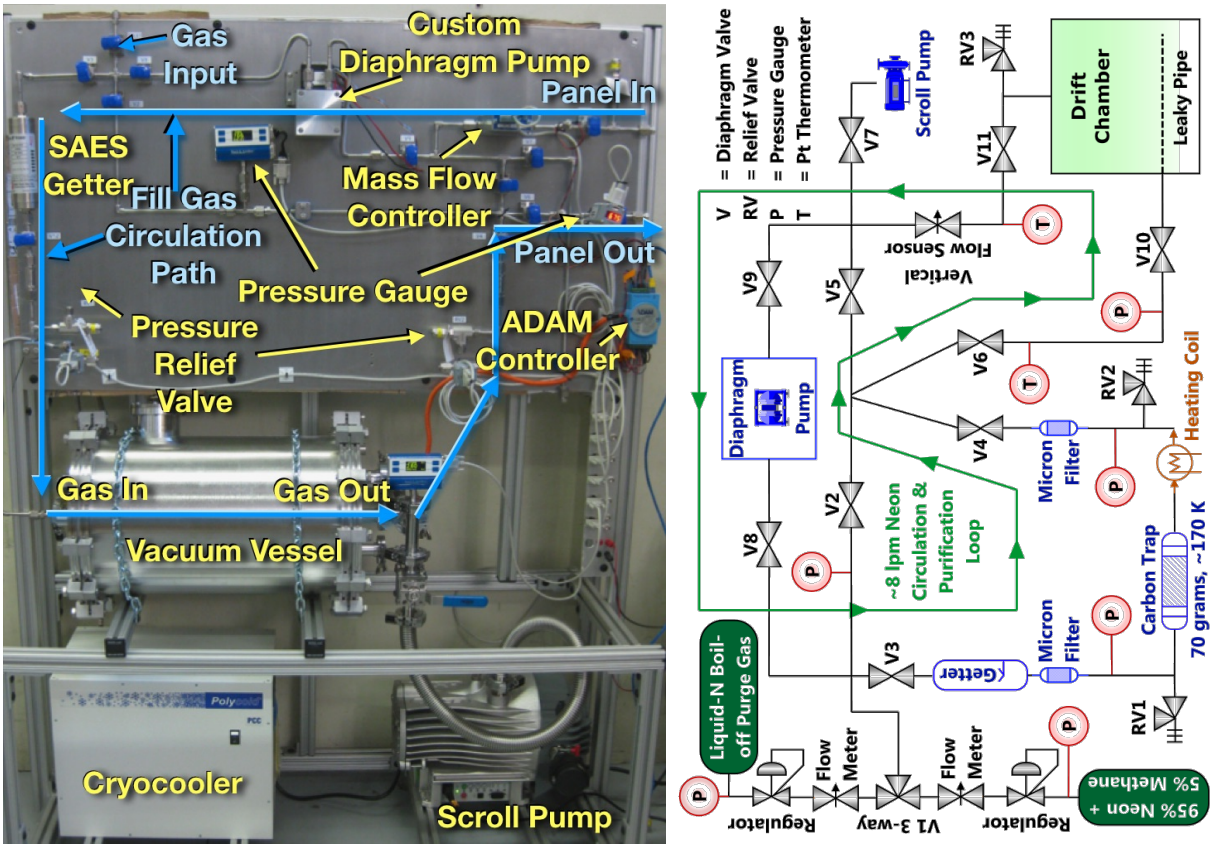

Figure 6.6: Left: BetaCage gas panel photo taken by Eric Miller. The gas panel has a carrier gas input (top left); the planned gases are neon or argon (less expensive, lower radiopurity) with 10% methane used as a quench gas. The circulation loop is shown (solid blue line) with a mass-flow controller with ethernet read-out, a custom diaphragm pump, an SAES getter, a vacuum vessel housing a copper cooling block and cryogenic carbon trap, and pressure relief valves, and pressure gauges. The panel in and out (top right) connect to the cleanroom feedthrough Resistive temperature devices (RTDs) measure the carrier gas temperature at 5 locations. An ADAM-6015 module reads out the temperature of the RTDs. The large vacuum vessel houses a copper cooling block surrounding a carbon trap through which the carrier gas passes. The copper block is cooled by a Brooks Polycold compressor. The Edwards scroll pump evacuates the vessel to rough vacuum $P \approx 3.6$ mTorr which allows more efficient cooling of the copper trap and carrier gas passing through trap, compared to cooling the trap in the ambient atmospheric environment. **Right:** Piping and instrumentation diagram (P&ID) for the BetaCage gas handling system.

The BetaCage will connect to a gas handling panel (shown left panel of **Fig. 6.6**) designed to

circulate and purify the fill gas along the blue path. The main components of the gas handling system (P&ID shown right in **Fig. 6.6**) are the fill gas–neon or argon doped (5–10%) with a methane quenching gas–and nitrogen dewars (not shown), the SAES getter and vacuum vessel housing a cryogenic carbon trap (not shown) to scrub the fill gas, a mass flow controller (MFC) and a custom diaphragm pump to circulate the gas. The gas temperature is measured with 6 temperature gauges (resistive temperature devices–RTDs) readout with an ADAM-6015 module connected to a PC. The fill gas will be circulated through the getter, carbon trap to clean the gas of gaseous impurities. The temperature gauges will be used to monitor the fill gas temperature as it passes through the carbon trap housed in a vacuum vessel and subsequently through a heating jacket. The vacuum vessel houses a copper block cooled with a Polycold cryocooler through which the gas will pass before entering a carbon trap, to improve the radon adsorption. Since argon and neon are unsafe for breathing, a scroll pump and low-radon boil-off liquid nitrogen dewar (not pictured) will be used to fill and flush the vessel volume of the fill gas before opening the chamber to operate or troubleshoot the detector in the low-radon cleanroom. During operation, a custom diaphragm pump and mass flow controller at the panel input circulate the gas through the detection vessel and gas panel. A getter in the loop removes electronegative impurities which will attract and neutralize the drifting electrons of the ionization tracks. A cryogenic-temperature carbon trap, similar to the one employed in the radon emanation system, see *e.g.* **Section 4.6**, will capture radon in the fill gas that emanated from the detector components and gas panel. By using a load-lock mechanism for sample placement, we can avoid wasting the fill gas which is already purified by the circulation loop.

The BetaCage will be operated at a vessel pressure $P_{\text{B.C.}} = 760\,\text{Torr}$. The atmospheric pressure in South Dakota $P_{\text{SD}} \lesssim 700\,\text{Torr} < P_{\text{B.C.}}$, so we expect that leaks in the gas panel or acrylic containment vessel will not let radon from the surrounding lab enter the gas panel or the detection volume. The radon concentration ($C \equiv R/V$) (decay rate per volume in the vessel), in the BetaCage will obey

$$\frac{\partial C}{\partial t} = \frac{Q}{V\tau} + \frac{FC_{\text{trap}}}{V} - \frac{FC}{V} - \frac{C}{\tau}. \tag{6.3.5}$$

depends on the emanation Q of the vessel and the gas panel, the vessel volume V, the flow rate F (STP gas volume per unit time), the output concentration of the cryogenic trap C_{trap}, and the proportional radioactive decay of radon with its mean lifetime τ. The characteristic volume-exchange rate of the detector and gas panel

$$\phi^{-1} = F/V, \tag{6.3.6}$$

is the number of vessel volumes of carrier gas flowed per unit time ($\frac{\mathrm{d}N_{\text{Vol}}}{\mathrm{d}t}$). This exchange rate allows Eqn. 6.3.5 to be recast

$$\frac{\partial C}{\partial t} = \frac{Q}{V\tau} + \frac{C_{\text{trap}}}{\phi} - \frac{C}{\phi} - \frac{C}{\tau}. \tag{6.3.7}$$

The steady-state concentration is important for BetaCage since radon in the gas could be the largest detector background. I will compare the steady-state solution to Eqn. 6.3.7 in two cases of trap performance. The first case (ideal) assumes the trap will provide 100% reduction of the radon input concentration. The second case (real) carries a reduction that includes the non-zero contribution of radon from the trap's output. The radon-reduction performance of the gas handling is strongly dependent on the flow rate and will also be impacted by the radon breakthrough time.

6.3.1 Ideal Radon Trap

Before the radon breakthrough time $t_{\text{B.T.}}$, the trap provides radon-free gas ($C_{\text{trap}} \equiv 0\,\text{Bq/m}^3$) so the steady-state concentration depends only on the output flow and the proportion of radon decaying in the vessel which reduce the radon concentration C in the BetaCage by ϕ^{-1} and τ^{-1} respectively, so that with an ideal trap, the concentration

$$C\left(\frac{F}{V}+\frac{1}{\tau}\right)=\frac{R}{V}\left(\frac{1}{\phi}+\frac{1}{\tau}\right)=\frac{Q}{V\tau}. \tag{6.3.8}$$

This equation may be rearranged to give the radon decay rate R in the chamber

$$R \;=\; \frac{Q}{\tau/\phi+1}. \tag{6.3.9}$$

It is useful to quantify the ratio of radon decays R actually occurring in the BetaCage to the vessel's radon emanation Q. The reduction factor for a perfect trap is simply

$$f_{\text{ideal}} \equiv R/Q = (\tau/\phi+1)^{-1}\,. \tag{6.3.10}$$

At high flow, the replacement time for the vessel decreases and $\tau/\phi = F\tau/V \gg 1$ so the ideal reduction

$$f_{\text{ideal}} \approx \frac{\phi}{\tau} = \frac{V}{F\,\tau} \qquad (F\tau \gg V) \tag{6.3.11}$$

in the BetaCage is inversely proportional to flow; in practice, we won't use flow rates much higher than 20 L/min. At this flow, the corresponding characteristic volume-replacement rate is

$$\phi^{-1} = F/V = \frac{0.02\,\text{m}^3/\text{min}}{0.6\,\text{m}^3} \times 1440\,\text{min/day} = 48\,\text{exchanges per day}, \tag{6.3.12}$$

about one entire vessel volume replacement every half hour. Then, the number of volume exchanges occurring during the radon mean lifetime $F\tau/V \approx (48\,\text{per day}) \times 5.52\,\text{days} = 265$, and the overall reduction for the perfect trap

$$f_{\text{ideal}}(20\,\text{L/min}) = (\tau/\phi+1)^{-1} = \left(\frac{1}{265+1}\right) \approx 0.38\% \tag{6.3.13}$$

leaves less than 4 parts per thousand of the emanated radon in the vessel. This flow is excessive, but meets the radon reduction goal $\times 100$ and is sufficient to keep the radon backgrounds subdominant

to the backgrounds intrinsic to the detector materials. A planned flow $F = 5\,\mathrm{L/min}$, $F\tau/V \approx 66$, reduces the radon decays to

$$f_{\mathrm{ideal}}(5\,\mathrm{L/min}) \approx \left(\frac{1}{66+1}\right) \approx 1.49\% \tag{6.3.14}$$

of the total emanation. and with data-selection cuts, the rate is reduced by another factor of 10 so that If the total decay radon rate $R_{\mathrm{Rn}} \approx 650^{222}\mathrm{Rn}$ decays per day, the reduction$f_{\mathrm{ideal}} = 1.5\%$, and quality cuts reducing reduced the background rate to $\varepsilon_{\mathrm{bgd}} = 10\%$, then the total background rate

$$\varepsilon_{\mathrm{bgd}}\, R_{\mathrm{Rn}} \cdot f_{\mathrm{ideal}} \approx 0.1 \times 650\,\mathrm{decays/day} \cdot 1.5\% \lesssim 1\,{}^{222}\mathrm{Rn}\,\mathrm{decays\ per\ day} \tag{6.3.15}$$

and the goal is met! While the carbon in the trap may be cooled well below 200 K, thus leading to excellent radon-trapping performance, we expect that the we cannot practically expect to trap all the radon from the vessel. Below I consider a realistic trap which allows some radon to breakthrough after some time.

6.3.2 Realistic Radon Trap

A real trap will not capture radon indefinitely. Generally, after a time $t_{\mathrm{B.T.}}$ when radon at a concentration C entering the trap has finally broken through, the concentration C_{trap} exiting the trap will be reduced by a factor

$$\eta(t_{\mathrm{B.T.}}) \equiv \exp\left(\frac{-t_{\mathrm{B.T.}}}{5.52\,\mathrm{d}}\right) \tag{6.3.16}$$

according to the exponential decay of radon with mean lifetime $\tau = 5.52\,\mathrm{days}$. The breakthrough time $t_{\mathrm{B.T.}}$ of radon passing through the carbon trap can be experimentally measured or, in the case of very effective traps, lower bound. The breakthrough time rises exponentially with the inverse of the trap temperature T

$$t_{\mathrm{B.T.}} \propto \exp(1/T)\,\frac{m_{\mathrm{trap}}}{F}, \tag{6.3.17}$$

so at larger flows F, less time is available $< t_{\mathrm{B.T.}}$ with radon-free gas at the trap output. The radon concentration at the output of the trap

$$C_{\mathrm{trap}} \equiv C \cdot \eta(t_{\mathrm{B.T.}}) = (R/V)\exp\left(\frac{-t_{\mathrm{B.T.}}}{5.52\,\mathrm{d}}\right). \tag{6.3.18}$$

The breakthrough time $t_{\mathrm{B.T.}}$ of radon passing through the carbon trap determines how close the reduction in concentration is to the ideal case above. At high enough flow rates, a significant fraction of radon that has broken through the trap, contributing a concentration increase C_{trap} to the vessel, may *enter the trap a second time* where it will spend another $t_{\mathrm{B.T.}}$, on average. The flow rate has a strong effect on the equilibrium activity, as we'll see, even for somewhat ineffective traps.

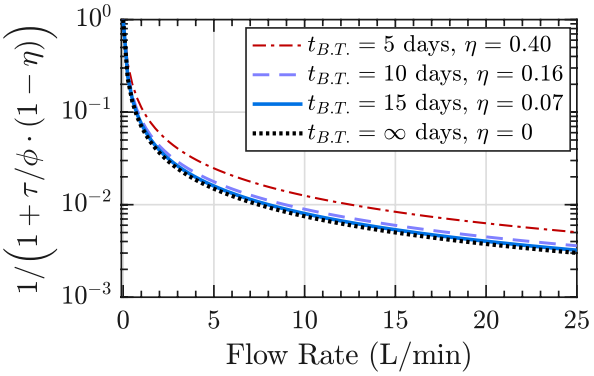

Figure 6.7: Fraction of emanated radon that decays in the BetaCage as a function of the flow rate. The ideal reduction (Eqn. 6.3.10) of a perfect trap (*i.e.* $t_{\text{B.T.}} = \infty, \eta = 0$, dotted black), and real traps f_{real} from Eqn. 6.3.21 with breakthrough times $t_{\text{B.T.}} = (5, 10, 15)$ days are shown (dash-dotted, dashed, solid lines respectively). The real reduction for a 15 day breakthrough is very close to the ideal reduction for all flows. The total reduction f_{real} varies less strongly as a function of flow, however, the reduction is limited more by the flow than the breakthrough times *i.e.* the different breakthrough curves are closer than the improvement from increasing the flow.

The steady-state concentration of radon decays in the BetaCage can be determined by the outgoing gas flow, radon emanation and decay in the vessel, and the radon at the trap output

$$\frac{C}{\tau} + \frac{C}{\phi} - \frac{C_{\text{trap}}}{\phi} = \frac{Q}{V\tau}. \tag{6.3.19}$$

The rate of radon decays in the BetaCage can be found by multiplying Eqn 6.3.19 by τ

$$\frac{R}{V}\left(1 + \frac{\tau}{\phi} - \frac{\eta\tau}{\phi}\right) \quad = \quad \frac{Q}{V}. \tag{6.3.20}$$

The reduction f for a realistic trap, the ratio of decays occurring in the BetaCage divided by the total production rate, is given by

$$f_{\text{real}} = \left(1 + \tau/\phi - \eta\tau/\phi\right)^{-1}. \tag{6.3.21}$$

It is clear that the reduction for a perfect trap is obtained when $t_{\text{B.T.}} = \infty$ and therefore $\eta = 0$. The reduction is shown in **Fig. 6.7** as a function of the flow rate a perfect trap, $\eta = 0$, (dotted black), and for a real trap with three breakthrough times $t_{\text{B.T.}} = (5, 10, 15)$ days corresponding to reductions $\eta = (0.4, 0.16, 0.07)$ respectively. As expected, the output of the trap ηC weakens the overall reduction from the ideal case, where the denominator is simply $1 + \tau/\phi$. At high flow, the replacement time for the vessel decreases and $\tau/\phi = {}^{F\tau}/_{V} \gg 1$, so the fraction f_{real} of radon emanated decaying in the vessel

$$f_{\text{real}} \approx \frac{1}{\tau/\phi(1-\eta)} \qquad \left(F\tau(1-\eta) \gg V\right). \tag{6.3.22}$$

in the BetaCage are inversely proportional to flow. In practice, we won't use flow rates as high as 20 L/min. The BetaCage gas panel is currently outfitted with a diaphragm pump and a mass flow controller which can be read a maximum flow $F = 5$ L/min. At this flow, the volume replacement

rate

$$\frac{F}{V} = \frac{5\,\mathrm{L/min}}{0.6\,\mathrm{m}^3} = 0.5\,\text{volume exchanges per hour.} \tag{6.3.23}$$

Even at low flows $F \sim 1\,\mathrm{L/min}$, radon decays $\lambda_{\mathrm{Rn}} = 7.60 \times 10^{-3}\,\mathrm{hr}^{-1}$ are slow enough to occur that radon re-entering the BetaCage from the trap output has a much higher probability of going back into the trap a second time than decaying in the vessel. So for modest flow rates, the reduction is still considerable. The planned flow $F_{\mathrm{nom}} \approx 5\,\mathrm{L/min}$ is not expected to influence the ionization tracks produced in the drift gas. The reduction at $5\,\mathrm{L/min}$

$$f_{\mathrm{real}}(5\,\mathrm{L/min}) \approx \left(\frac{1}{66}\right) \frac{1}{1 - \exp\left(\frac{-t_{\mathrm{B.T.}}}{5.52\,\mathrm{d}}\right)}. \tag{6.3.24}$$

Let us consider the impact on reduction for a real trap with non-zero radon concentration at the trap output. The decay factor $\eta \equiv \exp(-t_{\mathrm{B.T.}}/\tau)$ to demonstrate a given reduction is

$$\begin{aligned} f_{\mathrm{real}}^{-1} &= 1 + \tau/\phi - \eta\tau/\phi \\ \eta\tau/\phi &= 1 + \tau/\phi - f_{\mathrm{real}}^{-1} \\ \eta &= \phi/\tau\Big(1 + \tau/\phi - f_{\mathrm{real}}^{-1}\Big). \end{aligned} \tag{6.3.25}$$

The breakthrough time needed to demonstrate a given (real) reduction is

$$t_{\mathrm{B.T.}} = -\tau \ln\Big(\phi/\tau \times \big(1 + \tau/\phi - f_{\mathrm{real}}^{-1}\big)\Big). \tag{6.3.26}$$

We plan to demonstrate the trapping is sufficient so that the equilibrium concentration at the output of the trap provides some fraction of the ideal reduction

$$\varepsilon \equiv \frac{f_{\mathrm{ideal}}}{f_{\mathrm{real}}}. \tag{6.3.27}$$

The real reduction is weaker than the ideal reduction, and so leaves a larger fraction of the emanated radon, than the ideal reduction so that $\varepsilon < 1$. Then plugging in the ideal reduction (Eqn. 6.3.10) with flow and decay terms

$$f_{\mathrm{real}} = \varepsilon^{-1} f_{\mathrm{ideal}} = \frac{\varepsilon^{-1}}{\tau/\phi + 1} \tag{6.3.28}$$

to the decay factor (Eqn. 6.3.25) gives

$$\eta = \phi/\tau \times \big(1 + \tau/\phi - \varepsilon(\tau/\phi + 1)\big) = \phi/\tau\,(1 - \varepsilon)\,(1 + \tau/\phi)$$

Then the decay needed in the real case to achieve a certain fraction of the ideal reduction

$$\eta = (1 - \varepsilon)\,(1 + \phi/\tau)\,. \tag{6.3.29}$$

As expected, the breakthrough time for a real trap with the same reduction as a perfect trap *i.e.* $\varepsilon = 1$

is infinite. For a flow $F = 5\,\mathrm{L/min}$, the ratio ϕ/τ is the BetaCage vessel volume V divided by the characteristic replacement volume $F \times \tau$

$$\frac{\phi}{\tau} = \frac{0.6\,\mathrm{m}^3}{(5\times10^{-3}\,\mathrm{m}^3/\mathrm{min})\,1440\,\mathrm{min/day}\times 5.52\,\mathrm{days}} = \frac{0.6\,\mathrm{m}^3}{39.7\,\mathrm{m}^3} = 0.015. \tag{6.3.30}$$

So, to provide $\varepsilon \approx 90\%$ of the reduction of a perfect trap, a real trap needs a decay factor

$$\eta(0.9) = (1-0.9)\times(1+0.015) = 0.1015 \tag{6.3.31}$$

and a corresponding a breakthrough time $t_{\mathrm{B.T.}} = -\tau\cdot\ln\eta$

$$t_{\mathrm{B.T.}}(0.9) = -5.52\,\mathrm{days}\cdot\ln(0.1015) = -5.52\cdot(-2.28) = 12.6\,\mathrm{days} \tag{6.3.32}$$

of $F = 5\,\mathrm{L/min}$ flow without radon breakthrough. It is crucial to test the performance of the gas handling system to estimate the reduction of the radon-induced backgrounds.

It is somewhat more intuitive to cast the radon breakthrough time as a volume

$$V_{\mathrm{B.T.}} = F\cdot t_{\mathrm{B.T.}} \tag{6.3.33}$$

because with a fast flow rate and radon breakthrough will occur quickly, and at zero flow, ignoring diffusion, the radon will never breakthrough. The performance of the trap, *i.e.* the trap's breakthrough time or volume determines the reduction. **Fig. 6.8** shows the reduction f_{real} for five flow rates $F = (2.5\text{–}25)\,\mathrm{L/min}$ as a function of the breakthrough time $t_{\mathrm{B.T.}}$ (left panel) and volume $V_{\mathrm{B.T.}}$ (right panel). For a trap with a 15 day breakthrough, the reduction f_{real} is *very close* the ideal reduction f_{ideal}. The left panel shows the reduction does not improve beyond a 10 day breakthrough time for all flow rates shown. The difference in reduction indicated by the curves indicates that the reduction is a very strong function of the flow rate (curves). In practice we won't flow at $\gtrsim 15\,\mathrm{L/min}$, but if breakthrough time is larger than a few days, the radon reduction will be flow limited.

6.3.3 Lower Limits on Radon Breakthrough (137 K)

To trap radon in the BetaCage, coming from the fill gas and emanated from components, a 70 gram sample of Saratech synthetic carbon [393] (GmbH 102688) obtained from Wolfgang Rau was placed in a stainless steel tube by R. Bunker and undergraduate D. Noble. Eric Miller installed the carbon trap on the gas handling system. At low temperatures, radon will adsorb to the surface of the carbon and be trapped before the breakthrough time. In order to achieve sufficient radon trapping with such a small mass of carbon, a cryocooler must be able to cool the gas entering the carbon trap to cryogenic temperatures. A copper cooling block (shown dark orange in **Fig. 6.9**) cools gas at the vacuum vessel input, before it passes through the carbon trap. The cold finger of the compressor is fed through to the inner volume of the vacuum jacket shown (blue) in the left panel

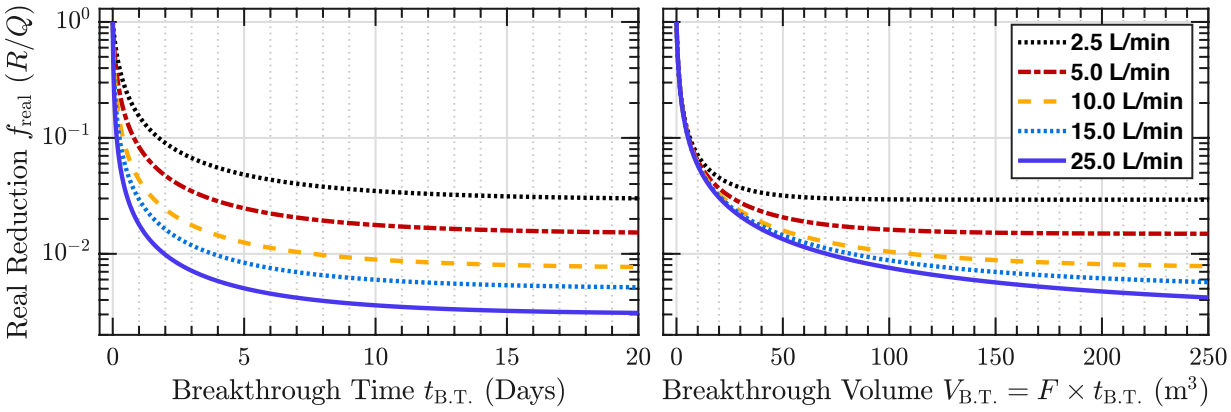

Figure 6.8: Fraction f_{real} of emanated radon that decays in the BetaCage (Eqn. 6.3.21) for 5 flow rates (in legend) as a function of the breakthrough time $t_{\text{B.T.}}$ (**left**), and the breakthrough volume $V_{\text{BT}} = F \times t_{\text{B.T.}}$ (**right**). The deviation from the ideal case (Eqn. 6.3.10) for a 10 day breakthrough time is very small! For the planned flow $F = 5\,\text{L/min}$, we need only demonstrate a $t_{\text{B.T.}} \approx 10\,\text{day}$ breakthrough time to essentially have a perfect trap.

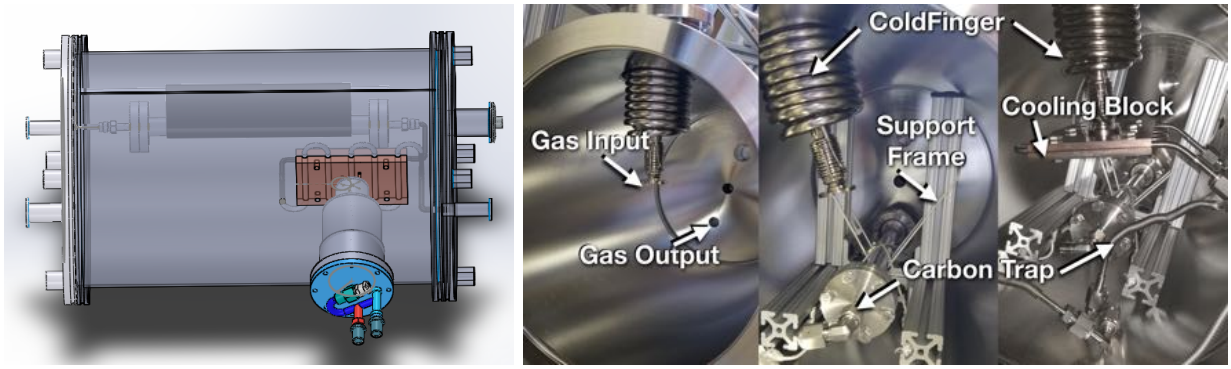

Figure 6.9: Left: Vacuum vessel with copper block (orange), and cold finger feedthrough (blue) which cools gas passing through the copper block to $T_{\text{gas}} = 137\,\text{K}$, before reaching a carbon trap where incoming radon is expected to spend $\gtrsim$weeks before breaking through the trap. CAD drawing by undergraduate John Ziadat. **Right:** Components inside the vacuum jacket as they are chronologically installed: carbon trap, support frame, and the copper cooling block. The input and output gas ports are on the circular flanges. The cold finger connects the Polycold cryocooler (not pictured) to the copper cooling block, and support frames hold the carbon trap in place. Pictures adapted courtesy of S. Aviles.

of **Fig. 6.9**. The cold finger is attached to a copper block which acts as a thermal reservoir that cools the fill gas to cryogenic temperatures before entering the trap. The left panel of **Fig. 6.9** shows the copper blocks surrounding the gas line which feeds to the tube containing the activated-carbon radon filter supported by t-slotted framing in the vacuum vessel. The right panel of **Fig. 6.9** shows the components being installed sequentially inside the vacuum jacket. Following the (external) application of a silicone heating tape, reaching $T \approx 300\,^\circ\text{F}$ for 6 hours, to bake-out the inner volume of the vacuum jacket, the vacuum vessel can be evacuated to a pressure $P_{\text{vac}} \approx 3.7\,\text{mTorr}$. We use resistive temperature devices (RTDs) connected to an ADAM module sending temperature data at 5 locations in the gas panel: 2 attached to the copper cooling block, 1 attached after the cooling block, 1 after the heating jacket before the gas panel output, and 1 after the gas panel input before the mass flow controller (MFC) and diaphragm pump. When the vacuum vessel is evacuated to

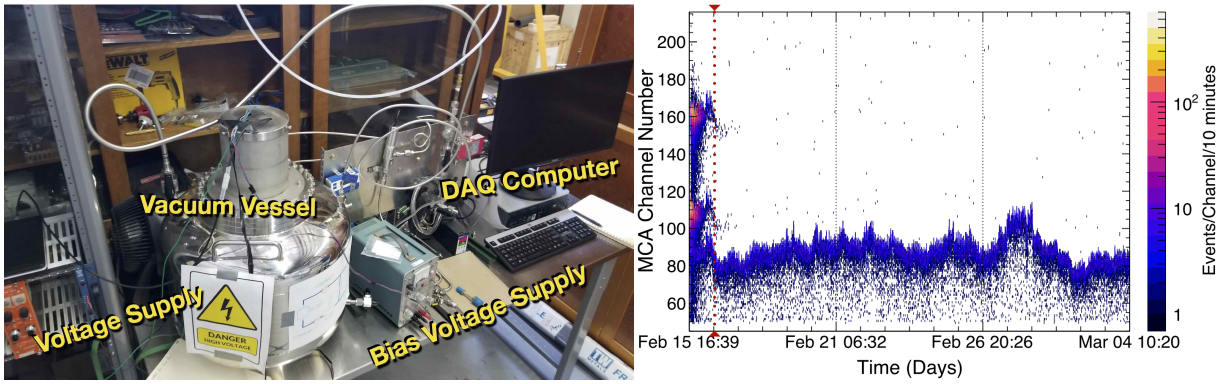

Figure 6.10: Left: The radon monitor with a 70 L vacuum vessel housing a Hamamatsu alpha detector biased to $V_{\text{bias}} = 50\,\text{V}$. The gas ports of the vacuum vessel were connected to the BetaCage gas handling system to measure the breakthrough of the cryogenic carbon trap. This detector works identically to the radon emanation system detector described in **Section 4.3**. By placing the detector at an offset voltage $V_{\text{offset}} = -1.5\,\text{kV}$, polonium ions are electrostatically collected to infer the radon decay rate in the vessel using data stored on the DAQ computer. **Right:** (Colormap) Pulse height spectrum as a function of time showing the analog-to-digital converted (ADC) counts per channel per 10 minute interval during the breakthrough test of the carbon trap. The test was performed at a trap temperature $T = 137\,\text{K}$, and a flow rate $F = 5\,\text{L/min}$. The small $^{218/4}$Po decay rate (between MCA channel numbers 100 and 160) from the Pylon calibration source decreases to the level of the detector background over a period of 1 day (vertical dotted). The ^{210}Po alpha decays are fluctuating near channel 80; this gain fluctuation does not impede measurement and the observed lower limit on breakthrough time $t_{\text{B.T.}} \gtrsim 16\,\text{days}$ of the carbon trap in the BetaCage gas handling system is essentially perfect.

such low pressures the gas passing through the carbon trap may be cooled to a temperature

$$T_{\text{trap}} = 137\,\text{K} \tag{6.3.34}$$

well below the planned 180 K. To measure the breakthrough time of the $m_{\text{trap}} = 70\,\text{gram}$ carbon trap inside the BetaCage gas panel, the input and output gas lines of the BetaCage gas panel were connected to a radon monitor in preparation for a long measurement of the radon concentration at the trap output. The vacuum vessel was held at a pressure $P_{\text{vac}} \approx 4\,\text{mTorr}$ and the gas temperature was indirectly measured by RTDs inside the vacuum jacket connected to the gas line at the trap output. Before the test began, the gas passing through the trap was a consistent temperature $T_{\text{trap}} = 137\,\text{K}$. The radon monitor, shown in the left panel of **Fig. 6.10**, consists of a photodiode detector in a

$$V_{\text{det}} = 70\,\text{L} \tag{6.3.35}$$

vacuum vessel, commissioned by Luke Corwin's group at SDSM&T with the help of Jungho So, Eric Morisson, and David Molash. The detector collects positively charged radon daughters similar to the R.E.S. α detector. Eric Morrison determined an upper-limit on the radon daughter decay background $R_{\text{bkgd}} \sim 2\,\text{cts/day}$ so the radon monitor is sensitive to radon activities $C_{\text{sens}} \sim 10\,\text{mBq/m}^3$. To test the breakthrough time $t_{\text{B.T.}}$ of the carbon trap, I sealed the pylon source for $t_{\text{build}} = 2\,\text{minutes}$. The initial rate of radon decays (Eqn. 4.2.8)

$$R_0 = \lambda\, R_{\text{py}} \times t_{\text{build}} = 14.6\,\text{Bq/min} \times 2\,\text{min} \approx 29.2\,\text{Bq}. \tag{6.3.36}$$

transferred to the $V_{\rm det} = 70\,\mathrm{L}$ radon monitor, had an initial concentration

$$C_0 = {}^{R_0}\!/_{V_{\rm det}} = {}^{29.2\,\mathrm{Bq}}\!/_{70\times10^{-3}\,\mathrm{m}^3} \approx 400\,\mathrm{Bq/m}^3.$$

This radon activity is sufficient to last 5 radon decay half-lives $5 \times 3.82\,\mathrm{days} \approx 19\,\mathrm{days}$ for the breakthrough test since the overall concentration

$$C(19\,\mathrm{days}) = C_0 \exp({}^{-19\,\mathrm{days}}\!/_{5.52\,\mathrm{days}}) \approx 400\,\mathrm{Bq/m}^3 \times 3.2\% \approx 12\,\mathrm{Bq/m}^3 \gg C_{\rm sens}$$

would remain well above the sensitivity of the detector. Given the nature of a breakthrough test, very low radon daughter levels are measured which then smoothly reach an equilibrium, exact knowledge of the polonium collection and detection efficiencies in the detector is not necessary to interpret the result. The results of the breakthrough measurements are shown in the right panel of **Fig. 6.10**. The measurement of backgrounds in the $^{218/214}$Po for 2 weeks correspond to a lower limit on the breakthrough time

$$t_{\rm B.T.}(137\,\mathrm{K}) \gtrsim 16\,\mathrm{days} \tag{6.3.37}$$

and a breakthrough volume of carrier gas no less than

$$V_{\rm B.T.} = F\,t_{\rm B.T.} = 16\,\mathrm{days} \times 5\,\mathrm{L/min} \times 1440\,{}^{\mathrm{min}}\!/_{\mathrm{day}} \times {}^{1\,\mathrm{m}^3}\!/_{10^3\mathrm{L}} \approx 115\,\mathrm{m}^3. \tag{6.3.38}$$

The breakthrough volume at this flow indicates a radon decay reduction $\varepsilon \approx 95\%$ of the ideal reduction will be achievable in in the BetaCage. Assuming the radon emanation produces $Q \lesssim 1,300\,{}^{222}$Rn decays/day in the BetaCage (Eqn. 6.2.5), and the radon $R_{\rm Ar} \lesssim 520\,{}^{222}$Rn decays per day in argon (Eqn. 6.3.3), the $t_{\rm B.T.} \gtrsim 16\,\mathrm{day}$ breakthrough time will give (Eqn. 6.3.24) a radon decay rate

$$\begin{aligned} R &\lesssim f_{\rm real}(5\ \mathrm{L/min}) \times (Q + R_{\rm Ar}) \\ &= \left(\frac{1}{66}\right) \frac{1}{1 - \exp\left(\frac{-t_{\rm B.T.}}{5.52\,\mathrm{d}}\right)} \times 1820\,\mathrm{decays/day} \\ &\approx \frac{27.6\,\mathrm{decays/day}}{1 - \exp(-16/5.52)} \approx 30\,{}^{222}\mathrm{Rn\,decays/day}. \end{aligned} \tag{6.3.39}$$

Only $\varepsilon_{\rm bgd} = 10\%$ of the decays are expected to produce backgrounds in the BetaCage, so the total background rate from radon daughters

$$\begin{aligned} R_{\rm Rn} &= \varepsilon_{\rm bgd} \times R && (6.3.40)\\ &\approx 0.1 \times 30\,{}^{222}\mathrm{Rn\,decays/day} && (6.3.41)\\ &= 3\,{}^{222}\mathrm{Rn\,decays/day} && (6.3.42) \end{aligned}$$

within a factor of three to the goal of 1 ^{222}Rn decay/day, at which point the surface-lead gamma background dominates over the radon emanation and U/Th backgrounds from the TPC materials

themselves. The trap is expected to have a significantly larger breakthrough time, however the reduction demonstrated here can only be improved by $\approx 5\%$, which is negligible compared to the reduction of radon sources achieved with better materials and gas, which are both costly.

As shown in **Fig. 6.7**, the radon reduction is flow-limited since only so much radon enters the trap per unit time. By meeting the radon emanation goal 10 ^{222}Rn decays/day, which is 130× lower than assumed above, and using high-purity gas[1] with a radon concentration $C_{\mathrm{Rn}} \lesssim 2\,\mathrm{mBq/m^3}$ (104 decays/day), 5× lower than assumed above, the radon backgrounds

$$R_{\mathrm{Rn}} = \varepsilon_{\mathrm{bgd}} \frac{1}{66} \frac{10+104}{0.994} \approx 0.18\,^{222}\mathrm{Rn\,decays/day} \tag{6.3.43}$$

will be subdominant to both the lead-surface gammas and the U/Th gamma-backgrounds from the detector materials by ∼2 orders of magnitude!

A Diffusion Digression

The diaphragm pump on the BetaCage gas panel has a flow rate $F = 5\,\mathrm{L/min}$ and is expected to fully replace the inner volume of the radon monitor over a period

$$t_{\mathrm{exp}} = \frac{V_{\mathrm{det}}}{F} = \frac{70\,\mathrm{L}}{5\,\mathrm{L/min}} \approx 15\,\mathrm{minutes}. \tag{6.3.44}$$

This replacement rate is only possible if the gas mixes on time scales much shorter than this. However, this is an under estimate since the gas won't mix perfectly in such a short time. Some large number of these replacement times should serve to fully remove the initial concentration of radon placed in the detector. The right panel of **Fig. 6.10** shows that the time for the radon activity in the detector to shrink to the level of the backgrounds is $t_{\mathrm{rep}} \approx 1\,\mathrm{day}$ much larger than naively expected $t_{\mathrm{exp}} = 15\,\mathrm{min}$ from the flow rate. We don't expect the flow through the detector to be uniform so some radon atoms may not be near enough to the output port to escape the radon monitor. It is useful to consider the impact radon diffusion may have on this replacement falltime measured during the breakthrough test.

I could not find a measurement of the radon diffusion coefficient in nitrogen in the literature. The radon diffusion in air at atmospheric pressure

$$D_{\mathrm{air}} \sim 1.2 \times 10^{-5}\,\mathrm{m^2/sec} \tag{6.3.45}$$

is within a factor of 4 of the radon diffusion in hydrogen, helium, neon, and argon [125, 394]. The detection vessel (shown in left panel **Fig. 6.10**) is nearly cylindrical with dimensions ∼15" tall with a ∼25" diameter. The vessel may be said to have a rough characteristic dimension

$$x_{\mathrm{det}} \approx 18\,\mathrm{inches} = 0.46\,\mathrm{meters}. \tag{6.3.46}$$

[1] Or by waiting for radon initially present in fill the gas to decay before beginning an assay!

Then, the characteristic time Δt_{diff} radon atoms in the vessel will diffuse across the detector and eventually get close enough to the output port to be removed will be determined by the characteristic vessel size

$$x_{\text{det}} = \sqrt{6\, D_{\text{air}}\, \Delta t_{\text{diff}}}, \tag{6.3.47}$$

since the radon will diffuse in three dimensions [376, 395]. Then the time Δt for radon atoms in the vessel to diffuse across the whole detector

$$\Delta t_{\text{diff}} = \frac{x_{\text{det}}^2}{6\, D_{\text{air}}} \sim \frac{1}{6}\frac{(0.46\,\text{m})^2}{1.2\times10^{-5}\,\text{m}^2/\text{sec}} \approx 2.9\times10^3\,\text{sec} \approx 49\,\text{min} \tag{6.3.48}$$

is still far from the observed replacement time–about a day–in (right panel) **Fig. 6.10**. This seems to indicate that the radon diffusion does not effectively mix the gas contents in the radon monitor when the through-going flow $F = 5\,\text{L/min}$. To understand this disagreement and quantify the difference between the expected and measured replacement I performed a rudimentary fit to the total counts

$$\tilde{\mathcal{C}} = \frac{1}{V_{\text{det}}}\sum_{\text{chan}} \text{counts measured} \tag{6.3.49}$$

measured in 10 minute time bins, divided by the radon monitor volume $V_{\text{det}} = 70\,\text{L}$, in the first day period at which time the Po-218/214 counts are well above the ∼cts/day background. The total counts in a given bin

$$\sum_{\text{chan}} \text{counts measured} = \underbrace{{}^{218}\text{Po} + {}^{214}\text{Po}}_{\text{decreases with replacement}} + \underbrace{{}^{210}\text{Po} + \text{ noise events}}_{\text{constant}} \tag{6.3.50}$$

will include fast radon daughters: ^{218}Po and ^{214}Po, which decrease with gas replacement (which we know to occur over a day), the slow daughter ^{210}Po decays on the detector surface, and some noise and backgrounds events. Between the times $t = (3.5\text{–}24)\,\text{hrs}$, the data are modeled by an exponentially decreasing function

$$y_{\text{fit}} = A\,\exp(-t/B) + C \tag{6.3.51}$$

where A is the amplitude of the counts measured per unit volume, B is the (exponential) falltime of the concentration, and C is a constant offset. In this model, the coefficient C corresponds to the rate of detected Po-210 decays and the random noise events. Since this is a counting experiment, the statistical uncertainties on this pseudo-concentration $\tilde{\mathcal{C}}$ in each time bin

$$\sigma_{\tilde{\mathcal{C}}} = \frac{1}{V_{\text{det}}}\sqrt{\sum_{\text{chan}} \text{counts measured}} \tag{6.3.52}$$

can be used to determine the best-fit model. To determine the best fit parameters, I first computed the best-fit constant C, representing the rate of ^{210}Po and noise events, by a weighted average of

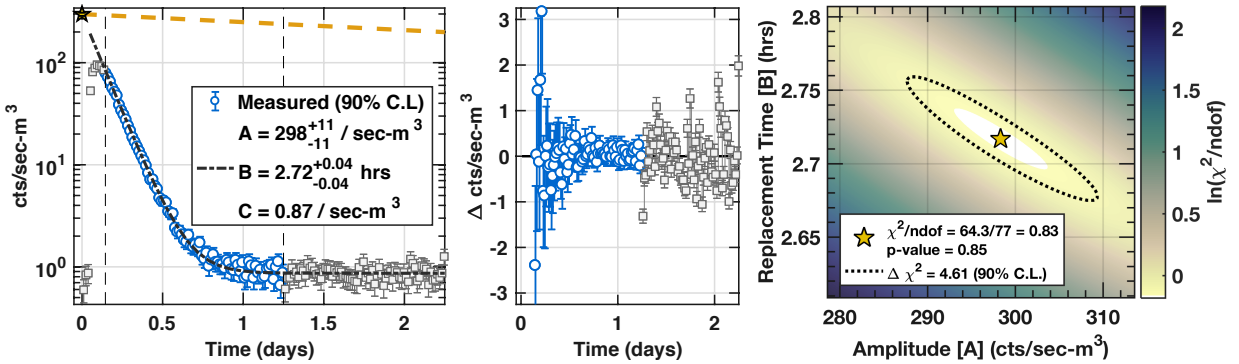

Figure 6.11: Left: (Log-scale) Time-dependent pseudo-concentration $\tilde{\mathcal{C}}$ shown with 90% C.L. statistical uncertainties1.28$\sigma_{\tilde{\mathcal{C}}}$ (rebinned $\times 2$). The data taken at early times $t = (3.5\text{–}30)$ hrs shown (blue dots) determine the best-fit model $y_{\rm fit}$ (Eqn. 6.3.51, dot-dash). The unfit data are shown (gray squares) with the expected radon decay rate shown (★, dashed) scaled to the best-fit amplitude $A \approx 300\,\text{cts sec}^{-1}\,\text{m}^{-3}$. **Middle:** (Linear scale) Difference Δ between the data $\tilde{\mathcal{C}}$ and the best-fit decay model $y_{\rm fit}$ shown (blue dots) for fitted data are $\Delta \sim 1$ of order one. The unfit residuals are shown (gray squares) scaled by $\times 5$ indicating that the best-fit C predicts the noise and ^{210}Po event rate. **Right:** Two-dimensional histogram of the natural logarithm of the χ^2/number of degrees of freedom, as a function of the replacement time B, and decay amplitude A. The $\chi^2_{\rm ndof} \approx {}^{64.3}/_{77} = 0.83$ and p-value ≈ 0.85. The dotted band corresponds to the $\Delta\chi^2 = 4.61$ and the extent of the band gives the 90% C.L. for each parameter.

the pseudo-concentrations $\tilde{\mathcal{C}}$ to times $t > 1.25$ days. The average rate of noise and Po-210 events

$$C = 0.87\,\text{cts}\,\text{sec}^{-1}\,\text{m}^{-3} \tag{6.3.53}$$

was then used in the model (Eqn. 6.3.51) and the values of A and B were determined. The amplitude A and falltime B were determined by minimizing a goodness-of-fit parameter

$$\chi^2(A,B) = \sum_{t=(3.5\text{–}30)\,\text{hrs}} \left(\frac{\tilde{\mathcal{C}} - y_{\rm fit}(A,B)}{\sigma_{\tilde{\mathcal{C}}}} \right)^2 \tag{6.3.54}$$

on a lattice of amplitudes A and falltimes B, with the weighted C determined from the weighted average of the late-time pseudo-concentrations. The left panel of **Fig. 6.11** shows the pseudo-concentrations $\tilde{\mathcal{C}}$ for the first 3 days of the breakthrough test and the best-fit prediction. The fitted data are shown (blue dots) with 90% C.L. statistical uncertainties, and the gray squares were not used to determine the best-fit model parameters. The middle panel of **Fig. 6.11** shows the residuals

$$\Delta = \tilde{\mathcal{C}} - y_{\rm fit}(A,B) \tag{6.3.55}$$

between the best-fit model $y_{\rm fit}$ and the data $\tilde{\mathcal{C}}$ and $\Delta \sim 1$ are of order one, even for the largest pseudo-concentrations at early times ≈ 3.5 hours. In the middle panel, the unfit data are shown (gray squares) scaled by $\times 5$ to increase the detail on the since the differences $5 \times \|\Delta\| \sim 1$ are of order one. The best-fit C, used as a constant in the χ^2 minimization appears reasonable from this plot. A two-dimensional colormap of $\ln(\chi^2)$/number of degrees of freedom, is shown in the right panel of **Fig. 6.11** with the best-fit (A,B) shown (★) with 90% C.L. bounds (dashed) on the model

parameters A and B. The best-fit amplitude

$$A \approx (300 \pm 10)\,\mathrm{cts\,sec^{-1}\,m^{-3}}. \tag{6.3.56}$$

is close to the nominal radon concentration $C_{\mathrm{nom}} = 400\,\mathrm{Bq/m^3}$, and the difference can be reasonably accounted from the systematic uncertainty arising from the inexact build-up time for the calibration sample. I made two attempts to add radon to the radon monitor: the first attempt partially failed due to poor gas connections from the source enclosure to the radon monitor input valve, the leak was significant enough to hear. Afterwards, I purged and resealed the source for a short time to prepare more radon. The nominal concentration is a conservative lower limit based on the expected radon decay rate from a $t \sim 2\,\mathrm{min}$ build up from the second (successful) attempt to and transfer the radon to the detector. The best-fit falltime

$$B = (2.72 \pm 0.04)\,\mathrm{hrs} \approx 162\,\mathrm{minutes} \qquad (\mathrm{at}\,90\%\,\mathrm{C.L.}) \tag{6.3.57}$$

is inconsistent with the expected flow-replacement time $t_{\mathrm{rep}} \approx 15\,\mathrm{minutes}$ (from Eqn. 6.3.44). Even though the $B = 2.7\,\mathrm{hr}$ falltime is so much larger than the diffusion time $\Delta t \approx 0.8\,\mathrm{hrs}$ (from Eqn. 6.3.48), if the gas really is perfectly mixed, the corresponding flow

$$\frac{V_{\mathrm{det}}}{B} = \frac{70\,\mathrm{L}}{2.7\,\mathrm{hrs}\cdot 60\,\mathrm{min/hr}} \approx 43\,\mu\mathrm{L/min} \ll 5\,\mathrm{L/min} \tag{6.3.58}$$

is 6 orders of magnitude lower than the nominal flow. It appears reasonable to assume the mixing is not dominated by the presumably imperfect flow but rather the diffusion of radon in the presence of turbulent flow. Assuming the mixing is diffusion dominated, then the computed diffusion coefficient

$$D_{\mathrm{comp}} = \frac{x_{\mathrm{det}}^2}{6\,B} \approx \frac{1}{6}\,\frac{(0.46\,\mathrm{m})^2}{9.7\times 10^3\,\mathrm{sec}} \approx 0.36\times 10^{-5}\,\mathrm{m^2/sec} \approx 30\%\,D_{\mathrm{air}} \tag{6.3.59}$$

is only $\times 3$ smaller than the assumed diffusion coefficient of radon in other gases (hydrogen, helium, neon, and argon) which themselves differ by a factor of 4 [125, 394]. Moreover, uncertainties on radon diffusion coefficient measurements in solids are generally as large as a factor of two, so this discrepancy seems reasonable. Radon diffusion throughout the detector does play a large role for the radon monitor at flows $F \sim 5\,\mathrm{L/min}$.

6.4 BetaCage Sensitivity to ^{32}Si Beta Decays

As described in **Section 1.3.1** and **Section 1.4.2**, the presence of low energy beta-emitter ^{32}Si in solid state detectors needs to be reduced to improve the WIMP sensitivity of dark matter detectors such as SuperCDMS SNOLAB, and the CCD-based DAMIC. Silicon-based experiments are expected to bear non-zero Si-32 contamination either through the bulk or on detector surfaces. There are several vectors of Si-32 introduction to non-radioactive silicon [119] shown in **Fig. 6.12**. The Si-32 could be intrinsic to the raw silicon ore; this is potentially the hardest vector to mitigate against. It

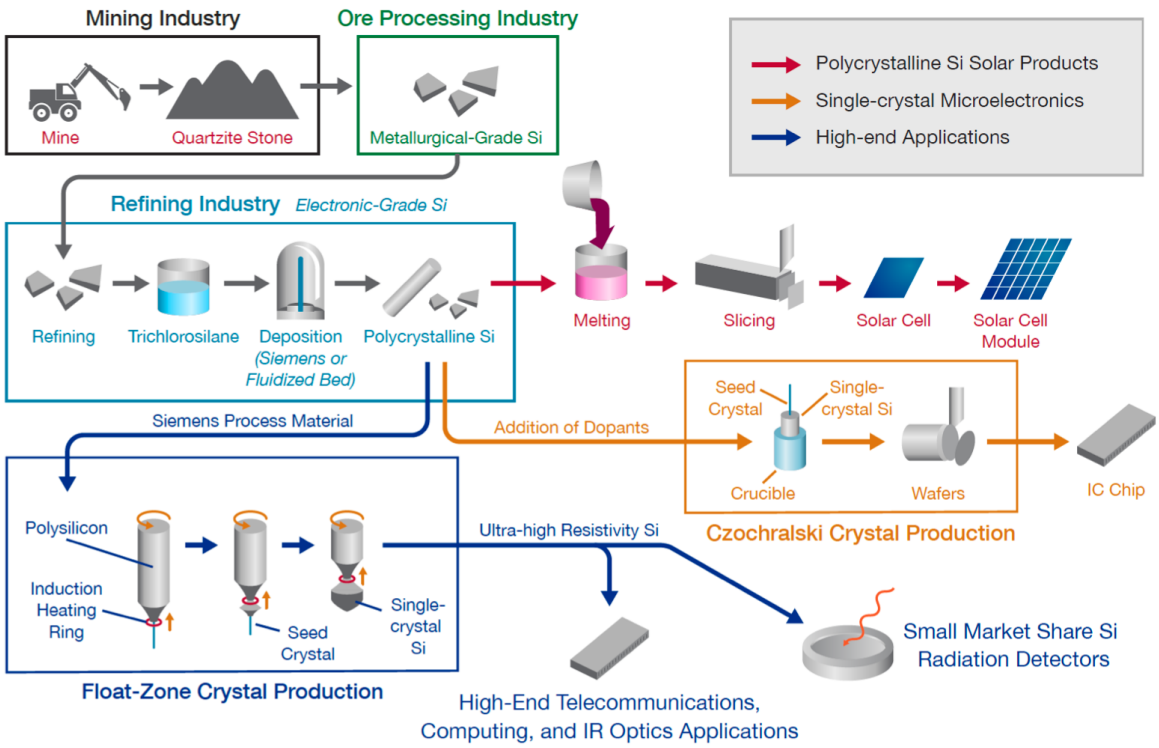

Figure 6.12: Diagram outlining the commercial silicon production cycle, from [119]. Silicon is mined, processed, refined, and further process before the final device, *e.g.* radiation detector, is produced. Si-32 may be introduced directly or indirectly, through contact with materials, at basically any stage of the cycle. There are more vectors for Si-32 to be introduced to the bulk of the material from batch processes than those that would lead to surface deposits via processing contact.

could be introduced to the raw ore during mining when in contact with surface waters containing Si-32 precipitates *i.e.* rain and snow [117, 118]. Since, chlorine has a nonzero Si-32 spallation cross section [114--116], the Si-32 may be introduced indirectly during the chemical refinement stage. When growing the crystal from refined materials, the Si-32 may be come from material recycling, or objects with Si-32 in them, such as processing crucibles. Si-32 may also be introduced during the detector fabrication and Si-containing films might leave behind a small amount of Si-32 on the device surface. To ensure ^{32}Si contamination is a sub-dominant background in the upgraded or future SuperCDMS SNOLAB detectors, we would assay silicon batches from production facilities to determine which fabrication step introduces the Si-32 to mitigate contamination in the final devices. See [119] and references therein for further description of the steps of the silicon production cycle. Ultimately, it is likely difficult to determine the source of silicon contaminant within the production cycle.

The beta-decay endpoint energy $Q_{\mathrm{Si}} = 225\,\mathrm{keV}$ gives rise to low-energy electrons [396--398]. Silicon-32 β-decays with a long half-life $t_{1/2} \approx 172\,\mathrm{yrs}$, to the short-lived ^{32}P as shown in **Fig. 6.13**. The Phosphorus-32 then beta-decays, with an endpoint energy $Q_{\mathrm{P}} = 1.71\,\mathrm{MeV}$, to the stable Sulfur-32 producing higher energy electrons, after a half-life $t_{1/2} = 14.3\,\mathrm{days}$. In the early 1990's, researchers measured the decay rate of Si-32 in their early generation WIMP detectors [400] concluding the

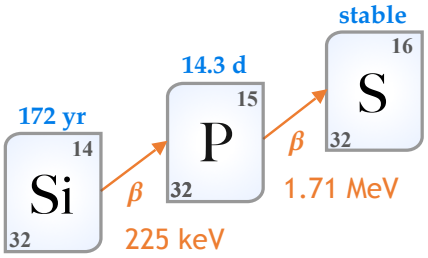

Figure 6.13: Si-32 β decay chain with half-lives and endpoint energies. ^{32}Si decays with a half-life $t_{1/2} \approx 172$ yrs, and endpoint energy $Q = 225$ keV into ^{32}P. Phosphorus beta decays with a half-life $t_{1/2} = 14.3$ days, $Q = 1.71$ MeV) to the stable ^{32}S. Both beta decays are accompanied by anti-(electron) neutrino emission (not shown). Data from NIST [399].

contamination in the solid-state detectors was at the level

$$\mathcal{A} \approx 300\,\text{decays/kg/day}. \tag{6.4.1}$$

As described in **Section 1.3.1**, DAMIC measured the rate of ^{32}Si/^{32}P decays in their CCDs to $\lesssim$ 100 events/kg/day [109, 110], drawn from spatially- and temporally-correlated electron recoils in the bulk of their CCDs. A recent measurement of the Si-32 bulk activity in DAMIC detectors had a low central value

$$\mathcal{A}^{\text{new}}_{\text{Si}-32} = (11.5 \pm 2.4)\,\text{events/kg/day} \qquad (\text{at } 95\%\text{ C.L.}) \tag{6.4.2}$$

with small uncertainties [110, 120]. Previous measurements of the bulk contamination had a larger central value

$$\mathcal{A}^{\text{old}}_{\text{Si}-32} = 80^{+110}_{-65}\,\text{events/kg/day} \qquad (\text{at } 95\%\text{ C.L.}) \tag{6.4.3}$$

with larger uncertainties on the order of the measurement itself [109]. The CCDs DAMIC used to make the two measurements [109, 110] were fabricated by TOPSIL [121] from two different silicon ingots, produced in different years. DAMIC has strong evidence that the ^{32}Si is spread through the bulk of the CCDs, not merely concentrated on the surface from contaminants deposited late in the ingot processing.

The ^{32}Si β-emission spectrum shown in the left panel of **Fig. 6.14** is the probability of an electron produced by athe radioactive decay of an atom with energy $\in [E,\, E + \mathrm{d}E]$. In natural units ($c = 1$), the differential number of events per energy

$$\frac{\mathrm{d}N}{\mathrm{d}E} = C_L(T)\, F(Z,T) \sqrt{E^2 - 2\,E \cdot m_e}\,(E + m_e)\,(Q - E)^2 \tag{6.4.4}$$

depends on the electron mass m_e, the total energy E, the endpoint energy Q of the radioactive decay–determined by the excess energy producing the decay, and a shape function C_L that depends on the forbidden-ness of the decay which is 1 for allowed decays (such as ^{32}Si and ^{32}P decays) [401], and the Fermi Function $F(Z,T)$– which I have also assumed to be 1. The right panel of **Fig. 6.14** shows

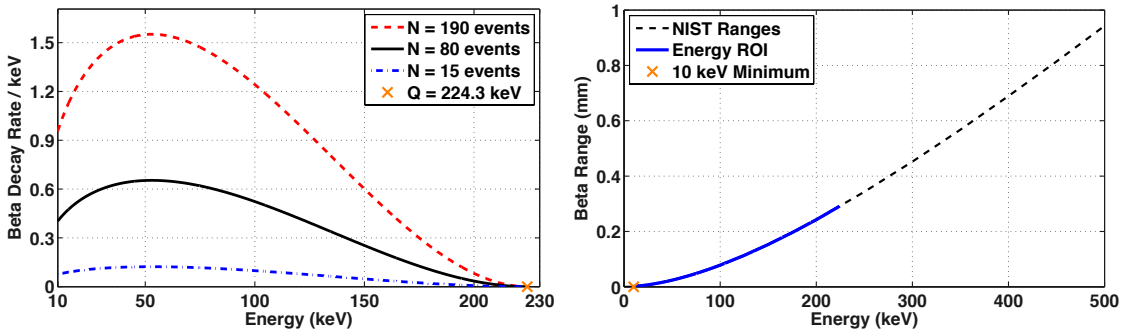

Figure 6.14: Left: Beta emission spectrum for ^{32}Si, normalized to bulk contamination measurements by DAMIC [109], with the corresponding 95% C.L. uncertainties. The endpoint energy $Q \approx 224.3\,\text{keV}$ is shown ($\times$), **Right:** Electron range in silicon vs kinetic energy from NIST [399] under the continuous slowing-down approximation described in **Section 6.4.4** are shown (dotted line). The Range-energy relation relevant to Si-32 beta decays are indicated by a solid line. No range values are givens for below 10 keV ($\times$).

the electron range d_β in solid silicon as a function of kinetic energy taken from the National Institute of Standards and Technology (NIST) [399]. The β emission-spectrum $\mathrm{d}N/\mathrm{d}E_0$, range $d_\beta(E)$, and the dimensions (*i.e.* thickness) of a sample of interest will determine the rate of electrons which can be measured by a screening device such as the BetaCage.

In this **Section 6.4**, I estimate the β-decay rate from ^{32}Si contamination of silicon wafers, due to surface and bulk contamination using order of magnitude estimates and simulations. I use the results of Boqian's simulations to determine the sensitivity of the BetaCage, with backgrounds (Eqn. 6.2.7). In **Section 6.4.1**, I describe HPGe photon spectra measurements and a simple photon flux model for a device with larger backgrounds derived from the measurements. These scaled measurements are used as a stand-in for backgrounds of a small-scale prototype device called the *ProtoCage*, deployed at SDSM&T; this detector is the focus of **Chapter 7**. **Section 6.4.2** describes the GEANT4 simulation framework used to simulate Si-32 and P-32 decays within and on the surface of bulk of thin wafers. In **Section 6.4.4**, I use semi-analytic and algorithmic calculations to compute the escape spectra from bulk contaminants. To more accurately estimate the BetaCage's sensitivity to arising from bulk betas (**Section 6.4.5**), I developed a GEANT4 simulation. I describe the results of a simulation of consecutive beta decays and calculate the rate of such events from silicon and the short-lived phosphorus, though the analysis presented here is generalizable to other radioactive decay chains with multiple daughters. The BetaCage is designed to measure Pb-210 which is long-lived, as ^{32}Si, with a half-life $t_{1/2} \approx 22\,\text{years}$, and has a short-lived daughter Bi-210, as ^{32}P to silicon. The short-lived daughters in both decay chains have half-lives $t_{1/2} \sim 10\,\text{days}$. While this section focuses on the capabilities of the BetaCage to detect silicon-32, I conclude by commenting on the potential discovery of Pb-210 on thin silicon devices.

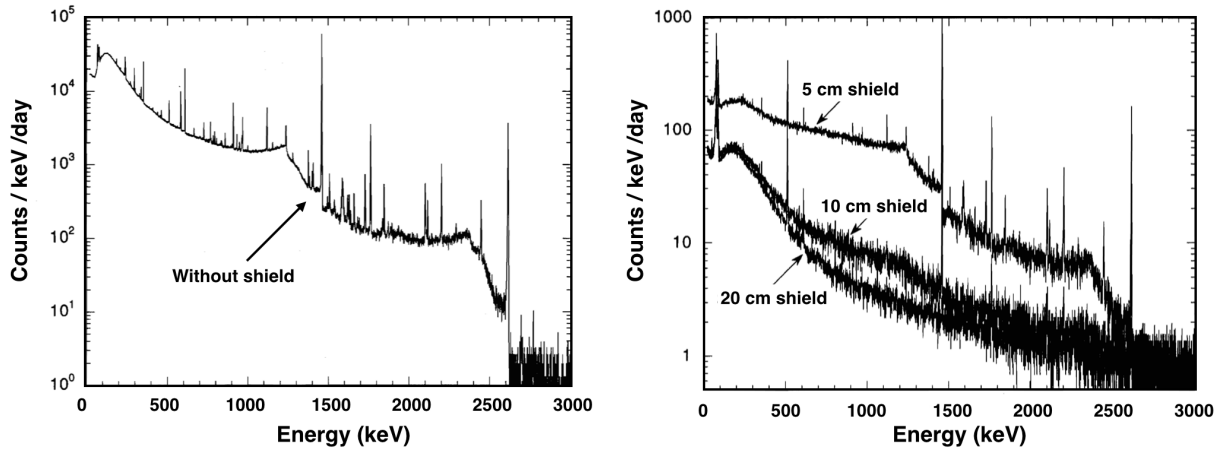

Figure 6.15: High purity Germanium (HPGe) spectrometer measurement of photon backgrounds at Stanford Underground Facility (SUF) adapted from [402]. **Left:** Ambient photon background without any lead shielding to attenuate the ambient gamma flux. **Right:** Photon background B with 5, 10, and 20 cm of lead shielding. Below 300 keV, the rate with no lead shield is *near* $2{\times}10^4$ events/keV/day, and is reduced to around 200 events/keV/day with 5 cm shielding. For 10 cm of lead, the γ rate is ~ 60 events/keV/day and there is an essentially negligible reduction at 20 cm due to the surface contamination of the lead itself.

6.4.1 Modeling the BetaCage ProtoType Photon Backgrounds

A prototype device to the BetaCage: the so-called *ProtoCage*, described in **Chapter 7**, has been installed and operated at SDSM&T. The ProtoCage is fully unshielded for the time being, although this will change with funding. To estimate the sensitivity of this unshileded device to Si-32, I use the measurements detailed in A.J. Da Silva's thesis [402] describing the effect on the rate of gamma interactions of increasing the levels of lead shielding. These measurements were made with a HPGe detector at the Stanford Underground Facility (SUF) with a modest < 20 m.w.e. overburden. In this environment, the photon backgrounds are as many as $\times 100$ higher than an underground lab. We can use the measured spectra to estimate the effect of adding up to 20 cm of lead shielding to the ProtoCage; since the BetaCage will be operated underground with 20 cm of lead shielding and another cm of copper.

Fig. 6.15 shows the ambient photon rate for a few shielding configurations at the Stanford underground Facility (SUF). It is useful to consider the background rate B_τ as a function of the shielding thickness τ in centimeters. I will take the ratio of photon backgrounds in the HPGe detector for less shielding to estimate backgrounds of the ProtoCage and describe the sensitivities for these detectors. **Table 6.2** shows a summary of the average background rate near energies $E \approx$ (0–300) keV relevant to Si-32 decays, as a function of the thickness of lead shield τ. The ratio of the background rate to the shield-free (0 cm) case. Without shielding $B_0 \approx 3 \times 10^4$ events/keV/day, whereas $B_5 \approx 200$ events/keV/day–a rate reduction of $B_0/B_5 \sim 150$. With $B_{10} \approx 80$ events/keV/day a further reduction factor of 2.5×, and overall 375× lower than the unshielded case ($B_0 \approx 375\, B_{10-20}$). The rate isn't much lower with 20 cm of lead due to ^{210}Pb decays on the surface of the lead shield itself which is evident from the rate of gammas near (46–80) keV. The presence of these decays

Table 6.2: Backgrounds in the HPGe detector at SUF near (0–300) keV with as a function of lead shielding thickness.

Lead Shield τ (cm)	0	5	10	20
B_τ (events/keV/day)	2×10^4	200	80	<60

is not reduced with more shielding due the the surface radiopurity. Obtaining an inner shield of ancient lead–samples which have been processed more than 300 years ago is costly but useful for low-background experiments needing photon shielding [403]. We might expect the Compton-scatter backgrounds due to the ambient photon spectrum s to increase roughly by a factor of 100 by removing the shielding. Then, a moderate estimate of the backgrounds in the unshielded ProtoCage

$$R_{\text{P.C.}}^{\text{moderate}} \approx 100 \cdot R_{\text{B.C.}} = 3,500/\text{day} \tag{6.4.5}$$

could be $\geq \times 100$ higher than the well-shielded BetaCage. The backgrounds for the prototype could be higher, I use this simple estimate to move forward. A more conservative, worst-case estimate of the background rate in the unshielded ProtoCage

$$R_{\text{P.C.}}^{\text{worst}} \approx 375 \cdot R_{\text{B.C.}} = 375 \cdot 35/\text{day} \approx 13 \times 10^3/\text{day} \tag{6.4.6}$$

could be up to $375\times$ greater than the BetaCage. These estimates do not account for the ProtoCage being above ground, its smaller active area, some

$$f_{\text{Active}} = \frac{A_{\text{P.C.}}}{A_{\text{B.C.}}} = \frac{40 \times 40\,\text{cm}^2}{4500\,\text{cm}^2} \approx 35\% \tag{6.4.7}$$

that of the BetaCage, or the less stringent cleanliness strategies employed during the HPGe detector commissioning at SUF which could have reduced the shielded γ spectra, using *e.g.* old lead inside the 10 cm shield.

6.4.2 Geant4: Simulation Toolkit for Particle Transport

Monte Carlo transport codes are used by many screening and rare-event search experiments to calculate expected rate of background, calibration, and signal interactions in a given detector. Applications which include energy loss fluctuations and straggling in matter allow users to obtain statistical expectations for the behavior of particles passing through > centimeters of shielding, and resulting in energy deposition spectra in a detector. Software such as the Stopping and Range of Ions in Matter (SRIM) [283] is a popular particle transport code and is among the most accurate particle range calculators, employing Projected Range ALgorithm (PRAL) equations[2] to determine the projected range; it only computes simple physics quantities with *very* simple detector geometries and doesn't run on macOS without an emulator. Other codes include Penelope a system for electron

[2]PRAL solutions are found with iterative difference equations depending on the moments of the nuclear-energy loss distribution.

and photon transport [404], and the Monte Carlo code for Neutron and Phonon transport (MCNP) which is distributed by the Radiation Safety Information Computational Center (RSICC) in Oak Ridge, Tennessee, and one must obtain permission from the DOE to use the program.

GEometry ANd Tracking (GEANT4) [405--408] is a C++-based particle physics Monte Carlo simulation toolkit obtainable by download from CERN [409] used for high-energy, nuclear, and accelerator physics, medical, biological, space science and low-background applications. GEANT4 utilizes Monte Carlo methods to simulate the passage of particles through matter based on user-chosen physics. GEANT4 employs an object-oriented approach to particle simulation. To run a simulation, one must construct the detector, choose the physics processes and particles to include and which physics quantities to read-out, and the production mode and primary particles for each event. It is useful to track spatial (*e.g.* decay-, emission-, or transmission-angle, and track length), timing (isotopic decay time or time of flight), and energy (initial kinetic energy, energy deposition) of a given particle species such as hadrons/ions, α's, β's, γ's, μ's, ν's, or particles with user-defined optical, quantum, etc. properties. The GEANT4 toolkit is useful because many useful tutorials (*e.g. /extended/radioactive/rdecay02*) can be found which may include exactly the materials, physics processes, and physics quantity readout of interest to an experiment such as a screening device.

By constructing polytopes (euclidean solids) in 3-space specifying the location, shape, size, material, in the mandatory action class: *DetectorConstruction* the full geometry of (a) radiation detectors and shielding can be realized. Particle transport is dictated by the interaction cross sections per unit distance. GEANT4 allows one to specify material components of an experiment by defining the isotopic content, temperature, density, and state of matter in geometric shapes corresponding to the detector geometry. Since a simulation can take a long time to run to obtain statistically significant results, which also depends on the complexity of the detector, the user chooses relevant physics processes; it is useful to eschew irrelevant physics in the *PhysicsList* class. GEANT4 simulates particle *transportation* (transmission, reflection, etc) and continuous (*e.g. electromagnetic* ionization) and discrete (*e.g.* nuclear and electromagnetic decay) *physics processes*. Particle transport in GEANT4 is modeled as a *Markovian* process, so that physical processes, undergone by primary and secondary particles, depend strictly on the current, instantaneous particle properties— *i.e.* no hysteresis effects are included in any native GEANT4 physics calculation. A step in GEANT4 invokes a state change to the particle, *e.g.* transportation, as determined by the physics invoked by the user.

The stopping power of a particle in a given material is calculated along each step and the behavior of the particle is determined by interaction cross sections of competing physics processes. Naturally occurring silicon, as defined in GEANT4 [407], has 3 stable isotopes, mostly Si-28 (≈92%), at the levels as shown in **Table 6.3**. The material density has a mild impact on the results here since the energy deposition of ionizing particles increases with the density of the substrate. For the simulations described in this section, I use a silicon substrate with this composition.

Primary particles are made in the *PrimaryGeneratorAction* class. The type of particle can be forced in the class, or manipulated in a macro file after the application (simulation) is compiled.

Table 6.3: List of isotopes, neutrons ($Z - A$), density N, and fractional abundance (%) of natural silicon in GEANT4.

(A)	$(A - Z)$	N (g/mole)	(%)
^{28}Si	14	27.98	92.230
^{29}Si	15	28.98	4.683
^{30}Si	16	29.97	3.087

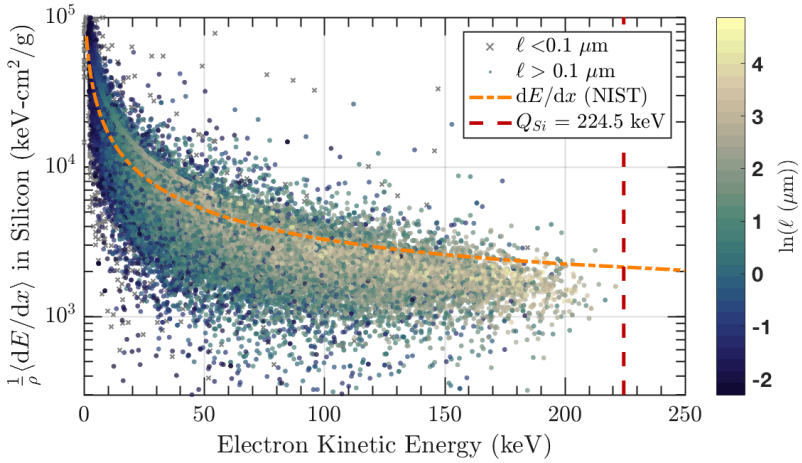

Figure 6.16: Simulated electron stopping power in silicon as a function of kinetic energy and step length (colormap). The NIST prediction is shown (dot dashed) along with the endpoint energy $Q = 224.5$ keV of Si-32 decays (vertical dashed).

physics quantities of particles relevant to the simulated experiment can be tracked in other action classes such as the *SteppingAction* class, which is evoked for every step of every particle, the *TrackingAction* class, which may be evoked for the birth and death of every (primary and secondary, etc.) particle created. Physics process cannot be evoked continuously, instead physics calculations, *e.g.* ionization, are done discretely according to the appropriate interaction cross section; physics lists may also be evoked or removed in a macro file.

Low-energy electron interactions in silicon are important to predict the escape spectra for bulk contaminants, and back scatter effects. The GEANT4 simulated stopping power dE/dx of electrons traveling through silicon in GEANT4 is shown in **Fig. 6.16** as a function of kinetic energy step length (colormap) with the NIST expectation [399]. I chose to use the low-energy electromagnetic package EMOPT4 which is expected to be reliable for physical processes (such as the photoelectric effect, Compton and Rayleigh scattering, and gamma conversion) corresponding to particle energies as low as 250 eV [410], below the expected sensitivity of the BetaCage. Based on results of an optimal noise filter study in Boqian's Thesis [371], we expect to the noise of the electronics to peak at 0.6 keV, therefore this effect is not included in my simulations.

6.4.3 ^{32}Si Surface Contaminants

This sensitivity analysis assuming a wafer mass $m_{\rm CCD} = 2.9 \times 10^{-3}\,{\rm kg}$ and a surface area $A_{\rm CCD} = 19\ {\rm cm}^2$ per side similar to the CCDs deployed in DAMIC discussed in Ref. [109]. I have scaled the contamination density for these calculations the (larger) ^{32}Si DAMIC measurement (Eqn. 6.4.3) Ref. [109]. To first order, the escape rate of Si-32 electrons coming from such a sample of silicon

$$\begin{aligned} \mathcal{R}_{\rm surf} = \mathcal{A}_{\rm Si-32} \cdot \left(\frac{m_{\rm CCD}}{A_{\rm CCD}}\right) &= 80^{+110}_{-65}\,{\rm kg}^{-1}{\rm day}^{-1} \cdot \left(2.9\,{\rm g}/19\,{\rm cm}^2\right) \\ &= 1.22^{+1.68}_{-1.00} \times 10^{-2}\,{\rm cm}^{-2}{\rm day}^{-1}\ ({\rm at}\,95\%\,{\rm C.L.}). \end{aligned} \tag{6.4.8}$$

Assuming the signal selection efficiency $\epsilon_{\rm sel}$ for identifying electrons decaying upwards into the trigger MWPC is limited by the geometric detection efficiency

$$\epsilon_\Omega \equiv \epsilon_{\rm sel} = 50\% \tag{6.4.9}$$

the ^{32}Si β escape rate for a large sample of area $A = 76\,{\rm cm}^2$

$$\begin{aligned} R_{\rm surf} \equiv \epsilon_{\rm sel} \times \mathcal{R}_{\rm surf} \times A &= 0.5 \cdot \left(1.22^{+1.68}_{-1.00} \times 10^{-2}{\rm cm}^{-2}{\rm day}^{-1}\right) \cdot 76^2\,{\rm cm}^2 \\ &= 35.3^{+48.5}_{-28.8}/{\rm day} \qquad ({\rm at}\,95\%\,{\rm C.L.}) \end{aligned} \tag{6.4.10}$$

is very close to the BetaCage Compton background expectation $R_{\rm B.C.} \approx 35\,{\rm events/day}$.

One caveat to this simplistic calculation is that the SNOLAB high-voltage detectors are cylindrical, not rectangular, and couldn't possibly fully cover the active area of the planned screener. It is more accurate to consider the packing fraction $\mathcal{F}$ of circles in a two-dimensional plane, which can be done in at least two ways. A naive packing of circles in a simple rectangular lattice, called square packing, is shown in (the left panel of) **Fig. 6.17**. The ratio $\mathcal{F}$ of the areas of a circle of diameter D to the unit cell square of area $A_{\rm sq} = D \times D$ is

$$\mathcal{F}_{\rm sq} = \frac{A_{\rm circ}}{A_{\rm sq}} = \frac{\pi D^2/4}{D^2} = \pi/4 = 78.5\%. \tag{6.4.11}$$

In this case, the rate of backgrounds expected from Compton scatters in the same would be 21.5% lower than computed above in Eqn. 6.4.10. For hexagonal packing, shown (right panel) in **Fig. 6.17**, 6 circles are arranged in a honeycomb geometry with their centers at the vertices of an equilateral hexagon of side length D with one at the center. The hexagonal unit cell has one circle and two circles cut in thirds. This packing was proven to be the highest-density packing fraction

$$\mathcal{F}_{\rm hex} = \frac{3 \cdot A_{\rm circ.}}{A_{\rm hex.}} = \frac{\pi}{\sqrt{12}} \approx 90.7\% \tag{6.4.12}$$

in the Euclidean plane [411]. A hexagon of side length D, has a surface area

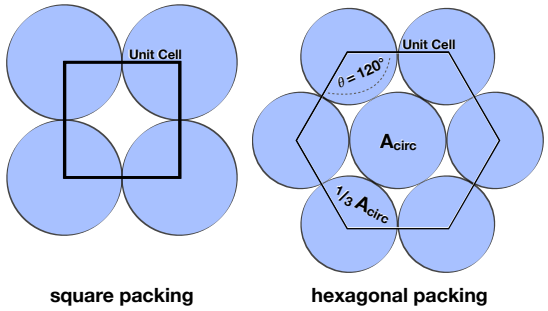

Figure 6.17: Two examples of circle packing in a euclidean plane with two units cells: square and hexagonal. **Left:** Square packing circles onto a grid bears a packing fraction $\mathcal{F}_{\rm sq} \approx 78.5\%$. **Right:** Hexagonal packing circles into a honeycomb bears a packing fraction $\mathcal{F}_{\rm hex} \approx 90.7\%$.

$$A_{\rm hex} = {}^{3\sqrt{3}D^2}/_{2}. \tag{6.4.13}$$

With hexagonally packed wafers, the Compton backgrounds and the signal would be reduced by the same ratio; only 10% lower than the available surface area. According to Eqn. 6.2.8, the signal-to-noise ratio ${}^{S}/\sqrt{B}$ for $\mathcal{F} = 90.7\%$ packing efficiency of the nominal active area $A_{\rm nom}$

$$\frac{S(\mathcal{F})}{\sqrt{B(\mathcal{F})}} \propto \sqrt{A_{\rm sample}} = \sqrt{\mathcal{F}\, A_{\rm nom}} \approx \sqrt{0.907\, A_{\rm nom}} \propto 0.952 \frac{S}{\sqrt{B}} \tag{6.4.14}$$

is reduced by only 4.8%. For this reason, these packing arrangements are ignored in the following sensitivity calculations. With well-characterized backgrounds from Eqn. 6.2.6, and a surface rate (Eqn. 6.4.10) mimicing the DAMIC result [109]) a 14 day assay period would produce a discovery significance

$$\frac{S}{\sqrt{B}} = \frac{35^{+48}_{-29}/\text{day} \times 14 \text{ days}}{\sqrt{35/\text{day} \times 14 \text{ days}}} \approx 22^{+30}_{-18} \qquad (\text{at } 95\%\,\text{C.L.}) \tag{6.4.15}$$

no worse than a 4σ, so the BetaCage is well-suited for this measurement. Counting the surface contamination of a very large sample completely filling the unshielded ProtoCage, with a background level given by Eqn. 6.4.5, the surface emission rate gives

$$\frac{S}{\sqrt{B}} = \frac{35^{+48}_{-29}/\text{day} \times 31 \text{ days}}{\sqrt{3500/\text{day} \times 31 \text{ days}}} \approx 3.3^{+4.5}_{-2.7} \qquad (\text{at } 95\%\,\text{C.L.}) \tag{6.4.16}$$

3.3σ significance after a 31 day measurement. An assay lasting $t_{\rm asy} = 60$ days, with a worst-case background $R_{\rm P.C.} \sim$13k/day (Eqn. 6.4.6) would yield

$$\frac{S}{\sqrt{B}} = \frac{35^{+48}_{-29}/\text{day} \times 60 \text{ days}}{\sqrt{13,000/\text{day} \times 60 \text{ days}}} \approx 2.4^{+3.3}_{-2.0}\sigma \qquad (\text{at } 95\%\,\text{C.L.}) \tag{6.4.17}$$

a 5.7σ significance at best. Two months is probably the longest time available to count a single sample. However, counting for 3 months with high backgrounds we could obtain a significance

$$\frac{S}{\sqrt{B}} = 35^{+48}_{-29}/\text{day} \sqrt{\frac{90 \text{ days}}{13,000 \text{ evts day}^{-1}}} \approx 2.9^{+4.0}_{-2.4}\sigma \qquad (\text{at } 95\%\,\text{C.L.}). \tag{6.4.18}$$

These naive calculations underestimate the β escape rate since about half of the electrons we hope to identify will be aimed into the sample itself and of these will back-scatter upwards and out of the sample towards the trigger MWPC.

Low-Energy Electron Back-Scatter

Electron tracks typically deposit ionization in tracks that form long strands during the initial energy deposition, then generally curl up as they scatter through increasingly large angles. This is sometimes colloquially referred to as 'spaghetti and meatballs' respectively (visually) representing the tail (start) and head (end) of the track. Low-energy electrons scatter at increasingly large angles due to electron-nucleus interactions, giving rise to the 'meatballs'. The escape fraction of β's near at the surface is 50% with the distribution exactly matching the β-decay function, without accounting for backscattering. Backscattering is described in Sec 2.5.2 of Leo's *Particle Physics Techniques* [395]. Backscattering is more important for surface contaminants since only a small fraction of electrons will be produced near the surface for decays originating throughout the bulk of a sample.

Using GEANT4, I determined that 35% of downwards-aimed electrons originating from the beta-decay of Si-32, will turn around in the upper layers of the wafer and leave the sample. So then, for events originating very close to the sample surface, we might expect 50% (already aimed up) + 50% (aimed down)$\times$ 35% (back-scattered) so that $\mathcal{B}_f \sim 66\%$ of the total number of betas emitted from the surface are back-scattered, leading to a measurable signal

$$\begin{aligned} R_{\text{surf.}} &= \mathcal{B}_f \times \mathcal{R}_{\text{surf.}} \times A \\ &= 0.675 \cdot \left(1.22^{+1.68}_{-1.00} \times 10^{-2}/\text{cm}^2/\text{day}\right) \cdot 76^2\text{cm}^2 \\ &= 47^{+65}_{-39}/\text{day} \quad (\text{at } 95\% \text{ C.L.}). \end{aligned} \tag{6.4.19}$$

Then, with well-characterized BetaCage backgrounds [371], accounting for backscattering of the downwards events, measuring a sample with the largest possible area $A = 0.5\,\text{m}^2$ for 14 days we would have

$$\frac{S}{\sqrt{B}} = \frac{47^{+65}_{-29}/\text{day} \times 14 \text{ days}}{\sqrt{35/\text{days} \times 14 \text{ days}}} \approx 30^{+41}_{-11} \qquad (\text{at } 95\% \text{ C.L.}) \tag{6.4.20}$$

achieving a minimum discovery significance 19σ. After a single day, the worst discovery significance

$$\frac{\min(S)}{\sqrt{B}} = {}^{(47-29)}/_{\sqrt{35}} \approx 3\sigma \tag{6.4.21}$$

is still 3σ! For a modest sample of area $A = 40\,\text{cm}^2$, we expect

$$\begin{aligned} R_{\text{surf.}} &= 0.675 \cdot \left(1.22^{+1.68}_{-1.00} \times 10^{-2}/\text{cm}^2/\text{day}\right) \cdot 40\,\text{cm}^2 \\ &= 0.33^{+0.45}_{-0.27} \text{ signal events/day}, \quad (\text{at } 95\% \text{ C.L.}) \end{aligned} \tag{6.4.22}$$

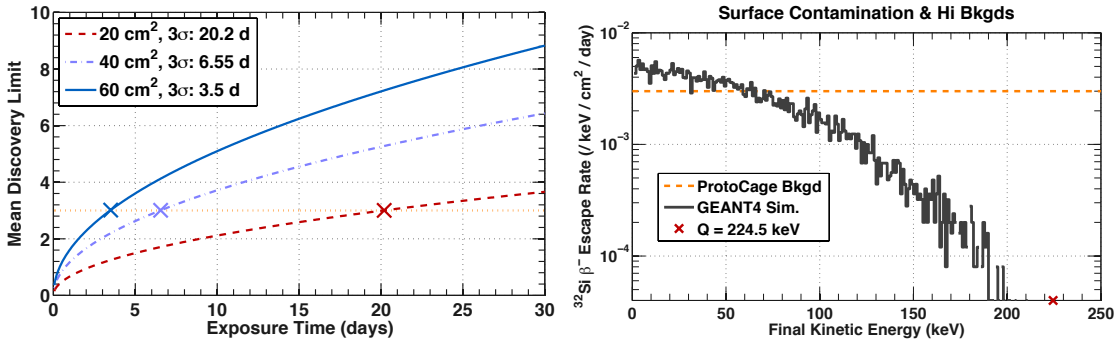

Figure 6.18: Left: Discovery limit for ^{32}Si surface contamination from the mean rate in Eqn. 6.4.19 for β's emitted from modest samples of area $A_{\rm samp.} = (20,\ 40,\ \&\ 60)\,{\rm cm}^2$ shown (dashed, dot-dash, and solid) with 3σ detection significance above backgrounds at (20, 6.5, and 3.5) days (×). **Right:** Simulated kinetic energy spectrum from ^{32}Si β's leaving the surface of a 500 μm thick silicon sample. The spectra is scaled to the (larger) ^{32}Si decay rate DAMICreported [109].

which we can compare to the expected Compton scatter backgrounds for such a small sample

$$\begin{aligned} R_{\rm B.C.} &= \mathcal{R}_{\rm B.C.} \times \Delta E \times A = 3 \times 10^{-5}\,{\rm keV}^{-1}\,{\rm cm}^{-2}\,{\rm day}^{-1} \cdot 225\ {\rm keV} \cdot 40\ {\rm cm}^2 \\ &\approx 0.27\ {\rm events/day}, \end{aligned} \tag{6.4.23}$$

is a little less than the surface-emission rate and we can conclude that the BetaCage is well suited to make such a measurement! The left panel of **Fig. 6.18** shows the achievable discovery significance using the central rate (Eqn. 6.4.19) as a function of time. The energy spectrum for surface-events decaying isotropically, with an energy spectrum drawn from the ^{32}Si β-spectrum is shown (solid) in the right panel of **Fig. 6.18**. The figure shows an over estimate of the expected average BetaCage backgrounds $R_{\rm P.C.} = 100 \cdot R_{\rm B.C.} = 3,500$/day from Eqn. 6.4.5. The low-energy $E < 50\,{\rm keV}$ emission spectra above backgrounds (shown dashed horizontal) will provide evidence of ^{32}Si contamination.

In the unlikely event that ^{32}Si is introduced during the processing phase and truly is on the surface (or weakly implanted), it will be easy to measure the rate of β-decays from silicon samples With such low backgrounds, the BetaCage could easily identify surface contamination from silicon wafers well below the rate DAMIC measured. Assuming the ProtoCage has a background even (100–1,000)× larger than this, surface contamination at the level DAMIC measured will be significant. For isotropically-aimed electrons (drawn from Eqn. 6.4.4) coming from material surfaces, electron back-scattering produces an abundance of lower energy events. The rate of ^{32}P betas, $Q \approx 1.7\,{\rm MeV}$, would increase the low-energy event rate what is depicted above, where the signal selection efficiency $\epsilon_{\rm sig.} \sim 90\%$. The above calculations ignore the P-32 decay which will contribute significantly to the spectra at much higher energies leading to a larger rate of events depositing energy in the bulk grid. The vetoed events will speed up the discovery significance for consecutive beta-emitters such as the long-lived Pb-210 ($Q = 64\,{\rm keV}$, $t_{1/2} = 22\,{\rm yrs}$) which will correlate with the increased rate of Bi-210 ($Q = 1.16\,{\rm MeV}$, $t_{1/2} = 5\,{\rm days}$) beta decays. Lead shielding would further improve the detection sensitivity of the prototype device.

6.4.4 Semi-Analytic ^{32}Si Bulk Escape Rate

I continue here with two semi-analytic approximations and a GEANT4 simulation of electrons arising from the ^{32}Si bulk contamination. I calculate the one-sided β-escape spectra from a thin silicon sample of thickness $\tau_{\text{CCD}} = 500\,\mu\text{m}$ similar to the CCDs DAMIC used to report their spin-independent WIMP-nucleon cross-section exclusion sensitivity [109, 232]. The first approximation will include no energy-losses as the electrons are released from the Si→P β decay. The second approximation includes first order energy losses E_{loss} along straight line travel through a thin silicon sample. Both approximations ignore backscattering which is considered above in **Section 6.4.3**, but a final GEANT4 simulation includes this (small) effect.

Lossless Escape Spectrum

In the simplest model, let us assume electrons will escape the surface of a plane material of thickness τ which is taken to be larger than the maximum decay energy imparted to an electron from a Si-32 decay. Neglecting electron backscattering, 50% of isotropically aimed β-decays occurring on the surface will 'escape' the sample, and the beta escape spectra

$$\left.\frac{\mathrm{d}N}{\mathrm{d}E}\right|_{\text{surf.}} = 1/2 \times \frac{\mathrm{d}N}{\mathrm{d}E_{\text{emis.}}} \tag{6.4.24}$$

will be identically equal, at all energies, to half of the emission spectrum. The escape spectrum will become distorted at increasing implantation depths d_β until the maximum electron range $R(Q)$–corresponding to the endpoint energy Q of the beta decay. At this depth, electrons aimed at the surface with the endpoint energy will very nearly escape the sample surface, and the emission spectrum vanishes.

$$\left.\frac{\mathrm{d}N}{\mathrm{d}E}\right|_{d_\beta = R(Q)} \equiv 0. \tag{6.4.25}$$

Ignoring these spectral distortions in the emission spectrum and angular information (will be shown to be ignorable) due to energy loss, the escape fraction f_{esc} at a given depth will decrease from 50% to 0% The left panel of **Fig. 6.19** shows this effect as a function of implantation depth, for a few example electron ranges (*i.e.* initial energies). However, the above is only true, ignoring energy loss in the sample, and if the fraction of the solid angle of a sphere (since decays are assumed to be isotropic) is linear long the polar axis z, which connects its poles. The left panel of **Fig. 6.19** shows the coordinates used to derive the surface area of a sphere along the polar axis. Because a sphere exhibits azimuthal symmetry along ϕ, it is a surface of revolution, and so the surface area per unit z is a constant. Then, by finding the arc-length of a semi-circle *e.g.* $f(z) = \sqrt{r^2 - z^2}$, shown in the right panel of **Fig. 6.19**, we account for the creation of a surface of revolution by multiplying the calculated semi-circular arc-length $\ell(\Delta z)$ by 2π. Then, the arc-length as a function of vertical

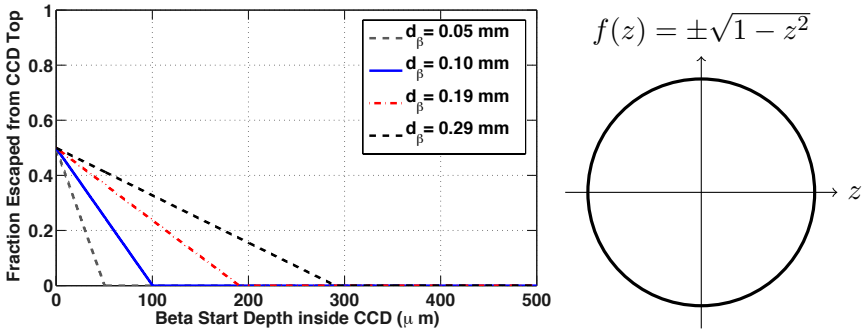

Figure 6.19: Left: Fraction of β's escaping a silicon sample as a function of implantation depth. The fraction is shown or a few β ranges $d_\beta = (0.05, 0.10, 0.19, 0.29)$ mm. For the maximum ^{32}Si electron range $R_Q = 290\,\mu$m (dashed black) the surface escape fraction $p_{\rm esc}(z=0) = 50\%$ and the fraction $p_{\rm esc}(z=R_Q) = 0\%$. **Right:** A circle of radius 1, centered on the origin.

distance z is

$$\ell(z_i, z_f) = \int_{z_i}^{z_f} f(z) \sqrt{\left(\frac{{\rm d}f}{{\rm d}z}\right)^2 + 1}\,{\rm d}z \tag{6.4.26}$$

Then the area of surface of revolution of $f(z)$ about the z-axis and its derivative $f' = -z/\sqrt{r^2-z^2}$ to the starting at the above integral is

$$\begin{aligned} A(z_i, z_f) &= 2\pi \int_{z_i}^{z_f} \sqrt{r^2-z^2} \sqrt{\left(\frac{-z}{\sqrt{r^2-z^2}}\right)^2 + 1}\,{\rm d}z \\ &= 2\pi \int_{z_i}^{z_f} \sqrt{r^2-z^2} \sqrt{\frac{z^2}{r^2-z^2} + 1}\,{\rm d}z = 2\pi \int_{z_i}^{z_f} \sqrt{z^2+r^2-z^2}\,{\rm d}z \\ &= 2\pi r \int_{z_i}^{z_f} {\rm d}z = 2\pi r\,(z_f - z_i) \end{aligned} \tag{6.4.27}$$

So, the surface area of a sphere is indeed proportional to the length along the polar axis. From the left panel of **Fig. 6.19**, beta's of initial energy E have an escape fraction that linearly decreases from $f_{\rm esc}(z=0, E) = 0.5$ at the surface to $f_{\rm esc}(z = d_\beta(E), E) = 0$ at all implantations z beyond their range d_β

$$f_{\rm esc}\big(z < d_\beta(E), E\big) = \left(\frac{1/2 - 0}{0 - d_\beta(E)}\right) z + 1/2 = \frac{1}{2}\left(1 - \frac{z}{d_\beta(E)}\right). \tag{6.4.28}$$

Then, integrating the escape fraction of beta's at an energy E and range $d_\beta(E)$, the escape probability

$$\begin{aligned} p_{\rm esc}(E) = \int_0^{d_\beta} f_{\rm esc}\big(z, d_\beta(E)\big)\,{\rm d}z &= \frac{1}{2}\int_0^{d_\beta}\left(1 - \frac{z}{d_\beta}\right){\rm d}z \\ &= \frac{1}{2}\left(d_\beta - \int_0^{d_\beta}\frac{z}{d_\beta}\,{\rm d}z\right) \\ &= \frac{1}{2}\left(d_\beta - \frac{z^2}{2\,d_\beta}\Big|_0^{d_\beta}\right). \end{aligned} \tag{6.4.29}$$

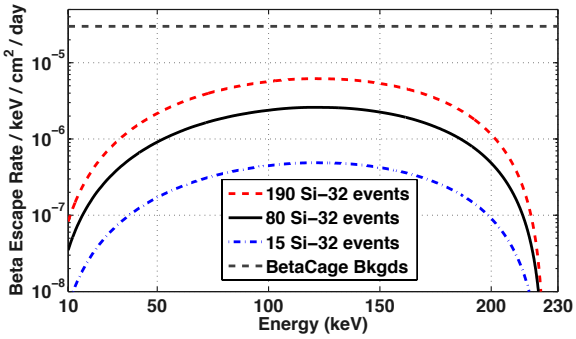

Figure 6.20: ^{32}Si βrate (solid) with 95% C.L. (dot-)dash escaping the top of a thin slab of silicon versus initial kinetic energy, and the average BetaCage background $\mathcal{R}_{\text{B.C.}}$ is shown (gray dashed). The distribution lower than the expected background rate. Implementing background subtraction would improve the sensitivity to these silicon decays. This calculation does not include the expected emission spectra from phosphorus-32 decays which would contribute at energies well above 200 keV.

As expected, the escape probability of electrons at a given energy, just the integral under the line representing the escape fraction, is

$$p_{\text{esc}}(E) = \frac{1}{4} d_{\beta}(E) \tag{6.4.30}$$

will be 25% of all the electrons emitted at that energy. This escape fraction for all energies can be weighed by the with normalized beta-emission spectrum to determine the rate of electrons, isotropically aimed and spread in z, that escape one side of a thin silicon sample. The approximate rate escaping the top of an infinite slab can be found by weighing these probabilities $p_{\text{esc}}(E)$ with normalized beta-decay spectrum. Combining the expected beta-decay rate density, the probability of escaping for a given start depth, and the density $\rho_{\text{Si}} \approx 2.33\,\text{gm/cm}^3$ of silicon, the rate density (in units of $\text{keV}^{-1}\,\text{cm}^{-2}\,\text{day}^{-1}$) of β's escaping the surface of a thin silicon sample for a given decay energy E will be given by

$$\mathcal{R}_{\text{esc.}}(E) = \rho_{\text{Si}} \left(\frac{p_{\text{esc}}(E) \cdot N(E)}{\int N(E)\, dE} \right) \tilde{A}_{\text{DAMIC}}. \tag{6.4.31}$$

In the best case, we would completely fill an area $A = 76^2\,\text{cm}^2$ of the BetaCage with as many wafers as possible! Using the energy-dependent signal-selection efficiency $\epsilon(E)$ (**Fig. 6.5**) determined in by Boqian [371] the rate of electrons emitted from the bulk the BetaCage is

$$R^{\beta}_{\text{bulk}} = A \int_{E_{\text{thr.}}}^{Q} \epsilon \cdot \mathcal{R}_{\text{esc.}}\ \text{d}E = 1.48^{+2.03}_{-1.19}/\text{day} \qquad (95\%\,\text{C.L.}) \tag{6.4.32}$$

where the energy threshold $E_{\text{thr.}} = 10\,\text{keV}$ is chosen since the range–energy relations given by NIST only extend down to 10 keV. Assuming the BetaCage background of 35 events/day, then counting a sample bearing ($80\,^{32}\text{Si decays}\,\text{kg}^{-1}\,\text{day}^{-1}$) throughout the bulk for 60 days gives a significance of

$$\frac{S}{\sqrt{B}} = \frac{1.48^{+2.03}_{-1.19}/\text{day} \times 60\ \text{days}}{\sqrt{35/\text{day} \times 60\ \text{days}}} \approx 1.9^{+2.7}_{-1.6}. \tag{6.4.33}$$

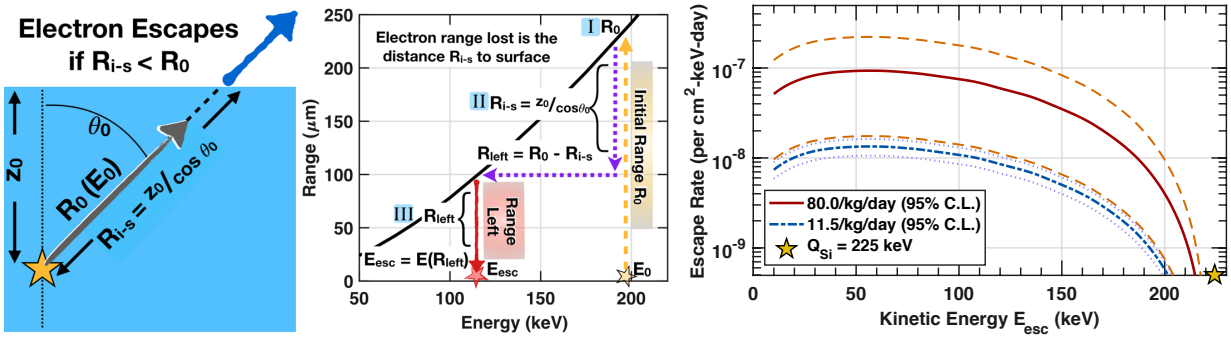

Figure 6.21: Left: Diagram of the variables of the lookup table for ^{32}Si decays at a given implantation depth z_0, initial kinetic energy E_0, and decay direction θ_0. The initial energy from the βdecay sets the maximum range. **Middle:** Algorithm for calculating the escape energy $E_{\rm esc}$ with an example initial energy, and $R\mathrm{i}-\mathrm{s}$ corresponding to an energy loss $\Delta E = \langle {}^{\mathrm{d}E}/_{\mathrm{d}x}\rangle \cdot R_{\mathrm{i-s}}$. **Right:** Electron escape rate computed from the algorithm in the middle panel for both DAMIC measurements [109, 110].

While this calculation is useful to estimate the expected sensitivity of the TPC, it does not include the energy losses within the silicon (which I discuss below), but it also ignores the effect of the subsequent phosphorus-32 decay which is discussed **Section 6.4.5**.

Escape Spectrum including CSDA Energy Loss

The continuous-slowing-down approximation (CDSA) can be used to obtain a close approximation to a charged particle's expected range R. This approximation assuming the particle lose energy continuously determined by the stopping power ${}^{\partial E}/_{\partial x}$ of the particle in the material. The mean range

$$R(E_0) = \int_0^{E_0} \frac{\mathrm{d}E'}{{}^{\mathrm{d}E'}/_{\mathrm{d}x}(E')}. \tag{6.4.34}$$

as a function of the initial kinetic energy E_0 is shown for electrons in silicon in (the right panel of) **Fig. 6.14**. The energy deposited to a material along a track may be obtained by integrating the CSDA range from Eqn. 6.4.34. Though this is accurate to first order, energy-loss fluctuations during transit are neglected. This 'nuclear-free' approximation doesn't include effects from electrons curling from (low-energy-)electron–nucleus interactions.

I have constructed a very simple model whereby electrons originate throughout the bulk a material of thickness τat a depths $z_0 \in (0, \tau)$ are aimed upward and lose energy based on the CSDA expectation, as shown in the left panel **Fig. 6.21**. For the bulk contamination assumption, the distribution of depths is constant. These electrons will be aimed upward at an initial angle $\theta_0 \in (0, \pi/2)$, expected to propagate isotropically. By traveling along a straight line to the surface, the path length to the surface

$$R_{\mathrm{i-s}} = z_0/\cos\theta_0. \tag{6.4.35}$$

The electrons will lose the energy moving through the silicon to the surface and their initial range $R_0 = R(E_0)$ will be reduced corresponding to the energy loss as computed by the CSDA model (Eqn. 6.4.34). If the electron's initial kinetic energy E_0 exceeds the energy $E_\beta(R_{\text{i-s}})$ required to escape the surface, the resulting escape energy E_{esc} be the difference

$$E_{\text{esc}} = \begin{cases} E_0 - E_\beta(R_{\text{i-s}}), & \text{for } R_0(E_0) > R_{\text{i-s}} \\ 0, & \text{for } R_0(E_0) \leq R_{\text{i-s}} \end{cases} \tag{6.4.36}$$

as depicted in the middle panel of **Fig. 6.21**; this difference will also be given by $E_0 - \langle \mathrm{d}E/\mathrm{d}x \rangle \cdot R_{\text{i-s}}$, where the average stopping power is computed between the initial and escape energies. Using the functional form (Eqn. 6.4.36) to calculate the escape spectra is simpler in practice. The distribution of escape energies

$$\mathcal{S}(E_{\text{esc}}; E_0, z_0, \cos\theta_0) \tag{6.4.37}$$

is a function of the escape energy E_{esc} given the electron emission properties E_0, z_0, and $\cos\theta_0$. Then weighing the distribution $\mathcal{S}(E_{\text{esc}}; E_0)$ at a given initial kinetic energy E_0, for all initial depths z_0 and angles θ_0, with the beta-emission spectrum $N(E_0)$, the correct escape distribution

$$N(E_{\text{esc}}) \equiv N(E_0) \sum_{z_0,\, \cos\theta_0} \mathcal{S}(E_{\text{esc}}; E_0, z_0, \cos\theta_0). \tag{6.4.38}$$

is obtained. The right panel of **Fig. 6.22**) shows the energy distribution of electrons escaping the wafer surface, scaled to the wafer geometry $(A_{\text{wafer}}, m_{\text{wafer}})$ and activities $\mathcal{A}$ reported in (solid, Eqn. 6.4.3) [109] and (dot dash, Eqn. 6.4.2) [110]. This energy distribution is considerably lower than the expected backgrounds $\sim 10^{-5}\,\text{keV}^{-1}\,\text{cm}^{-2}\,\text{day}^{-1}$ in the BetaCage, but still ignores the effect of phosphorus where significant energy losses would make this approximation significantly weaker. Instead of calculating the sensitivity, I move to describe simulation results incorporating energy loss, ^{32}P decays, and position dependence for sequential beta decays.

6.4.5 Simulating ^{32}Si Bulk Contamination in Thin Wafers

None of the above estimations include range straggling due to fluctuations in electron energy loss, and the ^{32}Si beta-decay endpoint energy $Q \approx 225\,\text{keV}$ corresponds to an expected maximum electron range $d_\beta = 0.29\,\text{mm}$ which is close to the thickness $\tau_{\text{CCD}} = 0.5\,\text{mm}$ of the DAMIC CDDs. I wrote a simple GEANT4 simulation to determine the escape spectra resulting from bulk ^{32}Si contamination in a thin silicon sample as previously described. In this section, I describe the results of my simulation to find the expected emission spectrum and the spatial dependence for the sequential silicon and phosphorus beta-decays (β-β) which exit the sample from the same side. In this section, I estimate the sensitivity to sequential ^{32}Si and P β-decays in the shielded BetaCage with the expected backgrounds (Eqn. 6.2.6) and scaled backgrounds (Eqn. 6.4.5, 6.4.6) as a stand

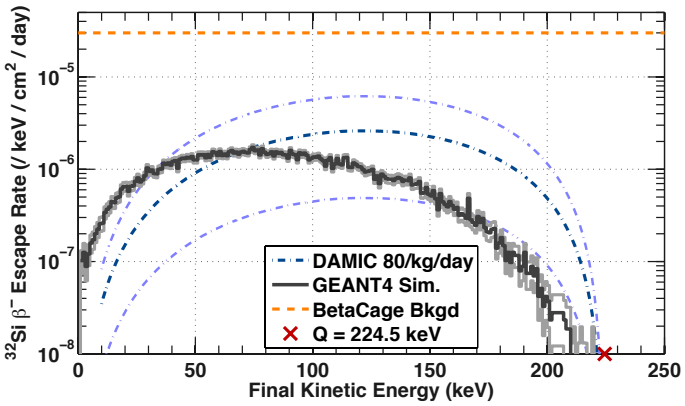

Figure 6.22: Simulated ^{32}Si beta-emission spectrum ('GEANT4 sim', dark histogram) with 1σ statistical uncertainties (light histograms). The analytically calculated lossless escape spectra (Eqn 6.4.31) is shown for comparison. The average expected BetaCage backgrounds are shown (orange dashed) before background subtraction. While only $\sim 3\%$ of the electrons escape the wafer, the some $\sim 70\%$ of the phosphorus-32 electrons escape.

in for the the ProtoCage.

I used the `G4RadioactiveDecayPhysics` module[3] to produce consecutive β-decays from ^{32}Si and ^{32}P throughout the bulk of very simplistic physical geometry of silicon wafer of area $A = 19\,\mathrm{cm}^2$ and thickness $\tau_{\mathrm{wafer}} = 500\,\mu\mathrm{m}$. I chose to use the low-energy electromagnetic package EMOPT4 which is expected to be reliable for physics processes corresponding to particle energies as low as 250 eV [410], below the expected sensitivity of the BetaCage. The decays occurred at $(x, y) = (0, 0)\,\mathrm{mm}$ in the center of the wafer at random starting depths $z_0 \in (0, 500)\,\mu\mathrm{m}$. After the beta-decay occurs, the radioactive decay module produces three daughters: the recoiling ^{32}P ion (`trackID`=2), an anti-neutrino (`trackID`=3), and the electron (`trackID`=4) we hope to identify. These particles share the ^{32}Si parent atom. I identified electrons from ^{32}Si decays (from events whose `parentID`=1 and `trackID`=4) escaping the wafer *i.e.* changing physical volumes. I recorded the post-step kinetic energy of these electrons and tallied their energy distribution, as shown in **Fig. 6.22**.

The energy distribution of electrons escaping the wafer surface is shown (dark histogram) with 1σ statistical uncertainties (light histograms) in **Fig. 6.22** is scaled to an activity

$$\mathcal{A} = 80^{+110}_{-65}\,\mathrm{events\ kg^{-1}\,day^{-1}} \tag{6.4.39}$$

from Eqn. 6.4.3, as reported by DAMIC [109]. The figure also shows the previously calculated lossless spectrum (Eqn 6.4.31, dot-dash) and the average BetaCage background (dashed). The difference between the simulated distribution and the lossless spectrum is reasonable since electrons will lose energy, and the higher energy electrons that do leave the sample will be attenuated to lower energies.

[3] I modified the tutorial example */extended/radioactive/rdecay02*.

Si-P Beta Decay Multiplicity

Using GEANT4, I computed the escape probability for electrons from each parent originating throughout the bulk of a 500 μm silicon sample. Due to the low energy imparted to the betas, an average $\langle E_{\mathrm{Si}-32}\rangle \approx 80\,\mathrm{keV}$, from ^{32}Si decays have an escape probability

$$\mathcal{P}_{\mathrm{esc}}^{\mathrm{Si}} = (3.707 \pm 0.019)\,\% \qquad (68\%\,\mathrm{C.L.}). \tag{6.4.40}$$

Because phosphorus betas $Q_{\mathrm{P}} = 1.7$ MeV, the average $\langle E_{\mathrm{P}-32}\rangle \approx 713\,\mathrm{keV}$, a much larger fraction of the electrons successfully escape the thin wafer. A silicon sample of area $A = 0.5\,\mathrm{m}^2$ and thickness $\tau = 0.05\,\mathrm{cm}$ will have a mass $m \equiv \rho\, V = \rho\, A\, \tau$, with an activity $\mathcal{A} = 80\,^{32}\mathrm{Si\ decays\,kg^{-1}\,day^{-1}}$, the average beta-emission rate

$$\begin{aligned} R_{\mathrm{Si}} &= \mathcal{P}_{\mathrm{esc}}^{\mathrm{Si}}\, \mathcal{A}\, m = \mathcal{P}_{\mathrm{esc}}^{\mathrm{Si}}\, \mathcal{A}\, \rho\, A\, \tau \\ &\approx 4\% \times 80\,^{32}\mathrm{Si\ decays\,kg^{-1}\,day^{-1}} \times 2.33\,\mathrm{g/cm^3}\,(0.5\,\mathrm{m^2})\,0.05\,\mathrm{cm} \\ &= 1.8\,^{32}\mathrm{Si}\beta' s\,\mathrm{day^{-1}}. \end{aligned} \tag{6.4.41}$$

Then, if the BetaCage backgrounds 27 backgrounds/day for a similarly sized sample, a 60 day assay gives a

$$\frac{S}{\sqrt{B}} = 1.8\,/\mathrm{day}\sqrt{\frac{60\,\mathrm{days}}{27\,/\mathrm{day}}} \approx 2.8 \tag{6.4.42}$$

discovery significance. The spectrum of silicon-32 electrons is not very strong, the escape probability

$$\mathcal{P}_{\mathrm{esc}}^{\mathrm{P}} = (69.752 \pm 0.0835)\,\% \qquad (68\%\,\mathrm{C.L.}) \tag{6.4.43}$$

is a large fraction of the production rate of ^{32}Si beta decays arising from bulk ^{32}Si contamination in thin samples , which will increase the discovery potential for samples with such contamination.

To take full advantage of the power of the BetaCage's (x, y) position sensitivity, I found the expected spatial distribution of these sequential electron pairs sharing the same ^{32}Si parent atom *i.e.* shared starting location and depth $(x_0,\ y_0,\ z_0)$. Given that ^{32}Si decays will impart beta's with a maximum range $d_\beta = 0.29\,\mathrm{mm}$ which is only 6% of BetaCage the wire pitch $s = 5.08\,\mathrm{mm}$, we generally the (x, y) escape location of electron to be very close to the parent atom. If the electron from the phosphorus decay travels far in the sample before escaping then the spatial correlation would be too weak to advantageously use. The left panel of **Fig. 6.23** shows the distribution $N_{\beta\beta}$ of escape location $(x_{\mathrm{esc}}, y_{\mathrm{esc}})$ separation (the x and y difference) for the atoms

$$N(x, y) \equiv N(x_{\mathrm{esc}}^{\mathrm{Si}} - x_{\mathrm{esc}}^{\mathrm{P}}, y_{\mathrm{esc}}^{\mathrm{Si}} - y_{\mathrm{esc}}^{\mathrm{P}}) \tag{6.4.44}$$

as a two-dimensional (log-scale) colormap. The simulations indicate that the sequential electron-pair escape locations are very tightly packed on the surface the silicon, as expected. The average radial

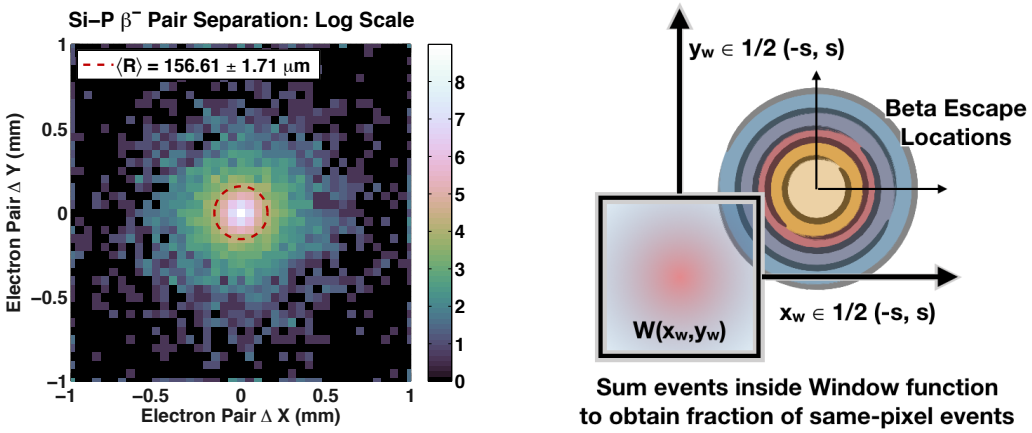

Figure 6.23: Two-dimensional log-scale histogram of (x, y) escape separation of electrons induced from Silicon and subsequent Phosphorus β decays. The average separation (dashed red) $\langle r \rangle \lesssim 200\,\mu$m, only 3% of the BetaCage wire pitch $s = 5.08$ mm). A back-of-the-envelope calculation using the average surface escape separation indicates that no fewer than 94% of subsequent decays will occur within the same (x, y) pixel, the other 6% occurring at the edges will eject sequential electrons in adjacent pixels. **Right:** Window function algorithm. The number of beta-escape separations are summed for each of the Window function locations $W(x_w, y_w)$.

deviation of the escape locations

$$\langle r \rangle = \left\langle \sqrt{(x_{\rm esc}^{\rm Si} - x_{\rm esc}^{\rm P})^2 + (y_{\rm esc}^{\rm Si} - y_{\rm esc}^{\rm P})^2} \right\rangle = (156.6 \pm 1.7)\,\mu{\rm m} \tag{6.4.45}$$

is shown (red dotted circle). This radial deviation $\langle r \rangle \approx 3.07\%\, s$ is only 3% of the wire pitch. To obtain the exact fraction of same-pixel electrons, I used the escape-position distribution $N(x, y)$ to algorithmically calculate the fraction of events contained in the same $s \times s = 1\,{\rm cm}^2$ pixel. To determine the fraction of same-pixel events, I summed the number of events appearing in a window function $W(x, y)$ spanning a 1 cm in each direction as depicted in the right panel of **Fig. 6.23**. Moving the window function to the extent of the pixel area *i.e.* $(x_i, y_i) \in ([0, s], [0, s])$ in a 1,000-by-1,000 grid of linearly spaced points, the fraction of spatially-correlated events

$$f_{\rm same-pixel} = 98.9\% \sim 100\% \tag{6.4.46}$$

is basically 100% and essentially all consecutive electrons will escape the surface of the silicon in the same xy location! Moving forward, I will assume all sample electrons from Si-P-32 decays with a shared atomic parent will occur at the same (x, y) position on the sample surfaces.

The BetaCage will be a screener with world-leading sensitivity to low-energy beta decays. Given that the ionization track reconstruction will be performed using the (x, y) spatial information, especially to reject events coming from the outside of the detector, the ability to localize sequential surface-events from a sample will lend increased sensitivity to those radioactive chains which emit more than one electron in a short time such as ^{32}Si and ^{210}Pb.

For a significant contamination, the rate of emitted electrons will be large enough that we will expect a large number of spots from which 2 consecutive electrons will be located. The event

multiplicity η can be tallied for an assay. During a background run where the average event-rate per-(x,y)-bin μ, the frequency of bins with a multiplicity η can be calculated from the poisson distribution

$$P(\eta;\mu) = \exp(-\mu)\frac{\mu^{\eta}}{\eta!}. \tag{6.4.47}$$

The spatial resolution (*i.e.* the number of bins N_{bins}) of the screener will strongly effect the event multiplicity distribution for a given signal rate. Since the spatial distribution of escaping electrons is so tightly packed around the original (x,y) location, I assume signal events will occur in the same pixel of the screener. For smaller enough backgrounds, the rate of $(\eta = 2)$ bins 'double hits', will be large enough to be detected above the noise of the backgrounds-alone. For a given total event rate, the maximum event multiplicity will increase with decreasing bin size until the experiment is just a counting experiment bearing no position dependence, and the event multiplicity will correspond tot he total rate. An empty bin, where no ^{32}Si/P ions decayed and no Compton backgrounds occurred, has an event multiplicity $\eta = 0$. A bin with a single hit $\eta = 1$ will be populated with either backgrounds alone or a single electron from ^{32}Si/P beta decay. The focus of this analysis is to determine if the increase in double hits $\eta = 2$, arising from ^{32}Si in and on the surface of thin samples is statistically significant over the rate of backgrounds which produce double hits for a given assay period.

The number of signal events N_S simulated is then dictated by the corresponding level of contamination for surface or bulk contamination respectively. The number N_S of ^{32}Si events is

$$N_S = \mathcal{R}\cdot t_{\text{asy}} \tag{6.4.48}$$

determined by the simulated assay time t_{asy} and the electron escape rate $\mathcal{R}$ corresponding to the level of bulk (Eqn. 6.4.32) or surface (Eqn. 6.4.10) contamination. For this analysis, I assumed the ^{32}Si were already close to their equilibrium, long half-life $t_{1/2}^{\text{Si}} \approx 170\,\text{yrs}$, and so would occur at random times t_{Si} distributed evenly throughout the assay period. The short phosphorus-32 half-life $t_{1/2}^{\text{P}} = 14.3\,\text{d}$ is useful since events close enough in time will be identified as from the same parent atom. To determine if the assay would include the ^{32}P electron, the radioactive decay times t_{P} for the ^{32}P were drawn from an exponential distribution and if the summed decay time

$$t_{\text{asy}} < t_{\text{Si}} + t_{\text{P}} \tag{6.4.49}$$

is longer than the assay time t_{asy}, the ^{32}P would not contribute to the assay. In this case, the parent atom will contribute only a *single* electron from the ^{32}Si decay to the distribution of signal events in the screener. The number of background N_B events was determined from the assumed level of shielding. I took the rate of background events $R_B = 60\,\text{m}^{-2}\,\text{day}^{-1}$ in the BetaCage (Eqn 6.2.6), and used for the prototype device a background rate $100\times$ higher, as discussed in **Section 6.4.1**.

The event multiplicity η–the rate events-per-pixel–in the BetaCage is generally determined by

the signal rate R_{Si}, and assay time t_{asy}, the sample area A, and the number of bins

$$N_{\mathrm{bins}} = \frac{A}{\Delta_{1\mathrm{D}}^2} \tag{6.4.50}$$

which is inversely proportional to the surface area $\Delta_{1\mathrm{D}}^2$, the square of the linear resolution or wire pitch, of each distinct pixel in the screener. I simulated signal and background events at random locations drawn from flat distributions spanning an oversized active area

$$A_{\mathrm{B.C.}} = (76 \times 76)\,\mathrm{cm}^2 \approx 0.57\,\mathrm{m}^2. \tag{6.4.51}$$

The spatial dependence of the backgrounds and signal events (beta decays from ^{32}Si/P) are drawn from flat distributions in x and y each with a frequency $\mathcal{R}$ (events per unit area)

$$\mathcal{R} = \frac{N_{\mathrm{sim}}}{A_{\mathrm{B.C.}}} \tag{6.4.52}$$

which is a function of the spatial extent $A_{\mathrm{B.C.}}$ of the BetaCage, assuming the background rate ($\sim$ 35 events/day). I have estimated the impact of double-signal hits on the signal discovery potential $S/\sqrt{B}$ for counting periods $t_{\mathrm{asy}} \sim$ (14–60) days for two cases of spatial resolution: a conservative and an idealized case. While the electronics noise on each wire will increase as the number of channels increases, and electronics are generally expensive, the ideal case outlined here is used to consider the impact of implementing a large number of channels in the BetaCage to gain increased sensitivyt to these double hits ($\eta = 2$). The wire planes of the BetaCage will have a pitch

$$s_{\mathrm{MWPC}} = 5.08\,\mathrm{mm}, \tag{6.4.53}$$

we conservatively expect one-dimensional $\Delta x_{\mathrm{res}} \approx 1\,\mathrm{cm}$ position resolution in both wire plane directions. I calculated the event multiplicity assuming a very conservative spatial resolution $\Delta_{1\mathrm{D}} = 1.0\,\mathrm{cm}$, and in the interest of seeing the possible power of implementing a large number of channels on the BetaCage approaching such a fine one-dimensional resolution,

$$\sigma_{2\mathrm{D}} = (\Delta_{1\mathrm{D}})^2 = (10\,\mathrm{mm})^2 \sim 1\,\mathrm{cm}^2 \qquad \text{(conservative)} \tag{6.4.54}$$

corresponding to $N_{\mathrm{bins}} = \frac{A_{\mathrm{B.C.}}}{\Delta_{1\mathrm{D}}^2} \approx 5,776\,\mathrm{cm}^2/1\,\mathrm{cm}^2 \lesssim 6\times10^3$ bins.

Fig. 6.24 shows the simulated position of the signal events from ^{32}Si and ^{32}P β's (left panel), and the total signal and backgrounds (middle panel). The right panel shows the event multiplicity η distribution for each of the events types signal, background, and the total (black dots) resulting from their sum. The top panel shows the results of surface events in a high-background ($R_B \equiv 100\times R_{\mathrm{B.C}}$) TPC screener such as the *ProtoCage*. indicating a huge discrepancy between the maximum event multiplicity due to backgrounds alone: $\eta = 4$ counts per bin, and the signal alone appears to give rise to more than a hundred pixels with an event multiplicity ($\eta = 5$)–for the given assay, the number of pixels with 5 counts per bin is less than 1. As expected, the rate significance (neglecting all position information) above the backgrounds is quite large. It would be possible to correlate the

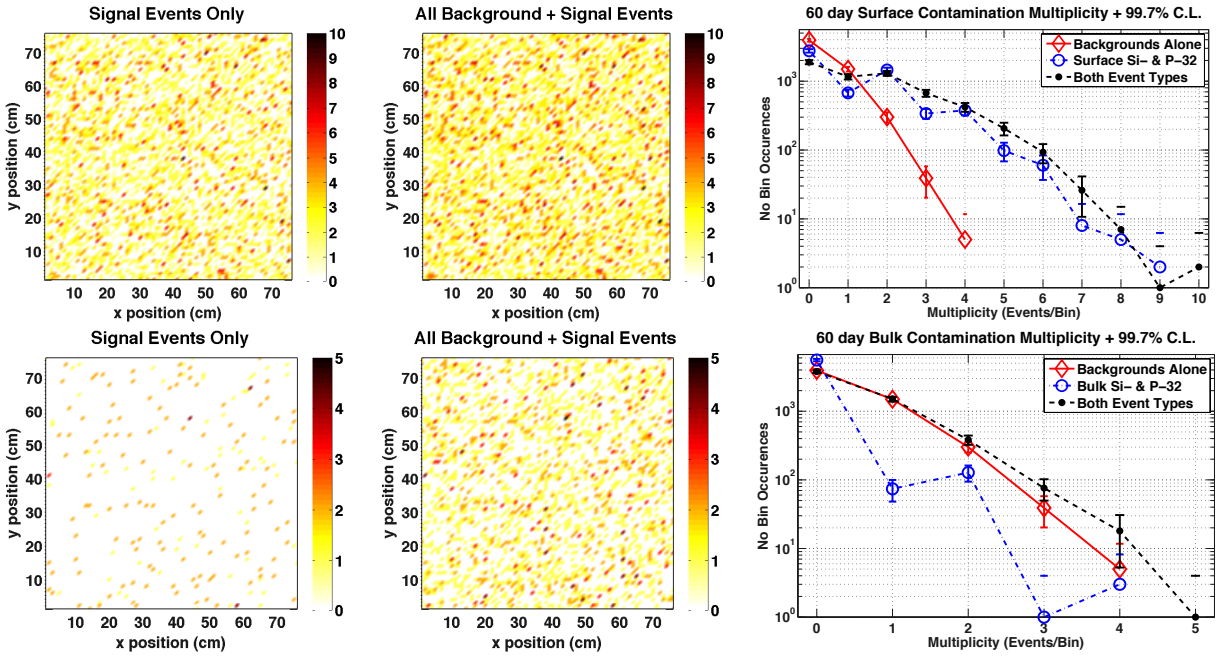

Figure 6.24: Simulated event multiplicity histograms for 60 days of counting a silicon wafer with Si-32 (*Top:* surface, *Bottom:* bulk) contamination with low backgrounds: 35 events/day. **Left:** 2-D histogram of ^{32}Si and ^{32}P signal events. **Middle:** 2-D histogram of all signal and background events. **Right:** Histogram of event multiplicity for backgrounds events (◊), signal events (◯), and all events (dots) with 3σ statistical uncertainty. Detecting surface emission will be easy in the case of large backgrounds! Detecting bulk contamination in thin samples, even with double hits would be difficult and take a long time.

maximum number event multiplicity expected for a given assay and compare with the maximum multiplicity from backgrounds alone to determine the rate and perhaps inform subtraction efforts for samples with lower levels of contamination. It might also be possible to characterize the track reconstruction efficiency of surface-events originating at the detector edges which would normally be vetod a large fraction of the time. We infer from this that screening samples with ^{210}Pb and ^{210}Bi with a half-life $t_{1/2} = 5$ days $3\times$ smaller the ^{32}P, with much shorter assay times $t_{\rm asy} \sim 10$ days would provide sensitivity to significantly lower rates.

The simulation shows the number of pixels with 2 hits from ^{32}Si/P β's $S_{\rm II} \approx (100 \pm 10)$, and backgrounds contribute $B_{\rm II} \approx (300 \pm 30)$ double hits. The discovery significance

$$\frac{S_{\rm II}}{\sqrt{B_{\rm II}}} \approx \frac{100}{30} > 3\sigma \tag{6.4.55}$$

3σ discovery significance from detection double hits, which is confirmed by the pixels with 3 events ($\eta = 3$), which has an event more clearly separated ratio of total events to background alone events.

In the interest of understanding the impact increasing the number of channels and thus the spatial resolution, of a screening device such as the BetaCage, I simulated events on a smaller, more idealized grid size. One-dimensional wire detectors, with a pitch s, have an ideal 'sub-pixel' position

resolution

$$\Delta x_{\rm res} = \frac{s}{\sqrt{12}} \approx 28\%\, s \tag{6.4.56}$$

some three times smaller than the actual wire spacing [376, 377]. In the ideal case, the one-dimensional spatial resolution

$$\Delta_{\rm 1D} = {}^{5\rm mm}/_{\sqrt{12}} = 1.44\,\rm mm \tag{6.4.57}$$

gives rise to pixels with a surface area

$$\sigma_{\rm 2D} = (\Delta_{\rm 1D})^2 = (1.44\,\rm mm)^2 \sim 0.0207\,\rm cm^2 \qquad \text{(ideal)}. \tag{6.4.58}$$

corresponding to $N_{\rm bins} = \frac{A_{\rm B.C.}}{\Delta^2_{\rm 1D}} \approx 5,776\,\rm cm^2/0.028\,cm^2 \sim 270\times10^3$ bins. The left (right) panel of **Fig. 6.25** shows the resulting event multiplicity histograms for a $t_{\rm asy} = 60$ day assay of a silicon sample with surface (bulk) contamination at 3σ (99.7% C.L.) assuming the rate densities calculated previously. For 60 days of counting a surface contaminated sample, we expect $N_B = (2,235 \pm 47)$ background events, $4,232 \pm 65$ ^{32}Si events and $2,839 \pm 53$ ^{32}P counted events with $1,393 \pm 37$ ^{32}P events (32%) uncounted. The bottom panel of **Fig. 6.24** shows the simulated position dependence and event multiplicity histogram arising from bulk contamination. The single hits are expected to be swamped by backgrounds, but the double hits from backgrounds are swamped by the 10× larger signal event rate. Counting the backgrounds alone, with no sample in place, we get only 7 doubles. Counting a sample with surface contamination for 60 days indicates 2,796 doubles from the signal alone. The coincident ^{32}Si/P signal and background events has fewer doubles than signal alone since there are 8 backgrounds coincident in a double-hit bin, bumping the triple-hit bin for measured total up by $2,804 - 2,796 = 8$. Then the signal purity of the doubles bin for surface contaminants would be

$$\frac{S^{\rm surf.}_{\rm II}}{\sqrt{B_{\rm II}}} \approx \frac{2,800 \text{ total doubles}}{\sqrt{10 \text{ bkgd doubles}}} \approx 885 \tag{6.4.59}$$

in the doubles bin $\eta = 2$, carrying an signal-to-background $S_{\rm II}/B_{\rm II} = 2,800/10 \sim 280$, excellent discrimination capability. However it is obvious the rate significance alone would be clearly distinguishable above the backgrounds. For every background-induced double hit (in a 60 day period) we's get about 250× more signal-induced doubles. In the case of bulk contaminants, the signal purity of doubles we see

$$\frac{S^{\rm bulk}_{\rm II}}{\sqrt{B_{\rm II}}} \approx \frac{135 \text{ signal doubles}}{\sqrt{10 \text{ bkgd doubles}}} \approx 42 \tag{6.4.60}$$

which is still a great discrimination capability. So using the BetaCage, to count for 60 days, we expect an order of magnitude more signal-induced doubles (135) than background-induced doubles (10). Moreover, the number of bins with 3 hits ($\eta = 3$) would contribute to the discovery potential. So using event multiplicity and pushing the counting time to 2 months gives us the ability to identify bulk ^{32}Si contamination in samples.

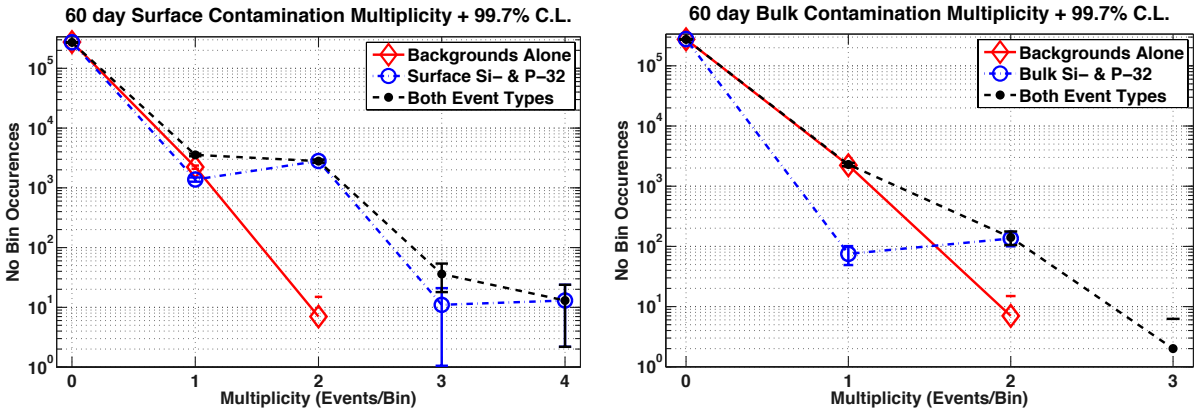

Figure 6.25: Simulated event multiplicity histograms (with 3σ poisson uncertainties) for 60 days of counting of background events alone (red diamonds) from 6.2.6, bulk signal (^{32}Si and ^{32}P) events alone (blue circles), and both event types together (black dots). **Left:** Surface contaminants with a $S = 2116$ ^{32}Si events/month with 2,796 doubles in total ($S_{\rm II} + B_{\rm II}$), and only 7 doubles from the backgrounds alone. **Right:** Bulk contaminants $S = 105$ ^{32}Si events/month with 141 doubles in total, and 7 doubles from the backgrounds and a very large signal discovery potential.

6.4.6 Conclusions for Detecting Si-32 and Pb-210

These simulations indicate that for ^{32}Si nuclei that are spread throughout the bulk as DAMICbelieves [110], the escaping β's could be discoveredm by identifying an increased number of double hits, at the level DAMIC reported for 500 μm thick wafers. The discovery potential for these such events increases with decreasing sample thickness, due to the low endpoint energy $Q \approx 220$ keV of Si-32. The very high-energy $\langle E_{\rm P-32} \rangle \gtrsim 500$ keV beta's from the P-32 decay would provide a significant rate well above the expected Compton scatter backgrounds of the well-shielded BetaCage. While these many of the higher energy events $E_{\rm dep}300$ keV would normally be vetoed, but using timing and spatial correlation the BetaCage would be sensitive to levels lower than 20 events/kg/day. A more sophisticated simulation of the events would provide a method for validating very low levels of contamination.

The results indicate that for ^{32}Si contamination appearing on the surface of such wafers at a level of contamination even $^1/_{50}\times$ the rate observed in the DAMIC CCDs, we can achieve a 5σ discovery significance within a day, in a low-background screener like the BetaCage. The implications of this are that consecutive betas from samples with surface contamination from ^{210}Pb could be discovered in a similar manner from the secondary beta from ^{210}Bi. These decays are separated by $t_{1/2} \approx 5$ days, 30% the ^{32}P halflife $t_{1/2} = 14.3$ days, and so by having a contaminated sample bearing even quicker beta decays from a single atoms, assays could proceed more quickly than described here, and the discovery significance would be improved even further!

Chapter 7

The BetaCage ProtoType: Small-Scale Surface-Alpha Screener

As we work towards commissioning the very-low background BetaCage, we have operated a small-scale prototype detector dubbed the *ProtoCage* at SDSM&T. The ProtoCage was constructed at Caltech in 2011 where two MWPCs were configured as a time projection chamber (TPC) [375]. Each MWPC was strung with 3 layers (cathode-anode-cathode) with 79 wires per layer spanning an area

$$A_{\text{P.C.}} = (40.1 \times 40.1)\,\text{cm}^2 \approx 0.16\,\text{m}^2 \tag{7.0.1}$$

about 30% of the BetaCage planned area. The MWPCs of the ProtoCage are spaced with a drift region length

$$z_{\text{drift}} = 20\,\text{cm} \tag{7.0.2}$$

half the size of the planned drift dimension of the BetaCage. The gas gain and energy resolution were characterized using an low-energy ^{55}Fe γ-source, in a single channel configuration with an argon/methane (P-10) gas [375]. Eric Miller transported the ProtoCage, the associated electronics, and vacuum vessel to SDMS&T from Caltech with a truck in Spring 2016. Eric, myself, and undergraduate Fernando Boo installed the device in the reduced-radon cleanroom at our local laboratory above ground. The ProtoCage is made from less radiopure materials than the planned BetaCage, lacks the extensive lead and copper gamma shielding, and acrylic containment gas vessel. The detector is operated with an argon-based gas (P-10, 10% methane quench gas) instead of a more expensive neon-based fill gas. Since the device is above ground, it will have a larger cosmic-ray flux than the BetaCage, which will be deployed at a nearby underground laboratory. The detector does not have any appreciable shielding and it is expected to be ineffective at screening for low-energy beta's due to the ambient photon flux. This small-scale device is intended to demonstrate the sensitivity of such a TPC as a surface-alpha screener. The use of argon gas, and the lack of shielding

should not impede the α sensitivity. The ProtoCage is shown in (the left panel of) **Fig. 7.1** after installation in our cleanroom. The TPC consists of two noryl MPWC frames (black) for the trigger and bulk grids. An acrylic frame (clear) evenly spaces the copper electric-field shapers. G10 (green) cathode and anode boards send the ionization signals produced by the proportional avalanching occurring near the anodes sense wires of the trigger MWPC as described in **Section 6.1**. The TPC sits on a feedthrough flange inside a vacuum vessel operated with a winch system which lifts the vessel cap. The signals are connected to the feedthrough flange with kapton-insulated wires. Two G10 boards (yellow) sandwich the TPC to protect the sense wires from accidental damage and dust accumulation during troubleshooting. A lattice of holes allow calibration sources to be placed consistently in (x, y) on either side of the device. The feedthrough flange has 5 high-voltage feedthroughs that allow 22 channel readout, 2 gas feedthroughs for fill gas input and output, and one gaseous evacuation port to fill and flush the volume. The prototype is configured to readout 6 channels, 3 of which are used to identify events occurring near the (x, y) center of the device, and the other three channels are intended as a veto near the outer edges.

As in the middle panel of **Fig. 7.1**, the TPC sits on a stainless steel platform that sits in a metal frame outfitted with a winch system that helps to place the vacuum vessel cap over the detector. The cap prevents the neon- or argon-based gas from mixing with the cleanroom air, and photon interactions from swamping the event rate or destroying the high-voltage device. The vessel cap protects the (argon- or neon-based) fill gas from mixing with the cleanroom. The clearance of the copper feedthroughs from the cathode and anode wires extending from the bulk and trigger MWPCs is only a few inches from the vessel cap on each side, so care must be taken when operating the winch. The vessel cap can be safely closed with two people on opposite sides of the structure to guide the vessel cap towards the feedthrough flange and align the bolts which secure the cap to the flange. The middle panel of **Fig. 7.1** shows the ProtoCage TPC after the readout wire were soldered to the G10 boards and feedthrough flange. I am operating the winch system which helps remove or replace the vacuum vessel cap before and after troubleshooting, commissioning, and calibration source deployment. The readout channels from the ProtoCage vacuum vessel are processed by a preamp with 6 channel input/output. The analog signal is then sent through the cleanroom feedthrough to the laboratory outside. The feedthroughs of the low-dust, reduced-radon cleanroom at SDSM&T, the electronics racks, and data acquisition (DAQ) system for the ProtoCage are shown (right panel) in **Fig. 7.1**. The feedthrough includes connections for the high voltage, signal electronics, gas input and output from the gas handling system, an evacuation port, and pressure readout. The gas handling system I characterized as described in **Section 6.3**, connects to the cleanroom feedthroughs to supply the fill gas, or to provide nitrogen and a vacuum for flushing the detector after opening the vacuum vessel cap.

This chapter describes the ProtoCage data acquisition system and electronics (**Section 7.1**), the first data taken here at SDSM&T, readout software, and improvements to the electronics (**Section 7.1.1**), and initial measurements and deployment of a ^{210}Pb α source (**Section 7.2**). I also

Figure 7.1: Left: The ProtoCage demonstration screening time projection chamber without readout wires following installation in the reduced-radon cleanroom at SDSM&T. The $(40\times40\times20)\,\mathrm{cm}^3$ TPC is made with an acrylic frame, copper electric-field shapers, and noryl MWPC frames. The TPC itself sits atop a feedthrough flange underneath a vessel cap during operation. The trigger and bulk MWPC frames (noryl) are each strung with a single anode plane sandwiched by 2 cathode planes. To achieve proportional avalanching in the anode grid, the anode and cathode grids are separated by 5.08 mm with a voltage separation $V_{\mathrm{MPWC}} \sim 2\,\mathrm{kV}$. The wire planes each have 79 sense wires spaced $s = 5.08\,\mathrm{mm}$ apart. Two square G-10 boards (yellow) protect the sense wires and, on the visible side, help to consistently aim calibration sources. The (acrylic) frame separates the trigger and bulk MWPCs by $z_{\mathrm{drift}} = 20\,\mathrm{cm}$ and holds the (copper) electric-field shapers. **Middle:** The ProtoCage TPC wired with 6 channels of readout from the trigger MWPC. I am using the wench system to place the cap over the vacuum vessel. For now, the ProtoCage data readout consists of many fewer channels (6) than the planned BetaCage configuration, with an active area $\approx 3\times$ larger. **Right:** ProtoCage data acquisition system (DAQ), electronics rack, and control PC. The rack has a pressure gauge indicating the inner vessel pressure, a computer with solid-state disk drives for data storage, a high voltage supply, a timing unit to control the digitization rate and a field programmable gate array (FPGA) which digitizes and records the pulses to send to the computer.

describe a GEANT4 simulation of alpha and beta tracks, that includes a Monte Carlo parameterization of electron diffusion, used by undergraduate Michael Thompson to develop track reconstruction software (**Section 7.3**). I conclude with plans for future upgrades (**Section 7.4**) as work continues towards demonstrating surface-alpha screening sensitivity of prototype detector.

7.1 Electronics and Data Acquisition

The signal cables are connected to a digitization board called a Field Programmable Gate Array (FPGA). The FPGA continuously receives pulses from a timer determining the rate the analog signals are digitized. Pulses on each of the channels consist of $N_{\mathrm{samp}} = 2^{15}$ samples recorded at a digitized frequency $f_{\mathrm{pulse}} = 748\,\mathrm{MHz}$ over a period

$$t_{\mathrm{pulse}} = \frac{N_{\mathrm{samp}}/\mathrm{pulse}}{f_{\mathrm{pulse}}} = \frac{2^{15}\,\mathrm{samples/pulse}}{748\,\mathrm{MHz}} \approx 43.8\,\mu\mathrm{sec/pulse}. \tag{7.1.1}$$

The 12-bit digital pulses have a dynamic range $(2^{12} - 1) = 4095$ analog-to-digital converted (ADC) units. When no pulse is recorded, the baseline naturally fluctuates about a mean

$$\mu \approx 2048\,\text{ADCs} \tag{7.1.2}$$

due to electronics noise. To record these pulses, we use a PYTHON script which employs the `katcp` protocol, developed by the astronomy experiment CASPER at Berkley [412]. The FPGA records the digitized pulses (automatically) when a predetermined ADC threshold is reached. The ADC trigger threshold is determined in the PYTHON script which controls the data-taking. A trigger is recorded in the FPGA and transferred over an ethernet cable to a 100 MBPS switch to a computer running a python script controlling the data readout from the ROACH board. I wrote a PYTHON script to record 100 triggers across 6 channels with 2^{15} ADC samples per pulse of unsigned 16-bit integers (int16, at 2 bytes per sample) to an HDF file which also stores trigger number information a ~ 1 Mb/trigger.

To understand the behavior of the detector as we apply increasing voltage to the MWPCs and across the drift region of the TPC, I wrote a live-monitoring script which prints statistical quantities in analog-to-digital converted units (ADCs) and timing quantities for each pulse to the terminal screen where the code runs. As a trigger pulse is recorded, the minimum m, maximum M, average μ, and standard deviation σ (in ADCs) of the pulse on each channel are printed to identify events with significant pulse heights. The average time between consecutive triggers and the instantaneous time since the last trigger t_{wait} are also displayed. Before we can take a measurement, we ramp the voltage up on the trigger grid *slowly*: about 100 Volts every 3 seconds with a BERTAN high-voltage (HV) supply, or by repeatedly incrementing a KEITHLEY high-voltage supply 100 Volts over a period of a minute. With the script output, we interpret the data as it is recorded which helps us to avoid potentially harmful conditions such as excessive or sustained arcing.

During this period, where the voltage is not yet in the proportional regime, arcing from the TPC materials causes large pulses. These events may indicate sparks from the high-voltage wire to the surrounding detector materials as the surface charge density changes under the influence of the increasing electric field. We monitor these 'railed' events *i.e.* pulses which maximally deviate from the baseline to either end of the 12-bit dynamic range with a minimum $m = 0$ or a maximum $M = 4095$ or a standard deviation $\gtrsim$25% of the dynamic range. We take as many as 1,000 triggers during this ramp up period and never exceed the nominal MWPC voltage separation

$$V_{\text{MWPC}} = 2\,\text{kV}. \tag{7.1.3}$$

We monitor the trigger behavior before taking data in order to protect the wires from incurring damage from repeated sparking during the ramp up period. For some periods of data taking, the voltage separation $V_{\text{MWPC}} \approx 1.8$ kV we could set the MWPC to without spark-induced pulses triggering the device as fast as possible; the operational voltage does vary by ~ 150 V. We begin a run after making sure the device is not triggering constantly due to sparks by verifying that the

time between triggers varies and that the pulses are not all railed.

7.1.1 First Data Taken at SDSM&T

Before deploying a radioactive source to calibrate the energy scale of α's, we took random pulses to understand the ambient event rate in the detector. The left panel of **Fig. 7.2** shows the an example pulse on 3 fiducial channels taken after the TPC installation at a voltage separation $V_{\mathrm{MWPC}} = 2\,\mathrm{kV}$. Each channel of the pulse is shown (to scale) baseline-subtracted, *i.e.* not centered at the nominal $\mu = 2048\,\mathrm{ADCs}$. The middle panel of **Fig. 7.2** shows a (log-scale) histogram of the ADCs recorded for the given trigger in each channel. As expected, the distributions are gaussian, but the full-width at half maximum (FWHM) due to the electronics noise in each of the channels

$$\Gamma_{\mathrm{noise}} \sim 100\,\mathrm{ADCs}. \tag{7.1.4}$$

This is quite large a fraction of the pulse height $H_{\mathrm{trig}} \equiv M - \mu \sim 300\,\mathrm{ADCs}$ for the given trigger

$$H_{\mathrm{trig}} \sim 3\,\Gamma_{\mathrm{noise}}. \tag{7.1.5}$$

Generally, the pulse height of interesting (*i.e.* signal) events should be well separated from the noise so that as many real events as possible may be identified, *i.e.* they are not buried in the noise distribution. As indicated by the average noise level on all channels, the pulse quality was poor. The right panel of **Fig. 7.2** shows a histogram of the time between pulses *i.e.* the time since the last trigger. The average time between consecutive triggers and the current time since the last trigger $t_{\mathrm{wait}} \approx 350\,\mathrm{millisec}$ (in the figure) help to identify any significant increase in the event rate from sparking as the voltage between the anode and cathode MWPC sense wires is ramped up to the nominal $V_{\mathrm{MWPC}} \approx 2,000\,\mathrm{V}$. We considered the case that the noise might have been significantly lower at a smaller applied voltage. After many periods of data taking at multiple voltage separations $V_{\mathrm{MWPC}} \sim 1.5\,\mathrm{kV}$ lower than nominal with consistently noisy traces, we inferred that the preamp may have been damaged.

Luckily, our collaborators at CalTech who had possession of the prototype before us sent several preamps along with Eric when he transported the TPC and associated materials to SDSM&T. So, Michael Thompson and I installed another preamp and found that the pulses taken with this new preamp had a significantly lower level of noise that is not a function of the applied voltage. The left panel of **Fig. 7.3** shows an example 3 signal channel pulse taken at an MWPC voltage separation $V_{\mathrm{MWPC}} = 1.8\,\mathrm{kV}$. The middle panel shows a zoom on the pulse near times $t = (4\text{–}8)\,\mu\mathrm{s}$. The middle channel (green) has a pulse height

$$H \sim 450\mathrm{ADCs} \tag{7.1.6}$$

and is easily distinguished from the noise. The right panel of **Fig. 7.3** shows a histogram of the pulse ADCs (light) and due to the pre-pulse electronics noise (dark) in each channel, and the

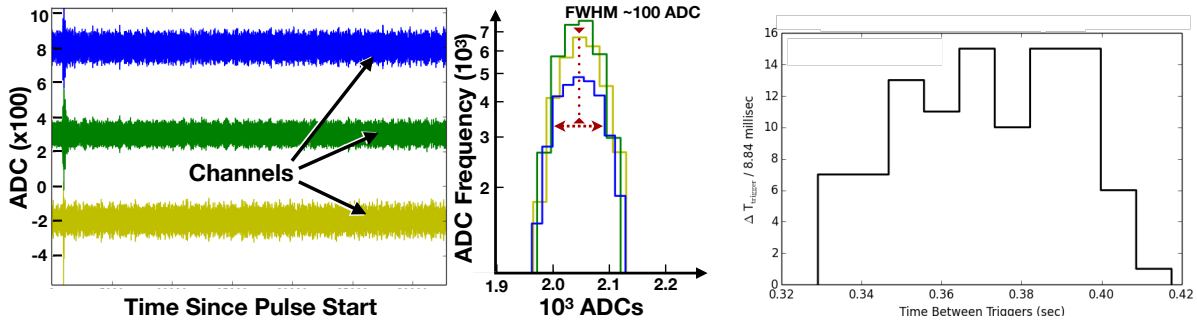

Figure 7.2: Left: An example read-out pulse from the ProtoCage at SDSM&T (ADCs vs time) for 3 channels with an cathode-anode (MWPC) voltage separation $V_{\rm MWPC} = 2\,{\rm kV}$. The baseline ADC count (2048) has been subtracted and each channel is vertically stacked by 500 ADCs. The triggered pulse height $H_{\rm trig} \equiv M - \mu \sim 300$ ADCs, but the initial pulses we recorded were *very* noisy. **Middle:** (Log-scale) Histogram of the ADCs recorded for each of the channels with an approximate full width at half-maximum $\Gamma_{\rm noise} \sim 100$ ADCs indicating significant electronics noise approximately $\sim {}^1\!/_3\, H_{\rm trig}$ the triggered pulse height. **Right:** Histogram of the time between triggers for 100 pulses. For the time being, the PYTHON readout and data storage are slow with an average time $t_{\rm wait} \approx 350\,{\rm millisec}$ between the pulses.

summed pre-pulse noise (line). The pre-pulse electronics noise are scaled by 1/5 to clarify the ADC width in each channel. The electronics noise shown in the histogram corresponds to the pre-pulse ADC samples taken before $t_{\rm pulse} \approx 5\,\mu{\rm sec}$. While there are many fewer sample after the pulse, no systematic effects–such as the afterpulsing in middle (green) channel mentioned below–from the electronics are in the pre-pulse samples. The full-width at half maximum of the pre-pulse electronics noise indicated in the histogram[1] for each of the channels appears to be about 2 bin widths (each 2 ADCs wide) corresponding to a full-width at half maximum

$$\Gamma'_{\rm noise} \lesssim 10\,{\rm ADCs} \tag{7.1.7}$$

some ten times better than the previous preamplifier! The pulse on the middle channel has a pulse height $H \gg \Gamma'_{\rm noise}$ much larger than the ADC deviations due to the noise. After the second preamp was installed, the pulse quality was deemed good enough to take alpha spectra data with a calibration source.

7.2 Deploying a ^{210}Pb α Source

The intention of the BetaCage is to measure the surface emission of low-energy $E_\beta \sim 50\,{\rm keV}$ beta spectra of ^{210}Pb and its progeny, as well as the ^{210}Po α. The ProtoCage will be subject to a large photon and beta background, but we expect to be able to measure the larger energies $E_\alpha \sim 5\,{\rm MeV}$ of surface alphas. Calibrating the prototype α-demonstration device with ^{210}Po alphas is a necessary step working towards the BetaCage. Our group, under Richard Schnee, does not possess a direct source of these long-lived U/Th daughters. Luckily, Juergen Reichenbacher allowed us to borrow his ^{210}Pb α source which he measured in his ALPHABACH detector [413, 414]. The rate of the

[1] The y-scale is logarithmic.

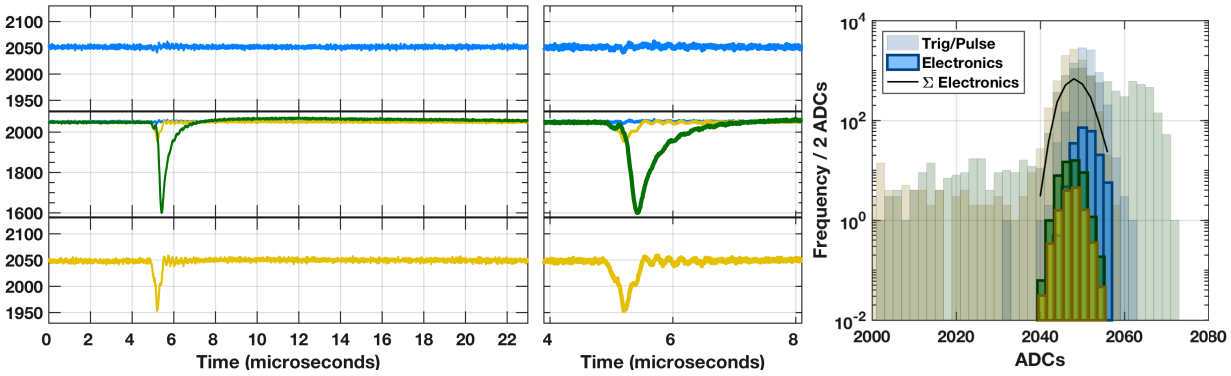

Figure 7.3: Left: Improved read-out pulses after installing a new preamp (ADCs vs time) for 3 working channels. The y-scale for the bottom and top channels are the same, and those pulse are shown in the middle axis to show the different ADC-deviations for triggered events. The maximum pulse height $H \approx 450$ ADCs (middle). **Middle:** Zoom from (4–8) µs period near pulse. These pulses have a significantly better pulse-height sensitivity since the noise has been reduced by $\sim 10\times$. **Right:** (Log-scale) Histogram of the ADCs (with 2 ADC bin width) recorded for each of the channels. The whole-pulse ADC histogram is shown (light, 'Trig/Pulse'). The pre-pulse ADC electronics noise shown (dark, 'Electronics') sequentially scaled by $\times 5$. The 3-channel sum (line, 'Σ Electronics') of the pre-pulse noise distributions indicates an approximate full width half-maximum $\Gamma' \sim 5$ ADCs significantly improved over the damaged preamp.

source, specified by Juergen, is an enormous $\Gamma_{\rm Pb} \approx 52\,$Bq. The probability of obtaining a number of events N–sometimes called successes–in a given time (or space) is

$$P(N) = \frac{\exp(-\mu)\,\mu^N}{N!}. \tag{7.2.1}$$

The probability of getting event pile-up (2 or more hits) in a given a pulse window $\Delta t = 42.3\,$µs is small since the probability of zero triggers (*i.e.* no decay) is an overwhelming fraction

$$P(0) = \exp\left(-42.3\times10^{-6}\,\text{sec} \times 52\,\text{Bq}\right) = \exp(-2.20\times10^{-3}) \approx 0.9978. \tag{7.2.2}$$

In any event, we decided to reduce the overall rate of incident alphas by constructing a pin-hole collimator. I designed and machined an acrylic source holder in which fits the disk source, depicted in the left panel of **Fig. 7.4**. Eric Miller included a thumb tab for easy source removal. I drilled screw holes in a metal plate to fit over the source and suppress alphas which are not emitted normal to the surface of the α-source. I drilled a $D_{\rm p} = 0.003$" diameter pinhole with an area

$$A_{\rm p} = \pi\left(1/2 \cdot 0.003" \times 25.4\,{\rm mm/in}\right)^2 \approx 45\,\mu{\rm m}^2 \tag{7.2.3}$$

in a thin metal cover plate. The metal plate is installed very close acrylic and blocks most of the alphas emitted from the disk source. The ^{210}Pb source was placed in an *AlphaDuo* commercial alpha counter from Ortec [415]. The right panel of **Fig. 7.4** shows the resulting pulse height spectrum from a 15 hour assay of the ^{210}Po alpha emission. The total rate of ^{210}Po alphas detected

$$R_\alpha = 2424\,\alpha' s/15\,{\rm hr} \approx 44.88\,{\rm mBq}\,(1 \pm 2\%) \tag{7.2.4}$$

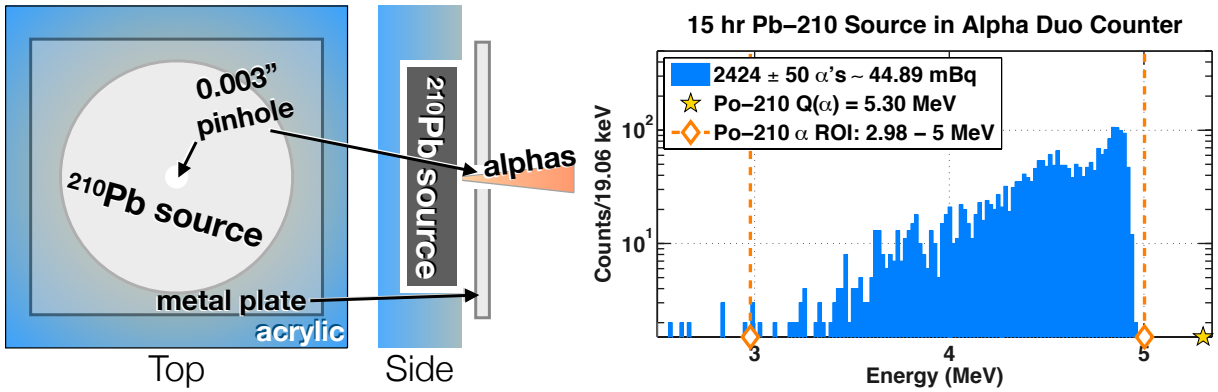

Figure 7.4: Left: Diagram of acrylic ^{210}Pb source holder, with metal cover plate. A 3/16" pinhole significantly reduces the rate of alphas from the long-lived ^{210}Po. I measured the reduced alpha rate with a commercial alpha detector. **Right:** ^{210}Pb α energy spectrum recorded during the 15 hour Run 294 by the *AlphaDuo* [415] detector at SDSM&T. Thanks to Joseph and Eric for helping operate the detector, supplying me with the pulse height data, and energy calibration. The total α rate $R = 45\,(1 \pm 0.02)$ milliHz determined by summing the events of energy $E_\alpha = (2.98\text{–}5.30)$ MeV. If the calibration, is accurate no events had an energy $E_\alpha > 5.0$ MeV. The typical ^{210}Po α rate in the R.O.I. (vertical dashed) is less than a few counts per day. The expectation rate of background events $N_{\text{bgds}} < 1$ ct for this $t_{\text{asy}} = 15$ hr measurement.

with 2% statistical uncertainty. The alpha backgrounds for this detector in the region of interest (3–5) MeV are of order 1 α/day. Presumably, due to the pinhole collimation, all the alphas were perfectly aimed into the small alpha-detector and no efficiency corrections need to be applied to the *AlphaDuo* spectrum. The measured rate indicates an overall reduction

$$\eta_\alpha = \frac{44.88 \times 10^{-3}}{52} \approx 0.086\% \tag{7.2.5}$$

of the true alpha-emission rate. After verifying the alpha emission in the *AlphaDuo*, Michael Thompson helped me install the ^{210}Pb source and rate-reducing holder. The left panel of **Fig. 7.5** shows the source holder (inset) taped to the wire-protecting G10 boards with Kapton tape. This unreliable method of source placement was improved by screwing slats of acrylic together to hang off the top 'side' of the TPC frame. This holder helps the user the place the ^{210}Pb more carefully, and allows for crude readjustment of the location. The right panel of **Fig. 7.5** shows an improved plastic holder made of acrylic slats that is much less likely to erroneously fall down from the top of the TPC (inset) during operation.

A complete TPC calibration would consist of verifying the α track reconstruction efficiency as a function of location (x_0, y_0) and emission angle (θ, ϕ). A small subset of alphas emitted from a sample surface will be aimed along the anode wire and track reconstruction may be more difficult. In the future, it would be useful to design an improved source holder to precisely control these factors. An ideal source holder will be as close to the trigger grid as possible so the entire alpha energy can be measured. Once the G10 boards protecting the trigger grid wires are removed, the source will need a placement tray where the emission location can be systematically controlled. A practical source holder would have a small pinhole, perhaps outfitted with an iris, to allow only

Figure 7.5: Left: Juergen's ^{210}Pb α source in an acrylic source holder and $D_{\rm p} = 0.003$” pinhole drilled into metal plate (inset). The source is secured behind the metal plate, which is screwed into an acrylic thumb-tab accessible disk-holder. Initially, we secured the source to the wire-protecting G10 board with Kapton tape. The source is placed at $\vec{r}_{\rm sce}(x, y) = (0, 0)$ aimed into the G10 board nearest the trigger MWPC. To improve the reliability of the source placement, we assembled some acrylic slats to use instead of Kapton. **Right:** ^{210}Pb α-source secured to an improved source holder made of acrylic slats with zip-ties. The holder hangs off the top to the TPC wiring (inset) and can be moved more easily.

well-aimed alphas emitted perpendicular to the source holder.

7.3 On Track Reconstruction

Michael Thompson and I have attempted to measure the energy spectra many times with the ^{210}Pb source in place. The energy spectra are expected to have consist of $E_\alpha = 5.3\,\text{MeV}$ alphas from ^{210}Po decay as shown in the pulse spectra of **Fig. 7.4**. Since there is a nonzero radon concentration $C_{\rm Ar} \lesssim 10\,\text{mBq/m}^3$ in the argon gas (Eqn. 6.3.3) [392] we also expect some

$$R_{\rm Rn} \lesssim C_{\rm Ar} \times V_{\rm trig} \sim 10\,\text{mBq/m}^3 \times (40 \times 40 \times 3)\,\text{cm}^3 \approx 48 \times 10^{-6}\,\text{Bq}$$

$E_\alpha = 5.48\,\text{MeV}$ ^{222}Rn alpha decays in the 3 cm tall trigger region. There should be a small amount of $E_\alpha = 6.0\,\text{MeV}$ (7.9 MeV) events from ^{218}Po (^{214}Po) alpha decays. These events would be $10^3\times$ smaller than the ^{210}Pb rate (Eqn. 7.2.4). Unfortunately, measured pulse-height spectra of the ^{210}Pb alpha emission do not have the features measured in the AlphaDuo spectrum, or any of these other low-level characteristic features. The spectra are inconclusive and there are a few potential reasons why this is the case.

It is possible the energy resolution of the detector is poor as a result of being too far from the proportional avalanching regime, *i.e.* $V_{\rm MWPC}$ is too large (or small). In any event, the spectra is expected to be complicated by the geometry of the distance of the source to the anode wires of the trigger grid. The machined holes in the G10 board near the trigger MWPC help to place the source consistently and protect the trigger MWPC wires from being damaged during commissioning

and source replacement. These boards prevent the α-source from being deployed very close to the trigger grid. The MWPC frames are 3.0 cm tall [375]. The anode wires of the trigger grid are centered 1.5 cm from the G10 boards. The closest the source can be deployed from the trigger region $d_\alpha \gtrsim 1.5\,\text{cm}$. The range of alphas in argon, neon, and methane (CH_4) is shown in the left panel of **Fig. 7.6**. This is potentially problematic because the ProtoType operates with an argon-methane gas (at a 90-10 ratio), and a $E_\alpha = 5.3\,\text{MeV}$ alpha only has a range

$$\ell_\alpha \approx 3.8\,\text{cm}$$

in argon, approximately $2.5\times d_\alpha$ the distance to the grid. Also, the measured alpha spectra shown in the right panel of **Fig. 7.4**) from the ^{210}Pb disk source, many alphas will have less than $E_\alpha = 4.5\,\text{MeV}$ to deposit in the gas.

Since the alpha range in methane $\ell_\alpha \approx 4.7\,\text{cm}$ is 23% bigger than in argon, the true alpha range will be ∼4.0 cm. Unfortunately, this introduces a complicating factor for alpha-spectroscopy in the ProtoCage with argon. These alphas traveling $d_\alpha \sim 2\,\text{cm}$ before depositing their energy in the trigger region will have lost a significant fraction ∼2 MeV of their kinetic energy. For alpha spectroscopy, neon naively appears to be a better gas since the alpha tracks will be twice as long $\ell_\alpha \approx 9.0\,\text{cm}$. Though we could not make meaningful conclusions regarding the alpha sensitivity of the ProtoCage, I mentored undergraduate Michael Thompson in developing ionization track reconstruction software in Python.

Time projection chambers are designed with an electric (and sometimes magnetic) field to drift the ionized charges to a collection grid and the timing profile (in the bulk and trigger MWPCs) will determine the spatial information in the z-direction. I generated ionization tracks alphas and low-energy (10–200) keV betas in argon-methane and neon-methane gases using my own Geant4 simulation designed to mimic signal events. These simulated events were aimed upward into the bulk of the gas detector, from the origin–the (x, y) center of the trigger grid. The initial angle was generated randomly spanning the upper 2π by Geant4's internal random number generator. Some events aimed parallel to an anode or cathode are expected to be difficult to reconstruct due their potentially ambiguous signal produced on along the length of a single wire. To obtain three-dimensional ionization information, as would be the case for the BetaCage, I read out every instance of energy deposition E and position (x, y, z) for the simulated the event tracks and saved them to Root [416] files for offline analysis.

The right panel of **Fig. 7.6** shows an example α track in neon-methane mixture. The upper left panel shows the 3D track and each of the panels shows a two-dimensional colormap projected on each pairs of spatial dimensions (xy, xz, and yz from left to right). For $E_\alpha \sim 5\,\text{MeV}$ ($E_\beta \sim 100\,\text{keV}$) alphas (betas) the Root files for each event were a reasonably small 1 MB (50 kB). I used Root to loop over all energy deposition locations and break up the ionization into 3D voxels with 5 mm (x, y)-spacing with $\sim 2\,\text{mm}$ z-slices and saved the location-binned energy deposition.

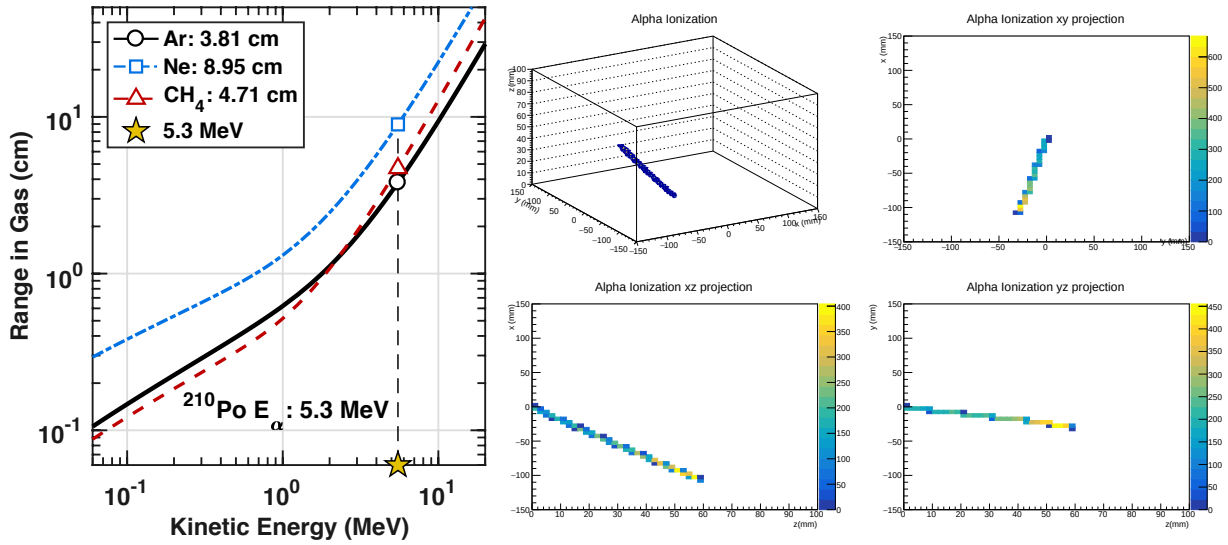

Figure 7.6: Left: NIST α ranges under the CSDA approximation as a function of alpha energy in argon (solid), neon (dot-dash), and methane (dashed) gases. The factor of 2 difference in (5.3 MeV) alpha range between argon and neon is primarily due to the gas density. We use argon-methane (P-10) gas in the prototype which means the highest energy alphas will travel $\ell_\alpha \sim 4\,\text{cm}$ instead of $\ell_\alpha \sim 9\,\text{cm}$ as they would in neon. As a result, the alpha spectra are nondescript because the alpha travels $\sim 2\,\text{cm}$ before depositing ionization in the sensitive region of trigger MWPC where avalanching will occur. Using simulated tracks could help to understand the pulse height spectra whose features are less clear than we initially expected. **Right:** Simulated alpha energy deposition in neon gas (3D representation upper left) with two-dimensional projected histograms. From left to right, top to bottom, the plots are: x vs y, x vs z, and y vs z. The z-axis (colormap) corresponds to energy (keV) deposited per voxel (or projected 2D voxel) where the (x, y, z) voxels are $(5{,}5{,}2)\,\text{mm}^3$.

Without an external electric field, electrons and ions freed by ambient radiation will diffuse uniformly from the ionizing event location colliding with the material (*e.g.* gas molecules) losing energy until they reach thermal equilibrium and recombine. The charges are accelerated, and they collide with the gas, and they re-accelerate until they reach the MWPC grid where they undergo avalanching and are subsequently collected. So, these simulated ionization tracks of electrons produced by GEANT4 are physically incorrect. In reality, the electrons in the gas will undergo longitudinal and transverse diffusion while they travel from the drift region of the TPC, above the trigger grid, before they are imaged by the bulk grid.

7.3.1 Electron Diffusion in Gases

Here, I discuss electron diffusion following works by W. Leo [395], F. Sauli [376], B. Sadoulet [417], and Blum, Riegler, and Rolandi [377] to incorporate the diffusion of electrons as the track drifts upwards from above the trigger grid towards the bulk grid. The velocity distribution of thermalized charges of mass m, at temperature T, are Maxwell distributed with a mean speed

$$\langle v \rangle = \sqrt{\frac{8}{\pi}} \sqrt{\frac{k_B\, T}{m}}$$

is derived based on molecular collisions under the kinetic theory of gases [395]. At room temperatures, diatomic nitrogen gas has a mean speed

$$\langle v_{N_2} \rangle = \sqrt{\frac{8}{\pi}} \sqrt{\frac{8.617\,\mathrm{J/mol\,K} \cdot\ 300\,\mathrm{K}}{0.028\,\mathrm{kg/mol}}} \approx 500\,\mathrm{m/s}.$$

Under the kinetic theory model, diffusion is gaussian [376, 395]. For a one-dimensional charge distribution f of total charge q, initially distributed at the origin $x = 0$

$$f(x, t = 0) \equiv q\,\delta(x) \tag{7.3.1}$$

thermalizing in a gas with a diffusion coefficient D for a time t will evolve according

$$f(x, t > 0) = \frac{q}{\sqrt{2\pi}\sigma_{1D}} \exp\left(\frac{-x^2}{\sigma_{1D}^2}\right). \tag{7.3.2}$$

where the time-dependent cloud will diffuse $\sigma_{1D} = \sqrt{2\,D\,t}$ and spread with the square root of time. Three dimensional isotropic diffusion is spherically symmetric and gaussian distributed with a spread

$$\sigma_{3D} = \sqrt{6\,D\,t}. \tag{7.3.3}$$

The distance $z_{\mathrm{drift}} = 40\,(20)\,\mathrm{cm}$ between the trigger and bulk MWPC of the BetaCage (ProtoCage). As a compromise, I chose a simulated (maximum) drift distance $z_{\mathrm{drift}} = 30\,\mathrm{cm}$ to determine the standard deviation of a gaussian distribution that is then applied to simulate spherical diffusion from every deposit of ionization along the track, as a function of the drift distance. The deviation

$$\sigma_D = \tilde{D}\sqrt{z_{\mathrm{drift}}} \tag{7.3.4}$$

increases with the square root of the drift distance. The standard deviation of the diffusive spread σ was determined experimentally for argon-methane (90-10) for the planned operating conditions of the BetaCage: (atmospheric) pressure $P = 760\,\mathrm{Torr}$, and a modest electric field $|E| = 50\,\mathrm{V/cm}$. The diffused distance for electrons drifting under these conditions is shown for two values

$$\tilde{D} \approx 600\,\mu\mathrm{m}/\sqrt{\mathrm{cm}} \tag{7.3.5}$$

in **Fig. 7.7**. I used a value for the electron spread based on Magboltz [418] simulations by Blair Stringfellow from 1995 [419] used for the Solenoid Tracker (STAR) at the Relativistic Heavy Ion Collider (RHIC). The calculated transverse and longitudinal diffusion $\tilde{D} \approx 600\,\mu\mathrm{m}/\sqrt{\mathrm{cm}}$ of electrons in P10 gas differ by only 2% [420]. As a result, the Monte Carlo parameterization I perform assumes these coefficients are equal, and thus the diffused clouds produced by point-like ionization deposits are spherically symmetric.

During the loop over each location where energy deposition occurred, I used a Monte Carlo parametrized diffusion model, shown in the left panel of **Fig. 7.7**, determined by the distance the ionization travels before being readout by the bulk MWPC. At each point, treated as a

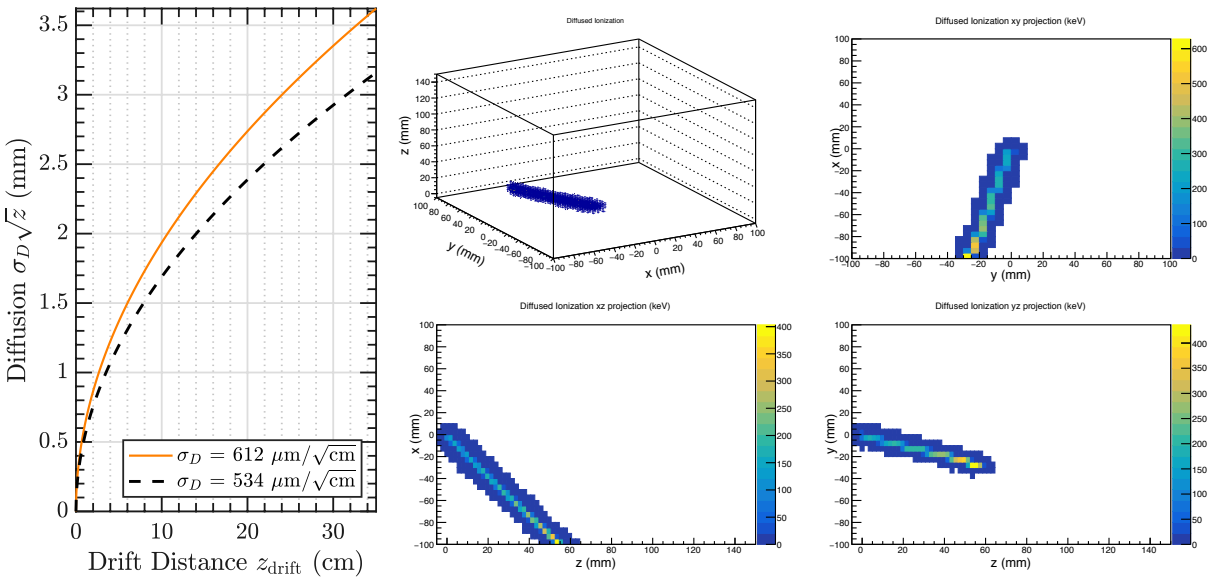

Figure 7.7: Left: Diffusive spread of an electron cloud as a function of drift distance. **Right:** Simulated alpha energy deposition in neon gas (3D representation upper left) with two-dimensional projected histograms. From left to right, top to bottom, the plots are: x vs y, x vs z, and y vs z. The z-axis (colormap) corresponds to energy (keV) deposited per voxel (or projected 2D voxel) with (x, y, z) bins = (5,5,5) mm.

delta distribution, I generated a 3D gaussian distribution (Eqn. 7.3.2) with a standard deviation determined by the drift distance. I redistributed the ionization $\mathrm{d}E$ deposited at each location, independent of the others, according to a spherically symmetric gaussian distribution

$$g(r, z_{\text{drift}}) = \mathrm{d}E \cdot \exp\left(\frac{-r^2}{z_{\text{drift}} \cdot \tilde{D}^2}\right) \tag{7.3.6}$$

where r is the distance from the initially deposition location, and the spread $\tilde{D}$ taken from simulation (Eqn. 7.3.5). The distribution is independent of angle, so each fraction of the ionization $\mathrm{d}E$ is relocated to a randomly chosen angle with a flat probability per unit solid angle to create diffused charge clouds. These diffused tracks were voxel-ized, saved, and analyzed by an undergraduate Michael Thompson. I mentored Michael in developing a Python script to implement track reconstruction for these more physically accurate diffused tracks which implements Djikstra's search algorithm that solves the single-source shortest path problem for a graph by producing the shortest path tree. Understanding the measured energy spectrum will be enhanced using simulated tracks such as these.

7.4 Future Work

Collaborators at the University of Alberta have built and shipped 16 preamps, with 6 channels per preamp. We received them at SDSM&T in July of 2018. We cannot yet install these preamps because we are currently waiting for the power supply to the preamps to arrive. After we can

power the preamps, each preamp will be paired with an FPGA. Currently, the vacuum vessel supporting the TPC has enough signal feedthroughs to accommodate 22 channels. In the very near future, will we employ 4 preamp/FPGA pairs to increase the spatial resolution of the ProtoCage. In the future, using a lower density neon-based fill gas will allow surface and calibration α's to travel $2\times$ farther in the TPC so that the bulk MPWC can image the tracks significantly better. Additionally, fiducialization against background events from the anode wire surfaces from ^{222}Rn daughter plate-out onto the ProtoCage wires may be improved beyond what has already been described. Using simulated tracks to obtain the energy deposition before the alpha's enter the trigger region will help to understand and verify the alpha spectra from calibration sources. After improving the position resolution to ionization produced in the TPC with new electronics, the track reconstruction software may be applied to real α tracks and the alpha sensitivity of the device can be demonstrated and it is possible that even with a higher ambient photon background than the BetaCage, measuring consecutive beta-emitters will be possible.

Chapter 8
Conclusions

Directly discovering dark matter will require detector calibration and a detailed understanding of detector backgrounds. The work performed in this thesis entails three major components. The first is the energy calibration of the Cryogenic Dark Matter Search (CDMS II) silicon dark matter detectors with a ^{252}Cf neutron source. The second is the improvement of ^{222}Rn backgrounds for SuperCDMS SNOLAB by commissioning a system to measure the radon emanation and by constructing an apparatus to measure the radon diffusion of gaskets in order to identify a low-cost seal. The third is work on a novel surface-α and -β screener (the BetaCage) including the development and use of a GEANT4-based simulation and the characterization of a gas panel.

Calibrating a detector's nuclear-recoil energy scale is one of the major challenges for dark matter experiments because of the generally featureless spectra produced by common radioactive sources. Many experiments are pursuing expensive, complicated, dedicated experiments for such calibrations, using fixed-energy neutron sources and an array of secondary detectors. The nuclear-recoil energy resulting from a neutron scatter may be reconstructed using the secondary detector array to identify the neutron's time-of-flight with timing coincidence and the neutron recoil angle. Instead, this thesis describes the determination of the nuclear-recoil energy scale for CDMS II silicon detectors using a systematic comparison between the nearly featureless nuclear-recoil spectra measured in-situ from a ^{252}Cf neutron source and a Monte Carlo simulation with a flux-based correction to the nuclear-recoil calibration livetime. Results imply a phonon collection efficiency $\eta^{\varphi}_{\mathrm{NR}} = 95^{+0.9}_{-0.7}\%$ down to nuclear-recoil energies $\sim$10 keV.

With the recalibrated energy scale, I determined that the ionization yield for low-energy $E_{\mathrm{R}} \lesssim 20$ keV nuclear recoils in CDMS II silicon detectors is lower than the Lindhard prediction, but in agreement with recent measurements [232, 233]. Additionally, the resulting nuclear-recoil ionization measurement supports the hypothesis that the phonon collection efficiency $\eta^{\varphi}_{\mathrm{NR}} = 95\%$, since the yield with the recalibrated energy scale agrees better with other measurements. The ionization collection efficiency of nuclear recoils is consistent with 100% at energies $E_{\mathrm{R}} \sim 20$ keV and decreases to $\sim$75% at 100 keV. Presumably, ionization produced by nuclear recoils at higher energies is too

dense to be completely separated by the electric field and collected by the low-bias charge sensors of the CDMS II detectors.

The radioactively decaying noble gas ^{222}Rn is a critical problem for direct-detection dark matter experiments. This thesis describes the commissioning of a radon emanation system. The radon detector and gas panel were characterized to determine the standard operating procedures for sample preparation and radon transfer with our gas handling system. We found that the diffusion of radon into and back out of teflon in the radon detection vessel can contribute significantly to the detector backgrounds. Based on simulations of data, I developed a method to determine the wait-time needed for a low-background measurement to avoid cross-contaminating a sample with back-diffused radon from a previous measurement.

We measured the radon transfer efficiency free of systematic uncertainties, and determined that about 96% of emanated radon from our 13 L vacuum vessel can be transferred to the small detector volume. The small-volume radon detector typically has very low backgrounds $\sim$2 counts/day resulting in a sensitivity to radon decay rates $\sim$0.2 mBq. Emanation of large sample in the 300 L vacuum vessel provides a world-leading potential for detecting samples with ultra-low radon levels.

We used the system for measurements of non-metal gaskets, which typically emanate significant amounts of radon. We measured two samples of EPDM produced in different batches by Lemer Pax. The radon emanation per unit length for the batches was found to differ by a factor of 16, emphasizing the importance of assaying actual materials to be used. Two rubber gasket samples were determined to be consistent with zero radon emanation: one 30-cm-long Silicone sample from Lemer Pax, and a second, commercially available sample of caulking substance Zip-A-Way. These materials have the lowest radon emanation found in the literature, and may be useful for other low-background experiments as low-cost, easy-to-use gaskets.

Further, this thesis work helped to construct a low-cost apparatus to measure the radon diffusion, solubility, and permeability of the same gasket materials. Measuring the radon diffusion properties of gaskets is difficult since the radon permeability of materials in air is a strong function of the relative humidity. Consecutive measurements of radon diffusion and permeability of a gasket that we fabricated from a commercial caulking substance Zip-A-Way indicate that the radon diffusion properties of soft materials may change, with the material even becoming more radon-hard with time. For such a fabricated gasket, it would be useful to repeatedly measure the radon diffusion of several similar gaskets to determine this change as a function of time since gasket fabrication.

We also determined that a 1.5 cm thickness of EPDM would be sufficient for the SuperCDMS SNOLAB radon purge. The radon concentration in the SNOLAB cavern underground at Sudbury, Canada where SuperCDMS will be deployed would contribute excessively to the single-scatter electron-recoil backgrounds, at a rate $\sim 3.5\times$ larger than all other experimental backgrounds, if it were not purged. A radon barrier surrounding the detectors will be sealed with a low-radon 4.8 mBq/m EPDM gasket and purged with low-radon gas at a flow rate $F \lesssim 8$ L/min. With

this gasket, the radon-induced backgrounds are expected to be $\gtrsim 200\times$ lower than the dominant electron-recoil backgrounds from ^{32}Si and ^{3}H within the bulk of the detectors.

Finally, to make further progress on background reduction for dark matter searches, ultra-low-background surface-screening devices like the BetaCage will be critical to determine *e.g.* which batches of silicon are sufficiently free of ^{32}Si and ^{210}Pb. In this thesis, progress was made on a prototype device and we demonstrated that the gas handling system will reduce radon $60\times$ to keep the radon-induced background subdominant. GEANT4 simulations I performed in this thesis show that the BetaCage will have a considerably greater sensitivity than originally calculated for radionuclides, such as ^{32}Si and ^{210}Pb, that beta-decay twice in moderate succession ($t_{1/2} \lesssim 14\,\text{days}$).

Significant work remains developing screeners that will help researchers to further mitigate the backgrounds of direct dark matter experiments. It is my hope that the work performed in this thesis will help experimentalists to inform aspects of future detector generations that will finally directly detect dark matter. With luck, graduate students will soon be comparing unambiguous recoil spectra from WIMPs in many targets, determining systematic uncertainties in nuclear physics models, and providing benchmarks for indirect dark matter observations and future collider experiment efforts!

Appendices

Appendix A
Nuclear Recoil Ionization Yield

This appendix contains plots of the resulting ionization yield (and recoil energy) for the three rescaling hypotheses which were not compared in the publication [2]: the average rescaling $\eta^{\varphi}_{\mathrm{NR}} = 95.2^{+0.9}_{-0.7}\%$, detector-dependent rescaling as shown in **Fig. 2.11** and **Table 2.2**, and no rescaling.

Table A.1 shows the values of the flux-weighted livetimes by detector, for each neutron source position, for nuclear recoils $E_{\mathrm{R}} = (10\text{–}100)\,\mathrm{keV}$.

Fig. A.1 shows nuclear recoil (NR) events passing quality cuts, as outlined in **Section 2.3.1**, in the ionization yield–recoil energy plane for each of the hypotheses. Two-dimensional histograms of

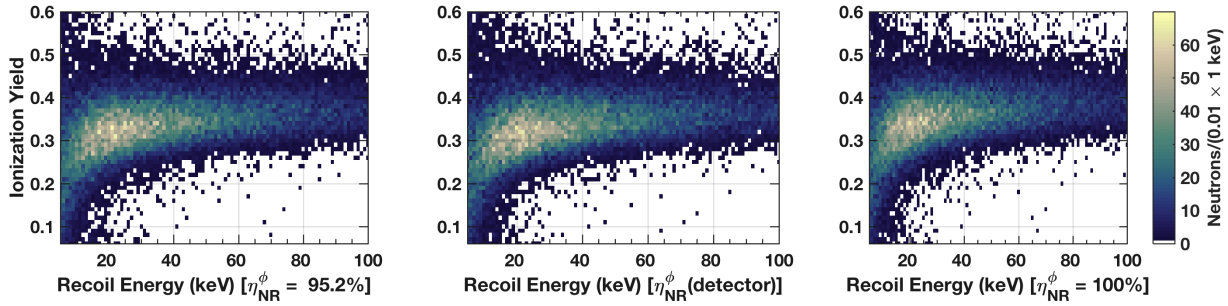

Figure A.1: Two-dimensional histograms of selected neutrons-induced nuclear recoils (per 1 keV per 0.01 yield) for all ^{252}Cf calibrations as a function of rescaled ionization yield and nucelar-recoil energy (Eqns. 2.6.1, 2.6.2) for three rescaling hypotheses. **Left:** The average rescaling (Eqn. 2.5.3) used in Ref. [227]. **Middle:** The detector-dependent rescaling as shown in (right panel) **Fig. 2.12** and **Table 2.2**. **Right:** No rescaling applied *i.e.* the apparent nuclear-recoil energy and corresponding ionization yield are accurate. The best-fit rescalings (for both hypotheses) do not significantly effect the energy-dependent distribution of ionization yield. **perhaps more?**

nuclear recoils as a function of ionization yield and recoil energy for ^{252}Cf calibration events passing selection criteria are shown in **Fig. A.2**, shown with the average (top), detector-dependent (middle), and no (bottom) nuclear recoil rescaling. The vertical lines representing the energy thresholds which are described in Kevin's McCarthy's thesis [228], and used in the 2013 PRL paper [227].

The results of the gaussian fits to the ionization yield (with detector-dependent $\eta^{\varphi}_{\mathrm{NR}}$) for selected neutrons is shown, grouped by energy, in **Fig. A.3**, and with no rescaling in **Fig. A.4**, *i.e.* assuming

Table A.1: Flux-Weighted Livetimes by series and detector in silicon detectors. Bad series are shown as X. The horizontal lines separate each of the relevant CDMS II runs: 123–128. The series number shows the data-taking start time increasing sequentially.

Series	^{252}Cf Source	T1Z4	T2Z1	T2Z2	T2Z4	T3Z3	T4Z1	T4Z3	T5Z3
1709271227	NE	1087	1525	X	1704	1704	1704	1691	1703
1709271531	SW	733	1055	X	1179	1179	1179	1169	1179
1712171212	NE	982	1271	X	X	1478	1477	1467	1477
1712171457	SW	717	916	X	1068	1068	1068	1060	1068
1712171748	SW	X	X	X	X	X	X	X	X
1712180520	SW	X	X	X	X	X	X	X	X
1802080804	SW	X	X	1497	1497	1497	1497	1497	1497
1802081014	NE	X	1181	1442	1442	1442	1442	1442	1442
1802081333	NE	X	X	X	X	X	X	X	X
1804250825	SW	X	1344	1674	1674	1675	1675	1674	1674
1804251235	NE	X	1440	1786	1785	1786	1786	1786	1786
1807211133	SW	X	1609	2078	2078	X	2079	2078	2078
1807211340	NE	X	1278	1654	1654	X	X	X	1654
1809151037	SW	X	1482	1897	1897	1897	1897	1897	1897
1809151324	NW	X	1283	1579	1579	1579	1579	1579	1579
1809151524	NW	X	497	588	588	588	588	587	588

the phonon collection efficiency for nuclear recoil is the same as for electron recoils of the same deposited energy.

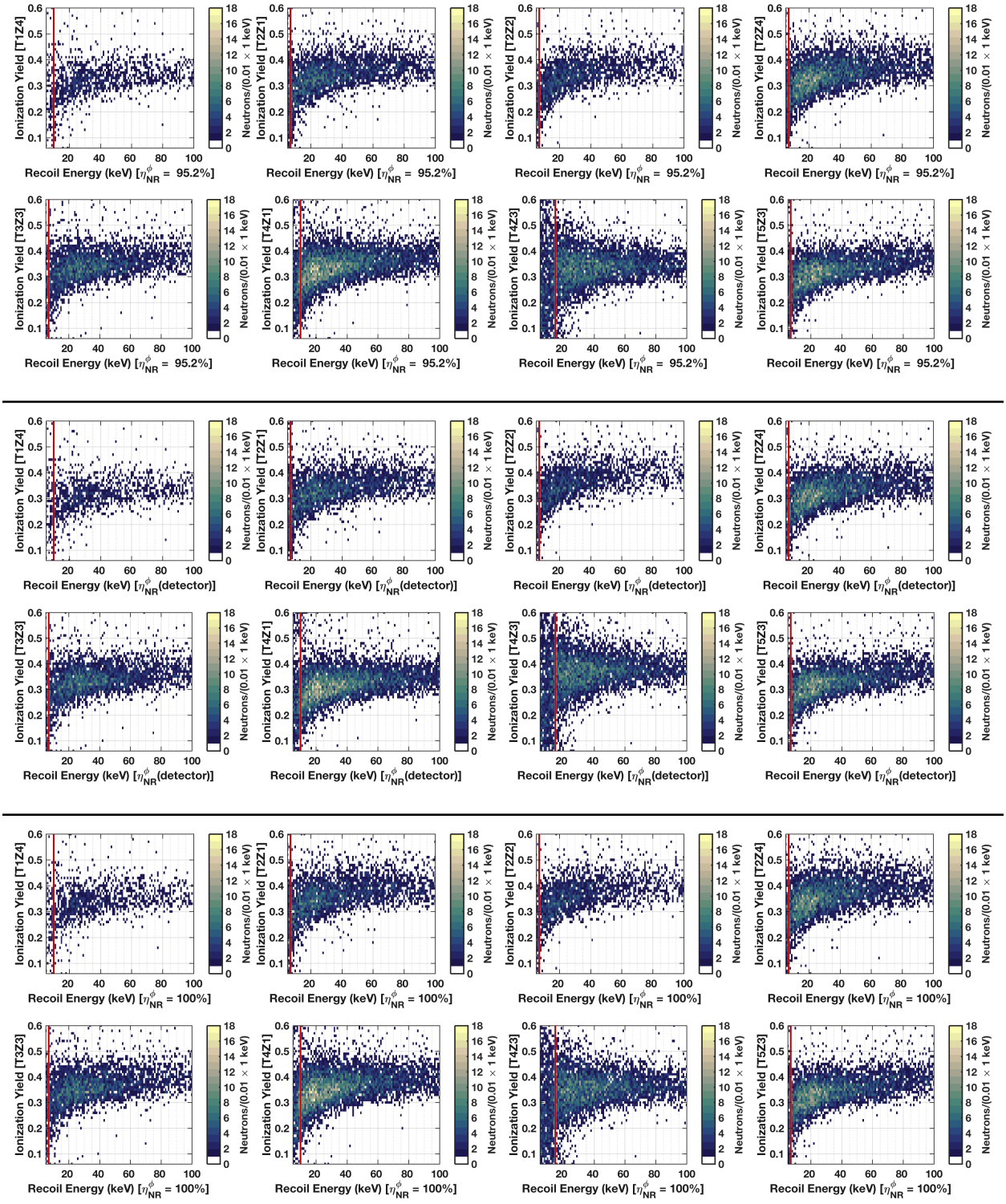

Figure A.2: Two-dimensional histograms of neutron-induced nuclear recoils passing quality cuts as a function of ionization yield and recoil energy for three rescaling hypotheses: **top:** the average rescaling (Eqn. 2.5.3) used in Ref. [227], **middle:** the detector-dependent rescaling as shown in **??** and **Table 2.2**, and **bottom:** no rescaling applied.

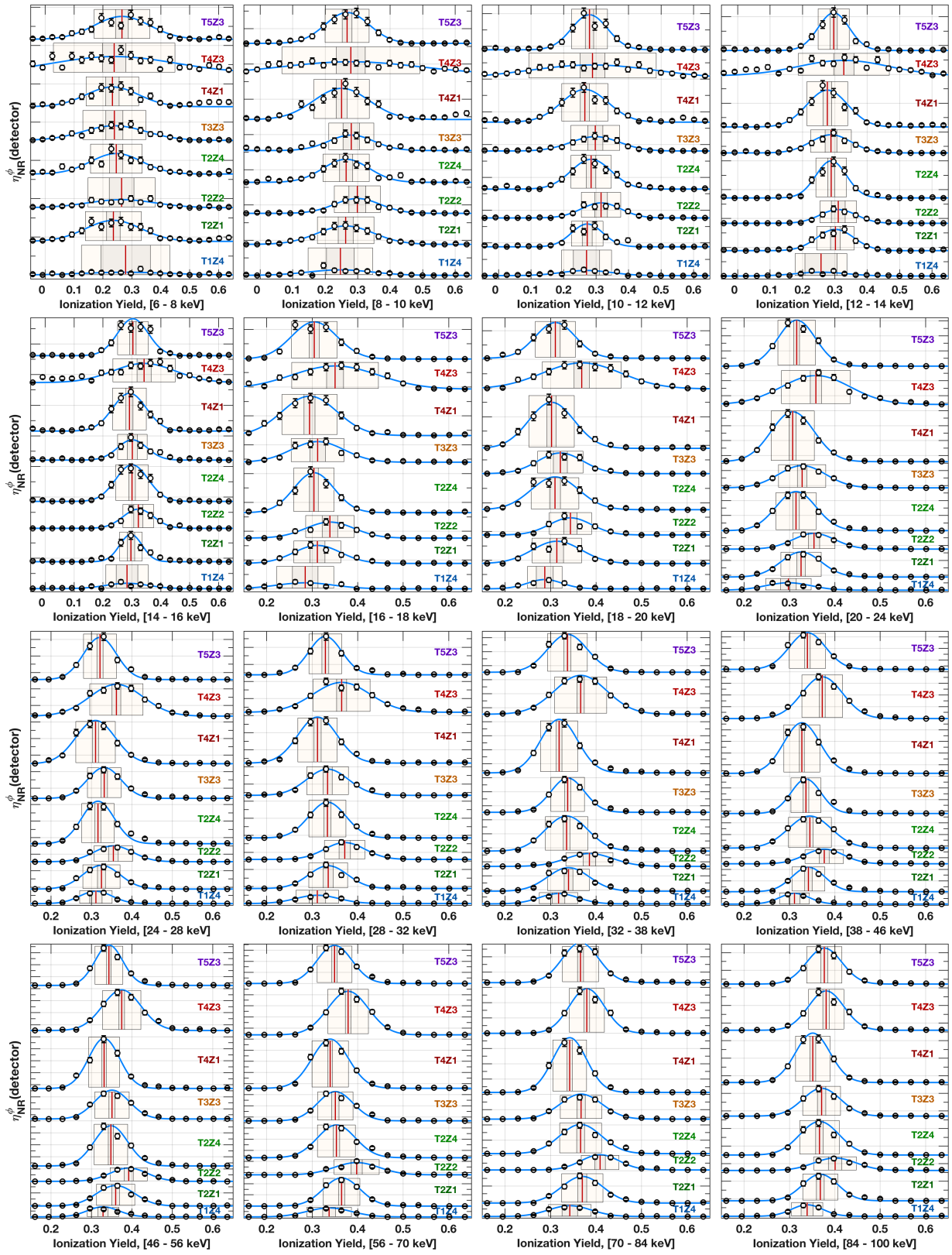

Figure A.3: Histograms of ionization yield (∘ with 68% C.L. statistical uncertainties) for neutrons in the eight working CDMS II silicon detectors for 16 energy ranges (labeled on the x-axis) with the detector-dependent rescaling. Gaussian Fits (solid curves) to the number of events (with a 0.33 yield bin width) with fitted means $\langle y \rangle$ are shown (red vertical line), with $3\sigma_{\langle y \rangle}$ (99.7% C.L.) fit uncertainties on the mean ionization (dark fill), and fitted standard deviation (light fill).

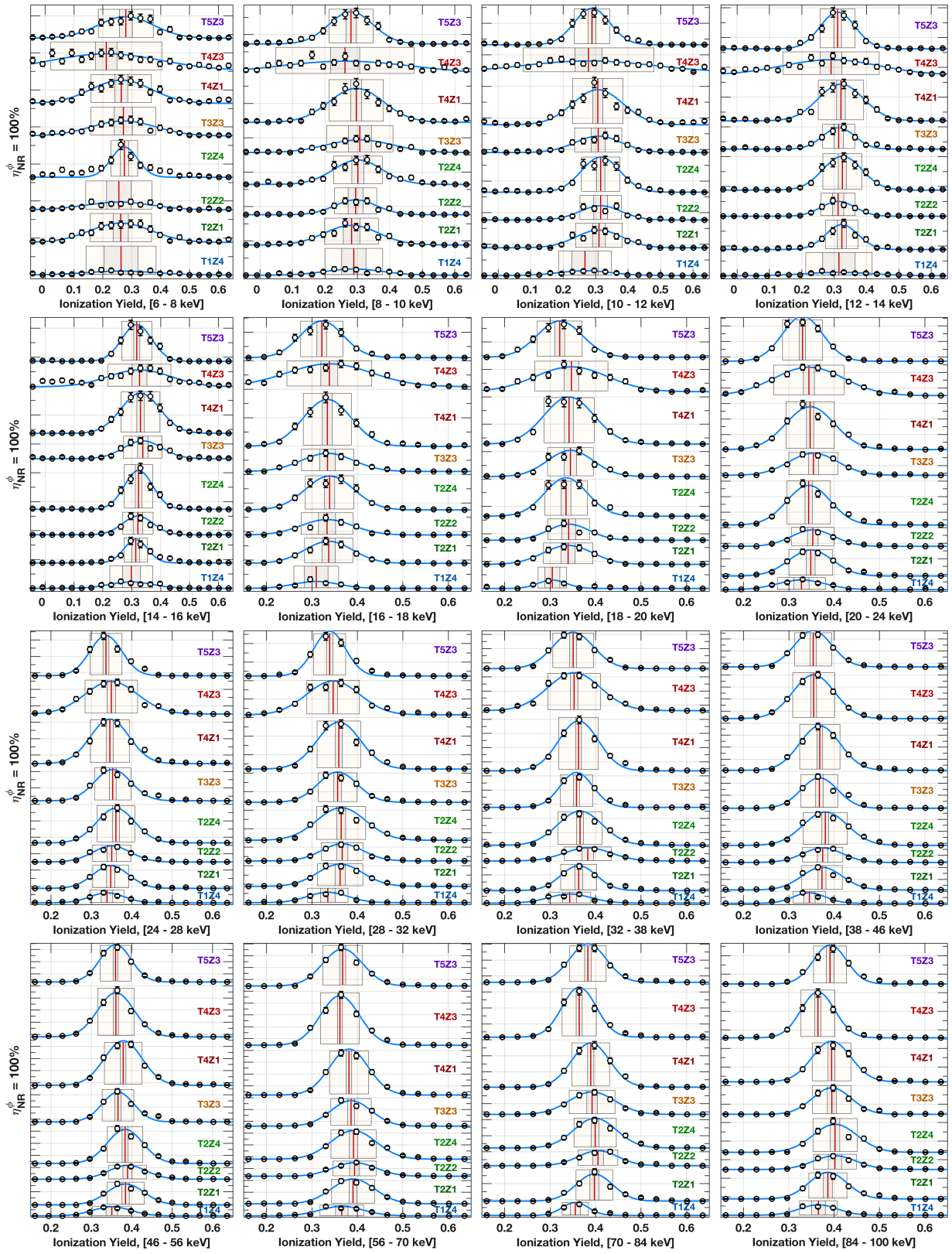

Figure A.4: Histograms of ionization yield (∘ with 68% C.L. statistical uncertainties) for neutrons in the eight working CDMS II silicon detectors for 16 energy ranges (labeled on the x-axis) with no energy rescaling. Gaussian Fits (solid curves) to the number of events (with a 0.33 yield bin width) with fitted means $\langle y \rangle$ are shown (red vertical line), with $3\sigma_{\langle y \rangle}$ (99.7% C.L.) fit uncertainties on the mean ionization (dark fill), and fitted standard deviation (light fill).

Bibliography

[1] M. Tanabashi, K. Hagiwara, K. Hikasa, et al. Review of particle physics. *Phys. Rev. D*, 98:030001, Aug 2018.

[2] R. Agnese, A. J. Anderson, T. Aramaki, et al. Nuclear-recoil energy scale in CDMS II silicon dark-matter detectors. *Nucl. Instrum. Meth. A*, 905:71--81, July 2018.

[3] H. Andernach and F. Zwicky. English and Spanish Translation of Zwicky's (1933) The Redshift of Extragalactic Nebulae. *arXiv e-prints: 1711.01693*, November 2017.

[4] M. W. Goodman and E. Witten. Detectability of certain dark matter candidates. *Phys. Rev. D*, 31:3059--3063, 1985.

[5] Neil Spooner. *Directional detectors*, chapter 22, pages 437--466. Cambridge University Press, Cambridge, UK, 2010.

[6] G. Jungman, M. Kamionkowski, and K. Griest. Supersymmetric Dark Matter. *Phys. Rept.*, 267:195--373, 1996.

[7] Gianfranco Bertone, editor. *Particle Dark Matter: Observations, Models and Searches*. Cambridge University Press, Cambridge, UK, 2010.

[8] Gianfranco Bertone, Dan Hooper, and Joseph Silk. Particle dark matter: Evidence, candidates and constraints. *Phys. Rept.*, 405:279--390, 2005.

[9] Steven Weinberg. *Cosmology*. 2008.

[10] A. R. Liddle and D. H. Lyth. *Cosmological Inflation and Large-Scale Structure*. Cambridge University Press, Cambridge, UK, 2000.

[11] Edwin Hubble. A relation between distance and radial velocity among extra-galactic nebulae. *Proceedings of the national academy of sciences*, 15(3):168--173, 1929.

[12] Wolfgang Rindler. *Essential relativity: special, general, and cosmological*. Springer Science & Business Media, 2012.

[13] Stephanie Blondin, Tamara Maree Davis, Kevin Krisciunas, et al. Time dilation in type ia supernova spectra at high redshift. *The Astrophysical Journal*, 682(2):724, 2008.

[14] Jerome Martin. Everything you always wanted to know about the cosmological constant problem (but were afraid to ask). *Comptes Rendus Physique*, 13(6-7):566--665, 2012.

[15] R Capasso, A Saro, JJ Mohr, et al. Galaxy kinematics and mass calibration in massive

sze-selected galaxy clusters to z= 1.3. *Monthly Notices of the Royal Astronomical Society*, 482(1):1043--1061, 2018.

[16] D. Clowe, A. Gonzalez, and M. Markevitch. Weak-Lensing Mass Reconstruction of the Interacting Cluster 1E 0657-558: Direct Evidence for the Existence of Dark Matter. *Astrophys. J.*, 604:596--603, April 2004.

[17] Planck Collaboration, P. A. R. Ade, N. Aghanim, et al. Planck 2015 results. XIII. Cosmological parameters. 594:A13, 2016.

[18] E. Komatsu, J. Dunkley, M. R. Nolta, et al. Five-Year Wilkinson Microwave Anisotropy Probe Observations: Cosmological Interpretation. *Astrophys. J. Supp.*, 180:330--376, February 2009.

[19] David R. William. Nasa planetary fact sheet. Accessed Mar 2, 2019, `https://nssdc.gsfc.nasa.gov/planetary/factsheet/`.

[20] K. G. Begeman, A. H. Broeils, and R. H. Sanders. Extended rotation curves of spiral galaxies - Dark haloes and modified dynamics. *Mon. Not. Royal Ast. Soc.*, 249:523--537, April 1991.

[21] G. G. Raffelt. Dark matter: motivation, candidates and searches. In *1997 European School of High-Energy Physics*, pages 235--278, Jan 1998.

[22] C. Patrignani et al. Review of Particle Physics. *Chin. Phys.*, C40(10):100001, 2016.

[23] Pieter van Dokkum, Shany Danieli, Yotam Cohen, et al. A galaxy lacking dark matter. *Nature*, 555(7698):629--632, Mar 2018.

[24] Pieter van Dokkum, Shany Danieli, Roberto Abraham, Charlie Conroy, and Aaron J. Romanowsky. A Second Galaxy Missing Dark Matter in the NGC 1052 Group. *apj*, 874(1):L5, Mar 2019.

[25] A. Einstein. Die Grundlage der allgemeinen Relativitätstheorie. *Annalen der Physik*, 354(7):769--822, Jan 1916.

[26] ESA NASA and L. Calada. Gravitational lensing in action. `https://www.spacetelescope.org/images/heic1106c/`, April 12, 2011.

[27] V Belokurov, NW Evans, PC Hewett, et al. Two new large-separation gravitational lenses from sdss. *Monthly Notices of the Royal Astronomical Society*, 392(1):104--112, 2008.

[28] Henk Hoekstra, Jan Hartlap, Stefan Hilbert, and Edo van Uitert. Effects of distant large-scale structure on the precision of weak lensing mass measurements. *Monthly Notices of the Royal Astronomical Society*, 412(3):2095--2103, 04 2011.

[29] Douglas Clowe, Marusa Bradac, Anthony H. Gonzalez, et al. A direct empirical proof of the existence of dark matter. *Astrophys. J.*, 648:L109--L113, 2006.

[30] David Harvey, Richard Massey, Thomas Kitching, Andy Taylor, and Eric Tittley. The non-gravitational interactions of dark matter in colliding galaxy clusters. *Science*, 347:1462--1465, 2015.

[31] C. L. Bennett, A. J. Banday, K. M. Gorski, et al. Four-Year COBE DMR Cosmic Microwave Background Observations: Maps and Basic Results. 464:L1--L4, June 1996.

[32] A. A. Penzias and R. W. Wilson. A Measurement of Excess Antenna Temperature at 4080 Mc/s. *Astrophys. J.*, 142:419--421, July 1965.

[33] E. W. Kolb and M. S. Turner. *The Early Universe*. Addison-Wesley, Reading, MA, 1990.

[34] Andrew Liddle. *An introduction to modern cosmology*. John Wiley & Sons, 2015.

[35] D. J. Fixsen. The temperature of the cosmic microwave background. *The Astrophysical Journal*, 707(2):916, 2009.

[36] D. J. Fixsen, E. S. Cheng, D. A. Cottingham, et al. Cosmic microwave background dipole spectrum measured by the COBE FIRAS instrument. *Astrophys. J.*, 420:445--449, 1994.

[37] D. J. Fixsen, A. Kogut, S. Levin, et al. The temperature of the cosmic microwave background at 10 ghz. *The Astrophysical Journal*, 612(1):86, 2004.

[38] B. D. Fields and S. Sarkar. Big Bang Nucleosynthesis. *Phys. Lett. B*, 592:20.1--20.11, July 2004.

[39] P Sikivie. Experimental tests of the "invisible" axion. *Physical Review Letters*, 51(16):1415, 1983.

[40] Pierre Sikivie. Axions 05. In *AIP Conference Proceedings*, volume 805, pages 23--29. AIP, 2005.

[41] C Alcock, RA Allsman, TS Axelrod, et al. The macho project-a search for the dark matter in the milky-way. In *Sky Surveys. Protostars to Protogalaxies*, volume 43, page 291, 1993.

[42] Bernard Carr, Martti Raidal, Tommi Tenkanen, Ville Vaskonen, and Hardi Veermäe. Primordial black hole constraints for extended mass functions. *Phys. Rev. D*, 96:023514, Jul 2017.

[43] AG Doroshkevich and M Yu Khlopov. Formation of structure in a universe with unstable neutrinos. *Monthly Notices of the Royal Astronomical Society*, 211(2):277--282, 1984.

[44] Scott Dodelson and Lawrence M. Widrow. Sterile neutrinos as dark matter. *Phys. Rev. Lett.*, 72:17--20, Jan 1994.

[45] Joel R. Primack, David Seckel, and Bernard Sadoulet. Detection of Cosmic Dark Matter. *Ann. Rev. Nucl. Part. Sci.*, 38:751--807, 1988.

[46] Jonathan L. Feng, Arvind Rajaraman, and Fumihiro Takayama. Superweakly-interacting massive particles. *Phys. Rev. Lett.*, 91:011302, 2003.

[47] Ya B Zeldovich. Survey of modern cosmology. In *Advances in astronomy and astrophysics*, volume 3, pages 241--379. Elsevier, 1965.

[48] Gary Steigman. Cosmology confronts particle physics. *Annual Review of Nuclear and Particle Science*, 29(1):313--338, 1979.

[49] Gary Steigman, Basudeb Dasgupta, and John F Beacom. Precise relic wimp abundance and its impact on searches for dark matter annihilation. *Physical Review D*, 86(2):023506, 2012.

[50] Rouven Essig, John A Jaros, William Wester, et al. Dark sectors and new, light, weakly-coupled particles. *arXiv preprint arXiv:1311.0029*, 2013.

[51] M Kachelriess, OE Kalashev, and M Yu Kuznetsov. Heavy decaying dark matter and icecube high energy neutrinos. *Physical Review D*, 98(8):083016, 2018.

[52] Nicolao Fornengo, L Maccione, and Andrea Vittino. Constraints on particle dark matter from cosmic-ray antiprotons. *Journal of Cosmology and Astroparticle Physics*, 2014(04):003, 2014.

[53] Patrick J Fox, Roni Harnik, Joachim Kopp, and Yuhsin Tsai. Missing energy signatures of dark matter at the lhc. *Physical Review D*, 85(5):056011, 2012.

[54] M. C. Smith, G. R. Ruchti, A. Helmi, et al. The RAVE Survey: Constraining the Local Galactic Escape Speed. *Mon. Not. Roy. Astron. Soc.*, 379:755--772, 2007.

[55] Richard W Schnee. Introduction to dark matter experiments. In *Physics of the Large and the Small: TASI 2009*, pages 775--829. World Scientific, 2011.

[56] J. D. Lewin and P. F. Smith. Review of mathematics, numerical factors, and corrections for dark matter experiments based on elastic nuclear recoil. *Astropart. Phys.*, 6:87--112, 1996.

[57] J Engel. Nuclear form factors for the scattering of weakly interacting massive particles. *Physics Letters B*, 264(1-2):114--119, 1991.

[58] F Donato, N Fornengo, and S Scopel. Effects of galactic dark halo rotation on wimp direct detection. *Astroparticle Physics*, 9(3):247--260, 1998.

[59] SuperCDMS Collaboration, R. Agnese, A. J. Anderson, et al. Low-Mass Dark Matter Search with CDMSlite. *arXiv e-prints*, page arXiv:1707.01632, Jul 2017.

[60] A Liam Fitzpatrick, Wick Haxton, Emanuel Katz, Nicholas Lubbers, and Yiming Xu. Model independent direct detection analyses. *arXiv preprint arXiv:1211.2818*, 2012.

[61] A. Liam Fitzpatrick, Wick Haxton, Emanuel Katz, Nicholas Lubbers, and Yiming Xu. The effective field theory of dark matter direct detection. *Journal of Cosmology and Astroparticle Physics*, 2013(02):004--004, feb 2013.

[62] Nikhil Anand, A Liam Fitzpatrick, and WC Haxton. Model-independent wimp scattering responses and event rates: a mathematica package for experimental analysis. *arXiv preprint arXiv:1308.6288*, 2013.

[63] Nikhil Anand, A Liam Fitzpatrick, and WC Haxton. Model-independent analyses of dark-matter particle interactions. *Physics Procedia*, 61:97--106, 2015.

[64] K. Schneck, B. Cabrera, D. G. Cerdeño, et al. Dark matter effective field theory scattering in direct detection experiments. *Phys. Rev. D*, 91(9):092004, May 2015.

[65] J. Engel and P. Vogel. Spin-dependent cross sections of weakly interacting massive particles on nuclei. *Phys. Rev. D*, 40(9):3132--3135, Nov 1989.

[66] D. S. Akerib, M. S. Armel-Funkhouser, M. J. Attisha, et al. Limits on spin-dependent WIMP-nucleon interactions from the Cryogenic Dark Matter Search. *Phys. Rev. D*, 73(1):011102/1--5, January 2006.

[67] R. Bunker. *A Low-threshold Analysis of Data from the Cryogenic Dark Matter Search Experiment*. PhD thesis, University of California, Santa Barbara, December 2011.

[68] Marcello Messina. Status of direct search of wimp dark matter. *PoS*, page 080, 2017.

[69] Elena Aprile and Laura Baudis. *Liquid noble gases*, chapter 21, pages 413--436. Cambridge University Press, Cambridge, UK, 2010.

[70] Marc Schumann. Dark matter search with liquid noble gases. *arXiv preprint arXiv:1206.2169*, 2012.

[71] D.P. Snowden-Ifft, C.J. Martoff, and J.M. Burwell. Low Pressure Negative Ion Drift Chamber for Dark Matter Search. *Phys. Rev. D*, 61:101301/1--5, 2000.

[72] S. Burgos et al. First results from the DRIFT-IIa dark matter detector. *Astropart. Phys.*, 28:409--421, 2007.

[73] Q Arnaud, D Asner, J-P Bard, et al. First results from the news-g direct dark matter search experiment at the lsm. *Astroparticle Physics*, 97:54--62, 2018.

[74] R. Agnese, A. J. Anderson, T. Aramaki, et al. Projected Sensitivity of the SuperCDMS SNOLAB experiment. *Phys. Rev.*, D95(8):082002, 2017.

[75] R Agnese, T Aralis, T Aramaki, et al. First dark matter constraints from a supercdms single-charge sensitive detector. *Physical review letters*, 121(5):051301, 2018.

[76] S. A. Hertel. *Advancing the Search for Dark Matter: from CDMS II to SuperCDMS*. PhD thesis, Massachusetts Institute of Technology, 2012.

[77] N. Kurinsky. *The Low-Mass Limit: Dark Matter Detectors With Ev-Scale Energy Resolution*. PhD thesis, Stanford University, August, 2018.

[78] S. A. Hertel, M. Pyle, and for the SuperCDMS Collaboration. Phonon Pulse Shape Discrimination in SuperCDMS Soudan. *ArXiv e-prints*, September 2011.

[79] L. Bond, J. I. Collar, J. Ely, et al. Development of bubble chambers with sensitivity to WIMPs. *New Astron. Rev.*, 49:271--275, May 2005.

[80] W. J. Bolte, J. I. Collar, M. Crisler, et al. A bubble chamber for dark matter detection (the COUPP project status). *J. Phys. Conf. Ser.*, 39:126--128, May 2006.

[81] E. Behnke, J. I. Collar, P. S. Cooper, et al. Improved Spin-Dependent WIMP Limits from a Bubble Chamber. *Science*, 319:933--936, 2008.

[82] C. Eric Dahl. COUPP progress report: results from the 4kg test chamber. at the 9th UCLA Symposium on Sources and Detection of Dark Matter and Dark Energy in the Universe, 2010. www.physics.ucla.edu/hep/dm10/talks/dahl.pdf.

[83] Frederick Seitz. On the theory of the bubble chamber. *The Physics of Fluids*, 1(1):2--13, 1958.

[84] A. E. Robinson. *Dark Matter Limits From A 2 L C3f8 Filled Bubble Chamber*. PhD thesis, University of Chicago, 2015.

[85] Danielle Speller. *A Background-Subtracted Search for Annual Modulation in CDMS II*. PhD thesis, UC Berkeley, 2017.

[86] Chris Kouvaris and Ian M Shoemaker. Daily modulation as a smoking gun of dark matter with significant stopping rate. *Physical Review D*, 90(9):095011, 2014.

[87] D. S. Akerib, S. Alsum, H. M. Araújo, et al. 3d modeling of electric fields in the lux detector. *Journal of Instrumentation*, 12(11):P11022, Nov 2017.

[88] R. Agnese, A. J. Anderson, D. Balakishiyeva, et al. Demonstration of surface electron rejection with interleaved germanium detectors for dark matter searches. *Applied Physics Letters*, 103(16):164105, October 2013.

[89] Z. Ahmed, D.S. Akerib, S. Arrenberg, et al. Dark Matter Search Results from the CDMS II Experiment. *Science*, 327(5973):1619--1621, 2010.

[90] GJ Davies, JD Davies, JD Lewin, PF Smith, and WG Jones. Liquid xenon as a dark matter detector. prospects for nuclear recoil discrimination by photon timing. *Physics Letters B*, 320(3-4):395--399, 1994.

[91] M. G. Boulay and A. Hime. Technique for direct detection of weakly interacting massive particles using scintillation time discrimination in liquid argon. *Astropart. Phys.*, 25:179--182, 2006.

[92] Eric W Hoppe, Allen Seifert, Craig E Aalseth, et al. Cleaning and passivation of copper surfaces to remove surface radioactivity and prevent oxide formation. *Nuclear Instruments and Methods in Physics Research Section A: Accelerators, Spectrometers, Detectors and Associated Equipment*, 579(1):486--489, 2007.

[93] CD Christofferson, N Abgrall, SI Alvis, et al. Contamination control and assay results for the majorana demonstrator ultra clean components. In *AIP Conference Proceedings*, volume 1921, page 060005. AIP Publishing, 2018.

[94] D Akimov, JB Albert, P An, et al. Observation of coherent elastic neutrino-nucleus scattering. *Science*, 357(6356):1123--1126, 2017.

[95] S Westerdale and Peter Daniel Meyers. Radiogenic neutron yield calculations for low-background experiments. *Nuclear Instruments and Methods in Physics Research Section A: Accelerators, Spectrometers, Detectors and Associated Equipment*, 875:57--64, 2017.

[96] G.A Wagner, G.M Reimer, B.S Carpenter, et al. The spontaneous fission rate of u-238 and fission track dating. *Geochimica et Cosmochimica Acta*, 39(9):1279 -- 1286, 1975.

[97] Jacob G. and Fantidis. The comparison between simple and advanced shielding materials for the shield of portable neutron sources. *International Journal of Radiation Research*, 13(4), 2015.

[98] B. J. Mount, S. Hans, R. Rosero, et al. LUX-ZEPLIN (LZ) Technical Design Report. *arXiv e-prints*, page arXiv:1703.09144, March 2017.

[99] Yu Chen. *High-energy Neutron Backgrounds for Underground Dark Matter Experiments*. PhD thesis, Syracuse University, 2017.

[100] D.-M. Mei and A. Hime. Muon-induced background study for underground laboratories. *Phys. Rev. D*, 73(5):053004--+, March 2006.

[101] Raul Hennings-Yeomans and D. S. Akerib. A Neutron Multiplicity Meter for Deep Underground Muon- Induced High Energy Neutron Measurements. *Nucl. Instrum. Meth.*, A574:89--97, 2007.

[102] E Armengaud, Q Arnaud, C Augier, et al. Measurement of the cosmogenic activation of germanium detectors in edelweiss-iii. *Astroparticle Physics*, 91:51--64, 2017.

[103] Georg Meierhofer. *Neutron capture on 76 Ge*. PhD thesis, University of Tubingen, 2010.

[104] Megha Bhike, B. Fallin, Krishichayan, and W. Tornow. Measurement of the neutron-capture cross section of 76ge and 74ge below 15 mev and its relevance to 0 decay searches of 76ge. *Physics Letters B*, 741:150 -- 154, 2015.

[105] Laura Baudis, Alexander Kish, Francesco Piastra, and Marc Schumann. Cosmogenic activation of xenon and copper. *The European Physical Journal C*, 75(10):485, 2015.

[106] SuperCDMS Collaboration. SuperCDMS Final Design Report.

[107] Rafael F Lang and Wolfgang Seidel. Search for dark matter with CRESST. *New Journal of Physics*, 11(10):105017, oct 2009.

[108] CRESST Collaboration, A. H. Abdelhameed, G. Angloher, et al. Geant4-based electromagnetic background model for the CRESST dark matter experiment. *arXiv e-prints*, page arXiv:1908.06755, Aug 2019.

[109] Aguilar-Arevalo, A. and Amidei, D. and Bertou, X. and Bole, D. and Butner, M. and Cancelo, G. and Castañeda Vázquez, A. and Chavarria, A. E. and de Mello Neto, J. R. T. and Dixon, S. and D'Olivo, J. C. and Estrada, J. and Fernandez Moroni, G. and Hernández Torres, K. P. and Izraelevitch, F. and Kavner, A. and Kilminster, B. and Lawson, I. and Liao, J. and López, M. and Molina, J. and Moreno-Granados, G. and Pena, J. and Privitera, P. and Sarkis, Y. and Scarpine, V. and Schwarz, T. and Sofo Haro, M. and Tiffenberg, J. and Torres Machado, D. and Trillaud, F. and You, X. and Zhou, J. Measurement of radioactive contamination in the high-resistivity silicon CCDs of the DAMIC experiment. *Journal of Instrumentation*, 10(08):P08014, 2015.

[110] G.C. Rich. Status and plans for the DAMIC Experiment at SNOLAB and Modane. `https://indico.cern.ch/event/699961/contributions/3043431/attachments/1694413/2726984/2018-07-27_G.C.Rich_damic.pdf`, 2018. IDM Conference.

[111] K. Abe, J. Hosaka, T. Iida, et al. Distillation of liquid xenon to remove krypton. *Astroparticle Physics*, 31:290--296, May 2009.

[112] S. Li, X. Chen, X. Cui, et al. Krypton and radon background in the PandaX-I dark matter experiment. *Journal of Instrumentation*, 12(02):T02002, 2017.

[113] P. Privitera. Damic: a novel experiment for low mass dark matter. `http://cosmo2014.uchicago.edu/depot/talk-privitera-paolo.pdf`, 2014. International Conference on Particle Physics and Cosmology (COSMO 2014).

[114] D. Lal, E. D. Goldberg, and M. Koide. Cosmic-ray-produced silicon-32 in nature. *Science*, 131(3397):332--337, 1960.

[115] D. Lal, J. R. Arnold, and M. Honda. Cosmic-Ray Production Rates of Be^{7} in Oxygen, and P^{32}, P^{33}, S^{35} in Argon at Mountain Altitudes. *Physical Review*, 118:1626--1632, June 1960.

[116] Manfred Lindner. New nuclides produced in chlorine spallation. *Science*, 91(3):642--643, Aug 1953.

[117] U. Morgenstern, R. Gellermann, D. Hebert, et al. 32si in limestone aquifers. *Chemical Geology*, 120(1):127 -- 134, 1995.

[118] U. Morgenstern, C. B. Taylor, Y. Parrat, H. W. Gaggeler, and B. Eichler. ^{32}Si in precipitation: evaluation of temporal and spatial variation and as dating tool for glacial ice. *Earth and Planetary Science Letters*, 144:289--296, October 1996.

[119] John L Orrell, Isaac J Arnquist, Mary Bliss, Raymond Bunker, and Zachary S Finch. Naturally occurring 32si and low-background silicon dark matter detectors. *Astroparticle Physics*, 99:9--20, 2018.

[120] Radomir Smida. The damic dark matter experiment: status and prospects, May 15 2019. CoSSURF 2019.

[121] Topsil website. `www.topsil.com/en.aspx`. Not secure.

[122] Vanessa Chisté, Marie-Martine Bé, and Christophe Dulieu. Evaluation of decay data of radium-226 and its daughters. In *International Conference on Nuclear Data for Science and Technology*, pages 77--80. EDP Sciences, 2007.

[123] Radium-226 decay chain. `https://www.nist.gov/image-23773`. Accessed: Jan. 17, 2019.

[124] G. Audi, O. Bersillon, J. Blachot, and A.H. Wapstra. The nubase evaluation of nuclear and decay properties. *Nuclear Physics A*, 729(1):3 -- 128, 2003. The 2003 NUBASE and Atomic Mass Evaluations.

[125] W. Hirst and G. E. Harrison. The Diffusion of Radon Gas Mixtures. *Proceedings of the Royal Society of London Series A*, 169:573--586, March 1939. https://royalsocietypublishing.org/doi/pdf/10.1098/rspa.1939.0016.

[126] Gerald L. Schroeder, Hobart W. Kraner, and Robley D. Evans. Diffusion of radon in several naturally occurring soil types. *Journal of Geophysical Research*, 70(2):471--474, 1965.

[127] International Atomic Energy Agency. *Measurement and Calculation of Radon Releases from NORM Residues*. Number 474 in Technical Reports Series. Vienna, 2013.

[128] M. Wojcik. Measurement of radon diffusion and solubility constants in membranes. *Nucl. Instrum. Meth. B*, 61:8--11, 1991.

[129] M Wjcik, W Wlazo, G Zuzel, and G Heusser. Radon diffusion through polymer membranes used in the solar neutrino experiment borexino. *Nuclear Instruments and Methods in Physics Research Section A: Accelerators, Spectrometers, Detectors and Associated Equipment*, 449(1):158 -- 171, 2000.

[130] S. J. Schowalter, C. B. Connolly, and J. M. Doyle. Permeability of Noble Gases through Kapton, Butyl, Nylon, and 'Silver Shield'. *Nucl. Instrum. Meth.*, A615:267--271, 2010.

[131] et al. F. Mamedov. Measurement of radon diffusion through shielding foils for the supernemo experiment. *Journal of Instrumentation*, 6(01):C01068, 2011.

[132] E.D. Hallman J. Bigu and L. Kendrick. Permeability of different materials to radon (^{222}Rn) gas. `https://sno.phy.queensu.ca/sno/str/SNO-STR-91-069.pdf`, Sudbury Neutrino Observatory Project Report SNO-STR-91-069. Elliot Lake Laboratory, November 1991.

[133] A. Piepke and K. Pushkin. Estimate of the EXO-200 radon production inside the TPC. Internal Memo, 2011. EXO Internal Memo.

[134] M. Jirnek and M. Kotrbat. Radon diffusion coefficients in 360 waterproof materials of different chemical composition. *Radiation Protection Dosimetry*, 148(2):274, 2012.

[135] M. Durcik and F. Havlik. Experimental study of radon and thoron diffusion through barriers, Dec 1995.

[136] K. Rovenska M. Jiranek and A. Fronka. Radon diffusion coefficient: a material property determining the applicability of waterproof membranes as radon barriers. In *Proceedings of the American Association of Radon Scientists and Technologists (AARST) : 2008*, International Radon Symposium, Las Vegas, NV, 2008.

[137] Grzegorz Zuzel. Highly sensitive measurements of 222rn diffusion and emanation. *AIP Conference Proceedings*, 785(1):142--149, 2005.

[138] Fadahat Mamedov, Ivan Štekl, and Karel Smolek. Measurement of the radon diffusion through a nylon foil for different air humidities. In *AIP Conference Proceedings*, volume 1672, page 140007. AIP Publishing, 2015.

[139] Lee H. Sur, B. and B.C. Robertson. Radon control options for the cavity liner. `https://sno.phy.queensu.ca/sno/str/SNO-STR-92-017.pdf`, Sudbury Neutrino Observatory Project Report SNO-STR-92-017. Apri 21, 1992.

[140] Matthew Stein, Dan Bauer, Ray Bunker, et al. Radon daughter plate-out measurements at SNOLAB for polyethylene and copper. *Nuclear Instruments and Methods in Physics Research Section A: Accelerators, Spectrometers, Detectors and Associated Equipment*, 880:92 -- 97, 2018.

[141] J. A. Formaggio and C. J. Martoff. Backgrounds to sensitive experiments underground. *Ann. Rev. Nucl. Part. Sci.*, 54:361--412, 2004.

[142] A. Hallin. Radon reduced laboratory. Unpublished; private communication.

[143] P. Pagelkopf and J. Porstendrfer. Neutralisation rate and the fraction of the positive 218po-clusters in air. *Atmospheric Environment*, 37(8):1057 -- 1064, 2003.

[144] J. Kiko. Detector for ^{222}Rn measurements in air at the 1 mBq/m^3 level. *Nuclear Instruments and Methods in Physics Research A*, 460:272--277, March 2001.

[145] M.L. Maiello and N.H. Harley. Determining the charged fractions of 218po and 214pb using an environmental gamma-ray and rn detector. `https://www.ncbi.nlm.nih.gov/pubmed/2745097`, Jul, 1989. Environmental Measurements Laboratory, U.S. Department of Energy, New York, NY. PMID: 2745097.

[146] E. S. Morrison, T. Frels, E. H. Miller, R. W. Schnee, and J. Street. Radon daughter plate-out onto teflon. *AIP Conference Proceedings*, 1921(1):090002, 2018.

[147] AlphaLab Inc. The TriboElectric Series. https://www.trifield.com/content/tribo-electric-series/, 2009. Accessed: 2019-05-16.

[148] H. Simgen. Radon assay and purification techniques. In L. Miramonti and L. Pandola, editors, *American Institute of Physics Conference Series*, volume 1549 of *American Institute of Physics Conference Series*, pages 102--107, August 2013.

[149] Yue Meng, Jerry Busenitz, and Andreas Piepke. A new method for evaluating the effectiveness of plastic packaging against radon penetration. *Applied Radiation and Isotopes*, 156:108963, 2020.

[150] Adam Jonathan Anderson. *A search for light weakly-interacting massive particles with SuperCDMS and applications to neutrino physics.* PhD thesis, Massachusetts Institute of Technology, 2015.

[151] D. Barker. *SuperCDMS Background Models for Low-Mass Dark Matter Searches*. PhD thesis, University of Minnesota, 2018.

[152] Katayun Kamdin. First evidence for radon daughter mobility in liquid xenon. `https://indico.cern.ch/event/699961/contributions/3043385/attachments/1694116/2726418/IDM2018_Radon_kkamdin.pdf`, 2018. IDM Conference.

[153] Alissa Erin Monte. Alpha radiation studies and related backgrounds in the darkside-50 detector. Technical report, Fermi National Accelerator Lab.(FNAL), Batavia, IL (United States), 2018.

[154] P. Agnes, I. F. M. Albuquerque, T. Alexander, et al. Measurement of the ion fraction and mobility of ^{218}Po produced in ^{222}Rn decays in liquid argon. *Journal of Instrumentation*, 14(11):P11018--P11018, Nov 2019.

[155] A. Bradley, D. Akerib, H. M. Araújojo, et al. Radon-related backgrounds in the LUX dark matter search. *Physics Procedia*, 61:658--665, 2015.

[156] D. S. Akerib et al. Radiogenic and Muon-Induced Backgrounds in the LUX Dark Matter Detector. *Astropart. Phys.*, 62:33--46, 2015.

[157] A. W. Bradley. *LUX thermosyphon cryogenics and radon-related backgrounds for the first wimp result*. PhD thesis, Case Western Reserve University, 2014.

[158] N. Chott. Status of the lz experiment. `https://meetings.undergroundphysics.org/indico/getFile.py/access?contribId=49&sessionId=16&resId=0&materialId=slides&confId=2`, May 16, 2019. CoSSURF 2019.

[159] G. Zuzel and H. Simgen. High sensitivity radon emanation measurements. *Applied Radiation and Isotopes*, 67:889--893, 2009.

[160] W. Rau and G. Heusser. 222Rn emanation measurements at extremely low activities. *Applied Radiation and Isotopes*, 53:371--375, 2000.

[161] M. Liu, H. W. Lee, and A. B. McDonald. ^{222}Rn emanation into vacuum. *Nuclear Instruments and Methods in Physics Research A*, 329:291--298, May 1993.

[162] C. Cerna, B. Soule, and F. Perrot. Radon emanation based material measurement and selection for the supernemo double beta experiment. *AIP Conference Proceedings*, 1672(1):050002, 2015.

[163] I. Blevis, J. Boger, E. Bonvin, et al. Measurement of ^{222}Rn dissolved in water at the Sudbury Neutrino Observatory. *Nuclear Instruments and Methods in Physics Research A*, 517:139--153, January 2004.

[164] H. Simgen. Radon and radium assay of water for real-time solar neutrino experiments. *Progress in Particle and Nuclear Physics*, 48(1):25 -- 26, 2002.

[165] Xin Ran Liu. Ultra-low level radon assays in gases. *AIP Conference Proceedings*, 1672(1):070002, 2015.

[166] S Grhardt, J Bonn, L Bornschein, et al. Impact of a cryogenic baffle system on the suppression of radon-induced background in the katrin pre-spectrometer. *Journal of Instrumentation*, 13:T10004--T10004, 10 2018.

[167] Pattavina L. Radon-induced surface contaminations in neutrinoless double beta decay and dark matter experiments. Master's thesis, Universit Claude Bernard - Lyon I; Universita degli Studi di Milano - Bicocca, 2011. https://tel.archives-ouvertes.fr/tel-00640789/document.

[168] EH Miller, J Busenitz, TK Edberg, et al. Constraining radon backgrounds in lz. In *AIP Conference Proceedings*, volume 1921, page 050003. AIP Publishing, 2018.

[169] N. Rupp. Radon background in liquid xenon detectors. *Journal of Instrumentation*, 13:C02001, February 2018.

[170] E. H. Miller, J. Busenitz, T. K. Edberg, et al. Constraining radon backgrounds in LZ. volume 1921 of *American Institute of Physics Conference Series*, page 050003, January 2018.

[171] K. Pushkin, C. Akerlof, D. Anbajagane, et al. Study of radon reduction in gases for rare event search experiments. *Nuclear Instruments and Methods in Physics Research A*, 903:267--276, September 2018.

[172] S. Lindemann. *Intrinsic ^{85}Kr and ^{222}Rn Backgrounds in the XENON Dark Matter Search.* PhD thesis, Heidelberg University, 2013.

[173] Aprile, E., Aalbers, J., Agostini, F., et al. Intrinsic backgrounds from rn and kr in the xenon100 experiment. *Eur. Phys. J. C*, 78(2):132, 2018.

[174] K. Abe, K. Hieda, K. Hiraide, et al. Radon removal from gaseous xenon with activated charcoal. *Nuclear Instruments and Methods in Physics Research A*, 661:50--57, January 2012.

[175] D. Jardin and R. Schnee. Construction, Testing, and Analysis of Radon Mitigation System. In *APS Division of Nuclear Physics Meeting Abstracts*, October 2011.

[176] J. Street, R. Bunker, C. Dunagan, et al. Construction and Measurements of an Improved Vacuum-Swing-Adsorption Radon-Mitigation System. In J. L. Orrell, editor, *Topical Workshop on Low Radioactivity Techniques: LRT 2015*, American Institute of Physics Conference Series, June 2015.

[177] J. Street, R. Bunker, C. Dunagan, et al. Construction and measurements of an improved vacuum-swing-adsorption radon-mitigation system. In *American Institute of Physics Conference Series*, volume 1672 of *American Institute of Physics Conference Series*, page 150004, August 2015.

[178] J. Street, R. Bunker, E. H. Miller, et al. Radon mitigation for the SuperCDMS SNOLAB dark matter experiment. 1921:050002, January 2018.

[179] G. Benato et al. Radon mitigation during the installation of the cuore-0 decay detector. *Journal of Instrumentation*, 13(01):P01010, 2018.

[180] C. Arpesella, H. O. Back, M. Balata, et al. Measurements of extremely low radioactivity levels in BOREXINO. *Astroparticle Physics*, 18:1--25, August 2002.

[181] G. Heusser, W Rau, B. Freudiger, et al. 222Rn detection at the $\mu Bq/m^3$ range in nitrogen gas and a new Rn purification technique for liquid nitrogen. *Applied Radiation and Isotopes*, 52:691--695, 2000. https://www.mpi-hd.mpg.de/biblio/preprints/2000:031.pdf.

[182] G. Zuzel. Experience of gas purification and radon control in borexino. *AIP Conference Proceedings*, 1921(1):050001, 2018.

[183] J. Golightly. *Characterization of a carbon radon filter, and Radon detection.* PhD thesis, Queens University, 2008.

[184] Yuuki Nakano and Super-Kamiokande Collaboration. Radon background study in super-kamiokande. *Journal of Physics: Conference Series*, 888(1):012191, 2017.

[185] Y. Nakano, H. Sekiya, S. Tasaka, et al. Measurement of radon concentration in super-kamiokandes buffer gas. *Nuclear Instruments and Methods in Physics Research Section A: Accelerators, Spectrometers, Detectors and Associated Equipment*, 867:108 -- 114, 2017.

[186] J. B. Albert et al. Investigation of radioactivity-induced backgrounds in exo-200. *Phys. Rev. C*, 92:015503, Jul 2015.

[187] R. W. Schnee, R. Bunker, G. Ghulam, et al. *Construction and measurements of a vacuum-swing-adsorption radon-mitigation system*, volume 1549 of *American Institute of Physics Conference Series*. August 2013.

[188] A. Pocar. *Low Background Techniques and Experimental Challenges for Borexino and its Nylon Vessels*. PhD thesis, Princeton University, 2003.

[189] H. Diamond and J.E. Gindler. Alpha half-lives of 216-Po, 217-At and 218-Rn. *Journal of Inorganic and Nuclear Chemistry*, 25(2):143 -- 149, 1963.

[190] E. Figueroa-Feliciano for the CDMS Collaboration. Towards Direct Detection of WIMPs with the Cryogenic Dark Matter Search. In *SUSY09: 7th International Conference on Supersymmetry and the Unification of Fundamental Interactions*, volume 1200, pages 959--962, Boston, Massachusetts, 2010. American Institute of Physics Conference Proceedings.

[191] P. Bernardini, G. Fogli, E. Lisi, and C.J. Jillings. Proceedings of the neutrino oscillation workshop the science program at snolab. *Nuclear Physics B - Proceedings Supplements*, 188:130 -- 132, 2009.

[192] P. Cushman. Exploring low mass dark matter in SuperCDMS, 2019. April APS Meeting.

[193] N. Mirabolfathi, J. P. Filippini, V. Mandic, et al. Detector commissioning for the CDMS-II final run at the Soudan Underground Laboratory. *Nucl. Instrum. Meth.*, A559:417--419, 2006.

[194] R. Agnese, A. J. Anderson, M. Asai, et al. Improved WIMP-search reach of the CDMS II germanium data. *Phys. Rev. D*, 92:072003, Oct 2015.

[195] M. Pyle, B. Serfass, P. L. Brink, et al. Surface Electron Rejection from Ge Detector with Interleaved Charge and Phonon Channels. In B. Young, B. Cabrera, & A. Miller, editor, *American Institute of Physics Conference Series*, volume 1185 of *American Institute of Physics Conference Series*, pages 223--226, December 2009.

[196] Matthew Hollister, D A Bauer, Ram Dhuley, et al. The cryogenics design of the SuperCDMS SNOLAB experiment. *IOP Conference Series: Materials Science and Engineering*, 278:012118, 12 2017.

[197] M. Pyle. *Optimizing the Design and Analysis of Cryogenic Semiconductor Dark Matter Detectors for Maximum Sensitivity.* PhD thesis, Stanford University, 2012.

[198] R. Agnese, A. J. Anderson, D. Balakishiyeva, et al. Maximum likelihood analysis of low energy CDMS II germanium data. *Phys. Rev. D*, 91:052021, Mar 2015.

[199] R. Agnese, A. J. Anderson, M. Asai, et al. Search for low-mass weakly interacting massive particles using voltage-assisted calorimetric ionization detection in the supercdms experiment. *Phys. Rev. Lett.*, 112:041302, Jan 2014.

[200] R. Agnese, A. J. Anderson, T. Aramaki, et al. New results from the search for low-mass weakly interacting massive particles with the cdms low ionization threshold experiment. *Phys. Rev. Lett.*, 116:071301, Feb 2016.

[201] Kent D Irwin and Gene C Hilton. Transition-edge sensors. In *Cryogenic particle detection*, pages 63--150. Springer, 2005.

[202] J. J. Yen, B. Shank, B. A. Young, et al. Measurement of quasiparticle transport in aluminum films using tungsten transition-edge sensors. *Applied Physics Letters*, 105(16):163504, 2014.

[203] J. Yen. *Phonon Sensor Dynamics For Cryogenic Dark Matter Search Experiment.* PhD thesis, Stanford University, 2015.

[204] V. S. Vavilov. Radiation ionization processes in germanium and silicon crystals. *Soviet Physics Uspekhi*, 4(5):761--769, May 1962.

[205] F. Scholze, H. Rabus, and G. Ulm. Measurement of the mean electronhole pair creation energy in crystalline silicon for photons in the 501500 ev spectral range. *Applied Physics Letters*, 69(20):2974--2976, 1996.

[206] Z. He. Review of the Shockley-Ramo theorem and its application in semiconductor gamma-ray detectors. *Nuclear Instruments and Methods in Physics Research A*, 463:250--267, May 2001.

[207] Glenn F Knoll. *Radiation detection and measurement; 4th ed.* Wiley, New York, NY, 2010.

[208] B. S. Neganov and V. N. Trofimov. Colorimetric method measuring ionizing radiation. *Otkryt. Izobret.*, 146:215, 1985.

[209] P. N. Luke. *J. App. Phys.*, 64:6858--6860, 1988.

[210] B. S. Neganov and V. N. Trofimov. *JETP Letters*, 28:328--329, 1978.

[211] EDELWEISS Collaboration, A. Broniatowski, X. Defay, et al. A new high-background-rejection dark matter Ge cryogenic detector. *Physics Letters B*, 681:305--309, November 2009.

[212] Ritoban Basu Thakur. *The Cryogenic Dark Matter Search Low Ionization-threshold Experiment.* PhD thesis, University of Illinois at Urbana-Champaign, 2015.

[213] P.N. Luke, J. Beeman, F.S. Goulding, S.E. Labov, and E.H. Silver. Calorimetric ionization detector. *Nuclear Instruments and Methods in Physics Research Section A: Accelerators, Spectrometers, Detectors and Associated Equipment*, 289(3):406 -- 409, 1990.

[214] Louis E Strigari. Neutrino coherent scattering rates at direct dark matter detectors. *New Journal of Physics*, 11(10):105011, 2009.

[215] John N Bahcall, Aldo M Serenelli, and Sarbani Basu. New solar opacities, abundances, helioseismology, and neutrino fluxes. *The Astrophysical Journal Letters*, 621(1):L85, 2005.

[216] D Z Freedman, D N Schramm, and D L Tubbs. The weak neutral current and its effects in stellar collapse. *Annual Review of Nuclear Science*, 27(1):167--207, 1977.

[217] S. Yellin. Finding an upper limit in the presence of an unknown background. *Phys. Rev. D*, 66(3):032005, Aug 2002.

[218] S Yellin. Extending the optimum interval method. *arXiv:0709.2701*, 2007.

[219] Bento A. Bucci C. et al. Angloher, G. Results on light dark matter particles with a low-threshold CRESST-II detector. *Eur. Phys. J. C*, 2016.

[220] D. S. Akerib, H. M. Araújo, X. Bai, et al. Improved limits on scattering of weakly interacting massive particles from reanalysis of 2013 lux data. *Phys. Rev. Lett.*, 116:161301, Apr 2016.

[221] F. Ruppin, J. Billard, E. Figueroa-Feliciano, and L. Strigari. Complementarity of dark matter detectors in light of the neutrino background. *Phys. Rev. D*, 90:083510, Oct 2014.

[222] D. S. Akerib, M. J. Attisha, L. Baudis, et al. Low-threshold analysis of CDMS shallow-site data. *Phys. Rev. D*, 82:122004, Dec 2010.

[223] S. Fallows. *Measurement of Nuclear Recoils in the CDMS II Dark Matter Search*. PhD thesis, University of Minnesota, 2014.

[224] R. Bernabei, P. Belli, F. Cappella, et al. New results from DAMA/LIBRA. *Eur. Phys. J.*, C67:39--49, 2010.

[225] C. E. Aalseth, P. S. Barbeau, N. S. Bowden, et al. Results from a search for light-mass dark matter with a p-type point contact germanium detector. *Phys. Rev. Lett.*, 106:131301, Mar 2011.

[226] G. Angloher, M. Bauer, I. Bavykina, et al. Results from 730 kg days of the CRESST-II Dark Matter search. *European Physical Journal C*, 72:1971, April 2012.

[227] R. Agnese, Z. Ahmed, A. J. Anderson, et al. Silicon detector dark matter results from the final exposure of CDMS II. *Phys. Rev. Lett.*, 111:251301, Dec 2013.

[228] K. A. McCarthy. *Detector Simulation and WIMP Search Analysis for the Cryogenic Dark Matter Search Experiment*. PhD thesis, Massachusetts Institute of Technology, 2013.

[229] D. Moore. *A Search for Low-Mass Dark Matter with the Cryogenic Dark Matter Search and the Development of Highly Multiplexed Phonon-Mediated Particle Detectors*. PhD thesis, California Institute of Technology, 2012.

[230] M. A. Bowles. Implications on silicon ionization yield from nuclear recoil energy scaling. `http://titus.stanford.edu/cdms_restricted/Soudan/R125-128/ebook/NR_escale_notes_MB/17_04_23/`, 2017. "CDMS Internal Note NR-18 Note".

[231] D. Moore. Constraints on nr energy scale from ionization yield. `http://titus.stanford.edu/cdms_restricted/Soudan/R125-128/ebook/101220/`, 2010. "CDMS Internal Note c58 note 199".

[232] A. E. Chavarria, J. I. Collar, J. R. Peña, et al. Measurement of the ionization produced by sub-keV silicon nuclear recoils in a CCD dark matter detector. *Phys. Rev. D*, 94:082007, Oct 2016.

[233] F. Izraelevitch, D. Amidei, A. Aprahamian, et al. A measurement of the ionization efficiency of nuclear recoils in silicon. *JINST*, 12(06):P06014, 2017.

[234] D Speller, SuperCDMS Collaboration, et al. Dark matter direct detection with supercdms soudan. In *Journal of Physics: Conference Series*, volume 606, page 012003. IOP Publishing, 2015.

[235] D. S. Akerib, P. D. Barnes, Jr., P. L. Brink, et al. Design and performance of a modular low-radioactivity readout system for cryogenic detectors in the CDMS experiment. *Nuclear Instruments and Methods in Physics Research A*, 591:476--489, July 2008.

[236] R.W. Ogburn. *A Search for Particle Dark Matter Using Cryogenic Germanium and Silicon Detectors in the One- and Two-Tower Runs of CDMS-II at Soudan.* PhD thesis, Stanford University, 2008.

[237] A. J. Anderson, S. W. Leman, M. Pyle, et al. Simulations of Noise in Phase-Separated Transition-Edge Sensors for SuperCDMS. *J. Low Temp. Phys.*, 167(3):135--140, 2012.

[238] S. W. Leman. Invited Review Article: Physics and Monte Carlo techniques as relevant to cryogenic, phonon, and ionization readout of Cryogenic Dark Matter Search radiation detectors. *Review of Scientific Instruments*, 83(9):091101--091101, September 2012.

[239] S. R. Golwala. *Exclusion Limits on the WIMP-Nucleon Elastic-Scattering Cross Section from the Cryogenic Dark Matter Search.* PhD thesis, University of California, Berkeley, 2000.

[240] Z. Ahmed. *A dark-matter search using the final CDMS II dataset and a novel detector of surface radiocontamination.* PhD thesis, California Institute of Technology, 2012.

[241] Alan E. Robinson. New libraries for simulating neutron scattering in dark matter detector calibrations. *Phys. Rev.*, C89(3):032801, 2014.

[242] A. E. Robinson. The effect of mis-modelling anisotropic scattering on simulations of neutron recoils from silicon. `http://titus.stanford.edu/cdms_restricted/Soudan/R125-128/ebook/170713/si_dxs_ebook.html`, 2017. "CDMS Internal Note".

[243] Z. Ahmed, D. S. Akerib, S. Arrenberg, et al. Results from a Low-Energy Analysis of the CDMS II Germanium Data. *Physical Review Letters*, 106(13):131302--+, April 2011.

[244] Keiichi Shibata, Osamu IWAMOTO, Tsuneo NAKAGAWA, et al. Jendl-4.0: A new library for nuclear science and engineering. *Journal of Nuclear Science and Technology*, 48(1):1--30, 2011.

[245] J. P. Filippini. *A Search for WIMP Dark Matter Using the First Five-Tower Run of the Cryogenic Dark Matter Search,.* PhD thesis, University of California, Berkeley, 2008.

[246] S. Fallows. CDMS II 5-tower nuclear recoil energy scale, monte carlo chi-squared analysis: Si detectors. `http://titus.stanford.edu/cdms_restricted/Soudan/R125-128/ebook/130402/`, 2013. "CDMS Internal Note NR-13 Note".

[247] J. Lindhard, V. Nielsen, M. Scharff, and P. V. Thomsen. *Mat. Fys. Medd. K. Dan. Vidensk. Selsk.*, 33:10, 1963.

[248] P. Zecher, D. Wang, J. Rapaport, C. J. Martoff, and B. A. Young. Energy deposition of energetic silicon atoms within a silicon lattice. *Phys. Rev. A*, 41:4058--4061, Apr 1990.

[249] G. Gerbier, E. Lesquoy, J. Rich, et al. Measurement of the ionization of slow silicon nuclei in silicon for the calibration of a silicon dark-matter detector. *Phys. Rev. D*, 42:3211--3214, Nov 1990.

[250] Brian L. Dougherty. Measurements of ionization produced in silicon crystals by low-energy silicon atoms. *Phys. Rev. A*, 45:2104--2107, Feb 1992.

[251] Javier Tiffenberg. Results from the antonella experiment. `https://kicp-workshops.uchicago.edu/2015-lowecal/depot/talk-tiffenberg-javier.pdf`, Sept. 24 2015. KICP 2015.

[252] A. R. Sattler. Ionization produced by energetic silicon atoms within a silicon lattice. *Phys. Rev.*, 138:A1815--A1821, Jun 1965.

[253] A. Chavarria. private communication, 2016.

[254] J. Crank. *The mathematics of diffusion*. Clarendon Press Oxford [England], 2nd ed. edition, 1975.

[255] R. M. Barrer. Diffusion in and through solids. *The Journal of Physical Chemistry*, 46(4):533--534, 1942.

[256] Vern Child Rogers, RF Overmyer, KM Putzig, et al. Characterization of uranium tailings cover materials for radon flux reduction. Technical report, Argonne National Lab., 1980.

[257] E. A. Lepel, W. B. Silker, V. W. Thomas, and D. R. Kalkwarf. Comparison of field-measured radon diffusion coefficients with laboratory-measured coefficients. Technical report, United States, May 24, 1983. NUREG/CR--2769.

[258] G Keller and B Hoffmann. The radon diffusion length as a criterion for the radon tightness. In *IRPA10 conference proceedings, Hiroshima*, 2000.

[259] D. Grant, A. Hallin, S. Hanchurak, et al. Low Radon Cleanroom at the University of Alberta. In R. Ford, editor, *American Institute of Physics Conference Series*, volume 1338 of *American Institute of Physics Conference Series*, pages 161--163, April 2011.

[260] Marcin Wójcik and Grzegorz Zuzel. Radon permeability through nylon at various humidities used in the borexino experiment. *Nuclear Instruments and Methods in Physics Research Section A: Accelerators, Spectrometers, Detectors and Associated Equipment*, 524(1-3):355--365, 2004.

[261] Lemer pax. `https://www.lemerpax.com/en/`. Accessed: Jun. 4, 2016.

[262] A Malki, N Lavi, M Moinester, et al. Measurement of radon diffusion length in thin membranes. *Radiation protection dosimetry*, 150(4):434--440, 2012.

[263] KH Folkerts, G Keller, and H Muth. An experimental study on diffusion and exhalation of 222rn and 220rn from building materials. *Radiation Protection Dosimetry*, 9(1):27--34, 1984.

[264] P. V. Danckwerts. Absorption by simultaneous diffusion and chemical reaction. *Trans. Faraday Soc.*, 46:300--304, 1950. `http://dx.doi.org/10.1039/TF9504600300`.

[265] Andreas Maier, Uli Weber, Jannis Dickmann, et al. Method for measurement of radon diffusion and solubility in solid materials. *Nuclear Instruments and Methods in Physics Research Section B: Beam Interactions with Materials and Atoms*, 416:119 -- 127, 2018.

[266] Xuan QuangáNguyen, Quang TrongáNguyen, et al. Methods for the determination of transport parameters of gases in membranes. *Journal of the Chemical Society, Faraday Transactions*, 88(24):3553--3560, 1992.

[267] Durridge RAD7 website. https://durridge.com/products/rad7-radon-detector/. Accessed: Feb. 4, 2019.

[268] W. H. Press, S. A. Teukolsky, W. T. Vetterling, and B. P. Flannery. *Numerical Recipes in C: The Art of Scientific Computing*. Cambridge University Press, Cambridge, 1992.

[269] Zip-a-way removable sealant. https://www.reddevil.com/index.php?l=product_detail&p=920. SKU: 0606, Accessed: Apr. 8, 2019.

[270] E. Bellotti, C. Broggini, G. Di Carlo, M. Laubenstein, and R. Menegazzo. Precise measurement of the 222rn half-life: A probe to monitor the stability of radioactivity. *Physics Letters B*, 743:526 -- 530, 2015.

[271] Jin Wang, Oliver Meisenberg, Yongheng Chen, Erwin Karg, and Jochen Tschiersch. Mitigation of radon and thoron decay products by filtration. *Science of The Total Environment*, 409(19):3613--3619, 2011.

[272] A. Pocar. Low background techniques for the Borexino nylon vessels. In B. Cleveland, R. Ford, and M. Chen, editors, *Topical Workshop on Low Radioactivity Techniques: LRT 2004.*, volume 785 of *American Institute of Physics Conference Series*, pages 153--162, September 2005.

[273] M. Wojcik. Behavior of the 222Rn daughters on copper surfaces during cleaning. In P. Loaiza, editor, *AIP Conf. Proc. 897: Topical Workshop on Low Radioactivity Techniques: LRT 2006*, pages 53--58, Melville, NY, October 2007. American Institute of Physics.

[274] G. Zuzel and M. Wójcik. Removal of the long-lived ^{222}Rn daughters from copper and stainless steel surfaces. *Nuclear Instruments and Methods in Physics Research A*, 676:140--148, June 2012.

[275] R. W. Schnee, M. A. Bowles, R. Bunker, et al. Removal of long-lived 222Rn daughters by electropolishing thin layers of stainless steel. https://arxiv.org/pdf/1404.5843.pdf, August 2013.

[276] Kurt j. lesker company: Basic Outgassing Concepts. https://www.lesker.com/newweb/technical_info/vacuumtech/outgas_00_basicconcept.cfm. Accessed: Jan. 17, 2019.

[277] John F. O'Hanlon. *A User's Guide to Vacuum Technology*. 01 1980.

[278] Swagelok company. https://www.swagelok.com/en. Accessed: Feb. 8, 2018.

[279] J. B. R. Battat, J. Brack, E. Daw, et al. Radon in the DRIFT-II directional dark matter TPC: emanation, detection and mitigation. *Journal of Instrumentation*, 9:P11004, November 2014.

[280] M. Liu. Radon emanation into vacuum, MSc Thesis, 1991.

[281] A.P. ET AL Yallin. Summary of radon measurements on urethane o-rings. https://sno.phy.queensu.ca/sno/str/SNO-STR-93-027.pdf, Sudbury Neutrino Observatory Project Report SNO-STR-93-027. June 1993.

[282] Lee H. Fallas I.and MacDonald A. Liu, M.Q. Radon emanation from stainless steel. https://sno.phy.queensu.ca/sno/str/SNO-STR-90-075.pdf, Sudbury Neutrino Observatory Project Report SNO-STR-90-075. June 17, 1990.

[283] J. F. Ziegler, M. D. Ziegler, and J. P. Biersack. SRIM - The stopping and range of ions in matter (2010). *Nuclear Instruments and Methods in Physics Research B*, 268:1818--1823, June 2010.

[284] Uline kimtech low-lint wipers. https://www.uline.com/BL_6957/Kimtech-Low-Lint-Wipers. Accessed: Jan. 16, 2019.

[285] Berkshire cleanroom supplies. https://www.berkshire.com/shop/lint-free-clean-room-wipes.html. Accessed: 2019-01-16.

[286] R. A. Smith. Packaging materials outgassing study final report. https://www.osti.gov/servlets/purl/1340589, September 26, 2006. Y-12 National Security Complex Oak Ridge for the U. S. Department Of Energy.

[287] Agilent high and ultra-high vacuum for science research seminar handbook. https://www.agilent.com/cs/library/training/Public/UHV_Seminar_Handbook.pdf. Accessed: Apr. 18, 2019.

[288] Karl Jousten. Thermal outgassing. Nov. 1999. https://cds.cern.ch/record/455558/files/p111.pdf.

[289] Vacuum technology seminar by varian (now a part of agilent). Accessed: Apr. 18, 2019, https://www.agilent.com/cs/library/training/Public/UHV_Seminar_Handbook.pdf.

[290] Sean R. Koebley, Ronald A. Outlaw, and Randy R. Dellwo. Degassing a vacuum system with in-situ uv radiation. *Journal of Vacuum Science & Technology A*, 30(6):060601, 2012.

[291] Swagelok. *VCR FITTINGS Metal Gasket Face Seal Fittings*. MS-01-24, RevQ, May 2018.

[292] Bolt tightening sequence for flanges using 24 bolts. https://www.woodcousa.com/24-bolt-sequence.htm. Accessed: Jan 21, 2019.

[293] Pfeiffer vacuum website: Multipurpose. https://www.pfeiffer-vacuum.com/en/products/leak-detection/leak-detectors/multipurpose/. Pfeiffer Vacuum Inc., Accessed: July 18, 2015.

[294] JE Lennard-Jones. Processes of adsorption and diffusion on solid surfaces. *Transactions of the Faraday Society*, 28:333--359, 1932.

[295] K. P. Strong and D. M. Levins. Dynamic adsorption of radon on activated carbon. pages 627--639, United States, 1979. CONF-780819--P2.

[296] R. D. Ackley. Removal of Radon-220 from HTGR fuel reprocessing and refabrication off-gas streams by adsorption (based on a literature survey). *Oak Ridge National Lab., Tenn. (USA)*, April, 1975. https://www.osti.gov/biblio/4212719.

[297] Radon Removal From Gaseous Xenon For The Enriched Xenon Observatory. Beauchamp, e. Master's thesis, Laurentian University of Sudbury, 2014.

[298] G Drexlin, F Harms, A Jansen, et al. Calculations and tpmc simulations of the reduction of radioactive decays of a noble gas by cryo-panels. *Vacuum*, 138:165--172, 2017.

[299] L. Zikovsky. Temperature dependence of adsorption coefficients of 222rn on activated charcoal determined by adsorption-desorption method. *Health Physics*, 80(2), 2001.

[300] P. Paewpanchon and S. Chanyotha. Development of the charcoal adsorption technique for determination of radon content in natural gas. *Radiation Protection Dosimetry*, 177(1-2):40--44, Sep 2017.

[301] R Noel, Jose Busto, and Vanessa Fierro. Measurements and understanding of radon adsorption in nanoporous materials. March 2015.

[302] Bin Long, Jun-Li Li, Qun-Shu Wang, et al. Dynamic adsorption of xe on a fixed-bed adsorber at 77 k. *Nuclear Science and Techniques*, 28(8):118, 2017.

[303] A. Kuper, H. Letaw, L. Slifkin, E. Sonder, and C. T. Tomizuka. Self-diffusion in copper. *Phys. Rev.*, 96:1224--1225, Dec 1954.

[304] Svante Arrhenius. *Über die Dissociationswärme und den Einfluss der Temperatur auf den Dissociationsgrad der Elektrolyte*. Wilhelm Engelmann, Leipzig, 1889.

[305] S. Pauly. Permeability and diffusion data. *The Wiley Database of Polymer Properties*, 2003.

[306] R. Eichler and M. Schdel. Adsorption of radon on metal surfaces: a model study for chemical investigations of elements 112 and 114. *The Journal of Physical Chemistry B*, 106(21):5413--5420, 2002.

[307] Pylon electronics website. `https://pylonelectronics-radon.com/radioactive-sources/`. Rn-1025.

[308] Earl O. Knutson. Radon and Its Decay Products in Indoor Air: Modeling indoor concentrations of radon's decay products. pages 161--202, 1988.

[309] Pfeiffer vacuum: Introduction to vacuum technology. `https://www.pfeiffer-vacuum.com/en/know-how/introduction-to-vacuum-technology/fundamentals/mean-free-path/`. Pfeiffer Vacuum Inc., Accessed: Jan 9, 2019.

[310] Manjeera Mantina, Adam C. Chamberlin, Rosendo Valero, Christopher J. Cramer, and Donald G. Truhlar. Consistent van der waals radii for the whole main group. *The Journal of Physical Chemistry A*, 113(19):5806--5812, May 2009.

[311] J. Verbus. Low background 222-rn counting for the large underground xenon dark matter detector. `https://casgroups.case.edu/physics-senior-projects/files/2009/05/JamesVerbusPoster.pptx`. Poster at Case Western Reserve University.

[312] Ortec/Ametek products: Radiation detectors. `https://www.ortec-online.com/products/radiation-detectors`. AS-300, Accessed: Jan. 19, 2013.

[313] Laurence W. Nagel and D.O. Pederson. Spice (simulation program with integrated circuit emphasis). Technical Report UCB/ERL M382, EECS Department, University of California, Berkeley, Apr 1973.

[314] Ortec/Ametek models 142A/B/C preamplifiers. `https://www.ortec-online.com/products/electronics/preamplifiers/142a-b-c`. Accessed: Feb. 4, 2013.

[315] Models 142a, 142b, and 142c preamplifiers operating and service manual. `https://www.ortec-online.com/-/media/ametekortec/manuals/142abc-mnl.pdf`. Accessed: Feb. 4, 2013.

[316] Ortec/Ametek 575a amplifier. `https://www.ortec-online.com/products/electronics/amplifiers/575a`. Accessed: Feb. 4, 2013.

[317] Model 575a amplifier operating and service manual. `https://www.ortec-online.com/-/media/ametekortec/manuals/575a-mnl.pdf`. Accessed: Feb. 4, 2013.

[318] MAESTRO multichannel analyzer emulation software. https://www.ortec-online.com/products/application-software/maestro-mca. Accessed: June, 2015.

[319] MAESTRO-32 manual. https://www.ortec-online.com/-/media/ametekortec/manuals/a65-mnl.pdf. Accessed: June, 2015.

[320] National center for biotechnology information. pubchem compound database; cid=61773. https://pubchem.ncbi.nlm.nih.gov/compound/61773. Radon RN-222, accessed Jan. 22, 2019.

[321] National center for biotechnology information. pubchem compound database; cid=23987. https://pubchem.ncbi.nlm.nih.gov/compound/23987. Helium, accessed Jan. 22, 2019.

[322] National center for biotechnology information. pubchem compound database; cid=6328554. https://pubchem.ncbi.nlm.nih.gov/compound/6328554. Po-218, accessed Jan. 22, 2019.

[323] J. Porstendorfer and T. T. Mercer. Influence of electric charge and humidity upon the diffusion coefficient of radon decay products. *Health Physics*, 37(2):191--199, 1979.

[324] S. K. Dua, P. Kotrappa, and P. C. Gupta. Influence of relative humidity on the charged fraction of decay products of radon and thoron. *Health Physics*, 45(1):152--157, 1983.

[325] Scott D. Goldstein and Philip K. Hopke. Environmental neutralization of polonium-218. *Environmental Science & Technology*, 19(2):146--150, Feb 1985.

[326] Kai Dee Chu and Philip K. Hopke. Neutralization kinetics for polonium-218. *Environmental Science & Technology*, 22(6):711--717, Jun 1988.

[327] D. Seymour. 2016. "(Untitled) LUX Internal Note".

[328] D. Seymour. Monte Carlo Simulations of Polonium Drift from Radon Progeny in an Electrostatic Counter. https://www.brown.edu/academics/physics/sites/physics/files/images/Seymour-2017.pdf, 2017.

[329] X. C. Quintana. Radon measurement for neutrinoless double beta decay. Master's thesis, University of New Mexico, 2018.

[330] Comsol Multi-Physics website. https://www.comsol.com/comsol-multiphysics. Accessed: Jan. 19, 2019.

[331] Motukuru S Naidu. *High voltage engineering*. Tata McGraw-Hill Education, 2013.

[332] J.S. Townsend. *Electricity in Gases*. Oxford, Clarendon Press, 1915.

[333] F. Paschen. *Wied. Ann., 37, p. 69*. 1889.

[334] RS Nema, SV Kulkarni, and E Husain. On calculation of breakdown voltages of mixtures of electron attaching gases. *IEEE Transactions on Electrical Insulation*, (5):434--440, 1982.

[335] P. C. Johnson and A. B. Parker. The dielectric breakdown of low density gases. In *Proceedings of the Royal Society of London. Series A, Mathematical and Physical Sciences. pp 529-541*, volume 325 Issue 1563. Royal Society, Dec. 7, 1971.

[336] David B. Go. Gaseous ionization and ion transport: An introduction to gas discharges. February 13, 2012. Accessed: Feb. 7, 2019.

[337] E.M. Bazelyan and Yu. P. Raizer. *Spark Discharge*. CRC Press, Boca Raton, 1998.

[338] Y. Chen. Electrical breakdown of gases in subatomic pressure. Master's thesis, Auburn University, 2016.

[339] W J. Carey, A J. Wiebe, R D. Nord, and L L. Altgilbers. Characterization of paschen curve anomolies at high p*d values. pages 741--744, 06 2011.

[340] Kapton polyimide film. http://www.dupont.com/products-and-services/membranes-films/polyimide-films/brands/kapton-polyimide-film.html/. Accessed: Feb. 7, 2019.

[341] http://catalog.wshampshire.com/Asset/psg_teflon_ptfe.pdf. Accessed: April 9, 2019.

[342] Adolf Fick. Ueber diffusion. *Annalen der Physik*, 170(1):59--86, 1855.

[343] Durridge RAD7 manual. http://durridge.com/documentation/RAD7%20Manual.pdf. Accessed: Sept. 19, 2015.

[344] Milton Abramowitz and Irene A. Stegun, editors. *Handbook of Mathematical Functions with Formulas, Graphs, and Mathematical Tables*. Dover, New York, 1964.

[345] B. Soulé, SuperNEMO Collaboration, et al. Radon emanation chamber: High sensitivity measurements for the supernemo experiment. In *AIP Conference Proceedings*, volume 1549, pages 98--101. American Institute of Physics, 2013.

[346] R Strauss, G Angloher, A Bento, et al. Beta/gamma and alpha backgrounds in cresst-ii phase 2. *Journal of Cosmology and Astroparticle Physics*, 2015(06):030, 2015.

[347] R. Strauss, G. Angloher, A. Bento, et al. A detector module with highly efficient surface-alpha event rejection operated in cresst-ii phase 2. *The European Physical Journal C*, 75(8), Jul 2015.

[348] R Strauss, G Angloher, A Bento, et al. The cresst-iii low-mass wimp detector. In *Journal of Physics: Conference Series*, volume 718, page 042048. IOP Publishing, 2016.

[349] R. Budnik, E. Aprile, B. Choi, et al. The XENON1T Demonstrator. In *APS April Meeting Abstracts*, page 9003, March 2012.

[350] Kaixuan Ni. Status and results of the XENON1T dark matter search. http://nigroup.ucsd.edu/wp-content/uploads/sites/22/2018/07/XENON1T-NDM2018.pdf, 2018. NDM, IBS.

[351] A. Wright for the DArkSIDE Collaboration. The DArkSIDE Program at LNGS. In *Proceedings of the DPF-2011 Conference*, Providence, RI, 2011.

[352] P.-A. Amaudruz, M. Batygov, B. Beltran, et al. Radon backgrounds in the deap-1 liquid-argon-based dark matter detector. *Astroparticle Physics*, 62:178 -- 194, 2015.

[353] C. A. Klein. Bandgap Dependence and Related Features of Radiation Ionization Energies in Semiconductors. *Journal of Applied Physics*, 39:2029--2038, March 1968.

[354] Gmx series coaxial HPGe detector. https://www.ortec-online.com/-/media/ametekortec/brochures/gamma-x.pdf. Accessed: May, 2019.

[355] Perkin Elmer. The 30-minute guide to icp-ms. *Perkin Elmer, Shelton CT*, pages 1--8, 2001.

[356] Steve Wilbur. A comparison of the relative cost and productivity of traditional metals analysis techniques versus icpms in high throughput commercial laboratories. *Agilent Technologies Application Note*, 2005.

[357] Yue Meng on behalf of University of Alabama LZ group. Low background counting techniques at the university of alabama. https://meetings.undergroundphysics.org/indico/getFile.py/access?contribId=66&sessionId=16&resId=0&materialId=slides&confId=1, May 15 2017. CoSSURF 2017, Low-Background Workshop.

[358] John L. Orrell et al. Assay methods for^{238}U,^{232}Th, and^{210}Pb in lead and calibration of^{210}Bi bremsstrahlung emission from lead. *J. Radioanal. Nucl. Chem.*, 309(3):1271--1281, 2016.

[359] W.K. Warburton and B. Dwyer-McNally. Electronic background rejection in a new ultra-low background alpha-particle counter. *Nuclear Instruments and Methods in Physics Research Section B: Beam Interactions with Materials and Atoms*, 263(1):221 -- 224, 2007. Industrial Radiation and Radioisotope Measurement Applications - Proceedings of the 6th Topical Meeting on Industrial Radiation and Radioisotope Measurement Applications, 6th Topical Meeting on Industrial Radiation and Radioisotope Measurement Applications.

[360] M. Z. Nakib, J. Cooley, V. E. Guiseppe, et al. Screening materials with the XIA UltraLo alpha particle counter at Southern Methodist University. In L. Miramonti and L. Pandola, editors, *Topical Workshop on Low Radioactivity Techniques: LRT 2013*, volume 1549 of *American Institute of Physics Conference Series*, pages 78--81, August 2013.

[361] B. D. McNally, S. Coleman, W. K. Warburton, et al. Sources of variability in alpha emissivity measurements at LA and ULA levels, a multicenter study. *Nuclear Instruments and Methods in Physics Research A*, 750:96--102, June 2014.

[362] Brendan D. McNally, Stuart Coleman, Jack T. Harris, and William K. Warburton. Improving the limits of detection of low background alpha emission measurements. *AIP Conference Proceedings*, 1921(1):030001, 2018.

[363] W.K. Warburton Brendan D. McNally, S. Coleman. Recent developments in low background alpha particle counting. https://meetings.undergroundphysics.org/indico/getFile.py/access?contribId=60&sessionId=16&resId=1&materialId=slides&confId=1, May 15 2017. CoSSURF 2017, Low-Background Workshop.

[364] JL Erchinger, John L Orrell, Craig E Aalseth, et al. Background characterization of an ultra-low background liquid scintillation counter. *Applied Radiation and Isotopes*, 126:168--170, 2017.

[365] R. W. Schnee. The BetaCage, an Ultra-sensitive Screener for Surface Contamination. Invited talk at the Topical Workshop on Low Radioactivity Techniques: LRT 2015, 2015. https://www.npl.washington.edu/indico/contributionDisplay.py?contribId=48&confId=5.

[366] T. Shutt, C. E. Dahl, L. de Viveiros, R. J. Gaitskell, and R. W. Schnee. Beta Cage: A New, Large-Area Multi-Wire Screening Detector For Surface Beta Contamination. In *Topical Workshop on Low Radioactivity Techniques: LRT 2004*, volume 785, pages 79--83, Melville, NY, September 2005. American Institute of Physics Conference Proceedings.

[367] R. W. Schnee, Z. Ahmed, S. R. Golwala, D. R. Grant, and K. Poinar. Screening Surface Contamination with BetaCage. In *Topical Workshop on Low Radioactivity Techniques: LRT 2006*, volume 897, pages 20--25, Melville, NY, October 2007. American Institute of Physics Conference Proceedings.

[368] Z. Ahmed, S. R. Golwala, D. R. Grant, et al. Status of BetaCage: an Ultra-sensitive Screener for Surface Contamination. In R. Ford, editor, *Topical Workshop on Low Radioactivity*

Techniques: LRT 2010, volume 1338 of *American Institute of Physics Conference Series*, pages 88--92, April 2011.

[369] R. H. Nelson, Z. Ahmed, S. R. Golwala, et al. The Prototype BetaCage: A prototype time-projection chamber material screener for radioisotope surface contamination. In L. Miramonti and L. Pandola, editors, *Topical Workshop on Low Radioactivity Techniques: LRT 2013*, volume 1549 of *American Institute of Physics Conference Series*, August 2013.

[370] R. Bunker, M. A. Bowles, M. Kos, et al. The BetaCage, an Ultra-sensitive Screener for Surface Contamination. In L. Miramonti and L. Pandola, editors, *Topical Workshop on Low Radioactivity Techniques: LRT 2013*, volume 1549 of *American Institute of Physics Conference Series*, pages 132--135, August 2013.

[371] Boqian Wang. *Alpha Background Study in Dark Matter Detection.* PhD thesis, Syracuse University, 2014.

[372] D-M Mei, C Zhang, K Thomas, and F Gray. Early results on radioactive background characterization for sanford laboratory and dusel experiments. *Astroparticle Physics*, 34(1):33--39, 2010.

[373] VA Kudryavtsev. Muon simulation codes MUSIC and MUSUN for underground physics. *Computer Physics Communications*, 180(3):339--346, 2009.

[374] N Abgrall, E Aguayo, FT Avignone III, et al. Muon flux measurements at the davis campus of the sanford underground research facility with the majorana demonstrator veto system. *Astroparticle Physics*, 93:70--75, 2017.

[375] Z. Ahmed, M. A. Bowles, R. Bunker, et al. A prototype low-background multiwire proportional chamber. *Journal of Instrumentation*, 9:1009P, January 2014.

[376] Fabio Sauli. Principles of operation of multiwire proportional and drift chambers. page 92, Geneva, 1977. CERN.

[377] W. Blum and L. Rolandi. *Particle Detection with Drift Chambers.* Springer-Verlag, Berlin, 1993.

[378] Serge Duarte Pinto and Jens Spanggaard. Gas Electron Multipliers versus Multiwire Proportional Chambers. In *Proceedings, 2nd International Beam Instrumentation Conference (IBIC2013): Oxford, United Kingdom, September 16-19, 2013*, page TUCL3, 2013.

[379] P. Vojtyla. Fast computer simulations of background of low-level ge γ-spectrometers induced by 210pb210bi in shielding lead. *NIM B: Beam Interactions with Materials and Atoms*, 117(1-2):189--198, 1996.

[380] Maria Tsagri. High Precision Gaseous Pixel Detectors. `https://www.nikhef.nl/~stanb/download/Tsagri_Thesis.pdf`, 2018.

[381] R. P. Beukens. *Annual Report, IsoTrace Laboratory, Canadian Centre for Accelerator Mass Spectroscopy at the University of Toronto.* University of Toronto, Toronto, 1992.

[382] G. Bonvicini, N. Harris, and V. Paolone. ‘‘the chemical history of ^{14}c in deep oilfields,’. *arXiv preprint hep-ex/0308025*, 2003.

[383] S. Burgos, J. Forbes, C. Ghag, et al. Track reconstruction and performance of DRIFT

directional dark matter detectors using alpha particles. *Nuclear Instruments and Methods in Physics Research A*, 584:114--128, January 2008.

[384] J. B. R. Battat, E. Daw, A. Dorofeev, et al. Reducing DRIFT backgrounds with a submicron aluminized-mylar cathode. *Nuclear Instruments and Methods in Physics Research A*, 794:33--46, September 2015.

[385] R. Bunker, Z. Ahmed, M. A. Bowles, et al. The BetaCage, an ultra-sensitive screener for surface contamination. In L. Miramonti and L. Pandola, editors, *Topical Workshop on Low Radioactivity Techniques: LRT 2013*, volume 1549 of *American Institute of Physics Conference Series*, pages 132--135, August 2013.

[386] et al. Bunker R. The betacage, an ultrasensitive screener for surface contamination. `https://meetings.undergroundphysics.org/indico/getFile.py/access?contribId=35&sessionId=20&resId=0&materialId=poster&confId=0`, May 2015. CoSSURF 2015, Poster.

[387] A. J. Da Silva. *Development of a Low Background Environment for the Cryogenic Dark Matter Search*. PhD thesis, University of British Columbia, 1996.

[388] D. Abrams, D. S. Akerib, M. S. Armel-Funkhouser, et al. Exclusion limits on the WIMP-nucleon cross section from the Cryogenic Dark Matter Search. *Phys. Rev. D*, 66:122003/1--35, December 2002.

[389] JC Loach, J Cooley, GA Cox, et al. A material assay database for the low-background physics community. In *AIP Conference Proceedings*, volume 1549, pages 8--11. AIP, 2013.

[390] E. Aprile, K. Arisaka, F. Arneodo, et al. Study of the electromagnetic background in the XENON100 experiment. *Physical Review D*, 83(8):082001, April 2011.

[391] V Alvarez, I Bandac, A Bettini, et al. Radiopurity control in the next-100 double beta decay experiment: procedures and initial measurements. *Journal of Instrumentation*, 8(01):T01002, 2013.

[392] H. Simgen and G. Zuzel. Analysis of the 222-Rn concentration in argon and a purification technique for gaseous and liquid argon. *Applied Radiation and Isotopes*, 67(5):922--925, may 2009.

[393] Blucher: High performance sorption technologies. `seewww.bluecher.com/en/technology`. Designation: GmbH 102688. Accessed: Jun. 24, 2019.

[394] TV Ramachandran. Environmental thoron (220Rn): A review. *IRANIAN JOURNAL OF RADIATION RESEARCH (IJRR)*, 2010.

[395] W.R. Leo. *Techniques for Nuclear and Particle Physics Experiments: A How-to Approach*. Springer, 1994.

[396] D. E. Alburger, G. Harbottle, and E. F. Norton. Half-life of ^{32}Si. *Earth and Planetary Science Letters*, 78:168--176, June 1986.

[397] H.J. Hofmann, G. Bonani, M. Suter, et al. A new determination of the half-life of 32si. *Nuclear Instruments and Methods in Physics Research Section B: Beam Interactions with Materials and Atoms*, 52(3):544 -- 551, 1990.

[398] R.L. Brodzinski, J.R. Finkel, and D.C. Conway. Beta-spectrum of si-32. *Journal of Inorganic and Nuclear Chemistry*, 26(5):677 -- 681, 1964.

[399] M. J. Berger, J. S. Coursey, and M. A. Zucker. ESTAR, PSTAR, and ASTAR Computer Programs for Calculating Stopping-Power and Range Tables for Electrons, Protons, and Helium Ions (version 1.21), 1999.

[400] D. O. Caldwell, B. Magnusson, M. S. Witherell, et al. Searching for the cosmion by scattering in si detectors. *Phys. Rev. Lett.*, 65:1305--1308, Sep 1990.

[401] P. Venkataramaiah, K. Gopala, A. Basavaraju, S. Suryanarayana, and Sanjeeviah H. A simple relation for the Fermi function. *Journal of Physics G: Nuclear Physics*, 11(3):359, 1985.

[402] A. Da Silva. *Development of a Low Background Environment for the Cryogenic Dark Matter Search*. PhD thesis, University of British Columbia, 1996.

[403] A. Alessandrello, C. Cattadori, G. Fiorentini, et al. Measurements on radioactivity of ancient roman lead to be used as shield in searches for rare events. *Nuclear Instruments and Methods in Physics Research Section B: Beam Interactions with Materials and Atoms*, 61(1):106 -- 117, 1991.

[404] J. M. Salvat, F.and Fernandez-Varea, E. Acosta, and J. Sempau. *Penelope - A code system for Monte Carlo simulation of electron and photon transport*. Organisation for Economic Co-Operation and Development - Nuclear Energy Agency, 2001.

[405] R. Brun and F. Carminati. *GEANT: detector description and simulation tool, long writeup W5013*. CERN Program Library. CERN, Geneva, 1993.

[406] J. Allison, K. Amako, J. Apostolakis, et al. GEANT4 developments and applications. *IEEE Transactions on Nuclear Science*, 53(1):270--278, Feb 2006.

[407] S. Agostinelli, J. Allison, K. Amako, et al. GEANT4: a simulation toolkit. *Nuclear Instruments and Methods in Physics Research A*, 506:250--303, July 2003.

[408] J. Allison, K. Amako, J. Apostolakis, et al. Recent developments in geant4. *Nuclear Instruments and Methods in Physics Research Section A: Accelerators, Spectrometers, Detectors and Associated Equipment*, 835:186 -- 225, 2016.

[409] GEANT4: A simulation toolkit. `https://geant4.web.cern.ch/`. Date accessed: June 12, 2019.

[410] Steffen Hauf, Markus Kuster, Matej Batič, et al. Radioactive decays in geant4. *IEEE Transactions on Nuclear Science*, 60(4):2966--2983, 2013.

[411] Hai-Chau Chang and Lih-Chung Wang. A simple proof of thue's theorem on circle packing. *arXiv preprint arXiv:1009.4322*, 2010.

[412] CASPER KATCP-protocol website. `casper.ssl.berkeley.edu/wiki/KATCP`. Accessed: Sept. 21, 2019.

[413] Juergen Reichenbacher. Large volume alpha beta screener for radon daughter plate-out studies at sdsmt, May 21 2015. AARM workshop at SDSMT.

[414] Juergen Reichenbacher. Radiopurity screening and radiological model for DUNE, May 15 2017. CoSSURF.

[415] ORTEC alpha spectrometers. https://www.ortec-online.com/products/radiochemistry-health-physics-research-industrial/alpha-spectroscopy/spectrometers/alpha-suite. Accessed: October, 2019.

[416] Rene Brun and Fons Rademakers. ROOTan object oriented data analysis framework. *Nuclear Instruments and Methods in Physics Research Section A: Accelerators, Spectrometers, Detectors and Associated Equipment*, 389(1-2):81--86, 1997.

[417] V. Palladino and B. Sadoulet. Application of classical theory of electrons in gases to drift proportional chambers. *Nuclear Instruments and Methods*, 128(2):323 -- 335, 1975.

[418] S.F. Biagi. Accurate three-dimensional simulation of straw chambers using slow, medium and fast gas mixtures. *Nuclear Instruments and Methods in Physics Research Section A: Accelerators, Spectrometers, Detectors and Associated Equipment*, 310(1):133 -- 136, 1991.

[419] Transverse diffusion in P10: STAR measurements. https://www.star.bnl.gov/public/tpc/hard/tpcrings/p10_measure.html. Accessed: Mar. 5, 2019.

[420] Diffusion in p10 (calculated). https://www.star.bnl.gov/public/tpc/hard/tpcrings/p10_magboltz1a.html. Accessed: Mar. 5, 2019.

Vita

Michael Bowles was born November 30, 1988 in GA. He graduated from Hiram High School in 2007, and earned a B.Sc. in physics and mathematics from Southern Polytechnic State University May 2011, and a M.Sc. at Syracuse University December 2013. Michael worked as a undergraduate tutor in the physics and math department, and as teaching assistant for the math department, and served as the SPS president for a semester. He began working under Dr. Richard Schnee in June 2011, before beginning graduate school at Syracuse University working on the SuperCDMS dark matter experiment. He moved to Rapid City to continue his Ph.D. work at the South Dakota School of Mines and Technology in June 2015. He has accepted an offer to begin work at the Johns Hopkins University Applied Physics Laboratory in January 2020.